PTB bericht Opt-89
Wissenschaftliche Veröffentlichungen
August 2020

Dissertation

Peter Micke

Quantum Logic Spectroscopy of Highly Charged Ions

ISSN 0341-6712
ISBN 978-3-95606-537-8

Physikalisch-Technische Bundesanstalt ■ Braunschweig und Berlin Nationales Metrologieinstitut

Die Serien der PTB-Berichte:

Dosimetrie	PTB-Dos
Elektrizität	PTB-E
Elektronische Entwicklung	PTB-EW
Fertigungsmesstechnik	PTB-F
Informationstechnik	PTB-IT
Mechanik und Akustik	PTB-MA
Medizinische Messtechnik	PTB-MM
Neutronenphysik	PTB-N
Optik	PTB-Opt
Physikalische Grundlagen	PTB-PG
Radioaktivität	PTB-Ra
Thermodynamik	PTB-Th
Explosionsschutz	PTB-Ex
Chemische Physik	PTB-CP

Eingestellte Serien:

Akustik	(bis 1985)	PTB-Ak
Forschungs- und Meßreaktor Braunschweig	(bis 1988)	PTB-FMRB
Institut Berlin	(bis 1985)	PTB-IB
Mechanik	(bis 1985)	PTB-Me
Neutronendosimetrie	(bis 1988)	PTB-ND
Sicherstellung und Endlagerung radioaktiver Abfälle	(bis 1989)	PTB-SE
Wärme	(bis 3/97)	PTB-W
Literaturzusammenstellungen und Veröffentlichungshinweise	(bis 2001)	PTB-L
Akkreditierung, Qualitätsmanagement, Zertifizierung	(bis 2003)	PTB-AQZ
Atomphysik	(bis 2003)	PTB-APh
Internationale Organisation für Gesetzliches Messwesen	(bis 2003)	PTB-OIML
Thermodynamik und Explosionsschutz	(bis 2003)	PTB-ThEx
Technisch-Wissenschaftliche Dienste	(bis 2003)	PTB-TWD

Physikalisch-Technische Bundesanstalt

Optik
PTB-Opt-89
Braunschweig, August 2020

Peter Micke

Quantum Logic Spectroscopy of Highly Charged Ions

ISSN 0341-6712
ISBN 978-3-95606-537-8

Herausgeber:
Physikalisch-Technische Bundesanstalt
ISNI: 0000 0001 2186 1887

Presse und Öffentlichkeitsarbeit

Bundesallee 100
38116 Braunschweig

Telefon: (05 31) 592-93 21
Telefax: (05 31) 592-92 92
www.ptb.de

Quantum Logic Spectroscopy of Highly Charged Ions

Von der QUEST-Leibniz-Forschungsschule der

GOTTFRIED WILHELM LEIBNIZ UNIVERSITÄT HANNOVER

zur Erlangung des akademischen Grades

Doktor der Naturwissenschaften
Dr. rer. nat.

genehmigte Dissertation von

PETER MICKE, M. Sc.

geboren am 15. Juni 1988 in Kassel

Braunschweig, 2020

Quantum Logic Spectroscopy of Highly Charged Ions

PETER MICKE

Referent:	Prof. Dr. Piet O. Schmidt Gottfried Wilhelm Leibniz Universität Hannover und Physikalisch-Technische Bundesanstalt, Braunschweig
Korreferent:	Prof. Dr. Christian Ospelkaus Gottfried Wilhelm Leibniz Universität Hannover und Physikalisch-Technische Bundesanstalt, Braunschweig
Korreferent:	Priv.-Doz. Dr. José R. Crespo López-Urrutia Ruprecht-Karls-Universität Heidelberg und Max-Planck-Institut für Kernphysik, Heidelberg
Tag der Disputation:	17. April 2020

Zusammenfassung

Struktur und Eigenschaften aller Materie werden durch fundamentale Wechselwirkungen und Symmetrien bestimmt. Dies gilt insbesondere für die kleinen Bausteine der sichtbaren Materie – die Atome. Aus diesem Grund ist die Untersuchung atomarer Spektren ein wesentliches Mittel, um unser Verständnis der Natur zu verbessern. Hochgeladene Ionen bilden den größten Teil aller atomarer Systeme, da jedes einzelne Element so viele Ladungszustände wie Elektronen besitzt und sie sind im Universum allgegenwärtig. Ihre systematische Untersuchung ist daher nicht nur integraler Bestandteil der Atomphysik, sondern von großer Bedeutung für viele weitere Bereiche, wie beispielsweise die Astrophysik, Kernphysik und Fusionsforschung. Vor Kurzem wurden optische Übergänge in hochgeladenen Ionen für empfindliche Tests unbekannter Physik jenseits des Standardmodells der Teilchenphysik und für neuartige optische Atomuhren vorgeschlagen. Unzureichende experimentelle Methoden haben die relative spektroskopische Genauigkeit allerdings auf nur wenig besser als 10^{-6} beschränkt und die Umsetzung solcher Vorhaben bislang verhindert.

In dieser Arbeit wird die erste kohärente Laserspektroskopie von hochgeladenen Ionen vorgestellt. Die Präzision konnte damit um etwa acht Größenordnungen, verglichen mit bisher üblichen spektroskopischen Methoden, gesteigert werden. Der optische $^2P_{1/2}$ – $^2P_{3/2}$ Feinstrukturübergang im hochgeladenen $^{40}\mathrm{Ar}^{13+}$-Ion wurde dazu exemplarisch untersucht. Ein einzelnes Ion dieser Spezies wurde aus einem heißen Plasma isoliert und zusammen mit einem lasergekühlten, einfach geladenen $^9\mathrm{Be}^+$-Ion als Zwei-Ionen-Kristall im harmonischen Potential einer kryogenen Paul-Falle gespeichert. Anschließend wurde dieses gekoppelte quantenmechanische System in den Bewegungsgrundzustand gekühlt – dem kältesten jemals erreichten Zustand eines hochgeladenen Ions. Durch den Einsatz der Quantenlogik konnte der elektronische Zustand des $^{40}\mathrm{Ar}^{13+}$-Ions präpariert und nach durchgeführter Spektroskopie auf das $^9\mathrm{Be}^+$-Logik-Ion übertragen und detektiert werden. Zusätzlich wurden die Lebensdauer und der g-Faktor des angeregten Zustandes gemessen – letzterer mit bislang unerreichter Genauigkeit, die die Auflösung von Effekten der speziellen Relativitätstheorie, elektronischer Wechselwirkungen und der Quantenelektrodynamik ermöglicht sowie eine Diskrepanz aus unterschiedlichen theoretischen Vorhersagen aufklärt.

Die demonstrierten Konzepte sind für hochgeladene Ionen universell einsetzbar. Damit erschließt diese Arbeit das Potential hochgeladener Ionen für vielfältige Tests fundamentaler Physik, für die Suche nach unbekannter Physik – wie etwa einer fünften Kraft, einer Variation von Fundamentalkonstanten und Dunkler Materie – sowie für den Einsatz in zukünftigen optischen Atomuhren.

Schlagworte: Hochgeladene Ionen, Spektroskopie, Quantenlogik, Frequenzmetrologie, Atomuhr, Atomphysik, fundamentale Physik

Abstract

Fundamental interactions and symmetries define the structure and properties of all matter, in particular of its small and diverse visible constituents—the atoms. The study of their distinctive spectra through precision spectroscopy is therefore a vital tool to advance our understanding of nature. Highly charged ions (HCIs) constitute the largest fraction of all atoms since every atom has as many charge states as electrons it can bind. Although most of the matter on Earth is neutral, HCIs are ubiquitous in the universe and their systematic study is essential not only for atomic physics but eminently for astrophysics, nuclear physics, and fusion research, among others. Recently, HCIs have been identified as ideal candidates for sensitive tests of physics beyond the Standard Model of particle physics and for use in future high-accuracy optical atomic clocks. However, the realization of such proposals has been hindered by the hitherto constrained laboratory control and limited spectroscopic accuracy of about parts-per-million fractional uncertainty levels.

This thesis reports the first coherent laser spectroscopy of HCIs, boosting the achievable spectroscopic precision by eight orders of magnitude compared to traditional spectroscopy methods. The $^2\mathrm{P}_{1/2}$–$^2\mathrm{P}_{3/2}$ fine-structure ground-state transition in highly charged $^{40}\mathrm{Ar}^{13+}$ at an optical wavelength of 441 nm was chosen as a proof-of-principle case. A single ion of this species was isolated from a megakelvin-hot plasma cloud and co-trapped together with a laser-cooled singly charged $^9\mathrm{Be}^+$ ion in a two-ion crystal, confined in the harmonic potential of a cryogenic linear Paul trap. This coupled quantum-mechanical system was then cooled to its ground state of axial motion, corresponding to the lowest temperature of a HCI ever achieved. The spectroscopy was realized by implementing quantum logic techniques which allow preparation of the quantum state of the HCI and to map its electronic state after spectroscopy onto the $^9\mathrm{Be}^+$ logic ion in order to detect it there with high efficiency through electron shelving. In addition to the increase of spectroscopic precision, the excited-state lifetime and g-factor were measured—the latter one to unprecedented accuracy, resolving effects from special relativity, interelectronic interactions, and quantum electrodynamics. Moreover, it settled a discrepancy between theoretical predictions.

The demonstrated techniques are not limited to the specific $^{40}\mathrm{Ar}^{13+}$ species but universally applicable to other HCIs. Thereby, this work unlocks the potential of HCIs for unrivaled tests of fundamental physics, the search for new physics—such as a 5th force, variations of fundamental constants and dark matter candidates—as well as the use of HCIs in novel optical atomic clocks.

Keywords: highly charged ion, spectroscopy, quantum logic, frequency metrology, atomic clock, atomic physics, fundamental physics

Contents

I Introduction

1 Highly charged ions 3
1.1 General scaling of the atomic structure 5
1.2 Laboratory studies and optical spectroscopy 7
2 Frequency metrology 11
2.1 Uncertainties and related technical terms 12
2.2 Microwave atomic clocks 13
2.3 Optical atomic clocks 15
3 Probing fundamental physics 27
3.1 Atomic structure and quantum electrodynamics 28
3.2 Variation of fundamental constants and dark matter 33
3.3 Lorentz violation 39
4 Thesis outline 41

II Background

5 The atomic systems 45
5.1 Spectroscopy ion $^{40}\mathrm{Ar}^{13+}$ 46
5.2 Logic ion $^{9}\mathrm{Be}^{+}$ 49
6 Ion traps 55
6.1 Electron beam ion trap 55
6.2 Paul trap 57
7 Atom-light interaction 65
7.1 Electronic transitions 65
7.2 Coherent excitation and manipulation 72
7.3 Laser cooling 79

III Experiment

8 Overview 85
9 Production of highly charged ions 87
10 Transfer of highly charged ions 91
10.1 Ion optical setup 91
10.2 Extraction 96
10.3 Charge-state separation and selection 98
10.4 Ion bunch characterization and deceleration 100
10.5 Recapture 102
11 Storage and preparation of cold highly charged ions 105
11.1 Stable, cryogenic environment 105
11.2 Paul trap, trap drive, and quantization field 110
11.3 Laser beams 111
11.4 Be^{+} loading, imaging, and state detection 115

11.5 Two-ion crystal preparation 117
12 Clock laser and frequency measurement 125
13 Quantum logic 129
13.1 Quantum logic-assisted state preparation 130
13.2 Quantum logic spectroscopy 131

IV Results and discussion

14 Rabi spectroscopy 137
14.1 Frequency scans 137
14.2 Rabi oscillations 141
15 Zeeman structure 143
15.1 Linear energy splitting and *g*-factors 146
15.2 Quadratic contribution to the energy splitting 150
16 Excited-state lifetime 155

V Conclusion

17 Summary 163
18 Outlook 167
18.1 Absolute transition frequency of Ar^{13+} 167
18.2 Isotope shift spectroscopy and King-plot nonlinearity . . . 168
18.3 An optical clock based on a highly charged ion 173

VI Appendix

P1 The Heidelberg compact electron beam ion traps 179
P2 Closed-cycle, low-vibration 4 K cryostat for ion traps and other applications 199
P3 A cryogenic radio-frequency ion trap for quantum logic spectroscopy of highly charged ions 215
P4 Coherent laser spectroscopy of highly charged ions using quantum logic 231

Bibliography 245

List of Figures

Figure 1.1 Parameterization of atomic systems 4
Figure 1.2 Coulomb crystal with a single highly charged ion . 6
Figure 1.3 In-EBIT spectroscopy of $^{40}\mathrm{Ar}^{13+}$ 8
Figure 3.1 Composition of the universe 27
Figure 3.2 Potential variation of α as a signature of dark matter 35
Figure 5.1 Level structure of $^{40}\mathrm{Ar}^{13+}$ 48
Figure 5.2 Level structure of $^{9}\mathrm{Be}^{+}$ 50
Figure 5.3 Level structure of neutral $^{9}\mathrm{Be}$ 52
Figure 6.1 Electrode configuration of the linear Paul trap . . . 58
Figure 7.1 Geometrical relations between quantization axis, wave vector, and polarization 69
Figure 7.2 Coupled system of qubit and quantum harmonic oscillator 75
Figure 7.3 Geometrical relations for the Raman beams 79
Figure 7.4 Pulsed resolved sideband cooling 81
Figure 8.1 Overview of the experimental setup 86
Figure 9.1 Longitudinal section of PTB-EBIT 88
Figure 10.1 90°-deflector unit 92
Figure 10.2 Deceleration unit 94
Figure 10.3 Ion detector with retarding-field analyzer 95
Figure 10.4 Highly charged ion transfer 97
Figure 10.5 Time-of-flight spectrum 99
Figure 10.6 $^{40}\mathrm{Ar}^{13+}$ ion bunch 100
Figure 10.7 Switching time of the pulsed drift tubes 101
Figure 10.8 Energy spread affected by the differential pulsed drift tube voltage 102
Figure 10.9 $^{40}\mathrm{Ar}^{13+}$ recapture 104
Figure 11.1 Cutaway view of the cryostat 107
Figure 11.2 Ar^{13+} lifetimes 109
Figure 11.3 Schematic circuit diagram of the elevated ground . 110
Figure 11.4 Laser beam geometry at the Paul trap 112
Figure 11.5 Two-ion crystal preparation 116
Figure 11.6 Axial ground-state cooling sequence 120
Figure 11.7 Axial ground-state cooling of the two-ion crystal . . 121
Figure 11.8 Heating rates of the axial modes 123
Figure 12.1 Simplified scheme for the stabilization and absolute frequency measurement of the clock laser 128
Figure 13.1 Quantum representation of the two-ion system . . . 130
Figure 13.2 Quantum logic-assisted electronic state preparation 131
Figure 13.3 Quantum logic spectroscopy sequence 132
Figure 14.1 Frequency scans across Zeeman component 1 . . . 138

Figure 14.2 Frequency scan with 50 ms probe time 139
Figure 14.3 Rabi oscillations between the clock states 140
Figure 15.1 Zeeman structure of the $^{40}\mathrm{Ar}^{13+}$ clock transition . . 144
Figure 15.2 Excited-state g-factor 148
Figure 16.1 Excited-state lifetime 156
Figure 17.1 Fractional frequency uncertainty of the $^2\mathrm{P}_{1/2}$–$^2\mathrm{P}_{3/2}$ Ar^{13+} fine-structure transition 164
Figure 18.1 Illustration of a King plot 170
Figure 18.2 Level structure of Ca^{14+} and Ca^{15+} 171
Figure 18.3 Ground-state fine structure in middle-Z highly charged ions 174
Figure 18.4 Level structure of sulfur-like Ni^{12+} 175

List of Tables

Table 1.1 Scaling of the atomic structure 5
Table 2.1 Atomic clock transitions and sensitivity to a variation of the fine-structure constant 15
Table 2.2 Scaling of frequency shifts in a hydrogen-like atom 23
Table 5.1 Ionization energies of highly charged argon 46
Table 5.2 Hyperfine constants of $^9\mathrm{Be}^+$ 51
Table 7.1 Geometrical coupling between a light field and E1 transitions 68
Table 7.2 Geometrical coupling between a light field and M1 transitions 72
Table 10.1 Ion optical elements of the ion transfer beamline . . 92
Table 11.1 Continuous wave laser beams at the Paul trap . . . 115
Table 11.2 Secular frequencies 119
Table 15.1 Measurements of the $^{40}\mathrm{Ar}^{13+}$ excited-state g-factor 147
Table 15.2 Theoretical predictions of the $^{40}\mathrm{Ar}^{13+}$ g-factors . . 149
Table 15.3 Second-order Zeeman shifts 152
Table 15.4 Electric-quadrupole shifts 153
Table 16.1 Excited-state decay parameters 157

Acronyms

ac	alternating-current
AOM	acousto-optic modulator
ASD	NIST Atomic Spectra Database
BBO	beta barium borate
BBR	black-body radiation
BSB	blue sideband
CAR	carrier
CERN	Conseil Européen pour la Recherche Nucléaire (European Organization for Nuclear Research)
CODATA	Committee on Data for Science and Technology
CPT	charge conjugation, parity transformation, and time reversal
CryPTEx	Cryogenic Paul Trap Experiment at the MPIK
cw	continuous wave
dc	direct-current
DESY	Deutsches Elektronen-Synchrotron (German Electron Synchrotron)
E1	electric-dipole
E2	electric-quadrupole
E3	electric-octupole
EBIT	electron beam ion trap
EMCCD	electron multiplying charge-coupled device
FAIR	Facility for Antiproton and Ion Research
FWHM	full width at half maximum
GSI	GSI Helmholtz Centre for Heavy Ion Research
GTR	general theory of relativity
HC-EBIT	Heidelberg compact EBIT

HCI	highly charged ion
HV	high-voltage
IP	in-phase
LLI	local Lorentz invariance
LPI	local position invariance
M1	magnetic-dipole
M2	magnetic-quadrupole
M3	magnetic-octupole
MCP	microchannel plate
MPIK	Max-Planck-Institut für Kernphysik
NEG	non-evaporable getter
NIST	National Institute of Standards and Technology
NPL	National Physical Laboratory
OP	out-of-phase
PDT	pulsed drift tube
PMT	photomultiplier tube
PPKTP	periodically-poled potassium titanyl phosphate
ppm	parts-per-million
PTB	Physikalisch-Technische Bundesanstalt
QCD	quantum chromodynamics
QED	quantum electrodynamics
QHO	quantum harmonic oscillator
QL	quantum logic
QLS	quantum logic spectroscopy
QPN	quantum projection noise
rf	radio-frequency
RIKEN	Institute of Physical and Chemical Research
rms	root-mean-square
RSB	red sideband

SHG	second harmonic generation
SI	Système international d'unités (International System of Units)
Si2	PTB's second silicon cavity
SM	Standard Model of particle physics
SNR	signal-to-noise ratio
TMP	turbomolecular pump
ToF	time-of-fight
UHV	ultra high vacuum
XHV	extreme high vacuum
XUV	extreme ultraviolet

Math symbols

α	fine-structure constant or angle between the ion's motion and the laser beam
β	angle between the quantization axis (z') and the Paul trap axis of dc confinement (z) or modulation index
$\delta\nu$	natural linewidth in frequency units
$\Delta\omega$	detuning in angular frequency units
Δf^{FWHM}	full width at half maximum in frequency units
$\hat{\varepsilon}$	unit vector of the polarization of the electric field
ε_0	vacuum permittivity
η	Lamb–Dicke parameter
Θ	electric-quadrupole moment
θ	polar angle
$\varkappa$	geometrical factor of a linear Paul trap
λ	wavelength in vacuum
λ_{air}	wavelength in air
μ	proton-to-electron mass ratio
μ_{B}	Bohr magneton

τ	averaging time, coherence time, or lifetime of either an electronic state or the highly charged ion in the trap
ω	angular frequency with $\omega = 2\pi \times f$
Ω_0	Rabi frequency
Ω_R	generalized Rabi frequency
Ω_rf	radio frequency that drives the Paul trap
ω_u	secular frequency of a motional mode along the direction of $u \in \{\tilde{x}, \tilde{y}, z\}$
A	mass number (nucleon number) of a specific isotope
a_0	Bohr radius of the hydrogen atom
a_u	Paul trap stability parameter a for the direction along u
B	magnetic flux density
b	coefficient, beat frequency, or fit parameter in Chapter 15
c	vacuum speed of light
$\hat{\vec{\mathcal{D}}}$	electric-dipole operator
$\mathcal{E}$	scalar electric field strength
e	elementary charge or excitation amplitude
$\vec{\mathcal{E}}$	electric field vector
F	total angular momentum quantum number or field-shift constant
f	frequency
g	g-factor or excitation amplitude
h	Planck constant
I	nuclear spin, laser intensity, or electron-beam current
J	total electronic angular momentum quantum number
K	sensitivity factor for a possible α variation or mass-shift constant
$\vec{k}$	wave vector
k_B	Boltzmann constant
L	orbital angular momentum quantum number
m	mass or magnetic quantum number
$\hat{\vec{\mathcal{M}}}$	magnetic-dipole operator

N	number of measurements or atoms, or frequency comb tooth number
n	principal quantum number, occupation number of the QHO mode, or particle density
P	excitation probability
p	pressure
$\widehat{p}_u$	momentum operator along the motional mode direction u
q	charge of the ion with $q = Z_\mathrm{ion} \cdot e$ or sensitivity factor for a possible α variation
$\widehat{Q}$	electric-quadrupole operator
q_u	Paul trap stability parameter q for the direction along u
r	modulus of the position vector or radius
$\vec{r}$	position vector
R_∞	Rydberg constant
r_0	characteristic geometrical distance of a linear Paul trap for the radial confinement
S	spin angular momentum quantum number, power spectrum, or signal strength
T	temperature
t	time
t_π	π-time, being the pulse length of a π-pulse
t_p	probe time
U	potential in units of an energy or an expression for the ground-state Zeeman splitting in Chapter 15
u	position coordinate, refers to a motional mode direction of the Paul trap frame $(\tilde{x}, \tilde{y}, z)$
$\widehat{u}$	position operator
$\hat{u}^*_{\Delta m}$	conjugated unit vector in the spherical basis
u_0	displacement of the ion's equilibrium position from the rf-free nodal line
u_a	amplitude of the secular motion of the mode along u; an additional index n refers to the corresponding occupation number of that mode

V	voltage
v	velocity
V_{ac}	ac amplitude voltage
V_{dc}	dc voltage
(x, y, z)	coordinates in the laboratory frame
$(\tilde{x}, \tilde{y}, z)$	coordinates in the Paul trap frame
(x', y', z')	coordinates in the atomic frame; $y' = y$ for a laser beam propagating in the xz plane
Z	proton number
z_0	characteristic geometrical distance of a linear Paul trap for the axial confinement
Z_{ion}	ion charge state

Part I

Introduction

oîda ouk eidōs
(I know, that I do not know.)

— Attributed to Socrates

The first part of this thesis intends to give an introduction into the different fields which are linked to the reported work. Chapter 1 addresses the atomic class of highly charged ions (HCIs) that are the subject of study in this experiment. In Chapter 2 a brief overview about the field of frequency metrology dealing with optical transitions in atoms and ions is given. Chapter 3 discusses some aspects of fundamental research-related atomic physics. In view of their unique properties, the potential of precision metrology with HCIs is emphasized. Finally, Chapter 4 provides an outline of this thesis.

1 Highly charged ions

The periodic table is composed of 118 known elements—all of them are either found in nature or have been synthetically produced in accelerator facilities. The idea to arrange elements in a periodic system came up in the 19th century and was mainly driven by chemistry. The relevance and meaning of this system for atomic physics became clear some decades later. However, the periodic table only represents a small fraction of all atomic systems since each atom has, besides its neutral state, $Z-1$ charge states, where Z is the proton number. For instance, up to plutonium with $Z=94$, a large number of 4465 different neutral and positively charged atomic systems is obtained, up to the hydrogen-like ones with only a single electron left in the atomic shell[1]. A corresponding parameterization is shown in Figure 1.1 which arranges the atomic systems as a function of their proton number Z and their electron number $Z-Z_{\mathrm{ion}}$, where Z_{ion} is the charge state. This also leads to the concept of *isoelectronic sequences* in which the number of electrons is constant and thereby, the electronic structure is fixed. Instead, the proton number is considered as the free parameter. Such isoelectronic sequences are represented by horizontal rows in Figure 1.1. Each element of the periodic table thus defines an isoelectronic sequence and gives the sequence a name, for instance, hydrogen-like or helium-like[2]. Atomic systems which are not neutral or singly charged are termed multiply or highly charged, although the latter term is not defined very rigorously. For simplicity, in this thesis the term highly charged ion (HCI) refers to every ion with more than one positive elementary charge. Most of the systems considered here will however have a charge state Z_{ion} on the order of 10.

Figure 1.1 also shows the number of observed optical transitions (color-coded) which were tabulated by the NIST Atomic Spectra Database (ASD) (Kramida et al., 2019)[3] in September 2018. Here, the term *optical* refers to the wavelength range of 200 to 1500 nm. Two areas are highlighted, which are dubbed by the community the ‘land of knowledge’ (blue rectangle), mostly composed of the neutral and singly charged atoms, and the ‘sea of ignorance’ with essentially all multiply and highly charged systems (red triangle) (Currell, 2003). Certainly striking, it emphasizes the general situation in HCI research:

---

[1] In fact, the number of atomic systems even further increases when considering different isotopes. Also the nucleus affects the electronic structure of the atoms and causes their spectroscopic fingerprint to be different. Furthermore, some negative ions with bound states exist as well.

[2] Apart from this naming, another nomenclature uses Roman numerals behind the elements, mostly used in spectroscopy, astrophysics, and chemistry. The Roman numeral indicates the ionization state, where ‘I’ starts with the neutral atom. For example, Ar^{13+}, boron-like Ar, and Ar XIV denote the identical atomic system.

[3] Note that the observation and measurement of some more optical transitions is published but not (yet) tabulated by the ASD.

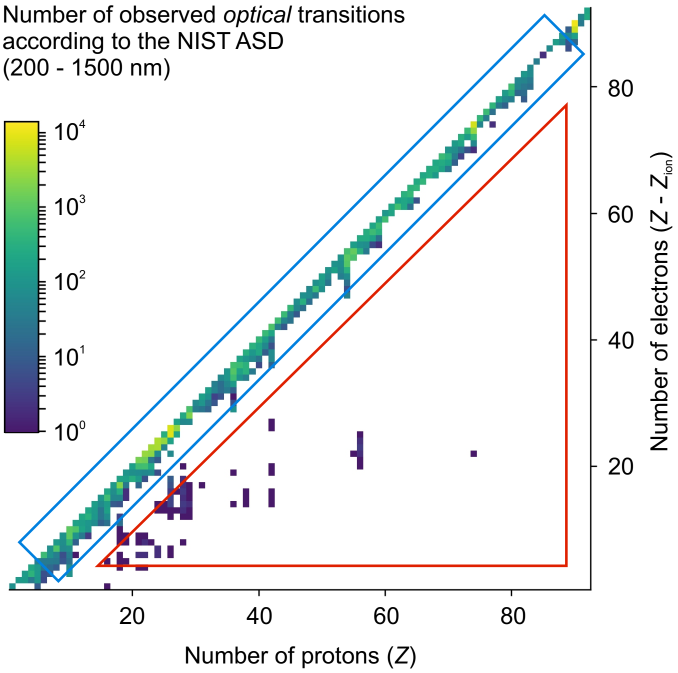

Figure 1.1: Parameterization of atomic systems with regard to their proton and electron number. As a function of both parameters, the number of observed optical transitions (color-coded) in the range from 200 to 1500 nm of the corresponding atomic system is shown as tabulated by the NIST Atomic Spectra Database (ASD) (Kramida et al., 2019). The presented data was extracted in September 2018. Note that some more data was published, but not yet tabulated. The blue rectangle highlights the 'land of knowledge', including the neutral systems on the outer diagonal, which transitions into the 'sea of ignorance' (Currell, 2003) marked by the red triangle. Adapted from a processing by S. Bernitt.

Although the number of atomic systems is significantly increased by the parameterization through the charge state, the number of observed optical transitions remains surprisingly small. Arguably, the number of available optical transitions in HCIs is also smaller than in neutral and singly charged atoms since scaling laws shift their electronic states and transitions to higher energies, out of the optical range. However, there are also other transitions which are in the microwave and radio-frequency (rf) regime for neutral and singly charged atoms and shift upwards eventually into the optical range for HCIs. Indeed, the situation is also not much different when not only optical, but all transitions throughout the entire range of the electromagnetic spectrum are considered—despite of a significant number of x-ray transitions showing up for lighter elements in higher charge states and also for some isonuclear sequences of heavier elements. This 'sea of ignorance' is also a result of the increasing demands imposed by the production and handling of HCIs which has kept the research community rather small compared to others.

Studies and in particular spectroscopy of HCIs provide the unique opportunity to systematically explore properties and scaling laws of atomic systems, including effects from special relativity, quantum electrodynamics (QED), interelectronic interactions, and the nucleus. The interaction between the electrons in the atomic shell and the nucleus can be essentially tuned as a function of the proton number, being discussed in the next Section 1.1. Furthermore, the study of HCIs by spectroscopy and spectrometry in the laboratory is vital for many fields far beyond atomic physics, such as fundamental research, cosmology, astronomy and astrophysics, plasma and fusion research, nuclear physics, and particle physics. A brief overview about state-of-the-art studies is given in Section 1.2.

1.1 General scaling of the atomic structure

Atomic properties are ruled by the electromagnetic interaction between the electrons and the nucleus. Considering a hydrogen-like system, the simple non-relativistic relation for the gross-structure binding energy of the electron in the potential of the nucleus

$$E_n \propto \frac{Z^2}{n^2} \tag{1.1}$$

features the important scaling with the proton number Z. n denotes the principal quantum number. In accordance with this relation, the field strength increases with increasing charge state Z_{ion}, where $Z_{\text{ion}} = Z - 1$ for the hydrogen-like sequence. Similarly, the field strength experienced by the outer valence electrons is in general significantly larger in all HCIs compared to neutral or singly charged atoms owing to the excess of positive elementary charges in the nucleus and the reduced screening by the inner electrons. As a consequence the valence electrons are more strongly bound to the nucleus with a smaller spatial extent of their electronic wave function. This also causes a substantially larger overlap with the finite-size nucleus. Contributions to the binding energies from special relativity, QED, and the nucleus can be enhanced by orders of magnitude. At the same time the sensitivity of the electronic states and transitions to perturbations from external electromagnetic

Effect	Scaling
Gross-structure transition ($\Delta n \neq 0$)	Z^2
Fine-structure transition	Z^4
Hyperfine-structure transition	Z^3
QED Lamb shift	Z^4
Bohr radius	Z^{-1}
Polarizability	Z^{-4}

Table 1.1: Scaling of the atomic structure of a hydrogen-like atom as a function of the proton number Z. Δn denotes the change in the principal quantum number n. Scaling laws are discussed in more detail in, e. g., Berengut et al. (2012a), H. F. Beyer, Shevelko, and Shevelko (2016), J. D. Gillaspy (2001), and Quint and Vogel (2014).

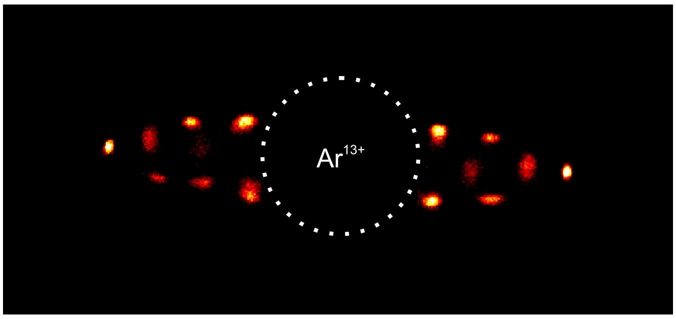

Figure 1.2: **Coulomb crystal with a single highly charged ion at the center.** Many fluorescing $^{9}Be^{+}$ ions surround a single $^{40}Ar^{13+}$, which appears as a dark void since it does not interact with the Doppler cooling laser. Due to the high charge state, it farther repels the $^{9}Be^{+}$ ions than they do among themselves. This effect makes $^{40}Ar^{13+}$ appear much larger, although the extent of its electronic wave function is much smaller than it is for $^{9}Be^{+}$.

fields, expressed by the polarizability, is substantially suppressed. The main scaling laws for hydrogen-like systems are summarized in Table 1.1 and illustrate this general trend for all HCIs. To account for the screening effect in many-electron systems, the concept of the non-integer effective nuclear charge number Z_{eff} which is experienced by the electron under consideration finds application. Alternatively, the non-integer effective principal quantum number ν in combination with the charge state Z_{ion} is occasionally used. A more detailed discussion can be found in the respective literature [see, e. g., Berengut et al. (2012a), M. G. Kozlov et al. (2018), and Quint and Vogel (2014)].

Due to these scaling laws the optical-wavelength transitions of HCIs are typically found between fine-structure and hyperfine-structure levels, and therefore they are electric-dipole-forbidden and narrow (Crespo López-Urrutia, 2008; Crespo López-Urrutia et al., 2014). Additionally, so-called level-crossings, where two electronic configurations are close in energy, provide forbidden optical transitions as well (Bekker et al., 2019; Berengut, Dzuba, and Flambaum, 2010). Such level crossings happen since the ordering of the electronic levels in the neutral-atom limit differs from the Coulomb ordering of the hydrogen-like ion. Thus, at some intermediate charge state the energies of the levels cross with an energy difference in the optical range. The involved levels can have significantly different quantum numbers (Berengut et al., 2012a). The latter fact is particularly interesting for fundamental physics studies as will be discussed later.

Another more technical aspect is related to the high positive charge of HCIs. As a result, the Coulomb interaction with their environment is enhanced and they appear larger when interacting with singly charged atoms, although they are smaller with regard to the extent of their electronic wave function. This is observed in the electrostatic equilibrium state of a mixed-species Coulomb crystal in an ion trap as shown by Figure 1.2. The distances between the fluorescing singly charged $^{9}Be^{+}$ ions are significantly smaller than the distances between the dark $^{40}Ar^{13+}$ ion and the $^{9}Be^{+}$ ions.

1.2 Laboratory studies and optical spectroscopy

Forbidden fine-structure transitions in HCIs were identified a long time ago as an explanation for coronal lines of the sun (Edlén, 1942). For laboratory studies, machines are required which are capable of producing HCIs and maintaining their high ionization state over the course of the experiment. The production necessitates an efficient mechanism to overcome the electronic binding energies, which are typically on a keV level for high charge states. Moreover, excellent vacuum conditions are needed to reduce the rate of charge exchange reactions with residual gas, and finally, a confinement mechanism is required in many cases. For these demands, electron beam ion traps (EBITs) or sources (EBIS'), electron cyclotron resonance ion sources (ECRIS'), plasma and fusion devices, Penning traps with integrated ion sources, or accelerators are typically employed and enable broad HCI studies, such as spectroscopy from the x-ray to the optical range [see, e. g., Beiersdorfer et al. (2005), Beilmann et al. (2011), Draganić et al. (2003), Epp et al. (2007), Gumberidze et al. (2005), Iwamae et al. (2007), Klaft et al. (1994), Machado et al. (2018), Shah et al. (2016), and Ullmann et al. (2017)], mass spectrometry [see, e. g., Blaum (2006) and Repp et al. (2012)], or measurements of atomic magnetic moments [see, e. g., Sturm et al. (2011) and Sturm et al. (2019)].

Optical spectroscopy involved in most cases grating spectrometers installed at EBITs and fusion devices (Bekker et al., 2018; Bieber et al., 1997; Brenner et al., 2009; Draganić et al., 2003; Iwamae et al., 2007; Morgan et al., 1995; Windberger et al., 2015). However, also in-EBIT laser spectroscopy has been demonstrated, the first successful attempt measuring a wavelength of 12 µm with a fractional uncertainty of 6×10^{-4} (Hosaka et al., 2004), later in the x-ray regime by operating an EBIT at free-electron laser (Bernitt et al., 2012; Epp et al., 2007) or synchrotron facilities (Rudolph et al., 2013; Simon et al., 2010), and finally, also in the optical range (Mäckel et al., 2011, 2013; Schnorr et al., 2013). Also collinear laser spectroscopy (Klaft et al., 1994; Seelig et al., 1998; Ullmann et al., 2017) in a storage ring was performed by tuning the ions into resonance with a fixed-frequency laser through the Doppler shift of the ion beam. Very recently and in parallel to the work of this thesis, laser spectroscopy of HCIs was demonstrated in a Penning trap at a fractional uncertainty of 9×10^{-9} (Egl et al., 2019). Before that measurement, the most accurate optical spectroscopy of HCIs was indeed done in an EBIT by observing the ion fluorescence with a grating spectrometer after electron-impact excitation. Such experiments achieved a fractional uncertainty of 2×10^{-7} (Draganić et al., 2003; Soria Orts et al., 2006). The accuracy was already high enough to reveal contributions to the transition energy from special relativity, many-body QED, and nuclear effects. Notably, these measurements were also about three orders of magnitude more accurate than corresponding state-of-the-art calculations, being on a 10^{-4} uncertainty level (Artemyev et al., 2013, 2007; Soria Orts et al., 2006).

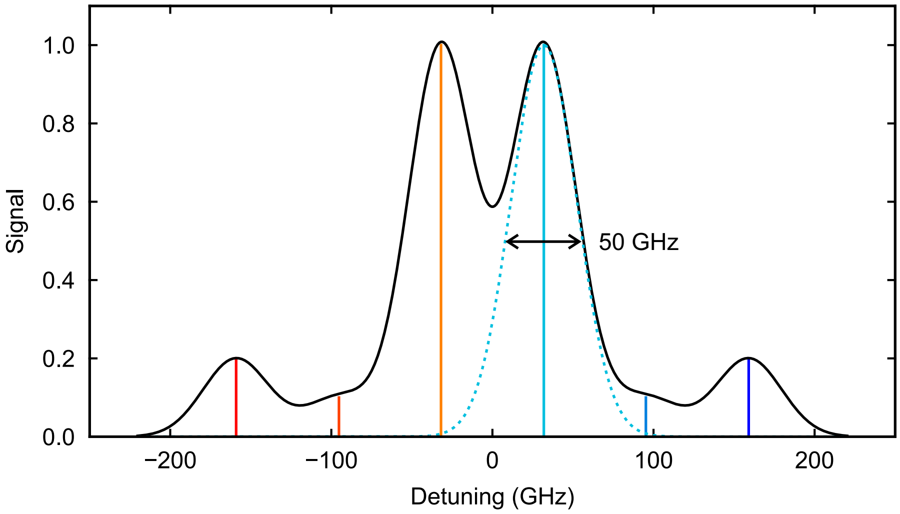

Figure 1.3: Typical in-EBIT spectroscopy of the ground-state fine-structure transition of ^{40}Ar^{13+} at 441 nm. The $^2P_{3/2}$–$^2P_{1/2}$ transition splits up into six Zeeman components (see for details Section 5.1) in the applied magnetic field of 6.82 T. Linewidths of about 50 GHz full width at half maximum (FWHM) can be achieved (Soria Orts et al., 2007).

Optical spectroscopy of HCIs in ion traps is typically limited by high ion temperatures. For instance in an EBIT, HCIs are produced and confined as a plasma, constantly heated by a mono-energetic electron beam, with a temperature on the order of a million kelvins. Spectral optical lines emitted by the thermal ion ensemble are Doppler-broadened with a full width at half maximum (FWHM) of

$$\Delta f^{\mathrm{FWHM}} = f \cdot \sqrt{8 \ln 2 \frac{k_{\mathrm{B}} T}{m c^2}}, \tag{1.2}$$

where f is the transition frequency, k_{B} the Boltzmann constant, T the temperature of the ions, m their mass, and c the vacuum speed of light. Putting numbers into this relation yields a FWHM linewidth of 50–100 GHz for an optical transition and a medium-light ion with a mass of 40 u (see Figure 1.3). Strategies to improve the resolution can be employed, such as operating the EBIT in the magnetic trapping mode by switching off the electron beam[4] (Beiersdorfer et al., 1996) and applying evaporative cooling. However, even in the best cases the FWHM linewidth remains on a level of a few ten GHz (Soria Orts et al., 2007). An additional broadening caused by an inhomogeneity of the magnetic field over the finite extent of the ion cloud was negligible here, but could become relevant when for instance Doppler-free methods are introduced or the plasma temperature can be significantly reduced. The magnetic field, employed by all plasma storage devices, is typically quite large (several teslas in superconducting EBITs, Penning traps, or stellarators). Depending on the Zeeman component of the electronic transition and its sensitivity to the magnetic field, a 100 µT field inhomogeneity (fractionally on the 10^{-5} level) over the spatial extent of the ion cloud would result in a line broadening on the order of 1 MHz.

---

[4] In the magnetic trapping mode, the radial confinement is purely given by the axial magnetic field which forces the ions to orbit the field lines.

Collinear laser spectroscopy in storage rings, in contrast, is limited by the uncertainty of the ion velocity. This quantity has to be measured accurately since it determines the Doppler shift of the ions and eventually the laser frequency which is seen by the ions. Additionally, the velocity spread of the ion bunches requires cooling. Both are accomplished by the use of an electron cooler in which the ion beam is overlapped with an electron beam of which the properties can be well controlled. In equilibrium, the measurement of the ion velocity is then realized through a measurement of the electron velocity and traced back to a high voltage measurement on the order of 100 kV (Ullmann et al., 2017). The accuracy of such a measurement is to date technically limited to the 10^{-6} uncertainty level. Among other contributions to the total uncertainty, this number defines the uncertainty level which can be realized with collinear laser spectroscopy in storage rings.

Until recently, the aforementioned reasons have limited the accuracy achieved in spectroscopy of HCIs with an uncertainty of a bit better than the parts-per-million (ppm) level. Optical spectroscopy on a metrological level, i. e., a few Hz absolute or a few 10^{-15} fractional, has been hindered by the lack of laser cooling combined with efficient state detection techniques. The atomic systems used in frequency metrology typically require a fast cycling transition for both purposes, as will be discussed in Chapter 2. Unfortunately, such an atomic structure is in general not available in HCIs. Therefore, sympathetic cooling through a second ion species which offers such a fast cycling transition for Doppler cooling was adopted (Gruber et al., 2001; Schmöger, Versolato, et al., 2015; Schmöger, 2017; Schneider, 1996; Schwarz et al., 2012) as a vital prerequisite. Combined with highly efficient state detection through quantum logic spectroscopy (QLS), this allowed for the first coherent laser spectroscopy of HCIs (Micke et al., 2020) on what this thesis will report. As mentioned above, incoherent laser spectroscopy of HCIs was demonstrated in the Penning trap *ALPHATRAP* (Egl et al., 2019) in parallel to this work as another new method in which the state detection is accomplished by a measurement of the atomic ground-state magnetic moment after excitation and spontaneous decay. Significant improvements can be expected in the future if the motional sideband structure of the transition can be resolved by a narrow-linewidth clock laser and sympathetic laser-cooling is implemented. Also the Penning trap experiment *ARTEMIS* at the *HITRAP* facility of the GSI Helmholtz Centre for Heavy Ion Research (GSI) (Kluge et al., 2008) aims at optical spectroscopy of HCIs (D. v. Lindenfels et al., 2013; Vogel et al., 2018; Vogel and Quint, 2010) by employing the laser-microwave double-resonance technique (Quint et al., 2008) with the prospect to measure simultaneously electronic and nuclear g-factors.

A leading motivation for the efforts which are made to advance the field of HCI spectroscopy is found in their inherent properties which make them promising candidates for tests of fundamental physics, as will be discussed in

Chapter 3. Laser spectroscopy at rest inside an ion trap unlocks their potential for such applications in frequency metrology. Nevertheless, a sufficient prior knowledge of the transition frequency is required since lasers are limited in their tuning range and the search for a narrow optical transition in a large frequency interval with a narrow-linewidth laser can take a long time. Therefore, techniques have to be developed and employed to bridge the uncertainty gap between theoretical predictions for the transition frequencies and spectroscopy on a metrological uncertainty level. Spectroscopy in EBITs remains an important method for this purpose, as recently demonstrated for the complex spectrum of the proposed HCI species Ir^{17+} (Berengut et al., 2011) by Windberger et al. (2015) in the optical and Bekker et al. (2015) in the extreme ultraviolet (XUV) range as well as for the first measurement of an optical level-crossing transition in a HCI, namely between the 5p and 4f orbitals (Bekker et al., 2019). Other strategies could employ the observation of decay-cascades of high-lying states which are excited with narrow-band x-ray radiation generated by synchrotrons, Doppler-free two-photon laser spectroscopy in EBITs[5], laser spectroscopy (Egl et al., 2019) and mass spectrometry[6] (Schüssler, 2019) in Penning traps, or dedicated spectroscopy schemes in Paul traps which allow to find narrow transitions quicker than it can be done through conventional frequency scanning of the spectroscopy laser[7] (Bekker et al., 2019; Hume et al., 2011; Wolf et al., 2016).

---

[5] Doppler-free two-photon laser spectroscopy in an EBIT has been proposed (Mäckel et al., 2011; Soria Orts et al., 2007), but it was never demonstrated.

[6] An electronic transition energy corresponds to a mass difference between the atom being in the excited and ground state, respectively. Mass differences can be measured with a fractional uncertainty of about 10^{-11} in Penning traps (Blaum, 2006; Repp et al., 2012; Schüssler, 2019). Recently, such a measured mass difference revealed metastable electronic states in $^{187}\mathrm{Re}^{29+}$ and $^{187}\mathrm{Os}^{30+}$ (Schüssler, 2019). These transitions are in the soft x-ray regime with a transition energy on the order of 200 eV and are very narrow with about 5×10^{-8} Hz linewidth for $^{187}\mathrm{Re}^{29+}$ and a correspondingly long lifetime of the upper state of about 200 d (neglecting effects of state mixing). Although the uncertainty is still limited to the eV level, this approach offers the potential to discover very long-lived optical clock states in the first place. In particular, this method is not just limited to metastable electronic states. Metastable nuclear states could be discovered in the same way.

[7] State-dependent oscillating optical dipole forces could be employed (Bekker et al., 2019), generated by counter-propagating laser beams with a detuning of the motional oscillation frequency of the HCI in the trap. Depending on the global frequency detuning of the laser beams, these forces would change the motional state of the ion which can be efficiently detected through the co-trapped other ion species which is used for sympathetic cooling.

2 Frequency metrology

Space and time define every event in nature and both coordinate concepts are closely linked as is shown by the theory of special relativity. The daily, monthly, and annual rhythm is ruled by periodic astronomical events—however, the accurate measurement and standardization of time was crucial along the evolution of civilizations and a continuous improvement was pursued. The tools for measuring time, known as clocks, have evolved from primitive sundials through mechanical pendulums and quartz oscillators to atomic clocks, which are today the most accurate human-made devices. While a little clock drift is typically not a big issue for the individual's daily life, it adds up to unacceptable deviations for various applications. For instance, until the 15th century nautic navigation was primarily done by sight and then complemented by astronomical observations and the use of a compass. While the determination of the latitude was rather simple by the observation of the height of the sun or stars above the horizon, measuring the longitude with a comparable uncertainty was a severe problem. It still took until the mid-eighteenth century to find a proper solution through mechanical clocks which were accurate and robust enough to provide the reference time of a place with known longitude. This allowed to calculate the local longitude from that reference time and the local solar time[1]. In that sense, nautics was certainly an important driving force for the development of modern clocks to allow for accurate positioning. Nowadays we have global navigation systems like the US *GPS*, the Russian *GLONASS*, the Chinese *BeiDou*, or the European *Galileo*, which even allow us to navigate via mobile phone. Such navigation systems rely on a proper time measurement and, therefore, the satellites are equipped with atomic clocks. For instance, other applications are found in very-long-baseline interferometry and even in height measurements, which are expected to become possible to unprecedented precision through the use of optical atomic clocks. A height difference of 1 cm in the gravitational field of the Earth (close to the sea level) corresponds to a fractional frequency shift of 10^{-18} and becomes measurable (Grotti et al., 2018; McGrew et al., 2018; Takano et al., 2016). Thereby, optical atomic clocks could serve as future height references (Mehlstäubler et al., 2018).

At the heart of each clock is a frequency standard which provides the reference through a periodic process. The term *clock* actually means more than the term *frequency standard* since it implies the capability of counting the periods to eventually measure and display time. However, outside the frequency metrology community not much attention is paid to that difference.

---

[1] In those days, the longitude could be also determined through the measurement of lunar distances to stars. However, this method was more complicated and was superseded by chronometers when they became affordable.

Indeed, both terms are used more or less interchangeably and also in this thesis the use is not very strict. Section 2.1 gives a concise description of some technical terms used in frequency metrology in order to qualify and quantify a frequency standard. The following Section 2.2 and Section 2.3 give a brief overview about atomic clocks and their state of the art. Details can be found in the literature [see, e. g., Ludlow et al. (2015), Poli et al. (2013), Riehle (2004), and references therein].

2.1 Uncertainties and related technical terms

The term uncertainty describes the lack of exact knowledge of a quantity. In accordance with the guides of the Joint Committee for Guides in Metrology (2008, 2012), uncertainties are classified into two categories referred to as 'A' and 'B', depending on their method of evaluation. A typ A uncertainty is evaluated by statistical methods from an observed distribution of many individual measurements. In this thesis, it usually corresponds to the statistical uncertainty. Typ B uncertainties account for systematic effects and are evaluated by other means[2]. Importantly, a known systematic effect can be corrected for. These corrections are usually expressed as additive frequency shifts for atomic clocks and have to be measured, which is one of the key tasks to evaluate a frequency standard. The residual lack of knowledge about the systematic effect is expressed as the corresponding systematic uncertainty. Both types of uncertainties are typically quantified by their $1\,\sigma$ standard deviation and sometimes the uncertainties are combined in order to state a total measurement uncertainty. Other terms such as *accuracy* and *precision* are understood as qualitative concepts according to the Joint Committee for Guides in Metrology (2012) and Taylor and Kuyatt (1994), describing the deviation of a measured quantity from the true value (accuracy) and the scattering of repeated measurements (precision). In accordance to those definitions, accuracy and precision are independent features of a measurement instrument. The instrument may be accurate but not precise and, therefore, a large number of measurements is required in order to obtain a small statistical uncertainty. In contrast, another instrument could offer an excellent precision, but the averaged result has a large offset from the true value and is therefore not very accurate. The ideal instrument is both accurate and precise. Furthermore, the term *resolution* is defined by the Joint Committee for Guides in Metrology (2012) as the smallest change of a quantity which can be perceived by a measurement instrument or a setup. However, in this thesis the term resolution refers to the ability to distinguish two peaks of a spectrum from each other and thereby follows the common use of this term in spectroscopy and spectrometry [see, e. g., International Union of Pure and Applied Chemistry (1997)]. The FWHM of the peak will be used in order to quantify the resolution.

---

[2] Note that according to the rigorous definition, the classification of uncertainties into categories 'A' and 'B' only depends on the methods used for their evaluation and the synonymous use of the terms statistical and systematic uncertainty, respectively, may be inappropriate.

Another term which is particularly important for atomic clocks is *stability* [see, e. g., Ludlow et al. (2015)]. It is closely linked to the terms precision and resolution as mentioned above, and it refers to the statistical uncertainty of a continuous measurement of a quantity over time, for instance the reference frequency of a frequency standard. Stability therefore also addresses how fast a measurement result can be acquired to achieve a given level of statistical uncertainty. For an optical atomic clock based on (single) ions, the typical dominant noise process is the quantum projection noise (QPN) (Itano et al., 1993) caused by the quantum-mechanical nature of the measurement. After probing the atom near its resonance, the detection puts the atom either into its excited state with the probability P or into its ground state with the probability $1-P$. The QPN of such a binomial process is then given by

$$\mathrm{QPN} = \sqrt{\frac{P\cdot(1-P)}{N}}, \tag{2.1}$$

where N accounts for the number of measurements (and atoms being probed simultaneously[3]). The signal-to-noise ratio (SNR) is given by

$$\mathrm{SNR} = \frac{P}{\mathrm{QPN}} = \sqrt{\frac{N\cdot P}{1-P}}. \tag{2.2}$$

With this white noise process, the fractional statistical uncertainty of the frequency mean yields

$$\frac{\sigma_f}{f_0}(\tau) \propto \frac{1}{\mathrm{SNR}\cdot f_0}\sqrt{\frac{\Delta f}{\tau}} \tag{2.3}$$

with the reference frequency f_0 of the atomic clock transition, the Fourier-broadened linewidth Δf at which the clock transition is probed (being equal or greater than the FWHM natural linewidth of the clock transition), and the averaging time τ, in other words the total measurement duration. Note that Δf is proportional to the inverse probe time of the clock transition as will be discussed later in Section 7.2. For atomic clocks (or other frequency references), the stability is usually given as a fractional statistical frequency uncertainty for an averaging time τ. Various types of Allan deviations provide the common toolbox for its evaluation (Allan, 1987; Benkler, Lisdat, and Sterr, 2015).

2.2 Microwave atomic clocks

The first atomic clock was developed in 1949 at the National Institute of Standards and Technology (NIST), in those days named *National Bureau of Standards*, by Lyons (1949a,b,c). This device marked a milestone in timekeeping since it introduced the atom as an intrinsically better frequency reference than the common quartz oscillators, which appeared in the late 1920s. It was based on a 23.8 GHz microwave transition of the ammonium molecule. Shortly afterwards, the first caesium beam clock was built and commissioned at the National Physical Laboratory (NPL) (Essen and Parry, 1955) and outperformed the earlier ammonium clock. During that time, methods were developed and refined by Rabi, Ramsey and others [see, e. g., Rabi (1937), Rabi et al. (1938), Ramsey (1983, 1985), and Ramsey (1949)] for molecular beam experiments with oscillatory magnetic fields, that laid the foundations for modern optical atomic clocks. Still until 1967 the SI second was defined as a fraction of the year (ephemeris second), but then was redefined in terms of the 9.2 GHz hyperfine splitting of the electronic ground state in ^{133}Cs. Apart from ^{133}Cs, also other atomic microwave frequency standards are in common use, based on the ground-state hyperfine transitions in ^{87}Rb or ^{1}H (see Table 2.1). The latter standard is known as the hydrogen maser, and actually references the prominent 21 cm line as known from radioastronomy. The accuracy of the best microwave standards is at a low 10^{-16} uncertainty level with a stability of several $10^{-14}/\sqrt{\tau/\mathrm{s}}$ (Guéna et al., 2014, 2017; Weyers et al., 2018). Hydrogen masers may provide a better medium-term stability with the drawback of a long-term drift. A solution can be realized by steering the maser on a daily basis by a ^{133}Cs clock (Bauch et al., 2012).

---

[3] Note that for optical lattice clocks, in which a large atom ensemble is simultaneously probed, the stability is typically limited through the *Dick-effect*, caused by the diffusion of the clock laser phase during the dead time of a measurement cycle in which the atoms are not probed by the clock laser (Ludlow et al., 2015).

System	K	Frequency (Hz)	Wavelength (nm)
^{1}H	0.00	1.42×10^{9}	microwave
^{87}Rb	0.34	6.83×10^{9}	microwave
^{133}Cs	0.83	9.19×10^{9}	microwave
^{87}Sr	0.06	429×10^{12}	698
^{171}Yb	0.31	518×10^{12}	578
^{199}Hg	1.16	1129×10^{12}	266
^{27}Al^{+}	0.008	1121×10^{12}	267
^{40}Ca^{+}	0.15	411×10^{12}	729
^{88}Sr^{+}	0.43	445×10^{12}	674
^{171}Yb^{+} E2	0.88	688×10^{12}	436
^{199}Hg^{+}	−3.19	1065×10^{12}	282
^{171}Yb^{+} E3	−5.95	642×10^{12}	467
Pr^{9+} E2	5.28	735×10^{12}	∼ 408
Pr^{9+} M3	6.32	663×10^{12}	∼ 452
Ir^{17+}	145.00	152×10^{12}	∼ 1978

Table 2.1: Atomic clock transitions and sensitivity coefficients *K* for a potential time variation of the fine-structure constant. See the text of this chapter and Section 3.2 for further details. Clock experiments with the species Pr^{9+} and Ir^{17+} have not yet been experimentally realized, but are proposed among other HCI species. The list is not exhaustive. Numbers extracted from Bekker et al. (2019), M. G. Kozlov et al. (2018), Ludlow et al. (2015), M. S. Safronova et al. (2018), and Uzan (2011).

2.3 Optical atomic clocks

Great improvements in clock performance have been facilitated by increasing the frequency of the reference oscillator. This can be understood as a consequence of Equation 2.3, which has the reference frequency f_0 in the denominator. The larger f_0 is, the smaller the fractional frequency uncertainty becomes for a given averaging time τ. Of course, the clock can only benefit from that when the systematic uncertainty can be controlled on a comparable level, which is the case for typical optical clocks.

Therefore, the next logical step was to move forward from hyperfine-structure transitions in the microwave range to optical transitions of the atomic gross structure. The laser, invented not much after the first atomic clocks (Maiman, 1960; Schawlow and Townes, 1958), could be employed as the so-called *local oscillator* to probe the optical transition, being the equivalent of the microwave source. However, in the beginning it was very difficult to reference the optical frequency of many hundred THz through complex harmonic frequency chains to countable frequencies in the rf domain. Eventually, the key development was the invention of the frequency comb (Reichert et al., 1999; Telle et al., 1999; Udem, Holzwarth, and Hänsch, 2002) which bridges the optical and rf domain through the operation of a mode-locked femtosecond laser in a much more convenient and reliable way. A few years later, optical frequency standards outperformed their microwave counterparts (Poli et al., 2013) and are nowadays more than two orders of magnitude more accurate and stable.

The concept of an optical atomic clock includes three main components. First, the frequency reference is provided by an optical transition of a specific atomic system. Second, a stable and narrow-linewidth laser, dubbed as *clock laser*, is used as a local oscillator which probes the optical transition. Third, the optical frequency of the clock laser is divided through a frequency comb to countable radio frequencies from which the optical frequency can be accurately determined. In that sense, the frequency comb serves as a clock work. The countable radio frequencies are referenced to a microwave standard, such as a hydrogen maser or a ^{133}Cs clock, to determine the optical frequency in hertz. However, in this case the lowest achievable uncertainty would be limited by the definition of the SI second itself. As a possible solution the frequency ratio f_1/f_2 of two optical clocks can be measured, which is independent of the SI definition. Still, this is more or less limited to clocks which are linked by optical fibers [see, e. g., Grotti et al. (2018), Lisdat et al. (2016), and Xu et al. (2019)] since clock comparisons through satellite techniques are still limited at the 10^{-16} uncertainty level (Riedel et al., 2020). To continuously operate the optical clock, the clock laser is not just repeatedly scanned across the transition but instead locked to it. The transition can be symmetrically probed for this purpose at two points on the line profile with identical excitation probability: one point on the increasing and one point on the decreasing slope. The transition frequency is then calculated as the mean of both probe frequencies. A difference in the probed excitation probabilities indicates a drift of the clock laser with respect to the atomic transition. An error signal is calculated from such a difference and fed back to the clock laser to steer its frequency back to the transition. Such a locking strategy is sometimes referred to as *two-point sampling*.

Efficient state detection is another crucial requirement since Equation 2.3 calls for narrow transitions which have a long lifetime and are therefore not suitable for fluorescence detection. For this purpose, a double-resonance technique (Brossel and Bitter, 1952) can be employed in the optical range by monitoring the fluorescence of a strong electric-dipole transition, also used for Doppler cooling, while probing the narrow and long-lived clock transition (Bergquist et al., 1986; Dehmelt, 1973; Itano et al., 1988; Itano, Bergquist, and Wineland, 1987). Once the clock transition has been excited, the fluorescence of the Doppler cooling transition vanishes. This technique provides essentially a unity detection efficiency since only a discrimination is required between a bright state and a dark state, where the bright state can be detected with typically about 10^4–10^5 photon counts per second on a photomultiplier tube (PMT) from a single atom while the dark state gives a vanishing background signal. It became known as *electron shelving* since the valence electron is shelved into the metastable upper clock state.

Two conceptually different types of optical atomic clocks have been developed in the past: first, clocks based on single ions confined in an ion trap and following the pioneering ideas of Dehmelt (1982), and later, clocks based on thousands of neutral atoms trapped in an optical lattice (Katori, 2002; Takamoto et al., 2005). Each of the two approaches provide distinct advantages and disadvantages which can be only briefly summarized here [see literature for details, e. g., Ludlow et al. (2015), Poli et al. (2013), and references therein]. Optical lattice clocks offer a superior stability since N atoms (see Equation 2.1) on the order of one thousand are interrogated simultaneously. However, lattice clocks suffer from delicate systematics, such as light shifts (Katori et al., 2015; Nemitz et al., 2019). In contrast, single-ion clocks might offer better control over systematic effects with the drawback of an instability due to the quantum projection noise of only a single atom. Therefore multi-ion clocks are being developed, which could offer an improved stability at the cost of higher complexity (Herschbach et al., 2012; J. Keller, Burgermeister, Kalincev, Didier, et al., 2019; J. Keller, Kalincev, et al., 2019; Kienzler et al., 2020; Schulte et al., 2016; Tan et al., 2019). Another strategy from the optical trapping side is the use of optical tweezer arrays which allow for larger atom distances and improved spatial control with potentially lower systematics (Norcia et al., 2019). A further approach to improve the clock performance is the use of schemes which overcome the QPN limit of Equation 2.3 by correlating atoms (Leroux, Schleier-Smith, and Vuletić, 2010; Shaniv, Manovitz, et al., 2018). A fractional instability of only $4.8 \times 10^{-17} / \sqrt{\tau/\mathrm{s}}$ was recently demonstrated for two ^{87}Sr lattice clocks (Oelker et al., 2019) which accesses the 10^{-19} instability range for averaging times on the order of one hour. A systematic uncertainty of 2×10^{-18} is demonstrated with shifts on the mid-10^{-15} level which have to be accurately corrected for (Bothwell et al., 2019). Single-ion clocks, such as $^{171}\mathrm{Yb}^{+}$ (Huntemann et al., 2016) and $^{27}\mathrm{Al}^{+}$ have demonstrated systematic uncertainties of 3.2×10^{-18} and 9.5×10^{-19}, respectively. However, they only achieve a stability on the $10^{-15} / \sqrt{\tau/\mathrm{s}}$ level.

$^{27}\mathrm{Al}^{+}$ is a special case for a single-ion clock, since it does not provide the typical atomic structure required for laser cooling and electron shelving detection. Actually, only a few atoms and ions are available for these techniques, which imposes a considerable limitation for frequency metrology since some of the other atomic systems offer superior properties. To overcome this limitation, quantum logic spectroscopy (QLS) has been invented by Wineland et al. (2002) and demonstrated by P. O. Schmidt et al. (2005) as a method which still realizes electron shelving by coupling two different ions in a common harmonic potential. $^{27}\mathrm{Al}^{+}$ as the *clock ion* is sympathetically laser cooled, prepared, and detected through the second, so-called *logic ion*. QLS and variations thereof have been demonstrated with $^{27}\mathrm{Al}^{+}$ (C. W. Chou et al., 2010; Rosenband et al., 2008), molecular ions such as $^{24}\mathrm{MgH}^{+}$ (Wolf et al., 2016) and $^{40}\mathrm{CaH}^{+}$ (C.-w. Chou et al., 2017), and broad transitions (Hempel et al., 2013; Wan et al., 2014). Details of this technique will be discussed later in Chapter 13.

In fact, the most accurate optical atomic clock is currently the ^{27}Al^{+} ion clock at NIST (Brewer et al., 2019), which offers a very narrow transition linewidth of 8 mHz at 267.4 nm without electric-quadrupole moment and a small Zeeman shift, only arising from the nucleus. Many other optical atomic clocks are however competitive and have reached fractional uncertainties on the low 10^{-17} and 10^{-18} level, based on single ions like ^{171}Yb^{+} (Huntemann et al., 2016), ^{199}Hg^{+} (Diddams et al., 2001; Rosenband et al., 2008), ^{88}Sr^{+} (Dubé et al., 2013; Madej et al., 2012) or thousands of neutral atoms, such as ^{87}Sr (Bloom et al., 2014; Bothwell et al., 2019; Takano et al., 2016) or ^{171}Yb (McGrew et al., 2018). A compilation of some clock species is given in Table 2.1, noting that this list is not exhaustive.

2.3.1 Frequency shifts of single-ion clocks

The exceptional stabilities of optical atomic clocks allow for statistical uncertainties on the 10^{-18} level within hours or days of averaging. Thereby, systematic perturbations from external electric or magnetic fields and the ion's motion are resolved on such fractional uncertainty levels and need to be corrected for when measuring the unperturbed transition frequency. The magnitudes of these perturbations are governed by corresponding atomic properties, such as polarizabilities, magnetic moments, electric-quadrupole moments and the mass. In general, these properties depend on the specific electronic state and consequently, cause different shifts for different states. Eventually, except for the motional shifts, the differential shifts of both electronic states which make up the transition have to be considered. Each of these frequency shifts is characterized with a corresponding uncertainty. A typical strategy to calibrate a shift is to measure the transition frequency as a function of the perturbation and finally extrapolate the transition frequency to zero perturbation.

All individual uncertainties of the shifts are then combined to a total systematic uncertainty of the clock transition which is on the 10^{-18} level for the best clocks, and thus comparable to their statistical uncertainties. However, the shifts themselves can be significantly larger, sometimes by several orders of magnitude. Therefore, the accurate assessment of these shifts and their uncertainties is a crucial task in frequency metrology. In the following, important single-ion-clock frequency shifts are briefly addressed [see, e. g., Ludlow et al. (2015) for details], some of them will become relevant in the future, building on the experiment reported in this thesis.

Stark shift

Atoms do not possess a permanent electric-dipole moment. However, an external electric field $\vec{\mathcal{E}}$ induces an electric-dipole moment which depends on the polarizability of the ion and the field itself. This induced dipole then interacts with the field that causes it. The corresponding energy shift is thus proportional to $\mathcal{E}^2$ and dubbed *second-order Stark shift*. The polarizability has a scalar and a tensor part, depending on the quantum numbers, and is frequency-dependent. As mentioned earlier, the differential polarizability of both clock states is relevant for the shift of the transition. The Stark shift can be split into an alternating-current (ac) and direct-current (dc) part with respect to the oscillation frequency of the external field, where only the ac part is relevant in an ion trap since the ion in an equilibrium position is by definition not subject to a static electric field. Furthermore, the oscillation periods of the electric fields are much shorter than the probe time with the clock laser. Therefore, the time average $\overline{\mathcal{E}^2}$ has to be considered only. The term *Stark shift* thus always refers to the time-averaged second-order ac Stark shift here, since it is the only relevant Stark shift for optical clocks.

An ac Stark shift caused by a laser is also known as *light shift*. To characterize this shift, the transition frequency can be measured as a function of the laser intensity and extrapolated to zero intensity. Additionally, the spatial extent of the quantum-mechanical wave function of the ion and in particular a possible displacement of the ion from the rf-zero of the Paul trap gives rise to an rf drive-induced Stark shift. Furthermore, the thermal black-body radiation (BBR) from the environment induces a Stark shift. Both effects are more complicated to calibrate since $\overline{\mathcal{E}^2}$ cannot be simply varied to extrapolate the induced shifts towards zero. They are typically characterized by the dc limit of the polarizability, dubbed *static polarizability*, since the involved field frequencies are much lower than the transition frequency[4]. In particular for the BBR shift not only accurate knowledge of the dc polarizability is required, but also of the thermal environment of the ion. However, in a cryogenic setup the BBR shift is tremendously suppressed due to the T^4 scaling originating from the Stefan-Boltzmann law, where T is the temperature.

Electric-quadrupole shift

States with total electronic angular momentum quantum numbers $J \geq 1$ possess quadrupole moments[5] Θ. In such a case the coupling of Θ with an electric-field gradient at the position of the ion in a linear Paul trap results in a quadrupole shift ΔE_{qps} of the electronic state, which depends on the magnetic quantum number m. Following Itano (2000), the time averaged[6] quadrupole shift can be expressed as

$$\Delta E_{\mathrm{qps}} = -\frac{\partial \mathcal{E}_z}{\partial z} \frac{\langle \xi, J || \widehat{Q} || \xi, J \rangle \left[3 m_J^2 - J\,(J+1)\right] \left(3\cos^2\beta - 1\right)}{2\sqrt{(2J+3)\,(2J+2)\,(2J+1)\,2J\,(2J-1)}}\,, \quad (2.4)$$

---

[4] For the BBR shift a dynamic correction is usually still applied.

[5] If state mixing effects cannot be neglected, even states with $J < 1$ can have a relevant quadrupole moment.

[6] The probe time with the clock laser should be long against the rf period of the trap drive of the Paul trap.

in the absence of hyperfine structure[7] with $\langle \xi, J \,||\widehat{Q}||\, \xi, J \rangle$ being the reduced matrix element of the electric-quadrupole operator $\widehat{Q}$ from which the quadrupole moment can be derived, commonly defined as

$$\Theta(\xi, J) = \langle \xi, J, m_J = J \,|\widehat{Q}_0|\, \xi, J, m_J = J \rangle \tag{2.5}$$

with the $q = 0$ component of $\widehat{Q}$ in a spherical basis. $\partial \mathcal{E}_z / \partial z$ is the electric-field gradient which is in an ideal linear Paul trap typically aligned along the trap axis of the dc confinement (z-axis) (Itano, 2000). β is the angle between the quantization axis and this electric-field gradient. Thereby, β describes the rotation of the atomic frame against the Paul trap frame. The angle dependence allows to cancel the quadrupole shift by rotating the atomic frame through an appropriate rotation of the magnetic quantization axis (Itano, 2000). Alternatively, this shift can be canceled by averaging an appropriate set of Zeeman components (Dubé et al., 2005). Note that the quadrupole shift has a term which is quadratic in m and a term which gives an energy offset, similar to the second-order Zeeman shift (see next paragraph).

Zeeman shift

An external dc magnetic field with flux density B is generally required to define a quantization axis for the ion and lift the degeneracy of the magnetic substates in a controlled manner. With a non-zero total angular momentum, the corresponding first-order or linear Zeeman shift for an electronic state is given by

$$\Delta E_{\text{Zeeman}} = m\, g\, \mu_{\text{B}}\, B \tag{2.6}$$

where m is the magnetic quantum number of the substate, g is the g-factor of the considered state, and μ_{B} is the Bohr magneton. The differential shift of both involved substates with magnetic quantum numbers m and m' matters for a transition. Hence, when at least one of the involved states possesses a magnetic-dipole moment with magnetic quantum numbers different from zero, the transition splits up into several Zeeman components. If available, a component with $m = m' = 0$ is unperturbed and thus (to first order) magnetic field insensitive. The linear Zeeman effect can also be removed by symmetrically averaging over some or all Zeeman components that shift in opposite directions.

The second-order or quadratic Zeeman shift, in contrast, can be described in a simplified picture by the relation

$$\Delta E^{(2)}_{\text{Zeeman}} = \frac{C_1\, (\mu_{\text{B}}\, B)^2 + C_2\, (m\, \mu_{\text{B}}\, B)^2}{\text{splitting}}\,, \tag{2.7}$$

where C_1 and C_2 are constants. The term involving C_1 gives an energy offset independent of the magnetic quantum number m while the other term involving C_2 depends quadratically on m. $\Delta E^{(2)}_{\text{Zeeman}}$ scales quadratically with

---

[7] If the ion has a nuclear moment, J has to be replaced by F.

B and decreases with an increasing 'splitting' which denotes the relevant energy splitting to the nearby hyperfine- or fine-structure state. A more exact description considers all other states as well [see, e. g., Glazov et al. (2013) and D. v. Lindenfels et al. (2013) for details]. The second-order Zeeman shift cannot be removed by averaging the Zeeman components. A characterization is possible, for instance with input from atomic structure calculations and/or fitting a quadratic term to the Zeeman structure of the state plus a careful magnetic field evaluation. In particular, while a linear Zeeman shift from the rf drive of the Paul trap averages to zero within the clock laser probe time, a quadratic Zeeman shift does not. This also applies for power line noise and high-frequency magnetic field noise.

If the Zeeman shift is purely caused by a nuclear magnetic moment, it is suppressed by more than three orders of magnitude, namely by the factor $\mu_\mathrm{N}/\mu_\mathrm{B} = m_\mathrm{e}/m_\mathrm{p}$, where μ_N is the nuclear magneton and $m_\mathrm{e}/m_\mathrm{p}$ the electron-to-proton mass ratio.

Motional shifts

The motion of the ion causes the ion to see the clock laser frequency f at a shifted frequency f' due to the relativistic Doppler effect. This shifted frequency

$$f' = f \cdot \gamma \cdot \left(1 - \frac{v \cdot \cos\alpha}{c}\right) \tag{2.8}$$

is purely governed by the ion's velocity v and the angle α between the direction of motion and the clock laser propagation direction. c is the vacuum speed of light and

$$\gamma = \frac{1}{\sqrt{1 - \left(\frac{v}{c}\right)^2}} \tag{2.9}$$

the Lorentz factor. The clock laser pulse is much longer than the time scale of microseconds on which the motion of the ion takes place and the laser frequency is stabilized in a way that the frequency seen by the ion matches the clock transition at a frequency f_0. Therefore, the relation $\overline{f'} = f_0$ applies, where the bar denotes the time average, and the laser frequency f is assumed to be constant. The resulting fractional frequency shift $(f - f_0)/f_0$ is then obtained through a Taylor expansion as

$$\frac{f - f_0}{f_0} \approx \underbrace{\frac{\overline{v} \cdot \cos\alpha}{c}}_{\substack{\text{First-order}\\ \text{Doppler shift}}} - \underbrace{\frac{\overline{v^2}}{2c^2}}_{\substack{\text{Second-order}\\ \text{Doppler shift}}} . \tag{2.10}$$

The first term on the right in Equation 2.10 is the first-order Doppler shift and would be zero on time average in an ideal case of purely harmonic motion of the ion. In reality, the ion might be exposed to slightly changing dc trapping or patch potentials. Additionally, the entire Paul trap might be subject to low-frequency vibrations or even move due to mechanical or thermal relaxation processes. In an unfortunate case, a periodic motion of the ion is synchronous with the probe period of the clock laser. All such effects would cause a drift (or virtual drift) of the ion's location against the laboratory frame and result in a first-order Doppler shift which has been measured to be on a 5×10^{-17} fractional frequency level in other experiments (Brewer et al., 2019). This corresponds to a drift velocity on the $10\,\mathrm{nm\,s^{-1}}$ level. In order to eliminate this shift, the clock laser can be interferometrically phase stabilized to the trap[8], or the ion can be probed in an alternating manner by counter-propagating clock beams. The averaged frequency of both probe directions is then free from a first-order Doppler shift, thereby also removing shifts from drifting dc electric fields.

The second term on the right in Equation 2.10 is the second-order Doppler shift, also known as the *time-dilation shift*. It gives always a non-zero result for a moving ion[9]. The only solution is to properly characterize the motion of the ion. According to the dynamics in a Paul trap, which will be discussed later in Section 6.2 in detail, two contributions to the second-order Dopper shift have to be considered. The first one is a consequence of the so-called *secular motion* and depends on the secular frequencies and the occupation number distributions of the ion as a quantum harmonic oscillator (QHO). From the energy stored in the QHO, the mean kinetic energy and $\overline{v^2}$ can be estimated with the virial theorem. Even for the pure quantum-mechanical ground state of motion, the zero-point energy results in a residual velocity which depends on the magnitude of the secular frequencies. Low ion heating rates are crucial in order to keep the occupation number low during the probe time with the clock laser (Chen et al., 2017). The second contribution results from *micromotion* at the trap-drive radio frequency. First, intrinsic micromotion cannot be avoided and depends on the spatial extent of the QHO wave function and thereby also on the occupation number distributions. Second, excess micromotion arises when the ion is not exactly situated in the rf field minimum. The corresponding velocity term increases with increasing displacement of the ion from this rf-zero. Therefore, compensation of excess micromotion is crucial to minimize the corresponding motional shift (Berkeland et al., 1998b). The residual excess micromotion shift can be evaluated by measuring the micromotion sidebands for example (J. Keller et al., 2016, 2015).

Collisional shift

Collisions with molecules or atoms of the background gas cause heating and a transient shift of the clock states through the temporary interaction of the electronic wave functions of target and projectile. This results in a finite shift of the clock transition on time average. Recently, the room-temperature collisional fractional frequency shift for $^{27}\mathrm{Al}^+$ at a background gas pressure of about 3.8×10^{-10} mbar ($\mathrm{H_2}$) was estimated to be 0.6×10^{-19} with an uncertainty of

---

[8] Such a stabilization eliminates the shift only if the ion and trap strictly move together.

[9] The heavier the ion's mass m, the smaller is the motional shift for a given kinetic energy E_kin because of the scaling of the ion's velocity $v = \sqrt{2E_\mathrm{kin}/m}$.

Shift	Scaling
Second-order Stark shift	Z^{-4}
Black-body radiation shift	negligible
Electric-quadrupole shift	Z^{-2}
First-order Zeeman shift	Z^0
Second-order Zeeman shift	suppressed
Motional shifts	Z^0
Collisional shift	negligible

Table 2.2: Scaling of frequency shifts in a hydrogen-like atom as a function of the proton number *Z*. The black-body radiation shift scales with Z^{-4} as the second-order Stark shift. Additionally, it is suppressed in the required cryogenic environment by a factor of about $(4\,\mathrm{K}/300\,\mathrm{K})^4$ compared to room-temperature setups and is therefore negligible. The second-order Zeeman shift depends on the fine and hyperfine structure of the transition. It is generally suppressed in HCIs, but a specific scaling law cannot be given in general (Berengut et al., 2012a). The collisional shift is negligible owing to the several orders of magnitude lower background gas particle density in the cryogenic environment and the by a factor of $4\,\mathrm{K}/300\,\mathrm{K}$ lower kinetic energy of the residual gas particles. Furthermore, collisions are typically noticed by the loss of the HCI due to a charge exchange reaction. See, e. g., Berengut et al. (2012a), Derevianko, Dzuba, and Flambaum (2012), J. D. Gillaspy (2001), M. G. Kozlov et al. (2018), Quint and Vogel (2014), and text for more details.

2.4×10^{-19} [see Brewer et al. (2019) and Hankin et al. (2019) for the the given numbers as well as complementary calculations by Davis, Dubé, and Vutha (2019)]. In contrast, a collisional shift is strongly suppressed in a cryogenic environment for two reasons: First, the background gas particle density is several orders of magnitude lower, which drastically reduces the rate at which collisions happen. Second, the kinetic energy of the cryogenic background gas is significantly reduced by a factor of $4\,\mathrm{K}/300\,\mathrm{K} \approx 0.01$. As a result of both aspects, the collisional shift is considerably smaller for cryogenic frequency standards.

2.3.2 An HCI clock

As discussed in Chapter 1, forbidden optical transitions are available in HCIs. More than ten years ago, a proposal emphasized ‘attractive features’ of HCIs for the use as frequency references based on optical hyperfine transitions in hydrogen-like ions (Schiller, 2007). More specifically with the idea to study fundamental physics (being discussed in Section 3.2.1), the suppression of systematic frequency shifts in HCIs was addressed, which was in principle already known before [see, e. g., J. D. Gillaspy (2001)]. The scaling of frequency shifts with the charge state was further evaluated and assessed by Berengut et al. (2012a) with the result that HCI-based optical atomic clocks on the 10^{-19} fractional frequency uncertainty level might be feasible (Derevianko, Dzuba, and Flambaum, 2012)[10]. In the following years a large number of further theoretical works appeared, suggesting many more HCI species (Bekker et al., 2019; Dzuba, Derevianko, and Flambaum, 2012a,b; Dzuba, Flambaum, and Katori, 2015; Dzuba et al., 2015; A. Kozlov, Dzuba, and Flambaum, 2013; Nandy and Sahoo, 2016; Oreshkina et al., 2017; M. S. Safronova et al., 2014a,b,c; U. I. Safronova, Flambaum, and M. S. Safronova, 2015; Y.-m. Yu and Sahoo, 2016, 2018, 2019; Yudin, Taichenachev, and Derevianko, 2014). The most relevant systems with narrow optical ground-state transitions have been reviewed by M. G. Kozlov et al. (2018). However, up to the work presented in this thesis no experiment existed to realize any of these proposals.

In brief summary of all these proposals, HCIs are inherently less sensitive to most of the external perturbations than the neutral or singly charged species which are in use today as references in optical atomic clocks. Table 2.2 summarizes the scaling of the above discussed frequency shifts as a function of the proton number Z for hydrogen-like ions. The scalings become more complicated when not considering hydrogen-like ions but a general HCI instead. Then, an effective nuclear charge number Z_{eff} is typically introduced and the charge state Z_{ion} utilized to quote a scaling behavior [see, e. g., Berengut et al. (2012a) and M. G. Kozlov et al. (2018)]. However, also in that case many of the systematic shifts are highly suppressed, accompanied with considerably reduced systematic uncertainties.

For HCI clocks, two systematic effects are expected to be dominant: The linear Zeeman shift and shifts resulting from the ion's motion. While the linear Zeeman shift can be removed in real time by averaging over Zeeman components, motional shifts are more severe and require a careful calibration. In fact, HCIs are rather sensitive to spurious electric fields from patch potentials for example and, therefore, to changes in the ambient electric field which would increase excess micromotion. As a consequence, the excess micromotion amplitude was estimated to scale linearly with the charge state Z_{ion} (M. G. Kozlov et al., 2018). Thus, careful minimization of the micromotion by adjusting the HCI position in the rf potential with additional compensation electrodes is crucial.

The Stark shift and the electric-quadrupole shift are strongly suppressed. In particular, the BBR shift is not only strongly suppressed as a Stark shift, the experiment requires a cryogenic environment anyway to prevent charge exchange reactions due to collisions with background gas, which further suppresses this temperature-dependent shift by a factor of about $(4\,\mathrm{K}/300\,\mathrm{K})^4$ compared to a room-temperature setup. As a result, the BBR shift becomes negligible. The electric-quadrupole moment of the $^2\mathrm{P}_{3/2}$ state in $^{40}\mathrm{Ar}^{13+}$, for instance, was estimated to be about $2.4 \times 10^{-2}\,e a_0^2$ (Müller, 2019), which is about two orders of magnitude smaller than typical for singly charged ions and on a comparable level as for the $^{171}\mathrm{Yb}^+$ E3 transition. The collisional shift is negligible since a collision typically causes the immediate loss of the HCI species. As long as the charge state is preserved, no severe collision has happened. However, future theoretical investigations might be helpful in order to assess what magnitude a shift of a glancing collision can have, in which the minimum distance is still larger than the critical distance for a charge exchange reaction. The latter one grows with $\sqrt{Z_{\text{ion}}}$ according to the classical over-barrier model (Micke et al., 2019; Schmöger, 2017).

---

[10] Other proposals even lowered this number to the 10^{-20}–10^{-21} uncertainty level [see, e. g., Yudin, Taichenachev, and Derevianko (2014)].

2.3.3 A nuclear clock

Even some years before the first HCI proposal for applications in frequency metrology, Peik and Tamm (2003) suggested a nuclear clock based on $^{229}\text{Th}^{3+}$ confined in a Paul trap. The excited metastable $^{229\text{m}}\text{Th}$ isomer offers the only known near-optical nuclear ground-state transition, and further theoretical evaluations (Campbell et al., 2012) certified excellent properties for optical clock applications. In particular, a high sensitivity for fundamental physics studies is expected (Flambaum, 2006). In that sense, a nuclear clock has a close relation to clocks based on HCIs since both will find applications in comparable fields. Above that, higher charge states of the ^{229}Th atom are required which offer a greater electronic binding energy than the nuclear transition energy to avoid the auto-ionizing internal conversion process. Recently, the first direct observation of this nuclear transition was reported (Wense et al., 2016) and since then, increasing effort was undertaken to characterize the nuclear isomer (Müller, Volotka, and Surzhykov, 2019; Thielking et al., 2018). According to Seiferle et al. (2019) the transition was pinned down to a wavelength of $149.7(31)$ nm in the vacuum ultraviolet range. Alternatively to a single-ion clock, doping of a crystal with ^{229}Th was also proposed for a solid-state-based nuclear optical clock (Rellergert et al., 2010), but this approach might suffer from difficulties owing to the ionizing clock-photon energy. Once the ^{229}Th system has proven controllable in the laboratory, exciting applications in frequency metrology and fundamental physics can be expected, which will complement the more evolved HCI research discussed here.

3 Probing fundamental physics

Our knowledge about nature and our understanding of the basic interactions and symmetries have rapidly evolved in the past 150 years. However, there are still serious challenges in modern physics, e. g., dealing with the unification of the Standard Model of particle physics (SM) and the general theory of relativity (GTR) or the composition of the content of our universe (see Figure 3.1). Studies of the cosmic microwave background (Ade et al., 2014; Hinshaw et al., 2013) show that in a scenario where GTR would be valid on all scales[1], only about 5 % of the universe can be related to normal matter. The other 95 % are assigned to other ingredients which we call dark matter and dark energy. Both are introduced as a possible explanation for various astrophysical observations and the cosmological evolution. For instance, the observed structure and dynamics of spiral galaxies showed an inconsistency with the expected gravity from the visible matter therein (Faber and Gallagher, 1979; Rubin and Ford, 1970), suggesting that there might be a form of massive dark matter. Moreover, the existence of dark matter is supported by our understanding of the evolution of the structures in the universe and the effect of gravitational lensing (Bertone and Hooper, 2018). Dark energy is by contrast proposed as an explanation for the accelerated expansion of the universe and is represented through the cosmological constant Λ in the Einstein field equations (Peebles and Ratra, 2003). But in fact, our understanding of dark matter and dark energy beyond their potential existence is very humble. Another challenge is to understand why the visible universe essentially only contains matter and no antimatter. In the process of baryogenesis of the early universe an almost equal, but apparently not identical amount of matter and antimatter has been created. The subsequent annihilation during the cool-down of the universe (Particle Data

---

[1] In contrast, MOND (*MOdified Newtonian Dynamics*) models were suggested to explain some observations (Bekenstein, 2004; Milgrom, 1983) but would imply that GTR fails to describe gravity on all scales.

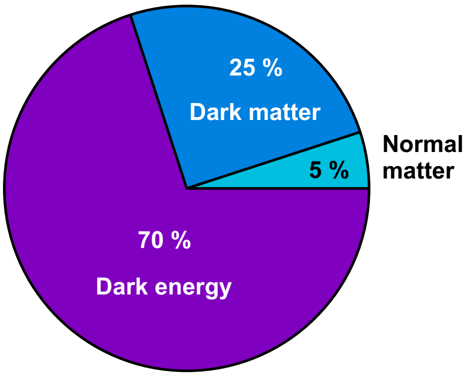

Figure 3.1: Composition of the universe. The current ingredients were estimated to be about 5 % normal matter, 25 % dark matter, and 70 % dark energy, inferred from recent measurements of the cosmic microwave background by the WMAP and Planck space telescopes (Ade et al., 2014; Hinshaw et al., 2013).

Group, 2018) has left over a small amount of matter but no antimatter. The reason for this matter-antimatter asymmetry is unknown.

These and other fundamental physics questions have been addressed over the last few decades in two complementary approaches, namely through studies at highest energy or at highest precision. The first approach requires astronomical observations with advanced telescopes or large accelerator facilities. The second one is carried out in more numerous experiments in smaller physics laboratories, which admittedly require a demanding infrastructure regarding stability requirements and reliable measurement references and standards, but experiments are still realized more or less as table-top setups. The following sections focus on the latter approach of precision experiments, primarily performed in the optical range of the electromagnetic spectrum, and make a link to HCI experiments or possible applications of HCIs in future studies. The listed experiments are not intended to be exhaustive. In Section 3.1 the atomic structure of simple atomic systems, such as HCIs, is addressed including a brief discussion of nuclear effects and isotope shift spectroscopy. Section 3.2 deals with a possible variation of fundamental constants and the use of atomic clocks as detectors. Finally, in Section 3.3 studies of a possible Lorentz violation are briefly addressed. A more comprehensive discussion on all these topics can be found in the latest literature [see, e. g., M. G. Kozlov et al. (2018), Quint and Vogel (2014), M. S. Safronova et al. (2018), and Uzan (2003), as well as references therein].

3.1 Atomic structure and quantum electrodynamics

An important field in atomic physics is high-precision optical spectroscopy of simple atomic systems since it allows us to refine our knowledge about both atomic structure and the underlying fundamental interactions. The advent of quantum mechanics facilitated the development of a proper understanding of atomic spectra, in particular of the hydrogen atom as a prime example. At first, the non-relativistic description by Heisenberg (1925) and Schrödinger (1926a,b,c,d) could explain the discrete electronic level structure postulated by N. Bohr (1913a,b) as a function of the principal quantum number n. Soon, the electron's spin s could be understood within Dirac's relativistic formulation of quantum mechanics (Dirac, 1928). The related fine structure of the hydrogen spectrum appeared as a consequence of the coupling of s with the orbital angular momentum l and the relevance of the total angular momentum j became clear. Later in the framework of the so-called *second quantization*, the electromagnetic field was quantized and a relativistic quantum field theory of electrodynamics (QED) developed. Thereby, also the Lamb shift (Lamb and Retherford, 1947)—the small energy shift of the $2\,\mathrm{s}_{1/2}$ state which lifts the degeneracy with the $2\,\mathrm{p}_{1/2}$ state—could be explained as a result of radiative corrections such as vacuum energy fluctuations.

Present-day atomic structure calculations for one or a few electron atoms within the framework of QED[2] achieve an excellent precision [e. g. the Lamb shift in the hydrogen atom (Karshenboim et al., 2019; Yerokhin, Pachucki, and Patkóš, 2019)], and the comparison with experimental results allows for extremely sensitive tests of theory. In particular, systems with strong relativistic and QED effects are generally preferred for this purpose. For atomic systems with more electrons, such calculations are significantly more demanding owing to electronic correlations. Therefore, a comparison with an experiment typically rather benchmarks how well electronic correlations, also dubbed interelectronic interactions, can be described. This also limits the predictive power for electronic energy levels and transitions. For instance, the most accurate theoretical calculations of the $^2\mathrm{P}_{1/2}$–$^2\mathrm{P}_{3/2}$ fine-structure transition in the five-electron system boron-like Ar^{13+} at a wavelength of about 441 nm, or 680 THz, have an uncertainty level of 100 GHz (Artemyev et al., 2013, 2007)[3] which appears limited by the missing computation of third and higher-order QED diagrams. In cases, useful predictions are possible with a significantly larger number of electrons, when a sufficient description of these systems through closed shells with only single valence electrons or electron holes within the closed electronic shells (Berengut et al., 2011; Dzuba, Derevianko, and Flambaum, 2012a) is possible. Likewise, the spectra of singly charged or neutral molecular hydrogen can be predicted with higher accuracy (Biesheuvel et al., 2016; Komasa et al., 2019; Pachucki and Komasa, 2016) than it is possible for molecules which involve more particles[4].

Experiments aiming at high-precision optical spectroscopy rely on atomic systems which can be sufficiently controlled. This includes the production and handling of these systems as well as the application of methods to reduce or avoid broadening mechanisms of the usually narrow-linewidth transitions, typically caused by thermal and translational motion. Prominent experiments were done with atomic hydrogen from which the Rydberg constant R_∞ can be determined to unprecedented accuracy on a 10^{-12} fractional uncertainty level (Mohr, Newell, and Taylor, 2016; Tiesinga et al., 2019). Such experiments have specifically measured the 1s–2s transition (M. Fischer et al., 2004; Matveev et al., 2013; Niering et al., 2000; Parthey et al., 2011), the 1s–3s transition (Fleurbaey et al., 2018), the 2s–4p transition (A. Beyer et al., 2017), and the $n = 2$ Lamb shift (Bezginov et al., 2019). A more sensitive hydrogen-like system with enhanced QED effects is He^+ since the electron is stronger bound to the two-proton nucleus. Two-photon spectroscopy at 61 nm (M. Herrmann et al., 2009) and Ramsey-comb spectroscopy (Krauth et al., 2019) of the 1s–2s transition was proposed, however coherent XUV radiation is needed to excite the 30 nm transition and poses further demands on such experiments. Helium-like systems involve two electrons and their study allows to benchmark the theoretical description of the simplest case of electron correlations. For this purpose, precision spectroscopy of the two helium isotopes ^{3}He and ^{4}He was carried out between the ortho- and parastates (Rengelink et al., 2018; Rooij et al., 2011). Beyond atomic systems, molecular systems involve many-body QED effects as well. Spectroscopy of optical, vibrational, or rotational transitions in the neutral and singly charged hydrogen molecules H_2 (Altmann et al., 2018), HD (Cozijn et al., 2018), D_2 (Dickenson et al., 2013), and HD^+ (Alighanbari et al., 2018; Biesheuvel et al., 2016; Patra et al., 2017) were carried out to benchmark QED and molecular theory as well as to constrain 5th forces and extra dimensions (Biesheuvel et al., 2016; Cozijn et al., 2018; Salumbides et al., 2013). Further important atomic physics experiments with the goal to probe fundamental physics are carried out with antimatter, hybrid, and exotic systems. These include studies of the antiproton (Smorra et al., 2017, 2019; Ulmer et al., 2015) and antihydrogen (ALPHA collaboration, 2017, 2018a,b) with the primary goal to test the fundamental charge conjugation, parity transformation, and time reversal (CPT) symmetry and search for the reason of the matter-antimatter asymmetry. Hybrid matter-antimatter systems, such as antiprotonic helium (Hori, 2018), positronium $\mathrm{Ps} = \mathrm{e}^+\mathrm{e}^-$ (Cassidy, 2018), its negative ion $\mathrm{e}^-\mathrm{e}^+\mathrm{e}^-$ (Nagashima, 2014), even the molecule Ps_2 (Cassidy and Mills, 2007), and more exotic atoms of higher lepton generations such as muonium $\mu^+\mu^-$ and tauonium $\tau^+\tau^-$ (Brodsky and Lebed, 2009), can also serve for those purposes as well as for QED tests. However, handling of these systems can be very complicated, meaning that they are in cases only proposed and require unique facilities, e. g., CERN with the production capability of antiproton beams (Hori and Walz, 2013)[5]. Spectroscopy of muonic hydrogen (Antognini et al., 2013; Pohl et al., 2010), in which the electron is replaced by the short-lived but much heavier muon μ^-, a lepton of the second generation, has heralded the so-called *proton radius puzzle* as a still unsolved discrepancy between various measurements aiming at an accurate determination of the proton root-mean-square (rms) charge radius r_p. Such experiments strongly disagreed with electron-proton scattering experiments and atomic hydrogen spectroscopy. From the latter one, r_p can be extracted by a comparison with QED calculations which include the effect of the finite size of the nucleus, being the proton. Compared to ordinary atomic hydrogen, muonic hydrogen is significantly more sensitive to QED (e. g. the Lamb shift) and nuclear effects due to the much smaller Bohr radius of the orbiting μ^-. Also the rms charge radius of muonic deuterium (Pohl et al., 2016) has shown a significant deviation from the CODATA value towards a smaller magnitude. Recently, the muonic hydrogen spectroscopy found ever more support, by an independent measurement of the 2s–4p transition (A. Beyer et al., 2017), the $n = 2$ Lamb shift in ordinary atomic hydrogen (Bezginov et al., 2019), and a new electron-proton scattering experiment at the Jefferson Laboratory (Xiong et al., 2019)[6]. These results strongly suggest that the reason for the discrepancies is hidden in unknown systematic effects of the older experiments[7] and not in a fundamental difference of the interaction between the proton and leptons of different generation. This issue shows as a prime example how close nuclear and even particle physics can be linked with atomic physics.

---

[2] The QED effects discussed in this work relate exclusively to the *bound-state* QED. Therefore, the term bound-state is usually omitted in the following.

[3] Other theoretical calculations, e. g., Bilal et al. (2018) and Tupitsyn et al. (2005) do not provide an uncertainty. Their deviations from the experimental values, e. g., Draganić et al. (2003) and Egl et al. (2019), are on a comparable level as the calculations by Artemyev et al. (2013, 2007).

[4] In this sense, particles are the atomic nuclei and the electrons which mediate the covalent bond.

---

[5] FAIR, an expansion of GSI which is under construction, will provide a future second source for antiprotons (Durante et al., 2019).

[6] The proton charge radius can in principle be also calculated through lattice quantum chromodynamics (QCD), although the accuracy level is still too poor to contribute here.

Conceptually, the discussed experiments can be significantly different, since one class deals with neutral, the other one with charged systems. For the first one, experiments are done with atomic/molecular beams or in optical traps, while for the latter one, ion traps are usually employed based on the storage and control through electric and magnetic fields. For HCIs only the latter approach is feasible. As already mentioned earlier, HCIs are promising systems with a similar motivation as for muonic atoms. While for the latter ones the Bohr radius is smaller due to the larger mass of μ^-, it is smaller for HCIs owing to the larger effective nuclear charge. This results in both cases in an increased sensitivity to special relativity, QED, and nuclear effects. A specific advantage of studies of HCIs over muonic systems is the ability to systematically tune the sensitivity by varying the proton number along an isoelectronic sequence. Based on these aspects, experiments with HCIs have proven extremely valuable to benchmark our understanding of atomic theory and state-of-the-art calculations [see, e. g., Indelicato (2019), M. G. Kozlov et al. (2018), Quint and Vogel (2014), and Shabaev et al. (2018) and references therein]. A prominent example is optical spectroscopy of the $^2\mathrm{P}_{3/2}$–$^2\mathrm{P}_{1/2}$ fine-structure transition in Ar^{13+}, performed in EBITs. The comparison of the measured transition energy with advanced calculations probed contributions from QED (Draganić et al., 2003). Furthermore, the Zeeman structure of this transition was studied (Soria Orts, 2005) and the isotope shift between $^{40}\mathrm{Ar}$ and $^{36}\mathrm{Ar}$ measured and calculated (Soria Orts et al., 2007) to test the relativistic recoil effect. Notably, isotope shifts can be calculated with a smaller absolute uncertainty than the transition energy owing to the cancellation of terms which limit the theoretical uncertainty of the transition energy. Moreover, the excited-state lifetime was experimentally (Lapierre et al., 2006, 2005) and theoretically (Tupitsyn et al., 2005) studied with uncertainties small enough to be sensitive to QED contributions and interelectronic interactions. However, a persisting discrepancy of more than five standard deviations between the measurement and the calculations remains unresolved. Beyond the optical range, important experiments have tested the ground-state Lamb shift of hydrogen-like $^{238}\mathrm{U}^{91+}$ in a storage ring (Gumberidze et al., 2005) and the Lamb shift in lithium-like $^{209}\mathrm{Bi}^{80+}$ (Beiersdorfer et al., 1998), $^{238}\mathrm{U}^{89+}$ (Beiersdorfer et al., 2005), $^{141}\mathrm{Pr}^{56+}$, and beryllium-like $^{141}\mathrm{Pr}^{55+}$ (Beiersdorfer et al., 2014) in an EBIT. Another important bunch of experiments with HCIs is performed in Penning traps. HCIs can be either produced in-situ in some cases or injected from an external source, for instance an EBIT. Penning traps have been proven as excellent tools to measure their atomic magnetic moments and related g-factors (Sturm et al., 2019, 2017). Also here, a comparison with theoretical calculations tested contributions from QED to the ground-state g-factor in hydrogen-like $^{12}\mathrm{C}^{5+}$ (Häffner et al., 2000) and $^{28}\mathrm{Si}^{13+}$ (Sturm et al., 2011) as well as in lithium-like $^{28}\mathrm{Si}^{11+}$ (Wagner et al., 2013). Furthermore, nuclear effects to the g-factor were probed by comparing the ground-state magnetic moments of lithium-like $^{40}\mathrm{Ca}^{17+}$ and $^{48}\mathrm{Ca}^{17+}$ (Köhler et al., 2016). The recent measurement of the ground-state g-factor of the five-electron system boron-like $^{40}\mathrm{Ar}^{13+}$ (Arapoglou et al., 2019) particularly demonstrated the increased contribution from interelectronic interactions. Measurements of excited states are however hindered by the long measurement time in Penning traps which is typically on the order of days for such experiments.

---

[7] It should be noted that the Rydberg constant R_∞ and the proton rms charge radius r_p are heavily correlated through the comparison of the experiment with the corresponding QED calculations (Pohl et al., 2017). An error in the Rydberg constant R_∞ would also shift r_p.

3.1.1 Nuclear physics effects

Accurate spectroscopy of the atomic structure provides a window to nuclear physics. Apart from the proton number of the nucleus itself that defines the element, nuclear properties affect the atomic spectra through three main mechanisms. First, a non-zero nuclear spin, only present in nuclei with an odd number of protons and/or neutrons[8], gives the atomic system a hyperfine structure, which further splits the spectral lines through the coupling of the nuclear spin with the total angular momentum of the electrons. Second, the finite mass of the nucleus causes a recoil effect and third, the non-zero size of the nucleus slightly changes its potential around it[9]. The latter two effects have to be considered for various processes and are known as *mass shift* and *field shift*, but are typically summarized as the so-called *isotope shift*. Thereby, the electronic energy levels and atomic spectra are slightly adjusted for each isotope. In neutral and singly charged atoms isotope shifts of transition energies on the order of a few hundred MHz up to a few GHz were measured (Gebert et al., 2015; Knollmann, Patel, and Doret, 2019; Miyake et al., 2019; Shi et al., 2016). Since the electronic wave functions of HCIs are more compact, their relative overlap with the nucleus is increased. Therefore, nuclear effects are generally larger than they are in neutral or singly charged atoms, albeit the specific magnitudes significantly depend on the involved atomic structure. For instance in Ar^{13+}, the isotope shift of the $^2\mathrm{P}_{3/2}$–$^2\mathrm{P}_{1/2}$ fine-structure transition was measured to be about 1.9 GHz (Soria Orts et al., 2006). The hyperfine splittings of the 1s state in heavy hydrogen-like ions can even shift into the optical range and provide laser-accessible transitions [see, e.g., Beiersdorfer et al. (2001), Crespo López-Urrutia et al. (1998), Crespo López-Urrutia et al. (1996), Klaft et al. (1994), and Seelig et al. (1998)]. The contribution to the transition energy from the nuclear size can be on the order of several percent and allows to study nuclear properties, such as nuclear charge and magnetization distributions. However, large nuclear contributions can also impede rigorous tests of strong-field QED. Therefore, the so-called *specific*

---

[8] For nuclei which are not in the nuclear ground state, the corresponding nuclear isomer can possess a non-zero nuclear spin with an even number of protons and neutrons.

[9] For a hyperfine-structure system, this effect is described by the Breit-Rosenthal correction for the nuclear charge distribution (Rosenthal and Breit, 1932) and the Bohr-Weißkopf correction for the nuclear magnetization distribution (A. Bohr and Weisskopf, 1950).

difference between hyperfine splittings in hydrogen- and lithium-like ions was introduced, for which nuclear effects cancel. Following this idea, hyperfine collinear laser spectroscopy of $^{209}\mathrm{Bi}^{82+}$ and $^{209}\mathrm{Bi}^{80+}$ was recently performed in a storage ring and gave rise to a $7\,\sigma$ deviation of the specific difference between the measured and calculated value which became known as the *hyperfine puzzle* (Ullmann et al., 2017). Finally, the reason was found in an insufficient knowledge of the nuclear magnetic moment of $^{209}\mathrm{Bi}$ and thereby resolving the puzzle again (Skripnikov et al., 2018).

Another important topic is isotope shift spectroscopy (Gebert et al., 2015; Holliman, Fan, and Jayich, 2019; Imgram et al., 2019; Knollmann, Patel, and Doret, 2019; Miyake et al., 2019; Shi et al., 2016) in combination with a King-plot analysis (W. H. King, 1963, 1984) to test fundamental physics and search for a potentially unknown 5th force and new particles (Berengut et al., 2018; Flambaum, Geddes, and Viatkina, 2018; Frugiuele et al., 2017). An unknown interaction between the electrons of the atomic shell and the neutrons of the nucleus could be represented by the Yukawa-type potential

$$U_\phi \propto \frac{\mathrm{e}^{-\frac{m_\phi c}{\hbar} r}}{r}, \tag{3.1}$$

where m_ϕ is the mass of the unknown boson which mediates the interaction, c the vacuum speed of light, $h = 2\pi\hbar$ the Planck constant and r the modulus of the position vector of the electron under consideration. A consequence of this interaction would be a nonlinearity in the King plot. However, nonlinearities are also expected within the SM framework owing to next-to-leading order effects, such as the quadratic nuclear recoil effect (Yerokhin et al., 2020). The calculation of those nonlinearities with sufficiently low uncertainties has to be under control before studies of physics beyond the SM are enabled. The use of HCIs in isotope shift spectroscopy would offer two advantages. First, this would significantly extend the number of useful transitions due to the sheer number of different species in which the nucleus could be studied. It particularly provides the opportunity to employ significantly different atomic systems and transitions of which some can be very sensitive while others are very insensitive to King-plot nonlinearities. Second, nonlinearities which originate within the SM framework can be calculated for HCIs with much higher accuracy compared to neutral and singly charged atoms.

3.2 Variation of fundamental constants and dark matter

The Standard Model of particle physics (SM) comes with a set of 18 fundamental constants[10] (Uzan, 2011), namely six masses for the quarks, three masses for the leptons, a mass for the W, Z, and Higgs boson each, the electromagnetic coupling constant, the strong coupling constant[11], and four independent parameters of the Cabibbo–Kobayashi–Maskawa matrix, which describes the mixing of the quarks through an interaction with a W boson. One further constant might be present for describing a potential violation of the CP-symmetry in the strong interaction, but there is still no experimental evidence for that (Dobrin, 2017), though there is also no obvious reason why this symmetry should be preserved[12]. The existence of three, possibly all massive, neutrinos which show flavor oscillations (Gonzalez-Garcia and Maltoni, 2008; Wolfenstein, 1999) raises the need for up to seven further fundamental constants and, in principle, represents already an extension of the SM. This gives a total number of up to 26 fundamental constants, all being dimensionless quantities (masses are divided by the Planck mass). They cannot be calculated from first principles and, therefore, have to be measured—indeed we do not know why they have their specific magnitudes.

---

[10] There are different sets of fundamental constants which can be chosen. For instance, Yukawa coupling constants can be used instead of the quark and lepton masses.

The electromagnetic interaction is the dominant interaction for atomic physics. It binds electrons to the atomic nucleus and allows atoms to form molecules. Its strength is expressed by the electromagnetic coupling constant α, being known as the *fine-structure constant*[13]. It is linked to the elementary charge e, the vacuum permittivity ε_0, the Planck constant h, and the vacuum speed of light c through

$$\alpha = \frac{e^2}{2\,\varepsilon_0\,h\,c} \approx \frac{1}{137}\,. \tag{3.2}$$

α was introduced by Sommerfeld as a spectroscopically useful quantity to describe the fine structure of the hydrogen atom[14]. It can be precisely determined by comparing Penning trap measurements of the electron's gyromagnetic anomaly (Hanneke, Fogwell, and Gabrielse, 2008) with extensive QED calculations within the SM framework, involving more than ten thousand Feynman diagrams (Aoyama et al., 2015). More recently, α was independently measured with a matter-wave interferometer (Parker et al., 2018), in which phase differences were measured which matter waves accumulated through photon-atom interactions. The recoil energy and thereby h/m_{at} was extracted from the phase differences and allowed to determine α with known atom-to-electron mass ratio $m_{\mathrm{at}}/m_{\mathrm{e}}$ and the Rydberg constant R_∞. Importantly for this, the latter one is deeply linked to the fine-structure constant through the relation

$$R_\infty = \alpha^2\, m_{\mathrm{e}}\, \frac{c}{2\,h}\,. \tag{3.3}$$

The recommended CODATA value is $\alpha^{-1} = 137.035\,999\,084(21)$ with a fractional uncertainty of 1.5×10^{-10} (Tiesinga et al., 2019).

---

[11] The coupling constant for the weak force is calculated from the other constants.

[12] This is part of another unsolved question in the SM, known as the fine-tuning problem.

[13] In particle physics, the coupling constants depend on the energy scale on which they are measured. Per definition the fine-structure constant expresses the coupling in the zero-energy limit.

[14] For instance, α is the ratio of the electron's velocity on the first Bohr orbit in the hydrogen atom to the vacuum speed of light.

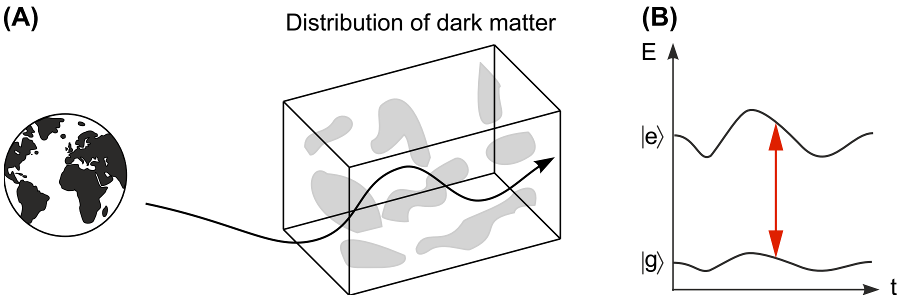

Figure 3.2: Potential variation of the fine-structure constant as a signature of dark matter. (**A**) In a simple scenario, dark matter is inhomogeneously distributed and can be described by a scalar background field. While the Earth travels through space, the background dark matter density would change with time. (**B**) A small coupling between matter and dark matter would cause the energy levels of the matter atoms to vary depending on the background dark matter density. When the coupling to the energy levels is different, also the observable transition frequency would vary with time. A comparison of two different electronic transitions could be interpreted as an apparent time variation of α.

Another important dimensionless fundamental constant in atomic physics is the proton-to-electron mass ratio (or occasionally the reciprocal as electron-to-proton mass ratio)

$$\mu = \frac{m_\mathrm{p}}{m_\mathrm{e}} \approx 1836\,. \tag{3.4}$$

The recommended CODATA value is $\mu = 1836.152\,673\,43(11)$ with a fractional uncertainty of 6×10^{-11} (Tiesinga et al., 2019). The most accurate evaluation on the 10^{-11} uncertainty level was achieved by independent Penning trap mass measurements of the proton mass m_p (Heiße et al., 2017) and the electron mass m_e (Sturm et al., 2014) with almost identical uncertainty contributions. It is noteworthy that the measurement of the electron mass was realized by measuring the atomic magnetic moment in a hydrogen-like HCI, namely $^{12}\mathrm{C}^{5+}$. A different approach determines μ by spectroscopic measurements of ro-vibrational or rotational transitions in HD^+ (Alighanbari et al., 2018; Biesheuvel et al., 2016; Patra et al., 2017) and relies on accurate QED calculations. However, the uncertainty through this approach is still almost two orders of magnitude larger.

The SM only describes 5 % of the universe—the ordinary matter (see Figure 3.1). The link to the remaining ingredients dark matter and dark energy is missing. In certain conceivable scenarios [see for instance Derevianko and Pospelov (2014)], dark matter is described by an inhomogeneous scalar background field in space as illustrated in Figure 3.2A. Assuming that a small coupling between normal and dark matter exists, electronic energy levels of atoms of the normal matter would shift while the Earth moves through this dark matter distribution (see Figure 3.2B). The corresponding electronic transitions measured in laboratories on Earth would then experience a time variation of their frequencies, provided that the coupling to the upper and lower level is different. This could be interpreted as a variation of the fine-structure constant α and therefore as a signature of dark matter.

The question whether dimensionless fundamental constants are truly constant or only to some extent, is at the heart of our understanding of nature. The reason is that an unexplained variation could imply a violation of Einstein's equivalence principle (Uzan, 2011), being the backbone of GTR. Hence, it would have strong implications to the commonly accepted standard model of cosmology, which involves dark energy and cold dark matter and is known as the ΛCDM model. If an additional field is identified as explanation for the variation, the obvious consequence were that the current SM is not complete. Although the SM is undisputably a success story, as for instance recently demonstrated by the observation of the predicted Higgs boson (ATLAS collaboration, 2012), it is also clear that extensions to it are required to answer many still-open questions. These deal in particular with the evolution of the early universe, where the energy scales involved were much higher than those on which we can test the SM with our most powerful particle accelerators. Indeed, fundamental constants appear to be constant on relevant scales for humankind, but there is no good reason to assume this to be a given axiom. Extensions of the SM and the GTR and also a more general concept of an underlying theory, for instance quantum gravity, allow for or even suggest a variation of fundamental constants [see, e. g., Calmet and M. Keller (2015), Dent, Stern, and Wetterich (2008), Uzan (2003, 2011), and Wetterich (2003) and references therein].

Experimentally, a possible time variation of fundamental constants can be investigated in very different systems [see for example the review by Uzan (2011)], for instance through astronomical observations. Webb et al. (2011) reported on an extensive survey which evaluated so-called *quasar absorption spectra*. The data was taken with two observatories—the Keck telescope in Hawaii and the Very Large Telescope in Chile—probing different directions of the universe. Quasars were used as distant light sources that backlit gas clouds of the interstellar or intergalactic medium in which absorption of the quasar radiation took place. The resulting atomic absorption spectra were observed on Earth at high redshifts owing to the large distance to the gas clouds. After accounting for effects from all conceivable physical properties of the gas clouds, residual shifts of the absorption lines were attributed to a possible spatial variation of the fine-structure constant. Finally, the evaluation indicated a spatial dipole variation of α, which became known as the *Australian dipole*. A few years later, Whitmore and Murphy (2015) discussed systematic errors which were previously not considered and might weaken this indication. Dumont and Webb (2017) objected again. Thus far, a clear conclusion is still pending. Similarly, also a possible variation of the proton-to-electron mass ratio is studied through astronomical observations of molecular spectra of H_2 (Reinhold et al., 2006; Ubachs et al., 2016) or even larger molecules (Bagdonaite et al., 2013; Ubachs, 2017). In contrast to these examples, laboratory studies can only probe a potential variation of fundamental constants at much smaller scales of time and space compared to these cosmological ones. However, owing to a much higher precision and accuracy, stringent constraints can be inferred through laboratory spectroscopy which is carried out on a time scale of years and is addressed in the next section.

3.2.1 Atomic clocks as detectors

While the uncertainty of the absolute value of the fine-structure constant α (proton-to-electron mass ratio μ) is currently limited to the 10^{-10} (10^{-11}) uncertainty level, a variation can be constrained to a much lower level. This is feasible owing to the significantly lower uncertainty levels achieved in frequency metrology. Accurate QED calculations on a comparable level are not required for such studies. In laboratory experiments the constancy of fundamental constants is monitored through the frequency of clock transitions, or more exactly the ratio of such frequencies which can be measured in the best cases on the 10^{-18} uncertainty level for optical clocks. In general, transitions depend differently on the magnitude of fundamental constants. However, optical electronic transitions in particular depend purely on the fine-structure constant and can be used for exclusive tests of the constancy of α. The most stringent constraint from a single optical clock comparison was obtained by Rosenband et al. (2008) as

$$\frac{\dot{\alpha}}{\alpha} = -1.6(23) \times 10^{-17}\,\mathrm{yr}^{-1}\,. \tag{3.5}$$

Hyperfine-structure transitions, such as employed in today's microwave clocks based on, e. g., ^{133}Cs (Weyers et al., 2018) or ^{87}Rb (Guéna et al., 2014), in contrast depend on the product of the nuclear magnetic moment and the electron mass. This can be rewritten as a dependence on the proton-to-electron mass ratio μ and the nuclear g-factor. The latter one relates to the light-quark masses with respect to the QCD energy scale and, therefore, to the strong interaction (M. G. Kozlov et al., 2018; M. S. Safronova et al., 2018; M. S. Safronova, 2019). Combined measurements with microwave clocks are therefore suitable to study the constancy of μ and nuclear g-factors [for the latter one see, e. g., M. S. Safronova et al. (2018) and references therein for details]. Combined measurements of several clock comparisons including microwave clocks (Godun et al., 2014; Huntemann et al., 2014) thus yielded the most stringent limits for a temporal variation of both, the fine-structure constant and the proton-to-electron mass ratio[15] as

$$\frac{\dot{\alpha}}{\alpha} = -2.0(20) \times 10^{-17}\,\mathrm{yr}^{-1} \tag{3.6a}$$

$$\frac{\dot{\mu}}{\mu} = 0.2(11) \times 10^{-16}\,\mathrm{yr}^{-1}\,. \tag{3.6b}$$

---

[15] Ultracold molecules are also highly sensitive and promising systems for testing the constancy of μ without invoking nuclear models since they directly involve inertial masses. However, constraints are two orders of magnitude weaker (Kobayashi, Ogino, and Inouye, 2019) than those from atomic clock comparisons.

How sensitive a transition to possible changes of fundamental constants is, can be theoretically estimated through the calculation of the transition energies by varying the constants in the computation. A useful uncertainty on the order of 1–10 % is typically obtained (M. S. Safronova, 2019). In the case of α, the two sensitivity factors q and K are usually employed (M. G. Kozlov et al., 2018; M. S. Safronova et al., 2018) based on the (linearized) relation

$$f = f_0 + q \cdot \frac{2\,(\alpha - \alpha_0)}{\alpha_0} \quad \Leftrightarrow \quad \frac{\Delta f}{f_0} = \underbrace{\frac{2q}{f_0}}_{=:\,K} \cdot \frac{\Delta \alpha}{\alpha_0}\,, \tag{3.7}$$

where f is the current transition frequency, $\Delta f = f - f_0$ and $\Delta\alpha = \alpha - \alpha_0$ respectively, and the index 0 refers to the common reference point. The definition of q is not consistent in the literature since it possesses a unit and can be related to the energy, frequency, or angular frequency of an electronic state or an electronic transition[16]. In contrast, the dimensionless sensitivity factor K links the relative change of α to the relative change of the transition frequency f. When comparing q and K factors, the type of transition must be considered, since optical transitions can be measured to much higher accuracy and precision. Therefore, microwave transitions must have significantly higher K factors compared to optical transitions in order to compete for time-variation tests of α. Expressed in terms of K, one obtains for the measurement of a frequency ratio

$$\frac{\Delta\,(f_1/f_2)}{(f_1/f_2)_0} = (K_1 - K_2)\,\frac{\Delta\alpha}{\alpha_0}\,. \tag{3.8}$$

Typical values for K are summarized in Table 2.1 for various atomic clock systems. Recently, the community became aware that HCIs are promising systems for such tests. Many systems have been proposed in the last few years with large K factors (Bekker et al., 2019; Berengut, Dzuba, and Flambaum, 2010, 2011; Berengut et al., 2011, 2012a,b; Dzuba, Derevianko, and Flambaum, 2012b; Dzuba, Flambaum, and Katori, 2015; Dzuba et al., 2015; Nandy and Sahoo, 2016; Oreshkina et al., 2017; M. S. Safronova et al., 2014a,b,c; U. I. Safronova, Flambaum, and M. S. Safronova, 2015; Schiller, 2007). In particular, level crossing transitions are exceptionally sensitive. The reason for the high sensitivity lies in enhanced relativistic effects, particularly for heavy HCIs with a correspondingly large proton number and a large ionization energy. Additionally, the sensitivity is increased for a significant change in the involved electronic wave functions with respect to their quantum numbers and for nearly-filled shells (Berengut et al., 2012a). A proposed model system is Ir^{17+} (Berengut et al., 2011) which should offer a K factor about two orders of magnitude larger than for all evaluated neutral or singly charged atomic systems (see Table 2.1). Also hyperfine-structure transitions are interesting, since they can shift into the optical range in HCIs, which would also allow for sensitive tests of a potential time variation of μ and nuclear g-factors. Applications of HCIs for such fundamental physics studies were recently reviewed by M. G. Kozlov et al. (2018).

---

[16] Here, q refers to the electronic transition (Equation 3.7) and represents the differential sensitivity of both involved electronic states.

As discussed in the previous Section 3.2, the variations of fundamental constants can be closely linked to a coupling between dark and normal matter. Thus, atomic clocks can serve as sensitive detectors for dark matter. In particular, whole networks of clocks were proposed for this purpose to increase the sensitivity (Derevianko, 2018). Apart from a slow continuous drift (Stadnik and Flambaum, 2015), variations can in principle happen on different time scales. Oscillations (Arvanitaki, Huang, and Van Tilburg, 2015; Stadnik and Flambaum, 2015, 2016), owing to a scalar bosonic field which oscillates with the Compton frequency of the particle that mediates the coupling, or step changes (Derevianko and Pospelov, 2014; Kouvaris et al., 2019; Roberts et al., 2017), caused by macroscopic dark matter objects such as topological defects (monopoles, strings, or domain walls) or boson stars, could happen as well. Constraints were evaluated also for such scenarios (Roberts et al., 2020; Van Tilburg et al., 2015).

3.3 Lorentz violation

Another fundamental physics application of atomic clock experiments, which shall only briefly mentioned here, addresses tests of Einstein's theory of relativity [see for details Ludlow et al. (2015), M. S. Safronova et al. (2018), and references therein]. As the foundation, Einstein's equivalence principle postulates the universality of free fall, local Lorentz invariance (LLI), and local position invariance (LPI). LLI relates to the independence of a (local) experiment from velocity or orientation, whereas LPI refers to the independence of the position in a certain gravitational potential. Studies of Lorentz violation are therefore strongly motivated, since a violation would directly imply new physics and set bounds for the development of an underlying quantum field theory of gravity (M. S. Safronova et al., 2018). Atomic clock comparisons are ideal experiments for such tests. While LPI can be probed by operating a clock in a spacecraft, LLI can be tested with high accuracy in laboratories on Earth. Recently, LLI was confirmed on the 10^{-21} uncertainty level by an optical clock comparison (Sanner et al., 2019). This result even exceeded the confirmation on the 10^{-19} uncertainty level which was also recently achieved with a $^{40}\mathrm{Ca}^{+}$ trapped-ion experiment (Megidish et al., 2019). Apart from the use of singly charged ions as done in these experiments, also HCIs were suggested. They offer a particularly high sensitivity to a possible violation of LLI (Bekker et al., 2019; M. G. Kozlov et al., 2018; Shaniv, Ozeri, et al., 2018).

4 Thesis outline

Part I of this thesis addressed two different fields of atomic physics: physics with highly charged ions (HCIs) and the field of (optical) frequency metrology and atomic clocks. A stunning number of HCI proposals and theoretical studies for their use in frequency metrology has been published in the last decade, most of them mentioned here. They all follow the idea to make use of the excellent properties of HCIs for the development of novel optical clocks and the exploration of fundamental physics. However, the first experiment which would be able to realize one of these proposals was missing until recently. This thesis reports on that first experiment which demonstrated the successful application of common techniques used in frequency metrology for unprecedented spectroscopy of HCIs.

In Part II of this thesis, some background for this work is detailed and provides relations and equations, which are used later on. Even so, Part II cannot give a full compilation of all the physics involved in the experiment but rather focuses on some specific aspects. More details and a deeper discussion are found in the corresponding literature.

Part III introduces the experimental setup. The focus lies on the production, transfer, isolation, and preparation of a single HCI as well as the implementation of ground-state cooling of the two-ion crystal $^{40}\mathrm{Ar}^{13+}$–$^{9}\mathrm{Be}^{+}$ and quantum logic spectroscopy (QLS) with an ultrastable clock laser. This part is closely linked to two previous works: Schmöger (2017) demonstrated methods for the HCI transfer, recapture, and sympathetic laser cooling in the Cryogenic Paul Trap Experiment (CryPTEx) of the Max-Planck-Institut für Kernphysik (MPIK), and Leopold (2018) set up the cryogenic Paul trap at the Physikalisch-Technische Bundesanstalt (PTB) used in this work and implemented full coherent control of $^{9}\mathrm{Be}^{+}$ ions in the optical and microwave regime, including single-ion ground-state cooling of all motional modes and a thorough characterization of the setup by means of $^{9}\mathrm{Be}^{+}$ spectroscopy.

The results of this thesis are summarized in Part IV. Employing cutting-edge techniques as used in frequency metrology, the first coherent laser spectroscopy of cold HCIs is demonstrated. Optical Rabi spectroscopy of the Zeeman structure of the electric-dipole-forbidden ground-state fine-structure transition in $^{40}\mathrm{Ar}^{13+}$ is presented and measurements of the excited-state g-factor and lifetime are shown. This kind of novel HCI spectroscopy constitutes an improvement upon the precision of the previous state-of-the-art in-EBIT spectroscopy (Draganić et al., 2003; Soria Orts et al., 2006) by about eight orders of magnitude and by more than six orders of magnitude over the recently published laser spectroscopy in a Penning trap (Egl et al., 2019), which was performed in parallel to this work.

Part V concludes this work and gives an outlook about a possible future roadmap of the experiment.

During the work of this thesis, four articles have been published in peer-reviewed journals, describing various parts of the experiment. This thesis intends to provide additional information to these publications and to arrange them in a more general context of this work. The content of the articles is however not repeated in detail. Instead, they are referred to in the text where appropriate. Copies are included in the Appendix.

Part II

Background

> *Das Spektrum eines beliebigen Atoms ist sehr ähnlich dem Spektrum des einfach positiv geladenen Atoms, das im Periodischen System folgt.*
> (The spectrum of any atom is very similar to the spectrum of the singly charged atom that follows in the periodic table.)
>
> — W. Kossel, A. Sommerfeld
> Spektroskopischer Verschiebungssatz
> (Sommerfeld–Kossel displacement law)

The second part of this thesis provides some basic background on the reported experiment. Chapter 5 introduces the atomic systems $^{40}\mathrm{Ar}^{13+}$ and $^{9}\mathrm{Be}^{+}$. In Chapter 6 the two ion traps used in this work, an electron beam ion trap (EBIT) and a Paul trap, are briefly discussed. Finally, Chapter 7 deals with the interaction between light and atoms. Three different coordinate frames are introduced in these chapters, namely the laboratory frame (x, y, z), the Paul trap frame $(\tilde{x}, \tilde{y}, z)$, and the atomic frame (x', y', z'). The purpose of this part is to assist understanding of the experimental concepts and to provide equations and relations for later reference. Still, it is not intended to cover all background needed, which can be found in the respective textbooks and literature.

5 The atomic systems

This work involves two specific atomic systems—boron-like $^{40}\mathrm{Ar}^{13+}$ and lithium-like $^{9}\mathrm{Be}^{+}$—which are being discussed in this chapter. $^{40}\mathrm{Ar}^{13+}$ was chosen to demonstrate for the first time coherent laser spectroscopy of highly charged ions (HCIs) in general. It is therefore referred to as the *spectroscopy ion*. $^{9}\mathrm{Be}^{+}$ is deeper linked to this experiment since it serves as the indispensable auxiliary ion species to implement laser cooling and the spectroscopy technique known as quantum logic spectroscopy (QLS), even when the HCI species is changed in the future. It is referred to as the *logic ion*.

Before both atomic systems are introduced, the Zeeman effect shall be briefly addressed again. Known for more than 120 years, this effect is of crucial importance to implement modern atomic physics experiments and applies to both ion species equally. In this work, a homogeneous and static magnetic field of about $160\,\mu\mathrm{T} = 1.6\,\mathrm{G}$ is applied with external coils in order to define a quantization axis and thereby the atomic coordinate frame (x', y', z'). This magnetic quantization field with flux density B separates the electronic energy levels of the Zeeman substates with total angular momentum numbers J or $F \neq 0$ for fine and hyperfine structure, respectively. For weak magnetic fields the splittings between the substates are equidistant with energy shifts of $\Delta E_{\mathrm{Zeeman}} = m\,g\,\mu_{\mathrm{B}}\,B$ (Equation 2.6), being linear in the magnetic quantum numbers m and the magnetic flux density B. The g-factor g describes the sensitivity of the electronic state to the linear Zeeman shift. Since m and g are on the order of 1, the Bohr magneton $\mu_{\mathrm{B}} = (e\hbar)/(2m_{\mathrm{e}}) \approx h \times 1.4\,\mathrm{MHz\,G}^{-1}$ sets the order of magnitude for the energy shifts. As a result, the Zeeman shifts in this work are on a MHz level, and the corresponding Zeeman substates can be addressed individually with narrow-linewidth lasers. In contrast, B cannot be considered small anymore when the internal splittings, owing to fine or hyperfine structure, are not large against the Zeeman shift—then this weak field limit breaks down and the energy shifts of the Zeeman substates are not linear anymore in m and B (cf. the second-order Zeeman shift in Equation 2.7). Depending on the magnitude of the external magnetic field, the internal magnetic moments of the atom are partially decoupled or even fully decoupled in the strong-field limit, known as the Paschen-Back effect. For instance, the hyperfine splitting of the $^{2}\mathrm{P}_{3/2}$ state in $^{9}\mathrm{Be}^{+}$ is on the order of 5 MHz while the calculated linear Zeeman shifts would also be on a comparable level in the $160\,\mu\mathrm{T}$ magnetic field. Indeed in this case, the total angular momentum quantum number F is not a good quantum number anymore and cannot be used to describe the $^{9}\mathrm{Be}^{+}$ $^{2}\mathrm{P}_{3/2}$ state. The Zeeman effect is classified into a normal (with total electronic spin $S = 0$) and an anomalous effect. Both atomic systems of this work, $^{40}\mathrm{Ar}^{13+}$ and $^{9}\mathrm{Be}^{+}$, are spin-½ systems and therefore feature the anomalous Zeeman effect.

Table 5.1: Ionization energies of highly charged argon. The left column gives the charge state and the right column states the minimum energy needed to produce the next charge state. For example to produce Ar^{13+} an energy of at least 686 eV is required. A large step appears when the next closed shell is reached, as shown for He-like Ar^{16+}. A binding energy of more than 4 keV has to be overcome in order to produce H-like Ar^{17+}. Energies from the ASD (Kramida et al., 2019).

Charge state	Ionization energy (eV)
0	16
+5	91
+10	540
+11	619
+12	686
+13	755
+14	856
+15	918
+16	4121
+17	4426

5.1 Spectroscopy ion $^{40}\mathrm{Ar}^{13+}$

$^{40}\mathrm{Ar}^{13+}$ was chosen for this work to demonstrate QLS with HCIs. The main reason was the fact that it offered the most accurately known transition in any HCI with a $1\,\sigma$ uncertainty of about 154 MHz (Draganić et al., 2003; Soria Orts et al., 2006). This came with two advantages: first, the time needed to find the E1-forbidden transition with a natural linewidth of 17 Hz with a Hz-narrow clock laser was expected to be acceptable. Second, the most accurately known transition would be an excellent benchmark to demonstrate the potential of QLS for HCIs in general. Other advantages certainly are that argon is easy to handle in the laboratory, offers a high natural abundance of 99.6 % of the isotope $^{40}\mathrm{Ar}$ and features a ‘clock’ transition wavelength of 441 nm in the optical range which is easily accessible with a frequency-doubled diode laser. To generate the required charge state $Z_{\text{ion}} = +13$, high binding energies have to be overcome as shown in Table 5.1. This is experimentally accomplished by means of a keV electron beam and will be discussed later in Section 6.1 and Chapter 9 [see also Micke et al. (2018) in Appendix P1].

Boron-like Ar^{13+} is a five-electron system with a single valence electron. It has an electronic ground-state configuration of $1\mathrm{s}^2 2\mathrm{s}^2 2\mathrm{p}^1$ with the ground state $^2\mathrm{P}_{1/2}$. The nuclei of all stable isotopes have an even number of protons and neutrons, therefore no nuclear spin and thus no hyperfine structure exists. The first excited state is the $^2\mathrm{P}_{3/2}$ state, which is linked through an E1-forbidden fine-structure transition to the ground state. The transition wavelength of 441 nm is shifted into the optical range for Ar^{13+} owing to the high charge state, whereas this transition is in the very far infrared at 654 µm in neutral boron. The Zeeman structure of this transition is shown in Figure 5.1 with the non-relativistic Landé g_J-factors, which can be calculated according to

$$g_J \approx \frac{3}{2} + \frac{S\,(S+1) - L\,(L+1)}{2J\,(J+1)} \tag{5.1}$$

with the orbital g-factor $g_L = 1$ and the approximation for the spin g-factor $g_S \approx 2$. L is the orbital angular momentum quantum number, S the spin angular momentum quantum number, and J the total electronic angular momentum quantum number. According to Equation 2.6 the spacing between two adjacent Zeeman components of this $^2\mathrm{P}_{1/2}$–$^2\mathrm{P}_{3/2}$ transition with $\Delta(m_J g_J) = 2/3$ (see Figure 5.1) calculates to

$$\frac{\Delta E}{B}\,[\Delta(m_J g_J) = 2/3] \approx h \times 0.933\,\mathrm{MHz\,G}^{-1}\,. \tag{5.2}$$

The transition is by far dominated by its magnetic-dipole (M1) transition amplitude, being five orders of magnitude larger than the next largest amplitude of the E2 contribution (Bilal et al., 2018; C. F. Fischer, 1983). Theoretical calculations of the transition energy, transition probability, and the excited-state lifetime were carried out (Artemyev et al., 2013, 2007; Bilal et al., 2018; Soria Orts et al., 2006; Tupitsyn et al., 2005), of the isotope shift (Nazé et al., 2014; Soria Orts et al., 2006; Zubova et al., 2016), as well as of the ground-state and excited-state g-factors (Agababaev et al., 2018, 2019; Arapoglou et al., 2019; Glazov et al., 2013; Maison, Skripnikov, and Glazov, 2019; Marques et al., 2016; Shchepetnov et al., 2015; Verdebout et al., 2014). Also, higher-order Zeeman effects were calculated in perturbation theory. Predictions for the quadratic Zeeman shift in magnetic fields at the T level (Agababaev et al., 2017; Glazov et al., 2013; D. v. Lindenfels et al., 2013; Varentsova et al., 2018) imply that for the 160 μT quantization field as used in this work, the shift would be on the mHz level. Experimentally, the transition energy has a long measurement history (Bieber et al., 1997; Draganić et al., 2003; Edlén, 1982; Egl et al., 2019; Lyot and Dollfus, 1953; Mäckel et al., 2011, 2013; Morgan et al., 1995; Soria Orts et al., 2007, 2006). Also the excited-state lifetime was previously measured (Lapierre et al., 2006, 2005; Serpa, J. D. Gillaspy, and Träbert, 1998; Träbert et al., 2000), the ground-state g-factor (Arapoglou et al., 2019; Soria Orts et al., 2007), the excited-state g-factor (Egl et al., 2019; Soria Orts et al., 2007), and the isotope shift between $^{40}\mathrm{Ar}^{13+}$ and $^{36}\mathrm{Ar}^{13+}$ (Soria Orts et al., 2006).

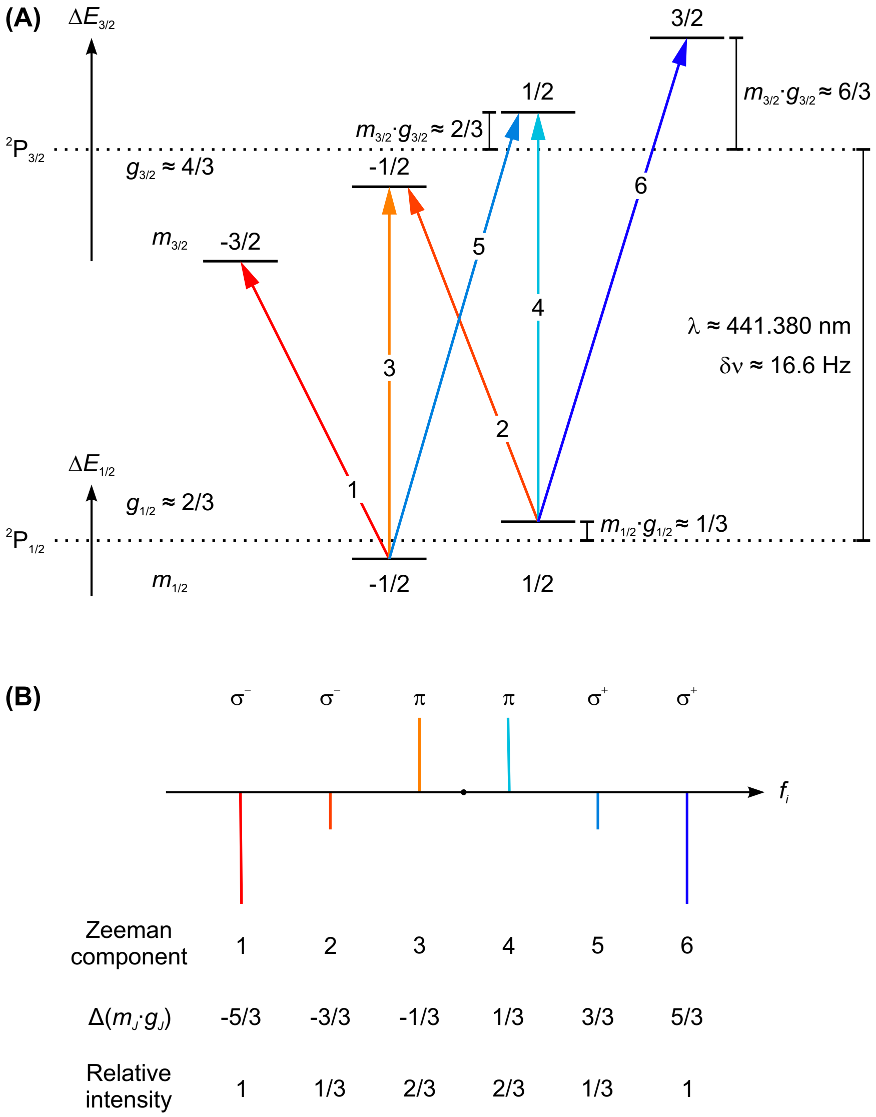
(A)
ΔE_3/2
3/2
1/2
$m_{3/2}\cdot g_{3/2} \approx 6/3$
$m_{3/2}\cdot g_{3/2} \approx 2/3$
$^2P_{3/2}$
$g_{3/2} \approx 4/3$
-1/2
6
$m_{3/2}$
-3/2
5
4
λ ≈ 441.380 nm
3
δν ≈ 16.6 Hz
2
ΔE_1/2
$g_{1/2} \approx 2/3$
1
$m_{1/2}\cdot g_{1/2} \approx 1/3$
$^2P_{1/2}$
$m_{1/2}$
-1/2
1/2
(B)
σ⁻
σ⁻
π
π
σ⁺
σ⁺
f_i

Zeeman component	1	2	3	4	5	6
$\Delta(m_J \cdot g_J)$	-5/3	-3/3	-1/3	1/3	3/3	5/3
Relative intensity	1	1/3	2/3	2/3	1/3	1

Figure 5.1: Kastler diagram and Zeeman transitions of ^{40}Ar^{13+}. (**A**) Level diagram of the ^{2}P$_{1/2}$–^{2}P$_{3/2}$ ground-state fine-structure transition at a transition wavelength of $\lambda = 441.380\,$nm in vacuum [corresponding to a transition wavelength of $\lambda_{\text{air}} = 441.256\,$nm in air (Draganić et al., 2003; Soria Orts et al., 2006)]. The two ^{2}P$_{1/2}$ Zeeman substates and four ^{2}P$_{3/2}$ Zeeman substates are separated by a small magnetic quantization field in accordance with the linear Zeeman shift (see Equation 2.6). Note that the given Landé g_J-factors and splittings are the non-relativistic predictions. The excited-state lifetime is $\tau \approx 9.57\,$ms and corresponds to a transition rate of $1/\tau = 2\pi \times \delta\nu = 104.5\,\text{s}^{-1}$ (Bilal et al., 2018; Lapierre et al., 2006; Tupitsyn et al., 2005), with the natural linewidth $\delta\nu$. (**B**) Zeeman components which are observed from this transition, following the convention of π components above and σ components below the horizontal line. The heights of the vertical lines correspond to the observed relative intensities of the Zeeman components (squared Clebsch-Gordan coefficients). Note that the notation π and σ refers to the change of the magnetic quantum number m and that the polarization of the electromagnetic radiation is different for M1 transitions compared to E1 transitions (see Section 7.1 for details). $\Delta(m_J g_J) = m_{3/2} g_{3/2} - m_{1/2} g_{1/2}$ corresponds to the differential shifts of the Zeeman components.

5.2 Logic ion $^9\mathrm{Be}^+$

QLS relies on a second ion species which offers a suitable level structure for extensive quantum control. In particular, QLS of HCIs requires a high charge-to-mass-ratio of that ion species in order to approximate the charge-to-mass-ratio of a typical HCI for enhanced motional coupling of both ions in an ion trap. $^9\mathrm{Be}^+$ is an excellent species for both demands with its relevant electronic level structure shown in Figure 5.2. Specifically, a fast cycling transition (orange) and a long-lived *qubit* transition (red) are required. The latter one is a forbidden and narrow transition, which can be still quickly manipulated by means of a strong coupling mechanism. The idea behind the name qubit is the ability to store binary information in either ground state $|\downarrow\rangle \equiv |0\rangle$ or excited state $|\uparrow\rangle \equiv |1\rangle$. The long lifetime guarantees that this information is preserved. Both transitions share the same ground state and thereby enable electron shelving with nearly unity detection efficiency. The fast cycling transition allows for Doppler cooling and the qubit transition for resolved sideband cooling beyond the Doppler cooling limit in order to access the quantum-mechanical ground state of motion.

Lithium-like $^9\mathrm{Be}^+$ is a three-electron system with the electron configuration $1\mathrm{s}^2 2\mathrm{s}^1$. The wave function of the ground state $^2\mathrm{S}_{1/2}$ is tighter bound to the nucleus in comparison to the two excited fine-structure states $^2\mathrm{P}_{1/2}$ and $^2\mathrm{P}_{3/2}$, which reduces screening through the inner two $1\mathrm{s}^2$ electrons. As a consequence, the $^2\mathrm{S}_{1/2}$ state lies much lower than the P states, linked to both via electric-dipole (E1) transitions at 313 nm. As for all alkali(-like) atomic systems, these transitions are denoted as *D-lines*, named by Fraunhofer himself, and appear as the doublet D_1 and D_2 corresponding to the $^2\mathrm{P}_{1/2}$ and $^2\mathrm{P}_{3/2}$ states, respectively. The nuclear spin of $I = 3/2$ results in a hyperfine structure as also shown in Figure 5.2. This hyperfine structure is typically three orders of magnitude smaller than the fine structure[1] and is characterized by the total angular momentum numbers F. The corresponding electronic structure was extensively studied in theory and experiment [see, e. g., Bollinger et al. (1985), Nörtershäuser et al. (2009), Nörtershäuser et al. (2015), Puchalski and Pachucki (2009), U. I. Safronova and M. S. Safronova (2013), Vetter et al. (1976), Wineland, Bollinger, and Itano (1983), and Yerokhin (2008)] and can be calculated from the magnetic-dipole and electric-quadrupole hyperfine constants $\mathcal{A}$ and $\mathcal{B}$ according to

$$\Delta E_{\mathrm{hfs}} = \frac{\mathcal{A}}{2} \cdot \mathcal{C} + \mathcal{B} \cdot \frac{\frac{3}{4} \cdot \mathcal{C}\,(\mathcal{C}+1) - I\,(I+1) \cdot J\,(J+1)}{2I\,(2I-1) \cdot J\,(2J-1)} \tag{5.3}$$

with

$$\mathcal{C} = F\,(F+1) - I\,(I+1) - J\,(J+1)\,, \tag{5.4}$$

---

[1] The reason is that the nuclear magneton is three orders of magnitude smaller than the Bohr magneton, owing to the proton-to-electron mass ratio.

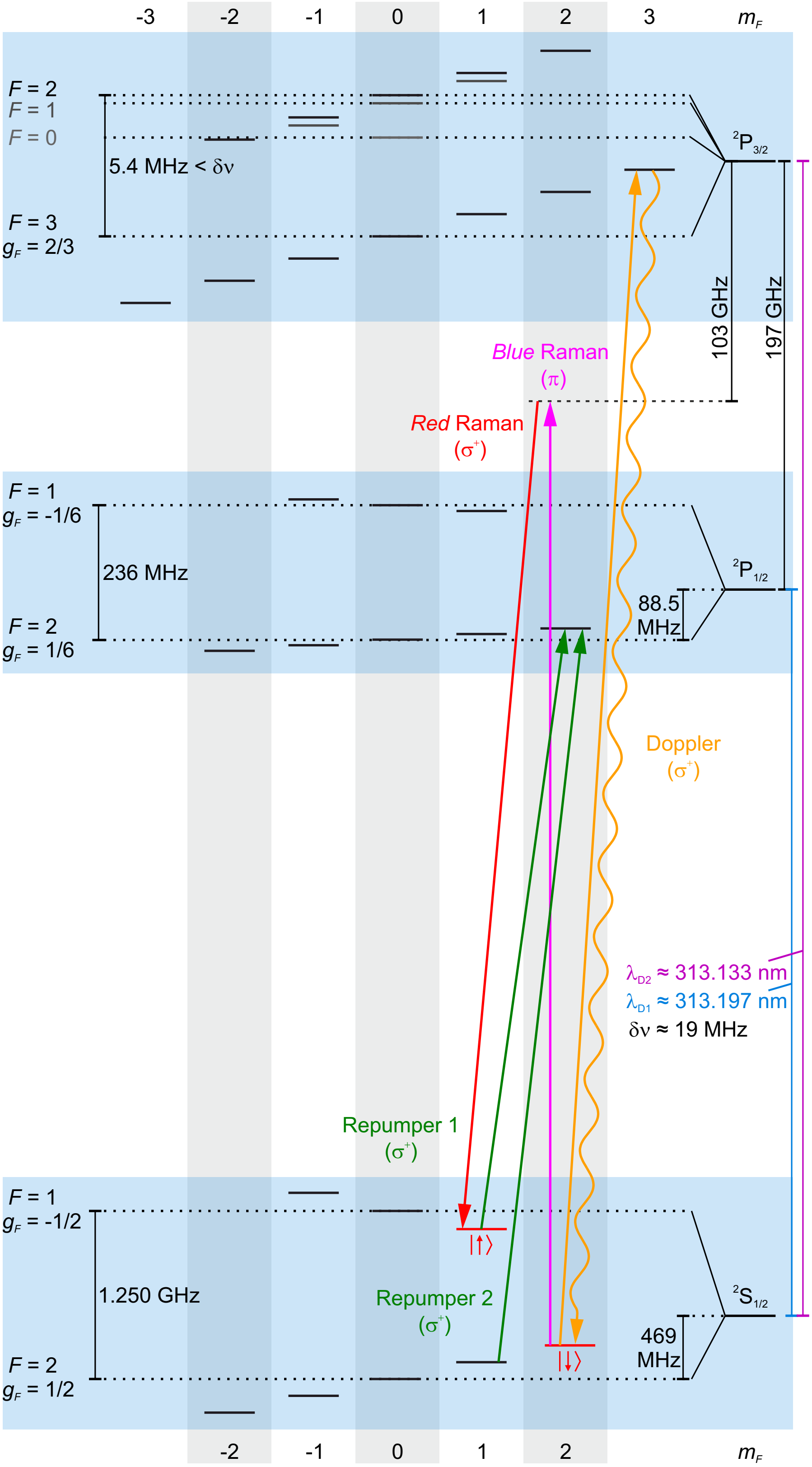
-3 -2 -1 0 1 2 3 m_F
$F = 2$
$F = 1$
$F = 0$
5.4 MHz < δν
$F = 3$
$g_F = 2/3$
$^2P_{3/2}$
103 GHz
197 GHz
Blue Raman
(π)
Red Raman
(σ^+)
$F = 1$
$g_F = -1/6$
236 MHz
$^2P_{1/2}$
88.5 MHz
$F = 2$
$g_F = 1/6$
Doppler
(σ^+)
$\lambda_{D2} \approx 313.133$ nm
$\lambda_{D1} \approx 313.197$ nm
δν ≈ 19 MHz
Repumper 1
(σ^+)
$F = 1$
$g_F = -1/2$
$|\uparrow\rangle$
1.250 GHz
Repumper 2
(σ^+)
$^2S_{1/2}$
469 MHz
$|\downarrow\rangle$
$F = 2$
$g_F = 1/2$
-2 -1 0 1 2 m_F

Figure 5.2: Kastler diagram of $^9\mathrm{Be}^+$ in the limit of a weak magnetic quantization field. The ground state $^2\mathrm{S}_{1/2}$ and the fine-structure states $^2\mathrm{P}_{1/2}$ and $^2\mathrm{P}_{3/2}$ are shown (highlighted in blue) with their hyperfine structure owing to the nuclear spin of $I = 3/2$. All wavelengths λ stated in vacuum. $\delta\nu$ is the natural linewidth. Non-relativistic g_F-factors are given with the approximation that $g_I \ll g_J$. For the $^2\mathrm{P}_{3/2}$ state, it is $g_F = 2/3$ for all $F \neq 0$ hyperfine states. Levels are not to scale. See text for further details.

State	$\mathcal{A}$ (MHz)	$\mathcal{B}$ (MHz)	Reference
^{2}S$_{1/2}$	$-625.008\,837\,048(10)$	0	Wineland, Bollinger, and Itano (1983)
^{2}P$_{1/2}$	$-118.00(4)$	0	Nörtershäuser et al. (2009)
^{2}P$_{3/2}$	$-1.026(3)$	$-2.299\,40(3)$	Puchalski and Pachucki (2009)

Table 5.2: Hyperfine constants of ^{9}Be$^+$. The references for the ^{2}S$_{1/2}$ and ^{2}P$_{1/2}$ states are measurements, whereas the hyperfine constants of the ^{2}P$_{3/2}$ state are based on theoretical calculations. Note that for the ^{2}P$_{3/2}$ state also other independent calculations exist (Yerokhin, 2008). Deviations are sufficienty small that they have no relevance here.

where ΔE_{hfs} is the additional energy shift for the hyperfine state with total angular momentum quantum number F from the fine structure energy. J and I are the quantum numbers for the total electronic angular momentum and the nuclear spin, respectively. The hyperfine constants are shown in Table 5.2 for the respective states. Note that for the $J = 1/2$ states no electronic electric-quadrupole moment exists and, therefore, $\mathcal{B} \equiv 0$. Also, the non-relativistic Landé g_F-factors can be calculated from the involved quantum numbers L, S, J, I, and F as

$$g_F \approx g_J \cdot \frac{F\,(F+1) - I\,(I+1) + J\,(J+1)}{2F\,(F+1)} \tag{5.5}$$

with the approximation of a vanishing nuclear g-factor with respect to the total electronic g-factor ($g_I \ll g_J$) and g_J calculated from Equation 5.1. A useful quantity for the ^{2}S$_{1/2}$ ground state is again the spacing between two adjacent Zeeman components of the hyperfine transition $|^2\mathrm{S}_{1/2}, F = 2\rangle$–$|^2\mathrm{S}_{1/2}, F' = 1\rangle$ which calculates according to Equation 2.6 as

$$\frac{\Delta E}{B}\,[\Delta(m_F\,g_F) = 1/2] \approx h \times 0.7\,\mathrm{MHz\,G^{-1}}\,. \tag{5.6}$$

Red-detuned Doppler cooling and on-resonance detection is performed with the Doppler cooling beam (straight orange line in Figure 5.2) on the $|^2\mathrm{S}_{1/2}, F = 2, m_F = 2\rangle$–$|^2\mathrm{P}_{3/2}\rangle$ σ^+-transition. This is a closed-cycling transition and therefore the upper state decays only into the same initial Zeeman substate (wavy orange line). The Doppler cooling beam together with a repumper beam (green, referred to as repumper 1), addressing the $|^2\mathrm{S}_{1/2}, F = 1\rangle$–$|^2\mathrm{P}_{1/2}, F' = 2\rangle$ σ^+-transition, serve for initial optical pumping of all Zeeman substates of the ^{2}S$_{1/2}$ ground state into $|^2\mathrm{S}_{1/2}, F = 2, m_F = 2\rangle$ thanks to the sufficiently broad upper P states. The qubit (red) is realized through the 1.25 GHz hyperfine splitting of the ^{2}S$_{1/2}$ ground state as $|^2\mathrm{S}_{1/2}, F = 2, m_F = 2\rangle$–$|^2\mathrm{S}_{1/2}, F' = 1, m_{F'} = 1\rangle$ and is driven by stimulated Raman transitions with two Raman beams and a common detuning of 103 GHz from the ^{2}P$_{3/2}$ state. The Raman beam displayed in pink operates at the higher frequency and is therefore referred to as the *blue Raman beam*. It has an appropriate polarization in order to induce a π-transition. Thus, the other Raman beam

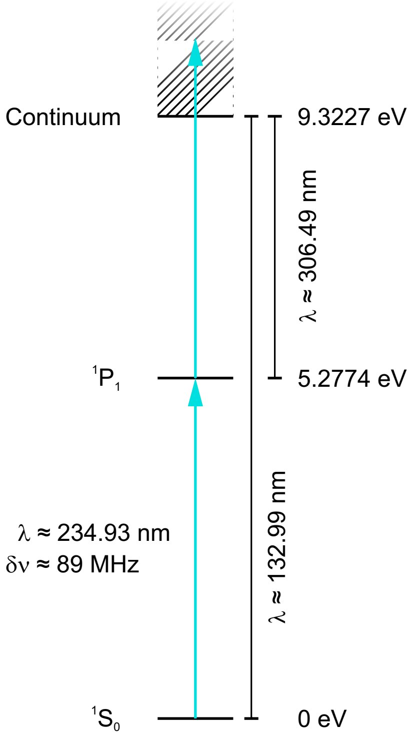

Figure 5.3: Level structure of neutral ^{9}Be for photoionization. The ^{1}P$_1$ state is resonantly populated with laser radiation at 235 nm from the ^{1}S$_0$ ground state. In a second step, ionization into the continuum is accomplished by absorption of a photon of the same wavelength. The intermediate excited state is rather broad with a FWHM natural linewidth of $\delta\nu = 89\,\mathrm{MHz}$ for the ^{1}S$_0$–^{1}P$_1$ E1 transition (Tachiev and C. F. Fischer, 1999). This is still orders of magnitude smaller than the several GHz Doppler broadening of the laser-ablated atoms (Leopold, 2018). All wavelengths λ stated in vacuum.

denoted as the *red Raman beam* needs to induce a σ^+-transition. The upper qubit state can be depopulated with the aforementioned repumper beam through the ^{2}P$_{1/2}$ state. Furthermore, a second repumper beam (also green, referred to as repumper 2) is used to depopulate the $|^2\mathrm{S}_{1/2}, F = 2, m_F = 1\rangle$ substate, also through a σ^+-transition involving the ^{2}P$_{1/2}$ state, in order to cope with σ^+-decay from this state, or σ^+-decay from the ^{2}P$_{3/2}$ state after unwanted π-excitation with the Doppler cooling laser when its polarization is not perfectly pure. Note that this reported laser scheme differs from the former scheme described by Leopold (2018) where σ^--transitions were used instead. All laser beams were swapped to the right in the Kastler diagram in order to select the redmost ^{2}S$_{1/2}$ hyperfine Zeeman component as qubit transition to suppress off-resonant excitation of other transitions when driving red sidebands of the qubit, which is the most important operation.

The electronic levels shown in Figure 5.2 are not to scale. However, the Zeeman splittings still indicate the magnitude of the g_F-factors, and the hyperfine splittings in the ^{2}P$_{3/2}$ state are approximately to scale. The indicated Zeeman shifts in the ^{2}P$_{3/2}$ state would actually correspond to a magnetic quantization field of 90 µT which is the right order of magnitude for this experiment. This points out that the Zeeman shifts are not small anymore against the hyperfine splittings of the ^{2}P$_{3/2}$ state. Thus, J and I are partially decoupled. F and m_F are therefore not good quantum numbers any more and cannot serve to describe the ^{2}P$_{3/2}$ state. In fact, only the Zeeman structure of the ground state can be spectrally resolved, either with microwaves or the Raman lasers. In contrast, the short lifetimes of about 9 ns of both excited P states (Andersen, Jessen, and Sørensen, 1969; B. E. King, 1999; U. I. Safronova and M. S. Safronova, 2013) result in FWHM natural linewidths of $\delta\nu \approx 19\,\mathrm{MHz}$, being larger than the Zeeman shifts. Therefore, the Zeeman substates of the $^2P_{1/2}$ state can only be selectively addressed by an appropriate choice of the laser polarizations in order to induce σ^-, π, or σ^+-transitions. For the $^2P_{3/2}$ state, this selectivity is even further constrained since the different hyperfine states cannot be resolved as mentioned before.

Loading of ^{9}Be$^+$ is accomplished through laser ablation from a solid beryllium wire with a natural abundance of 100 % and subsequent photoionization with the relevant laser geometry shown in Figure 11.4. The photoionization is realized in a two-step absorption process with a resonant first step (E1 transition) at a wavelength of 235 nm as shown in Figure 5.3. This allows to overcome the binding energy of the valence electron of 9.3 eV which would correspond to vacuum ultraviolet radiation (Beigang, D. Schmidt, and West, 1983; Kramida and Martin, 1997).

6 Ion traps

Trapping ions at rest in the laboratory frame is impossible with purely electrostatic potentials. According to Earnshaw's theorem, a local minimum of such a potential can never be generated in free space since it would not satisfy the Laplace equation $\nabla^2 U = 0$, where U is the electric potential energy. Therefore, ion traps typically employ magnetic fields, space charge, or oscillating electric fields to enable three-dimensional confinement. In order to isolate the ions from perturbations caused by other atoms or molecules, such traps are usually operated at ultra high vacuum (UHV) or even extreme high vacuum (XHV). In the following, two ion traps are briefly discussed which are operated in this work. Details can be found in the respective literature [see, e. g., Currell (2003), Ghosh (1995), Wineland, Monroe, Itano, B. E. King, et al. (1998), and Wineland, Monroe, Itano, Leibfried, et al. (1998)].

6.1 Electron beam ion trap

Electron beam ion traps (EBITs) are devices which aim at the study of highly charged ions (HCIs), produced and stored in a hot plasma. As the name implies, the main tool for these purposes is an electron beam which provides the energy to overcome the binding energies of the outer electrons in HCIs, which are much larger than in neutral atoms, and to provide radial confinement. More specifically, the trap has a cylindrical geometry with the electron beam along the symmetry axis. Along this axial direction, the confinement is realized with an electrostatic potential generated by so-called *drift tubes*. Three such tubes are sufficient to generate a potential well by applying a dc voltage to the outer ones which is larger than the voltage of the inner one. In the radial plane, the ions are trapped in the electrostatic potential of the negative space charge of the electron beam itself. This is no contradiction to Earnshaw's theorem since the space is not free and, instead of the Laplace equation, the Poisson equation $\nabla^2 U = -\rho / \varepsilon_0$ with the charge density ρ and the vacuum permittivity ε_0 applies. The charge density of the electron beam can be described approximately by a top-hat profile with

$$\rho = \frac{I}{\pi r_{\mathrm{H}}^2 v_z} \tag{6.1}$$

where I is the electron-beam current (typically tens to many hundreds of mA in superconducting EBITs), v_z the velocity of the electrons along the symmetry axis, and r_{H} the electron-beam radius (on the order of about 50 µm) which can be calculated within the Herrmann theory (G. Herrmann, 1958). One then obtains for the radial part of the negative space-charge potential, considering the geometry and the boundary conditions,

$$U_{\mathrm{nsc}}(r) = U_0 \cdot \begin{cases} \left(\frac{r^2}{r_{\mathrm{H}}^2} + \ln\frac{r_{\mathrm{H}}^2}{r_{\mathrm{D}}^2} - 1\right) & r \leq r_{\mathrm{H}} \\ \ln\frac{r^2}{r_{\mathrm{D}}^2} & r_{\mathrm{H}} \leq r \leq r_{\mathrm{D}}\,, \end{cases} \tag{6.2}$$

where the upper case corresponds to the region inside the electron beam and the lower case to the region outside. r is the distance from the symmetry axis, r_{D} is the inner radius of the cylindrical drift tube which surrounds the beam, and

$$U_0 = q \cdot \frac{I}{4\pi\varepsilon_0 v_z} \tag{6.3}$$

is the potential difference between the edge of the electron beam and the symmetry axis with the charge q of the HCI under consideration[1]. U_{nsc} is partially compensated by the positive space-charge potential U_{psc} of typically millions of trapped HCIs per mm^3. Finally, the overall space-charge potential $U_{\mathrm{sc}} = U_{\mathrm{nsc}} + U_{\mathrm{psc}}$ is the relevant quantity for the trapped HCIs.

A strong and inhomogeneous magnetic field is also present along the axial direction with its maximum at the trap center. The purpose is focusing of the electron beam to achieve a high current density for efficient ionization. An EBIT can even be operated in the so-called *magnetic trapping mode* (Beiersdorfer et al., 1996) by switching off the electron beam. Then, the trap operates like a Penning trap with the radial confinement provided by the magnetic field, forcing the ions to orbit the field lines.

A wealth of atomic physics interaction processes happen in such a system between free electrons, atoms, and ions in different charge states. A comprehensive description would exceed the scope of this chapter, but can be found in textbooks [see, e. g., Currell (2003) and J. Gillaspy (1999)]. The most important processes for this work are electron impact ionization of the ion $\mathrm{X}^{Z_{\mathrm{ion}}+}$ by a beam electron e^- to attain the next higher charge state

$$\mathrm{X}^{Z_{\mathrm{ion}}+} + \mathrm{e}^- \rightarrow \mathrm{X}^{(Z_{\mathrm{ion}}+1)+} + 2\,\mathrm{e}^- \tag{6.4}$$

and recombination processes which lower the charge state again. These are, for instance, radiative recombination through the capture of a free electron and the emission of an x-ray photon γ

$$\mathrm{X}^{Z_{\mathrm{ion}}+} + \mathrm{e}^- \rightarrow \mathrm{X}^{(Z_{\mathrm{ion}}-1)+} + \gamma \tag{6.5}$$

or charge exchange with, for example, a neutral atom Y from the background gas

$$\mathrm{X}^{Z_{\mathrm{ion}}+} + \mathrm{Y} \rightarrow \mathrm{X}^{(Z_{\mathrm{ion}}-1)+} + \mathrm{Y}^+\,. \tag{6.6}$$

---

[1] U_0 is also a measure for the electron-beam energy spread, where the charge q then represents the charge of the electron. This energy spread is typically on the order of a few eV up to many tens of eV.

Electron-impact ionization requires the free electron to have a kinetic energy larger than the binding energy of the bound electron which is released. The dominant recombination processes strongly depends on the parameters of the EBIT operation. For this work, the main purpose of the EBIT is to serve as a source for HCIs. Thus, the operation parameters are chosen in order to maximize the production of a specific HCI species within the charge state distribution. A distribution of charge states is always present in such a machine and governed by the ionization and recombination rates.

The temperature of the HCI plasma in the EBIT is typically on the order of a megakelvin since the electron beam continuously introduces energy and the trap is quite deep (typically several ten up to hundreds of eV). Coulomb crystallization as a prerequisite for spectroscopy at highest precision is in such an environment excluded as the Coulomb coupling parameter

$$\Gamma = \frac{\text{Coulomb energy}}{\text{Thermal energy}} \tag{6.7}$$

would need to overcome values of about 200 (Drewsen, 2015; Dubin, 1990) with a Coulomb energy between the ions on a meV level. Switching off the electron beam and operating the EBIT in the magnetic trapping mode in order to accomplish Coulomb crystallization was never demonstrated (for instance by means of sympathetic laser cooling with an auxiliary ion species) owing to the drawback of the multitude of different charge states and other elements simultaneously present in the plasma. Inhomogeneities of the strong magnetic field would be a further obstacle. However, a possible solution is the isolation of a single HCI of the desired species from this plasma and its transfer into another ion trap (for instance a Paul trap). There, efficient laser cooling can be realized and established techniques employed which are used in frequency metrology with optical atomic clocks.

6.2 Paul trap

A Paul trap confines ions by means of a dynamic radio-frequency (rf) electric field. Several types of Paul traps have been developed which have their distinct advantages and disadvantages. In this work, a linear Paul trap is used, in which an rf field provides confinement in the radial plane. An additional electrostatic (dc) axial field is superimposed in order to accomplish three-dimensional confinement. The electrodes are realized by four blades as shown in Figure 6.1 [see also Leopold (2018) and Leopold et al. (2019) in Appendix P3] and define the Paul trap coordinate frame $(\tilde{x}, \tilde{y}, z)$[2] which is obtained by rotating the laboratory frame (x, y, z) by $-45°$ around the z-axis. Two opposing blades (referred to as dc blades and pointing along the $\tilde{y}$-axis) are segmented and thereby provide a central segment at a common ground potential and two endcap electrodes on either side for dc voltages and axial confinement along

---

[2] In the following, we assume a perfect trap in which the principal axes of motion line up with the principal axes of the trap. In reality a slight tilt can be present.

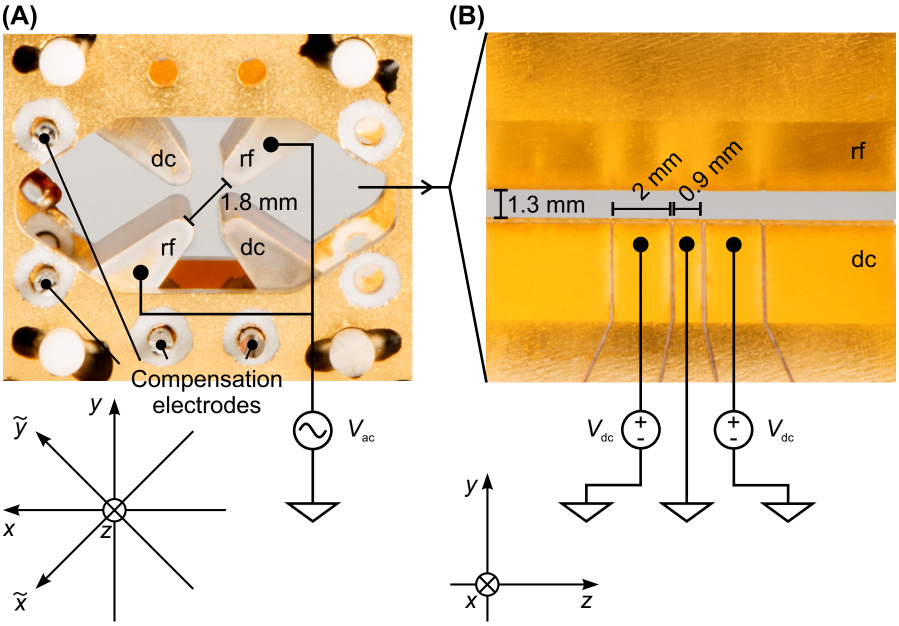

Figure 6.1: Electrode configuration of the linear Paul trap in use by this work. (**A**) View along the Paul trap axis (z-axis). The coordinate frame of the Paul trap is rotated by $-45°$ around the z-axis with respect to the laboratory frame (x, y, z). The Paul trap principal axis $\tilde{x}$ points along the rf blades, $\tilde{y}$ points along the dc blades. $\tilde{x}\tilde{y}$ defines the plane of the radial ac confinement with the amplitude voltage V_{ac} and the radio frequency Ω_{rf}. Four rod-type compensation electrodes, parallel to the z-axis, provide dc voltages for micromotion compensation. (**B**) Side view onto the Paul trap from the right. The rf blade (top) is not structured while the dc blade (bottom) provides five dc electrode segments. The central one is connected to the common ground potential of the trap, while the adjacent ones are biased to a dc voltage V_{dc}.

the z-axis. The other two opposing blades (referred to as rf blades and pointing along the $\tilde{x}$-axis) are not segmented and carry the ac voltage for the radial confinement along the principal axes $\tilde{x}$ and $\tilde{y}$. The choice to provide the dc voltage for the axial confinement only through the two opposing dc blades breaks the symmetry and lifts the degeneracy of the $\tilde{x}$ and $\tilde{y}$ directions, but will be omitted for now. At the end of this section we will come back to the consequences of this choice. The basic idea of a linear Paul trap is that, in contrast to a spherical rf trap, a string of ions can be trapped on the symmetry axis[3] z without being exposed to the rf field which vanishes on this nodal line. This is an important feature for quantum logic spectroscopy (QLS) in which a two-ion crystal is handled. In the following, the basic relations are summarized for the specific Paul trap operated in this work [see Leopold (2018) for more details]. Further information about Paul traps in general can be found in the literature [see, e. g., Berkeland et al. (1998b), Ghosh (1995), Leibfried et al. (2003), and Wineland, Monroe, Itano, Leibfried, et al. (1998)].

---

[3] A stronger confinement in the radial plane than in the axial direction is required.

The electric potential U of an ideal symmetric linear Paul trap, described in the Paul trap frame $(\tilde{x}, \tilde{y}, z)$ with $z = \tilde{z}$, seen by a single trapped ion with charge q is given by

$$U(\tilde{x},\tilde{y},z,t) = \frac{\varkappa}{z_0^2}\left[z^2 - \frac{1}{2}\left(\tilde{x}^2+\tilde{y}^2\right)\right] q V_{\mathrm{dc}} + \left(\frac{\tilde{x}^2-\tilde{y}^2}{2r_0^2}+\frac{1}{2}\right) q V_{\mathrm{ac}} \cos\left(\Omega_{\mathrm{rf}} t\right), \tag{6.8}$$

where V_{dc} and V_{ac} are the dc and ac amplitude voltages applied to the dc endcaps and rf blades, respectively, Ω_{rf} is the angular frequency at which the ac voltage oscillates, z_0 and r_0 are characteristic geometrical distances of the trap, and $\varkappa < 1$ is a geometrical factor [see, e. g., Berkeland et al. (1998b)]. The z-axis corresponds to the nodal line with vanishing rf field. With the electric field, obtained from the derivative of the potential, one deduces the equations of motion for the radial plane

$$\ddot{u}(t) + \frac{\Omega_{\mathrm{rf}}^2}{4}\left[a_u - 2q_u \cos\left(\Omega_{\mathrm{rf}} t\right)\right] u(t) = 0 \qquad u \in \{\tilde{x},\tilde{y}\}, \tag{6.9}$$

known as the *Mathieu equations*. These are linear ordinary differential equations with a coefficient nonlinear in t. The two stability parameters a_u and q_u for each radial principal axis $u \in \{\tilde{x},\tilde{y}\}$ are given by

$$a_u = -\frac{4\varkappa}{z_0^2}\frac{q}{m}\frac{V_{\mathrm{dc}}}{\Omega_{\mathrm{rf}}^2} \tag{6.10a}$$

$$q_u = \mp\frac{2}{r_0^2}\frac{q}{m}\frac{V_{\mathrm{ac}}}{\Omega_{\mathrm{rf}}^2}. \tag{6.10b}$$

Both stability parameters are notably proportional to the charge-to-mass ratio q/m of the ion with charge q and mass m. Stable ion trapping is achieved for a certain parameter space of a_u and q_u, referred to as the *stability region*. This includes the region with $|q_u| < 0.4$ and $|a_u| \ll |q_u|$ for which the so-called *adiabatic approximation* can be applied. Within this approximation, the motion in the radial plane can be decomposed into a slower motion (*secular motion*), which happens on a timescale defined by the trapping potential and characterized by the secular frequency ω_u, and a significantly faster motion (*micromotion*), taking place on a timescale defined by the trap drive frequency Ω_{rf}. ω_u is typically about one order of magnitude smaller than Ω_{rf}. Generalizing Equation 6.8 and Equation 6.9 by allowing for a small radial dc field due to, e. g., patch potentials or electric stray fields, this adiabatic approximation yields the solution for the radial motion of the ion

$$\begin{aligned} u(t) \approx u_0 &+ \underbrace{u_\mathrm{a} \cos(\omega_u t)}_{\text{secular motion}} \\ &+ \underbrace{\frac{u_\mathrm{a} q_u}{4} \left(\cos\left[(\Omega_\mathrm{rf} + \omega_u)\, t\right] + \cos\left[(\Omega_\mathrm{rf} - \omega_u)\, t\right]\right)}_{\text{intrinsic micromotion}} \\ &+ \underbrace{\frac{u_0 q_u}{2} \cos(\Omega_\mathrm{rf} t)}_{\text{excess micromotion}} \end{aligned} \tag{6.11}$$

with $u(t) \in \{\tilde{x}(t), \tilde{y}(t)\}$ and a corresponding starting condition of the ion. Four terms appear. u_0 is the displacement of the ion's equilibrium position from the rf-free nodal line due to a radial dc field[4]. In the ideal case, however, $u_0 = 0$ would apply. The second term describes the *secular motion* with amplitude u_a and the motional frequency ω_u, appearing as a harmonic motion as known from a harmonic oscillator. However, this motion is a consequence of the ponderomotive force. The third term expresses the unavoidable *intrinsic micromotion* at angular frequencies $\Omega_\mathrm{rf} \pm \omega_u$. It corresponds to oscillations producing sidebands around the trap drive frequency Ω_rf at a distance of the motional frequency ω_u. The amplitude is suppressed by the stability parameter q_u. The fourth term describes *excess micromotion*, an oscillation at the trap drive frequency Ω_rf which is caused by the displacement u_0 of the ion from the nodal line[5]. Therefore, additional dc compensation electrodes are operated, as shown in Figure 6.1, in order to control the radial displacement of the ion, minimizing $|u_0|$ and thus the excess micromotion term. Another source of excess micromotion would be a phase shift between the electric potentials of the rf electrodes, but is ignored here. Additionally, an imperfect trap electrode alignment can give rise to an axial rf component of the electric field, which causes axial excess micromotion. In general, excess micromotion can have a severe impact on the systematic frequency shift of an optical ion clock and should be minimized.

Neglecting micromotion, the secular motion of the ion can be also described within the pseudopotential approximation (Dehmelt, Bates, and Estermann, 1968, 1969) as originating from the static pseudopotential

$$U_\mathrm{p}(\tilde{x}, \tilde{y}) = \frac{m}{2} \omega_u^2 \left(\tilde{x}^2 + \tilde{y}^2\right) \tag{6.12}$$

with the mass m of the ion and where $\omega_u = \omega_{\tilde{x}} = \omega_{\tilde{y}}$ still applies. For the axial confinement we have the analogous expression

$$U(z) = \frac{m}{2} \omega_z^2 z^2 . \tag{6.13}$$

---

[4] Note that this position is actually not an equilibrium position because of the ponderomotive force, but rather the averaged ion position.

[5] Note that intrinsic and excess micromotion can be discriminated by the frequency at which they appear, $\Omega_\mathrm{rf} \pm \omega_u$ or Ω_rf, respectively.

As a conclusion, on time-average the ion is trapped along all directions $\tilde{x}$, $\tilde{y}$, and z in an overall three-dimensional harmonic (pseudo-)potential. Thus, there are three modes of harmonic motion with the motional angular frequencies $\omega_{\tilde{x}}$, $\omega_{\tilde{y}}$, and ω_z that characterize the strength of the confinement in the trap. In the beginning of this section, it was mentioned that the degeneracy in $\tilde{x}$ and $\tilde{y}$ is deliberately lifted by the design of the trap. This was realized by operating only two opposite blades of the total four ones with an axially confining dc voltage. As a result the radial motional frequencies are split and therefore $\omega_{\tilde{x}} \neq \omega_{\tilde{y}}$. They fulfill the equations (Leopold, 2018)

$$\omega_{\tilde{x}} = \frac{\sqrt{2}}{r_0^2} \frac{q}{m} \frac{V_{\mathrm{ac}}}{\Omega_{\mathrm{rf}}} \tag{6.14a}$$

$$\omega_{\tilde{y}} = \sqrt{\frac{2}{r_0^4} \left(\frac{q}{m}\right)^2 \left(\frac{V_{\mathrm{ac}}}{\Omega_{\mathrm{rf}}}\right)^2 - \frac{8\varkappa}{z_0^2} \frac{q}{m} V_{\mathrm{dc}}} \tag{6.14b}$$

$$\omega_z = \sqrt{\frac{2\varkappa}{z_0^2} \frac{q}{m} V_{\mathrm{dc}}} \tag{6.14c}$$

with the relation

$$\omega_{\tilde{x}}^2 = \omega_{\tilde{y}}^2 + \omega_z^2 . \tag{6.15}$$

6.2.1 Quantum harmonic oscillator

Until now, the description of an ion in the Paul trap was purely classical. The amplitude u_{a} is linked to the energy of the ion in that mode. Low energies in such a system call for a quantum-mechanical description. Each mode of motion corresponds to a quantum harmonic oscillator (QHO) with its Hamiltonian given by

$$\widehat{H} = \frac{\widehat{p_u}^2}{2m} + \frac{1}{2} m \omega_u^2 \widehat{u}^2 , \tag{6.16}$$

where $\widehat{p_u}$ is the momentum operator, $\widehat{u}$ is the position operator, m the mass of the ion, and ω_u the secular frequency of the mode with $u \in \{\tilde{x}, \tilde{y}, z\}$. The energy eigenstates $|n\rangle$, dubbed *Fock states*, fulfill the relation

$$\widehat{H}\,|n\rangle = E_n\,|n\rangle \tag{6.17}$$

with the discrete energy eigenvalues given by

$$E_n = \hbar\,\omega_u \left(n + \frac{1}{2}\right) \qquad n = 0, 1, 2, 3, \ldots \tag{6.18}$$

with $\hbar = h/(2\pi)$ being the reduced Planck constant. n is therefore dubbed the *Fock state number*, *occupation number*, or *phonon number* with which the mode is occupied. The former classical amplitude u_a of the oscillator can be linked with a thermal occupation number distribution

$$u_{\mathrm{a},n} = \sqrt{\frac{\hbar\,(\overline{n}+1/2)}{m\,\omega_u}}\,, \tag{6.19}$$

where $\overline{n}$ is the mean occupation number. A distinct feature of quantum mechanics is the zero-point energy

$$E_0 = \frac{1}{2}\hbar\,\omega_u \tag{6.20}$$

of the ground state $|0\rangle$. The amplitude

$$u_{\mathrm{a},0} = \sqrt{\frac{\hbar}{2m\,\omega_u}} \tag{6.21}$$

corresponds to the spatial extent of the motional ground-state wave function. According to the virial theorem, a residual kinetic energy of

$$E_{\mathrm{kin},0} = \frac{1}{2}E_0 \tag{6.22}$$

remains in the system and causes a second-order Doppler shift even in the ground state of motion.

6.2.2 Two-ion crystal

So far, the confinement of only a single ion was considered in the Paul trap. QLS, however, is performed with a two-ion crystal. This crystal has to be understood as a coupled QHO of both ions, coupled together through their repulsive Coulomb interaction in the three-dimensional harmonic (pseudo-)potential of the trap. This gives rise to six motional modes, instead of the former three modes of a single ion, since both ions can move in-phase[6] or out-of-phase[7] along each direction $\tilde{x}$, $\tilde{y}$, and z. As a result, the motion of either ion can be described as a superposition of these six modes, where each ion possesses an individual oscillation amplitude for each mode ruled by the ratio of the charge-to-mass ratios q/m of both ions [see, e. g., M. G. Kozlov et al. (2018) and Wübbena et al. (2012)]. Nonetheless, the motion is a common motion and both ions share the same oscillation frequencies with a fixed phase relation of their motion. The out-of-phase motional frequency of the axial motion is larger than the in-phase one. For the radial motion it is the other way around. In the following, these motional frequencies $\omega_{u,p}$ will be denoted with the additional index $p \in \{o,i\}$, referring to the out-of-phase and in-phase mode, respectively. Each mode is also characterized by its corresponding occupation number $n_{u,p}$.

---

[6] These modes are also dubbed as the *center-of-mass* modes.

[7] Along the axial direction, this mode is also referred to as *breathing* or *stretch* mode. In the radial plane the terms *rocking* or *bending* mode are used.

As mentioned earlier, the trap conditions are chosen to trap both ions on the nodal line (the symmetry axis z) of vanishing rf field and minimized micromotion. To achieve this, the radial confinement is made stronger than the axial one, resulting for the Paul trap of this work in

$$\begin{aligned}
\omega_{\tilde{x},i} &> \omega_{\tilde{y},i} > \omega_{z,o} && \text{(6.23a)}\\
\omega_{u,i} &> \omega_{u,o} \qquad \forall u \in \{\tilde{x},\tilde{y}\} && \text{(6.23b)}\\
\omega_{z,o} &> \omega_{z,i}\,. && \text{(6.23c)}
\end{aligned}$$

A mismatch of the charge-to-mass ratios q/m of both ions can lead to significantly different oscillation amplitudes for the radial motion. Motional frequencies and amplitudes have been calculated by Leopold (2018) for the two-ion crystal ${}^{40}\mathrm{Ar}^{Z_{\mathrm{ion}}+}$–${}^{9}\mathrm{Be}^{+}$ with varying charge state Z_{ion} for the highly charged argon and for reasonable trap parameters [see also M. G. Kozlov et al. (2018)]. It was found that the motional amplitudes in the radial modes of both ions can differ by almost two orders of magnitude while the amplitudes in the axial modes only differ by a factor of 2 or 3. Specifically, ${}^{40}\mathrm{Ar}^{13+}$ has a large radial oscillation amplitude in both radial in-phase modes. This condition complicates cooling in these modes in order to outperform heating processes and to suppress the motional frequency shift (Wübbena et al., 2012). The cooling efficiency through ${}^{9}\mathrm{Be}^{+}$ is reduced by the smaller coupling proportional to the square of the small ${}^{9}\mathrm{Be}^{+}$ oscillation amplitude (as will be discussed later in Section 7.2). A radial mode which is still relatively hot and possesses a particularly large oscillation amplitude of ${}^{40}\mathrm{Ar}^{13+}$ would cause a significant second-order Doppler shift. However, strategies can be employed to overcome this limitation, for example by twisting the two-ion crystal and thus coupling axial and radial modes [see supplement of Rosenband et al. (2008)].

7 Atom-light interaction

This chapter deals with the interaction of atoms with light. Relevant basic formulas for electric and magnetic dipole transitions are given in the first section with a focus on the geometrical coupling between the light and the atom for a typical laser spectroscopy experiment. The second section addresses coherent atom-light interaction and quotes important equations for describing the observed phenomena. In particular, coherent manipulation of the motional degrees of freedom with light is discussed. Finally, a brief section gives an overview of laser cooling techniques used in this work.

7.1 Electronic transitions

The interaction of electromagnetic radiation with an atom can induce electronic transitions. Using an appropriate gauge, a monochromatic plane wave can be described by the vector potential

$$\vec{A}\left(\vec{r},t\right) = \vec{A}_0 \mathrm{e}^{i\left(\vec{k}\cdot\vec{r}-\omega t\right)} + c.c. \tag{7.1}$$

which satisfies the wave equation and from which the electric and magnetic field components can be generated, being described by Maxwell's equations. Here, $\vec{k}$ is the wave vector, $\vec{r}$ the position vector where the atom is situated at the origin of the coordinate frame, ω the angular frequency and t the time. The term $\exp\left(i\,\vec{k}\cdot\vec{r}\right)$ can be expanded as a Taylor series (known as plane wave expansion or Rayleigh expansion)

$$\begin{aligned}\mathrm{e}^{i\,\vec{k}\cdot\vec{r}} = {} & \underbrace{1}_{\text{Electric-dipole transitions (E1)}} + \underbrace{i\,\vec{k}\cdot\vec{r}}_{\substack{\text{Magnetic-dipole transitions (M1),}\\ \text{Electric-quadrupole transitions (E2)}}} \\ & + \underbrace{\frac{\left(i\,\vec{k}\cdot\vec{r}\right)^2}{2!}}_{\substack{\text{Magnetic-quadrupole transitions (M2),}\\ \text{Electric-octupole transitions (E3)}}} + \ldots,\end{aligned} \tag{7.2}$$

where only the first few terms are relevant for $\vec{k}\cdot\vec{r} \ll 1$ which is the case when the typical dimension of the atomic system ($\sim 0.1\,\mathrm{nm}$) is small against the electromagnetic wavelength (hundreds of nm for optical light). It can be shown that the 0^{th}-order term of the expansion in $i\,\vec{k}\cdot\vec{r}$ describes the *electric-dipole* contribution [see, e. g., Auzinsh, Budker, and Rochester (2010) and Bransden and Joachain (2003)], which generally dominates the transition rate between the involved electronic states, as long as selection rules, derived from the corresponding *reduced matrix element* (Equation 7.4), do not cause this term to vanish. In the latter case, transitions from the next-order term in $i\,\vec{k}\cdot\vec{r}$ have to be considered. These have *magnetic-dipole* and *electric-quadrupole* character and are physically induced by the magnetic field and the electric-field gradient, respectively. In the following, the process of absorption of incoherent light will be discussed for electric- (E1) and magnetic-dipole (M1) transitions to understand the basic coupling between light and atoms. Without loss of generality, this coupling also holds for the absorption of coherent light, important for coherent laser spectroscopy. It will be shown, that the coupling can be substantially affected by the geometrical degrees of freedom, namely the angle of incidence of the light with respect to the quantization axis and its polarization. More details can be found in the pertinent literature [for example in Auzinsh, Budker, and Rochester (2010), Bransden and Joachain (2003), Sobelman (1992), and Walraven (2018)].

7.1.1 Electric dipole transitions

If allowed, electric-dipole (E1) transitions are the leading coupling between two states, denoted here as $|\,\xi, F, m_F\,\rangle$ for the initial and $|\,\xi', F', m_{F'}\,\rangle$ for the final state. Such transitions are driven in the lithium-like $^9\mathrm{Be}^+$ system and, since this ion features a hyperfine structure, the quantum numbers F for the total angular momentum and m_F for the Zeeman substates are used to describe the electronic state[1]. ξ represents the other quantum numbers which characterize the state. It can be shown that the interaction which corresponds to the 0^{th}-order term of the plane wave expansion in Equation 7.2 [see, e. g., Auzinsh, Budker, and Rochester (2010) and Bransden and Joachain (2003)] is described by the Hamiltonian

$$\widehat{H}^{\mathrm{E1}}(t) = -\widehat{\vec{\mathcal{D}}}\cdot\vec{\mathcal{E}}(t)\,, \tag{7.3}$$

where $\widehat{\vec{\mathcal{D}}}$ is the electric-dipole operator in its vector form and $\vec{\mathcal{E}}(t) = \mathcal{E}(t)\cdot\hat{\varepsilon}$ the electric component of the light field with the polarization unit vector[2] $\hat{\varepsilon}$ and the time-dependent electric field strength $\mathcal{E}(t)$. E1 transitions are allowed between states of different parity and follow the well-known selection rules [see, e. g., Auzinsh, Budker, and Rochester (2010) and Bransden and Joachain (2003)]. The atomic coordinate frame (x', y', z') is partially defined by an external, homogeneous dc magnetic field along the z'-axis, which is applied through large magnetic field coils far away from the atom. The direction of this magnetic field defines the quantization axis, in other words, it defines the orientation of $\widehat{\vec{\mathcal{D}}}$. According to time-dependent first-order perturbation theory, the strength of a one-photon transition is governed by the electric-dipole transition matrix element[3]

---

[1] Without losing generality, F and m_F can be replaced by J and m_J for a system without hyperfine structure.

[2] Note that in this thesis operators are denoted with a wide hat. In contrast, a narrow hat is used to denote a unit vector.

$$\langle\, \xi', F', m_{F'}\, |\vec{\widehat{\mathfrak{D}}}|\, \xi, F, m_F\, \rangle = \langle\, \xi', F', m_{F'}\, |\widehat{\mathfrak{D}}|\, \xi, F, m_F\, \rangle\; \hat{u}^{*}_{\Delta m_F}\,. \tag{7.4}$$

$\vec{\widehat{\mathfrak{D}}}$ can be conveniently expressed in a spherical basis [see, e. g., Bransden and Joachain (2003)] as shown on the right-hand side of this equation with its modulus $\widehat{\mathfrak{D}}$ and the spherical unit vector $\hat{u}^{*}_{\Delta m}$; the asterisk denoting the complex conjugate and $\Delta m \equiv \Delta m_F$. The selection rule

$$\Delta m_F = m_{F'} - m_F = 0,\ \pm 1 \tag{7.5}$$

corresponds to π, σ^+, or σ^--transitions[4]. Using the *Wigner-Eckart theorem*, the angular momentum coupling of the $m_{F'}$ and m_F substates can be separated from the matrix element by introducing the Clebsch-Gordan coefficients which we will denote as $C^{F,F'}_{m_F,\Delta m_F}$ here. Using the general expression of the Clebsch-Gordan coefficients we accordingly obtain $\left(\, j_1\, m_{j_1}\, j_2\, m_{j_2}\,|\, j_3\, m_{j_3}\right) \overset{!}{=} C^{j_1,j_3}_{m_{j_1},m_{j_2}} = C^{F,F'}_{m_F,\Delta m_F}$ with j_i and m_{j_i} as general total angular momentum quantum numbers and corresponding magnetic quantum numbers, where $j_1 = F$ and $m_{j_1} = m_F$ describe the initial state and $j_2 = 1$, $m_{j_2} = 0,\ \pm 1$ describe the absorbed photon. $C^{F,F'}_{m_F,\Delta m_F}$ is only non-zero for $\Delta m_F = m_{F'} - m_F$. Symmetry relations cause the Clebsch-Gordan coefficients to be identical for absorption and emission. Considering now the monochromatic plane wave in resonance with the electronic transition[5], with wave vector $\vec{k}$, an arbitrary polarization $\hat{\varepsilon}$ of the electric field $\vec{\mathcal{E}} = \mathcal{E}\cdot\hat{\varepsilon}$, and the time-averaged intensity $I_{\vec{k},\hat{\varepsilon}} \propto \overline{\mathcal{E}^2}$, the transition rate W^{E1} is given by

$$\begin{aligned} &W^{\mathrm{E1}}\left(\xi\, F\, m_F \rightarrow \xi'\, F'\, m_{F'}\right) \\ &\propto\ I_{\vec{k},\hat{\varepsilon}} \cdot \left|\langle\, \xi', F'\, ||\widehat{\mathfrak{D}}||\, \xi, F\, \rangle \cdot C^{F,F'}_{m_F,\Delta m_F} \cdot \left(\hat{\varepsilon}\cdot \hat{u}^{*}_{\Delta m_F}\right)\right|^2 . \end{aligned} \tag{7.6}$$

According to this equation and apart from the intensity, the main dependence of the transition rate can be decomposed into three relevant factors. First, we have the square of the so-called *reduced matrix element* $|\langle\, \xi', F'\, ||\widehat{\mathfrak{D}}||\, \xi, F\, \rangle|^2$ which only depends on the initial and final state without any contribution from the Zeeman substates. This term is referred to as the *line strength* (Auzinsh, Budker, and Rochester, 2010; Sobelman, 1992). The second factor is the square of the Clebsch-Gordan coefficients, which describes the angular momentum coupling of the involved Zeeman substates. Finally, the third factor $|\hat{\varepsilon}\cdot\hat{u}^{*}_{\Delta m_F}|^2$ is a geometrical factor which accounts for the light field propagation direction

---

[3] This expression essentially corresponds to *Fermi's golden rule*, according which the transition rate is proportional to the squared matrix element $|\langle f|\widehat{H}'|i\rangle|^2$, where $|i\rangle$ and $|f\rangle$ denote the initial and final state, eigenstates of the unperturbed Hamiltonian, and $\widehat{H}' = \widehat{H}^{\mathrm{E1}}$ is the perturbation, treated within time-dependent first-order perturbation theory. In contrast, the strength of a two-photon transition is obtained in second-order perturbation theory.

[4] For a σ^+-transition, m_F increases by one for absorption and decreases by one for emission per definition.

[5] In other words, we assume that the frequency of the light field matches the transition frequency.

$\left\lvert\hat{\varepsilon}\cdot\hat{u}^*_{\Delta m}\right\rvert^2$	π	σ^+	σ^-
$\Delta m = m' - m$	0	1	-1
$\hat{\varepsilon}_\alpha$	0	$\frac{1}{2}$	$\frac{1}{2}$
$\hat{\varepsilon}_\beta$	$\sin^2\theta$	$\frac{1}{2}\cos^2\theta$	$\frac{1}{2}\cos^2\theta$
$\hat{\varepsilon}_+$	$\frac{1}{2}\sin^2\theta$	$(1+\cos\theta)^2/4$	$(1-\cos\theta)^2/4$
$\hat{\varepsilon}_-$	$\frac{1}{2}\sin^2\theta$	$(1-\cos\theta)^2/4$	$(1+\cos\theta)^2/4$

Table 7.1: Geometrical coupling between a light field and E1 transitions. The geometrical factor $|\hat{\varepsilon}\cdot\hat{u}^*_{\Delta m}|^2$ (see Equation 7.6) is given for π, σ^+, and σ^--transitions as a function of the polar angle θ and for a specific light field polarization (first column), defined by $\overrightarrow{\mathcal{E}} = \mathcal{E}\cdot\hat{\varepsilon}$ with the electric field strength $\mathcal{E}$ and the unit vector $\hat{\varepsilon}$. $\hat{\varepsilon}_\alpha$ and $\hat{\varepsilon}_\beta$ refer to the orthogonal linear polarization directions as defined in Figure 7.1 while $\hat{\varepsilon}_+$ and $\hat{\varepsilon}_-$ refer to the helical polarization basis. θ is the angle of incidence between the wave vector $\overrightarrow{k}$ and the quantization axis z'. The sum of all geometrical factors for a specific polarization over all Δm is identical to one.

and its polarization with respect to the quantization axis. Values of this factor for a specific Δm_F, an angle of incidence θ between $\overrightarrow{k}$ and the z'-axis, and a specific polarization are given in Table 7.1. The two different basis sets of polarization are introduced in the next section.

Geometrical relations

The transition probability W^{E1} depends, according to Equation 7.6, on the geometrical factor $|\hat{\varepsilon}\cdot\hat{u}^*_{\Delta m_F}|^2$ which describes the entire geometry of the absorption experiment. The following discussion refers to the atomic coordinate frame (x', y', z'). Three physical directions are involved: the quantization axis z' with the unit vector $\hat{z}'$ defining the orientation of the dipole operator $\widehat{\overrightarrow{\mathfrak{D}}}$, the direction of incidence of the light field, given by the wave vector

$$\overrightarrow{k} = k\cdot\hat{k}, \tag{7.7}$$

where $\hat{k}$ is the corresponding unit vector, and an arbitrary polarization of the light field defined by the unit vector $\hat{\varepsilon}$. In fact, we can describe this arrangement already with just the polar angle θ between $\hat{z}'$ and $\hat{k}$ which we use to span the $x'z'$ plane as shown in Figure 7.1[6]. For this purpose we allow $\theta \in [-\pi, \pi]$ and obtain

$$\hat{k} = (\sin\theta, 0, \cos\theta)\ . \tag{7.8}$$

---

[6] Note that in a more general expression the azimuthal angle, usually referred to as ϕ, represents a second variable for the parameterization of the coordinate frame and allows $\hat{k}$ to tilt out of the $x'z'$ plane. This is not necessary here.

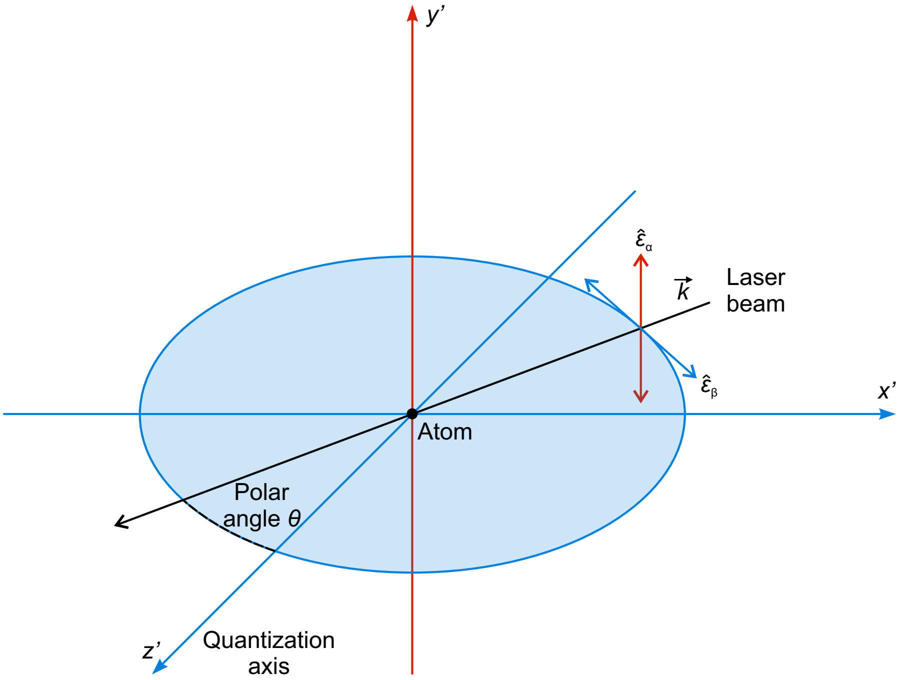

Figure 7.1: Geometrical relations between quantization axis, wave vector, and polarization. The light with wave vector $\vec{k}$ propagates in the $x'z'$ plane and reaches the atom at the origin of the coordinate frame at an angle θ with respect to the quantization axis z'. An arbitrary polarization $\hat{\varepsilon}$ can be decomposed as a superposition of the two orthogonal linear polarizations $\hat{\varepsilon}_\alpha$ and $\hat{\varepsilon}_\beta$, which are defined as being perpendicular and parallel to the $x'z'$ plane.

We can now define the useful orthogonal linear polarization basis

$$\hat{\varepsilon}_\alpha = \frac{\hat{k}\times\hat{z}'}{\left|\hat{k}\times\hat{z}'\right|} = (0,-1,0) \tag{7.9a}$$

$$\hat{\varepsilon}_\beta = \hat{k}\times\hat{\varepsilon}_\alpha = (\cos\theta, 0, -\sin\theta)\,, \tag{7.9b}$$

as shown in Figure 7.1. As a result, the unit vector $\hat{\varepsilon}_\alpha$ describes the polarization perpendicular to the $x'z'$ plane and the unit vector $\hat{\varepsilon}_\beta$ lies in that plane. Another useful orthogonal basis is the helical basis, defined by

$$\hat{\varepsilon}_+ = -\sqrt{1/2}\left(\hat{\varepsilon}_\alpha + i\,\hat{\varepsilon}_\beta\right) = -\hat{\varepsilon}_-^* \tag{7.10a}$$

$$\hat{\varepsilon}_- = +\sqrt{1/2}\left(\hat{\varepsilon}_\alpha - i\,\hat{\varepsilon}_\beta\right) = -\hat{\varepsilon}_+^*\,, \tag{7.10b}$$

where the asterisk denotes the complex conjugate. The back transformation is given by

$$\hat{\varepsilon}_\alpha = -\sqrt{1/2}\,(\hat{\varepsilon}_+ - \hat{\varepsilon}_-) \tag{7.11a}$$

$$\hat{\varepsilon}_\beta = i\sqrt{1/2}\,(\hat{\varepsilon}_+ + \hat{\varepsilon}_-)\,. \tag{7.11b}$$

The helical basis describes circular polarization of the light field, where $\hat{\varepsilon}_+$ constitutes a positive helicity and $\hat{\varepsilon}_-$ a negative helicity[7]. Any arbitrary polarization can be described by a superposition in either the linear basis or the helical basis

$$\hat{\varepsilon} = a\,\hat{\varepsilon}_\alpha + b\,\hat{\varepsilon}_\beta = c_+\,\hat{\varepsilon}_+ + c_-\,\hat{\varepsilon}_- \tag{7.12}$$

with the complex coefficients a, b, c_+, and c_- and their normalization condition given by $1 = |a|^2 + |b|^2 = |c_+|^2 + |c_-|^2$.

Apart from linear and circular polarization, the terms π and σ polarization are occasionally used, when dealing with electronic transitions. This can be useful as it defines the polarization not directly through a specific geometry, but through the effect on the atom, namely inducing a π, σ^+, or σ^--transition for which the magnetic quantum number m changes by 0 or ± 1, respectively. However, also a certain geometry is naturally linked to these transitions. For an E1 transition, π polarization requires the electric field to be parallel to the quantization axis. In contrast, σ polarization requires the electric field to be perpendicular to the quantization axis and then induces transitions with a change of m. This can be accomplished, for instance, with linearly polarized $\hat{\varepsilon}_\alpha$ light. However, this would induce σ^+ and σ^--transitions with the same probability since the light can be decomposed into σ^+ and σ^- light with equal intensity according to Equation 7.11. The geometrical factors $|\hat{\varepsilon} \cdot \hat{u}^*_{\Delta m_F}|^2$ of Equation 7.6 would then give the same results according to Table 7.1. Pure σ^+-transitions can be excited with circularly polarized $\hat{\varepsilon}_+$ light at an angle of incidence of $\theta = 0°$, meaning the circularly polarized light then propagates along the quantization axis. Such considerations are essential to accomplish optical pumping in order to initialize the quantum state of $^9\mathrm{Be}^+$ for instance (see Section 5.2).

7.1.2 Magnetic dipole transitions

E1-forbidden transitions are governed by the next-order contributions of M1 and E2-transition probabilities, of which the magnetic-dipole contribution is typically larger. This is the case for the fine-structure transition in Ar^{13+} as discussed in Section 5.1, being five orders of magnitude larger than the E2-transition probability (Bilal et al., 2018; C. F. Fischer, 1983). Ar^{13+} has no hyperfine structure and therefore the total angular momentum quantum number J is used in the following equations instead of F to characterize the electronic state. Again, it can be shown that the M1 interaction, corresponding to one of the two summands obtained from the 1st-order term of the expansion in Equation 7.2, is described by the Hamiltonian

---

[7] Note that there are two contrary conventions in use whether a specific helicity is right- or left-handed-circularly polarized. This is just a matter of perspective: In the first convention the thumb points along $\hat{k}$ and away from the source (common convention in atomic and particle physics) while in the second one the thumb points towards the source (familiar convention in optics) which swaps the hand for a given rotation direction of the electric field vector.

$$\widehat{H}^{\mathrm{M1}}(t) = -\widehat{\vec{\mathcal{M}}} \cdot \vec{\mathcal{B}}(t)\,, \tag{7.13}$$

where $\widehat{\vec{\mathcal{M}}}$ is the magnetic-dipole operator and $\vec{\mathcal{B}}(t)$ the time-dependent magnetic component of the light field. $\widehat{\vec{\mathcal{M}}}$ follows slightly different definitions in the literature, depending on the conventions used for the angular momentum operators and the Bohr magneton [see Auzinsh, Budker, and Rochester (2010) and Sobelman (1992)], but it fulfills the relation

$$\widehat{\vec{\mathcal{M}}} \propto \frac{\mu_B}{c}\left(\widehat{\vec{L}} + 2\widehat{\vec{S}}\right) = \frac{e\,a_0\,\alpha}{2}\left(\widehat{\vec{L}} + 2\widehat{\vec{S}}\right) \tag{7.14}$$

with the Bohr magneton μ_{B}, the angular momentum operators for orbit and spin, $\widehat{\vec{L}}$ and $\widehat{\vec{S}}$ respectively, a typical electric-dipole moment of $e\,a_0$, where e is the elementary charge and a_0 the Bohr radius, the fine-structure constant α, and the vacuum speed of light c. From the right-hand side of this equation it can be seen that the transition rate (proportional to the square of the matrix element) is suppressed by a factor of α^2 compared to an E1 transition, four to five orders of magnitude typically.

The M1-transition probability for absorption is then given in an analogous manner to the E1-transition probability in Equation 7.6 as

$$\begin{aligned} &W^{\mathrm{M1}}\left(\xi\,J\,m_J \rightarrow \xi'\,J'\,m_{J'}\right) \\ &\propto\ I_{\vec{k},\hat{\varepsilon}} \cdot \left|\langle \xi', J' \,||\widehat{\mathcal{M}}||\, \xi, J\rangle \cdot C^{J,J'}_{m_J,\Delta m_J} \cdot \left(\left[\hat{k} \times \hat{\varepsilon}\right] \cdot \hat{u}^*_{\Delta m_J}\right)\right|^2 \end{aligned} \tag{7.15}$$

with $\left|\langle \xi', J' \,||\widehat{\mathcal{M}}||\, \xi, J\rangle\right|^2$ being the squared reduced magnetic-dipole transition matrix element and a different geometrical factor $|\left(\hat{k} \times \hat{\varepsilon}\right) \cdot \hat{u}^*_{\Delta m_J}|^2$. In contrast to an E1 transition, the direction of the magnetic field matters here, which induces the M1 transition (see Equation 7.13). This is accounted for by the unit vector $\hat{k} \times \hat{\varepsilon}$ in the geometrical factor, which is identical to the unit vector of the magnetic field. Considering this, there is a full analogy between both types of dipole transitions. The values for the new geometrical factor are given in Table 7.2 where only the values for $\hat{\varepsilon}_\alpha$ and $\hat{\varepsilon}_\beta$ polarization are swapped compared to Table 7.1.

Another implication is, that the concept of the terminology of π or σ polarization of the light field breaks down for magnetic transitions as a result of the incompatibility with the definition of the polarization through the electric field. This even caused an inconsistent use of these terms in the literature [cf. Soria Orts (2005) and D.-F. F. v. Lindenfels (2015)]. To avoid that, this thesis defines π-transitions purely associated with $\Delta m = 0$ and σ-transitions with $\Delta m = \pm 1$. Expressions like π or σ polarization are avoided.

$\left\|(\hat{k}\times\hat{\varepsilon})\cdot\hat{u}^{*}_{\Delta m}\right\|^{2}$	π	σ^{+}	σ^{-}
$\Delta m = m' - m$	0	1	-1
$\hat{\varepsilon}_{\alpha}$	$\sin^2\theta$	$\frac{1}{2}\cos^2\theta$	$\frac{1}{2}\cos^2\theta$
$\hat{\varepsilon}_{\beta}$	0	$\frac{1}{2}$	$\frac{1}{2}$
$\hat{\varepsilon}_{+}$	$\frac{1}{2}\sin^2\theta$	$(1+\cos\theta)^2/4$	$(1-\cos\theta)^2/4$
$\hat{\varepsilon}_{-}$	$\frac{1}{2}\sin^2\theta$	$(1-\cos\theta)^2/4$	$(1+\cos\theta)^2/4$

Table 7.2: Geometrical coupling between a light field and M1 transitions. The geometrical factor $|(\hat{k}\times\hat{\varepsilon})\cdot\hat{u}^{*}_{\Delta m}|^2$ (see Equation 7.15) is given for π, σ^{+}, and σ^{-}-transitions as a function of the polar angle θ and for a specific light field polarization (first column), defined by $\vec{\mathcal{E}} = \mathcal{E}\cdot\hat{\varepsilon}$ with the electric field strength $\mathcal{E}$ and the unit vector $\hat{\varepsilon}$. $\hat{\varepsilon}_{\alpha}$ and $\hat{\varepsilon}_{\beta}$ refer to the orthogonal linear polarization directions as defined in Figure 7.1 while $\hat{\varepsilon}_{+}$ and $\hat{\varepsilon}_{-}$ refer to the helical polarization basis. θ is the angle of incidence between the wave vector $\vec{k}$ and the quantization axis z'. The sum of all geometrical factors for a specific polarization over all Δm is identical to one. Note that the only difference to Table 7.1 is that the values for linear $\hat{\varepsilon}_{\alpha}$ and $\hat{\varepsilon}_{\beta}$ polarization are swapped.

7.2 Coherent excitation and manipulation

Coherent control over the electronic and motional degrees of freedom of a trapped atom is a key capability in cutting-edge frequency metrology. This requires stable phase relations between interrogating lasers or microwaves and the electronic wave function of the atom. In this section relevant equations are briefly discussed to describe an electronic two-level system studied through Rabi spectroscopy [see the pertinent literature, e. g., Riehle (2004) and references therein]. Afterwards, the coupling of the two-level system with the motion of the atom is addressed [see, e. g., Leibfried et al. (2003), Wineland, Monroe, Itano, Leibfried, et al. (1998), and references therein].

7.2.1 Rabi excitation

An electronic transition with of a small natural linewidth, being interrogated by a narrow-linewidth laser tuned close to the resonance, is typically well described by a two-level system of a ground state $|\downarrow\rangle$ and an excited state $|\uparrow\rangle$. The electronic wave function of this system is given by

$$|\Psi\rangle = e(t)\,|\uparrow\rangle + g(t)\,|\downarrow\rangle \tag{7.16}$$

with the complex time-dependent amplitudes $g(t)$ and $e(t)$. The probability of measuring the system in one of these states, also dubbed the *population* of the corresponding state, is given by the square of these amplitudes with the normalization condition $1 = |e(t)|^2 + |g(t)|^2$. When the system is initially prepared in the ground state $|\downarrow\rangle$ at time $t = 0$ and probed by a square pulse of monochromatic coherent radiation of increasing pulse length, *Rabi oscillations* are observed (also known as *Rabi flopping*). The time-evolution of the population of the excited state owing to the interaction with the monochromatic light is given by

$$P_{\mathrm{e}}(t) = |e(t)|^2 = \left(\frac{\Omega_0}{\Omega_{\mathrm{R}}}\right)^2 \sin^2\frac{\Omega_{\mathrm{R}}\,t}{2} \tag{7.17}$$

with the generalized Rabi frequency

$$\Omega_{\mathrm{R}} = \sqrt{\Omega_0^2 + \Delta\omega^2}, \tag{7.18}$$

where Ω_0 is the Rabi frequency, describing the strength of the coupling between the resonant radiation field and the transition, and $\Delta\omega$ is the detuning from the atomic resonance. In the case of an electric-dipole transition for instance, Ω_0 is given by[8]

$$\Omega_0 = \frac{|\langle\uparrow|\widehat{\vec{\mathcal{D}}}\cdot\vec{\mathcal{E}}_0|\downarrow\rangle|}{\hbar}, \tag{7.19}$$

where $\widehat{\vec{\mathcal{D}}}$ is the electric-dipole operator and $\vec{\mathcal{E}} \equiv \vec{\mathcal{E}}(t) = \vec{\mathcal{E}}_0\cos(\omega t)$ the monochromatic electric field oscillating at the angular frequency ω with the constant amplitude $\vec{\mathcal{E}}_0$. The *Rabi angle* is defined by

$$\Phi_{\mathrm{R}}(t) = \Omega_{\mathrm{R}}\,t \tag{7.20}$$

with Ω_{R} being the generalized Rabi frequency. A maximum of population is transferred from the ground into the excited state (and vice versa) for the angle

$$\Phi_{\mathrm{R}}(t = t_\pi) = \Omega_{\mathrm{R}}\,t_\pi \overset{!}{=} \pi \tag{7.21}$$

for a given detuning $\Delta\omega$. This is accomplished through probing the transition with a so-called *π-pulse* of pulse length t_π, dubbed the *π-time*. Only when the radiation frequency exactly matches the electronic resonance, i. e., $\Delta\omega = 0$ and $\Omega_{\mathrm{R}} = \Omega_0$, all population can be transferred according to Equation 7.17. In the following, the term π-time usually refers to the on-resonant excitation.

The stable phase relation between the radiation and the atom is perturbed by fluctuations and noise of experimental parameters or even interrupted by spontaneous decay of the excited state. The coherence time τ is a measure for the time scale of stable phase relations. To account for decoherence caused by white noise, we rewrite Equation 7.17 using the addition theorem $2\sin^2 x =$

---

[8] Note that Equation 7.19 corresponds to Equation 7.3 with the resulting coupling given in Equation 7.6. Thereby, Ω_0 also accounts for the geometrical coupling between the light and the atom.

$1-\cos(2x)$ and introduce the additional damping term $\mathrm{e}^{-t/\tau}$ in front of the oscillatory part. This yields the equation

$$P_\mathrm{e}(t)=\left(\frac{\Omega_0}{\Omega_\mathrm{R}}\right)^2\frac{1-\mathrm{e}^{-\frac{t}{\tau}}\cos(\Omega_\mathrm{R}t)}{2}, \tag{7.22}$$

capable to describe Rabi oscillations which happen on a time scale comparable to or even longer than the coherence time τ.

7.2.2 Rabi line shape

The line shape of a transition, observed by probing with a square pulse of monochromatic radiation with fixed pulse length t_p being short against the excited-state lifetime, is described by a *Rabi line shape*. It is obtained from Equation 7.17 as a function of the detuning $\Delta\omega$ as

$$P(\Delta\omega)=\left(\frac{\Omega_0 t_\mathrm{p}}{2}\right)^2\operatorname{sinc}^2\left(\sqrt{\Omega_0^2+\Delta\omega^2}\,\frac{t_\mathrm{p}}{2}\right), \tag{7.23}$$

where $\operatorname{sinc}x=\sin x/x$ is the unnormalized sinc function[9] and Ω_0 the Rabi frequency. When the transition is driven by a pulse corresponding to an on-resonance π-pulse, the probe time $t_\mathrm{p}=t_\pi$ and the relation $\Omega_0 t_\pi=\pi$ is applicable. The FWHM linewidth Δf^FWHM of $P(\Delta\omega)$ is then found numerically by solving the equation

$$\left(\frac{\pi}{2}\right)^2\operatorname{sinc}^2\left(\sqrt{\left(\frac{\pi}{2}\right)^2+\left(\pi\cdot\Delta f^\mathrm{FWHM}\cdot t_\pi\right)^2}\right)\overset{!}{=}\frac{1}{2}. \tag{7.24}$$

To a good approximation one then obtains the relation

$$\Delta f^\mathrm{FWHM}\approx\frac{0.8}{t_\pi}. \tag{7.25}$$

7.2.3 Coupled system of qubit and quantum harmonic oscillator

The laser field seen by an ion in a Paul trap is modulated by the ion's own motion at the secular frequencies ω_u, at the frequencies of the intrinsic micromotion $\Omega_\mathrm{rf}\pm\omega_u$, and at the trap drive frequency Ω_rf of the excess micromotion. This gives rise to *motional sidebands* around the narrow electronic transition (the qubit), which is itself dubbed the *carrier*. The sidebands appear at integer multiples of $\omega_{\tilde{x}}$, $\omega_{\tilde{y}}$, ω_z, and Ω_rf, as well as at sum or difference frequencies of those. When scanning across the transition, these sidebands can be resolved if the bandwidth of the radiation, for example of a laser or a microwave antenna, is smaller than the spacing between the sidebands. Moreover, sidebands of the

---

[9] The unnormalized sinc function differs by a factor of π in the argument from the normalized sinc function.

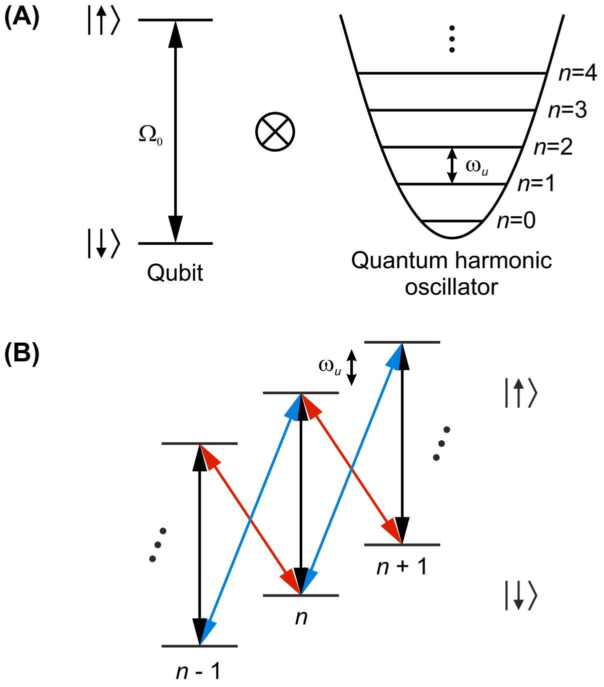

Figure 7.2: Coupled system of qubit and quantum harmonic oscillator. (**A**) The qubit (left) and the motional states of the quantum harmonic oscillator (QHO) (right) can be coupled with a narrow-linewidth laser. (**B**) This allows to selectively drive the qubit transition on the carrier (black arrows), the red sideband (red arrows), or the blue sideband (blue arrows). The motional state of the QHO is changed in the latter two cases.

qubit can be coherently driven on purpose in such a system as illustrated by Figure 7.2 for a specific secular mode with the motional frequency ω_u in order to manipulate the motional state of the ion. The sidebands appear at different signal strengths

$$S_i \propto |J_i(\beta)|^2 \,, \tag{7.26}$$

where J_i is the Bessel function of the modulation index

$$\beta = \vec{k} \cdot \vec{u_\mathrm{a}} = \frac{2\pi \cdot u_\mathrm{a}}{\lambda} \cos\alpha \tag{7.27}$$

with the motional amplitude u_a (u_a has to be replaced by $u_\mathrm{a} q_u/4$ in the case of intrinsic micromotion, see Equation 6.11), the wavelength λ of the electronic transition, and the angle α between the direction of motion and the laser beam. The index i refers to the corresponding sidebands, e. g., $i = 0$ for the carrier, $i = +1$ for the first-order blue sideband (BSB), and $i = -1$ for the first-order red sideband (RSB).

Lamb–Dicke regime

An important quantum regime which is a mandatory prerequisite for many trapped-ion experiments is the co-called *Lamb–Dicke regime*. It features a small coupling between the electronic transition and the quantized motion of the ion.

When the modulation index $\beta \ll 1$, one approximately obtains for the ratio of the first-order BSB to the carrier transition[10]

$$\frac{S_1}{S_0} = \left| \frac{J_1(\beta)}{J_0(\beta)} \right|^2 \approx \left(\frac{\beta}{2} \right)^2 , \tag{7.28}$$

i. e., the first-order sideband is weak in comparison to the carrier, and higher-order sidebands are even more strongly suppressed. The Lamb–Dicke parameter

$$\eta = \vec{k} \cdot \vec{u}_{\mathrm{a},0} = \frac{2\pi u_{\mathrm{a},0}}{\lambda} \cos\alpha \tag{7.29}$$

is defined as the modulation index for the motional ground state where the oscillation amplitude $u_{\mathrm{a},0}$ represents the spatial extent of the wave function of the motional ground state, given by Equation 6.21. The *Lamb–Dicke regime* is defined by demanding that the spatial extent of the ion's motion or in other words the spatial extent of the motional wave function $|\,\psi_{\mathrm{m}}\rangle$ is much smaller than the wavelength (Wineland, Monroe, Itano, Leibfried, et al., 1998), quantitatively expressed by

$$\sqrt{\langle\, \psi_{\mathrm{m}} | k_u^2 \widehat{u}^2 |\, \psi_{\mathrm{m}} \rangle} \ll 1 , \tag{7.30}$$

where k_u is the projection of the wave vector onto the motional mode with $u \in \{\tilde{x}, \tilde{y}, z\}$ and $\widehat{u}$ is the corresponding position operator. Using the definition in Equation 7.29 one obtains the expression

$$\eta \cdot \sqrt{2n+1} \ll 1 \tag{7.31}$$

for a specific Fock state $|\, n \rangle$ with the corresponding occupation number n of the motional mode[11]. As a consequence of this relation, n must be sufficiently reduced in order to access the Lamb–Dicke regime, in many experiments achieved through Doppler laser cooling (being discussed in Section 7.3.1). Importantly, the recoil energy

$$E_{\mathrm{recoil}} = \eta^2 \hbar\, \omega_u \tag{7.32}$$

transferred to the ion upon absorption or emission of a photon along the motional mode direction is by a factor of η^2 considerably smaller than the energy spacing $\hbar\, \omega_u$ between the QHO states. Therefore, transitions which change the occupation numbers n of the motional mode are basically negligible. In order to drive sidebands which change the motional state on purpose, the small Lamb–Dicke parameter η needs to be compensated by a high intensity of the laser field[12] and thereby a high Rabi frequency Ω_0. BSB, carrier, and RSB-transitions appear with a signal of

---

[10] If $\beta > 1$, the carrier can even be suppressed with respect to the sidebands.

[11] The spatial extent of the motional wave function is basically expressed by Equation 6.19 when replacing $\bar{n}$ through n. Mind the difference between the classical amplitude u_{a}, which corresponds to a thermal distribution of the occupation number n, and the spatial extent of a quantum state.

$$\begin{aligned}
&\text{First-order BSB} && \propto && \Omega_{n,n+1}^2 = (\Omega_0\,\eta)^2 \cdot (n+1) && \text{(7.33a)}\\
&\text{Carrier} && \propto && \Omega_0^2 && \text{(7.33b)}\\
&\text{First-order RSB} && \propto && \Omega_{n,n-1}^2 = (\Omega_0\,\eta)^2 \cdot n, && \text{(7.33c)}
\end{aligned}$$

where $\Omega_{n,n+1}$ and $\Omega_{n,n-1}$ are the Rabi frequencies for the first-order BSB and RSB transitions, respectively (Leibfried et al., 2003). Note that each system of coupled motional mode and electronic transition has its own Lamb–Dicke parameter, for instance we have $\eta_{\tilde{x}}$, $\eta_{\tilde{y}}$, and η_z.

Stimulated Raman transitions

Stimulated Raman transitions are used to control the electronic hyperfine qubit state of $^9\mathrm{Be}^+$ and the motional state of the two-ion crystal. For this two-photon process, the difference frequency of two laser beams, dubbed as *Raman beams*, is matched to the 1.25 GHz transition frequency of the qubit (see Figure 5.2). The higher-frequency Raman beam is denoted as the blue Raman beam, the other one as the red Raman beam. Both Raman beams use a common virtual state with a detuning of 103 GHz and 94 GHz from the intermediate electronic P states[13] in order to avoid population of these intermediate states. To scan across the Raman transition, the frequency of one Raman beam is fixed to define the detuning of the common virtual state and the frequency of the other Raman beam is then scanned across the qubit transition. The Rabi frequency of a stimulated Raman transition is given by (Wineland et al., 2003; Wineland, Monroe, Itano, B. E. King, et al., 1998)

$$\Omega_0^{\mathrm{Raman}} = \frac{\Omega_{0,1} \cdot \Omega_{0,2}}{\Delta\omega^{\mathrm{Raman}}}, \tag{7.34}$$

where $\Omega_{0,i}$ is the Rabi frequency of Raman beam i for a transition between the corresponding qubit state and the intermediate state. $\Delta\omega^{\mathrm{Raman}}$ is the detuning of the virtual state form the intermediate one, which is large against the involved natural linewidths[14].

For the selective coherent manipulation of a specific motional mode we have previously taken into account the wave vector $\vec{k}$ of a single laser beam. For a stimulated Raman transition the differential wave vector

$$\Delta\vec{k} = \vec{k}_1 - \vec{k}_2 \tag{7.35}$$

---

[12] This also implies that η should not be too small. Values on the order of 0.1 are typically preferred.

[13] The Raman beams couple to both P states roughly equally and the Stark shift is canceled to a high degree.

[14] In the specific case of this work, the virtual state lies in between of two intermediate P states with comparable couplings. Therefore, the coupling to both P states has to be taken into account for each Raman beam. In particular, interference between the coupling amplitudes has to be considered.

has to be considered instead of $\vec{k}$, where $\vec{k}_1$ and $\vec{k}_2$ are the individual wave vectors of the respective Raman beams (Wineland et al., 2003). Analogously, $\Delta\vec{k}$ needs to provide a projection onto the motional mode in order to couple and to manipulate it. In this work, two different sets of two Raman beams are employed, one for manipulating the axial modes of the two-ion crystal and one for the radial modes (see Figure 7.3 and for more details about the experimental implementation Figure 11.4). $\Delta\vec{k}_{\mathrm{ax}}$ points along the axial direction z. In contrast, $\Delta\vec{k}_{\mathrm{rad}}$ lies along x of the laboratory frame and has a projection through the angle $\alpha = 45°$ onto both radial mode directions $\tilde{x}$ and $\tilde{y}$. This means, that the radial set of Raman beams geometrically couples to both radial modes simultaneously. The selectivity for one of the radial modes is realized by the different secular frequencies $\omega_{\tilde{x}}$ and $\omega_{\tilde{y}}$.

The Lamb–Dicke parameter for the stimulated Raman transition is given by

$$\eta = \Delta\vec{k} \cdot \vec{u}_{\mathrm{a},0} \,. \tag{7.36}$$

$\Delta\vec{k}_{\mathrm{ax}}$ is parallel to $\vec{z}_{\mathrm{a},0}$. The projection of $\Delta\vec{k}_{\mathrm{rad}}$ onto the radial mode directions $\tilde{x}$ and $\tilde{y}$ through $\alpha = 45°$ further reduces η by $\cos\alpha \approx 0.71$. In the case of $^9\mathrm{Be}^+$, η is rather large due to the small ion mass of $m \approx 9\,\mathrm{u}$ (see Equation 6.21) and the small wavelength of $\lambda \approx 313\,\mathrm{nm}$. As reported by Leopold (2018), the $^9\mathrm{Be}^+$ Lamb–Dicke parameters with the chosen beam geometry for the three motional modes can be calculated by

$$\eta_z = 0.82\sqrt{\frac{2\pi \times 1\,\mathrm{MHz}}{\omega_z}} \tag{7.37a}$$

$$\eta_{\tilde{x}/\tilde{y}} = 0.34\sqrt{\frac{2\pi \times 1\,\mathrm{MHz}}{\omega_{\tilde{x}/\tilde{y}}}} \tag{7.37b}$$

with the secular angular frequencies ω_u.

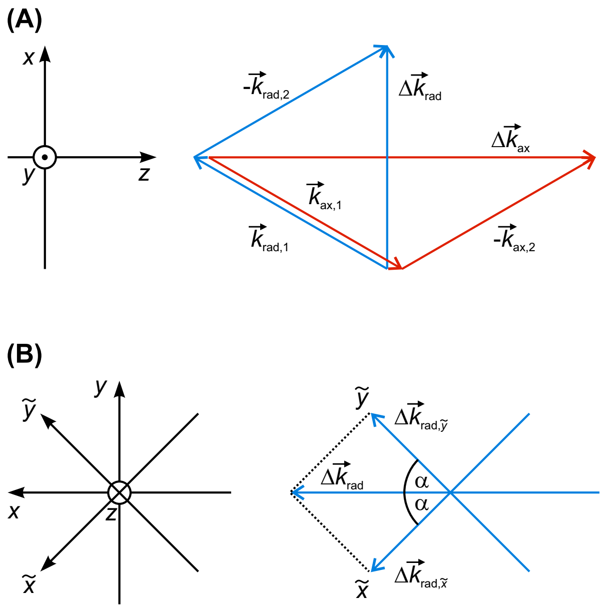
(A)
x
y
z
$-\vec{k}_{\mathrm{rad},2}$
$\Delta\vec{k}_{\mathrm{rad}}$
$\Delta\vec{k}_{\mathrm{ax}}$
$\vec{k}_{\mathrm{ax},1}$
$\vec{k}_{\mathrm{rad},1}$
$-\vec{k}_{\mathrm{ax},2}$
(B)
y
$\tilde{y}$
x
z
$\tilde{x}$
$\tilde{y}$
$\Delta\vec{k}_{\mathrm{rad},\tilde{y}}$
$\Delta\vec{k}_{\mathrm{rad}}$
α
α
$\tilde{x}$
$\Delta\vec{k}_{\mathrm{rad},\tilde{x}}$

Figure 7.3: Geometrical relations for the Raman beams. (**A**) Top view. Two Raman beams (1 and 2) are combined each to generate differential wave vectors for the axial and radial modes. The arrows represent the wave vectors $\vec{k}$ (or $-\vec{k}$ for the beams labeled with 2) and differential wave vectors $\Delta\vec{k}$ as labeled in the figure. (**B**) View along the Paul trap axis z. The radial differential Raman wave vector has projections onto both radial principal axes of the Paul trap. See text for further details.

7.3 Laser cooling

Laser cooling of $^9\mathrm{Be}^+$ is the essential method to remove kinetic energy from the trapped ions. Two types of laser cooling are employed in this work. First, *Doppler cooling* on the $|^2\mathrm{S}_{1/2}, F = 2, m_F = 2\rangle$–$|^2\mathrm{P}_{3/2}\rangle$ transition allows to Coulomb crystallize a large cloud of $^9\mathrm{Be}^+$ ions during $^9\mathrm{Be}^+$ loading, to dissipate the residual kinetic energy of the HCI during the recapture process in the Paul trap, and to sympathetically cool the HCI during the two-ion crystal preparation. Additionally, Doppler cooling periods are used in between of the QLS sequences. Second, *resolved sideband cooling* on the hyperfine qubit transition $|^2\mathrm{S}_{1/2}, F = 2, m_F = 2\rangle$–$|^2\mathrm{S}_{1/2}, F' = 1, m_{F'} = 1\rangle$ of $^9\mathrm{Be}^+$ via stimulated Raman transitions is applied to further cool the two-ion crystal (see Figure 5.2). This allows for cooling beyond the Doppler limit down to the quantum-mechanical ground state of motion. This section gives a brief summary about these techniques. Details can be found in the literature [see, e. g., Leibfried et al. (2003), Wineland and Itano (1979), and Wineland, Monroe, Itano, Leibfried, et al. (1998)].

7.3.1 Doppler cooling

Doppler cooling of an ion is based on the absorption of light from a laser beam, red-detuned from a fast cycling transition, followed by spontaneous emission. Most of the photons are absorbed by the ion when it moves towards the laser beam. Only then, the frequency of the red-shifted photons is closer to the resonance of the fast cycling transition of the moving ion. In contrast, the subsequent electronic decay does not prefer a specific direction. As a consequence, the ion experiences on average a momentum transfer along the laser beam direction which slows it down. Since the ion is confined in a trap, only a single Doppler cooling beam pointing along a direction which couples to all motional modes is sufficient for three-dimensional cooling. An E1 transition with a transition rate of

$$\gamma = 2\pi \times \delta\nu = \frac{1}{\tau} \tag{7.38}$$

on the order of several 10 MHz is typically used for this purpose in order to cool efficiently, where τ is the the natural lifetime and $\delta\nu$ the FWHM natural linewidth of the transition. The Doppler cooling limit is obtained by equating the average energy loss, owing to absorption from the cooling beam, and the competing heating, with a component from the isotropic spontaneous emission and another one again from the absorption. From this relation, the remaining energy at the Doppler limit

$$E_{\text{doppler}} = \frac{\hbar\left[4\Delta\omega^2 + \gamma^2\left(1+\frac{I}{I_0}\right)\right]\left(1+3\cos^2\alpha\right)}{48\,|\Delta\omega|\cos^2\alpha} \tag{7.39}$$

per motional mode is obtained[15] [see for details Wineland and Itano (1979) and Wübbena et al. (2012)]. $\Delta\omega$ is the detuning from the Doppler cooling transition, I the laser intensity of the Doppler cooling beam, I_0 the saturation intensity of the fast cycling transition, α the angle between the laser beam and the direction of the motional mode, and $\hbar$ the reduced Planck constant. The well-known Doppler limit

$$E_{\text{doppler}} = \frac{\hbar\gamma}{2} \tag{7.40}$$

is obtained for each mode with $I/I_0 \to 0$, $\Delta\omega = -\gamma/2$, and $\cos^2\alpha = 1/3$, corresponding to identical angles of $\alpha \approx 54.7°$ between the laser beam and each of the three motional mode directions. The maximum cooling rate is however realized for $I = 2I_0$ at the cost of an increased Doppler cooling limit by a factor of 2.

The remaining energy in each motional mode cooled to the Doppler limit is equally distributed between the kinetic and the potential energy of the mode. Expressed in terms of an occupation number of the QHO mode, one obtains a residual mean occupation number of

$$n_{\text{doppler}} \approx \frac{\gamma}{2\,\omega_u}, \tag{7.41}$$

where ω_u is the secular frequency of the mode. For instance, with $\omega_u = 2\pi \times 1\,\text{MHz}$ and $\gamma = 2\pi \times 20\,\text{MHz}$ this yields an occupation number of $n_{\text{doppler}} \approx 10$ in that mode.

---

[15] Equation 7.39 is also valid for a two-ion crystal. Both motional modes of a specific mode direction feature the identical Doppler cooling limit, independent of the individual oscillation amplitudes of the two ions. However, a smaller individual oscillation amplitude results in a longer cooling time.

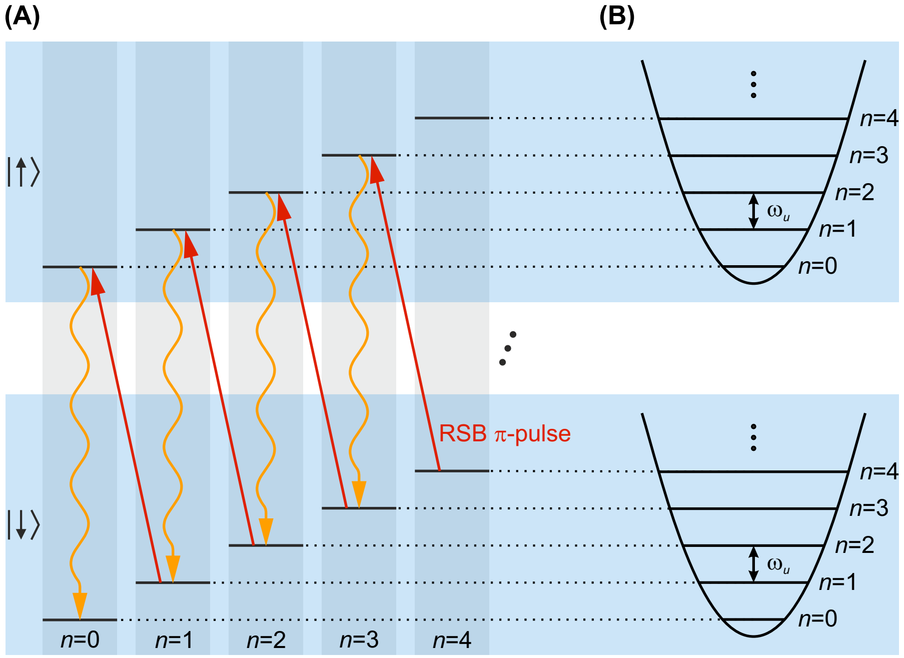

Figure 7.4: Pulsed resolved sideband cooling. (**A**) The alternating application of red sideband (RSB) π-pulses on the qubit transition (red arrows), followed by a dissipative step of spontaneous emission in order to re-initialize the qubit ground state (wavy orange arrows) allows to climb down the ladder of motional states until the motional ground state is reached. (**B**) Each of both qubit states (highlighted in blue) comprise the same ladder of QHO states. The spacing is given by the secular frequency ω_u. See text for further details.

7.3.2 Pulsed resolved sideband cooling

In order to bring the trapped ion into its ground state of secular motion, cooling beyond the Doppler cooling limit is required. This can be done through resolved sideband cooling [see, e. g., Leibfried et al. (2003), Monroe et al. (1995), and Wineland, Monroe, Itano, Leibfried, et al. (1998)] as illustrated in Figure 7.4. In contrast to Doppler cooling, a narrow electronic transition and a narrow-linewidth laser[16] are employed in order to resolve the sidebands of the secular modes. At first, through initial optical pumping and Doppler cooling the ion is deterministically prepared in the electronic ground state of the qubit and brought into the Lamb–Dicke regime according to Equation 7.31 with n on the order of $n_{\text{doppler}} \approx 10$. By driving a π-pulse on the first-order RSB of the qubit transition, the occupation number is reduced by one. Next, a dissipative step initializes the qubit ground state again, in the case of this work this is realized through repuming on the $^2\mathrm{S}_{1/2}$–$^2\mathrm{P}_{1/2}$ transition as shown in Figure 5.2. By repeating this cycle, the ion is sequentially cooled until the motional ground state with a mean occupation number of $\bar{n} \approx 0$ is reached.

---

[16] In this work, the Raman laser beams are operated for this purpose, derived from the same laser source. This has the distinct advantage that laser noise cancels for their frequency difference and the laser beams appear very coherent and narrow for the $^9\mathrm{Be}^+$ ion even without stabilization of any kind.

Resolved sideband cooling of both axial modes is performed in this work as a prerequisite of QLS. A Doppler cooling limit of n_{doppler} on the order of 10 is achieved. However, since the $^{9}\mathrm{Be}^{+}$ Lamb–Dicke parameters are with $\eta \approx 0.5$ rather large, $\eta \cdot \sqrt{2n+1}$ is on the order of 2 and does not fulfill the Lamb–Dicke criterion given by Equation 7.31. In that case, higher-order sidebands can be used to overcome this limitation [see Joshi et al. (2019), Leopold (2018), and Wan et al. (2015) as well as Leopold et al. (2019) in Appendix P3].

Part III

Experiment

Who ordered that?

— I. I. Rabi

The third part of this thesis describes the experimental implementation of quantum logic spectroscopy (QLS) and covers the entire procedure from the highly charged ion (HCI) production to the spectroscopy. An overview of the experimental setup is given in Chapter 8. The source of HCIs, the electron beam ion trap (EBIT), is discussed in detail in the publication Micke et al. (2018) in Appendix P1 and will therefore be only briefly addressed in Chapter 9, followed by a more comprehensive discussion of the $^{40}\mathrm{Ar}^{13+}$ extraction, transfer through a deceleration beamline, and recapture in a cryogenic Paul trap in Chapter 10. Chapter 11 focuses on the storage and preparation of cold HCIs in their motional ground state. The two publications Micke et al. (2019) and Leopold et al. (2019) in Appendix P2 and Appendix P3 provide further details. The clock laser stabilization and the concept of measuring its absolute frequency is described in Chapter 12. Finally, the realization of QLS by an experimental sequence is addressed in the last Chapter 13.

8 Overview

The experiment is distributed over several laboratories which are connected by optical fibers and transmission lines. The core setup is located in a single laboratory which extends over two rooms, one room designated as *laser laboratory*, the other one as *machine room*. This division allows to separate all components which cause acoustic noise and mechanical vibrations into the machine room, thereby allowing for a stable and quiet operation of the Paul trap and the laser systems. A top view is shown in Figure 8.1A.

Highly charged ions (HCIs) are produced in a compact room-temperature electron beam ion trap (EBIT), displayed in the top right corner of Figure 8.1A. From there, the ions are extracted in bunches. A beamline, operated under ultra high vacuum (UHV) conditions and mostly located in the laser laboratory, connects the EBIT and the Paul trap in order to transfer the HCIs. The beamline contains several ion optical elements and ion detectors to manipulate the beam and to accomplish a first electrodynamic deceleration step with a pair of pulsed drift tubes. This reduces the approximately $700\,q\mathrm{V}$ kinetic energy of the extracted HCIs to a level of about $150\,q\mathrm{V}$. Then, a second electrostatic deceleration step is realized by globally biasing the Paul trap voltages to about 150 V above the ground potential of the experiment in order to bring the HCIs to rest.

A closed-cycle cryostat is operated in the machine room and refrigerates the Paul trap in the laser laboratory to a temperature of below 5 K. Extreme high vacuum (XHV) conditions are achieved at such low temperatures through freezing out the residual gas and thereby enabling HCI storage times on the order of 45 min. The separation of the closed-cycle cryostat from the Paul trap allows the vibration level there to be reduce to about 10 nm, a crucial requirement to suppress motional frequency shifts and broadening mechanisms for spectroscopy.

Figure 8.1B shows a magnified side view onto the Paul trap region. Decelerated single HCIs enter from the left and are radially confined by the rf field of the Paul trap. They are reflected by a dc voltage applied to the outer endcap electrode downstream and recaptured by switching up the voltage of the mirror tube in front of the Paul trap in the meantime. $^9\mathrm{Be}^+$ ions, confined in the Paul trap, are imaged by exciting them with 313 nm laser radiation and collecting the fluorescence light by an in-vacuum biaspheric lens above the Paul trap. The fluorescence light is focused through a small-diameter aperture in the cryogenic shields and thereafter focused by an external lens system onto both a photomultiplier tube (PMT) and an electron multiplying charge-coupled device (EMCCD) camera with a 99:1 beamsplitter (not shown in Figure 8.1B) for counting the fluorescence photons and generating an ion image, respectively.

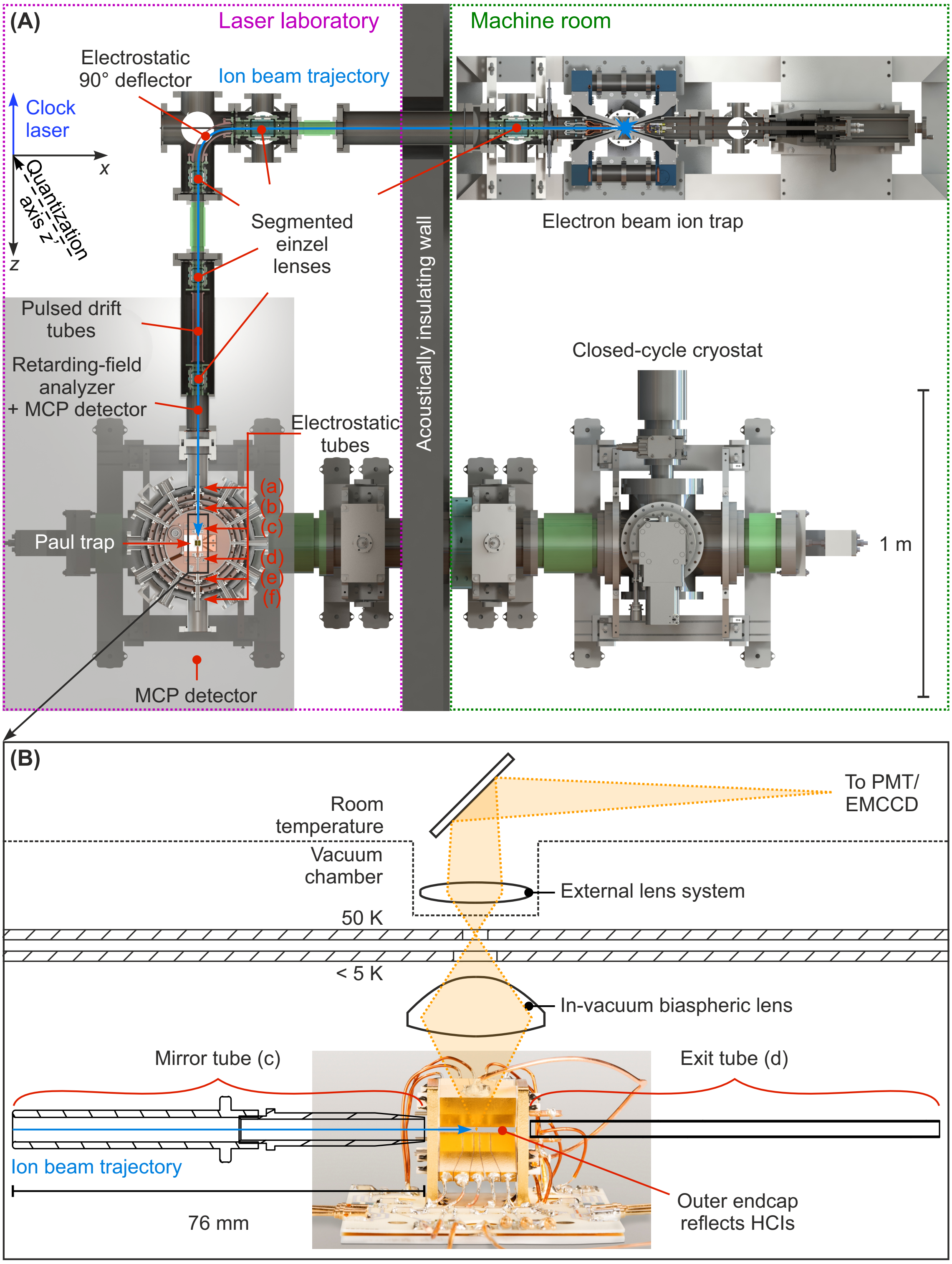
(A)
Laser laboratory
Machine room
Electrostatic 90° deflector
Ion beam trajectory
Clock laser
x
Quantization axis z'
z
Segmented einzel lenses
Pulsed drift tubes
Retarding-field analyzer + MCP detector
Electrostatic tubes
(a)
(b)
(c)
(d)
(e)
(f)
Paul trap
MCP detector
Acoustically insulating wall
Electron beam ion trap
Closed-cycle cryostat
1 m
(B)
Room temperature
Vacuum chamber
50 K
< 5 K
To PMT/ EMCCD
External lens system
In-vacuum biaspheric lens
Mirror tube (c)
Exit tube (d)
Ion beam trajectory
76 mm
Outer endcap reflects HCIs

Figure 8.1: Overview of the core setup. (**A**) Top view onto the laboratory and vacuum system. An acoustically insulating wall separates the two rooms. Six electrostatic tubes are symmetrically arranged around the Paul trap and along the ion beam trajectory referred to as (a) *first stage tube 1*, (b) *second stage tube 1*, (c) *mirror tube*, (d) *exit tube*, (e) *second stage tube 2*, and (f) *first stage tube 2*. (**B**) Magnified side view along the x-axis onto the Paul trap and imaging system. The upper part (< 5 K and 50 K thermal shields, room temperature stage) is only schematic and not to scale. See text for details. EMCCD—electron multiplying charge-coupled device, HCIs—highly charged ions, MCP—microchannel plate, PMT—photomultiplier tube.

9 Production of highly charged ions

The ionization energy of an ion scales roughly with the square of the charge state [J. D. Gillaspy (2001), see Table 5.1 as an example]. Thus, high energies are required for the production of high charge states in order to overcome the high ionization thresholds. Different types of machines, mentioned in Chapter 1, are operated for this purpose. Some of them are rather large and require a considerable amount of maintenance. To ease access to HCIs for various experiments, a new class of compact room-temperature electron beam ion traps (EBITs) were developed within this work, dubbed the *Heidelberg compact EBITs* (HC-EBITs). These EBITs are described in detail by Micke et al. (2018) in Appendix P1 and will be only briefly introduced in this chapter.

While traditional EBITs generate a strong magnetic field of many teslas by use of superconducting coils close to the Helmholtz configuration, the HC-EBITs are based on 72 NdFeB permanent magnets (see Figure 9.1), arranged in eight arrays of 3×3 magnets. The field is focused towards the trap center by a yoke, made from magnetic steel and soft iron. There, a magnetic flux density of 0.86 T is reached, larger than that reported for any other room-temperature EBIT. The choice of using permanent magnets eliminates the need to operate cryogenic superconducting coils and therefore reduces the required maintenance effort significantly. Multiple HC-EBITs have proved reliable and stable operation over years, and they demonstrated electron-beam currents and energies of up to 80 mA and 10 keV. Moreover, they allow to install detectors or fluorescence collecting elements at a close distance from the HCI plasma, thereby offering large solid angles for in-EBIT spectroscopy. This is more troublesome to achieve in superconducting EBITs with cryogenic shielding. A prototype and four upgraded HC-EBITs are currently in operation[1], three of the five machines are located at the MPIK. One is used as an HCI source for a novel cryogenic Paul trap experiment *CryPTEx-2*, aiming at direct frequency comb spectroscopy in the XUV range (Nauta et al., 2017), and two are used as HCI sources for the Penning trap experiments *ALPHATRAP* (Sturm et al., 2019) and *PENTATRAP* (Repp et al., 2012) for ground-state g-factor studies and high-precision mass spectrometry, respectively. Another one, named PTB-EBIT, produces HCIs for the work reported in this thesis, and the fifth one is equipped with an off-axis electron gun for x-ray laser spectroscopy at synchrotron and free-electron laser facilities [see, e. g., Kühn et al. (2020)] and

---

[1] Another HC-EBIT will be in operation shortly at the MPIK and another one is under construction at the Ulsan National Insitute of Science and Technology in Korea for operation at the *PAL-XFEL* free-electron laser in Pohang.

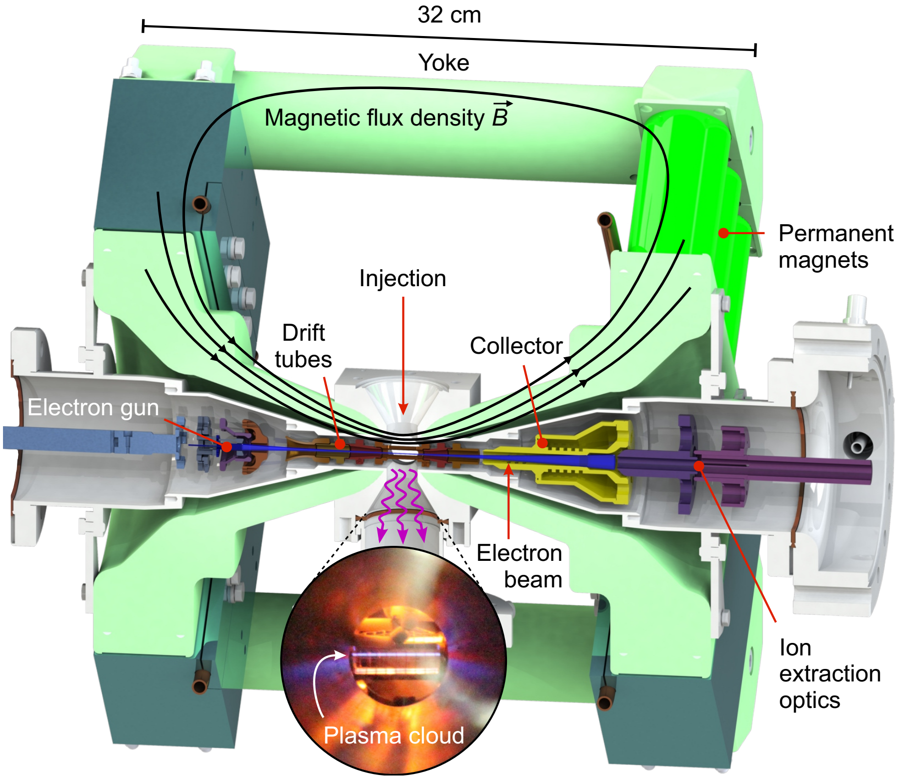
32 cm
Yoke
Magnetic flux density $\vec{B}$
Permanent magnets
Injection
Drift tubes
Collector
Electron gun
Electron beam
Ion extraction optics
Plasma cloud

Figure 9.1: Longitudinal section of PTB-EBIT. An electron beam (blue, labeled) is emitted from an electron gun, focused through the trap center by a magnetic field of increasing flux density B, decelerated again, and dumped on a collector electrode (yellow). The magnetic field is generated by permanent magnets (dark green) arranged in eight arrays and focused by a yoke (light green) towards the trap center. Highly charged ions (HCIs) are produced there by electron impact ionization of neutral atoms, injected perpendicular to the electron beam. The ions, in the form of a hot plasma cloud, are confined axially by the electrostatic potential of cylindrical drift tubes and radially by the negative space charge of the electron beam itself. The first electrostatic tube (purple) behind the collector is operated at a sufficiently negative potential to prevent the electron beam from passing through the collector. Additionally, this tube is used together with a second one as ion optical element to optimize the HCI extraction from the trap. The inset shows a photograph of the fluorescing HCI plasma.

is currently in operation at the *PETRA III* synchrotron of the DESY research center[2].

The monoenergetic electron beam is emitted from a thermionic cathode located in a true-zero magnetic field[3] and accelerated towards the trap center by the differential voltage applied between the central drift tube at a voltage V_t and the cathode at V_c. The kinetic electron-beam energy is then given by

---

[2] HC-EBITs equipped with an off-axis electron gun can run in a parasitic mode in line between the x-ray source and another experiment. With negligible transmission loss, HCIs are proposed to establish an unprecedented atomic standard for the calibration of the energy, intensity, and polarization of the x-ray radiation.

[3] In contrast to the magnetic field generated by Helmholtz coils, the magnetic field of the HC-EBITs possesses two locations at which the magnetic field inverts direction and the flux density becomes zero. The cathode and the collector are located there [see Micke et al. (2018) for details].

$$E_{\mathrm{kin}} = e \cdot (V_t - V_c) + U_{\mathrm{nsc}} + U_{\mathrm{psc}} + U_{\mathrm{offset}} \tag{9.1}$$

where U_{nsc} and U_{psc} are the negative and positive space-charge contributions from the electron beam and HCI cloud (as discussed in Section 6.1). U_{offset} is an offset energy on the order of a few eV owing to the work function of the electrode materials and reach-through of adjacent electric potentials. The magnetic flux density, increasing from zero field at the cathode up to 0.86 T at the trap center, compresses the electron-beam diameter[4] down to about 150 µm. This corresponds to an electron-beam current density of about 500 $\mathrm{A\,cm^{-2}}$ with an electron-beam current of 80 mA, to allow for a high ionization efficiency. After passing the trap center, the electron beam is decelerated again towards the collector electrode on ground potential and finally dumped there in order to close the electrical circuit. For this purpose, an electrostatic tube behind the collector is biased to a sufficiently negative potential to prevent the electron beam from passing through the collector. Typically, a fraction of 99 % of the emitted electron-beam is dumped on the collector electrode.

For the production of a specific HCI species, neutral atoms of the corresponding element can be introduced at the trap center as an atomic beam perpendicular to the electron-beam axis. If possible, a gas (sometimes isotopically enriched) of this element is directly leaked through a valve into a differentially pumped injection system. Alternatively, a vessel with a small amount of a volatile organometallic compound containing the element is installed at the inlet of the leak valve and, if needed, slightly warmed up. In both cases the inlet part is evacuated beforehand to less than 1 mbar in order to ensure low levels of contaminants. A 2 mm-diameter aperture separates the injection system from the main UHV of the EBIT. A different injection technique was recently developed for one of the HC-EBITs and employs *laser-induced desorption* for the study of rare isotopes (Schweiger et al., 2019) by modifying the *wire-probe technique* (Elliott and Marrs, 1995). There, an isotopically enriched sample of the respective element is prepared on the in-vacuum tip of a manipulator and moved towards the trap center to a sub-mm distance from the electron beam. Then, a pulsed laser with a few mJ pulse energy induces desorption of atoms from the sample and the close proximity to the electron beam ensures a high capture efficiency. With a 45 mA electron beam at 5.9 keV energy and a breeding time of 1 s, 2.3×10^4 pulses of highly charged $^{165}\mathrm{Ho}^{42+}$ with an integrated number of many million ions in that charge state were extracted from the EBIT, originating from a single sample of only 300 pg of holmium, corresponding to about 10^{12} atoms (Schweiger et al., 2019).

The electron beam dissociates molecules and ionizes neutral atoms by electron impact. Once ionized, the ions are immediately confined, as discussed in Section 6.1—axially by the electrostatic potential of the drift tubes and radially by the space-charge potential of the electron beam as well as the axial magnetic field. Then, sequential ionization takes place until a steady-state charge-state distribution has formed or the breeding is interrupted by dumping the trap, for instance through an extraction event. The maximum charge state is limited by the electron-beam energy, and the charge-state evolution (Penetrante et al., 1991) is governed by the ionization and recombination rates. The charge state of maximum abundance within the charge-state distribution can be well controlled by various EBIT parameters, such as the electron-beam energy and current, the injection pressure, and the breeding time. The latter one can be varied over several orders of magnitude from a few milliseconds up to many seconds for high charge states of heavy elements.

---

[4] The electron-beam diameter is given by twice the Herrmann radius as introduced in Section 6.1.

Various injection techniques and unspecific electron impact ionization allow an EBIT to produce a wide range of atomic systems. Experiments with the HC-EBITs and their demonstrated operation parameters suggest successful production of hydrogen-like systems up to the element iron and of helium-like or lithium-like systems up to the element xenon (Micke et al., 2018). Above that, a large range of intermediate charge states of heavier elements is accessible, as demonstrated with $^{165}\mathrm{Ho}^{45+}$ by Schweiger et al. (2019). The production of $^{40}\mathrm{Ar}^{13+}$ for this work is accomplished by leaking argon gas of natural abundance into the injection system of PTB-EBIT. For that purpose, the injection-system base pressure is raised from the low 10^{-9} mbar range by about one order of magnitude. An electron-beam current of 13 mA with 1 keV energy is used for ionization and radial ion confinement. The axial trap is established by operating the central drift tube at 460 V and the adjacent ones 40 V higher at 500 V. Taking the space-charge contribution into account, this corresponds to an axial trapping potential of about 50 V depth. The trap is partially dumped at a rate of 4 Hz by switching the central drift-tube potential up to 720 V for a period of 200 ns.

10 Transfer of highly charged ions

In the previous chapter the EBIT was introduced as the source for HCIs. This chapter addresses the transfer processes from the extraction of the HCIs to their recapture in the Paul trap and subsequent co-crystallization within a laser-cooled $^9\mathrm{Be}^+$ Coulomb crystal. A beamline was designed and set up for this purpose, following the concept of Schmöger, Schwarz, et al. (2015). The optimized HCI production, extraction, transfer, and recapture in the Paul trap has been stable for more than 1.5 yr without the need of readjustments, even for temperature changes on the order of a few kelvins in the machine room between summer and winter. The setup is introduced in the first section of this chapter. Thereafter, the extraction, charge-state selection, deceleration, and recapture are discussed in the following sections.

10.1 Ion optical setup

The ion optical elements used to transfer the HCIs from the EBIT into the Paul trap are shown in Figure 8.1A and are summarized in Table 10.1. The beamline comprises five segmented einzel lenses of two different sizes[1] (Mandal, Sikler, and Mukherjee, 2011), dubbed *Sikler lenses*, for focusing and steering the ion beam. The cutting of the central tube of such a Sikler lens is done in a diagonal manner to improve the ion optical properties in comparison to a conventional small-angle deflector with parallel cuts with respect to the ion beam axis. The resulting four segments are referred to as *top*, *bottom*, *left*, and *right* with regard to the moving ions (see Figure 10.1). Their corresponding individual voltages are V_top, V_bottom, V_left, and V_right. The outer tubes of these lenses are held on ground potential. The more convenient voltages

$$V_\mathrm{foc} = \frac{V_\mathrm{left} + V_\mathrm{right} + V_\mathrm{top} + V_\mathrm{bottom}}{4} \tag{10.1a}$$

$$V_\mathrm{ast} = \frac{V_\mathrm{left} + V_\mathrm{right} - \left(V_\mathrm{top} + V_\mathrm{bottom}\right)}{4} \tag{10.1b}$$

$$V_\mathrm{hor} = \frac{V_\mathrm{left} - V_\mathrm{right}}{2} \tag{10.1c}$$

$$V_\mathrm{ver} = \frac{V_\mathrm{top} - V_\mathrm{bottom}}{2} \tag{10.1d}$$

---

[1] Sikler lenses 1 and 2 are of the larger type with an inner diameter of 40 mm and 67 mm length of the central tube. Sikler lenses 3–5 have an inner diameter of 25 mm and a central tube length of 40 mm.

Ion optical element	Distance (mm)	Potential (V)
Central EBIT drift tube	−11	720
Extraction tube 1	111	−1620
Extraction tube 2	153	−760
Sikler lens 1	295	396
Sikler lens 2	1066	310
90° deflector	1194	34
Sikler lens 3	1387	314
Sikler lens 4	1685	200
Pulsed drift tubes	1756	548
Sikler lens 5	2001	57
First stage tube 1	2315	−82
Second stage tube 1	2395	−25
Mirror tube	2436	30
Paul trap	2514	138

Table 10.1: Ion optical elements for the HCI transfer from the EBIT to the Paul trap as seen by the transferred ions. The second column shows the distances of the front faces of the respective elements to the center of the central EBIT drift tube. This drift tube has a length of about 22 mm and the Paul trap blade length is 15 mm. The segmented einzel lenses are dubbed *Sikler lenses*. The third column presents the mean focusing electrostatic potential of the elements. Note that one electrode segment of Sikler lens 3 is used as a gate electrode and the corresponding high potential is not accounted for in the column 'potential'. The elements *first stage tube 1*, *second stage tube 1*, and *mirror tube* are the first three electrostatic tubes within the cryogenic environment, as shown in Figure 8.1A. Other elements required for the ion beam diagnostics are not shown. See text for details.

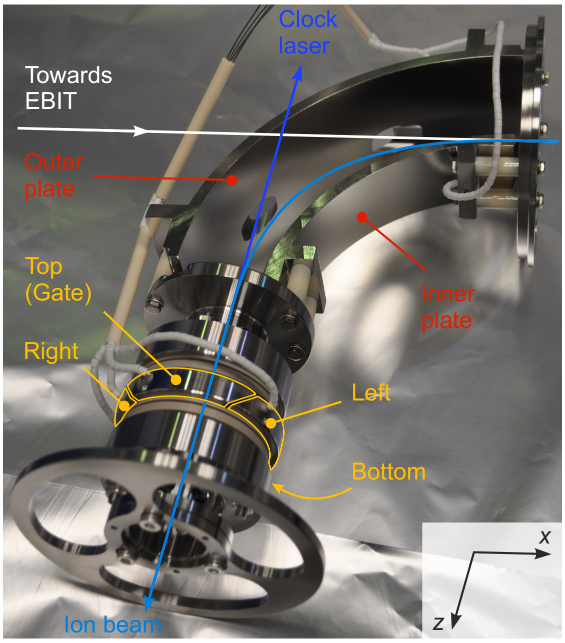

Figure 10.1: 90°-deflector unit of the ion transfer beamline. A double-focusing electrostatic 90° deflector (labeled in red) is followed by Sikler lens 3 (labeled in orange). The deflector is made of two quarter cylinder segments of different heights (inner and outer plate). The central tube of the Sikler lens is cut into four segments for small-angle deflection and astigmatism correction of which the outer surfaces can be seen. The top segment is also used as gate electrode for the charge-state selection. See text for further details.

are defined for accomplishing focusing, astigmatism correction, horizontal and vertical small-angle deflection. The differential potentials used for the last three purposes are small compared to the focusing voltage and typically on the level of a few volts.

A double-focusing electrostatic 90° deflector, following the design of Kreckel et al. (2010), is employed to guide the ion beam along a quarter-circular arc with a radius of 100 mm. This element is composed of two curved deflector plates biased to the voltages V_{outer} and V_{inner} for the outer and inner one respectively (see Figure 10.1). Geometrically, the plates are formed by quarter-cylinder segments with heights of 31 mm (inner plate) and 70 mm (outer plate). Both plates are 25 mm apart. Such a geometry allows for focusing in the vertical direction. The bias and deflection voltages[2] are given by the simple relations

$$V_{\mathrm{bias}} = \frac{V_{\mathrm{outer}} + V_{\mathrm{inner}}}{2} \tag{10.2a}$$

$$V_{\mathrm{def}} = \frac{V_{\mathrm{outer}} - V_{\mathrm{inner}}}{2} = \frac{\text{plate distance}}{\text{center radius}} \cdot \frac{E_{\mathrm{kin}}}{q} = \frac{1}{4}\left(V_{\mathrm{ext}} - V_{\mathrm{bias}}\right), \tag{10.2b}$$

where E_{kin} is the kinetic energy of the ion with charge q when entering the deflector. V_{ext} is the extraction voltage governed by the high potential (720 V was used in this work) of the central drift tube of the EBIT[3]. In the case discussed here, all HCI species obtain their kinetic energy from the same extraction potential and thus V_{def} is independent of the ion charge q. Therefore, no charge-state separation can be accomplished with the electrostatic deflector. The experimental optimization yielded values of $V_{\mathrm{def}} = [209\,\mathrm{V} - (-141\,\mathrm{V})]/2 = 175\,\mathrm{V}$ with $V_{\mathrm{bias}} = 34\,\mathrm{V}$, close to the prediction by Equation 10.2b. V_{bias} is used to control the astigmatism induced by the deflector. The subsequent Sikler lenses can be used to minimize any remaining astigmatism.

A pair of pulsed drift tubes, based on the work of Schmöger (2013), was made from a single tube with an inner diameter of 25 mm and a length of 212 mm. It is used for a first electrodynamic deceleration step and phase-space cooling of the ion bunches. This process will be described later in Section 10.4. The two interlaced tubes with a serrated structure are separated by a few millimeters along the symmetry axis z and generate a linear potential gradient along this direction (see Figure 10.2) by individually biasing both tubes to the voltages $V_{\mathrm{pdt1}} = 510\,\mathrm{V}$ and $V_{\mathrm{pdt2}} = 586\,\mathrm{V}$ for the $^{40}\mathrm{Ar}^{13+}$ transfer. The serrated structure allows for a homogeneous potential distribution in the xy-plane within a diameter of more than 12 mm around the z-axis, significantly larger than the ion beam diameter. The central voltage

$$V_{\mathrm{pdt}} = \frac{V_{\mathrm{pdt1}} + V_{\mathrm{pdt2}}}{2}, \tag{10.3}$$

---

[2] The relation for the deflection voltage is obtained in a few lines after equating the electric force between the deflector plates and the centripetal force.

[3] Note that the real extraction voltage deviates from the nominal voltage applied to that drift tube by the space charge contribution and the offset value as discussed in Section 6.1 and Chapter 9.

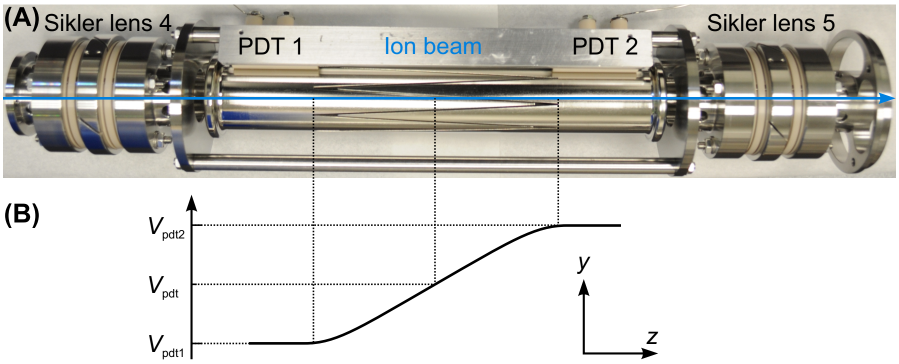

Figure 10.2: Deceleration unit of the ion transfer beamline. (**A**) A pair of pulsed drift tubes is located between the two Sikler lenses 4 and 5, the latter one being the last deflection element before the Paul trap. The two pulsed drift tubes (PDTs 1 and 2) are biased to the voltages V_{pdt1} and V_{pdt2}. (**B**) In the region of overlap a linear potential gradient is generated along the z-direction. In the xy-plane, the potential is uniform around the ion beam. The center potential V_{pdt} defines the potential used for the first electrodynamic deceleration step.

about 550 V for $^{40}\mathrm{Ar}^{13+}$, is used for the first electrodynamic deceleration step.

Six cylindrical electrostatic tubes are symmetrically arrange around the Paul trap inside the trap chamber, three before and three behind the Paul trap. The outer ones are installed on the first temperature stage of the cryostat (see Chapter 11 for more details) and referred to as *first stage tube 1* and *2*, labeled along the ion beam trajectory. The next inner ones are mounted on the second temperature stage and named accordingly as *second stage tubes*. The two innermost ones are mounted right before and after the Paul trap inside the second temperature stage. The first one is referred to as *mirror tube* and used for recapturing the HCIs inside the Paul trap by rapidly switching its voltage up.

Two retractable ion detector units are used for optimizing the ion yield and ion beam transmission through the Paul trap. The first detector unit is located about 390 mm before the ion beam enters the Paul trap (at a distance of 2125 mm from the center of the EBIT). It is composed of a retarding-field analyzer combined with a chevron microchannel plate (MCP) detector of 25 mm active diameter (see Figure 10.3). The MCP signal can be capacitively read out by an oscilloscope. The retarding-field analyzer comprises two parallel stainless-steel meshes, perpendicular to the z-direction, with a separation of about 3 mm. The first one is held on ground potential and the second one can be biased to an arbitrary voltage V_{grid}. With the MCP detector installed about 8.5 mm thereafter, this setup allows to measure the energy spread of the ion bunches along the z-direction. The second detector unit is used to maximize the transmission of the ion beam through the Paul trap and is therefore located inside a dedicated detection chamber behind it. It contains a second chevron MCP detector of 14 mm active diameter and a Faraday cup, of which one ion detector can be selected for ion yield measurements.

The beamline section between EBIT and Paul trap is pumped by a $300\,\mathrm{l\,s^{-1}}$ turbomolecular pump (TMP) and a $200\,\mathrm{l\,s^{-1}}$ non-evaporable getter (NEG)-ion

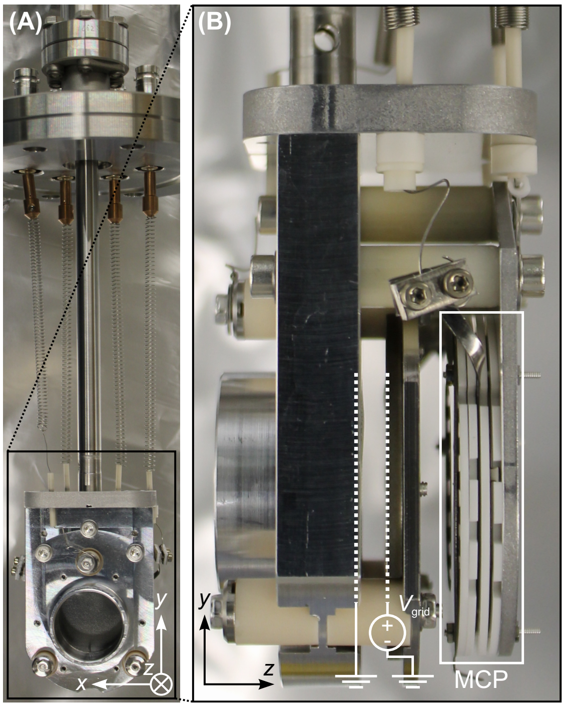

Figure 10.3: Ion detector with retarding-field analyzer. (**A**) The detector is mounted on a retractable manipulator. (**B**) Magnified side view of the detector. The retarding-field analyzer is composed of two stainless-steel meshes of which the first one is on ground potential. The second mesh can be biased to an arbitrary voltage V_{grid} in order to decelerate the ion bunch. The microchannel plate (MCP) detector behind the second mesh measures the ion yield as a function of V_{grid} to obtain the axial energy spread of the ion bunches.

combination pump. Above that, the beamline entrance and exit are pumped by another TMP located at the collector of the EBIT and the cryostat of the Paul trap. A base pressure of about 1×10^{-9} mbar is achieved. This beamline section can be isolated with gate valves from EBIT and Paul trap, e. g., when maintenance becomes necessary, such as a warm up of the cryostat which temporarily raises the pressure to about 10^{-7} mbar when releasing frozen gas from the cryosurfaces (see Chapter 11 for details). The detection chamber behind the Paul trap is pumped with another $200\,\mathrm{l\,s^{-1}}$ NEG-ion combination pump and can be also separated by a gate valve from the Paul trap chamber. Laser beams can propagate (anti-)collinear to the ion beam and Paul trap (z-direction) by passing through an aperture in the outer plate of the 90° deflector (see Figure 10.1) with optics mounted on a small breadboard behind the deflector.

Vibration decoupling of the Paul trap from the EBIT is accomplished by introducing two DN40CF edge-welded bellows into the beamline (see Figure 8.1A, green). The EBIT is resting on the vibration-damping screed of the machine room floor and is decoupled from the 90°-deflector unit with the first bellows. The deflector unit is rigidly anchored to the concrete floor of the laser laboratory. The second bellows, located between the deflector unit and the deceleration unit, establishes the second decoupling stage. The deceleration unit is directly installed on the pneumatically floating optical table. Externally installed mechanical springs balance the contractive atmospheric pressure force acting on these second bellows and prevent the optical table from being pulled towards the deflector unit.

10.2 Extraction

HCIs are confined in the EBIT as a hot plasma with a well-controllable charge-state distribution. The timing of the entire HCI transfer is controlled by a multi-channel digital pulse generator, which starts the extraction with a 200 ns extraction pulse on a push-pull high-voltage (HV) switch, which raises the central drift tube potential in < 100 ns from 460 V up to 720 V for an optimized set of $^{40}\mathrm{Ar}^{13+}$ extraction parameters (see Figure 10.4). This inverts the axial electrostatic potential well, thereby releasing an HCI bunch on a common extraction potential of $V_{\mathrm{ext}} \approx 700\,\mathrm{V}$. The electrostatic potential gradients between the central and both adjacent drift tubes accelerate the ions towards both axial exits. The ions which leave the trap towards the cathode are defocused by the other drift-tube and electron-gun potentials and do not damage the cathode. In contrast, the ions which are accelerated towards the beamline entrance are focused by appropriate voltages of the ion extraction optics (see Figure 9.1) behind the collector electrode. The phase-space state of the ion bunch is governed by the initial extraction parameters, such as the extraction potential, switching speed of the HV switch, and the extraction timespan, as well as the potential V currently experienced by the bunch in the beamline. The velocity v of the ions is then given by

$$v(V) = \sqrt{\frac{2E_{\mathrm{kin}}}{m}} = \sqrt{2\,(V_{\mathrm{ext}} - V)\,\frac{q}{m}} \tag{10.4}$$

and depends, importantly, on the charge-to-mass ratio q/m of the ion species. Typical ion velocities are on the (little more than) $100\,\mathrm{mm\,\mu s^{-1}}$ level for $^{40}\mathrm{Ar}^{13+}$ with kinetic energies of a few $100\,q\mathrm{V}$. Therefore, the passage time through ion optical elements is on the order of $\lesssim 1\,\mathrm{\mu s}$ and necessitates HV switching times for dynamical processes on the order of $\lesssim 100\,\mathrm{ns}$. The argon ion bunches are ejected from the EBIT at a rate of 4 Hz. The initial bunch duration is determined by the length of the extraction pulse.

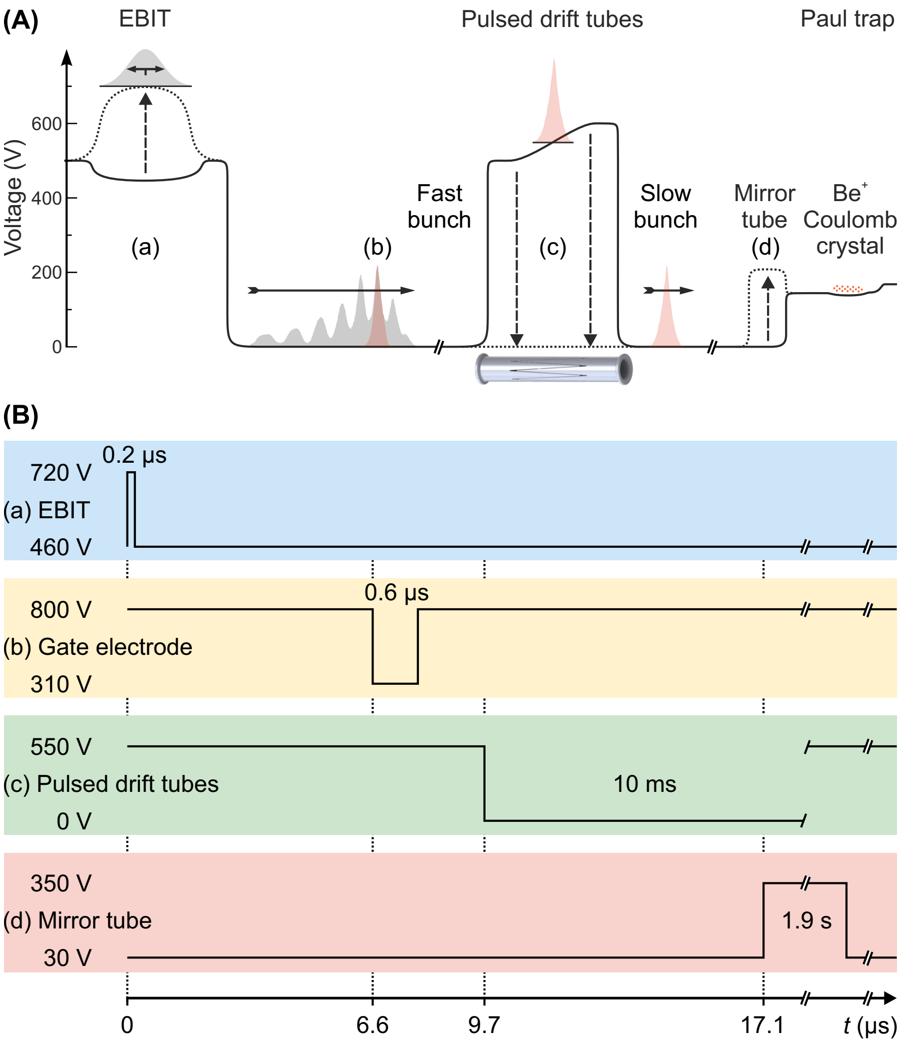
(A)
EBIT
Pulsed drift tubes
Paul trap
Voltage (V)
600
400
200
0
(a)
(b)
Fast bunch
(c)
Slow bunch
Mirror tube
(d)
Be+ Coulomb crystal
(B)
0.2 μs
720 V
(a) EBIT
460 V
0.6 μs
800 V
(b) Gate electrode
310 V
550 V
(c) Pulsed drift tubes
10 ms
0 V
350 V
(d) Mirror tube
1.9 s
30 V
0
6.6
9.7
17.1
t (μs)

Figure 10.4: Highly charged ion transfer. (**A**) Scheme with simplified schematics of the involved electric potentials. (**B**) Corresponding pulse sequence. (a) A HCI bunch is extracted by switching the central drift tube potential of the EBIT up. Ion species with different charge-to-mass ratio separate through their different time of flight. (b) A gate electrode is used to deflect all ion species except for the desired one [red in (A)] from the correct ion beam trajectory. (c) The selected ion bunch is electrodynamically decelerated using a pair of pulsed drift tubes. The slowed bunch is guided to the Paul trap, which is biased to a potential above ground to further decelerate the HCIs electrostatically. A laser-cooled ^{9}Be$^+$ Coulomb crystal has been prepared there beforehand. (d) A single HCI with a residual kinetic energy of a few qV is recaptured in the Paul trap by switching up the electric potential of a mirror tube in front of it.

10.3 Charge-state separation and selection

The HCI transport process is governed by the charge-to-mass-ratios q/m of the ion species[4]. Except for hydrogen and helium-3, this quantity varies for all stable isotopes between 0 for neutral atoms and $0.5\,e/\mathrm{u}$ for bare nuclei of light elements. With $0.325\,e/\mathrm{u}$ the q/m ratio of $^{40}\mathrm{Ar}^{13+}$ is above the middle of this range. The beamline can be understood as a q/m dispersive spectrometer. Equation 10.4 illustrates that ion species with a different q/m ratio separate spatially and thereby, time-of-fight (ToF) spectra such as shown in grey in Figure 10.5 are measured with the MCP detectors. The different peaks correspond to different q/m ratios of highly charged argon ions and are unambiguously identified by using the simple scaling law for the time of flight[5]

$$t_{\mathrm{ToF}} \propto \frac{1}{\sqrt{q/m}}, \tag{10.5}$$

which allows to convert the ToF axis into a q/m axis. The peaks separate more and more with increasing time of flight, but they also disperse more and more due to their initial energy spread. A multitude of different definitions for the resolution in a ToF spectrum is used. In this thesis we want the FWHM of the ToF peaks to be sufficiently small compared to the peak separation in order to properly isolate a specific species with a certain q/m ratio[6]. The 200 ns initial width of the ion bunches and their initial longitudinal energy spread result in a measured FWHM of 250 ns for a $700\,q\mathrm{V}$ $^{40}\mathrm{Ar}^{13+}$ bunch with a time of flight of slightly less than 12 µs to the first ion detector (see Figure 10.6A). The separation of two adjacent q/m peaks decreases for increasing q/m and, therefore, we consider the separation between q/m and $(q/m)'$ given by

$$\Delta t_{\mathrm{ToF}} = t_{\mathrm{ToF}} - t'_{\mathrm{ToF}} = t_{\mathrm{ToF}} \left(1 - \sqrt{\frac{(q/m)}{(q/m)'}}\right), \tag{10.6}$$

where $(q/m)'$ is the larger ratio. One obtains a prediction of 430 ns for the species $^{40}\mathrm{Ar}^{13+}$ and $^{40}\mathrm{Ar}^{14+}$ at the location of the first ion detector, larger by a factor of 1.7 than the FWHM of the $^{40}\mathrm{Ar}^{13+}$ peak. This value is also close to the measured one which is slightly larger with about 470 ns. The q/m resolution can be improved for a given beamline length by increasing the time of flight by means of a lower extraction voltage V_{ext} at the EBIT[7] or by reducing the initial temporal width of the HCI bunch by using a shorter extraction pulse, for example. This however significantly reduces the number of ions within

---

[4] In mass spectrometry the inverse quantity mass-to-charge ratio is more common.

[5] The relation in Equation 10.5 can be derived from Equation 10.4. Deviations may arise from the different focusing experienced by the different ion species which causes them to have slightly different path lengths on the way to the detector.

[6] We assume here, that the abundance of the element under consideration is relatively high. Since only the q/m ratio matters for the ion separation, in principle different ion species of different isotopes or elements can overlap with a similar q/m ratio. This is negligible, when the atoms, injected into the EBIT, have a high natural abundance or are isotopically enriched.

[7] The time of flight roughly scales with $t_{\mathrm{ToF}} \propto 1/\sqrt{V_{\mathrm{ext}}}$ according to Equation 10.4.

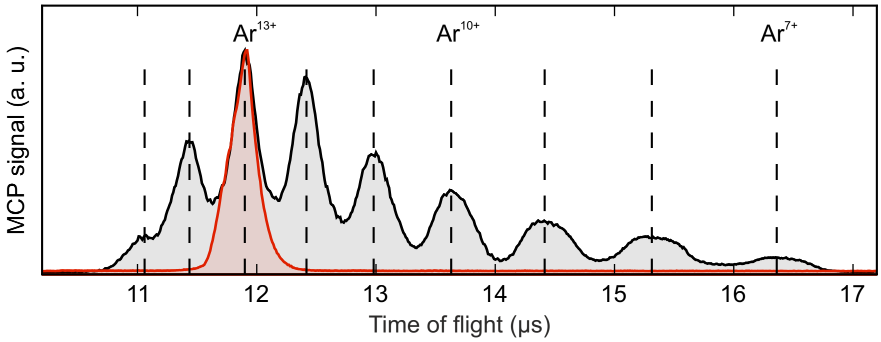

Figure 10.5: Time-of-flight spectrum of argon ions in different charge states. The ion yield, normalized to the highest peak, as measured by the first MCP detector is plotted as a function of the time of flight after ion extraction from the EBIT. The entire charge-state distribution is shown in black and the $^{40}\mathrm{Ar}^{13+}$ bunch in red, selected by a gate electrode of Sikler lens 3. Different time of flights correspond to different charge-to-mass ratios.

the bunch. Notably, HCI species with a much lower q/m ratio, such as Ir^{17+} and many other proposed HCI species for optical clock experiments, have a considerable longer time of flight according to Equation 10.5 which naturally improves the q/m resolution achievable with this beamline. In that sense, $^{40}\mathrm{Ar}^{13+}$ is a rather demanding HCI for the transport within the experiment.

The ToF separation is exploited to select the desired ion species with the *top* electrode of Sikler lens 3 (see Figure 10.1) which is used as a gate. On a high potential of 800 V it deflects all ion species from the correct ion beam trajectory towards the Paul trap until it is switched 6.6 µs after extraction for about 600 ns to the lower voltage of 310 V in order to properly focus and guide the $^{40}\mathrm{Ar}^{13+}$ bunch. Then, it is switched back to the high potential and deflects ion species with a lower q/m ratio again [see Figure 10.4B (b)]. The switching is done with a home-built push-pull HV switch, and the 600 ns switching time is experimentally adjusted to let most of the full $^{40}\mathrm{Ar}^{13+}$ bunch pass. This bunch features a very pure q/m selection as can be seen in red in Figure 10.5.

The ion yield for a specific q/m ratio depends on the focusing properties of the beamline. Optimization for a certain charge-to-mass ratio might even suppress the ion yield for other q/m ratios due to unfavorable ion optical focusing conditions for these ratios. It is also important to consider that the MCP detection efficiency depends not only on the operating voltages of the MCP detector, but also on the kinetic energy of the HCIs which is different for different q/m ratios and on the ion charge q itself. Therefore, the ion yield of different HCI species within the same ToF spectrum cannot be directly compared. The next higher charge state might contain a significantly lower number of ions while generating a higher signal on the MCP detector. During the optimization procedure it is exclusively the signal of a specific q/m peak which is required to be maximized.

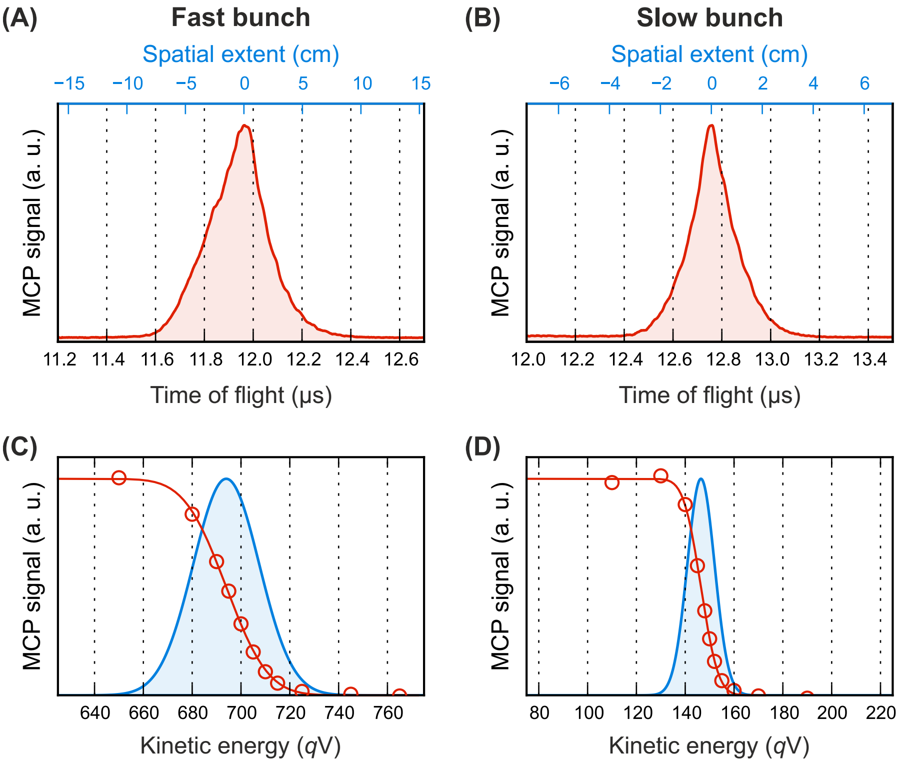

Figure 10.6: ^{40}Ar^{13+} ion bunch as analyzed by the first ion detector. The first row shows the normalized temporal (black scale) and spatial (blue scale) profile of (**A**) a fast $^{40}\mathrm{Ar}^{13+}$ bunch (250 ns FWHM) with a mean kinetic energy of 694 qV and (**B**) a slow $^{40}\mathrm{Ar}^{13+}$ bunch (185 ns FWHM) with 146 qV mean kinetic energy, averaged over 16 bunches each. The second row shows the corresponding normalized longitudinal kinetic energy distributions for (**C**) the fast bunch and (**D**) the slow bunch after electrodynamic deceleration and phase-space cooling. The integrated ion yield of 16 $^{40}\mathrm{Ar}^{13+}$ bunches is given by the red circles as a function of the retardation potential V_{grid} of the retarding-field analyzer. The red curve is a fit with a Gaussian error function. Differentiation yields the blue Gaussian energy distribution and reveals the mean kinetic energy and the longitudinal energy spread, 32 qV FWHM for the fast bunch and 13 qV FWHM for the slow bunch.

10.4 Ion bunch characterization and electrodynamic deceleration

An extracted HCI bunch has a certain initial FWHM duration, given by the length of the extraction pulse. Additionally, the HCIs have an initial energy spread, governed by the plasma temperature in the EBIT and affected by the switching speed of the HV switch used for the extraction. This causes the bunch to disperse along its trajectory through the beamline. The spatial and temporal profile of a bunch can be characterized with the MCP detectors, as shown in Figure 10.6A for an $^{40}\mathrm{Ar}^{13+}$ bunch with a kinetic energy of 694 qV after charge-state selection with the gate electrode and measured by the first ion detector. The energy spread can be determined with the retarding-field analyzer in front of the MCP (see Figure 10.3). While its first stainless-steel mesh is on ground potential, the second mesh is biased to a desired retardation voltage

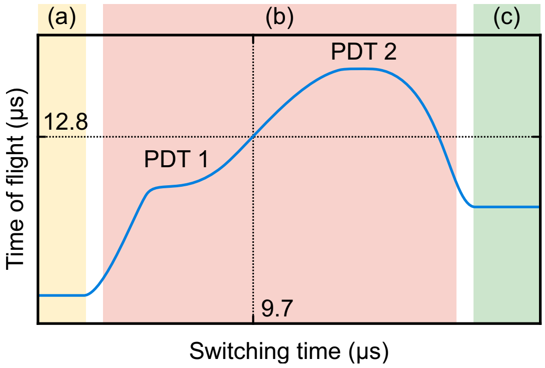

Figure 10.7: Schematic of the switching time of the pulsed drift tubes. The time of flight measured by an ion detector depends on the moment of switching both tubes. In region (a) and (c) switching happens too early and too late, respectively. For region (b) the bunch has been inside both tubes at the moment of switching. See text for details.

V_{grid}. Only ions with a kinetic energy larger than the retardation potential can pass through the mesh and are measured by the MCP detector. The ion yield of the bunch as a function of V_{grid} then yields, approximately, a Gaussian error function. By differentiating this function, the corresponding Gaussian energy distribution is derived with a mean kinetic energy and an energy spread. Such a measurement and evaluation is shown in Figure 10.6C.

The Paul trap only accepts HCIs within a specific phase-space volume. The pair of pulsed drift tubes is an ideal instrument to manipulate the phase-space state of the ion bunch in order to increase the overlap with the accepted phase-space volume of the trap. In practice, this requires to electrodynamically decelerate the HCIs and to reduce their longitudinal energy spread. Both pulsed drift tubes are biased to the individual voltages V_{pdt1} and V_{pdt2} to generate a mean potential V_{pdt} at the center of the potential gradient for this purpose (see Equation 10.3 and Figure 10.2). A potential of $V_{\text{pdt}} = 550\,\text{V}$ is chosen for $^{40}\text{Ar}^{13+}$. When the $^{40}\text{Ar}^{13+}$ bunch has reached the center and is exposed to that potential 9.7 µs after extraction, both pulsed drift tubes are rapidly switched to ground potential and the HCI bunch leaves the tubes with a kinetic energy reduced by $550\,q\,\text{V}$ [see Figure 10.4A (c) and B (c)].

Figure 10.7 illustrates the time of flight measured by the first ion detector as a function of this switching time. Three regions are observed. In region (a) (yellow) the pulsed drift tubes are switched to ground potential too early before the bunch has reached them. The time of flight is constant there. In region (c) (green) both tubes are switched to late when the bunch has already left the tubes. Also in that range, the time of flight is constant, but it is larger than in region (a) since the bunch has temporarily moved at a reduced velocity inside the tubes. In contrast, when the tubes are switched in region (b) (red) the kinetic energy of the bunch has been reduced and the time of flight follows a characteristic curve. Slightly before the middle of this region the time of flight approximately increases linearly with the switching time. There, the bunch is within the overlap region of both serrated tubes on the linear potential gradient along the z-direction. This is the right initial guess for experimentally adjusting the switching time. Next, the energy distributions has to be measured with the retarding-field analyzer. The mean kinetic energy of the decelerated bunch reveals the position of it at the moment of switching. When decelerated by

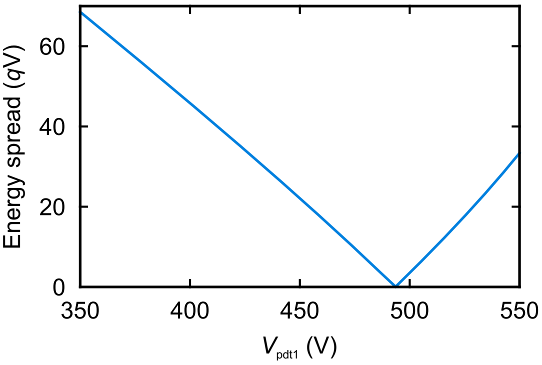

Figure 10.8: FWHM energy spread affected by the differential pulsed drift tube voltage. The energy spread of a 694 qV $^{40}\mathrm{Ar}^{13+}$ bunch with an initial energy spread of 32 V FWHM and decelerated to 146 qV is predicted as a function of the voltage V_{pdt1} of the first pulsed drift tube (PDT).

the aforementioned 550 qV, the bunch has been exactly in the middle between both tubes.

Above that, the individual potentials V_{pdt1} and V_{pdt2} have to be adjusted while fulfilling Equation 10.3 in order to minimize the energy spread of the decelerated bunch. In the idealized case, the energy spread can be reduced to zero for $V_{\mathrm{pdt1}} \approx 494\,\mathrm{V}$ as shown in Figure 10.8 [see the derivation in appendix A of Schmöger (2017)][8]. This cannot be accomplished in practice. Starting from the predicted ideal value, V_{pdt1} and V_{pdt2} have to be experimentally optimized by measuring the energy spread for the three parameter set V_{pdt1}, V_{pdt2}, and the switching time. Importantly, the mean kinetic energy of the decelerated bunch has to be kept close to the previously chosen value, here corresponding to $V_{\mathrm{pdt}} = 550\,\mathrm{V}$, to ensure switching at the correct moment when the ion bunch is at the center of the overlap region of both tubes[9]. For this work, the values $V_{\mathrm{pdt1}} = 510\,\mathrm{V}$, $V_{\mathrm{pdt2}} = 586\,\mathrm{V}$, and switching 9.7 µs after HCI extraction were found, yielding a minimized longitudinal energy spread. This set of parameters also slightly reduces the duration of the bunch. Figure 10.6B and D show the corresponding spatial and temporal profile of the decelerated $^{40}\mathrm{Ar}^{13+}$ bunch and its mean kinetic energy and energy spread. Note that a pure deceleration of an ion bunch without any energy spread would already reduce its spatial extent according to the relation

$$\Delta s_{\mathrm{f}} = \Delta s_{\mathrm{i}} \frac{v_{\mathrm{f}}}{v_{\mathrm{i}}} \tag{10.7}$$

with the initial velocity v_{i}, the final velocity v_{f}, and the initial spatial extent Δs_{i}. In the case shown here, the deceleration reduces the initial spatial extent from 52 mm to 17 mm FWHM.

10.5 Recapture

In the next step, a single $^{40}\mathrm{Ar}^{13+}$ of the slowed ion bunch with a mean kinetic energy of 146 qV has to be recaptured inside the Paul trap. The global potential of the Paul trap is biased to about 138 V in order to accomplish a second electrostatic deceleration step. This reduces the kinetic energy of the HCIs upon entry to a mean value of 8 qV. The transmission of the ion beam is first optimized with the second ion detector behind the Paul trap (see Figure 8.1A). The potential of the mirror tube has to be temporarily adjusted for this purpose to allow for appropriate focusing. Switching the mirror tube to a higher potential while the HCI bunch is inside this tube can even be used to accelerate the HCIs in order to increase the ion signal on the second detector. Once done, the correct switching time of the mirror tube has to be experimentally adjusted to accomplish the recapture of single HCIs within the accepted phase-space volume of the trap. The experimental parameters are chosen that on average less than one HCI per ion bunch is recaptured inside the Paul trap in order to avoid the need to remove excess HCIs if more than one were captured simultaneously. Inside the Paul trap, the rf field confines the HCI radially. It passes through a cigar-shaped Coulomb crystal of typically 50 to 100 $^9\mathrm{Be}^+$ ions which has been prepared beforehand (see later in Section 11.4), axially confined by the shallow potential of only 300 mV applied to the dc endcap electrodes on the side of the trap where the HCIs are injected. The opposite endcap electrodes are held at 12 V above the elevated ground potential and reflect the HCI (see Figure 8.1B). The $^9\mathrm{Be}^+$ ions are laser-cooled with two Doppler cooling beams (see Section 11.3 of the next chapter) of which one is 10 MHz red-detuned and used during the quantum logic (QL) sequence and a second one, 400 MHz farther red-detuned[10], is important to cool hot $^9\mathrm{Be}^+$ ions. In fact, we observe that the recapture efficiency and also the two-ion crystal preparation, which will be discussed in Section 11.5 of the next chapter, crucially relies on a sufficient laser power in that far-detuned Doppler cooling beam. In the meantime, the mirror tube in front of the Paul trap has to be switched up, optimized to 17.1 μs after HCI extraction, to a confining potential of 350 V, thereby recapturing the HCI[11] and resulting in an oscillatory axial motion of it. The sequential Coulomb interaction with the laser-cooled $^9\mathrm{Be}^+$ crystal dissipates the residual kinetic energy of the HCI. Finally, it joins the crystal and is observed as a dark void as large as the volume that a few $^9\mathrm{Be}^+$ ions would occupy owing to the enhanced repulsive force caused by the larger charge q (see Figure 10.9). In this state, the HCI is sympathetically cooled by the Doppler-cooled $^9\mathrm{Be}^+$ ions. The mirror tube remains on its high potential for 1.9 s to allow time for crystallization. If unsuccessful, the HCI injection is continued with the next extraction event. The extraction rate at the EBIT is 4 Hz and therefore only every eighth bunch is used for recapturing. This rate was chosen on purpose. It defines not only the breeding time inside the EBIT, optimized for the given set of EBIT parameters, but it is also high enough to allow for a convenient optimization of the HCI transfer process with sufficient statistics for the ion detection within seconds. The HCI recapture process typically succeeds in less than 30 s.

---

[8] V_{pdt2} is then defined by Equation 10.3.

[9] Minor deviations are tolerable since the overlap region is longer (about 90 mm) than the initial spatial extent of the ion bunch (52 mm here).

---

[10] The exact detuning of this beam is not very crucial. We also operated it successfully at a red-detuning of 300 MHz.

[11] The endcap electrodes of the Paul trap are filtered with cutoff frequencies of 34 kHz and cannot be used for rapid switching.

Figure 10.9: ^{40}**Ar**$^{13+}$ **recapture.** (**A**) A Coulomb crystal of ^{9}Be^{+} ions is prepared in the Paul trap, laser cooled and imaged by a lens above the trap. (**B**) ^{40}Ar^{13+} crystallizes after injection and sympathetic cooling. It appears dark since it does not interact with the Doppler cooling laser.

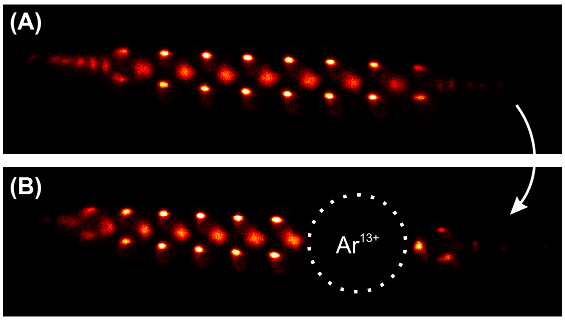

Note that after optimization of all focusing and deflecting voltages of the ion optical elements and all switching times of the HCI transfer sequence, it is practically impossible to trap an HCI of a wrong charge state inside the Paul trap, unless a very rare event of charge exchange with residual background gas happened. More frequently but still rare, an unfortunate event of early charge exchange might happen during the two-ion-crystal preparation when ^{9}Be^{+} loading becomes necessary while the ^{40}Ar^{13+} is still trapped inside the Paul trap (see Section 11.5). As will be described in the next chapter, the right charge state can be easily verified by measuring the motional frequencies in the two-ion-crystal sideband spectrum or just by measuring the atomic transition itself. The adjusted set of ^{40}Ar^{13+} production and transfer parameters were only given here as an example. The optimization procedure takes not more than a few days and is started with the EBIT. Once the set of EBIT parameters is fixed, the beamline parameters are optimized.

11

Storage and preparation of cold highly charged ions

Once recaptured, crystallized in a $^{9}\mathrm{Be}^{+}$ Coulomb crystal, and sympathetically cooled to the Doppler limit, the motional and electronic state of the HCI needs to be initialized for quantum logic spectroscopy (QLS). This chapter describes the cryogenic environment, the Paul trap, and the laser beams, addresses $^{9}\mathrm{Be}^{+}$ loading, imaging, and state detection, and finally discusses the $^{40}\mathrm{Ar}^{13+}$–$^{9}\mathrm{Be}^{+}$ two-ion crystal preparation and the cooling of both axial modes to the quantum-mechanical ground state of motion. The two publications Micke et al. (2019) and Leopold et al. (2019), of which copies are included in Appendix P2 and Appendix P3, and the thesis Leopold (2018) address many of those aspects in detail. Therefore, only a brief summary is provided here.

11.1 Stable, cryogenic environment

The necessity to store a single HCI for a period of a few ten minutes or even longer requires a sufficiently low background gas pressure to avoid charge exchange reactions on this time scale and the consequential loss of the HCI species by lowering the charge state. According to the previous sections, the HCI loading into the Paul trap is quite fast with an average time of 30 s. The prior loading of the $^{9}\mathrm{Be}^{+}$ crystal needs a few 10 s and could be fully automated. As will be discussed later, the preparation of the two-ion crystal and typical spectroscopy experiments are carried out on a time scale of 5 min each. Therefore the minimum useful HCI lifetime is on the order of 10 min. However, convenient experimental conditions and also the demands for operating an atomic clock, i. e., locking the clock laser to the optical transition for extended periods of time in order to average frequency measurements, call for significantly longer HCI lifetimes inside the Paul trap. Such conditions can only be realized for HCIs in a cryogenic environment where outgassing is drastically reduced and residual background gas is efficiently adsorbed on the cryogenic surfaces after impingement. This comes with the great benefit of much reduced collisional and black-body radiation (BBR) shifts[1] and corresponding small systematic uncertainties (Berkeland et al., 1998a; Ushijima et al., 2015), both being basically negligible for this experiment (see Section 2.3.2).

---

[1] The BBR shift is the dominant frequency shift for many non-cryogenic optical atomic clocks (Bothwell et al., 2019; Huntemann et al., 2016; McGrew et al., 2018).

Indisputably, the reported experiment comes with some complexity and, therefore, attention was paid that maintenance for the various parts is kept low. The choice was made to base the cryogenics on a closed-cycle pulse tube cryocooler. Unfortunately, such systems have intrinsic vibrations on a level of 10 µm at the cold head and require a sophisticated vibration-decoupling system for optical atomic clock operation in order to suppress vibration-induced Doppler shifts. For this reason, a cryostat (see Figure 11.1) was developed which fulfills all needs[2] [see Micke et al. (2019) and Leopold et al. (2019) in Appendix P2 and Appendix P3].

The pulse tube cryocooler provides two temperature stages for the experiment. The first (outer) one acts as a thermal shield for the second (inner) one, which offers the lowest temperature. The supplier specifies for the cold head temperatures of 45 K with 40 W cooling power for the first stage and 4 K with 1 W cooling power for the second stage. However, the realized temperatures at the experiment are defined by the thermal heat input onto both stages and the thermal conductance towards the cold head. Therefore, the conflicting needs of a high thermal coupling between both points combined with a low mechanical coupling had to be satisfied in order to reduce the transmission of vibrations. The developed system has proven capable to maintain temperatures of $< 5\,\mathrm{K}$ and $< 50\,\mathrm{K}$ at the Paul trap with an about three orders of magnitude reduction of the cold head vibrations to a level of about 10 nm in the relevant horizontal plane in which nearly all laser beams propagate.

The decoupling of acoustical noise and mechanical vibrations is realized by a variety of measures: Separating the pulse tube and its compressor in a dedicated room with a distance of about 1.4 m from the Paul trap reduces the acoustical noise by 20 dB. This room, dubbed *machine room* (see Figure 8.1), is equipped with a vibration-damping screed. The compressor and forevacuum pumps are situated on pneumatic vibration-insulation platforms and their helium and vacuum hoses are guided through quartz sand-filled boxes. The various segments of the cryostat are mounted on rubber feet, vibrations are decoupled along the system through edge-welded bellows on the room-temperature stage and through two interceptions of the rigid connection of the cold stages with flexible copper braid links and a 120 kg massive inertial copper pendulum in between. Finally, the optical table on which the last segment with the Paul trap is mounted, is pneumatically floating and acts, together with the inertial copper pendulum, as a 600 kg mechanical low-pass filter against high-frequency vibrations. The level of vibrations was characterized with three self-heterodyne interferometers probing vibrations at the position of the Paul trap from different directions. With the given measurement noise floor, no vibration peaks above 100 Hz were observed, although vibration sources such as the TMPs operate with revolution frequencies of 1000 and 1500 Hz in close proximity, directly mounted to the cold-head segment of the system. The lower vibration frequency spectrum is dominated by peaks from the 1.7 Hz operation of the pulse tube, 25 Hz operation of the forevacuum scroll pump, and harmon-

---

[2] Two replicas of this cryostat are in operation with different cryogenic Paul traps, at the MPIK for direct frequency comb spectroscopy of HCIs in the XUV range and at Aarhus university for the spectroscopy of molecular ions.

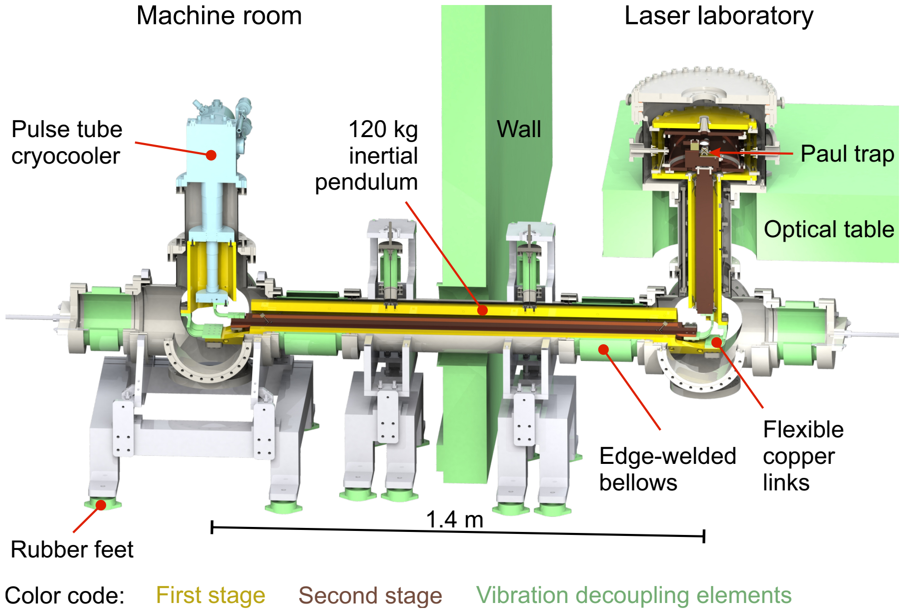

Figure 11.1: Cutaway view of the cryostat. A pulse tube cryocooler inside the machine room (left) provides two temperature stages at below 5 K (brown) and at below 50 K (yellow). Several vibration decoupling elements (light green) and a 120 kg inertial pendulum suppress vibrations at the Paul trap, installed on a pneumatically floating optical table in the laser laboratory (right). See text for further details.

ics thereof. From the residual vibration amplitude level of the order of 10 nm, a peak first order Doppler shift of about 10^{-16} is estimated. Such a Doppler shift results in a line broadening if the vibration period is shorter than the probe time, i. e., for higher frequency vibrations. Lower frequency vibrations are more severe and are preferably characterized by counter-propagating clock laser beams. Such a characterization or alternatives are important since the Paul trap could more or less continuously move with respect to the clock laser on a time scale of typical frequency averaging, for instance when the system is still not in thermal equilibrium and suffers from thermal contraction. As an example, a differential first-order Doppler shift of 4.6×10^{-17} was recently measured for the NIST $^{27}\mathrm{Al}^{+}$ ion clock between both opposing probe directions, but could be eliminated when averaging these (Brewer et al., 2019).

A high thermal conductance was realized by the use of vacuum-annealed ultra-pure copper (typically $> 99.99\,\%$) for all heat transfer elements as well as by maximizing their cross sections and minimizing their lengths within the given geometric boundaries. The dominant source of heat load onto the first temperature stage is thermal radiation from room-temperature surfaces due to the strong T^4 dependence of the Stefan-Boltzmann law. In contrast, thermal conduction through the suspension structure, based on stainless-steel spokes, is dominant for the second temperature stage. Both heat-load contributions were minimized by design. Thermal cycling of the entire system from 5 K to room temperature and back proved a position reproducibility at the Paul trap of better than a few 1–10 µm as judged by the need for only fine-tuning of the tightly focused laser beams (beam waists of a few 10 µm, see Table 11.1).

The background pressure of the cryogenic, residual gas at the Paul trap was estimated to be on a 10^{-15} mbar level. In contrast, other HCI experiments operating with Penning traps could realize lower vacuum pressures of less than 10^{-17} mbar, even with external ion injection capability (Sturm et al., 2019). There, the experimental vacuum is strictly separated from the isolation vacuum and prevents both, first, the continuous entering of warm residual gas from the outside which freezes out on the cryogenic surfaces, saturates them faster, and reduces their pumping speed over time and, second, the impact of ballistic room-temperature molecules or atoms onto the trapped HCI. The latter mechanism is ruled by the opening angle from the HCI towards the room-temperature stage and is independent of the cryogenic background gas pressure. It can have a significant contribution to charge exchange reactions. The separation of experimental and isolation vacuum is not realized in the experiment of this work. However, simple future improvements can approach this condition by closing ten out of twelve horizontal open access laser ports on the first or second temperature stage with cryogenic windows. Solely the two ports for HCI entrance and exit have to be permanently kept open[3]. A possible solution to close them as well would be the development of a home-built cryogenic valve as described in Sturm et al. (2019), but the effort associated with this might not justify the benefit for this experiment. In contrast to Sturm et al. (2019), typical measurement durations in this work are short and after a loss of the HCI species, experimental conditions can be restored within minutes. Additionally, a small amount of charcoal installed close to the Paul trap inside the second temperature stage significantly increases the cryopumping capacity. This amount can be further increased and an improved installation mechanism could allow for in-situ bake out of the charcoal to about 100 K to release adsorbed H_2, He, N_2, O_2, and other residual gas while the cryocooler is kept in operation. Currently, half-day warm up cycles on a two-week basis to approximately 30 K have proven to maintain HCI lifetimes on the order of 45 min with all twelve horizontal laser access ports still open (Micke et al., 2019). Such HCI lifetime measurements are a very sensitive method to estimate the background vacuum pressure. H_2 is the dominant background gas molecule at 5 K. In the Langevin model, the background particle density n is related to the lifetime τ_{HCI} through the relation

$$n = \left(\tau_{\mathrm{HCI}} \cdot k_{\mathrm{L}}\right)^{-1}, \tag{11.1}$$

where

$$k_{\mathrm{L}}\left(\mathrm{Ar}^{13+}, \mathrm{H}_2\right) = 1.957 \times 10^{-8}\,\mathrm{cm}^3\,\mathrm{s}^{-1} \tag{11.2}$$

---

[3] Additionally, four tipped laser ports exist. One of these is closed with a mirror used for vibration measurements.

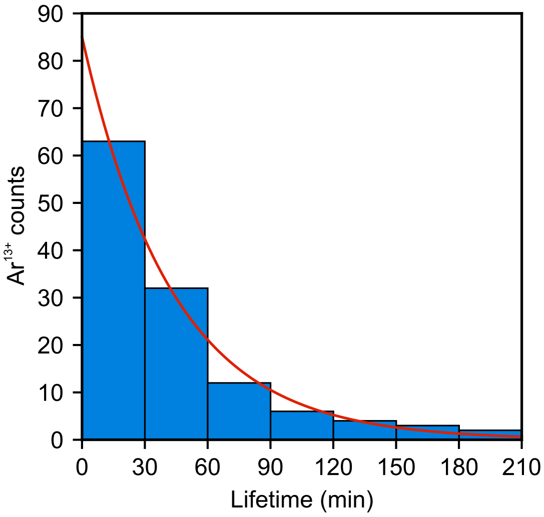

Figure 11.2: Ar^{13+} lifetime measurement. The lifetimes of a set of 122 Ar^{13+} ions are binned for this plot (blue columns). A maximum likelihood estimate with the unbinned data yields the exponential decay curve (red) and the mean lifetime of $\tau_{\mathrm{Ar}^{13+}} = 43.1(39)\,\mathrm{min}$.

is the Langevin rate coefficient for the specific charge exchange system Ar^{13+}–H$_2$ [see Micke et al. (2019), Schmöger (2017), and references therein for a more detailed discussion]. The ideal gas law

$$p = n \cdot k_{\mathrm{B}} \cdot T \tag{11.3}$$

then connects to the pressure p, k_{B} being the Boltzmann constant. Note that the pressure depends on the temperature T. This forbids any comparison of background gas pressures when not relating these with the corresponding temperature. The evaluation of the lifetimes of a set of 122 Ar^{13+} ions measured within two weeks after a warm up cycle, as shown in Figure 11.2, allowed for a maximum likelihood estimate of the mean lifetime of

$$\tau_{\mathrm{Ar}^{13+}} = 43.1(39)\,\mathrm{min}\,. \tag{11.4}$$

This corresponds to a particle density of

$$n < 1.98 \left({}^{+0.20}_{-0.16}\right) \times 10^{4}\,\mathrm{cm}^{-3} \tag{11.5}$$

and a pressure at 4.6 K of

$$p_{4.6\,\mathrm{K}} < 1.26 \left({}^{+0.12}_{-0.11}\right) \times 10^{-14}\,\mathrm{mbar} \tag{11.6}$$

as an upper estimate for the cryogenic background gas pressure. The effect of ballistic room-temperature gas collisions imposes a potentially significant systematic effect, which can be better quantified when several open access laser ports have been closed.

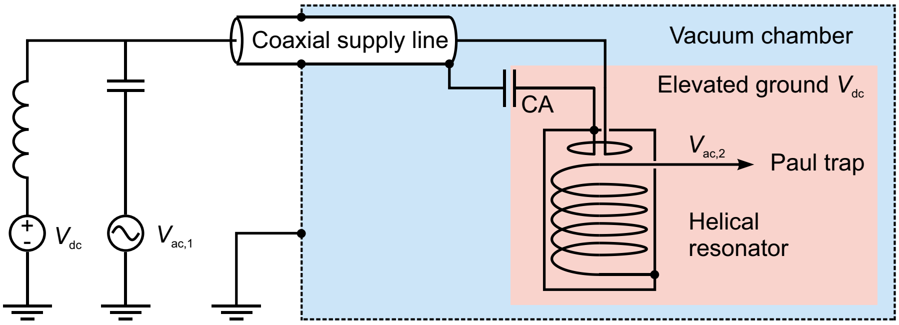

Figure 11.3: Schematic circuit diagram of the elevated ground. The elevated ground V_{dc} and the ac voltage $V_{ac,1}$ are fed into the vacuum chamber (blue) through a coaxial supply line. Inside the vacuum, the capacitor array (CA) breaks the dc connection between the shield of the coaxial supply line and the shield of the electrically insulated helical resonator. The helical resonator amplifies $V_{ac,1}$ to $V_{ac,2}$ for the radial ac confinement of the ions and is biased together with the Paul trap to the elevated ground V_{dc}. See text for further details. CA—capacitor array.

11.2 Paul trap, trap drive, and quantization field

The spectroscopy is performed in a segmented Paul blade trap which has been introduced in Section 6.2 and is discussed in detail by Leopold (2018) and Leopold et al. (2019) of which a copy can be found in Appendix P3.

The radial ac confinement of the trap is driven through an in-vacuum cryogenic helical resonator installed on the second temperature stage next to the Paul trap. Therefore, the resonator has a high temperature stability of typically better than 10 mK in thermal equilibrium over one day. Correspondingly, a highly stable rf resonance frequency is achieved. The elevated ground for the Paul trap is fed in through the signal wire of the coaxial in-vacuum supply line of the electrically insulated helical resonator (see Figure 11.3). An amplified low-noise signal generator couples the ac voltage with a bias-tee onto the signal wire on the air-side. The grounded shield of the coaxial cable is connected through a capacitor array to the shield of the helical resonator in order to break the dc ground while simultaneously providing a proper ac ground. This is an essential feature to allow biasing of the Paul trap ground for realizing the final HCI deceleration step in an electrostatic manner. The room-temperature quality factor of the loaded resonator was measured to 230 and increases to about 385 at a cryogenic temperature of below 5 K. The rf drive is then operated at the helical resonator resonance with an angular frequency of $\Omega_{rf} = 2\pi \times 24.1\,\mathrm{MHz}$.

Three-dimensional ground-state cooling of single $^9\mathrm{Be}^+$ ions outside the Lamb–Dicke regime was demonstrated in this trap with an axial heating rate of $\dot{\bar{n}}_z = 2.3(1)$ phonons / s at a secular frequency of 1 MHz. Radial heating rates of $\dot{\bar{n}}_{\tilde{x}} = 1.9(3)$ phonons / s and $\dot{\bar{n}}_{\tilde{y}} = 0.7(2)$ phonons / s were measured at secular frequencies of 2.5 MHz and 2.2 MHz, respectively. Such heating rates correspond to one of the lowest levels of electric field noise ever reported and they are about one to two orders of magnitude lower than in comparable

Paul traps which are operated at room temperature. Indeed, lower heating rates are expected for cryogenic operation since the thermal Johnson noise of the electric field is highly reduced (Deslauriers et al., 2006; Labaziewicz et al., 2008).

The magnetic quantization field with a magnitude of about 160 μT is generated with three pairs of passively driven magnetic field coils. A high stability of the field at the position of the trapped ions is facilitated through the two highly conductive copper enclosures of the first and second temperature stages which passively shield ac fluctuations with low-pass corner frequencies below 0.3 Hz. A magnetic field stability level of better than 1 nT from 1 to 100 s, corresponding to a fractional stability of better than 6×10^{-6} was inferred by measurements with a single $^9\mathrm{Be}^+$ ion (Leopold et al., 2019). Beyond that, the magnetic field is actively stabilized with additional compensation coils (operating at a much lower magnetic field) to suppress sudden field changes, for instance caused by the moving elevator of the building. For that purpose, a magnetic field sensor with a resolution of 200 pT measures the field as close as possible to the Paul trap outside the vacuum system in order to generate the error signal for the compensation coils. This improves the magnetic field stability on time scales below a few 10 s with an optimum stability of about 200 pT at about 1 s (Leopold et al., 2019), limited by the sensor resolution and the electric noise in the passive magnetic field coils.

Moreover, the axial excess micromotion of the trap was characterized by measuring the micromotion sidebands for compensated radial excess micromotion (using additional compensation electrodes, see Figure 6.1). A small imperfection of the Paul trap electrode alignment causes a second-order Doppler shift for the $^9\mathrm{Be}^+$ qubit transition on a fractional frequency level of 10^{-16}. The corresponding uncertainty was estimated to be on the 10^{-17} level (Leopold et al., 2019).

11.3 Laser beams

The atomic coordinate frame (x', y', z') is defined by the quantization axis z'. The transition probability of an electronic transition is strongly affected by the geometrical factor, $|\hat{\varepsilon} \cdot \hat{u}^*_{\Delta m}|^2$ for an electric and $|\left(\hat{k} \times \hat{\varepsilon}\right) \cdot \hat{u}^*_{\Delta m}|^2$ for a magnetic-dipole transition, and, therefore, depends on the polar angle θ between the z'-axis and the wave vector $\vec{k}$ as discussed in Section 7.1 and visualized in Figure 7.1. Ten continuous wave (cw) laser beams are operated for this work to probe and manipulate the spectroscopy ion $^{40}\mathrm{Ar}^{13+}$ (see Figure 5.1) and the logic ion $^9\mathrm{Be}^+$ (see Figure 5.2) plus a cw photoionization laser (see Figure 5.3) and a pulsed ablation laser with their beam geometry shown in Figure 11.4. Table 11.1 presents a summary with the typical laser powers and waists for the cw beams at the center of the Paul trap. All laser beams, except for the tipped clock beam, propagate in the horizontal plane. For all those beams, the transformation between the laboratory frame and the atomic frame is just given by a rotation around the vertical y-axis by 210° with $y = y'$

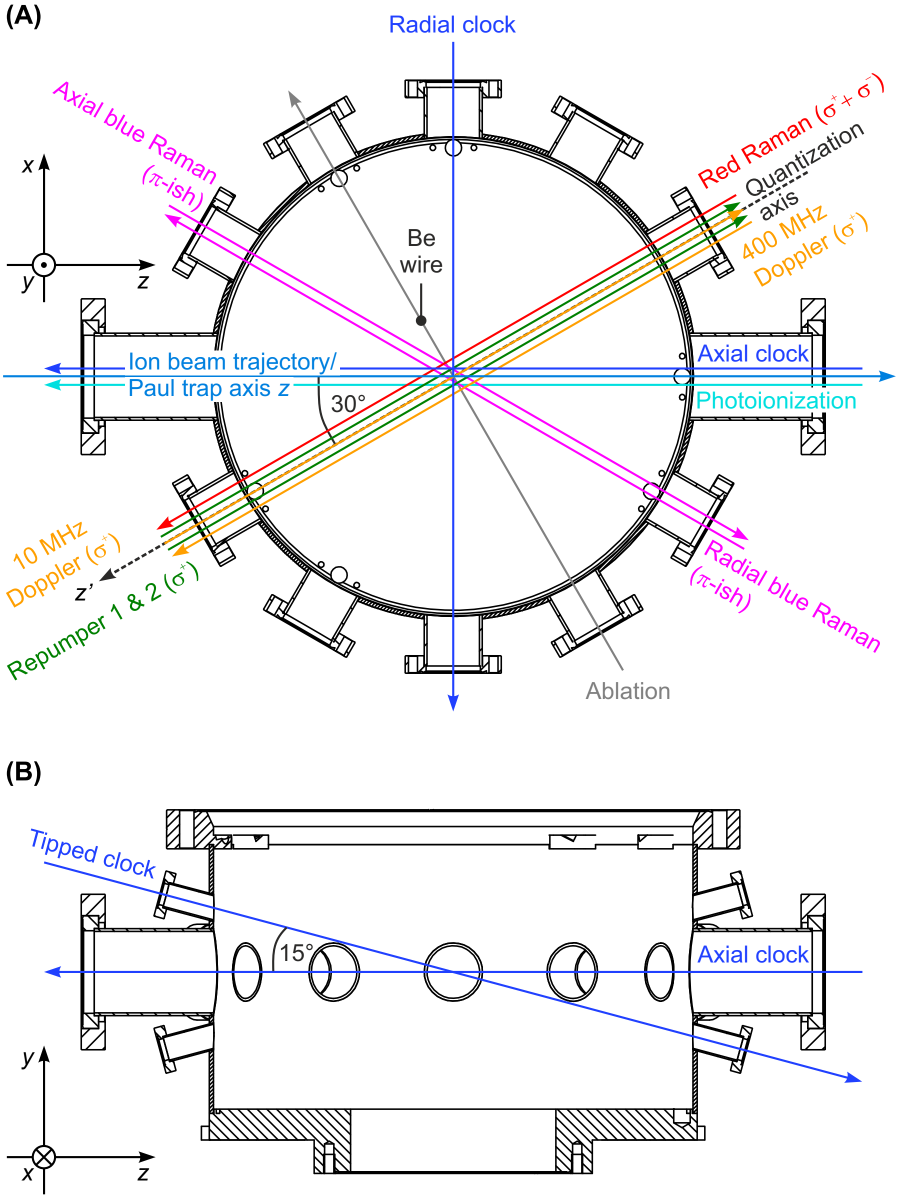
(A)
Radial clock
Axial blue Raman
(π-ish)
Red Raman (σ⁺+σ⁻)
Quantization
axis
400 MHz
Doppler (σ⁻)
x
y
z
Be
wire
Ion beam trajectory/
Paul trap axis z
30°
Axial clock
Photoionization
10 MHz
Doppler (σ⁺)
z'
Repumper 1 & 2 (σ⁺)
Radial blue Raman
(π-ish)
Ablation
(B)
Tipped clock
15°
Axial clock
y
x
z

Figure 11.4: Schematic laser beam geometry at the linear Paul trap. (**A**) Top view showing all laser beams for the loading and manipulation of $^{9}\mathrm{Be}^{+}$ and the two horizontal clock laser beams for probing $^{40}\mathrm{Ar}^{13+}$. The polarization of the 313 nm beams is given in parentheses. Note that a pure π polarization of both *blue Raman* beams (shown in pink) is not possible for their angles of incidence. The number in the label of the two Doppler cooling beams (orange) refers to their red detuning from the Doppler cooling transition. The laser beams are slightly displaced from the trap center to improve the visibility. (**B**) Side view, only showing the two clock laser beams in the vertical yz-plane. The two-ion crystal is aligned along the z-direction. See text for further details.

for the magnetic quantization-field direction as shown in Figure 11.4. The polar angles θ for those beams is a multiple of 30° and can be extracted from Figure 11.4. If a wave vector is tilted outside the horizontal plane, for example as for the tipped clock beam, the polar angle θ_{tipped} can be obtained by a two-step rotation of the unit vector $\hat{z}'$ in order to align it with the wave vector $\vec{k}$ and subsequently calculating the projection of the rotated unit vector onto the previous z'-axis through the relation $z' = \cos\theta_{\text{tipped}}$. The coordinate z' after rotation can be also expressed by using the corresponding rotation matrices. In the case of the tipped clock beam, we firstly rotate by $\varphi_1 = -30°$ about the y'-axis and secondly by $\varphi_2 = -15°$ about the new x-axis (see Figure 11.4). The coordinate z' of the rotated vector is then given by $z' = \cos\varphi_2 \cdot \cos\varphi_1$. Equating both expressions yields the polar angle[4]

$$\theta_{\text{tipped}} = \arccos\left(\cos\varphi_2 \cdot \cos\varphi_1\right), \tag{11.7}$$

being 33.2° for the tipped clock beam. Note that for all horizontal laser beams $\hat{\varepsilon}_\alpha$ and $\hat{\varepsilon}_\beta$ polarization as introduced in Section 7.1.1 are identical to the vertical and horizontal polarization in the laboratory frame, respectively. This does not apply for a laser beam tilted outside the horizontal plane.

Two Doppler cooling beams are operated with red-detunings of 10 MHz and 400 MHz, respectively. Their orientation with respect to the Paul trap coordinate frame $(\tilde{x}, \tilde{y}, z)$ was chosen to have sufficient projections onto all motional modes for efficient Doppler cooling. Axial modes along the z-direction are cooled under an angle of 30° while cooling of the radial modes (along the $\tilde{x}$ and $\tilde{y}$-directions) is slightly less efficient due to the larger angle of $\arccos(\cos 45° \cdot \cos 60°) \approx 69.3°$ between the Doppler cooling lasers and the principal radial axes (see Equation 7.39 for the angle dependence). The coupling of the Raman beams to the motional modes was discussed in Section 7.2.3. Although the *red Raman* beam is intended to purely drive σ^+ transitions, it is in fact operated with linear polarization in order to suppress the differential Stark shift of the qubit transition (Wineland et al., 2003) and to improve the coherence time and reduce the sensitivity for changes in the laser power (Leopold, 2018). The σ^- polarization component of the linearly polarized *red Raman* beam does not harm since it cannot resonantly couple with the *blue Raman* beam to any Zeeman substate.

The laser beams for loading and manipulating $^9\text{Be}^+$ are generated by several laser systems and discussed in detail by Leopold (2018). The ablation laser and photoionization laser are briefly addressed in the next section. The Doppler cooling and Raman laser beams are produced with a setup following the approach of Wilson et al. (2011). For each of the two systems, a common fiber laser at 1050 nm is combined with one out of two 1550 nm fiber lasers by single-pass sum-frequency mixing in a periodically-poled lithium niobate crystal to produce two 626 nm laser beams separated by about 50 GHz. The beam that is used for Doppler cooling is frequency stabilized by Doppler-free saturation spectroscopy of iodine while the other one, used to drive the Raman transition, is in fact not frequency stabilized. This is not required since a slow frequency drift is basically insignificant for the Raman transition and fast laser noise cancels since the Raman transition is driven by the frequency difference of two beams which are both derived from this beam. Both 626 nm beams are frequency-doubled by intracavity second harmonic generation (SHG) in two different cavities using beta barium borate (BBO) crystals as non-linear medium. With subsequent acousto-optic modulator (AOM) setups the three Raman beams and the two Doppler cooling beams at 313 nm are generated and appropriately frequency shifted. In particular, the laser powers of the 10 MHz red-detuned Doppler cooling laser beam and of all Raman laser beams are actively stabilized at the Paul trap on a pulse-by-pulse basis to guarantee stable Rabi frequencies and Stark shifts. The two repump laser beams at 313 nm are produced with a different setup, described in detail by S. A. King et al. (2018) and also Leopold (2018). For those two beams, 626 nm radiation is generated with a distributed Bragg reflector diode laser, which is self-injection-locked to the subsequent SHG cavity based on a BBO crystal. This significantly narrows the laser linewidth from a MHz level to about 20 kHz. The wavelength is long-term stabilized by a wavemeter, being sufficiently accurate for the 19 MHz broad transitions addressed with the repumper beams. Both 313 nm beams are generated and appropriately shifted with a subsequent AOM setup. All seven 313 nm laser beams are deliverd to the Paul trap through short hydrogen-loaded, large mode area optical fibers (Colombe et al., 2014) which eases the beam alignment onto the ion after adjustments to the laser setup since realignment is reduced to coupling the light into the fibers. The laser system producing the 441 nm clock laser beams is discussed in the next Chapter 12.

---

[4] With the same argumentation, the polar angle θ can be calculated for any arbitrary wave vector $\vec{k}$ tilted outside the horizontal plane. This relation can also be obtained by trigonometric considerations in a trirectangular tetrahedron with the same result.

Laser beam	Wavelength (nm)	Power (mW)	Waist (µm)
Photoionization	235	1	100
10 MHz Doppler laser	313	0.5×10^{-3}	20
400 MHz Doppler laser	313	1	40
Repumper 1	313	0.5×10^{-3}	20
Repumper 2	313	0.5×10^{-3}	20
Red Raman	313	5	20
Axial blue Raman	313	3	20
Radial blue Raman	313	3	20
Axial clock	441	0.2	50
Radial clock	441	0.2	50
Tipped clock	441	0.2	50

Table 11.1: Continuous wave laser beams at the Paul trap. The typical powers and approximate waists are given for the beams at the center of the Paul trap. The naming of the beams refers to Figure 11.4. The quoted waist of the photoionization laser beam is a theoretical value as expected for the applied focusing. For the clock laser beams, the typical maximum powers are quoted. Clock pulses are applied with a much reduced power (about 0.5 µW).

11.4 Be$^+$ loading, imaging, and state detection

^{9}Be$^+$ ions are loaded into the Paul trap through laser ablation and subsequent photoionization with the geometry shown in Figure 11.4A. A commercial pulsed laser system at 532 nm is used for the ablation process, focused to a spot size with about 120 µm waist onto a beryllium wire about 22 mm away from the trap center. This laser features pulse lengths of 4 ns and up to 10 mJ pulse energy. Pulses at a rate of 2 Hz and peak intensities of 1 GW cm^{-2} are used for the loading of tens of ions. A fraction of the ablated beryllium atoms can pass through a horizontal slit aperture about 13 mm away from the trap center. This slit aperture prevents coating of the trap electrodes. At the trap center the neutral beryllium atoms are resonantly excited and subsequently photoionized by 235 nm radiation (see Figure 5.3) and immediately trapped in the three-dimensional (pseudo-)potential of the trap. The 235 nm radiation of the photoionization beam is produced by a tapered amplifier diode laser operated at 940 nm, which is frequency-quadrupled in two subsequent SHG cavities using a periodically-poled potassium titanyl phosphate (PPKTP) crystal and a BBO crystal, respectively [similar to Lo et al. (2014)].

The Paul trap is equipped with an imaging system of high collection efficiency, illustrated in Figure 8.1B. 6.9 % of the total solid angle are covered by a custom in-vacuum biaspheric 22 mm-diameter lens installed inside the second temperature stage enclosure on a piezoelectric translation stage in order to fine-adjust the working distance of 20 mm from the trapped ions. A nearly diffraction-limited, 3-times magnified image is focused through a 5.5 mm aperture inside the first temperature stage in order to reduce the radiation heat load from the room-temperature stage onto the second temperature stage. A two-lens system on the air-side is partially located inside a reentrant viewport, simplified in Figure 8.1B, and further magnifies the image to produce a total magnification of 22. A beamsplitter with a splitting ratio of 99:1 allows to simultaneously count the fluorescence rate on a PMT and image the ion crystal on an EMCCD camera. The 10 MHz Doppler cooling laser is tuned to resonance of the Doppler cooling transition for state detection in order to maximize the photon count rate for a given level of off-resonant depopulation of the dark state. Then, the PMT counts a fluorescence rate of up to 340 kcps from the heavily saturated Doppler cooling transition of a single $^9\mathrm{Be}^+$ ion. In contrast, during the QL experiment the Doppler cooling laser is operated at 20 % of the saturation intensity corresponding to a count rate of 60 kcps to avoid saturation broadening and further off-resonant depopulation. A 200 µs time window is used for state detection in which on average 12 photons are counted when the ion is in the bright $|^2\mathrm{S}_{1/2}, F=2, m_F=2\rangle$ qubit state (see Figure 5.2). The background count rate from the PMT dark current and laser scatter is 2.1 cps, resulting in a mean photon number of 4.2×10^{-4} in the 200 µs interval[5]. This corresponds to a signal to background ratio of about 3×10^4, and both qubit states can be reliably discriminated by a standard threshold technique (Myerson et al., 2008) with a fidelity of 97 to 98 %, limited by off-resonant depumping of the dark $|^2\mathrm{S}_{1/2}, F=1, m_F=1\rangle$ state by the Doppler cooling laser. The threshold is usually set between 0 and 1 detected photon in the state detection window of 200 µs.

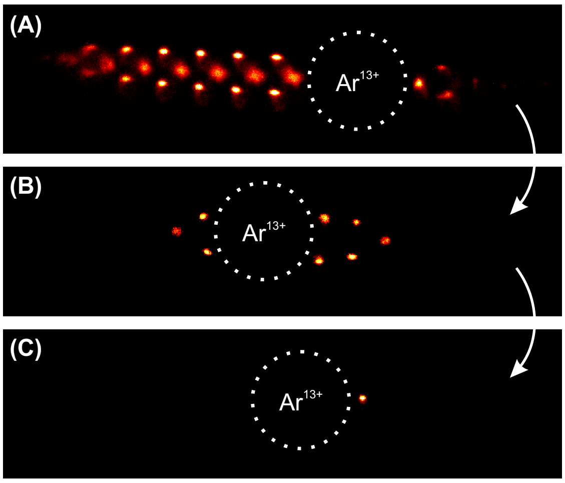

Figure 11.5: Two-ion crystal preparation. (**A**) $^{40}\mathrm{Ar}^{13+}$ appears as a dark void in the $^9\mathrm{Be}^+$ Coulomb crystal. (**B**) Changing the Paul trap parameters and modulating the ac trap drive allows to heat out excess $^9\mathrm{Be}^+$ ions. (**C**) Finally, an $^{40}\mathrm{Ar}^{13+}$–$^9\mathrm{Be}^+$ two-ion crystal is attained. Next, the confinement in the Paul trap is increased to a stable setting which allows for axial ground-state cooling and QLS.

11.5 Two-ion crystal preparation

Chapter 10 discussed the implantation of a single $^{40}\mathrm{Ar}^{13+}$ ion into a Coulomb crystal of about 50 to 100 $^{9}\mathrm{Be}^{+}$ ions (see Figure 11.5A). The kind of QLS demonstrated in this work is however based on an $^{40}\mathrm{Ar}^{13+}$–$^{9}\mathrm{Be}^{+}$ two-ion crystal, ground-state cooled in both axial motional modes of which one is used as a transfer bus to map the clock state of the $^{40}\mathrm{Ar}^{13+}$ spectroscopy ion onto the qubit state of the $^{9}\mathrm{Be}^{+}$ logic ion. To remove the excess ions, the axial dc and radial ac confinements of the Paul trap are both increased and the aspect ratio of the Coulomb crystal is changed from the cigar shape to a more spherical shape. Then, $^{9}\mathrm{Be}^{+}$ ions are intermittently heated without any laser cooling for periods of a few seconds after which the 400 MHz red-detuned Doppler cooling laser is switched on again[6]. Indeed, the secular spectrum of a mixed species Coulomb crystal can be quite involved, but secular resonances are observed close to the secular frequencies of the single ions (Ann et al., 2019). We therefore perform parametric heating of the $^{9}\mathrm{Be}^{+}$ ions by modulating the rf drive of the trap in order to modulate the radial pseudopotential near-resonantly to a secular frequency of a single $^{9}\mathrm{Be}^{+}$ ion. $^{9}\mathrm{Be}^{+}$ ions are then progressively lost until only a single one remains together with the HCI (see Figure 11.5). The latter one is more deeply confined due to the larger ion charge and quite insensitive to the parametric heating. In cases where all remaining $^{9}\mathrm{Be}^{+}$ ions are lost at once during a heating period, $^{9}\mathrm{Be}^{+}$ ions are reloaded again through laser ablation and photoionization. The HCI almost always remains trapped during that time and is again sympathetically cooled by the new $^{9}\mathrm{Be}^{+}$ ions. The entire process to attain the two-ion crystal usually takes less than 5 min. The right selection of the modulation depth of the radial trapping potential, the detuning of the modulation frequency from the secular resonance, and the heating time are as important as the availability of enough power in the far-red-detuned Doppler cooling beam.

In a next step, the Paul trap confinement is changed to the dc and ac settings selected for ground-state cooling and QLS. The radial micromotion is compensated with the compensation electrodes shown in Figure 6.1 by minimizing the shift of the ion image on the EMCCD camera when altering the ac confinement of the Paul trap[7]. Next, the motional sideband spectrum can be measured (see the black curve in Figure 11.7 for the axial modes) in order to verify trapping of the correct $^{40}\mathrm{Ar}$ charge state. If the charge state is lower by one, i. e., a charge exchange reaction has happened and $^{40}\mathrm{Ar}^{12+}$ is trapped, the axial motional frequencies are lower by about 30 to 40 kHz for typical trap

---

[5] Note that the background count rate can be significantly increased to up to two orders of magnitude owing to insufficient shielding of the PMT from room light.

[6] This Doppler cooling beam requires a sufficient power on the order of 1 mW with a waist of 40 µm in order to cope with the cooling of the more extended and much hotter remaining $^{9}\mathrm{Be}^{+}$ ions.

[7] This is in fact a rather imprecise method for micromotion compensation but has proven to be sufficient for the QLS as presented in this work. In order to achieve a better reproducibility and the lowest possible level of motional frequency shifts, more sophisticated quantification methods might find implementation [see, e. g., Berkeland et al. (1998b), J. Keller et al. (2015), and Ludlow et al. (2015)].

settings. This is easily resolved and on a much larger level than a drift of the motional frequency caused by a drift of the dc trapping voltages[8]. This can be quickly checked within seconds and, in such an unfortunate case, the ions are released and the recapture plus two-ion crystal preparation process is repeated within minutes. With the right charge state, the secular frequencies might be fine-adjusted. In particular, the secular frequency of the QL transfer mode needs to be set accurately for QLS within about 1 kHz since the FWHM of the Rabi line shape is only on the order of a few kHz for clock laser logic pulses with a duration on the order of 200 µs. Then, the preparation of the crystal can proceed with ground-state cooling.

Table 11.2 summarizes the approximate secular frequencies for the Paul trap spectroscopy settings used in this work. The axial out-of-phase (OP) mode was chosen as motional transfer mode for QLS and therefore needs to be addressed successfully by both the axial clock laser beam and the axial Raman beams. It was noted in Section 6.2.2 that the radial modes have significantly different oscillation amplitudes for the $^{9}\mathrm{Be}^{+}$ and the $^{40}\mathrm{Ar}^{13+}$ ions due to the mismatch of the charge-to-mass ratios by about a factor of 3. The higher frequency radial in-phase (IP) modes feature a large oscillation amplitude of the $^{40}\mathrm{Ar}^{13+}$ ion while the radial OP modes feature a large oscillation amplitude of the $^{9}\mathrm{Be}^{+}$ ion. Therefore, the radial OP modes are naturally easier to drive with the Raman beams since the coupling is proportional to the square of the oscillation amplitude (see Section 7.2.3). However, also the radial IP modes could be driven with the Raman beams, albeit with much longer pulses. In contrast, the radial clock laser could only successfully drive the radial IP modes of the two-ion crystal so far. In the settings described by Table 11.2 the radial motional modes were not reliably stable and drifted for an unacceptable amount of tens of kHz for radial ground-state cooling, owing to presumably not sufficiently stable trapping conditions. Three-dimensional ground-state cooling, including the four radial modes, is an ongoing effort for this experiment and indispensable for the ultimate suppression of motional frequency shifts and their quantification during long clock pulses owing to ion heating in the absence of cooling[9]. Axial ground-state cooling is addressed in the next section.

11.5.1 Axial ground-state cooling

Ground-state cooling of the motional QL transfer mode is an essential prerequisite for QLS. The other motional modes are preferably cooled close to the ground state as well in order to reduce motional frequency shifts, though in this work, the radial modes were only Doppler cooled[10]. The axial OP mode is chosen as the QL transfer mode since it is the higher frequency mode

---

[8] For comparison, the axial secular frequencies are stable at the sub-kHz level on a daily basis.

[9] Recently, more stable trapping conditions were found with $\omega_{z,o} = 2\pi \times 1.57\,\mathrm{MHz}$, $\omega_{z,i} = 2\pi \times 1.15\,\mathrm{MHz}$, $\omega_{\tilde{x},i} = 2\pi \times 4.0\,\mathrm{MHz}$, $\omega_{\tilde{y},i} = 2\pi \times 3.7\,\mathrm{MHz}$, $\omega_{\tilde{x},o} = 2\pi \times 1.094\,\mathrm{MHz}$, $\omega_{\tilde{y},o} = 2\pi \times 0.733\,\mathrm{MHz}$.

[10] The Doppler cooling limit corresponds to a mean occupation number of about $\bar{n} \approx 5$–10. The mean occupation number realized in practice can be higher owing to a low cooling efficiency

Motional mode	Secular frequency (MHz)
Axial out-of-phase	1.86
Axial in-phase	1.37
Radial $\tilde{x}$ in-phase	5.3
Radial $\tilde{y}$ in-phase	5.0
Radial $\tilde{x}$ out-of-phase	1.47
Radial $\tilde{y}$ out-of-phase	1.17

Table 11.2: Secular frequencies of the six motional modes. Note that $\omega_{u,p} = (2\pi \times \text{secular frequency})$ and the given values are approximate. The Paul trap coordinate frame is defined in, e. g., Figure 6.1.

along the axial direction and therefore offers a lower heating rate for the typical $1/f$-electric field noise. However, also the axial IP mode needs to be ground-state cooled in order to prevent dephasing. This is important, since the coupling between the interrogating lasers and the ions depends on the motional Fock state of the two-ion crystal as discussed in Section 7.2.3. If the motional state of the axial IP mode is a superposition of a thermal Fock state distribution, also the product state of the OP and IP mode is represented by such a distribution of product states with different IP Fock states. All these states would experience a different coupling strength for axial laser excitation with correspondingly different π-times, causing a dephasing of the excitation probability along an increasing probe time. Therefore, both axial modes require ground-state cooling in order to achieve the optimal contrast for carrier or sideband operations when probing along the axial direction. In contrast, the Doppler cooled radial modes do not couple to the axial laser beams owing to their orthogonal orientation and do not impede QLS with their thermal Fock state distributions.

Axial ground-state cooling is realized by resolved sideband cooling in a pulsed fashion using the axial Raman beams as was explained in Section 7.3.2. The ground-state cooling pulse sequence is realized with an experimental control system which accurately controls the microsecond timing of the entire pulse sequence as well as the frequencies, phases, and durations of the optical pulses with a top-hat temporal profile, generated from the 313 nm cw laser beams. Both axial modes start at their Doppler limit with a mean occupation number of about 10 (see Equation 7.41). Single $^9\text{Be}^+$ has rather large Lamb–Dicke parameters η of $0.48 \cdot \sqrt{2\pi \times 1\,\text{MHz}/\omega_u}$ for spontaneous emission and $0.82 \cdot \sqrt{2\pi \times 1\,\text{MHz}/\omega_z}$ for the stimulated Raman transitions with the axial Raman beams (see Section 7.2.3), where ω_u denotes the secular frequency. However, the Lamb–Dicke parameter in the two-ion crystal is smaller for a given value of ω_u since the energy stored in the QHO mode is shared between $^9\text{Be}^+$ and $^{40}\text{Ar}^{13+}$ and, therefore, the spatial extent of the $^9\text{Be}^+$ motional ground-state wave function is smaller. Still, the large spontaneous Lamb–Dicke parameter is somewhat troublesome since the dissipative step in the resolved sideband cooling sequence (see Figure 7.4), induced by excitation

---

of the IP modes or recoil and anomalous heating during periods when no Doppler cooling is applied.

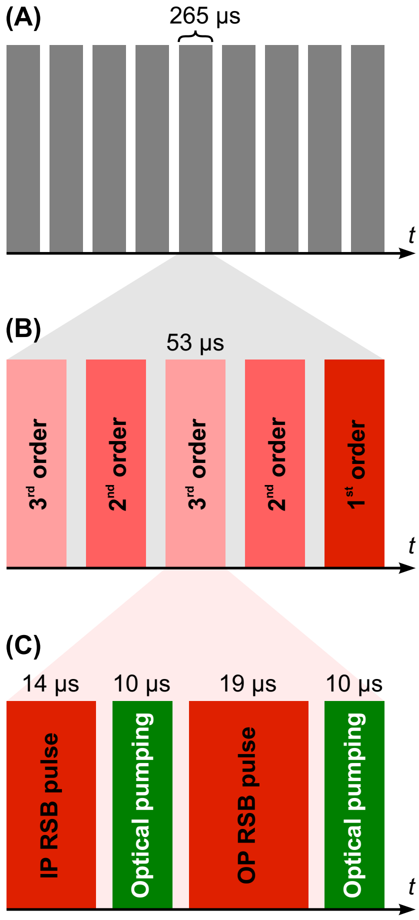

Figure 11.6: Axial ground-state cooling sequence. Pulsed resolved sideband cooling is employed in a multiple stage fashion. (**A**) A variable number of repetitions of the block shown in panel B is applied with a duration of about little less than 300 µs. (**B**) Each cooling block is composed of five sub-blocks in which different orders of red sidebands (RSBs) are used. (**C**) Each sub-block starts with a RSB π-pulse on the axial in-phase (IP) mode, followed by a dissipative step using both repumpers (referred to as *optical pumping*). This initializes the lower qubit state again. Next, a RSB π-pulse on the axial out-of-phase (OP) mode is applied, again followed by optical pumping. Note that the pulse lengths given in the scheme correspond to the settings used for QLS with 20 repetitions of the cooling blocks illustrated in panel A.

with the repumper lasers, relies on subsequent spontaneous emission which redistributes the initial Fock state distribution of the cooled mode into a wider and hotter Fock state distribution of the lower qubit state and thereby heats the two-ion crystal again. On the other hand, the large Lamb–Dicke factor for the stimulated Raman transitions can be exploited to efficiently drive higher-order RSBs in order to remove more than one phonon per pulse (Joshi et al., 2019; Wan et al., 2015; Y. Yu et al., 2018), as was demonstrated for single $^9\text{Be}^+$ ions in this system before [see Leopold (2018) and Leopold et al. (2019) in Appendix P3]. This higher-order sideband cooling is particularly important to overcome the zero-coupling nodes for a given RSB and specific occupation numbers which can lead to significant population being ‘trapped’ in a non-thermal distribution at higher occupation numbers. To cope with such ground-state cooling outside the Lamb–Dicke regime, the cooling is realized as a multi-stage sequence as shown in Figure 11.6 and follows previous simulations and experiences with single $^9\text{Be}^+$. The cooling blocks in Figure 11.6A are repeated many times (typically 15 to 20 times) and are composed of five sub-blocks each employing different RSB orders as shown in Figure 11.6B. In each sub-block, first, the axial IP mode is cooled by a RSB pulse and followed by a subsequent optical pumping phase using both repumper lasers simultaneously to initialize the lower qubit state again (see Figure 11.6C). Second, the cooling is analogously repeated on the axial OP mode with adjusted RSB pulse time.

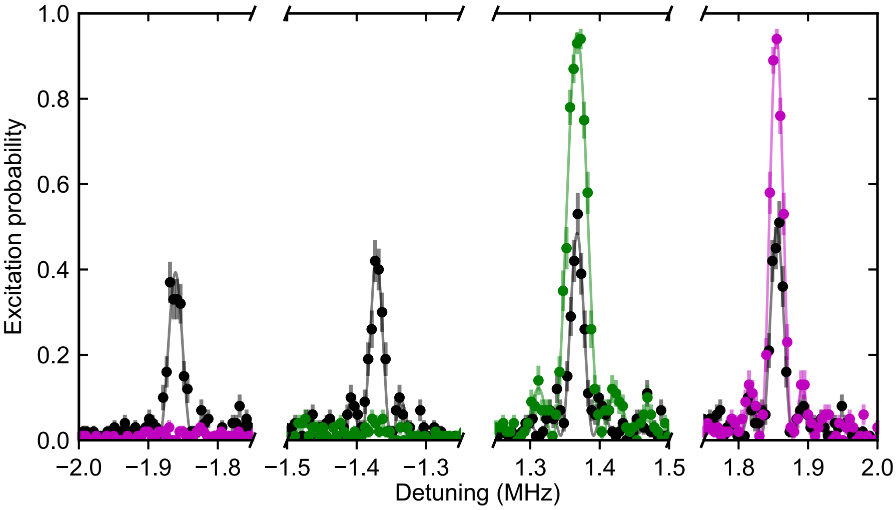

Figure 11.7: Axial ground-state cooling of the two-ion crystal. The secular sideband spectrum of the $^9\mathrm{Be}^+$ qubit transition shows the first-order sidebands of the axial IP mode at a detuning of $\pm 1.37\,\mathrm{MHz}$ (green) and of the OP mode at a detuning of $\pm 1.86\,\mathrm{MHz}$ (purple), measured with the axial Raman beams. The black data shows these sidebands measured just after Doppler cooling. After resolved sideband cooling of both axial modes, the sideband spectrum is measured again (green and purple data). The red sidebands of both modes (negative detuning) have vanished, revealing that these modes have been cooled to the quantum-mechanical ground state of motion. The sideband asymmetry yields mean occupation numbers of $\bar{n}_{z,i} = 0.053(11)$ and $\bar{n}_{z,o} = 0.017(6)$, respectively. The solid curves are least-square best fits of the sidebands with a Rabi line shape (Equation 7.23). The π-probe times were 36 µs for the measurement of the black and purple data and 24 µs for the green data. See text for further details.

The axial OP mode is cooled at last on purpose because it is the QL transfer mode in which the lowest mean occupation number $\bar{n}$ should be achieved. This sequence allows to smoothly sweep the excitation probability of higher Fock states down and finally ground-state cool both modes with high fidelity.

Pulse lengths on the order of 10 µs Fourier-broaden the sidebands to about 80 kHz (see Equation 7.25). Therefore, the resolved sideband cooling is quite insensitive to drifts of the motional frequencies on a typical sub-kHz level within one day. It is important to prevent so-called *coherent population trapping* (Morigi, 2003) when shining in both repumper lasers simultaneously during the optical pumping period of the ground-state cooling and also in the later discussed QL sequence. This is avoided by a sufficient detuning of the repumper difference frequency from the splitting of the involved hyperfine Zeeman substates $|^2\mathrm{S}_{1/2}, F = 1, m_F = 1\rangle$ and $|^2\mathrm{S}_{1/2}, F = 2, m_F = 1\rangle$ by about 4 MHz in order to efficiently depopulate the upper qubit state within significantly less than 10 µs [see Leopold (2018)]. Otherwise a significant fraction of the population could be 'trapped' in a coherent superposition of both involved Zeeman substates. Furthermore, the radial IP mode frequencies, in which $^{40}\mathrm{Ar}^{13+}$ has the large oscillation amplitude, are significantly larger than the axial mode frequencies (see Table 11.2). In contrast, the radial OP modes, in which $^9\mathrm{Be}^+$ has the large oscillation amplitude, are closer to the axial modes. The Paul trap settings must be chosen to avoid a close proximity or particularly any overlap of theses modes in order to prevent mode coupling which would impede ground-state cooling and QLS.

Figure 11.7 shows the axial sideband spectrum after successful axial ground-state cooling by operating the sequence as discussed here with 15 repetitions of the cooling blocks and π-times of about 24 and 36 µs for the axial IP and OP modes[11], respectively. This corresponds to a total number of 150 RSB pulses, accomplished within about 7.5 ms. The deviation from this cooling time achieved in practice and 6 ms as calculated by the values stated before is due to experimental overhead, i. e., additional dead times and wait times during the sequence. Mean occupation numbers of $\bar{n}_{z,i} = 0.053(11)$ and $\bar{n}_{z,o} = 0.017(6)$ were achieved, evaluated from the sideband asymmetry according to the relation

$$\bar{n} = \frac{P_{\mathrm{RSB}}/P_{\mathrm{BSB}}}{1 - P_{\mathrm{RSB}}/P_{\mathrm{BSB}}} \,. \tag{11.8}$$

This technique is known as Raman sideband thermometry (Turchette et al., 2000) with this formula being valid for first-order sidebands, as can be derived from Equation 7.33, measured with identical probe time, and a thermal Fock state distribution. P_{RSB} and P_{BSB} denote the peak excitations of the RSB and the BSB, respectively, of the corresponding motional mode. Note that this evaluation neglects a potentially long tail of the Fock state distribution after ground-state cooling with a low population fraction but extended towards high occupation numbers (Chen et al., 2017). To our knowledge, this is the first demonstration of ground-state cooling of such an exotic two-ion crystal composed of atomic species with both different charge and different mass.

Heating rates

Ion heating can impose severe issues. It does not only increase the motional frequency shift but can even compromise QLS when the ion cannot be kept in the ground state during the QL sequence. The heating rate, driven by electric field noise with the spectral density $S(\omega_{u,p})$, can be expressed as [see for instance Brownnutt et al. (2015), Kielpinski et al. (2000), and Turchette et al. (2000)]

$$\Gamma = S(\omega_{u,p}) \cdot \frac{e^2}{4\hbar\,\omega_{u,p}\, m_{\mathrm{Be}}} \cdot \left(b_{u,p}^{\mathrm{Be}} + Z_{\mathrm{ion}} \sqrt{\frac{m_{\mathrm{Be}}}{m_{\mathrm{HCI}}}}\, b_{u,p}^{\mathrm{HCI}} \right)^2 , \tag{11.9}$$

where $\omega_{u,p}$ is the angular secular frequency and $b_{u,p}$ are the normalized motional mode amplitudes of $^{9}\mathrm{Be}^{+}$ and $^{40}\mathrm{Ar}^{13+}$, respectively. They fulfill the normalization condition $1 = (b_{u,p}^{\mathrm{Be}})^2 + (b_{u,p}^{\mathrm{HCI}})^2$. m_{Be} and m_{HCI} are the respective ion masses, Z_{ion} the charge state of the HCI, here $Z_{\mathrm{ion}} = 13$ for $^{40}\mathrm{Ar}^{13+}$, e the elementary charge, and $\hbar$ the reduced Planck constant. According to

---

[11] The π-times achieved with the axial Raman beams could be later significantly reduced by a factor of almost 2 by tighter focusing the beams. These shorter π-times are shown in Figure 11.6 and were later in use for most of the QLS results.

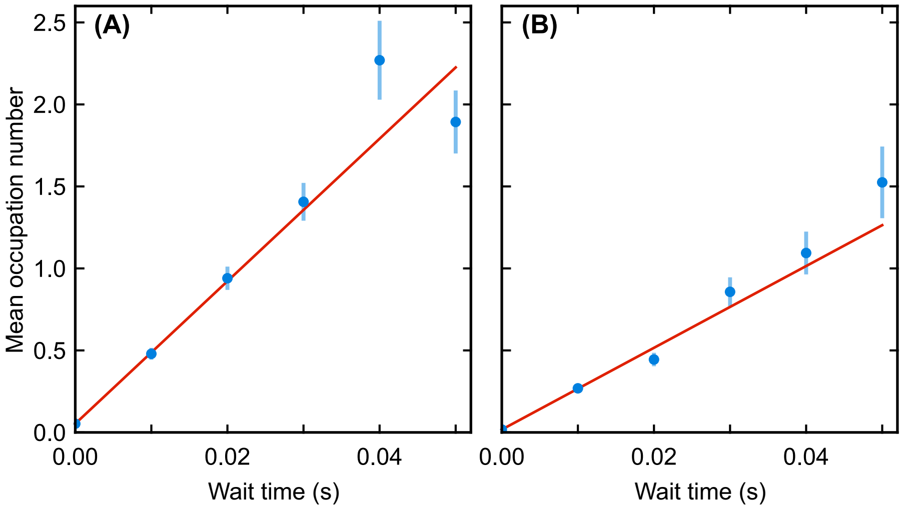

Figure 11.8: Heating rates of the axial modes of the two-ion crystal. The mean occupation number is measured by Raman sideband thermometry as a function of a wait time after ground-state cooling for (**A**) the axial in-phase mode and (**B**) the axial out-of-phase mode. Heating rates of $\dot{\bar{n}}_{z,i} = 43.4(24)$ phonons / s and $\dot{\bar{n}}_{z,o} = 24.9(15)$ phonons / s are obtained from the linear least-square best fits, respectively, where $\dot{\bar{n}}$ denotes the time derivative of the mean occupation number. Compared to the heating rate of a single $^9\mathrm{Be}^+$ ion, these measured rates are larger by a factor of about 20 as is expected from Equation 11.9.

Equation 11.9 the heating rate does not depend on the charge-to-mass ratios as many other quantities do but on the ratio q^2/m of the ions. The expression before the bracketed term in Equation 11.9 is the $^9\mathrm{Be}^+$ single ion heating rate. Correspondingly, it is expected that the ion heating increases by the factor of the squared bracket for the two-ion crystal with a HCI.

As mentioned earlier in Section 11.2, the Paul trap of this work features very low heating rates on the order of $\dot{\bar{n}} = 1$ phonon / s for a single $^9\mathrm{Be}^+$ ion [see Leopold et al. (2019) in Appendix P3]. Measurements of the heating rates for both axial modes of the $^{40}\mathrm{Ar}^{13+}$–$^9\mathrm{Be}^+$ two-ion crystal are shown in Figure 11.8. Here, $\bar{n}$ was measured by evaluating the sideband asymmetry (see Equation 11.8) as a function of a wait time after ground-state cooling. A linear fit yields both $\bar{n}$ for zero wait time and the heating rate $\dot{\bar{n}}$ expressed in terms of phonons / s, where the relation $\dot{\bar{n}} = \Gamma \cdot \bar{n}$ applies close to the ground state. We obtain the heating rates $\dot{\bar{n}}_{z,i} = 43.4(24)$ phonons / s and $\dot{\bar{n}}_{z,o} = 24.9(15)$ phonons / s for the axial IP and OP mode, respectively. In slightly different settings even lower heating rates of $\dot{\bar{n}}_{z,i} = 29.4(19)$ phonons / s and $\dot{\bar{n}}_{z,o} = 12.4(7)$ phonons / s for the axial IP and OP mode were achieved. These heating rates are about a factor of 20 larger than the $^9\mathrm{Be}^+$ single ion heating rates, which is indeed predicted by Equation 11.9. They are, however, low enough to keep the two-ion crystal in the ground state even for extended probe times with the clock laser. For instance, we obtain $\bar{n}_{z,i} \lesssim 0.5$ and $\bar{n}_{z,o} \lesssim 0.2$ for the axial IP and OP modes for wait times of 10 ms. Noteworthy, if required, the two-ion crystal could be even ground-state cooled during the clock laser interrogation due to the extremely low polarizability of the HCI, which would result in only a small second-order Stark shift.

12

Clock laser stabilization and frequency measurement

The electric-dipole forbidden transition of the $^{40}\mathrm{Ar}^{13+}$ spectroscopy ion has a FWHM natural linewidth of 17 Hz. A narrow-linewidth and highly stable clock laser is required in order to resolve this transition close to the natural linewidth and to perform spectroscopy with Hz-level uncertainty. The narrow linewidth is accompanied with a long coherence time of the clock laser radiation, which is also an essential property in order to perform the coherent operations which are discussed in the next chapter. For this purpose, a laser system was set up in the laser laboratory where the Paul trap is located and stabilized through a frequency comb to an ultrastable laser in a different building of PTB (see Figure 12.1).

The clock laser system, summarized by Figure 12.1D, is based on a commercial extended cavity diode laser operating at the fundamental wavelength of 882 nm, corresponding to a frequency of about 340 THz. It is prestabilized to an external reference cavity with a finesse of about 1000 with a high locking bandwidth of 4 MHz, using the pump current of the laser diode and the grating piezo as actuators. The prestabilization thus suppresses high-frequency laser noise and an instantaneous linewidth of about 2 kHz is achieved, limited by the reference cavity. Most of the available laser power is sent to an SHG cavity using a PPKTP crystal for frequency doubling to the $^{40}\mathrm{Ar}^{13+}$ transition wavelength of about 441 nm, corresponding to 680 THz. The frequency-doubled light is sent through a 5 m-long polarization-maintaining single-mode optical fiber to the other optical table in the laser laboratory to generate the different clock laser beams as shown in Section 11.3. Importantly, the clock laser is actively power stabilized on a pulse-by-pulse basis at the Paul trap in order to prevent fluctuations of the Rabi frequency.

A fraction of the fundamental clock laser light at 882 nm is sent to the frequency comb laboratory through a 300 m-long polarization-maintaining single-mode fiber. A fraction of that light is sent back to the laser laboratory in order to cancel the phase noise, introduced by the fiber, through a standard phase noise cancellation scheme (Falke et al., 2012; Ma et al., 1994). In the comb laboratory the clock laser light beats with a frequency-doubled and spectrally broadened erbium-doped fiber frequency comb (see Figure 12.1A), which provides a phase-coherent link to a hydrogen maser. This hydrogen maser is steered on a daily basis by the caesium fountain clock of PTB, which realizes the SI second as a primary frequency standard. Thus, the absolute frequency of the fundamental clock laser can be measured by measuring three radio frequencies, namely the carrier-envelope offset f_{ceo} of the frequency comb at about 20 MHz, the repetition rate f_{rep} of the frequency comb at about 253 MHz, and the beat frequency b_{882} between the clock laser and frequency comb at about 76 MHz using the relation

$$f_{882} = 2 \cdot f_{\text{ceo}} + f_{\text{rep}} \cdot N_{882} + b_{882} \,. \tag{12.1}$$

N_{882} is the number of the comb tooth[1] which is the closest one to $f_{882} \approx$ 340 THz. The factor 2 in front of f_{ceo} results from the frequency doubling of the comb light. In contrast, the comb tooth spacing f_{rep} is preserved in the nonlinear frequency-doubling process. Information about the basic operation and properties of frequency combs can be found elsewhere, e. g., in Udem, Holzwarth, and Hänsch (2002).

The 2 kHz instantaneous linewidth of the prestabilized clock laser was sufficiently narrow to observe the first QL signals from $^{40}\text{Ar}^{13+}$, but an improved clock laser stabilization is essential to resolve narrower transition linewidths. An ultrastable laser system operating at 1.5 μm, corresponding to a frequency of 194 THz, at PTB is employed for that purpose (see Figure 12.1B). This laser is itself stabilized to a cryogenic cavity cooled to 124 K, similar to the one described by Kessler et al. (2012). The cavity is made from crystalline silicon, has a finesse of about 500000, and is referred to as Si2. At averaging times between 1 and 50 s a fractional frequency instability of 4×10^{-17} at the thermal noise limit of the cavity mirrors is achieved. The laser features an instantaneous linewidth of below 10 mHz with a daily frequency drift on the order of 10 Hz (Matei et al., 2017). This ultrastable laser also beats with the frequency comb at $b_{\text{Si2}} \approx 23.5$ MHz, but different from above, with the fundamental of the comb. The laser frequency is analogously given by

$$f_{\text{Si2}} = f_{\text{ceo}} + f_{\text{rep}} \cdot N_{\text{Si2}} + b_{\text{Si2}} \,. \tag{12.2}$$

The residual noise of the 882 nm clock laser is suppressed by phase-locking it to the 1.5 μm ultrastable laser using the frequency comb as a transfer oscillator as illustrated in Figure 12.1C. This scheme is dubbed *transfer locking* and is an established technique [see, e. g., Scharnhorst et al. (2015), Stenger et al. (2002), and Telle, Lipphardt, and Stenger (2002)]. The idea is to generate a virtual beatnote, referred to as *transfer beat* b_{tb}, which contains the information about the relative phase and frequency fluctuations of the fundamental clock laser relative to the ultrastable laser and is free from the maser and other noise to which the frequency comb is exposed. To derive the relevant relations, we first multiply Equation 12.1 with N_{Si2}/N_{882} to obtain

$$f_{882} \cdot \frac{N_{\text{Si2}}}{N_{882}} = 2 \cdot f_{\text{ceo}} \cdot \frac{N_{\text{Si2}}}{N_{882}} + f_{\text{rep}} \cdot N_{\text{Si2}} + b_{882} \cdot \frac{N_{\text{Si2}}}{N_{882}} \tag{12.3}$$

---

[1] Note that f_{rep} is multiplied in Equation 12.1 by the large number $N_{882} = 1\,340\,321$. Therefore, the accurate value of this radio frequency is more important than for the other two. The more exact value is 253.378 286 MHz.

from which we subtract Equation 12.2. Finally, we arrive at another relation for the fundamental clock laser frequency

$$f_{882} = \frac{f_{\mathrm{Si2}} + b_{\mathrm{tb}}}{N_{\mathrm{Si2}}/N_{882}} \tag{12.4}$$

with the transfer beat b_{tb} given by

$$b_{\mathrm{tb}} = 2 \cdot \frac{N_{\mathrm{Si2}}}{N_{882}} \cdot \left(f_{\mathrm{ceo}} + \frac{b_{882}}{2}\right) - \left(f_{\mathrm{ceo}} + b_{\mathrm{Si2}}\right) . \tag{12.5}$$

Equation 12.4 shows that the optical frequency noise of the clock laser is represented by the frequency noise of the rf transfer beat, which has to be realized through the relation given by Equation 12.5. Therefore, the clock laser can be locked to the ultrastable laser by stabilizing b_{tb}. The generation of b_{tb} has to be accomplished through appropriate transfer electronics as illustrated by the simplified scheme in Figure 12.1C. In fact, the corresponding beat signals of both lasers with the comb, $b_{882}/2$ and b_{Si2}, are mixed with the carrier-envelope offset f_{ceo} of the comb in order to eliminate f_{ceo} and the corresponding noise. The factor $2 \cdot N_{\mathrm{Si2}}/N_{882}$ is realized by processing the rf signal through direct digital synthesis in the branch of the mixed beat of the clock laser. Finally, the difference frequency of both mixed rf signals is generated in order to eliminate the influence of f_{rep} and its noise. This difference frequency is the transfer beat b_{tb} which is used to generate the feedback signal for phase-locking the fundamental clock laser to the ultrastable laser. The feedback signal is applied to an AOM between the 882 nm diode laser and the reference cavity. The locking bandwidth of about 10 kHz is much lower than the one of the diode laser lock (4 MHz) to the prestabilization cavity and, thus, ensures that both loops do not compete. However, residual noise and drifts of the clock laser are suppressed, transferring the stability properties of the ultrastable laser to the clock laser at Fourier frequencies up to a few kHz. Owing to frequency doubling twice[2], we observe an expected daily frequency drift on the order of 40 Hz of the 441 nm beams, which could be eliminated through the link to the hydrogen maser via the frequency comb but was not implemented thus far. The clock laser linewidth could be in principle evaluated through the linewidth of a second out-of-loop transfer beat with another ultrastable laser under the assumption that the linewidth of that laser is much narrower. However, within this work no limitations from the residual clock laser linewidth were observed. From frequency scans across the narrow spectroscopy transition in $^{40}\mathrm{Ar}^{13+}$ one can conclude a clock laser linewidth not larger than about 10 Hz, representing a conservative estimate. Note that the clock laser stabilization scheme was recently changed by switching to a different frequency comb. Here, the comb itself is stabilized to the ultrastable laser and is therefore free from additional noise. The fundamental clock laser is then directly stabilized to the ultrastable frequency comb, removing the necessity for a transfer beat setup.

---

[2] First, the comb is frequency doubled for beating with the fundamental clock laser and second, the clock laser itself is frequency doubled.

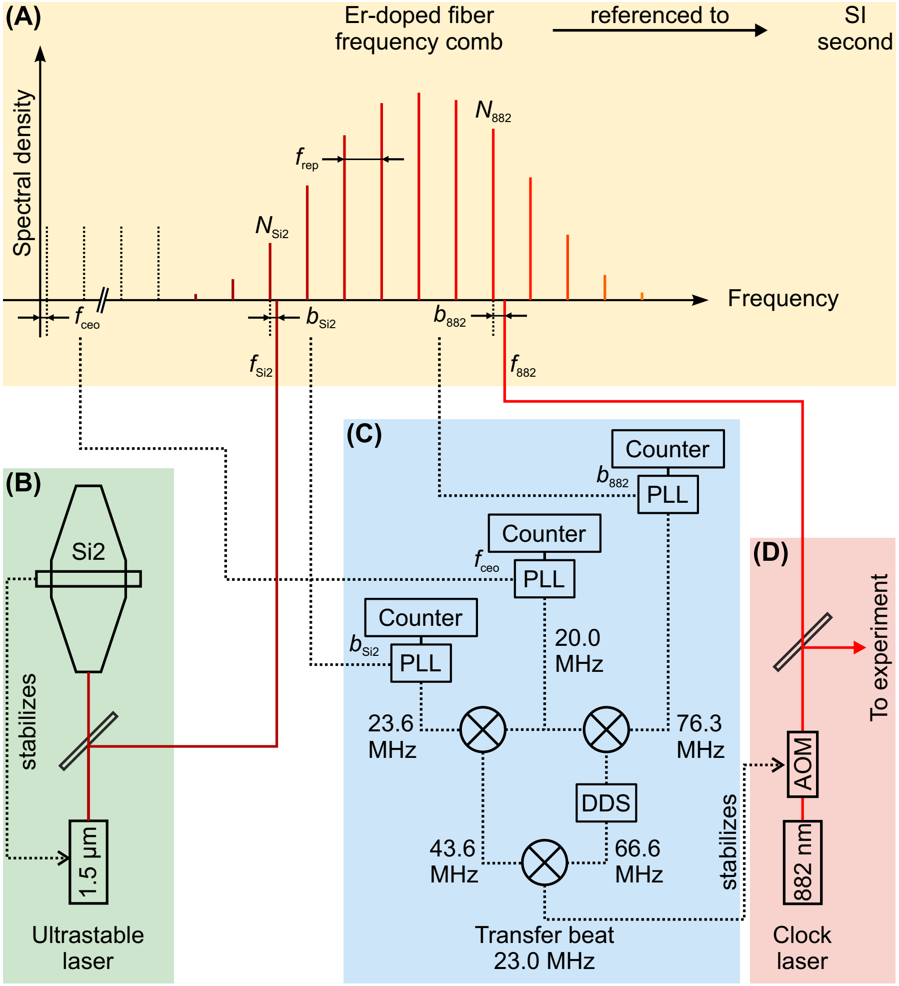
(A)
Er-doped fiber frequency comb
referenced to
SI second
Spectral density
Frequency
f_{rep}
N_{Si2}
N_{882}
f_{ceo}
b_{Si2}
b_{882}
f_{Si2}
f_{882}
(B)
Si2
stabilizes
1.5 µm
Ultrastable laser
(C)
Counter
PLL
b_{882}
Counter
f_{ceo}
PLL
Counter
b_{Si2}
PLL
20.0 MHz
23.6 MHz
76.3 MHz
DDS
43.6 MHz
66.6 MHz
stabilizes
Transfer beat 23.0 MHz
(D)
To experiment
AOM
882 nm
Clock laser

Figure 12.1: Simplified scheme for the stabilization and absolute frequency measurement of the clock laser. (**A**) A frequency comb allows to measure the optical frequencies of the involved lasers. It is also used as a transfer oscillator by fixing the frequency interval between the ultrastable laser and the fundamental clock laser. (**B**) A 1.5 µm laser is stabilized to the cryogenic silicon cavity Si2. (**C**) A transfer beat is generated by mixing the different beat signals and the carrier-envelope offset of the comb appropriately. Note that this is a simplified scheme which does not show various additional components for processing the rf signals. (**D**) A fraction of the fundamental clock laser is sent to the frequency comb. The other fraction is used for probing $^{40}\mathrm{Ar}^{13+}$. Note that the fundamental clock laser at 882 nm in fact beats with the frequency-doubled frequency comb. This results in a factor of 2 in front of f_{ceo} in Equation 12.1. The transfer beat used in the experiment was divided by 2 to reduce the attenuation in the transmission line to the laser laboratory. See text for further details. AOM—acousto-optic modulator, DDS—direct digital synthesis, PLL—phase-locked loop.

13 Quantum logic

This chapter addresses the realization of QL operations in this work. As discussed in Section 2.3, such techniques were employed at first in a Paul trap for the spectroscopy of the $^{27}\mathrm{Al}^{+}$ ion (P. O. Schmidt et al., 2005; Wineland et al., 2002) which does not offer an appropriate electronic level structure for direct laser cooling and electron shelving. HCIs suffer from this issue as well. A solution is possible by extending the spectroscopy to a two-ion crystal which is composed of the spectroscopy ion and a logic ion, here $^{40}\mathrm{Ar}^{13+}$ and $^{9}\mathrm{Be}^{+}$, respectively. The two-ion crystal represents a coupled system of the narrow clock transition of the $^{40}\mathrm{Ar}^{13+}$ spectroscopy ion, of a QHO constituted by one motional mode of the two-ion crystal and referred to as the *transfer mode*, and the narrow qubit transition of the $^{9}\mathrm{Be}^{+}$ logic ion as illustrated in Figure 13.1. The clock and the qubit transition are individually addressed by the clock laser and the axial Raman laser beams, respectively. Coherent excitation and de-excitation is realized by driving carriers (CARs) as well as red sidebands (RSBs) or blue sidebands (BSBs) involving exclusively the transfer mode. While driving the CARs only changes the electronic state, driving first-order RSBs or BSBs changes both the electronic and motional state by removing or adding a quantum of motion, respectively. Furthermore, the $^{9}\mathrm{Be}^{+}$ ion provides a fast closed-cycling transition which shares its lower electronic state with the lower qubit state $|\downarrow\rangle_\mathrm{L}$. The lower qubit state therefore appears as a bright state and the upper qubit state $|\uparrow\rangle_\mathrm{L}$ as a dark state when applying the $^{9}\mathrm{Be}^{+}$ Doppler cooling laser. This enables highly efficient state detection of the $^{40}\mathrm{Ar}^{13+}$ clock transition after a sequence of QL pulses through which $^{9}\mathrm{Be}^{+}$ is deterministically shelved into the upper dark qubit state and represents an extension of the conventional electron shelving technique. The fast closed-cycling transition is also used for Doppler laser cooling of the two-ion crystal.

The axial OP mode was chosen as the transfer mode here to map the clock transition onto the qubit transition. This mode is initially cooled to the motional ground state $|0\rangle_\mathrm{m}$ together with the axial IP mode as described in Section 11.5.1. The excitation to the first excited motional state $|1\rangle_\mathrm{m}$ is intermittently used for both electronic state preparation and to hold the information of a successful clock transition excitation during the QL sequence. Higher excited motional states $|n\rangle_\mathrm{m}$ are not involved in the protocols.

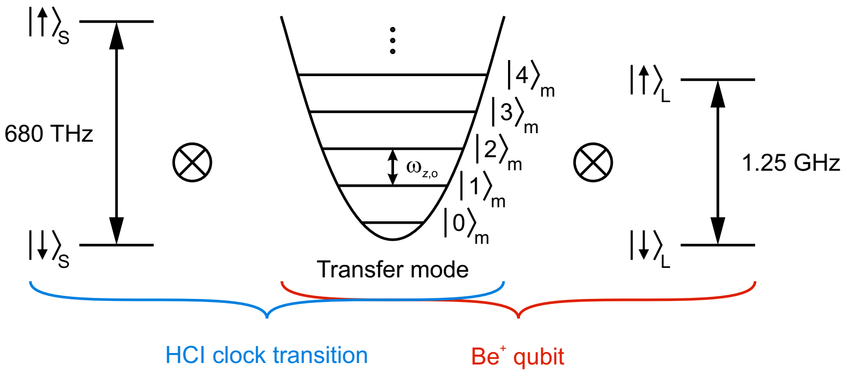

Figure 13.1: **Quantum representation of the coupled two-ion system.** The Ar^{13+} clock transition (blue) and the $^9\mathrm{Be}^+$ qubit transition (red) are individually addressed by the clock laser and the Raman laser system, respectively. Each electronic transition can be driven on the carrier or a red or blue sideband. The latter ones change the common motional state of the two-ion crystal and are used to transfer information between both ions. The spacing of the QHO states is governed by the secular frequency of the chosen transfer mode, here $\omega_{z,o}$ of the axial OP mode.

13.1 Quantum logic-assisted state preparation

The lower and upper electronic states of the $^{40}\mathrm{Ar}^{13+}$ clock transition split up in the magnetic quantization field into two and four Zeeman substates (see Figure 5.1). This results in a splitting of the clock transition into six Zeeman components. While the electronic state of the $^9\mathrm{Be}^+$ ion and the QHO state of the transfer mode is prepared through optical pumping with the Doppler cooling and repumper lasers and ground-state cooling, respectively, the electronic ground state of the $^{40}\mathrm{Ar}^{13+}$ ion is prepared through a series of five clock laser sideband π-pulses with π-times between 170 and 272 µs[1] as shown in Figure 13.2 for the $|^2\mathrm{P}_{1/2}, m_J = -1/2\rangle_\mathrm{S}$ Zeeman substate. RSB pulses are used for electronic de-excitation [(a, b) as well as (d, e)], and a BSB pulse is used for electronic excitation (c). This ensures unidirectional preparation since excitation with a RSB or de-excitation with a BSB pulse from the motional ground state $|0\rangle_\mathrm{m}$ is not possible owing to the nonexistence of the motional state $|-1\rangle_\mathrm{m}$. Therefore, each successful sideband pulse excites the transfer mode from $|0\rangle_\mathrm{m}$ to $|1\rangle_\mathrm{m}$. Ground-state cooling immediately after each sideband pulse returns the transfer mode back into the $|0\rangle_\mathrm{m}$ state. Interleaved ground-state cooling is realized analogously to the sequence shown in Figure 11.6 through RSB π-pulses with the axial Raman laser beams on the $^9\mathrm{Be}^+$ ion, but here only two cooling sub-blocks (Figure 11.6B) are used that comprise second-order at first and then first-order RSB pulses. Also in contrast to the full axial ground-state cooling sequence, five repetitions of the cooling blocks (Figure 11.6A) are used. The entire $^{40}\mathrm{Ar}^{13+}$ electronic state

---

[1] The different sideband π-times for the different Zeeman components result from the different Clebsch-Gordan coefficients and different geometrical couplings of the axial clock laser beam with given wave vector and polarization. The polarization was chosen to drive all Zeeman components with a rather similar strength.

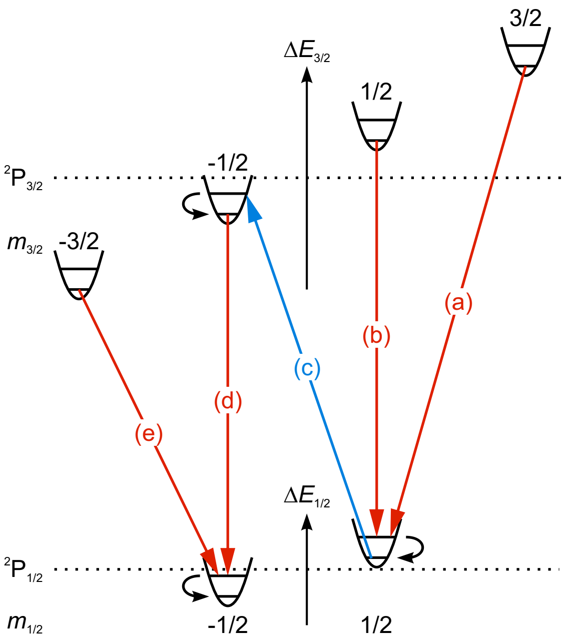

Figure 13.2: Quantum logic-assisted electronic state preparation. The $^{40}\mathrm{Ar}^{13+}$ Zeeman substates of the $^2\mathrm{P}_{1/2}$ ground and $^2\mathrm{P}_{3/2}$ excited state are visualized by the motional ground and first excited state of the transfer mode each. A series of five clock laser sideband π-pulses (a-e) with interleaved ground-state cooling (black curved arrows) deterministically prepares the $|^2\mathrm{P}_{1/2}, m_J = -1/2\rangle_\mathrm{S}$ state and guarantees unidirectional optical pumping. The other $^2\mathrm{P}_{1/2}$ Zeeman substate is analogously prepared. See text for further details.

preparation sequence with the five clock laser sideband pulses is repeated four times to ensure high-fidelity operation. This results in an overall $^{40}\mathrm{Ar}^{13+}$ state preparation time of about[2] 15 ms.

13.2 Quantum logic spectroscopy

The full pulse sequence for QLS is shown in Figure 13.3A with panel B illustrating the spectroscopy sequence itself on the quantum level. The sequence starts with 200 µs of Doppler cooling followed by 200 µs of state detection to quantify the bright qubit state photon count rate measured by the PMT. During the Doppler cooling period, the Doppler cooling laser with a red-detuning of 10 MHz and repumper 1 are applied in order to Doppler cool the two-ion crystal and to empty the $|^2\mathrm{S}_{1/2}, F = 1\rangle$ state manifold. This optically pumps the $^9\mathrm{Be}^+$ ion into the bright $|^2\mathrm{S}_{1/2}, F = 2, m_F = 2\rangle$ qubit state (see Figure 5.2). The first state detection of the sequence is then performed as described in Section 11.4 by additionally shining in repumper 1 in order to prevent losing the $^9\mathrm{Be}^+$ ion in the dark $|^2\mathrm{S}_{1/2}, F = 1, m_F = 1\rangle$ qubit state by a residual polarization component which could drive a π-transition with subsequent decay into this state. Next, a second 200 µs-long Doppler cooling period is performed, followed by a 10 µs-short period of optical pumping with both repumper lasers 1 and 2. This allows to prepare the bright $|^2\mathrm{S}_{1/2}, F = 2, m_F = 2\rangle$ qubit state with higher fidelity and is relevant since the last scatter event on the

---

[2] The quoted numbers would yield an expected state preparation time of 10.6 ms. In practice, this time is longer as a result of dead times and wait times for AOM switching as mentioned before in Section 11.5.1.

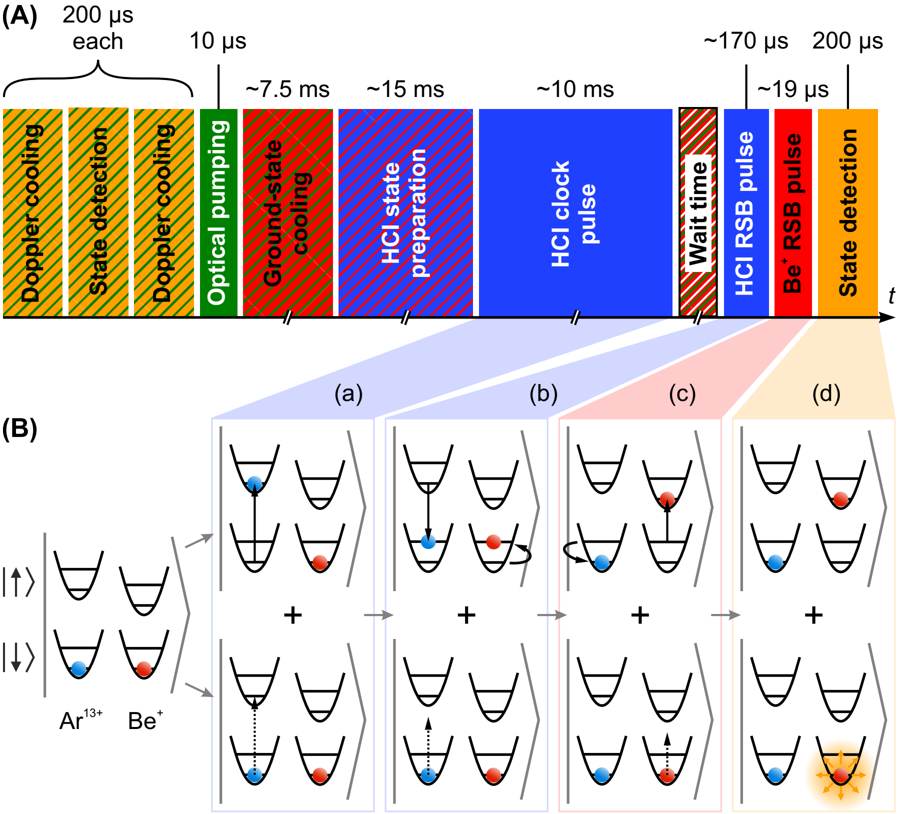
(A)
200 µs each
10 µs
~7.5 ms
~15 ms
~10 ms
~170 µs
200 µs
~19 µs
Doppler cooling
State detection
Doppler cooling
Optical pumping
Ground-state cooling
HCI state preparation
HCI clock pulse
Wait time
HCI RSB pulse
Be+ RSB pulse
State detection
t
(B)
(a)
(b)
(c)
(d)
|↑⟩
|↓⟩
Ar13+
Be+
+

Figure 13.3: Quantum logic spectroscopy sequence. (**A**) The pulse sequence starts with a Doppler cooling period followed by state detection in order to verify and quantify the count rate from the bright state of the $^9\mathrm{Be}^+$ logic ion. After another period of Doppler cooling and optical pumping with both repumper lasers, the $^9\mathrm{Be}^+$ bright qubit state is initialized again with high fidelity. Next, axial ground-state cooling and quantum logic-assisted electronic state preparation of $^{40}\mathrm{Ar}^{13+}$ is performed. The quoted times of about 7.5 and 15 ms are the values achieved in practice, including dead times of the experimental control system and wait times for AOM switching. The spectroscopy sequence (**B**) starts with (a) the clock laser pulse addressing the carrier transition of the $^{40}\mathrm{Ar}^{13+}$ spectroscopy ion. An optional wait time can be introduced to allow for measuring the excited-state lifetime. For clock pulses which are long enough that heating of the transfer mode is not negligible any more, a small number of repetitions of the axial ground-state cooling sequence (see Figure 11.6) is repeated. Next, (b) a red sideband (RSB) π-pulse is applied with the clock laser in order to map the clock transition onto the transfer mode. Thereafter, (c) another RSB π-pulse maps the transfer mode onto the qubit transition of the $^9\mathrm{Be}^+$ logic ion with the axial Raman laser beams. Finally, (d) state detection of the $^9\mathrm{Be}^+$ qubit state is performed. The colors of the pulse sequence refer to the lasers in use and correspond to the same convention as used in other figures, for instance in Figure 11.4. See text for further details.

Doppler cooling transition could result in losing the ion in the dark qubit state, again due to polarization impurities of the Doppler cooling laser. Repumper 1 could indeed depopulate this state, but subsequent decay into the $|^2\mathrm{S}_{1/2}, F = 2, m_F = 1\rangle$ substate is possible. The latter one can be depopulated with repumper 2 again through the $^2\mathrm{P}_{1/2}$ state. Importantly, the bright qubit state is finally a dark state for both repumper lasers in which the $^9\mathrm{Be}^+$ ion is then reliably pumped[3]. Then, axial ground-state cooling with the axial Raman laser beams as discussed in Section 11.5.1 and $^{40}\mathrm{Ar}^{13+}$ state preparation as discussed in the previous section follow. The two-ion crystal is now prepared in the

$$|\Psi\rangle = |\downarrow\rangle_\mathrm{S}|0\rangle_\mathrm{m}|\downarrow\rangle_\mathrm{L} \tag{13.1}$$

product state with a fidelity of about 80 %, where the indices S and L denote the electronic states (also dubbed the *internal states*) of the clock transition of the spectroscopy ion and the qubit transition of the logic ion, respectively. $|0\rangle_\mathrm{m}$ is the motional ground state of the transfer mode. The spectroscopy sequence is shown in Figure 13.3B. The black solid straight arrows in this panel denote a successful (de-)excitation and the black dashed straight arrows an unsuccessful (de-)excitation. The upper row shows the stepwise evolution of the system for a successful initial excitation of the clock transition with a clock pulse while the lower row shows its evolution with an unsuccessful initial clock pulse. The sequence starts with (a) the clock laser π-pulse of adjustable intensity, tuned close to the carrier of the clock transition. Lower intensities correspond to longer π-times and allow for a higher spectroscopic resolution (see Section 7.2.2). This lets the quantum system evolve to

$$|\Psi\rangle = (e|\uparrow\rangle_\mathrm{S} + g|\downarrow\rangle_\mathrm{S})\,|0\rangle_\mathrm{m}|\downarrow\rangle_\mathrm{L} \tag{13.2}$$

with the amplitudes $e = e(\Delta\omega)$ and $g = g(\Delta\omega)$ depending on the clock laser detuning $\Delta\omega$, and again the normalization condition $1 = |e|^2 + |g|^2$ applies (see Section 7.2.1). During an optional wait time after this first clock laser pulse (see Figure 13.3A), the upper clock state $|\uparrow\rangle_\mathrm{S}$ can spontaneously decay which would collapse the coherent superposition. Such a variable wait time allows to measure the excited-state lifetime as will be discussed in Chapter 16. Additionally, the transfer mode can heat up during long clock pulses which would reduce the contrast of the quantum logic signal by increasing the background signal. To counteract this systematic effect, a few repetitions of the axial ground-state cooling sequence (see Figure 11.6) can be repeated. Next, (b) a RSB π-pulse is applied on the clock transition, exactly on resonance. For a successful initial clock pulse, this RSB pulse simultaneously de-excites the clock transition and excites the transfer mode. If the initial clock pulse was unsuccessful, this RSB pulse is off-resonant and does not change the quantum state of the system. This operation ideally maps the clock transition one-to-one onto the transfer mode and therefore would evolve the system to

---

[3] As discussed in Section 11.5.1, a sufficient global detuning of the repumper laser frequency difference from the splitting of the involved $^2\mathrm{S}_{1/2}$ Zeeman substates has to be chosen to avoid coherent population trapping in those two states.

$$|\Psi\rangle = |\downarrow\rangle_{\mathrm{S}} \left(e|1\rangle_{\mathrm{m}} + g|0\rangle_{\mathrm{m}}\right) |\downarrow\rangle_{\mathrm{L}} \,. \tag{13.3}$$

In practice, the fidelity of the RSB clock laser pulse is not 1 and thus reduces the contrast of the quantum logic signal which will be later detected. In particular, if the Rabi angle of this RSB pulse is not π, the system is left in an entangled state. Next, (c) a RSB π-pulse is applied with the axial Raman laser beams on the $^{9}\mathrm{Be}^{+}$ qubit transition. This analogously maps the initial amplitudes e and g onto the $^{9}\mathrm{Be}^{+}$ qubit. Thereby, the system would ideally evolve to

$$|\Psi\rangle = |\downarrow\rangle_{\mathrm{S}} |0\rangle_{\mathrm{m}} \left(e|\uparrow\rangle_{\mathrm{L}} + g|\downarrow\rangle_{\mathrm{L}}\right) . \tag{13.4}$$

Again, in practice the non-ideal fidelity of the second RSB operation further reduces the QL contrast. The mapping of the initial clock transition excitation onto the qubit is now completed and in principle constitutes a variation of the electron shelving technique. Finally, (d) the qubit state is detected as described before but by applying only the 10 MHz Doppler cooling laser tuned into resonance with the qubit transition. A dark qubit is thereby identified as a successful initial excitation of the clock transition. The duration of the sequence is about 45 ms with clock pulses of 10 ms length and additional experimental overhead (dead time of about 10 ms).

The sequence is repeated multiple times (on the order of 100) for a given set of parameters in order to evaluate the excitation probability $P_e = |e|^2$ as the ratio of the number of detected dark qubit states to the total number of repetitions of the sequence. In particular, the obtained QPN (Equation 2.1) is ruled by the number N of these repetitions. Then, a chosen parameter is changed and the excitation probability $|e|^2$ of the new set of parameters is evaluated again by conducting the number of repetitions of the sequence again. Parameter scans are performed in this way, such as a frequency scan of the clock laser across the clock transition.

Part IV

Results and discussion

Never measure anything but frequency!

— Arthur Schawlow

The fourth part of this thesis summarizes the main results, which have recently been published in Micke et al. (2020) (see the copy in Appendix P4). Chapter 14 presents Rabi spectroscopy of a particular Zeeman component of the E1-forbidden ground-state fine-structure transition of $^{40}\mathrm{Ar}^{13+}$ at 441 nm, including frequency scans with a statistical uncertainty on the hertz-level and excited state lifetime-limited coherent population transfer between two clock Zeeman substates, known as *Rabi oscillations*. Measurements of all Zeeman components of the clock transition are reported in Chapter 15. Based on these measurements, the excited-state g-factor is determined to unprecedented accuracy and an existing discrepancy between different theoretical calculations settled. This chapter is concluded with a discussion of the leading quadratic contributions to the energy splitting, namely the second-order Zeeman shift and the electric-quadrupole shift. Chapter 16 presents and discusses a quantum logic-assisted excited-state lifetime measurement which is consistent with the most accurate previous measurement performed with an EBIT.

14

Rabi spectroscopy

This thesis reports on the first coherent laser spectroscopy of a HCI, demonstrated with the setup and by applying the techniques described in Part III. All measurements presented in this chapter address the spectroscopy of Zeeman component 1 of the $^{40}\mathrm{Ar}^{13+}$ $^2\mathrm{P}_{1/2}$–$^2\mathrm{P}_{3/2}$ clock transition at 441 nm (see Figure 5.1) with the axial clock laser beam, i. e., a first-order Zeeman sensitive σ^- transition[1]. This Zeeman component (and Zeeman component 6 as well) has a magnetic field sensitivity of about 23 Hz nT^{-1}.

14.1 Frequency scans

Figure 14.1 shows the excitation probability of the $|^2\mathrm{P}_{3/2}, m_J = -3/2\rangle$ Zeeman substate as a function of the clock laser detuning with respect to the center of Zeeman component 1 and for different clock laser intensities. The different intensities correspond to different π-times ranging from 2.6 to 20 ms. The solid curves are least-square best fits of the Rabi line shapes (Equation 7.23 with scaling factor and offset) which result from the time-dependent top-hat intensity profile of the clock laser pulses. The lengths of these π-pulses determine the observed linewidths of the clock transition (see Section 7.2.2) which has a FWHM natural linewidth of about 17 Hz. No additional line broadening is observed at these levels of resolution. This confirms previous measurements of the magnetic field stability of better than 1 nT (Leopold et al., 2019) on the time scale of data acquisition, achieved by passive shielding of ac magnetic fields and active magnetic-field stabilization (see Section 11.2). The observed contrast of the spectroscopy signal is mostly limited by the excited-state lifetime for probe times of several milliseconds. The fidelity of the $^{40}\mathrm{Ar}^{13+}$ electronic state preparation and of the sideband operations contribute to the achievable contrast as well. The latter ones limit the contrast at short probe times. A maximum contrast of about 70 % could typically be achieved with

---

[1] As a result of micromotion inside the Paul trap, the motion of the $^{40}\mathrm{Ar}^{13+}$ ion is modulated with the rf trap drive frequency of $\Omega_{\mathrm{rf}} = 2\pi \times 24.1$ MHz and, therefore, the spectroscopy signal is repeated at multiples of the 24.1 MHz in the frequency domain from the actual transition frequency (see Section 6.2). The excitation probability observed for these micromotion sidebands depends on the corresponding oscillation amplitude of $^{40}\mathrm{Ar}^{13+}$ at Ω_{rf} and the micromotion order [see Section 7.2.3 and J. Keller et al. (2016, 2015) for instance]. In particular for a measurement of the absolute transition frequency, spectroscopy at the ‘micromotion carrier’ must be guaranteed. This was verified early after the observation of the first QL signal by measuring the clock transition at multiples of 24.1 MHz. The carrier is then found at the center of the symmetric line structure. This result was later confirmed by slightly changing the trap drive frequency, showing an independence of the transition frequency from it.

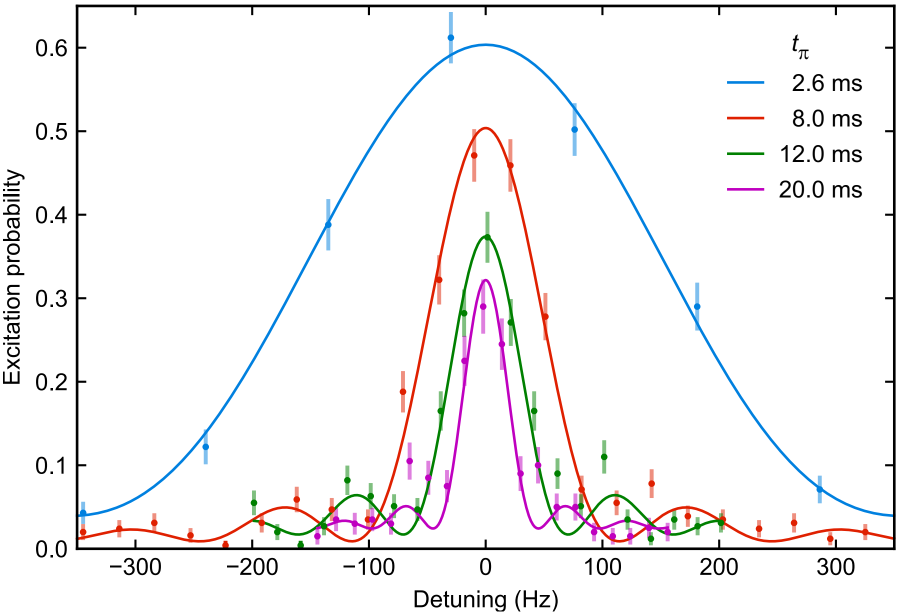

Figure 14.1: Frequency scans across Zeeman component 1 of the $^{40}\mathrm{Ar}^{13+}$ clock transition. The excitation probability of the $|^2\mathrm{P}_{3/2}, m_J = -3/2\rangle$ state is measured for various π-times t_π (color-coded) as a function of the clock laser detuning. Fourier-limited FWHM linewidths of about 307 Hz (blue), 100 Hz (red), 67 Hz (green), and 40 Hz (purple) are observed for probing with π-pulses. The solid curves are least-square best fits of the Rabi line shape. The error bars represent the QPN of 255 (blue, red, and green) and 200 (purple) measurements per data point.

π-times of 16 µs for the clock laser carrier pulse, about 200 µs for the clock laser RSB pulse, and 19 µs for the Raman laser RSB pulse.

The line center of the Zeeman component is determined with a statistical standard deviation of less than 2 Hz by the red, green, and purple fit. This corresponds to a fractional statistical uncertainty of better than 3×10^{-15} for the 680 THz clock transition obtained within an acquisition time of less than 7 min. These numbers suggest that a stability on the order of about $6 \times 10^{-14}/\sqrt{\tau/\mathrm{s}}$ can be expected, assuming white QPN as the dominant noise process. Up to recently, the state-of-the-art optical spectroscopy of HCIs was realized by emission spectroscopy with grating spectrometers installed upon EBITs. The most accurate measurement was carried out with the *Heidelberg EBIT* and measured the same transition as studied in this work (Draganić et al., 2003). In comparison, the reported coherent laser spectroscopy constitutes an improvement of the statistical uncertainty by eight orders of magnitude over that measurement. The spectroscopic resolution, expressed in terms of the FWHM linewidth, could be improved by about nine orders of magnitude, even compared to in-EBIT spectroscopy where evaporative cooling was applied in order to reduce the Doppler-broadened linewidths (Mäckel et al., 2011; Soria Orts et al., 2007). Notably, incoherent laser spectroscopy in the Penning trap *ALPHATRAP*, carried out in parallel to this work and also recently published (Egl et al., 2019), improved the uncertainty of the previous in-EBIT measurement of Draganić et al. (2003) by a factor of 24.

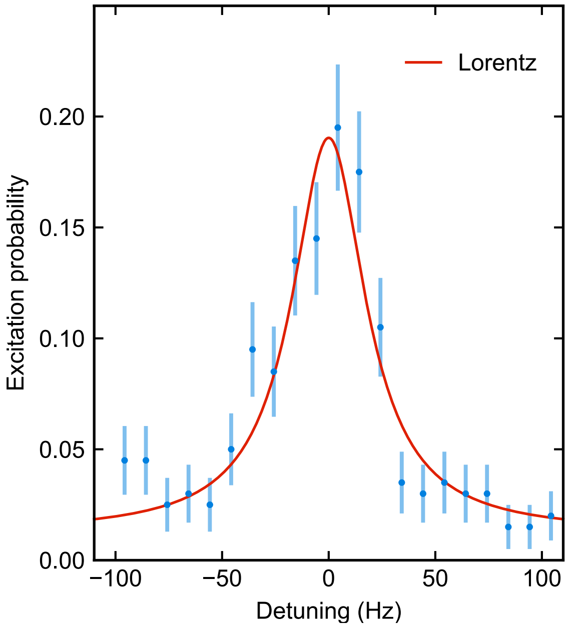

Figure 14.2: Frequency scan across Zeeman component 1 with 50 ms probe time. The residual magnetic field instability distorts the observed line (blue data points). Neither a Rabi line shape (Equation 7.23) nor a Lorentz profile (red, 42 Hz FWHM linewidth) can describe the 17 Hz-natural-linewidth transition properly at this level of resolution. The solid curve is a least-square best fit. The error bars represent the QPN of 200 measurements per data point.

The natural linewidth can in principle be resolved with the techniques demonstrated in this work and frequency scans of even longer probe times than shown in Figure 14.1. The residual magnetic field instability and the reduced excitation probability at such long probe times however impede spectroscopy with ultimate resolution. Figure 14.2 illustrates the limit of the spectroscopic resolution of this work. A typical frequency scan with pulses of 50 ms duration is shown, acquired within about 8 min (21 data points with 200 repetitions of the QL sequence per data point). The probe time is more than five times longer than the excited-state lifetime. Therefore, the line shape cannot be represented anymore by the Rabi line shape of Equation 7.23 which does not account for spontaneous emission as an important process which causes decoherence. A line shape closer to a Lorentz profile is expected at this level of resolution. However, distortions of the line profile are observed which result in many cases in asymmetric line shapes (see Figure 14.2). This can be explained by the known magnetic field fluctuations and drifts on the time scale of the data acquisition[2]. In contrast, the stability of the clock laser is far better, on a level of about 0.1 Hz at the level of the acquisition time and, essentially, does not contribute to the asymmetric line shape and broadening. The line is therefore neither well represented by a Rabi line shape (Equation 7.23) nor by a Lorentzian profile. Albeit the latter one seems to reproduce the data to some extent (see Figure 14.2), it leads to an overestimate of the instantaneous linewidth with about 42(7) Hz FWHM, which results from the aforementioned magnetic field noise during the data acquisition.

As a conclusion, this kind of Rabi spectroscopy based on simple frequency scans has its limitation at a level of about 50 Hz FWHM resolution for the present magnetic field instability and magnetic field sensitivity of the studied Zeeman component 1. The resolution could be further improved by better

---

[2] Mind that the magnetic field sensitivity of this Zeeman components is 23 Hz nT^{-1} and the magnetic field noise is on the order of 0.5–1 nT on the relevant time scale.

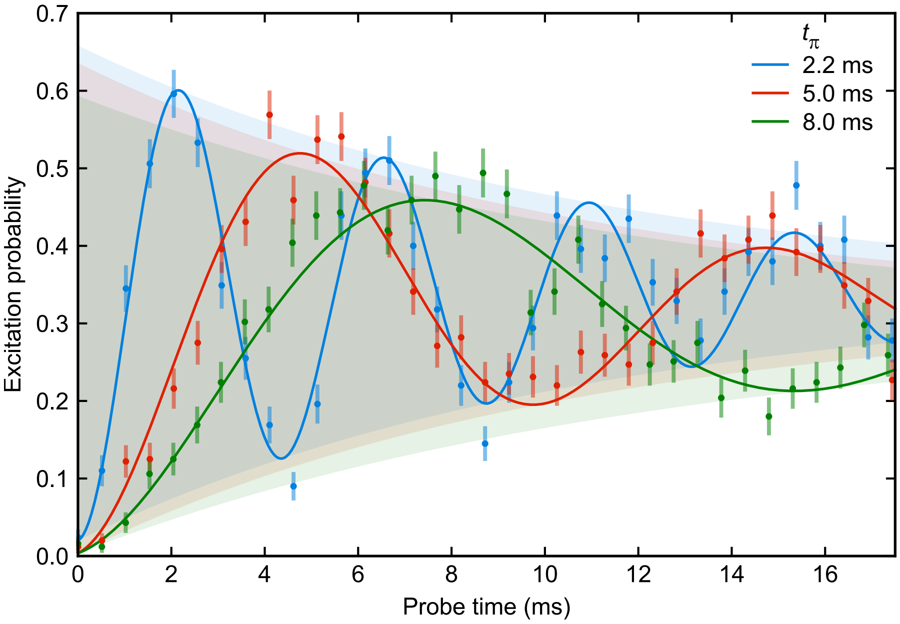

Figure 14.3: Rabi oscillations between the ^{40}Ar^{13+} clock states. The coherent population transfer between the lower and upper Zeeman substate of Zeeman component 1 of the clock transition is shown. The excitation probability of the upper $|^2\mathrm{P}_{3/2}, m_J = -3/2\rangle$ state is given as a function of the probe time for different π-times t_π (color-coded). The solid curves are least-square best fits of the oscillating signal and account for the decay of coherence with an exponential damping term and the obtained coherence times of $10.9(8)$ ms (blue), $10.6(9)$ ms (red), and $12.6(10)$ ms (green). The decay of coherence is visualized through the color-shaded exponential envelopes of the fit functions. The error bars represent the QPN of 255 measurements per data point for each curve. See text for details.

stabilization of the magnetic field and/or measuring Zeeman components of lower magnetic field sensitivity. In particular if available, magnetic field insensitive Zeeman components featuring $m = 0 \rightarrow m' = 0$ transitions are immune to first order against magnetic field noise, but are not present for the ^{40}Ar^{13+} clock transition. However, the implementation of other spectroscopy strategies such as sampling the line profile by quickly alternating between the rising and falling slope would allow to resolve the clock transition with a significantly better resolution for a given acquisition time, limited by the magnetic field noise during the alternation period. For an accurate measurement of the transition frequency, such a *two-point sampling* technique with Fourier-limited FWHM linewidths on the order of 100 Hz and corresponding π-times of about 8 ms seems favorable concluded from the measurements presented here. A robust signal with a symmetric Rabi line shape on an at least few-min time scale can be expected. A condition which is even mitigated for the inner Zeeman components 2–5 since they feature a lower magnetic field sensitivity (14 Hz nT^{-1} for components 2 and 5, 4.7 Hz nT^{-1} for components 3 and 4) resulting in a suppressed perturbation due to the residual magnetic field noise.

14.2 Rabi oscillations

Rabi oscillations between an upper and a lower Zeeman state of the clock transition are observed by scanning the probe time of the clock laser carrier pulse with a fixed clock laser frequency and intensity. Figure 14.3 shows the excitation probability of the upper $|^2\mathrm{P}_{3/2}, m_J = -3/2\rangle$ clock state of Zeeman component 1 with zero frequency detuning as a function of the probe time for different clock laser intensities, corresponding to different π-times. The solid curves represent least-square best fits (Equation 7.22 with scaling factor and offset). The color-shaded exponential envelopes of the fit functions visualize the coherence decay caused by the decay of the excited state with a lifetime of $9.573(4)_{\mathrm{stat}}(^{+12}_{-5})_{\mathrm{syst}}\,\mathrm{ms}$ (Lapierre et al., 2006). No indication of other decoherent processes is found on this timescale, neither from the clock laser nor from the magnetic field. In fact, the coherence times obtained from these fits are even slightly larger than the excited-state lifetime with values of $10.9(8)$ ms (blue), $10.6(9)$ ms (red), and $12.6(10)$ ms (green). The uncertainties, given in parentheses, are purely statistical and obtained from the fits. The fit does not account for a dephasing of the Rabi oscillations owing to an initial Fock state distribution instead of a pure state. Different Fock states show a different coupling to the light field and thus oscillate with slightly different Rabi frequencies. Therefore, these fits are not appropriate to accurately determine the excited-state lifetime. A dedicated excited-state lifetime measurement was carried out and is discussed in Chapter 16.

15 Zeeman structure

In the 160 µT magnetic quantization field, the $^{40}\mathrm{Ar}^{13+}$ $^2\mathrm{P}_{1/2}$–$^2\mathrm{P}_{3/2}$ clock transition at 441 nm splits up into six Zeeman components on a megahertz frequency scale. Figure 15.1A shows frequency scans performed with the axial clock laser beam across all six individual components (solid lines) with magnifications of the scanning ranges shown in panel B. The top axes represent the relative frequency detuning of the clock laser from the centers of the respective Zeeman components. The bottom axis in Figure 15.1B expresses the detuning from the degenerate center of the clock transition. The data was recorded with π-probe times of 5.3 to 6.0 ms and 200 measurements per data point. The solid curves represent least-square best fits of the Rabi line shapes with 130 to 150 Hz FWHM linewidths.

The upper graph of Figure 15.1C shows the reconstructed frequency shifts y_i of the $^2\mathrm{P}_{3/2}$ Zeeman substates, obtained by the relation

$$y_i\left(m_{3/2,i}\right) := \frac{\Delta E_{3/2,m_{3/2,i}}}{h} = f_i + \frac{\Delta E_{1/2,m_{1/2,i}}}{h}. \tag{15.1}$$

$\Delta E_{3/2,m_{3/2,i}}$ and $\Delta E_{1/2,m_{1/2,i}}$ are the energy shifts of the respective Zeeman substates of the $^2\mathrm{P}_{3/2}$ excited state and $^2\mathrm{P}_{1/2}$ ground state which depend on the involved magnetic quantum numbers m_J. f_i denote the measured frequency shifts of the six Zeeman components (i ranging from 1 to 6 according to the diagram in Figure 15.1D). h is the Planck constant. All shifts are referenced here to the degenerate centers of the fine-structure states or the transition[1]. The frequency shifts $\Delta E_{1/2,m_{1/2,i}}/h$ of the $^2\mathrm{P}_{1/2}$ ground state considered here are purely caused by the first-order (linear) Zeeman shift[2] (Equation 2.6) and were determined by measuring an appropriate combination of Zeeman components in order to eliminate both the magnetic field B and the ground-state g-factor $g_{1/2}$. The four inner Zeeman components 2–5, which are less sensitive to magnetic field noise than the two outer ones, are used for that purpose. As pairs, they share a common excited state ($m_{3/2} = -1/2$ for f_2 and f_3 as well as $m_{3/2} = 1/2$ for f_4 and f_5, see Figure 15.1D). Therefore, the ground-state

---

[1] A global frequency offset of the measured frequencies f_i from the degenerate center of the transition (on the order of 10 Hz) results in a global translation of the shifts of the $^2\mathrm{P}_{3/2}$ Zeeman substates. This is later accounted for by introducing an offset b in the fit functions (Equation 15.6 and Equation 15.7).

[2] The $^2\mathrm{P}_{1/2}$ state does not have an electric-quadrupole moment and therefore no electric-quadrupole shift. A second-order Zeeman shift would shift both substates equally into the same direction and not contribute to the observed Zeeman splitting.

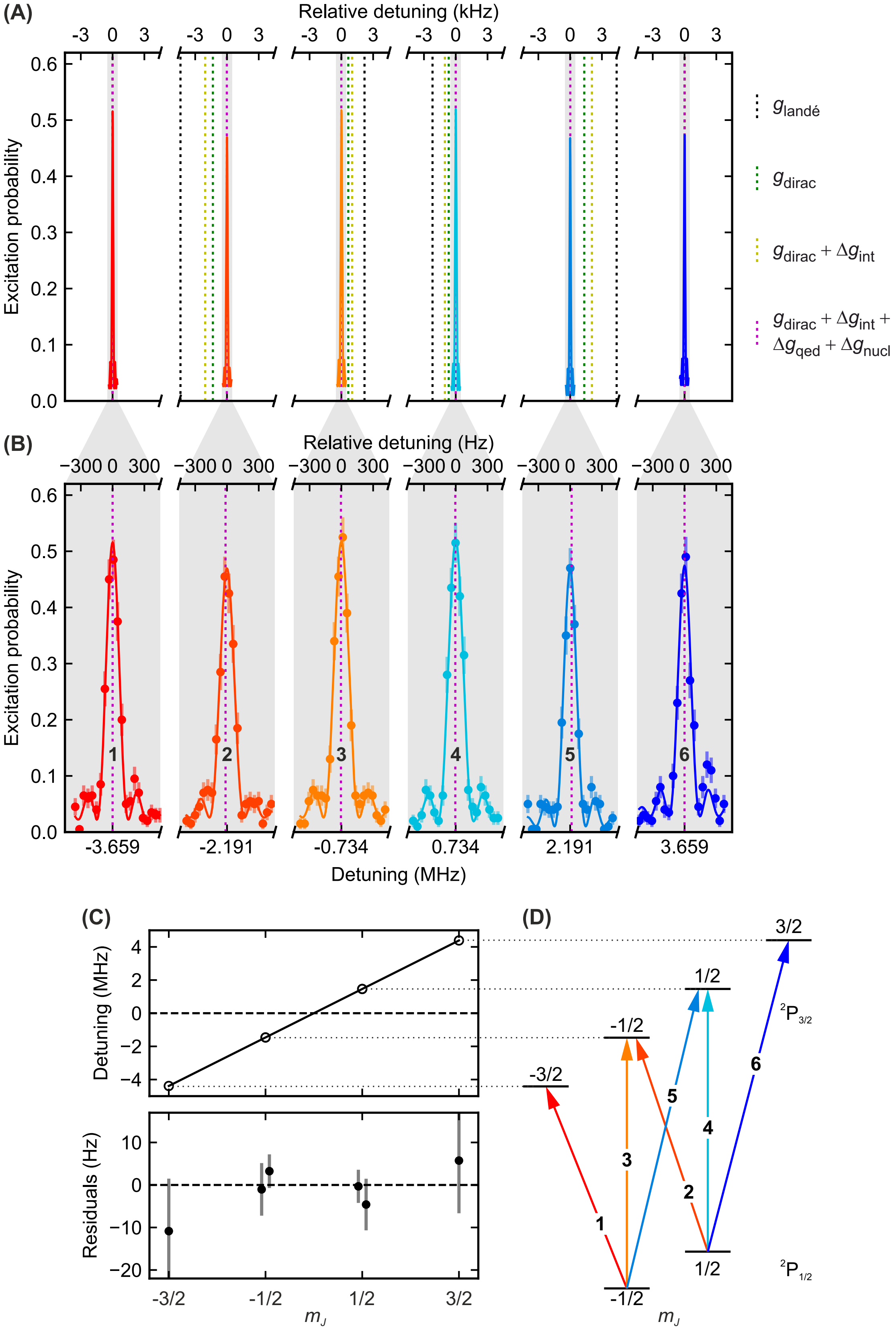

Figure 15.1: Zeeman structure of the 441 nm $^{40}\mathrm{Ar}^{13+}$ clock transition. (**A**) Excitation probability of the upper $^2\mathrm{P}_{3/2}$ state as function of the clock laser detuning. Six Zeeman components (solid curves) are observed. The dashed vertical lines visualize the predictions of the line positions based on different values of the involved g-factors (see Table 15.2). (**B**) Magnification of the scanning ranges shown in panel A. The error bars represent the QPN of 200 measurements per data point. (**C**) Reconstructed $^2\mathrm{P}_{3/2}$ state, fitted by a linear function. The error bars represent the 1 σ standard uncertainty. (**D**) $^{40}\mathrm{Ar}^{13+}$ clock transition level diagram. See text for details.

energy splitting is given by their frequency differences and does not rely on properties of the excited state. The two equivalent relations

$$B_1 = \frac{h\,(f_3 - f_2)}{g_{1/2}\,\mu_\mathrm{B}} \tag{15.2a}$$

$$B_2 = \frac{h\,(f_5 - f_4)}{g_{1/2}\,\mu_\mathrm{B}} \tag{15.2b}$$

are obtained for the magnetic field, where μ_B is the Bohr magneton, and are used to calculate an averaged magnetic field

$$B = \frac{B_1 + B_2}{2} \tag{15.3}$$

with a reduced uncertainty. For simplicity, the term

$$U = f_5 - f_4 + f_3 - f_2 \tag{15.4}$$

can be introduced. Inserting these relations into Equation 15.1 yields the excited-state frequency shifts

$$y_i\,(m_{3/2,i}) = f_i + m_{1/2,i}\,\frac{U}{2}\,, \tag{15.5}$$

which are purely based on frequency measurements of the involved Zeeman components. Six data points are generated from the six Zeeman components, where for the $m_{3/2} = \pm 1/2$ substates two data points are obtained each and are not distinguishable in the upper graph of Figure 15.1C. Details on the uncertainty propagation including a magnetic field instability of 0.5 nT can be found in the *Methods* section of Micke et al. (2020), see Appendix P4.

The first-order Zeeman shift (Equation 2.6) causes the dominant linear dependence of the excited-state frequency shifts on the magnetic quantum number $m_{3/2}$. A quadratic contribution in principle arises from the second-order Zeeman shift and the electric-quadrupole shift. However, no quadratic contribution could be measured with the Hz-level uncertainties of this measurement and the 160 µT magnetic field. A fit to the $^2\mathrm{P}_{3/2}$ Zeeman substates with a second-order polynomial

$$y_i\,(m_{3/2,i}) = a^{(2)} \cdot (m_{3/2,i})^2 + a^{(1)} \cdot m_{3/2,i} + b \tag{15.6}$$

yields a quadratic component $a^{(2)}$ which is consistent with zero (see Table 15.1). The order of magnitude of the expected quadratic contributions is discussed later in Section 15.2. A purely linear least-square best fit of the form

$$y_i\,(m_{3/2,i}) = a \cdot m_{3/2,i} + b \tag{15.7}$$

is shown in the upper graph of Figure 15.1C with its residuals in the lower graph. The data points of the $m_{3/2} = \pm 1/2$ substates are displaced for a better visibility. Note the different y-scales in both graphs of panel C.

15.1 Linear energy splitting and g-factors

The quality of the linear fit in Figure 15.1C (Equation 15.7) in combination with the finding that the quadratic term of a second-order polynomial fit (Equation 15.6) is consistent with zero proves that the energy shifts of the $^2\mathrm{P}_{3/2}$ Zeeman substates in the magnetic field of about 160 µT can be considered as purely linear within the uncertainty level of the measurements. As discussed before, we can substitute the magnetic field B in Equation 2.6 for the linear Zeeman shift with Equation 15.3 and using Equation 15.2. Then, introducing U again (Equation 15.4) yields the relation

$$y_i\left(m_{3/2,i}\right) = \frac{g_{3/2}U}{2g_{1/2}} \cdot m_{3/2,i}\,. \tag{15.8}$$

The linear fit (Equation 15.7) as shown in Figure 15.1C accounts with the offset b (on the 10 Hz level) for a global frequency offset of all measured Zeeman components[3]. The slope a of the fit and the measurement of U allows to calculate the excited-state g-factor $g_{3/2}$ as

$$g_{3/2} = \frac{2a}{U}g_{1/2} \tag{15.9}$$

with the well-known ground-state g-factor $g_{1/2}$, recently measured with a fractional uncertainty of 1.4×10^{-9} by the continuous Stern-Gerlach method in the Penning trap *ALPHATRAP* (Arapoglou et al., 2019). Note that a and U are functions of the measured frequencies f_i which feature statistical uncertainties from the individual Rabi line shape fits and systematic uncertainties due to the magnetic field instability. Details on the uncertainty analysis can be found in the *Methods* section of Micke et al. (2020), see the copy in Appendix P4, and are not repeated here.

The excited-state g-factor was evaluated as the weighted average $g_{3/2} = 1.332\,289\,5(13)_{\mathrm{stat}}(56)_{\mathrm{syst}}$ from the three individual measurement sets shown in Table 15.1, obtained on two different days[4]. The first parentheses give the statistical uncertainties and the second ones the systematic uncertainties. The statistical uncertainties of the individual measurements were combined for the statistical uncertainty of the average and the largest systematic uncertainty stated as a conservative estimate for the systematic uncertainty of the average. The uncertainties of $g_{3/2}$ are dominated in all cases by the systematic uncertainties resulting from the magnetic field instability [see the *Methods* section of Micke et al. (2020) in Appendix P4 for details]. Drifts or noise of the rf drive frequency of the AOM which is used to address the Zeeman components and to accomplish the frequency scanning are negligible since the rf drive is referenced to the maser-stabilized and SI second-referenced 10 MHz frequency reference of PTB. The experimental results are shown in Figure 15.2 in blue together with recent calculations shown in red. The blue horizontal line represents the experimental average with its 1 σ uncertainty band. The error

---

[3] Therefore, b does not further affect the evaluation presented below.

[4] Figure 15.1 shows the second measurement set.

#	$g_{3/2}$	σ_B/B	$a^{(2)}$ (Hz)
1	$1.332\,298\,9(19)_{\mathrm{stat}}(56)_{\mathrm{syst}}$	4.1×10^{-6}	$-2.5(57)$
2	$1.332\,289\,7(23)_{\mathrm{stat}}(43)_{\mathrm{syst}}$	3.2×10^{-6}	$-1.4(45)$
3	$1.332\,282\,8(24)_{\mathrm{stat}}(43)_{\mathrm{syst}}$	3.2×10^{-6}	$0.7(45)$
Average	$1.332\,289\,5(13)_{\mathrm{stat}}(56)_{\mathrm{syst}}$		

Table 15.1: Measurements of the ^{40}Ar^{13+} excited-state *g*-factor. The three measurement sets of the ^{2}P$_{1/2}$–^{2}P$_{3/2}$ ^{40}Ar^{13+} Zeeman structure are summarized. The second column shows the evaluated excited-state g-factors $g_{3/2}$. The third and fourth columns show the estimated magnetic field instabilities during the measurements and the evaluated quadratic terms in the fits of the ^{2}P$_{3/2}$ Zeeman substate-frequency shifts with a second-order polynomial (Equation 15.6). The parentheses show the statistical and systematic uncertainties separately for the g-factor. The last row shows the weighted average of the excited-state g-factor for which the statistical uncertainties of the individual measurements were combined and the systematic uncertainty conservatively estimated as the largest one of the individual measurements.

bars of the individual measurements are the root of the sum of the squared statistical and systematic uncertainties. All individual measurements are in agreement within their uncertainty level. Measurement 1 and the weighted average show the largest deviation of $1.6\,\sigma$.

The $g_{3/2}$ measurement of this work is an improvement by a factor of 351 over the previously best measurement of $g_{3/2} = 1.333(2)$ (Soria Orts et al., 2007) carried out at the *Heidelberg EBIT* through emission spectroscopy and an improvement by a factor of 26 over the recently published Penning trap measurement of $g_{3/2} = 1.332\,14(15)$ (Egl et al., 2019), which was performed through laser spectroscopy of the two Zeeman components 2 and 5 in parallel to this work[5]. The latter measurement lies outside the range which is shown in Figure 15.2, but it is with about $1\,\sigma$ deviation of its larger uncertainty level consistent with the measurement of this work.

The measurements presented here also settle a persisting discrepancy between previous theoretical predictions for $g_{3/2}$, confirming the work of the Saint Petersburg group, in particular the configuration-interaction calculations of Agababaev et al. (2019), Glazov et al. (2013), and Shchepetnov et al. (2015) and recent coupled-cluster calculations of Maison, Skripnikov, and Glazov (2019). In contrast, the deviations to the calculations of Verdebout et al. (2014) and Marques et al. (2016)[6] are significantly larger than the involved uncertainties and suggest that these predictions for the excited-state g-factor miss a small contribution in their calculations or significantly underestimate their uncertainties. The aforementioned recent Penning trap measurement of the ground-state g-factor by Arapoglou et al. (2019) also confirmed the

---

[5] Note that both previous measurements were performed in a much stronger magnetic field of about 6.8 and 4 T. The second-order Zeeman shift is therefore not negligible anymore for the uncertainty level of the Penning trap measurement, resulting in a shift on the MHz-level.

[6] Verdebout et al. (2014) used a multireference configuration interaction approach and Marques et al. (2016) employed the multiconfiguration Dirac-Fock method.

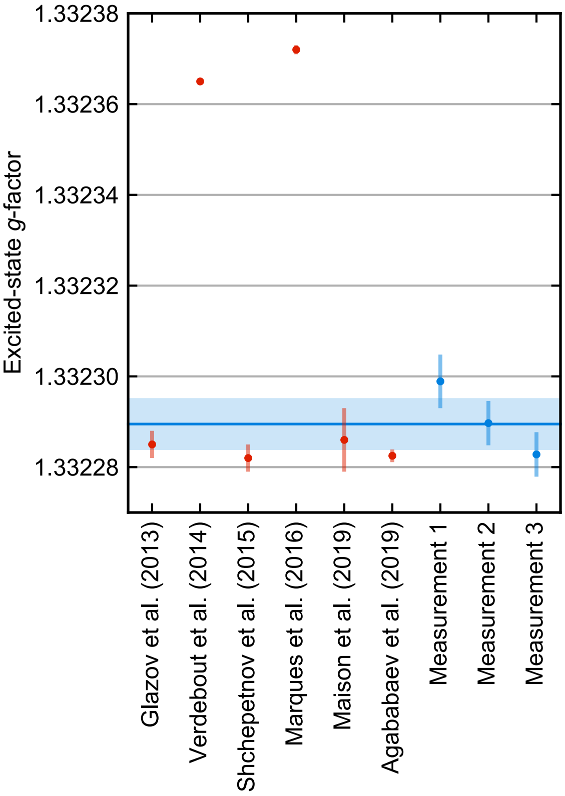

Figure 15.2: Excited-state *g*-factor. Theoretical predictions (red) and the measurements of this work (blue) are compared. The error bars represent the 1σ standard uncertainty. The blue horizontal line is the weighted average of the three measurements with its combined 1σ uncertainty band, dominated by the conservative estimate of the systematic uncertainty of measurement 1. The error bar of Marques et al. (2016) is of the size of the data point. Verdebout et al. (2014) does not provide an uncertainty. See text for further details.

calculations of the Saint Petersburg group. However, a measurement of the excited-state g-factor with a comparable uncertainty to the calculations was still pending. A measurement through the atomic magnetic moment as done for the ground-state g-factor is basically prevented by the excited-state lifetime of only 9.6 ms which is orders of magnitude shorter than typical measurement times in the Penning trap.

The $^{40}\mathrm{Ar}^{13+}$ g-factors $g_{1/2}$ and $g_{3/2}$ of the ground and excited state can each be described as the sum

$$g = g_{\mathrm{dirac}} + \Delta g_{\mathrm{int}} + \Delta g_{\mathrm{qed}} + \Delta g_{\mathrm{nucl}}\,, \tag{15.10}$$

where g_{dirac} describes the leading contribution obtained from solving the relativistic Dirac equation with a point-like nucleus [see Agababaev et al. (2018, 2019) and references therein for details]. Then, further corrections have to be included in order to obtain the state-of-the-art accuracy level for the theoretical prediction. The term Δg_{int} describes the interelectronic interactions and is calculated within perturbation theory in orders of $1/Z$. The first-order term can be calculated in a rigorous QED approach to all orders in αZ. The second-order term is calculated within the Breit approximation. Higher-order corrections are accounted for by an effective screening potential. Therefore, Δg_{int} already includes QED contributions. Δg_{qed} accounts for the one-loop (self-energy and vacuum polarization) and two-loop QED contributions[7]. Δg_{nucl} addresses the

---

[7] The magnitude of the vacuum polarization term is much smaller than the total theoretical uncertainty and also the two-loop QED contribution is either on a comparable level (ground state) or smaller than the total theoretical uncertainty.

	$g_{1/2}$	$g_{3/2}$
$g_{\text{landé}}$	$2/3$	$4/3$
g_{dirac}	0.663775447	1.331030389
Δg_{int}	$0.0006506(7)$	$0.0004787(6)$
Δg_{qed}	$-0.0007681(9)$	$0.0007783(12)$
Δg_{nucl}	$-0.0000091(2)$	$-0.0000049(4)$
Total g	$0.6636488(12)$	$1.3322825(14)$

Table 15.2: Theoretical predictions of the ^{40}Ar^{13+} g-factors and the various correction terms. The non-relativistic Landé g-factors $g_{\text{landé}}$ are calculated by Equation 5.1. The relativistic g-factors g_{dirac} can be calculated analytically (Agababaev et al., 2018) and were extracted with their various correction terms from the references Agababaev et al. (2018) for the $^2P_{1/2}$ ground state and Agababaev et al. (2019) for the $^2P_{3/2}$ excited state. The uncertainties are given in parentheses.

nuclear contribution which is significantly smaller than the interelectronic-interaction and QED contributions. This term is completely dominated by the nuclear recoil effect for ^{40}Ar^{13+} and a contribution from the nuclear size is negligible on this uncertainty level. Although small, the nuclear recoil contributes to $g_{1/2}$ and $g_{3/2}$ on a level of 10^{-5} and a few 10^{-6} (Glazov et al., 2018; Maison, Skripnikov, and Glazov, 2019; Malyshev et al., 2020), respectively, and cannot be neglected at this uncertainty level. The predicted magnitudes for the various terms of the $^2P_{1/2}$ ground state and $^2P_{3/2}$ excited state are summarized in Table 15.2 based on the calculations of Agababaev et al. (2018, 2019)[8]. In contrast, the non-relativistic Landé g-factors are calculated with Equation 5.1.

The various contributions of the g-factors shown in Table 15.2 can be used to predict the positions of the Zeeman components in a given magnetic field B. This illustrates in particular the sensitivity of a HCI such as ^{40}Ar^{13+} to the underlying physics in view of the uncertainty level of this experiment. These predictions are shown in Figure 15.1A and B as vertical dashed lines, where the outer Zeeman components were used to calibrate the magnetic field, i. e., the measured and predicted outer Zeeman components deliberately coincide. The use of the non-relativistic Landé g-factors for ground and excited state predict the positions given by the black vertical dashed lines. This results in a deviation of about 30 (15) Fourier-limited FWHM linewidths for the Zeeman components 2 and 5 (3 and 4). The use of the relativistic Dirac values of the g-factors without further corrections yield the green vertical lines. When including the interelectronic-interaction corrections the yellow vertical lines are obtained which deteriorate the predictions. With all corrections given in Table 15.2 the purple lines are obtained and agree well with the measured positions of all Zeeman components (see Figure 15.1B). The difference between including the nuclear contributions Δg_{nucl} or not is on the order of the width of the purple dashed lines in Figure 15.1B and corresponds to 12 Hz (6 Hz) for the Zeeman components 2 and 5 (3 and 4). Thereby, their magnitude is comparable with the experimental uncertainty and the nuclear contributions are not negligible. This is particularly important for future improvements of the experimental uncertainty.

---

[8] Independent calculations of $g_{1/2}$ are also published by Arapoglou et al. (2019) with about half of the uncertainty level stated by Agababaev et al. (2018). However, the latter one was chosen for the discussion here to compare g-factors which are calculated with exactly the same methods.

The measurements of this thesis and the recent laser spectroscopy in a Penning trap by Egl et al. (2019) resolve for the first time the relativistic, interelectronic-interaction, and QED contributions to an HCI excited-state g-factor. Additionally, the experiment of this work will be sensitive enough to properly resolve the nuclear contributions after implementing the *two-point sampling* technique which should significantly reduce the systematic uncertainty, which is the current limitation, and the statistical uncertainty as well. Furthermore, the experiment could in principle run at a ten-times larger magnetic field[9] of 1.6 mT. This would further reduce the uncertainty of the excited-state g-factor measurement by approximately one order of magnitude. The current fractional uncertainty of the excited-state g-factor of 4.3×10^{-6} might therefore be improvable by one to two orders of magnitude as a conservative estimate. This would then be significantly more accurate than the most accurate calculations and only two orders of magnitude less accurate than the ground-state g-factor measurement of *ALPHATRAP* with a fractional uncertainty of 1.4×10^{-9} (Arapoglou et al., 2019). Notably, a quadratic contribution to the energy shifts of the Zeeman substates has to be reconsidered then.

15.2 Quadratic contribution to the energy splitting

A quadratic contribution to the energy shifts of the Zeeman substates is not observed in the reported measurements. The quadratic term in a fit with a second-order polynomial of the from given in Equation 15.6 is consistent with zero for all three measurements (see Table 15.1). This section compares this experimental finding with the expected orders of magnitude of the leading quadratic contributions, namely the second-order Zeeman shift and the electric-quadrupole shift.

---

[9] If the fractional magnetic-field stability cannot be improved at the same time by about one order of magnitude, longer averaging of the Zeeman components is required. At even larger magnetic fields than about 1.6 mT, the addressing of the Zeeman substates, not only of $^{40}\mathrm{Ar}^{13+}$ but also $^{9}\mathrm{Be}^{+}$, requires larger frequency leaps and the replacement of several AOMs in the experiment.

15.2.1 Second-order Zeeman shift

The energy shifts of the Zeeman substates of the $^2\mathrm{P}_{3/2}$ excited state due to the second-order Zeeman effect include one term which adds an energy offset independent of the magnetic quantum number m_J and one term which depends quadratically on m_J (see Equation 2.7). The total shift can be conveniently expressed as

$$\Delta E^{(2)}_{J,m_J} = g^{(2)}_J(m_J)\,\frac{(\mu_\mathrm{B}B)^2}{m_\mathrm{e}c^2}\,, \tag{15.11}$$

where the symmetry relation $g^{(2)}_J(-m_J) = g^{(2)}_J(m_J)$ applies [see Agababaev et al. (2017), Glazov et al. (2013), D. v. Lindenfels et al. (2013), D.-F. F. v. Lindenfels (2015), and Varentsova et al. (2018) for details]. The coefficients $g^{(2)}_J(m_J)$ depend on m_J and account for both the energy offset and the term which is quadratic in m_J. They are calculated within perturbation theory. m_e an c are the electron mass and the vacuum speed of light. In contrast to the $^2\mathrm{P}_{3/2}$ excited state, the energy splitting of both $^2\mathrm{P}_{1/2}$ Zeeman substates is not affected by the second-order Zeeman shift since both substates shift by the same amount into the same direction. However, their shift contributes to the total $^2\mathrm{P}_{1/2}$–$^2\mathrm{P}_{3/2}$ transition energy as does the second-order Zeeman shift of the $^2\mathrm{P}_{3/2}$ state.

Table 15.3 summarizes the calculated $g^{(2)}_J(m_J)$ coefficients for the $^2\mathrm{P}_{1/2}$–$^2\mathrm{P}_{3/2}$ transition in $^{40}\mathrm{Ar}^{13+}$ as reported by D.-F. F. v. Lindenfels (2015). The last column calculates the expected second-order Zeeman shifts for the different Zeeman substates and the 160 µT magnetic quantization field of this experiment with Equation 15.11 and based on these coefficients. The uncertainties of the shifts are completely dominated by the theoretical uncertainties of the $g^{(2)}_J(m_J)$ coefficients. The shifts are three orders of magnitude smaller than the uncertainty level of the measurements presented in this work and are therefore negligible. No quadratic energy splitting due to the second-order Zeeman shift could be expected to be observed. For the future evaluation of the total transition energy, these results imply an expected maximum fractional second-order Zeeman shift of $4.828(13)\times10^{-18}$ between the substates $|^2\mathrm{P}_{1/2}, m_J = \pm1/2\rangle$ and $|^2\mathrm{P}_{3/2}, m_J = \pm1/2\rangle$ (Zeeman components 2-5). The uncertainty of this shift is on the 1.3×10^{-20} level. The Zeeman components 1 and 6 feature an even lower second-order Zeeman shift with a lower corresponding uncertainty. A second-order Zeeman shift resulting from ac magnetic fields, e. g., the rf trap drive or power line noise is negligible owing to the much lower magnetic flux densities involved and the high suppression of external ac magnetic fields as discussed in Section 11.2.

The calculated second-order Zeeman shift (uncertainty) compares favorably to the most accurate single-ion optical clocks, being more than two orders of magnitude (more than one order of magnitude) smaller than for the $^{27}\mathrm{Al}^+$ ion clock operated at NIST (Brewer et al., 2019) and about one order of magnitude (more than one order of magnitude) smaller than for the $^{171}\mathrm{Yb}^+$-1 ion clock operated at PTB (Huntemann et al., 2016). Note that this shift would quickly

State	$g_J^{(2)}(m_J)$	2^{nd}-order Zeeman shift (mHz)
$\lvert {}^2\mathrm{P}_{1/2}, m_J = \pm 1/2\rangle$	$-39.66(15) \times 10^3$	$-1.6097(61)$
$\lvert {}^2\mathrm{P}_{3/2}, m_J = \pm 1/2\rangle$	$41.20(15) \times 10^3$	$1.6722(61)$
$\lvert {}^2\mathrm{P}_{3/2}, m_J = \pm 3/2\rangle$	$1.007(15) \times 10^3$	$0.04087(61)$

Table 15.3: Second-order Zeeman shifts for the Zeeman substates of the $^{40}\mathrm{Ar}^{13+}$ clock transition. The calculated second-order Zeeman shift coefficients $g_J^{(2)}(m_J)$ are given in the second column according to D.-F. F. v. Lindenfels (2015). The third column shows the corresponding shift in the magnetic field of 160 µT. The uncertainties of the shifts (given in parentheses) are completely dominated by the uncertainties of the $g_J^{(2)}$ coefficients (also in parentheses).

increase when the experiment is operated at a larger magnetic quantization field owing to the quadratic dependence on B. For instance, for a magnetic flux density of about 560 µT, the second-order Zeeman shift would be on the same level as the electric-quadrupole shift (discussed in the next section) for Zeeman components 3 and 4 of the $^{40}\mathrm{Ar}^{13+}$ clock transition.

15.2.2 Electric-quadrupole shift

The electric-quadrupole energy shift arises from the electric-quadrupole moment of the corresponding electronic state coupling to an electric-field gradient present at the position of the ion in the linear Paul trap. However, only electronic states with total angular momentum quantum numbers J or $F \geq 1$ possess electric-quadrupole moments in the absence of state mixing. Therefore, the electric-quadrupole moment of the $^2\mathrm{P}_{1/2}$ ground state of $^{40}\mathrm{Ar}^{13+}$ is negligible. The electric-quadrupole moment of the $^2\mathrm{P}_{3/2}$ excited state was estimated to be about $\Theta \approx 2.4 \times 10^{-2}\, e a_0^2$ (Müller, 2019) with the elementary charge e and the Bohr radius a_0. This value is inherently small owing to the low polarizability of $^{40}\mathrm{Ar}^{13+}$ caused by the high charge state—it is by a factor of about 100 smaller than the most electric-quadrupole moments of clock states of singly charged atoms and it is on a comparable level as for the $^2\mathrm{F}_{7/2}$ excited state of the E3 clock transition in $^{171}\mathrm{Yb}^+$. The value of $\Theta \approx 2.4 \times 10^{-2}\, e a_0^2$ corresponds to a reduced matrix element of the electric-quadrupole operator $\widehat{Q}$ of approximately[10] $\langle \xi, J = 3/2 || \widehat{Q} || \xi, J = 3/2 \rangle \approx 10^{-1}\, e a_0^2$. Based on this value, Equation 2.4 yields the electric-quadrupole shifts shown in Table 15.4 for an estimated electric-field gradient of $\partial \mathcal{E}_z / \partial z = 8.33 \times 10^6\,\mathrm{V\,m^{-2}}$ [which is a typical value, see for instance Itano (2000)] and the angle $\beta = 30°$ between the Paul trap principal axis z and the quantization axis z'. The frequency shifts of the excited Zeeman substates of about $\pm 40\,\mathrm{mHz}$ imply expected fractional frequency shifts of about 6×10^{-17} for the total transition energies of the individual Zeeman components. This estimate points out that the electric-quadrupole shifts are more than one order of magnitude larger than

---

[10] Care must be taken here since different definitions used to calculate the reduced matrix element can lead to deviations by a factor of $\sqrt{2J+1} = 2$.

State	Electric-quadrupole shift (mHz)
$\vert{}^2\mathrm{P}_{1/2}, m_J = \pm 1/2\rangle$	0
$\vert{}^2\mathrm{P}_{3/2}, m_J = \pm 1/2\rangle$	40
$\vert{}^2\mathrm{P}_{3/2}, m_J = \pm 3/2\rangle$	−40

Table 15.4: Electric-quadrupole shifts for the Zeeman substates of the $^{40}\mathrm{Ar}^{13+}$ clock transition. The $^2\mathrm{P}_{1/2}$ state does not possess an electric-quadrupole moment and therefore experiences no shift. The shifts for the $^2\mathrm{P}_{3/2}$ Zeeman substates were calculated with Equation 2.4 with $\langle \xi, J \| \widehat{Q} \| \xi, J \rangle \approx 10^{-1}\, e a_0^2$, $\partial \mathcal{E}_z / \partial z = 8.33 \times 10^6\,\mathrm{V\,m^{-2}}$, and $\beta = 30°$ and should give the right order of magnitude. See text for further details.

the second-order Zeeman shifts in the magnetic field of 160 µT, but still about seven to eight orders of magnitude smaller than the linear Zeeman shifts. Notably, the term in the square brackets of the numerator in Equation 2.4

$$G(m_J, J) = 3 m_J^2 - J(J+1) \tag{15.12}$$

yields for $m_J = \pm 1/2$ and $m_J = \pm 3/2$ exactly the same modulus with inverted sign (see also Table 15.4),

$$G\left(\pm\frac{1}{2}, \frac{3}{2}\right) = -G\left(\pm\frac{3}{2}, \frac{3}{2}\right). \tag{15.13}$$

This fact allows to completely cancel the electric-quadrupole shift for the measurement of the total transition energy by averaging an appropriate set of Zeeman components addressing the $\vert{}^2\mathrm{P}_{3/2}, m_J = \pm 1/2\rangle$ and $\vert{}^2\mathrm{P}_{3/2}, m_J = \pm 3/2\rangle$ states. For instance, averaging of the outer Zeeman components 1 and 6 together with the innermost Zeeman components 3 and 4, which correspond to the π-transitions, allows to cancel the linear Zeeman shift together with the electric-quadrupole shift. Although the Zeeman components 2 and 5 could be used instead of 3 and 4, the latter choice has the benefit that these Zeeman components are less sensitive to magnetic field noise and offer larger squared Clebsch-Gordan coefficients. This causes the excited Zeeman states to spontaneously decay preferably into the same Zeeman ground-state from which the ion was excited and eases electronic state preparation of $^{40}\mathrm{Ar}^{13+}$. The averaging can be accomplished through the *two-point sampling* technique in a closed-loop operation. Above that, this method would allow to measure the electric-quadrupole moment of the $^2\mathrm{P}_{3/2}$ state from the quadratic energy shifts of the Zeeman substates with long averaging times so that the residual frequency instability allows to resolve these small shifts. In post-processing the predicted second-order Zeeman shifts as shown in Table 15.3 can be subtracted and then the reduced matrix element of the electric-quadrupole operator calculated by Equation 2.4 from which the electric-quadrupole moment can be obtained.[11]

---

[11] The theory publication Y.-m. Yu and Sahoo (2019) predicts an expected electric-quadrupole shift for the Ar^{13+} $^2\mathrm{P}_{3/2}$ state on a level of 0.1–10 Hz for electric-field gradients of the order

---

of $10^8\ \mathrm{V\,m^{-2}}$. Scaled to a typical value of $10^7\ \mathrm{V\,m^{-2}}$, the reported shift has a comparable order of magnitude as the estimate from this thesis. However, it is not clear how the corresponding quantity Θ for the electric-quadrupole moment given in Table IV of this publication links to the corresponding conclusion and shift stated in the text. The publication also predicts a fractional second-order Zeeman shift of below 10^{-20} for 'typical' magnetic fields of 10^{-8} T. Such low magnetic flux densities can only be achieved in shielded experiments since they were much lower than the Earth's magnetic field of about 5×10^{-5} T. Possibly, this number does refer to additional ac magnetic fields (but is not explicitly mentioned).

16 Excited-state lifetime

The observation of Rabi oscillation as shown in Chapter 14 represents an indirect method of estimating the excited-state lifetime through the decay of coherence, when all other decohering processes can be assumed to be negligible. This is indeed the case for these measurements. However, the scattering of the evaluated coherence times for different Rabi frequencies indicates a limitation of this method. The reason could be a dephasing of the Rabi oscillations when instead of a pure Fock state an initial Fock state distribution is present. The different Fock states are then driven with slightly different Rabi frequencies and the simple fit function (Equation 7.22) cannot sufficiently describe the evolution of the excitation probability for long probe times. Therefore, a direct measurement of the excited-state lifetime was performed by introducing a dedicated wait time into the QL sequence between the clock laser carrier pulse and the first RSB transfer pulse (see Figure 13.3) during which the excited state can decay through spontaneous emission. At the end of this wait time the remaining excitation probability $P_{\mathrm{e}}(t)$ of the $^{40}\mathrm{Ar}^{13+}$ $^{2}\mathrm{P}_{3/2}$ excited state was measured. Figure 16.1 shows the excitation probability as a function of the wait time t.

The direct lifetime measurement was carried out through the spectroscopy of Zeeman component 1 with the axial clock laser beam. The clock laser carrier π-pulse was applied with maximum laser intensity and populated the $|^{2}\mathrm{P}_{3/2}, m_J = -3/2\rangle$ excited Zeeman substate within a π-time of $t_\pi = 16\,\mu\mathrm{s}$. Series of ground-state-cooling pulses on both axial motional modes were applied every millisecond during the wait time. This counteracts ion heating (see Section 11.5.1) and keeps the axial modes in their QHO ground state with residual mean occupation numbers independent of the 1 ms-incremented wait time. After the wait time, the QL transfer protocol was carried out and completed with the $^{9}\mathrm{Be}^{+}$ qubit detection. The acquired data comprises a total number of 44 000 realizations of the QL sequence carried out through 440 individual measurements with 100 realizations each. In these 440 individual measurements, the excitation probability was measured for 40 different wait times and each wait time was thereby realized in 11 measurements. The individual measurements were arranged in a pseudo-random sequence in order to cancel effects from drifting experimental parameters. The 11 measurements for each wait time where averaged in order to visualize the data presented in Figure 16.1. Correspondingly, the error bars represent the QPN of 1100 QL sequences per wait time. The total measurement time was about two hours.

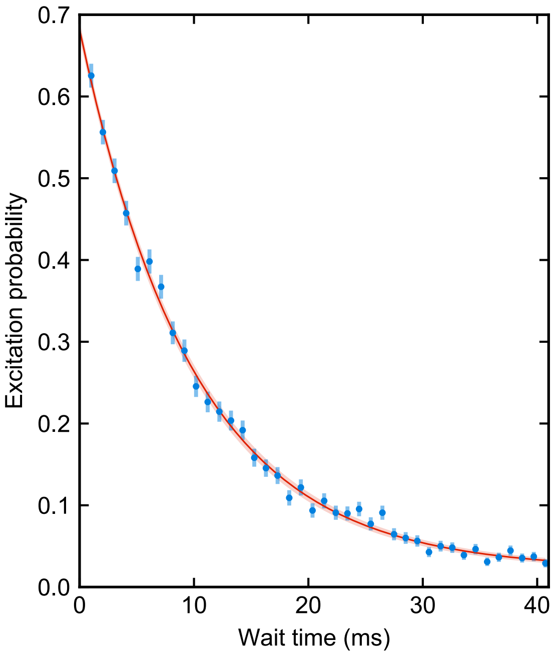

Figure 16.1: Excited-state lifetime measurement. The excitation probability of the $|^2\mathrm{P}_{3/2}, m_J = -3/2\rangle$ state is measured (blue) through QLS of Zeeman component 1 as a function of a wait time introduced into the QL sequence (see Figure 13.3). The error bars represent the QPN of 1100 measurements per data point. The red curve shows the result of a maximum likelihood estimate of the exponential decay with a lifetime of 9.97(27) ms. The narrow red-shaded area represents the $1\,\sigma$ uncertainty band of the estimate. See text for further details.

The observed exponential decay was analyzed with a three-parameter maximum likelihood estimate based on the function

$$P_\mathrm{e}(t) = a\mathrm{e}^{-\frac{t}{\tau}} + b. \tag{16.1}$$

For this purpose, the data were not averaged as described before, but the raw data of the 440 individual measurements directly processed. The maximum likelihood estimate yields the parameters given by Table 16.1 where τ is the $^2\mathrm{P}_{3/2}$ excited-state lifetime. The result of $\tau = 9.97(27)$ ms is about $1.5\,\sigma$ larger than the most accurate measurement of $9.573(4)_\mathrm{stat}(^{+12}_{-5})_\mathrm{syst}$ ms (Lapierre et al., 2006) and $1\,\sigma$ larger than the measurement of 9.70(15) ms (Träbert et al., 2000), both carried out through in-EBIT emission spectroscopy with the *Heidelberg EBIT* and *EBIT-2* at the Lawrence Livermore National Laboratory, respectively[1]. This result is also about $1.5\,\sigma$ larger than the most advanced calculations of 9.538(2) ms (Tupitsyn et al., 2005) and 9.5354(20) ms (Bilal et al., 2018). With regard to the involved uncertainties, the result of this work must be considered consistent with the aforementioned in-EBIT measurements and calculations.

In the following, systematic effects and their impact on the excited-state lifetime measurement are discussed. These include a drift of the magnetic field which was identified as the leading limitation for a more accurate measurement of the Zeeman structure as discussed in the last Chapter 15. A drifting magnetic

---

[1] Other measurements of the $^2\mathrm{P}_{3/2}$ excited-state lifetime were performed as well, summarized and discussed by, for instance, Brewer (2012) in figure 7.8. All of them measure shorter lifetimes and some of them are in mild disagreement with the aforementioned in-EBIT measurements and calculations as well as in severe disagreement with the result of this work. This might suggest an underestimate of their systematic uncertainties.

Parameter	Value
τ	$9.97(27)$ ms
a	$0.660(10)$
b	$0.0214(28)$

Table 16.1: Excited-state decay parameters. The table summarizes the parameters of Equation 16.1, estimated by the maximum likelihood method. τ is the excited-state lifetime, a is the initial contrast, and b represents the background signal. The uncertainties are given in parentheses.

field would shift the measured Zeeman component and lead to a drift of the contrast of the excitation probability. Correspondingly, this would result in a drift of the parameters a and b in Equation 16.1, the latter one through a change of the state preparation fidelity. The longer the total measurement time the more severe is such a drift. However, the effect is highly mitigated by the short π-times of $t_\pi = 16\,\mu\text{s}$ for the clock laser carrier pulse and $t_\pi = 225\,\mu\text{s}$ for the clock laser RSB pulse, leading to Fourier-limited FWHM linewidths of 50 kHz and 3.6 kHz, respectively. The typical short-term magnetic field drifts of this experiment lead to frequency shifts on the 10 Hz level and thus affect the measured excitation probability by less than 10^{-4}. Similarly, also drifts of the dc trapping voltages have to be considered as sources for systematic effects. Such drifts typically result in a shift of the axial trap frequency of below 100 Hz over the course of one day and therefore affect the excitation probability on a similar level for the two hours of total measurement time. Eventually, the pseudo-random measurement concept further mitigates the effect of systematic drifts. Additionally, the distribution of the data points is consistent with the expected QPN and rules out systematic drifts at the level of the statistical uncertainty. Another systematic effect could arise from residual clock laser light to which $^{40}\text{Ar}^{13+}$ would be exposed during the wait time. The clock laser pulses are generated by the first diffraction order of an AOM. An extinction of about 100 dB of the rf drive power is provided by an active rf switch. Although the optical extinction is on a lower level owing to scattered light within the AOM crystal, this scattered light is not frequency-shifted by the AOM and, therefore, off-resonant by the rf drive frequency of about 200 MHz. Thus, excitation by the unshifted scattered light is negligible. A severe systematic effect could be caused by spontaneous decay of $^{40}\text{Ar}^{13+}$ on the RSB which would be falsely detected as a persisting excitation of the $^2\text{P}_{3/2}$ state through the QL detection for long wait times. This effect would particularly bias the evaluated excited-state lifetime to a larger value and needs to be canceled. Anyhow, the RSB decay is suppressed by the square of the Lamb–Dicke parameter (see Section 7.2.3), $\eta^2 \approx 0.01$. The residual fraction of the RSB decays results in ion heating during the wait time, in particular also of the QL transfer mode. This is counteracted by the aforementioned ground-state-cooling pulses applied every millisecond during the wait time and just before the QL transfer protocol is carried out. As a result, the transfer mode is returned back into the QHO ground state, which should prevent a systematic bias of the measurement to longer lifetimes. The spontaneous decay probability of the residual excited-state population on the RSB during the first transfer pulse is of the order of 10^{-4} and independent of the wait time. Above that, off-resonant depumping of the $^2P_{3/2}$ state of $^{40}\mathrm{Ar}^{13+}$ during the wait time by the $^9\mathrm{Be}^+$ lasers is negligible owing to the narrow natural linewidth of the clock transition and the large corresponding detunings. Collision-induced decays as discussed by Barton et al. (2000) and Letchumanan et al. (2005) are also negligible owing to the low residual particle density in the XHV of the cryogenic environment and the fact that a collision would result in the loss of $^{40}\mathrm{Ar}^{13+}$ and immediately noticed. Note that an accurate measurement of the total wait time is crucial. A mere calculation of it by the numbers involved in the QL sequence could highly over- or underestimate the actual wait time, in particular since the exact duration of the ground-state-cooling pulses might not be accurately known and a deviation from the real value adds up for long wait times.

Based on this discussion, some possible improvements of the excited-state lifetime measurement can be identified. The magnetic field sensitivity of the measurement could be reduced by performing the measurement using Zeeman components 3 or 4 which feature the smallest linear Zeeman shifts and are therefore the least sensitive ones for a given magnetic field noise level. However, at the time of this measurement the $^{40}\mathrm{Ar}^{13+}$ state preparation was realized with the highest fidelity for the outer Zeeman components 1 and 6. Indeed, the electronic state preparation is eased for these components since decay in the other Zeeman ground state is impossible and the state preparation can be realized faster. Therefore, one of these components was chosen for this measurement. Furthermore, a mechanical shutter for the clock laser beam could be introduced into the setup in order to reliably prevent residual clock laser light from illuminating $^{40}\mathrm{Ar}^{13+}$ during the wait time. A significant improvement of the excited-state lifetime measurement is however only possible by significantly reducing the statistical uncertainty. For this purpose the excitation-probability offset b (see Equation 16.1) should be carefully characterized by measuring at very long wait times. Unfortunately, the maximum wait time of the here presented measurement was limited by the experimental control system, which is going to be resolved by switching to a new system. Above that, it should be possible to combine measurements carried out at different days and with varying adjustments of the experiment. When the offset b can be reliably measured for an effectively infinite wait time, then it can be subtracted from the data set. Finally, only the contrast realized in the data set has to be normalized by dividing the excitation probabilities of the data set through the initial contrast a. Such processed data sets would only follow the relation $P_e(t) = \exp(-t/\tau)$, could be accumulated, and analyzed with a one-parameter maximum likelihood estimate. This would improve on the lifetime estimate with a reduced uncertainty, presumably to a level comparable to the in-EBIT measurement of Lapierre et al. (2006) in an acceptable total measurement time. For now, no fundamental limitation of this method can be identified except for the required total measurement time.

Noteworthy, a second accurate experimental determination of the $^{40}\mathrm{Ar}^{13+}$ $^2P_{3/2}$ excited-state lifetime is urgently required to resolve a severe disagreement of more than 5 σ, existing between the in-EBIT measurement of Lapierre et al. (2006), which is by far the most accurate one, and the most accurate calculations of Tupitsyn et al. (2005) and Bilal et al. (2018).

Part V

Conclusion

> *The most dangerous phrase* [. . .] *is,*
> *'We've always done it that way.'*
>
> — Grace Brewster Murray Hopper

The last part of this thesis concludes the reported work by briefly summarizing the main achievements in Chapter 17 and providing an outlook about the work in progress and future plans in Chapter 18.

17 Summary

Highly charged ions (HCIs) are excellent atomic systems for the study of fundamental physics and the development of future high-accuracy optical atomic clocks. In comparison to neutral and singly charged atoms, the much higher binding energies of the outer electrons and the smaller spatial extent of the electronic wave functions result in an enhanced sensitivity of HCIs to effects from fundamental physics. Moreover, many perturbations that are induced by external electromagnetic fields and which limit the accuracy achievable in today's optical atomic clocks based on neutral and singly charged atoms are highly suppressed in HCIs, thereby resulting in considerably smaller frequency shifts. However, the uncertainty level achieved in optical spectroscopy of HCIs was limited for a long time to only a bit better than the parts-per-million (ppm) level (see Figure 17.1) and has lagged far behind the 10^{-18} uncertainty level which is state of the art in frequency metrology with optical atomic clocks.

Building on previous work which has been carried out with CryPTEx at the MPIK (Schmöger, Versolato, et al., 2015; Schmöger, 2017; Schwarz et al., 2012), a unique experiment was set up and commissioned at PTB which is capable to cope with two major demands: the production, handling, and preparation of HCIs, as well as the coherent manipulation of coupled electronic and motional degrees of freedom of single ions trapped in the harmonic potential of a Paul trap (Leopold et al., 2019; Leopold, 2018; Micke et al., 2018, 2019).

This thesis reported on the first coherent laser spectroscopy of a HCI (Micke et al., 2020), carried out with the new setup. The employed concepts break through the ppm-uncertainty barrier of traditional HCI spectroscopy, leading to an increase of precision by about eight orders of magnitude to a fractional uncertainty level of about 3×10^{-15} (see Figure 17.1). The spectroscopic resolution could be improved by nine orders of magnitude[1], expressed in terms of a resolving power to a value of about 1×10^{13}. This was enabled by isolating a single HCI from a megakelvin-hot plasma, reducing its temperature by about nine orders of magnitude, and preparing it in a two-ion crystal together with a logic ion inside the harmonic potential of a Paul trap. Two of the normal modes of the two-ion crystal were then cooled to their quantum-mechanical ground state of motion. This step constitutes the first demonstration of ground-state cooling of an exotic two-ion crystal with different ion charges and masses. Finally, the implementation of quantum logic (QL) techniques allowed for state preparation of the HCI and efficient detection through electron shelv-

---

[1] The terms *spectroscopic resolution* and *resolving power* refer here to the FWHM of the observed spectral lines.

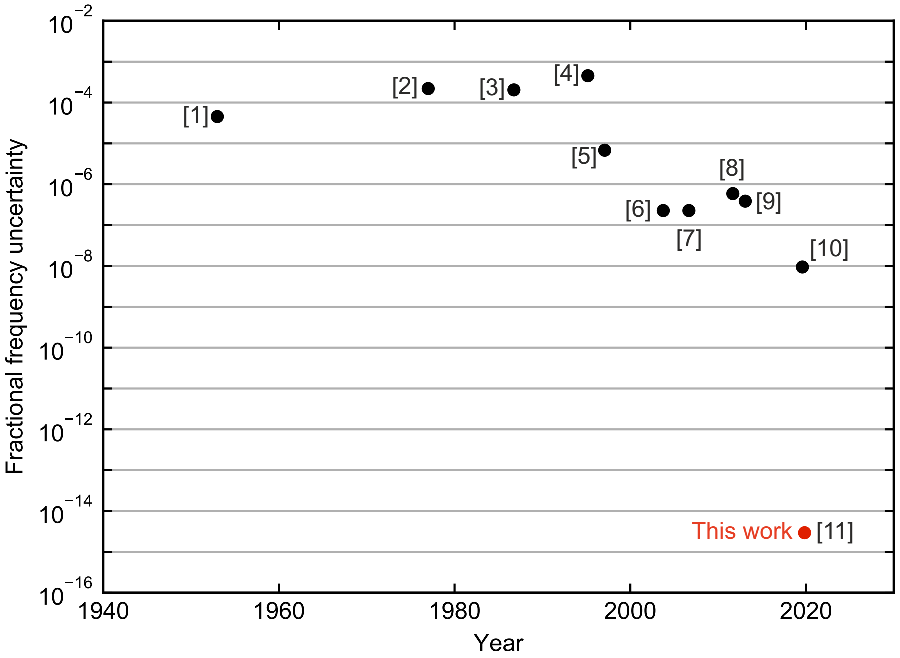

Figure 17.1: Fractional frequency uncertainties of the $^2P_{1/2}$–$^2P_{3/2}$ Ar^{13+} fine-structure transition at 441 nm achieved over the last decades. This optical transition is the most accurately measured transition in any HCI.
[1]—Lyot and Dollfus (1953)
[2]—Edlén (1977)
[3]—Prior (1987)
[4]—Morgan et al. (1995)
[5]—Bieber et al. (1997)
[6]—Draganić et al. (2003)
[7]—Soria Orts et al. (2006)
[8]—Mäckel et al. (2011)
[9]—Mäckel et al. (2013)
[10]—Egl et al. (2019)
[11]—This work [red, Micke et al. (2020)]
Traditional spectroscopy is carried out with spectrometers used to quantify the spectrum emitted by celestial or laboratory plasmas. [8] and [9] made use of a pulsed laser probing a laboratory plasma. The measurement of [10] and this work [11] herald a new era of optical spectroscopy with HCIs since these measurements are performed with single, cold HCIs probed with continuous-wave lasers. Sophisticated state-detection schemes are however required in order to obtain a sufficient 'spectroscopy signal' from an E1-forbidden transition of a single ion. The result of measurement [2] can be found in the compilation by Edlén (1982). The quoted uncertainty of the reported work of this thesis is the statistical uncertainty of about 3×10^{-15} obtained from the determination of the centers of the spectral lines. The evaluation of the additional systematic uncertainty is in progress but will be on a comparable or even better level. The plot makes no claim of being complete.

ing of the logic ion. Based on these reported advances and demonstrated with the specific system $^{40}\mathrm{Ar}^{13+}$–$^{9}\mathrm{Be}^{+}$, coherent population transfer (Rabi oscillations) were observed in a HCI for the first time. The Zeeman structure of the $^2\mathrm{P}_{1/2}$–$^2\mathrm{P}_{3/2}$ fine-structure transition of $^{40}\mathrm{Ar}^{13+}$ was measured with Hz-level uncertainty over a Zeeman splitting of about 7 MHz. From these measurements, the excited-state g-factor was determined with an unprecedented fractional uncertainty of 4.3×10^{-6}, resolving effects from special relativity, interelectronic interactions, and quantum electrodynamics (QED). This result also settles a discrepancy between previous theoretical calculations. Furthermore, a QL-assisted excited-state lifetime measurement was demonstrated, confirming the most accurate in-EBIT measurements and providing a new method to study lifetimes of metastable electronic states of HCIs in the much less perturbed environment of an ultracold two-ion crystal in comparison to an HCI plasma of MK-temperature in a strong magnetic field.

All of these measurements are intended as proof of principles. Further improvements are in preparation, in particular the evaluation of the absolute transition frequency of the $^2\mathrm{P}_{1/2}$–$^2\mathrm{P}_{3/2}$ fine-structure transition in $^{40}\mathrm{Ar}^{13+}$. The clock laser of this experiment is linked to the frequency-metrology network of PTB and enables absolute frequency measurements referenced to the SI second through PTB's fountain clocks and relative frequency comparisons with PTB's optical atomic clocks that are operating at the 10^{-18} fractional frequency uncertainty level. However, systematic frequency shifts have to be fully characterized with a target near-future total fractional frequency uncertainty of about 1×10^{-16}. $^{40}\mathrm{Ar}^{13+}$ is not an ideal clock candidate, primarily owing to the relatively large natural linewidth of 17 Hz of the studied fine-structure clock transition which strongly limits the achievable frequency stability. Nonetheless, it is an excellent system for this demonstration and is extensively studied in theory owing to its high sensitivity to fundamental effects combined with its rather simple, and therefore computable, atomic structure. For this reason, the atomic properties are important to be accurately measured, such as the optical transition frequency, the involved g-factors, the excited-state lifetime, and electric-quadrupole moment. Effects from special relativity, interelectronic interactions, QED, and the nucleus have to be included for an accurate theoretical prediction, and a comparison between experiment and theory allows to benchmark computational concepts and to verify or refine the underlying theories in general.

Importantly, the experiment is not limited to the specific HCI species $^{40}\mathrm{Ar}^{13+}$. The demonstrated techniques are universal and directly applicable to a large range of other species. This opens up the large and previously inaccessible atomic class of HCIs for use in frequency metrology and thereby to the most precise experimental techniques which have been developed so far. The combination of high sensitivity to fundamental effects with high experimental precision offers a promising potential to test fundamental physics and search for physics beyond the Standard Model, including possible variations of fundamental constants, a Lorentz violation, an unknown 5th force, and dark matter candidates. A large number of proposals suggesting an even larger number of HCI species for that purpose and as a basis for yet more accurate optical atomic clocks was published in the last decade. This work represents the first realization of the required experimental methods and brings these proposals into reach. Some of the future plans are briefly discussed in Chapter 18 which addresses an outlook of this work.

18 Outlook

The demonstration of coherent laser spectroscopy of HCIs enables a variety of experiments with a focus in fundamental physics-related research and frequency metrology. A growing number of similar experiments to the one reported here are under development, for example at the MPIK, where a novel superconducting cryogenic Paul trap has recently successfully trapped and laser-cooled $^{9}\mathrm{Be}^{+}$ ions (Stark, 2020) for sympathetic cooling of HCIs with the goal of direct frequency comb spectroscopy in the XUV range (Nauta et al., 2017). At RIKEN, another setup for an HCI-based optical clock is under development with the initial goal of demonstrating Doppler-free laser-induced fluorescence spectroscopy of the $^{2}\mathrm{P}_{1/2}$–$^{2}\mathrm{P}_{3/2}$ transition in indium-like Ba^{7+} at 424 nm (Kimura et al., 2019b) or of the $^{3}\mathrm{P}_{0}$–$^{3}\mathrm{P}_{1}$ transition of tin-like Ba^{6+} at 645 nm (Kimura et al., 2019a). At NIST in Gaithersburg, an experiment is set up which recently already demonstrated the recapture of bare Ne^{10+} nuclei in a room-temperature pseudo-hyperbolic Paul trap after production in the NIST EBIT (Dreiling et al., 2019). In the absence of any cooling mechanism, HCI storage times of 69 ms were achieved as a first result.

Following on the results of the work summarized in the previous chapter, the next sections address the planned measurements and future perspectives of the reported experiment.

18.1 Absolute transition frequency of Ar^{13+}

The accurate evaluation of the $^{2}\mathrm{P}_{1/2}$–$^{2}\mathrm{P}_{3/2}$ transition frequency of $^{40}\mathrm{Ar}^{13+}$ is the next major goal of this experiment. For this purpose, locking of the clock laser to the clock transition is currently implemented through *two-point sampling* (Bernard et al., 1999; Bernard, Marmet, and Madej, 1998) of four of the six Zeeman components. The simultaneous measurement of such four components allows to cancel the linear Zeeman shift and the electric-quadrupole shift as discussed in Section 15.2.2. The second-order Zeeman shift is known to be on a fractional level of 5×10^{-18} with an uncertainty at the 1×10^{-20} level (see Section 15.2.1). The BBR shift and the collisional shift are negligible (see Section 2.3.2). The highly suppressed second-order ac Stark shift (suppressed by about four orders of magnitude compared to singly charged ions, see Table 2.2) and the motional shifts have to be characterized in the next step. The first-order Doppler shift as a result of a drift of the ion's position against the clock laser was measured for the $^{27}\mathrm{Al}^{+}$ ion clock to be on a 5×10^{-17} uncertainty level corresponding to a drift-velocity of $10\,\mathrm{nm\,s^{-1}}$

(Brewer et al., 2019). Additionally, residual low-frequency vibrations at the Paul trap can result in a relevant first-order Doppler shift. Such shifts can be eliminated by probing the clock transition with counter-propagating clock laser beams. The negative second-order Doppler shift has to be evaluated in contrast by determining the residual kinetic energy stored in the secular motion and in the micromotion of the HCI. The corresponding residual velocity of the ion results in a relativistic time dilation relative to the laboratory frame. For its characterization, the occupation numbers of all six normal QHO modes of the two-ion crystal have to be measured and the residual micromotion level determined (see Section 2.3.1).

18.2 Isotope shift spectroscopy and the search for a King-plot nonlinearity

The element argon has the three stable isotopes ^{40}Ar, ^{38}Ar, and ^{36}Ar with natural abundances of about 99.6, 0.06, and 0.33 % (Sonzogni, 2020). Once the $^2\mathrm{P}_{1/2}$–$^2\mathrm{P}_{3/2}$ transition frequency of $^{40}\mathrm{Ar}^{13+}$ has been fully evaluated with a complete uncertainty budget, the measurement can be repeated with isotopically enriched ^{36}Ar. The frequency difference between both $^2\mathrm{P}_{1/2}$–$^2\mathrm{P}_{3/2}$ transition frequencies is called the *isotope shift* and was previously theoretically studied (Zubova et al., 2016) and measured (Soria Orts et al., 2006) to be $1.90(9)$ GHz with a fractional frequency uncertainty of about 5 %. The origin of this shift is found in the finite masses and non-zero sizes of the nuclei, which affect the electronic binding energies and therefore transition energies. This section briefly summarizes the formulation of the isotope shift and then addresses the search for an unknown 5th force and a corresponding particle which mediates this interaction [see, e. g., Breit (1958), Yerokhin et al. (2020), and references therein for details].

The nuclear contribution to the transition energy of a specific electronic transition i of an atomic isotope with mass number A is given by

$$\Delta f_i^A = \underbrace{\frac{1}{m_A} K_i}_{\text{Mass shift}} + \underbrace{r_A^2 F_i}_{\text{Field shift}} \quad , \tag{18.1}$$

where m_A is the mass and r_A the rms charge radius of the nucleus. The first term on the right of Equation 18.1 is mass-dependent and is referred to as the *mass shift*. It originates from the nuclear recoil and is more pronounced for lighter atoms. In more detail, this shift is composed of the *normal* and *specific mass shift*. Both terms are obtained by expressing the momentum of the nucleus in the kinetic energy term through the sum of all electron momenta. One then obtains a term $\propto \sum_i p_i^2$ (normal mass shift) and a second term $\propto 2\sum_{i<j} p_i p_j$ (specific mass shift), where p_i denotes the momentum of the i^{th} electron. The latter term involves the electron correlations and is more challenging to calculate. The second term in Equation 18.1 is the *field shift* and depends on the spatial extent of the nuclear charge distribution. It is

dominant for heavy atoms. The field shift is particularly large for transitions which involve electronic S states with a non-zero electronic wave function at the position of the nucleus. The field-shift contribution also increases with the charge state owing to the generally smaller spatial extent of the electronic wave functions. K_i and F_i are the corresponding mass-shift and field-shift constants[1] which are usually assumed to only depend on the electronic transition but not on the specific isotope.

By convention, the term isotope shift refers to the frequency difference

$$\delta f_i^{A,A'} := \Delta f_i^{A} - \Delta f_i^{A'} \tag{18.2}$$

observed for a specific electronic transition i between two different isotopes with the mass numbers A and A'. Introducing the inverse mass factor

$$\mu_{A,A'} = \left(1/m_A - 1/m_{A'}\right)^{-1}, \tag{18.3}$$

one obtains from Equation 18.1 the so-called *modified isotope shift*

$$\mu_{A,A'}\, \delta f_i^{A,A'} = K_i + F_i \;\; \mu_{A,A'} \left(r_A^2 - r_{A'}^2\right) \tag{18.4}$$

for the transition i. Considering now two different electronic transitions with $i \in \{1,2\}$, the difference of the squared charge radii can be eliminated. One then obtains the linear relation

$$\mu_{A,A'}\, \delta f_1^{A,A'} = K_1 - \frac{F_1}{F_2} K_2 + \frac{F_1}{F_2} \;\; \mu_{A,A'}\, \delta f_2^{A,A'} \tag{18.5}$$

between the modified isotope shifts of transition 1 and 2 for the isotope pair A,A'. The slope and the intercept of this linear function are given by the four quantities K_1, K_2, F_1, and F_2 which are assumed to not depend on the specific isotopes. When the isotope A is used as a reference from which the modified isotope shifts of other isotopes A' are measured, one obtains a so-called *King plot* (see Figure 18.1) in which the isotope pairs align according to Equation 18.5 (W. H. King, 1963, 1984).

Isotope shift spectroscopy and the evaluation of King plots allow to study nuclear parameters, such as the mass- and field-shift constants, and to extrapolate nuclear charge radii of short-lived isotopes. Recently, it was realized that an unknown 5th force and new particles could manifest in a subtle nonlinearity of the King plot [see Section 3.1.1 and Berengut et al. (2018), Flambaum, Geddes, and Viatkina (2018), Frugiuele et al. (2017), and M. G. Kozlov et al. (2018) for details]. For such studies, the measurement of two transitions in at least four isotopes is required in order to obtain at least three data points in the King plot. It is noteworthy that the two transitions can be studied in different atomic systems—merely the same nuclei are required. Therefore, one or even both transitions can be studied in HCIs. In particular, the possible use of HCIs extends the range of useful transitions that involve significantly

---

[1] Note that Equation 18.1 and the corresponding definitions of K and F are not consistent through literature.

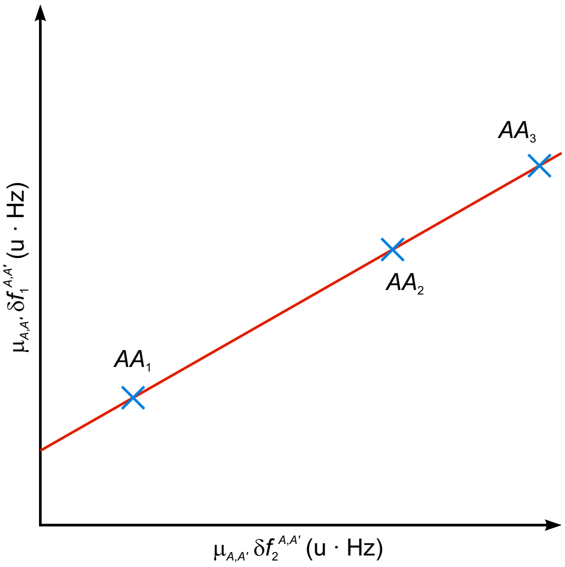

Figure 18.1: Illustration of a King plot. The modified isotope shifts $\mu_{A,A'}\,\delta f_1^{A,A'}$ and $\mu_{A,A'}\,\delta f_2^{A,A'}$ of the two different transitions 1 and 2 are shown for isotope pairs with mass numbers A and A', where $A' \in \{A_1, A_2, A_3\}$. Assuming isotope-independent mass- and field-shift constants, the isotope pairs must line up according to the linear relation in Equation 18.5 (red straight line). See text for further details.

different electronic wave functions in order to increase the sensitivity for such studies.

Resolving a possible nonlinearity in the King plot is a challenging task since small uncertainties of the frequency and mass measurements are required. Previous King-plot studies using E1 transitions in Ca^+ ions with a frequency uncertainty level of about 100 kHz (Gebert, 2015; Gebert et al., 2015; Shi et al., 2016) were consistent with the linear relation of Equation 18.5. Recently, measurements at a much smaller uncertainty level of a few Hz of an E2 transition in Ca^+ were performed by Knollmann, Patel, and Doret (2019), accomplished through simultaneous measurements of two different isotopes co-trapped in a Paul trap. In combination with an E1 transition, the King-plot analysis was again consistent with a linear scaling. Another work demonstrated the use of entangled states in Sr^+ to further improve on the uncertainty achievable in isotope shift spectroscopy (Manovitz et al., 2019). However, no King plot was evaluated here. Also neutral Sr atoms trapped in an optical dipole trap were recently used for a King-plot analysis. Here, the isotope shifts of four stable isotopes were evaluated for the 7.4 kHz wide ${}^1\mathrm{S}_0$–${}^3\mathrm{P}_1$ intercombination transition and the much narrower strictly forbidden ${}^1\mathrm{S}_0$–${}^3\mathrm{P}_0$ clock transition (mHz-wide) (Miyake et al., 2019). Uncertainties on the order of 10 kHz were achieved for both transitions and the King-plot analysis indicated a nonlinearity. However, a definite conclusion could not be drawn owing to an involved determination of the center of mass of the ${}^{87}\mathrm{Sr}$ ${}^3\mathrm{P}_1$ hyperfine structure. Also Ra^+ was recently used for a King-plot analysis with six isotopes and a frequency uncertainty level of about 10 MHz (Holliman, Fan, and Jayich, 2019). The analysis was consistent with a linear prediction.

Importantly, for the study of a nonlinearity in the King plot which could originate from physics beyond the SM, a proper understanding and careful evaluation of the nonlinearities that originate within the SM framework is vital (Yerokhin et al., 2020). A subtle dependence of the mass- and field-shift constants K and F on the isotopes would also result in a nonlinearity. Therefore,

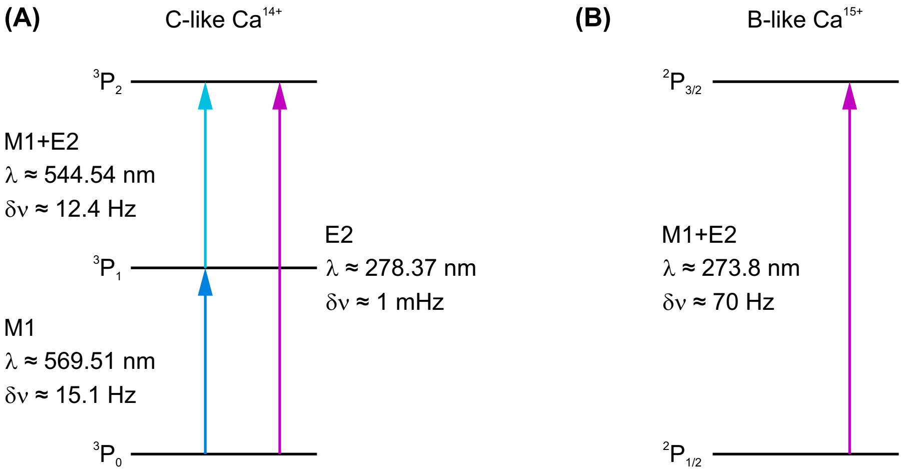

Figure 18.2: Level structure of carbon-like Ca^{14+} and boron-like Ca^{15+}. (**A**) The ground-state fine structure of Ca^{14+} is shown. It provides a $^3\mathrm{P}_0$–$^3\mathrm{P}_1$ ground-state M1 transition at a vacuum wavelength of $\lambda \approx 569.51$ nm and a $^3\mathrm{P}_0$–$^3\mathrm{P}_2$ ground-state E2 transition at about 278.37 nm. Notably, the $^3\mathrm{P}_0$ ground state has no additional Zeeman structure which significantly eases electronic state preparation. Spectroscopy data from Kramida et al. (2019). (**B**) The ground-state fine structure of Ca^{15+} features an E1-forbidden $^2\mathrm{P}_{1/2}$–$^2\mathrm{P}_{3/2}$ transition at a wavelength of about 273.8 nm. Spectroscopy data from Kramida et al. (2019) and Rynkun et al. (2012). All wavelengths stated in vacuum. Level schemes are not to scale. $\delta\nu$—FWHM natural linewidth, E2—electric-quadrupole transition, M1—magnetic-dipole transition.

the next-to-leading order term—the *quadratic mass shift*—was studied for transitions in highly charged argon. Nonlinearities on the order of 10 kHz were calculated (Yerokhin et al., 2020). This result is about four orders of magnitude larger than a previous estimate (Flambaum, Geddes, and Viatkina, 2018). However, it was also recently noted that for certain electronic states, such as the $\mathrm{P}_{1/2}$ state, the King-plot nonlinearity from the SM framework is enhanced and, therefore, such electronic states should be avoided for the use in such searches for new physics (Tanaka and Yamamoto, 2019).

Unfortunately, the three stable isotopes of argon are not sufficient for a King-plot analysis. Although in principle a fourth unstable isotope could be used, such as $^{42}\mathrm{Ar}$, this would impose additional safety requirements to the experiment. As an alternative, highly charged calcium could be used and is briefly addressed in the next section.

18.2.1 Highly charged calcium

The reported experimental techniques of this work allow for small uncertainties in King-plot studies of E1-forbidden transitions. As mentioned before, the study of a possible nonlinearity in the King plot requires at least four isotopes of an element in order to obtain three data points. To ease experimental conditions and to avoid a hyperfine structure of which the centers of mass would have to be determined, the availability of at least four stable isotopes (or primordial nuclides) without nuclear spin is highly preferred. This reduced the number of available elements significantly [see a chart of nuclides, e. g., Sonzogni (2020)]. Calcium is the lightest element which fulfills these demands and provides five useful isotopes, namely ^{40}Ca, ^{42}Ca, ^{44}Ca, ^{46}Ca, and ^{48}Ca with natural abundances of about 96.94, 0.65, 2.09, 0.004, and 0.19 %[2]. Additionally, the stable isotope ^{43}Ca with a nuclear spin of $I = 7/2$ exists. The fractional uncertainty of the atomic mass of neutral ^{40}Ca is for instance 5.5×10^{-10}. It is about one order of magnitude larger for the other isotopes except for ^{46}Ca for which the uncertainty is about two orders of magnitude larger (Wang et al., 2017). New Penning trap mass measurements could in principle improve the uncertainties to a fractional level of about 10^{-11} (Blaum, 2019).

The $^3P_0$–$^3P_1$ ground-state fine-structure transition in carbon-like Ca^{14+} at a vacuum wavelength of 569.51 nm and a natural linewidth of 15.1 Hz (Kramida et al., 2019) would be well suited for isotope shift spectroscopy and King-plot studies (see Figure 18.2A). This transition splits up into three Zeeman components in an external magnetic quantization field. The central component is to first order magnetic field insensitive. Since $J = 0$, the $^3P_0$ ground state possesses no electric-quadrupole moment and electronic state preparation of this system is significantly eased since the ground state does not have multiple Zeeman substates. Ca^{14+} also has a 1 mHz-narrow $^3P_0$–$^3P_2$ E2 transition at 278.37 nm. Unfortunately, the potential of this narrow excitation linewidth cannot be used with the QLS scheme as introduced in Section 13.2. The reason is the much faster decay of the $^3P_2$ excited state through an M1 channel with a natural lifetime of about 12.9 ms into the metastable $^3P_1$ state which further decays with a lifetime of about 10.5 ms into the ground state.

Combined with the isotope shift spectroscopy of the $^2S_{1/2}$–$^2D_{5/2}$ E2 transition of Ca$^+$ performed by Knollmann, Patel, and Doret (2019), a King-plot analysis could be done on an unrivaled uncertainty level employing very different kinds of transitions ($^2S_{1/2}$–$^2D_{5/2}$ and $^3P_0$–$^3P_1$). Alternatively, the $^2P_{1/2}$–$^2P_{3/2}$ fine-structure transition in boron-like Ca^{15+} at a wavelength of about 273.8 nm (Kramida et al., 2019) could be used (see Figure 18.2B)[3]. Compared to the $^3P_0$–$^3P_1$ transition in Ca^{14+} the wavelength is in the more inconvenient ultraviolet region, a more complex electronic state preparation is required, and this transition has no magnetic field insensitive Zeeman component. However, a distinct advantage of combining the two transitions of Ca^{15+} and Ca^{14+} exists: The accuracy achieved in calculations of boron-like and carbon-like systems allows to predict the King-plot nonlinearity originating within the SM framework with a fractional uncertainty of about 30%. It is expected to appear on a 10 kHz level (Yerokhin et al., 2020).

---

[2] ^{48}Ca is a primordial nuclide and indeed unstable but it has a lifetime of more than 10^{19} yr.

[3] This is the same transition as was studied in this work in ^{40}Ar^{13+}.

18.3 Towards an optical atomic clock based on a fine-structure transition of a highly charged ion

This section briefly addresses the idea of an optical atomic clock based on a single HCI in view of the capabilities of the reported experiment. A more general and comprehensive review on many proposed HCI species can be found in M. G. Kozlov et al. (2018), see also references therein. The reported experiment was specifically designed for the study of optical transition in HCIs within the enlarged fine structure or which originate from level crossings of electronic orbitals at specific charge states along the isoelectronic sequences. In contrast, (near-)optical transitions within the ground-state hyperfine structure of HCI are basically not accessible by this experiment since such transitions shift into this range only for very heavy HCIs, such as hydrogen-like Pb^{81+} or lithium-like Bi^{80+}. The production of these ions require energies in excess of the ionization potentials of the order of 100 and 25 keV. This is out of reach for the electron-beam energy of PTB-EBIT[4].

The suppression of many systematic frequency shifts induced by external electromagnetic fields is a strong argument for the use of HCIs in future optical atomic clocks. However, several additional criteria should be fulfilled in order to compete with the best optical clocks of today. First of all, the potential clock transition should be a (near-)optical transition in the wavelength range of about 200–2000 nm and preferably involve the electronic ground state. Moreover, the HCI should have a stable (or long-lived) nucleus. Importantly, the FWHM natural linewidth of the clock transition should be in the range of about 0.1–100 mHz. Generally, a narrower transition allows for a higher stability of the clock (see Equation 2.3) but since the linewidth of the most narrow and stable clock lasers is on the order of a few mHz, a much narrower clock transition does not help without a significant technological improvement of the lasers. A disadvantage of a much narrower clock transition would even be the higher laser intensity required in order to drive the transition which, in turn, increases the second-order ac Stark shift and reduces the maximum rate at which we can drive sidebands, making state preparation and QLS much slower. Since the QLS scheme relies on electronic state mapping through state-transfer laser pulses, the excited clock state should not decay back into the ground state through a much faster additional decay channel (as present in the level structure of Ca^{14+} for instance, cf. Figure 18.2A). In general, a simple level structure is highly preferred in order to ease electronic state preparation and to reduce the dead time of the clock. Although a hyperfine structure can be beneficial, it can also significantly complicate the electronic structure and impose the need of additional repumper lasers. Furthermore, the clock states should preferably have small total angular momentum quantum numbers J (or F in the case of hyperfine structure) in order to keep the number of Zeeman components low. Transitions which provide an $m = 0 \rightarrow m' = 0$ component are beneficial since

---

[4] Very heavy and highly charged ions are typically produced by particle accelerators or superconducting EBITs which are designed for HV operation on a 100 kV level.

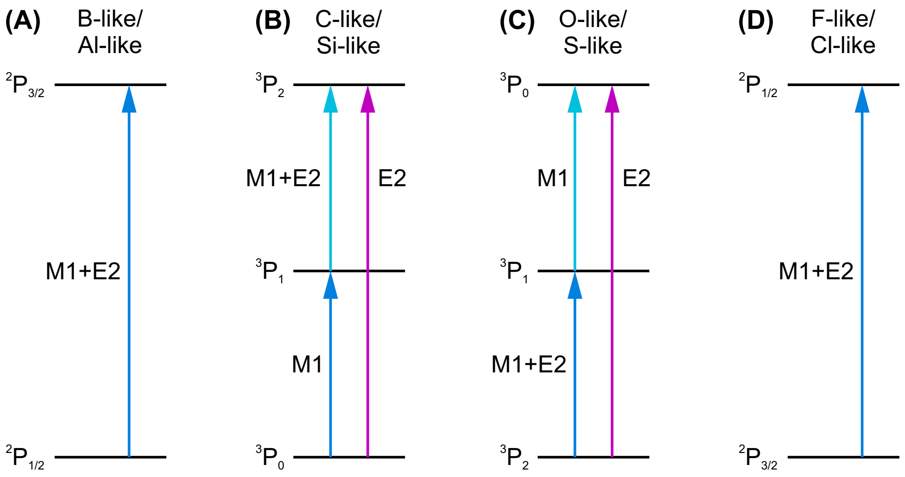

Figure 18.3: Ground-state fine structure in middle-*Z* highly charged ions. (**A**) Boron-like and aluminum-like systems feature a single fine-structure transition, dominated by the M1 channel, which splits up into six Zeeman components in an external magnetic field. (**B**) In carbon-like and silicon-like systems, three fine-structure transitions are present. Two of them are ground-state transitions of which the M1 transition (blue, three Zeeman components) is about three orders of magnitude faster than the E2 transition (purple, five Zeeman components). The $^3P_0$ ground state does not have multiple Zeeman substates. The decay of the upper $^3P_2$ state is dominated through the M1 channels. (**C**) The ordering of the electronic states in oxygen-like and sulfur-like systems is, in accordance with Hund's rules, different from the systems shown in panel B. The $^3P_2$ ground state has five Zeeman substates. Correspondingly, the faster ground-state transition (blue) has nine M1 Zeeman components and the slower E2 ground-state transition (purple) has five Zeeman components. (**D**) Similarly, the ordering of the level structure in fluorine-like and chlorine-like systems is different from the ordering shown in panel A. A single fine-structure transition is present with six M1 Zeeman components. The level schemes are not to scale. See text for further details. E2—electric-quadrupole transition, M1—magnetic-dipole transition.

such Zeeman components are to first order magnetic field insensitive. Clock states with J (F) < 1 have the advantage of no electric-quadrupole moment and no corresponding frequency shift. Additionally, heavier atoms have the advantage of smaller motional shifts.

Transitions within the ground-state fine structure are E1-forbidden. They only appear in eight specific electronic systems for all isoelectronic sequences of the first three periods of the periodic table of elements, shown in Figure 18.3 (in absence of hyperfine structure). While the fine-structure splittings are on a few meV to a few ten meV level in the neutral atomic systems, they shift into the optical range for the boron-like to fluorine-like systems for elements around $Z = 18$ (argon) and for aluminum-like to chlorine-like systems for elements around $Z = 27$ (cobalt). Most of the transitions have an M1 component which has a typical FWHM natural linewidth of a few Hz to a few 100 Hz. Those transitions are not ideal for an optical atomic clock since the linewidth is too large for a competitive stability compared to other single-ion optical clocks. Much narrower E1- and M1-forbidden E2 transitions with FWHM

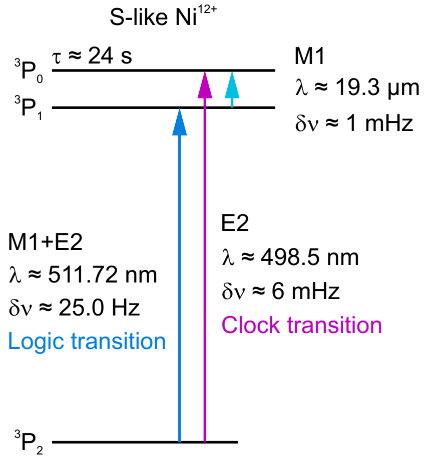
S-like Ni^{12+}
$^3P_0$
$\tau \approx 24$ s
M1
$\lambda \approx 19.3$ µm
$\delta\nu \approx 1$ mHz
$^3P_1$
M1+E2
$\lambda \approx 511.72$ nm
$\delta\nu \approx 25.0$ Hz
Logic transition
E2
$\lambda \approx 498.5$ nm
$\delta\nu \approx 6$ mHz
Clock transition
$^3P_2$

Figure 18.4: Level structure of sulfur-like Ni^{12+}. The $^3P_2$ ground state splits into five Zeeman substates. The E2 clock transition at a wavelength $\lambda \approx 498.5$ nm has a FWHM natural linewidth of $\delta\nu \approx 6$ mHz. The upper $^3P_0$ state has a natural lifetime of $\tau \approx 24$ s. The M1-dominated $^3P_2$–$^3P_1$ transition with a FWHM natural linewidth of about 25 Hz could be used as a dedicated logic transition for state preparation and detection, like the logic transition in $^{27}Al^+$. Level scheme is not to scale. All wavelengths stated in vacuum. Spectroscopy data from Kramida et al. (2019). See text for further details. E2—electric-quadrupole transition, M1—magnetic-dipole transition.

natural linewidths of a few mHz exist in carbon-like (silicon-like) and oxygen-like (sulfur-like) systems. However, in most cases the excited states of these transitions have a faster decay channel through an intermediate metastable state back into the ground state and are therefore not suitable for QLS. This situation changes for sulfur-like systems in which the intermediate $^3P_1$ state is much closer to the upper $^3P_0$ state, resulting in a significantly reduced transition rate of the $^3P_0$–$^3P_1$ M1 decay and, thus, in a much longer lifetime of the upper $^3P_0$ state. A particularly interesting case is sulfur-like nickel ($Z = 28$) in which the decay of the upper $^3P_0$ state is dominated by the E2 decay back into the ground state (see level structure shown in Figure 18.4). Between $Z = 28$ and 29 the $^3P_0$ and $^3P_1$ states cross. For higher Z, the E2 transition is then the lower-frequency ground-state transition[5]. However, sulfur-like copper ($Z = 29$) has two stable isotopes with a nuclear spin of $I = 3/2$ and a corresponding hyperfine structure. Another possible clock species would be sulfur-like zinc ($Z = 30$) with the clock transition in the ultraviolet range at about 378 nm (Kramida et al., 2019). For increasing Z, the E2 clock transition shifts deeper into the ultraviolet. Sulfur-like Ni^{12+} [also recently suggested by Y.-m. Yu and Sahoo (2018)] and sulfur-like Zn^{14+} would be even well suited for King-plot studies since both elements have four stable isotopes with zero nuclear spin[6] and natural abundances of $\gtrsim 1\,\%$ for each isotope. Moreover, both species offer a faster ground-state M1 transition with a wavelength similar to the one of the clock transition (see Figure 18.4). This M1 transition could be used as a dedicated logic transition for faster state preparation of the HCI. The upper $^3P_0$ clock state has no electric-quadrupole moment, and one of the five Zeeman components of the clock transition is to first order magnetic field insensitive. Another advantage of both HCI species is their charge-to-mass ratio of $q/m \approx 0.2e/\mathrm{u}$ which is much closer to the $^9Be^+$ charge-to-mass ration of about $0.11\,e/\mathrm{u}$ compared to the charge-to-mass ratio of $0.325\,e/\mathrm{u}$ for $^{40}\mathrm{Ar}^{13+}$ which was studied in this work. The smaller q/m mismatch would improve the efficiency of sympathetic Dopper and resolved sideband cooling of the two-ion crystal.

---

[5] The crossing of the upper and intermediate P states also occurs for oxygen-like systems, but in the ultraviolet range around 200 nm.

[6] Nickel and zinc are the second and third lightest elements after calcium which fulfill the demand of at least four stable isotopes with zero nuclear spin.

HCIs are also suited as species for future atomic clocks which could operate beyond the optical range at higher frequencies. Like the step from microwave clocks to optical clocks, clock operation at higher frequencies in the XUV or even x-ray domain would be an important technological development for frequency metrology which would boost clock stability significantly. In a first approach, the allied MPIK experiment aims at high harmonic generation of a frequency comb used for direct frequency comb spectroscopy of HCIs in the XUV range (Nauta et al., 2017).

18.3.1 Search for a variation of fundamental constants and dark matter candidates

In the previous section optical ground-state fine-structure transitions in HCIs were discussed. However, also aforementioned level crossings in HCIs, as recently observed (Bekker et al., 2019), can be well suited for optical atomic clocks. In particular, some of the corresponding transitions are promising for fundamental-physics research [see Windberger et al. (2015) and the review of M. G. Kozlov et al. (2018)] since they possess exceptionally high sensitivities to potential variations of fundamental constants—a research topic which is closely linked to the search for dark matter candidates (see Section 3.2 for details.). Such studies are another future perspective of the reported experiment.

Part VI

Appendix

P1 The Heidelberg compact electron beam ion traps

Journal: Review of Scientific Instruments

Copyright and license notice:
©2018 Author(s). All article content, except where otherwise noted, is licensed under a Creative Commons Attribution (CC BY) license.
(http://creativecommons.org/licenses/by/4.0/)

Reproduced from

P. Micke, S. Kühn, L. Buchauer, J. R. Harries, T. M. Bücking, K. Blaum, A. Cieluch, A. Egl, D. Hollain, S. Kraemer, T. Pfeifer, P. O. Schmidt, R. X. Schüssler, Ch. Schweiger, T. Stöhlker, S. Sturm, R. N. Wolf, S. Bernitt, and J. R. Crespo López-Urrutia (2018). “The Heidelberg compact electron beam ion traps.” *Review of Scientific Instruments* 89, 063109.
DOI: 10.1063/1.5026961

with the permission of AIP Publishing.

REVIEW OF SCIENTIFIC INSTRUMENTS **89**, 063109 (2018)

The Heidelberg compact electron beam ion traps

P. Micke,[1,2,a)] S. Kühn,[1] L. Buchauer,[1] J. R. Harries,[3] T. M. Bücking,[1] K. Blaum,[1]
A. Cieluch,[1] A. Egl,[1] D. Hollain,[1] S. Kraemer,[1] T. Pfeifer,[1] P. O. Schmidt,[2,4] R. X. Schüssler,[1]
Ch. Schweiger,[1] T. Stöhlker,[5,6,7] S. Sturm,[1] R. N. Wolf,[1,b)] S. Bernitt,[1,7,c)]
and J. R. Crespo López-Urrutia[1]
[1]*Max-Planck-Institut für Kernphysik, Saupfercheckweg 1, 69117 Heidelberg, Germany*
[2]*Physikalisch-Technische Bundesanstalt, Bundesallee 100, 38116 Braunschweig, Germany*
[3]*National Institutes for Quantum and Radiological Science and Technology, SPring-8, Kouto 1-1-1, Sayo-cho, Sayo-gun, Hyogo 679-5148, Japan*
[4]*Institut für Quantenoptik, Leibniz Universität Hannover, Welfengarten 1, 30167 Hannover, Germany*
[5]*GSI Helmholtzzentrum für Schwerionenforschung, Planckstraße 1, 64291 Darmstadt, Germany*
[6]*Helmholtz-Institut Jena, Fröbelstieg 3, 07743 Jena, Germany*
[7]*Institut für Optik und Quantenelektronik, Friedrich-Schiller-Universität Jena, Max-Wien-Platz 1, 07743 Jena, Germany*

(Received 26 February 2018; accepted 21 May 2018; published online 11 June 2018)

Electron beam ion traps (EBITs) are ideal tools for both production and study of highly charged ions (HCIs). In order to reduce their construction, maintenance, and operation costs, we have developed a novel, compact, room-temperature design, the Heidelberg Compact EBIT (HC-EBIT). Four already commissioned devices operate at the strongest fields (up to 0.86 T) reported for such EBITs using permanent magnets, run electron beam currents up to 80 mA, and energies up to 10 keV. They demonstrate HCI production, trapping, and extraction of pulsed Ar^{16+} bunches and continuous 100 pA ion beams of highly charged Xe up to charge state 29+, already with a 4 mA, 2 keV electron beam. Moreover, HC-EBITs offer large solid-angle ports and thus high photon count rates, e.g., in x-ray spectroscopy of dielectronic recombination in HCIs up to Fe^{24+}, achieving an electron-energy resolving power of $E/\Delta E > 1500$ at 5 keV. Besides traditional on-axis electron guns, we have also implemented a novel off-axis gun for laser, synchrotron, and free-electron laser applications, offering clear optical access along the trap axis. We report on its first operation at a synchrotron radiation facility demonstrating the resonant photoexcitation of highly charged oxygen. © *2018 Author(s). All article content, except where otherwise noted, is licensed under a Creative Commons Attribution (CC BY) license (http://creativecommons.org/licenses/by/4.0/).* https://doi.org/10.1063/1.5026961

I. INTRODUCTION

Highly charged ions (HCIs) constitute a large class of atomic systems since each element has as many ionization states as it has protons—in a sense, this extends the periodic table by a further dimension. As a consequence of virialization in deep gravitational potentials,[1] HCIs are the predominant forms in which most of the elements appear in the visible universe, be it in or around stars,[2] galaxies, and their clusters[3] or in the vast expanses of the intergalactic medium.[4–6] Consequently, for many decades, the study of HCIs has been essential for astrophysics and astronomy,[7–9] and many examples of recent laboratory work continuously show its importance not only for astrophysics (see, e.g., Refs. 10–13 and the references therein) but also for plasma and fusion research (e.g., in Refs. 14–24). In atomic physics, HCI studies often deal with fundamental interactions due to relativistic effects, quantum electrodynamics (QED), and nuclear-size contributions which are all enhanced by several orders of magnitude[25–28] compared to neutral or singly charged systems. This, for instance, facilitated the precise determination of the electron mass[29,30] and the electron magnetic moment[31] as well as stringent QED tests.[32–36] Moreover, several proposals contemplate HCIs as ideal laboratory probes of a possible variation of the fine-structure constant α[37–50] and as frequency references for optical clocks[51–57] superior to state-of-the-art optical lattice or singly charged ion clocks. The very low polarizability of their electronic wave function explains their insensitivity to both spurious external perturbations and laser-induced light shifts. Suitable forbidden optical transitions have been theoretically identified, and preliminary laboratory determinations of their energies have been carried out.[58] Other current applications are tumor ion therapy[59] and EUV nanolithography.[60–63] Nevertheless, the HCI research community has remained rather small as HCI production is perceived as demanding and, indeed, there are still open challenges before it becomes a standard routine.

One of the first ever mentions of an "ion trap" in the literature, by Pierce and others in the 1940s,[64–66] describes a system in which atoms were ionized by electron impact and their ions radially trapped by the negative space charge potential of the electron beam and axially by cylindrical electrodes forming an axial potential well. They carried out investigations

---

[a)] Author to whom correspondence should be addressed: peter.micke@mpi-hd.mpg.de
[b)] Current address: ARC Centre of Excellence for Engineered Quantum Systems, School of Physics, The University of Sydney, NSW 2006, Australia.
[c)] E-mail: sven.bernitt@mpi-hd.mpg.de

© Author(s) 2018

on ionic space charge and its effect on electron-beam propagation. Donets[67–69] and Arianer[70,71] introduced the electron beam ion source, with the addition of a magnetic field for electron-beam compression. The modern electron beam ion trap (EBIT) based upon this was developed in the 1980s at Lawrence Livermore National Laboratory (LLNL) by Marrs and Levine.[72–74] An EBIT operates by means of a focused mono-energetic electron beam. Emitted from an electron gun, this beam is accelerated, guided along the axis of a set of cylindrical electrodes (referred to as drift tubes), decelerated, and dumped on a collector electrode. A strong axial magnetic field of increasing flux density compresses the beam to a diameter of a fraction of a millimeter at the trap center, resulting in an extremely high current density (in certain EBITs on the order of 10^4 A/cm^2)—the key feature for efficient ionization and subsequent ion trapping. The beam energy results from the potential difference between the cathode and the central trap electrode, with corrections due to the space charge of both the electron beam and the trapped ions, the work function of the materials used for the electrodes, and adjacent potentials. Neutral atoms can be injected as an atomic beam by introducing a gas or a volatile organometallic compound through a differentially pumped injection system. Other techniques are also applied, employing a laser ion source[75] or a wire-probe target.[76] Ionized by electron-beam impact, the ions are immediately trapped radially by the negative space charge of the compressed electron beam itself, as well as by the magnetic field. Axially, the confinement is controlled by the electrostatic potentials applied to the drift tubes. Charge breeding is realized by further sequential ionization of the trapped ions by the electron beam. The highest possible charge state is limited by its kinetic energy. Finally, the charge-state distribution is determined by the ionization and recombination rates, depending on the electron beam energy and density, the confinement time, and the background pressure.[77] Details on the operating principle can be found elsewhere in the literature.[78–80]

With direct optical access to the confined ion cloud, mono-energetic excitation, narrow ion-charge distributions, and small source-volume sizes, EBITs have become essential spectroscopic tools in the last three decades, from the pioneering work on x-rays at LLNL, down to the optical range, there as well as in other groups.[58,81–106] Beyond electron-impact excitation and ionization of the trapped ions utilizing the electron beam, photoexcitation and photoionization by mono-energetic photons at synchrotrons[107–111] and free-electron laser (FEL) facilities[12,112,113] have also been reported, in part using the EBIT magnetic trapping mode,[114] for which the electron beam is switched off. However, these experiments are limited by Doppler broadening due to high ion temperatures (10^5–10^7 K). To overcome this limitation, HCIs can be extracted from an EBIT and loaded into Paul[115] or Penning traps[116–121] where advanced cooling techniques can be applied. Recently, Ar^{13+} ions have been re-trapped in a cryogenic radio-frequency trap[122] and sympathetically cooled down to below 100 mK by laser-cooled Be$^+$ Coulomb crystals.[123,124] This 8-order-of-magnitude cooling will finally allow high-precision spectroscopy on HCIs as it is routinely performed with atoms and singly charged ions, and the application of the most sensitive techniques for detection, like quantum logic spectroscopy,[125] aiming at resolving the natural linewidth of forbidden optical transitions, or direct frequency-comb spectroscopy from the optical to the extreme ultra-violet (XUV) range.[126] Furthermore, extraction and subsequent detection of ions can be used to determine the charge-state distribution in the trap and has been used to investigate resonant photoionization by synchrotron radiation.[107,108,111] EBITs also operate as versatile HCI sources in experiments investigating charge transfer processes[127] and HCI-surface interactions,[128–133] and for rapid charge breeding of radioactive ions.[134,135]

Most of the reported experiments have been carried out using high-performance EBITs, employing superconducting magnets with flux densities from 3 to 8 T. Room-temperature EBITs with permanent magnets have also been developed in order to reduce size as well as costs and to ease operation. After the pioneering apparatus built in Paris by Khodja and Briand,[137] soon several others followed in Dresden,[138,139] Tokyo,[140] Belfast,[141] Shanghai,[142] Clemson,[143] and at NIST.[144] Related devices based on permanent magnets were also recently developed.[145]

Here, we report on a novel class of devices with a stronger magnetic field than for any other previously built room-temperature EBIT. The operation with the newly designed electron gun, drift-tube assembly, and collector results in excellent performance parameters. Requirements of low cost, low maintenance, reliable and stable operation, high-numerical-aperture optical access for spectroscopy, easy transportability, and compact size have been fulfilled. These points are crucial for providing HCIs to a variety of new experiments and are in part prerequisites for measurements at synchrotron-radiation sources and FELs. Following our first prototype, already serving as an HCI source for a Penning trap, we have commissioned three further devices, PTB-EBIT [built for the Physikalisch-Technische Bundesanstalt (PTB)], PolarX-EBIT, and Tip-EBIT, of the upgraded HC-EBIT design on which this report will mainly focus.

II. DESIGN

A. Magnetic structure and central vacuum chamber

We chose a magnetic structure with a discrete four-fold rotational symmetry, allowing for a compact overall size and sufficient space around the trap (see Fig. 1). Close access for detectors, spectrometers, pumps, and target injection is offered through four radial DN40CF ports (see Figs. 2 and 3) machined on four sides of the central cubical chamber (side length of 70 mm). Four arrays of NdFeB permanent disk magnets (dark green in Fig. 2) for each of the two poles generate the magnetic field. Each disk magnet (N45 quality, diameter of 45 mm, height of 30 mm) is magnetized along its cylinder axis. The arrays consist of three parallel stacks of three magnets each and are mounted between magnetic-steel parts connected to four flux-return rods (soft iron) and two hollow conical pole pieces (soft iron), respectively, constituting the entire yoke (light green in Fig. 2). These pole pieces guide and concentrate a nearly fully rotationally symmetric magnetic field into the trap region while they are close to magnetic saturation. The pieces are bisected along their symmetry axis and are mounted surrounding two conical vacuum chamber sections,

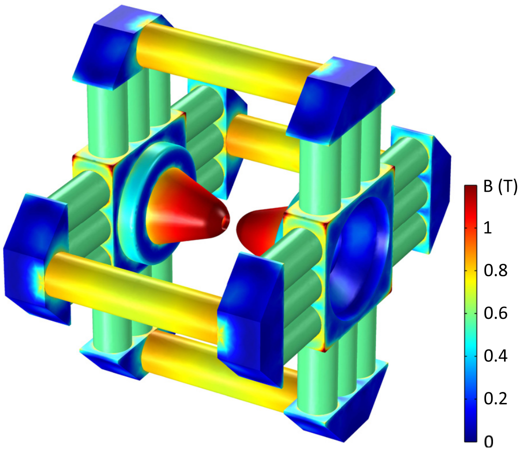
B (T)
1
0.8
0.6
0.4
0.2
0

FIG. 1. HC-EBIT magnetic structure: Color-coded absolute magnetic flux density on the outer surfaces (simulated with COMSOL[136]). Permanent magnets (appearing in green shades) produce the field, which is guided by magnetic-steel (blue shades) and soft-iron (yellow shades) parts, concentrated toward the gap at the trap center (reaching there 0.86 T), and displays its maximum at the tip (red shades) of the soft-iron pole pieces.

which contain the electron gun and the collector. These sections are welded at their respective narrow ends to the central cube, which has an inner bore of 16 mm along the trap axis and houses the drift-tube assembly. The two conical sections widen to DN63CF flanges and form together with the cube a symmetric 405-mm-long chamber. The pole pieces are fitted into conical bores on either side of the cube to reduce the magnetic gap (19 mm long, 19 mm bore diameter), while remaining outside of the vacuum. The sharp-edged geometry at their tips efficiently leaks out the field. The brittle magnets are mounted in stacked aluminum cartridges (see Fig. 3) providing mechanical protection and a water-cooling system to keep them below their Curie temperature of 80 °C during bake-out of the vacuum chamber.

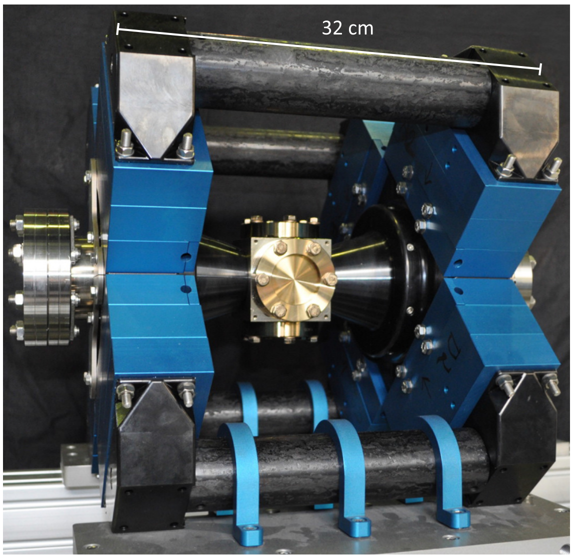

FIG. 3. Photograph of one of the commissioned magnetic structures with a vacuum chamber. Blue-anodized aluminum cartridges house the NdFeB magnets. Soft-iron and magnetic-steel elements were burnished to prevent rusting.

The whole magnetic structure has a footprint of 320 mm × 350 mm with a height of 350 mm and generates a magnetic flux density of more than 0.86 T at the trap center. Finite-element simulations (COMSOL[136]) were used to optimize the

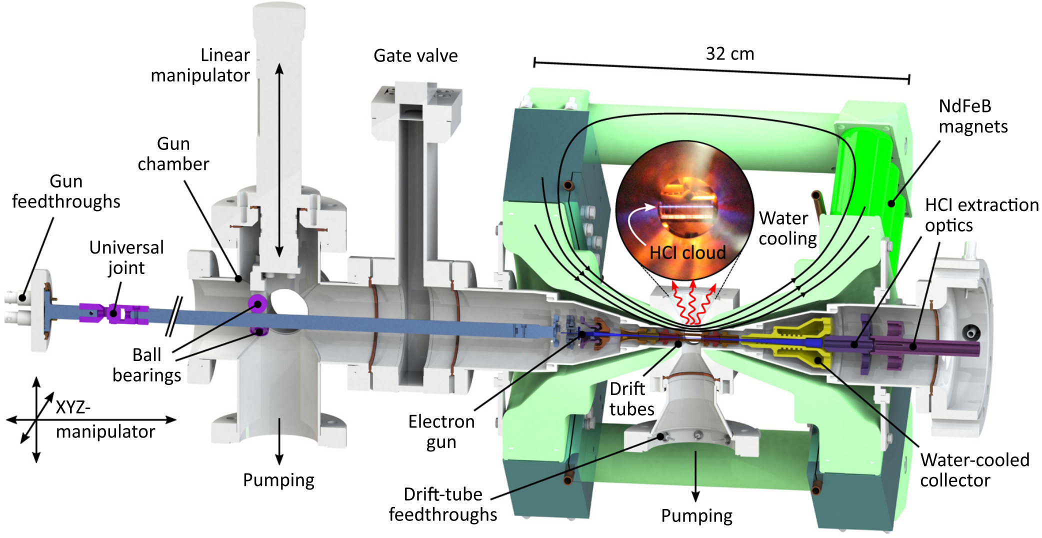
Linear manipulator
Gate valve
32 cm
NdFeB magnets
Gun chamber
Gun feedthroughs
Water cooling
HCI cloud
HCI extraction optics
Universal joint
Ball bearings
XYZ-manipulator
Drift tubes
Electron gun
Pumping
Drift-tube feedthroughs
Pumping
Water-cooled collector

FIG. 2. Simplified cross section of the HC-EBIT design. The magnetic field is generated by 72 NdFeB magnets arranged in eight arrays of 3 × 3 magnets (dark green, encased in protecting aluminum cartridges), guided and focused by soft-iron and magnetic-steel elements (light green). In the gap around the trap center, the field reaches 0.86 T. The electron gun is mounted on a long titanium rod and positioned with an XYZ-manipulator and a linear manipulator. The drift-tube assembly and the collector are mounted inside the central vacuum chamber. The inset shows a photograph of a bluish fluorescing HCI cloud excited by electron-beam impact.

setup with various simultaneous requirements in mind: maximum flux density at the trap center with zero field at the cathode position for electron beam compression according to Herrmann's theory[146] as well as sufficient flux density between the trap center and both the electron gun and collector for the beam transport. The magnetic flux density at the trap center was found to be limited by the material properties of the soft-iron pole pieces, resulting in the choice of three layers of magnets on each array. Adding a fourth layer would only increase the flux by about 3% according to our simulations. Figure 4(a) compares our simulations and the measured fields, which are slightly higher due to the underestimated permeability and saturation strength of both soft iron and magnetic steel as well as the magnetization of the NdFeB magnets. At 93.4(2.1) mm axial distance from the trap center, two locations with zero field are chosen for cathode and collector positions. At larger distances, the field reverses the direction and increases again in magnitude before decaying to zero [see Fig. 4(a)].

A further increase of the magnetic field requires in-vacuum pole pieces for a narrower bore. We follow this approach with a very similar prototype at SPring-8[147] using rectangular magnets and in-vacuum vanadium permendur pole pieces (VIC International) with a bore of only 8 mm diameter to reach field strengths of over 1 T (see Fig. 5). Measurements with this scalable apparatus and Finite Element Method Magnetics (FEMM) simulations of up to 6 magnet layers are compared in Fig. 5(a) indicating good agreement.

B. Assembling the magnetic structure

Mounting the strong permanent magnets requires particular care since forces acting on them can suddenly appear.

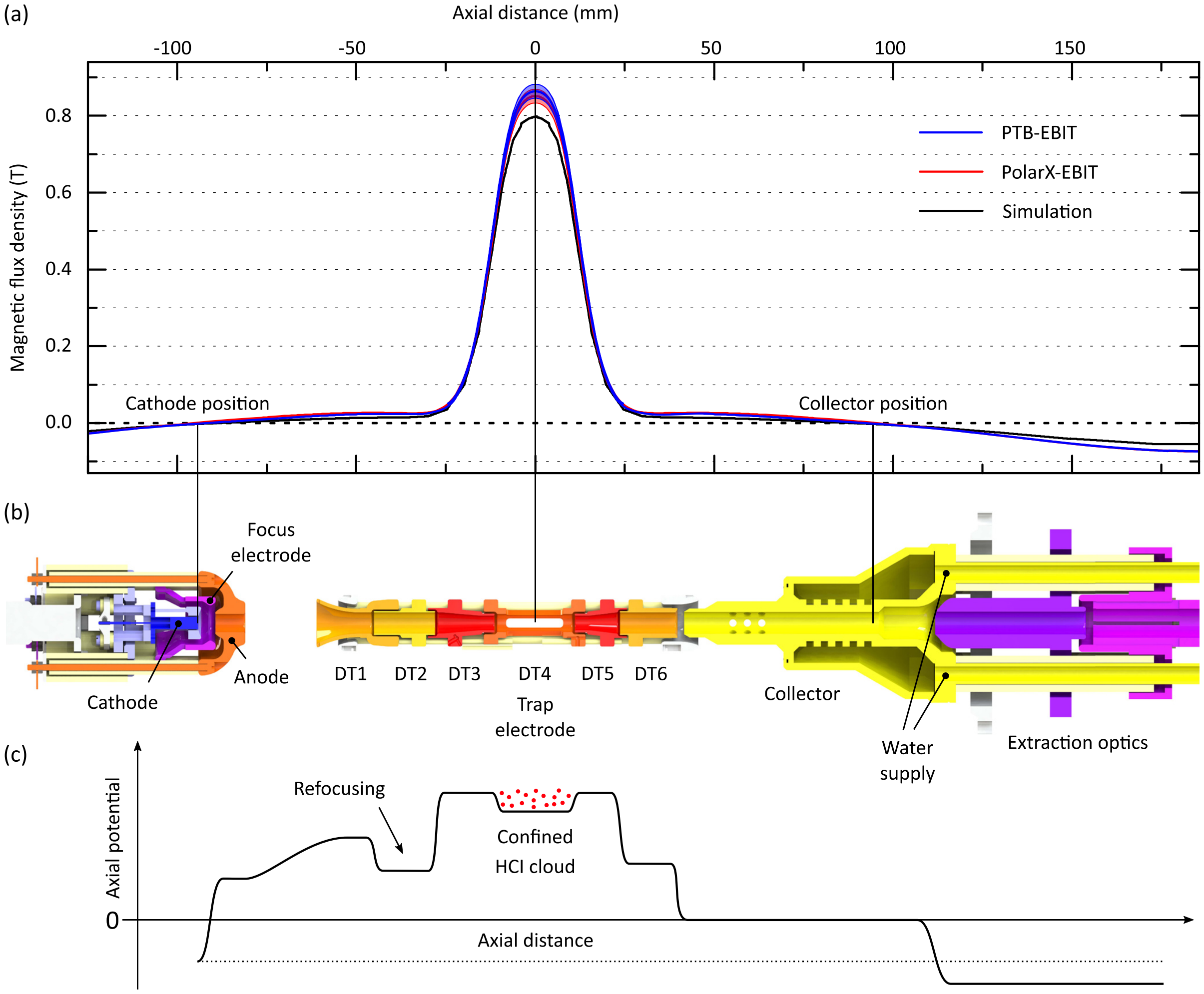

FIG. 4. Axial magnetic field and electrostatic system of the HC-EBIT design. (a) Simulated and measured magnetic flux densities on the electron beam axis are shown. The COMSOL simulations apparently underestimate the saturation magnetization and permeability of materials or the magnetization of the permanent magnets, resulting in slightly higher experimentally achieved values. The measurements (with gaussmeter 7010, F.W. Bell) match within uncertainties except for minor deviations between 30 and 110 mm from the trap center. (b) The electrostatic system including an on-axis Pierce-type electron gun, a drift-tube assembly with drift tubes 1–6 (DT1–DT6), a water-cooled collector, and ion extraction optics composed of two individual tubes for focusing is displayed. (c) An illustration of a typical axial electrostatic potential curve is shown. Here, DT1–DT3 are used to refocus the electron beam, while DT3–DT5 provide the axial ion trapping. The extraction optics electrodes are biased to a lower voltage than the cathode in order to prevent electrons from passing through.

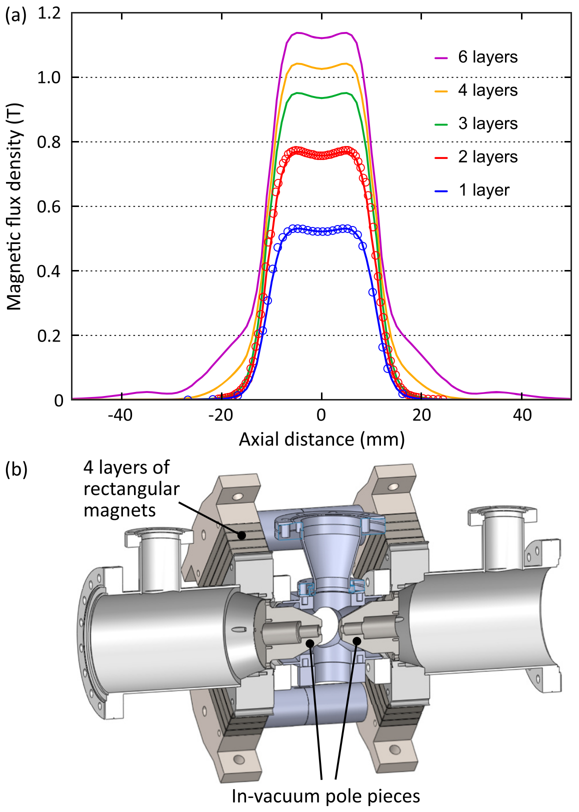

FIG. 5. SPring-8 prototype. (a) Axial magnetic field simulations (solid lines, FEMM) and measurements (circles) up to 2 magnet layers. The good agreement promises achievable magnetic flux densities of more than 1 T. Differing from the HC-EBIT design, the SPring-8 prototype uses rectangular magnets and in-vacuum pole pieces allowing for a narrower bore as shown in (b).

Their non-linear dependence on the magnetic gap easily makes them uncontrollable, causing injuries and destruction of the magnets. The magnets should only be individually unpacked and handled, and mounting of the magnetic structure should make use of tools that keep body parts far away from a potential squeezing hazard. To reduce such risks, we developed the following procedure: First, the central vacuum chamber is horizontally mounted on two holders for the DN63CF flanges which are firmly fixed to a heavy table (wooden or aluminum-top). The holders permit, when loosened, a rotation around the central axis of the vacuum chamber. Then, the bisected conical pole pieces are inserted into the grooves of the central cube and the similarly bisected square-profile yoke elements are mounted around the rim of the pole pieces with a 90° rotation between their respective cuts. The square-profile elements are screwed to the pole pieces and also to two rings welded to the vacuum chamber. The resulting stable structure protects the weld seam at the cube from a potential bending or torsion of the conical vacuum chamber extensions when, e.g., the DN63CF flanges are tightened. Prior to the mounting of the magnets, their field strengths were measured for their proper arrangement in the magnet arrays to accomplish the rotational symmetry for the magnetic field of the EBIT. Furthermore, the polarity of each magnet was clearly marked on it. The magnets can be individually handled, provided that no magnetic parts are close nearby. For the mounting procedure, we have designed a mounting tool capable of magnetically grabbing a single magnet on a magnetic-steel piston brazed to the end of a M10 threaded rod. This piston slides inside a 0.5 m-long hollow brass rod when screwing the threaded rod in or out. A grabbed magnet rests on the far end of the tool since the tool has the same outer diameter of 45 mm as the magnet. By moving the magnetic piston inwards, it slowly separates from the magnet and releases it safely. The tool can be held with two hands at a safe distance from the magnet and facilitates a careful manual insertion of each magnet into the corresponding hole of the cartridge. When the grabbed magnet approaches the yoke or the already mounted magnet beneath, eddy currents induced in the aluminum cartridges and the limited air-flow through the tight gap between the magnet and the cartridge reduce the attracting force and prevent damage when the magnet-magnet gap is closed. After partial filling of one array, repulsive forces start to appear at certain gap separations between the magnet being inserted and the layer of magnets below. The mounting tool helps one to push the magnet further in to overcome this repulsion. Then, the force immediately reverses the direction and the magnet is again pulled inwards. After completing two arrays by filling all six cartridges on one side, the outer flux-return rod is installed to complete that quarter of the magnetic structure. In this last step, the soft-iron rod, preinstalled to the magnetic-steel caps on either side, is lowered to the two magnet arrays by temporarily using long threaded rods to guide this motion. Further threaded rods are screwed through threads in the magnetic-steel caps and rest on the two topmost cartridges when the outer yoke part has slid toward the arrays. By screwing these rods out, the outer yoke part approaches the arrays further and the magnetic gap can be closed in a controlled way. After that, one proceeds to fill the cartridges on the opposite side to keep magnetic forces balanced. By rotating the whole structure as described earlier, one can always work in the horizontal direction. In principle, the stacked structure of cartridges also allows for removing possibly damaged magnets by sliding the aluminum cartridges sideways and gradually reducing the magnetic forces between the stacked magnets. However, no magnets were damaged during the assembly of all three EBITs of the new HC-EBIT design. We strongly recommend that the procedure described earlier is only performed by trained personnel following strict safety rules in order to avoid serious injuries.

C. Electron gun

1. Choice of the cathode

The strong electron beam of an EBIT, typically hundreds of milliamperes for a superconducting EBIT, can only be reliably sustained over long periods of operation by the use of thermionic dispenser cathodes. Among many available options, barium-impregnated tungsten dispenser cathodes have proven to be the most suitable cathode type for EBITs. Due to their low work function (≈2 eV), they can operate at rather low temperatures of around 1300 K and yield current emission densities of up to 10 A/cm^2. This dispenser-type cathode has been the most widely used choice in telecommunications, radar, aerospace, and related industries for decades. A depletion of barium on the emission surface is compensated by a constant replenishment from the tungsten-matrix reservoir of the dispenser cathode. This principle affords routine lifetimes of about 100 000 h of operation even at strong emission currents. The material itself is not brittle and can be machined and electron-beam welded. Molybdenum, alumina ceramic, and OFHC copper (provided it is not too close to the hot cathode) are compatible as adjacent materials inside an electron gun and do not induce poisoning of the cathode. Reliable commercial suppliers exist in the market. Compared to alternative cathode materials (e.g., IrCe or crystalline materials), barium-impregnated dispenser-type cathodes offer longer lifetimes, more stable emission behavior, resilience against experimental accidents, and a lower operation temperature. In particular, the latter advantage eases constraints on the choice of adjacent materials in the electron gun, allows for a better residual pressure there, and allows for a higher electron beam compression in a given magnetic field according to Herrmann's optical theory.[146]

2. *Pierce-geometry on-axis electron gun*

With its open structure, our new on-axis electron-gun design aims at being even more sturdy against unexpected thermal loads, voltage spikes, and discharges than our earlier models. This is particularly important for the parts that are close to the cathode since gaps have to be small. The Pierce-type[148] electron gun (shown in Fig. 6) is, despite the rotational symmetry of the electrodes around the electron beam, rotationally asymmetric to facilitate a more compact design. It employs a 3.4 mm-diameter thermionic barium-impregnated tungsten dispenser cathode (type "M" coating) with a concave spherical radius of 8.2 mm, which is clamped between two molybdenum parts. An OFHC copper anode, a molybdenum focus electrode, the cathode assembly, and a stainless-steel base are stacked along three alumina-ceramic rods [(A) in Fig. 6] with small dimensional tolerances to define the centering of the electrodes. These rods also act as spacers between the anode and base. The cathode assembly is tightened with two threaded rods to the base against alumina-ceramic tubes (B) which electrically insulate and set the correct distances. Thinner alumina-ceramic tubes (C) avoid sparkover to adjacent metal parts. The focus electrode and anode are similarly and independently clamped to the cathode assembly. The anode, focus electrode, and cathode are contacted on the back of the electron gun by shims on which wires are spot-welded. The cathode-heater filament is contacted with a triangular plate on the back of the cathode assembly through a lateral pin. All threaded rods, screws, and nuts near the cathode are made from molybdenum to resist the high temperature of the cathode of around 1400 K during operation. A crucial prerequisite for a reliable and strong long-term emission current, I_b, is a very low local residual pressure. The chosen open gun structure allows good pumping to facilitate this. The anode, with an aperture of 5 mm, is located at a distance of 5 mm in front of the cathode and controls the emission current independent of the potential difference between the cathode and trap-center electrode, determining the beam energy in the trap. Between the cathode and anode, the focus electrode compensates potential distortions to improve the beam transport. Furthermore, the focus-electrode voltage is dynamically adjusted to stabilize the emitted electron-beam current to better than $\Delta I_b/I_b \approx 10^{-4}$ on a >100 ms time scale to suppress long-term drifts when performing hour-long measurements. At the beginning of a measurement series, the gun position is carefully adjusted to optimize the current, current density, and beam transmission. For this, the electron gun is mounted on the far end of a horizontal titanium rod attached to an XYZ-manipulator by a universal joint on a DN40CF flange, also holding the high-voltage (HV) feedthroughs for the gun. The rod angle is set by a vertical, linear manipulator which supports the rod with a pivot point located roughly at the middle of the rod. Moreover, the gun can be completely retracted, sliding on ball bearings on that pivot point, into a dedicated gun chamber, which can be separated from the main chamber with a gate valve. In this setup, the on-axis electron gun has generated more than 80 mA of electron-beam current without approaching the temperature limit of the thermionic cathode.

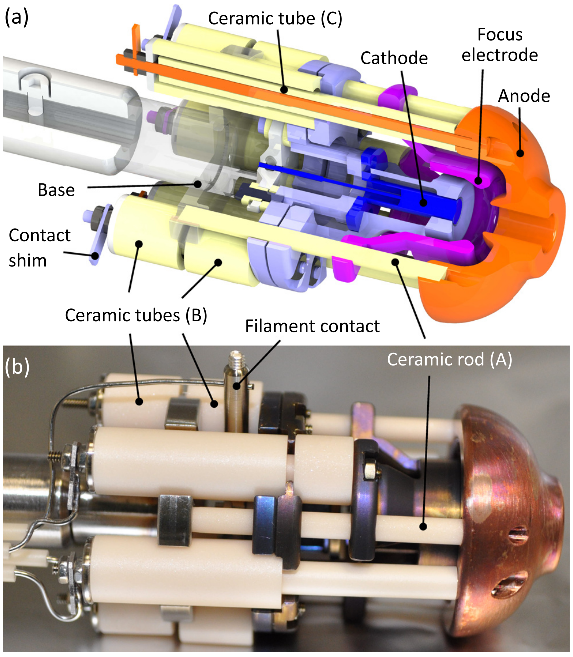

FIG. 6. Cross-sectional view (a) and photograph (b) of the Pierce-type on-axis electron gun. The electron-gun electrodes are held by a nested alumina-ceramic structure supported by a stainless-steel base on the back [transparent in (a)], providing high-voltage insulation with sufficiently large creeping distances. See the text for further details.

3. *Off-axis electron gun*

In the last decade, photoexcitation and photoionization in EBITs have become reliable techniques for investigating HCIs. The energy resolution in such studies allows one to resolve the natural line widths of the transitions involved and to study asymmetric line profiles due to quantum interference.

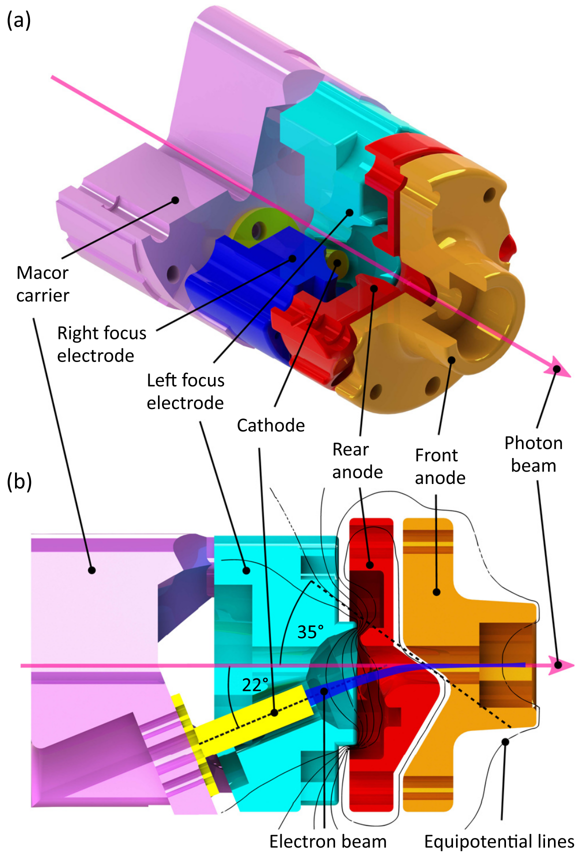

FIG. 7. Cross-sectional views of the off-axis electron gun. The cathode (yellow) points at an angle of 22° to the trap axis to allow an external photon beam to pass through the unobstructed central bore. The mirror-symmetric focus electrodes [light blue and blue in (a)] compensate for the drift of the electron beam due to the Lorentz force. Bending of the electron beam onto the trap axis is realized by splitting the anode into a rear (red) electrode and a front (orange) electrode, cut by a 35°-plane with respect to the horizontal. Simulated electrostatic potential lines (black) and electron beam trajectories (blue) are also shown in (b). See the text for further details.

Monoenergetic x-ray photon beams from both free-electron lasers[12,112,113] and synchrotron radiation sources[107–111] have been used for this purpose. Optical laser spectroscopy inside an EBIT has also been demonstrated.[103,106] Usually, the preferred method for these types of experiments is introducing the photon beam through the collector along the trap axis since a maximum overlap of the photon beam and the trapped HCI cloud is desirable. As a consequence, the photon beam is dumped onto the electron gun and, accordingly, discarded. Further disadvantages are vacuum degradation and HV problems since the photon beam can excessively produce photoelectrons at some of the electron-gun electrodes. Sputtered ions and pressure increases may damage the cathode and reduce its lifetime. Furthermore, alignment can be difficult.

To solve these problems, we have developed a novel off-axis electron gun as an alternative to the on-axis gun and equipped the PolarX-EBIT with it. Hence, a photon beam can propagate through the PolarX-EBIT without any obstructions while being axially overlapped with the trapped HCIs. For this reason, the cathode is separated from the trap axis by tilting it by an angle of 22° with respect to the horizontal plane [see Fig. 7(b)]. Directly mounted on a precisely machined Macor insulator, the cathode is located 9.5 mm in front of the anode. To optimize the deflection and focusing capability of the gun in the magnetic field, we simulated the electrostatic potentials and electron trajectories, using the software SIMION [see Figs. 7(b) and 8 for visualization of such simulations]. For steering the electron beam onto the trap axis, the anode is split into two separate electrodes by a 35°-plane with respect to the horizontal plane at the intercept of the electron beam [see Fig. 7(b)]. Whereas the rear anode is used to define the extraction potential inside the gun, the front anode is used to bend the beam into the horizontal to direct it toward the trap center. Since the electrons emerge non-coaxially to the magnetic field lines, their trajectories are deflected sideways due to the Lorentz force. To compensate for this, the focus element surrounding the cathode is vertically cut into two mirror-symmetric electrodes (left and right focus) on which different potentials are applied. Additionally, the focus electrodes are also used, similarly as for the on-axis gun, to regulate the emission current. These electrodes are mounted on the insulating Macor carrier. Owing to the high temperature of the nearby cathode, the focus electrodes are made of molybdenum. The rear and front anodes, in turn, are mounted on the focus electrodes and the Macor carrier by alumina-ceramic rods as spacers. They are made of OFHC copper to distribute the possible heat load by scattered electrons.

The central bore of the off-axis gun along the trap axis is 4 mm wide and, thus, in accordance with the requirements of typical photon beam diameters of less than 1 mm. The alignment with the aim to maximize the overlap between the photon and the electron beam for a high signal rate is eased by, first, the short trap length of our compact EBIT and, second, the capability to image the photon beam after passing through the EBIT.

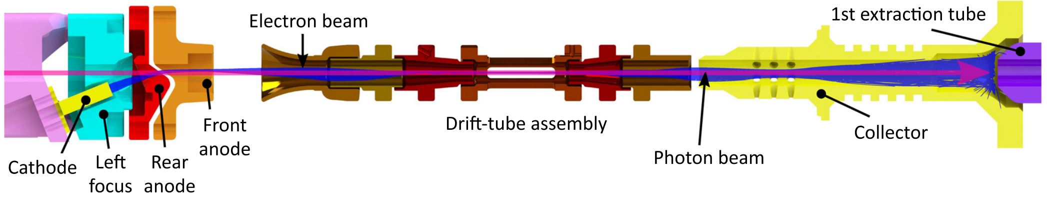

FIG. 8. Cross section through the electrostatic elements of the PolarX-EBIT. Electron trajectories are shown in blue. Due to the unobstructed trap axis, photon beams can pass through the EBIT, injected either from the gun or the collector side.

D. Drift tubes

A set of cylindrical electrodes (drift tubes) accelerates and guides the electron beam toward the collector [see Fig. 4(b)] and also shapes the axial ion-trapping potential [see Fig. 4(c)]. Six independent drift tubes (DT1–DT6, manufactured of grade 5 titanium alloy) are stacked along four alumina-ceramic rods [(A) in Fig. 9, diameter of 3 mm], which center these electrodes and terminate on either side in stainless-steel rings. Seven pairs of alumina-ceramic rods (B) (diameter of 2 mm), precisely cut to the correct length, set the different distances between the drift tubes and the stainless-steel rings as well as electrically insulate them, accounting for appropriate creeping distances. Two twisted copper wires, guided within a groove in each of the rings and slots filed on the ceramic rods (A) on either side, keep this asymmetric 100 mm-long assembly together. After assembling, the trumpet of DT1 is screwed with its outside thread into the body of DT1. Flexible silver-plated copper wires are used for connecting the drift tubes by M1.6 set screws. The wires need to be preinstalled since their electrode contact is not accessible after installation. Thin ceramic tubes (C) are used for insulating them within the 16-mm bore of the central vacuum chamber. Next, the assembly is inserted into this bore and clamped together by two stainless-steel holders on either side, pushing against the outer stainless-steel rings of the assembly. The central trap electrode (DT4) occupies the position of the maximum magnetic flux density and establishes a potential well of an effective trap length of 22 mm together with DT3 and DT5 (see Fig. 4). Four slits of 2.5 mm height by 16 mm length are aligned with the four DN40CF cube-side ports. To reduce reach-through from the ground chamber potential, the electrode apertures are covered with an electro-formed stainless-steel mesh of 2 mm × 2 mm grid size. This geometry offers an opening angle of 58° for each DN40CF port. One port is needed for HV feedthroughs and pumping. Another port is used for an atomic beam for trap loading. The two remaining ports are available for fluorescence detectors and spectrometers. Potentials applied to the first three drift tubes are tuned to optimize electron-beam focusing at the trap center [see Fig. 4(c)].

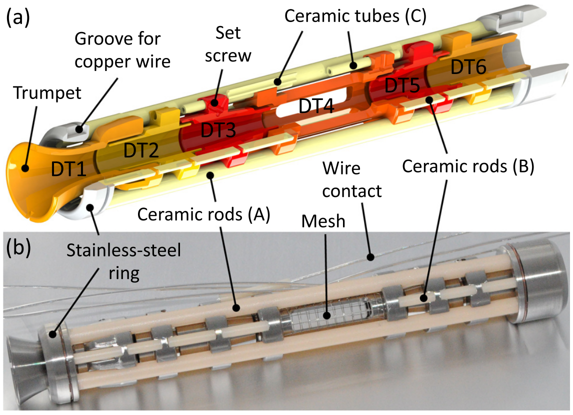

FIG. 9. Cross-sectional view (a) and photograph (b) of the drift-tube assembly. A set of six drift tubes is supported by alumina-ceramic rods and mounted between two stainless-steel rings. See the text for further details.

E. Collector

After passing the positively biased drift-tube section, the electron beam enters a region at the ground potential and is therefore slowed down. Finally, it is dumped on the inside of a hollow water-cooled collector electrode (OFHC copper) (see Figs. 4 and 10). The magnetic field strength at the collector is much lower than at the trap center, and thus the electron beam expands again and hits the wall. Behind the collector electrode, two extraction electrodes are installed. The first one has to be biased to a more negative potential than the cathode to prevent the electron beam from passing through the collector. Furthermore, both tubes are also used as ion optics for HCI extraction.

The collector is made of two copper parts, the inner collector electrode and the outer shell, enclosing a volume for cooling water. These elements and the copper pipes for the water inlet and outlet are electron-beam welded together. The collector, an aluminum mounting plate, and the two extraction tubes (OFHC copper) are stacked by using alumina-ceramic rods as spacers and two threaded rods to clamp the assembly together. Further ceramic shims and ceramic tubes around the water pipes are used for electrical insulation. Stainless-steel hydro-formed, braze-soldered flexible-bellow hoses connect the collector piping to insulated fluid feedthroughs. These feedthroughs lead the current deposited by the electron beam to the outside. The collector flange is mounted on its DN63CF side to the central vacuum chamber while it widens on the other side to DN100CF for attaching further extraction

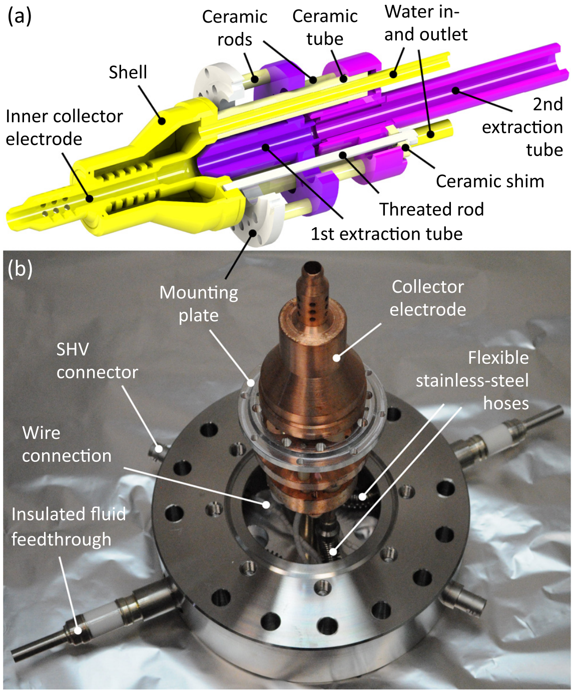

FIG. 10. Cross-sectional view (a) and photograph (b) of the collector. The water-cooled collector electrode [yellow in (a)], a mounting plate, and two extraction tubes are electrically insulated by ceramic elements against each other. Flexible stainless-steel hoses, brazed to hollow high-power feedthroughs, provide the collector with water. See the text for further details.

elements and a beamline. There, a 300 l/s turbomolecular pump (TMP) can be installed to pump the collector section from the back. Inside the central vacuum chamber, the collector assembly is mounted with the mounting plate. Two safe-high-voltage (SHV) connectors are welded on the collector flange for biasing the extraction tubes. The electrical insulation of the collector also allows for biasing it, provided a protecting enclosure is installed. However, in the current setups, it was operated very close to the ground potential by connecting it through a 10 Ω resistor or an ampere-meter measuring the current I_{col} for evaluating the transmission $T = I_{col}/I_b$. This is a key indicator for the quality of the electron beam, with typical values of $T \approx 99\%$. The missing current lost to the electron-gun anode and the six drift tubes is monitored and minimized during voltage adjustment.

F. Pumping and injection system

A low residual gas pressure is an essential prerequisite for achieving and keeping high charge states. We use a cascaded TMP system to achieve an ultra-high vacuum (UHV) at the low 10^{-9} mbar level: Four TMPs (preferably 70 l/s for the electron gun, 70 l/s for the trap, 300 l/s for the collector, and 70 l/s for the injection system, or better) share downstream a common intermediate high-vacuum stage, which is pumped by a single 70 l/s wide-range TMP, backed by an oil-free scroll pump. The use of this two-stage TMP system raises the compression ratio for H_2 by more than three orders of magnitude and prevents serious problems caused by a failure of either the intermediate TMP or one of the UHV TMPs. In the first case, the scroll pump can maintain the required backing pressure for the UHV TMPs. In the second one, the small intermediate TMP still manages to keep a vacuum in the 10^{-6} mbar range in the EBIT. Then, a vacuum-interlock safety system automatically turns off HV power supplies and the cathode heating unit. This level of protection is sufficient to prevent the cathode from permanent damage at the price of introducing the intermediate high-vacuum stage TMP. Additional protection is provided by a solenoid valve at the inlet of the scroll pump. It closes in case of a power failure and maintains, together with the forelines, a level of vacuum which is suitable for the continuing operation of the TMPs during their spin down. Again, the vacuum-interlock system immediately switches off the power supplies and also keeps them switched off when power is suddenly restored, up to their manual restart. In this way, the cathode has enough time to cool down since this process takes many minutes. Hot-cathode ion gauges are installed in the various chamber parts to monitor the pressure.

For immediate operation of the HC-EBITs after a transport between laboratories or cities, the electron gun can be isolated with gate valves in UHV in its own chamber. This protects the cathode from degradation and avoids a time-consuming re-activation after arrival. Additionally, we have installed a non-evaporable getter (NEG) pump close to the gun for the PolarX-EBIT to maintain a UHV pressure for an extended period without electrical power.

The gas-injection system has two UHV pumping stages to deliver a very low-density atomic or molecular beam to the central drift tube in order to introduce the element of choice into the EBIT. An UHV needle valve is connected to the first UHV stage, pumped by the aforementioned 70 l/s TMP. There, the pressure is typically in the range of 10^{-6} to 10^{-8} mbar. An aperture of 2 mm diameter allows the beam to enter the second UHV stage, which is pumped by the TMP attached to the central chamber. Moreover, the Tip-EBIT uses an implementation of the wire-probe method[76] in order to deliver minuscule quantities of heavy elements for ionization. The wire probe will be used for the study of rare isotopes.

III. OPERATION AND MEASUREMENTS

A. Commissioning

All devices of the HC-EBIT type showed a similar behavior during commissioning. At the beginning, the brand-new cathode is carefully heated up in a stepwise manner to the required activation temperature over a couple of days, dubbed "conditioning." This process causes a slow diffusion of the impregnants, driven by the high temperature and the concentration gradient, during which the barium aluminate reacts with some additives contained in the cathode, e.g., calcium oxide, and forms barium. Due to its low work function (≈2 eV), this substance builds a very efficient emission layer at the exterior surface of the cathode. The cathode suppliers recommend not to exceed a certain heating current since the type "M" coating evaporates at too high temperatures. At higher values, the cathode itself can be damaged. However, due to the open gun structure, the coupling through thermal radiation to the environment is relatively good and we expect to be clearly below the temperature limit. Because of the initial heating of the cathode and its environment, the pressure, measured by the gauge which is installed at the gun chamber, approaches the 10^{-7} mbar range while the pressure measured at the collector remains in the 10^{-9} mbar range. Increased ion bombardment of the cathode emission layer due to residual gas pressure removes some of the emitting barium and counteracts the diffusion process of the barium from the tungsten-matrix reservoir—initially limiting the maximum emission current.

After a few weeks of operation, the chemical-physical formation of the dispenser-cathode material has completed, the parts immediately surrounding the cathode have out-gassed, and the cathode heating can be reduced to prolong the lifetime, while maintaining the emission current. This process can be accelerated by baking the whole device while cooling the permanent magnets using the water-cooling of the protecting aluminum cartridges. After vacuum conditions have consistently improved (low 10^{-9} mbar pressure at the gun), currents of up to 80 mA for the on-axis gun and up to 30 mA for the off-axis gun could be achieved. Nonetheless, some of the commissioning measurements presented below were obtained at lower currents, either because of a higher residual gas pressure at the beginning or intentionally to achieve higher electron-beam energy resolution.

Electrical discharges between the gun electrodes can temporarily reduce or completely eliminate the emission layer. Reconditioning of the cathode layer after recovery of good vacuum conditions can be achieved, in most cases, in a matter of seconds or minutes. However, extended, strong discharges can completely sputter the emission layer or cover it with other materials from neighboring electrodes. Such an incident can require many hours or even days of reconditioning at higher cathode-heating currents, until the contaminating layers have been evaporated and a fresh barium emission layer has formed through permeation out of the reservoir. More serious problems can arise if an accidental leak occurs. In such cases, a vacuum-interlock system should instantly turn off the cathode heating and the high voltages applied to all the electrodes. Depending on how high the pressure rises during such an event and how long a high cathode temperature was maintained before restoring good vacuum conditions, several days of slow emission-current recovery can be required. In the worst case, the damage to the cathode is permanent.

1. *On-axis electron gun*

The Pierce-type electron guns operate in the space-charge limited regime. Appropriate high voltages have to be applied to the different electrodes. Typically, the focus electrode is initially biased to a more negative value than the cathode, thus completely blocking the emission. The anode voltage can be kept on ground or low positive potential of only a few hundred volts. By increasing the focus voltage, emission slowly starts and the position of the electron gun can be adjusted aiming at maximum transmission all the way through the drift tubes to the electron collector by monitoring the emission current and the collector current. A rough positioning of the gun was always sufficient to immediately measure the electron-beam current on the collector. In a second step, the current loss to the anode and the different drift tubes is minimized by fine positioning the gun and adjusting the drift-tube voltages. The reason for the anode current is essentially a partial reflection of the strongly focused electron beam by the strong magnetic-field gradient, hindering the electron beam from entering the drift-tube region. Consequently, the anode collects the largest part of the reflected beam since it is biased more positively than any other part there. Therefore, the anode current is a proxy for the quality of both the geometric alignment and the voltage adjustments. Once these steps are completed, having a typical transmission of 99% and a current loss to the anode and each drift tube well below 0.5 mA (even at emission currents of 80 mA), the anode voltage can be increased to obtain the desired electron-beam current. Possibly, the gun position, the focus voltage, and the drift tube voltages may need some readjustments then. The geometric alignment is very reproducible and hardly varies for a wide range of electron-beam energies and currents. However, for each beam energy, adjustments of the drift-tube and electron-gun potentials may be needed. Generally, also these parameters are reliably reproducible and can be maintained at constant values during long measurements.

The perveance $P = I_b/U^{3/2}$ is an important quantity to describe the relation between beam current I_b and extraction voltage U for space-charge limited, charged particle beams. In particular, it is often used to qualify the performance of electron guns. According to Child-Langmuir's law,[149,150] it is essentially determined by two geometrical quantities for a given particle beam: the diameter of the extracted beam and the distance between the cathode and anode. For our on-axis electron gun, we expect a perveance on the order of 1 μperv with the 3.4 mm-diameter cathode. However, in practice, this relation is not always fully applicable due to geometrical deviations and experimental conditions, for instance, in the presence of a magnetic field when the gun is operated in an EBIT. Figure 11 shows the emission current as a function of the electron-gun extraction voltage, i.e., the difference between anode and cathode voltages while the focus electrode is operated at the cathode potential. Fitting the data of 1.28 A cathode-heating current, the gun operating in the space-charge limited regime, we can confirm an electron-gun perveance on the order of 1 μperv. Note that the electron-beam current of the HC-EBITs, adjusted and regulated by the anode and focus-electrode voltages, respectively, is widely independent of the electron-beam energy which is determined by the voltage difference between the trap electrode and cathode. The measurement was carried out with 3.6 keV beam energy, for instance.

2. *Off-axis electron gun*

In first tests of the off-axis gun, the electrostatic deflection of the emitted electron beam was analyzed in a non-magnetic environment. In this setup, the electrons hit a phosphor-coated screen mounted in front of the gun. By changing the potentials of the electrodes, the electron beam could be steered along the horizontal and vertical directions independently. The focusing of the beam could be adjusted by changing the bias voltage of the focus electrodes. Then, the off-axis gun was mounted on an XYZ-manipulator and installed in the PolarX-EBIT. The manipulator allows positioning of the gun at the magnetic-field minimum, a crucial requirement. Starting with electrode potentials and a gun position optimized by simulations, the cathode emitted already electrons and the beam could be partially transmitted through the EBIT to the collector. After a

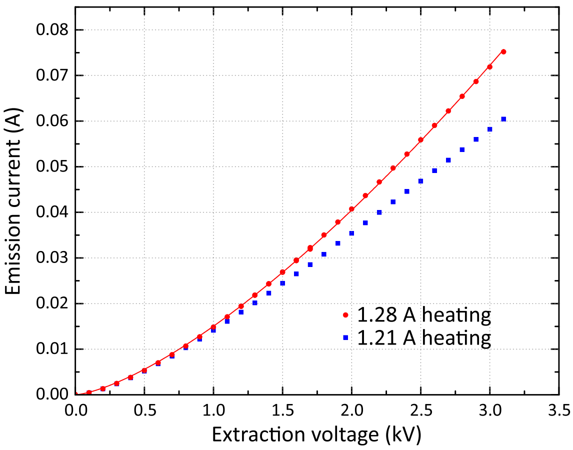

FIG. 11. Perveance measurement of the HC-EBIT on-axis electron gun. For two different cathode-heating currents, the emission current is shown as a function of the extraction voltage, i.e., the voltage difference between the anode and cathode while the focus electrode was kept on the cathode voltage. A heating with 1.21 A (blue squares) indicates emission not being fully space-charge limited. The fit function $I_b = aU^c$ yields the parameter $a = 0.78(2) \times 10^{-6}$ A/V^c and $c = 1.428(3)$ for the higher-temperature data (red circles).

manual optimization, stable beams with electron losses below 1% were achieved.

The Lorentz deflection strongly depends on the gun position. If the cathode is misaligned, compensating the beam drift calls for a voltage difference between the two focus electrodes of up to 50 V. Its optimal value does not strongly depend on the voltage difference between the cathode and anode. The potential between front and rear anodes, required for proper electron-beam steering, is in good agreement with the simulations. Positive voltages at the front anode are approximately half of those applied to the rear anode, a ratio which is not much affected by the electron-beam current. However, if the voltage difference between the cathode and rear anode is increased, i.e., essentially the beam energy is increased inside the gun, the voltage applied to the front anode also needs to be increased.

The PolarX-EBIT was operated with stable electron beams from a few hundred eV up to 8000 eV energy at the trap center. The cathode could be biased down to −4000 V, the limit of the cathode power supply. Stable space-charge limited currents of up to 30 mA were achieved, limited by the maximum voltage difference between the cathode and rear anode while a proper deflection of the electron beam onto the trap axis was still possible.

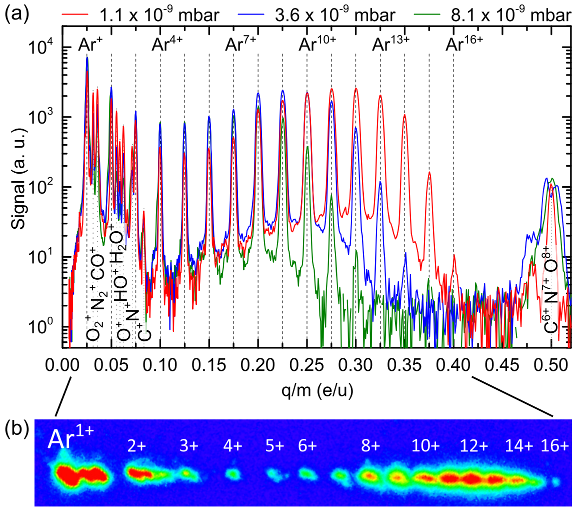

FIG. 13. (a) Microchannel-plate detector signal after charge-state separation (by the Wien filter) of extracted Ar HCI bunches using a 4 mA, 2.8 keV electron beam at different EBIT chamber pressures set by neutral Ar injection. Top labels: Ar charge states. Bottom labels: molecular and atomic ions from residual gas. (b) Charge-state distribution of a single Ar ion bunch impinging on the microchannel-plate detector. All charge states up to $q = 16$ are present at once, plus molecular and atomic ions from residual gas.

B. HCI extraction

To test ion breeding and extraction, we installed the prototype of the HC-EBITs at a beamline with charge-state separation and detection. This device has a slightly lower magnetic field of 0.74 T at the trap center, uses an older gun design, and delivered electron-beam currents of a few milliamperes at the time of the tests. Figure 12 illustrates the beamline setup. The HCIs leave the EBIT through an extraction electrode behind the collector [cf. Fig. 4(b)] and pass through a special, segmented einzel lens, dubbed Sikler lens, similar to our previous design.[151,152] The Sikler lens allows focusing and steering of the ion beam in spite of its short length. It forms a collimated beam toward a Wien-type velocity filter for separation according to the charge-to-mass ratio *q*/*m*. The electric field of the Wien filter is scanned for *q*/*m* analysis using alternatively either a Faraday cup measuring ion currents or a position-sensitive detector comprised of a microchannel plate (MCP) and a phosphor screen (PS), imaged onto a charge-coupled device camera (CCD).

For operating the EBIT in the pulsed mode, an axial trap depth of up to 100 V is applied. At the cost of a high ion temperature, this allows one to breed high charge states. By rapidly switching the trapping potential, an HCI bunch is released. We tested this mode with argon [see Figs. 13(a) and 13(b)] and isotopically enriched xenon-129 [see Fig. 14(a)]. We also carried out continuous extraction ("leaky" mode) with the prototype using a shallow axial trapping potential. Hereby, ions of the hot tail of the Maxwell-Boltzmann distribution overcome the axial trapping-potential barrier continuously. Figure 14(b) shows results for ^{129}Xe. Table I summarizes the main results of these experiments. The HCI charge-state distribution for the injected elements, and further peaks from molecular and atomic ions arising from residual gas, are visible in the figures. A superimposed, diffuse background between 0.03 and 0.06 e/u corresponds to ions not originating from the trap-center potential. With a 4 mA, 2.8 keV electron beam, Fig. 13(a) shows all Ar charge states up to He-like Ar^{16+}, the highest accessible charge state for Ar at that electron-beam energy. Figure 13(b) shows a CCD image of a single Ar HCI bunch spatially separated at low Wien-filter dispersion displaying simultaneously all produced charge states. This allowed one to quickly assess the whole charge-state distribution at once. Extraction of much heavier ^{129}Xe HCIs yielded charge states of up to $q = 37$

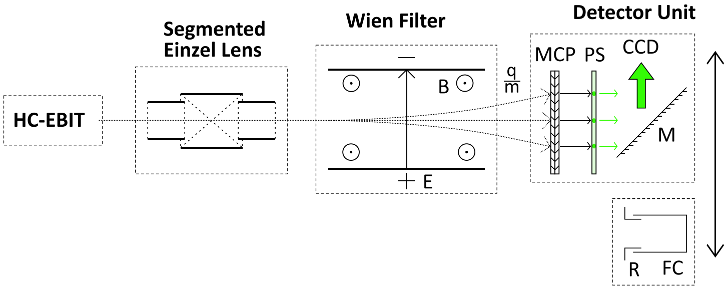

FIG. 12. HCI beamline setup. B—magnetic field, CCD—charge-coupled device camera, E—electric field, FC—Faraday cup, M—mirror, MCP—microchannel plate, PS—phosphor screen, R—repeller electrode.

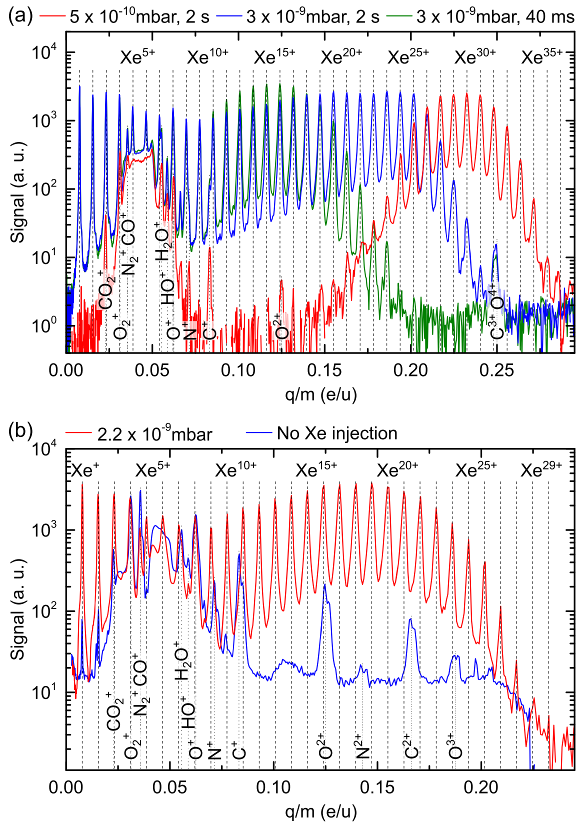

FIG. 14. Charge-state distribution of extracted ^{129}Xe. (a) Pulsed extraction for different EBIT pressures and breeding times with a 4.6 mA, 3 keV electron beam. (b) Continuous extraction with and without Xe injection employing a 4 mA, 2 keV electron beam. Top labels: Xe charge states. Bottom labels: molecular and atomic ions from residual gas.

[pulsed at 4.6 mA, 3 keV electron beam, see Fig. 14(a)] and q = 29 [leaky mode operation at 4 mA, 2 keV electron beam, see Fig. 14(b)], respectively, at sufficiently low pressures. Faraday-cup measurements yielded 100 pA of the total extracted ion current for the charge-state distribution shown in red in Fig. 14(b).

C. Dielectronic recombination

Dielectronic recombination[153] (DR) is a resonant interaction process of a free electron with an ion. The former one, having a kinetic energy of E_{kin}, is captured into an open shell of the latter one with binding energy E_B while a second, bound electron is excited to a higher level with energy difference ΔE by the released energy $E_{kin} + E_B$—fulfilling the resonance condition $\Delta E = E_{kin} + E_B$. A resulting excited, short-lived intermediate state is stabilized either by autoionization or radiative decay. *KLL* DR (notation akin to the Auger nomenclature referring to the electronic shells involved) is illustrated in Fig. 15 for an initially He-like ion. Observation of *KLL* DR is an excellent diagnostic of the charge-state distribution[143] since the energies of charge-state-resolved resonances are often well known. Hence, we carried out DR measurements on iron with the HC-EBITs, injecting an Fe-containing organometallic compound. While scanning the electron-beam energy over the *KLL* resonances, a high-purity germanium detector counted the *Kα* photons, which were emitted by stabilizing the intermediate state. Figure 16 presents results for two different HC-EBITs, the PTB-EBIT featuring the on-axis electron gun

TABLE I. Settings and results of HCI extraction obtained with the prototype.

Current (mA)	Energy (keV)	Mode	Element	Most abundant charge state	Highest charge state
4	2.8	Pulsed	Ar	12	16
4.6	3	Pulsed	Xe	30	37
4	2	Leaky	Xe	19	29

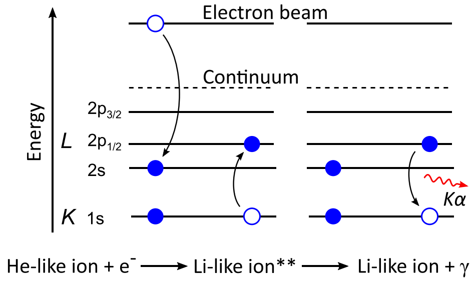

FIG. 15. Simplified energy scheme for resonant *KLL* dielectronic recombination of a He-like ion. A free electron from the beam is captured into the *L* shell while a second, bound *K*-shell electron is also excited into the *L*-shell. The intermediate hole state of the resulting Li-like ion decays through *Kα* emission.

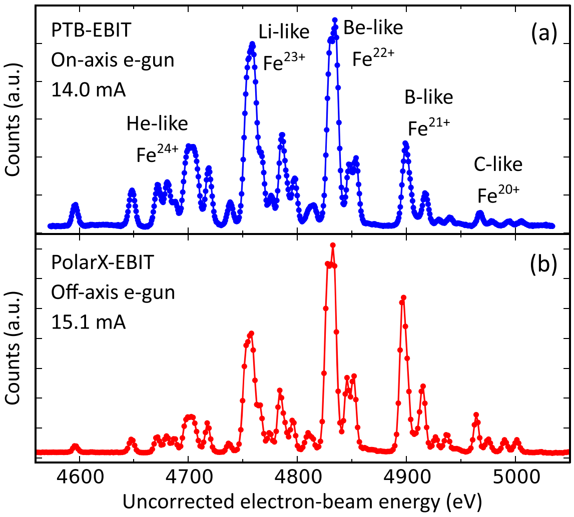

FIG. 16. Dielectronic recombination of iron ions. The *Kα* photons produced by the de-excitation of the intermediate hole states, populated by resonant dielectronic capture, were counted with a high-purity Ge detector while scanning the electron-beam energy. Shown are raw data, uncorrected for the space-charge potential and the influence of adjacent potentials. Since the *KLL* dielectronic recombination of Fe is well known,[98] the charge states can be unambiguously assigned. The upper panel shows a measurement with the PTB-EBIT and the on-axis electron gun with a 14 mA electron beam, while the lower panel shows a measurement of the PolarX-EBIT equipped with the off-axis electron gun operated with 15.1 mA.

(upper panel) and the PolarX-EBIT utilizing the novel off-axis electron gun (lower panel) with electron-beam currents of 14 mA and 15.1 mA, respectively. The appearing resonances give clear evidence of high charge states up to He-like Fe^{24+}. The HC-EBITs reach a remarkably high electron-beam energy resolution of $E/\Delta E > 1500$ for low electron-beam currents, even improving on that of previous work using evaporative cooling in cryogenic EBITs.[97,98] Arguably, this could be interpreted as a consequence of the higher residual gas pressure in the room-temperature HC-EBITs which provides low-atomic number HCIs for evaporative cooling by default.

D. Electron beam properties at the trap

1. On-axis electron gun

The size of an electron beam, compressed in a coaxial magnetic field B, can be described by the Herrmann radius r_H.[146] It contains 80% of the electron-beam current I_b, emitted by a cathode of radius r_c at a temperature T_c and in a residual magnetic field of B_c,

$$r_H = r_B\sqrt{\frac{1}{2}+\sqrt{\frac{1}{4}+\frac{8m_e k_B T_c r_c^2}{e^2B^2r_B^4}+\frac{B_c^2r_c^4}{B^2r_B^4}}}, \tag{1}$$

where r_B is the Brillouin radius

$$r_B = \sqrt{\frac{2m_eI_b}{\pi\epsilon_0 v_z e B^2}} \tag{2}$$

with the electron mass m_e, charge e, and velocity v_z, as well as the Boltzmann constant k_B.

Accordingly, in the magnetic field of 0.86 T at the trap center, as shown in Fig. 4(a), the electron-beam radius is compressed down to 72 μm, assuming a cathode temperature of 1400 K, a cathode diameter of 3.4 mm, an electron-beam current of 80 mA, an electron-beam energy of 5 keV, and a residual magnetic field at the position of the cathode of about or even below 100 μT. The latter one is a reasonable assumption since the structure of the magnetic field causes a true minimum where the field direction reverses. The minimum is only slightly shifted by the Earth's magnetic field or a weak magnetic background field in the laboratory. Photographic images of the ion cloud under electron-beam excitation (as displayed on the inset of Fig. 2) are, in spite of their limited spatial resolution, consistent with a radius below 150 μm. Based on the Herrmann radius of 72 μm, and also guided by the ionization efficiency, we estimate an approximate current density of 500 A/cm^2 and an electron density of 7×10^{11} cm^{-3} at 5 keV beam energy.

The electron-beam energy was limited by the power supplies to 10 kV so far. Higher values of up to 15 kV are likely to be possible in the future with other supplies and possibly exchanging HV feedthroughs. If required, modifications of the designs and lengths of the insulating parts can be implemented to increase creeping distances.

The energy shifts as a function of the electron-beam current observed in DR measurements by the space-charge potential of the electron beam and trapped ions at a trap depth of 10 eV were measured to be 0.397(8) eV/mA at about 2.2 keV electron-beam energy of argon *KLL* DR and 0.505(3) eV/mA at about 4.8 keV of iron *KLL* DR.

2. Off-axis electron gun

The observation of DR in argon at an electron-beam current of 10 mA while varying the nominal trap depth, i.e., the difference of the applied voltages of the central trap electrode and the two adjacent drift tubes, allows for a coarse estimate of the electron-beam radius through the electronic space-charge potential Φ_e, though Φ_e is partially compensated by the positive space-charge potential Φ_i of the trapped ions. The sum of these two contributions is the total space-charge potential $\Phi_{tot} = \Phi_e + \Phi_i$ and reduces the nominal electron-beam energy, defined by the acceleration voltage applied to the electrodes. Solving Poisson's equation by assuming, for simplicity, an infinitely long electron beam propagating coaxially to the trap axis with a top-hat charge density, the electronic space-charge potential only depends on the separation r from the axis (see also Refs. 77 and 80) and is given by

$$\Phi_e(r) = \Phi_0\left(\frac{r^2}{r_e^2} + \ln\frac{r_e^2}{r_D^2} - 1\right) \tag{3}$$

for $r \leq r_e$ and

$$\Phi_e(r) = \Phi_0 \ln\frac{r^2}{r_D^2} \tag{4}$$

for $r \geq r_e$, where r_e is the electron-beam radius, r_D is the inner radius of the cylindrical drift tube surrounding the beam, and

$$\Phi_0 = \frac{I_b}{4\pi\epsilon_0 v_z} \tag{5}$$

is the potential difference between the edge of the electron beam and the trap axis. I_b is the electron-beam current, v_z is the electron's velocity, and ϵ_0 is the vacuum permittivity.

The total space charge Φ_{tot} was determined by measuring the shifts in the nominal electron-beam energy, at which the DR resonances appear, as a function of the electron-beam current. A value of 0.462(9) eV/mA was obtained,[154] yielding a negative value of $\Phi_{tot} = -4.6$ eV for a 10 mA electron beam.

The space-charge contribution Φ_i of the trapped ions, at this constant electron-beam current of 10 mA, could be estimated by increasing the nominal trap depth from a trapping condition to its inversion and even higher, to, first, gradually reduce the number of trapped ions and, then, push transient ions out of the trap volume. In addition to the trap depth, the electron-beam energy was repeatedly scanned as the second parameter of this measurement to cover the argon *KLL* DR resonances. Figure 17 shows the $K\alpha$ fluorescence as a function of both, the nominal trap depth and the nominal electron-beam energy, calibrated with atomic structure calculations using the Flexible Atomic Code.[155] The loss of positive charges when flattening the trap, resulting in a change in the space-charge potential and, therefore, in a shift of the resonance positions on the electron-beam energy axis, is not very large until a nominal trap depth of +13(2) V when the trapped HCIs begin to escape along the trap axis. From here, the space-charge compensation is noticeably decreased and a significantly higher nominal electron-beam energy is needed to fulfill the DR

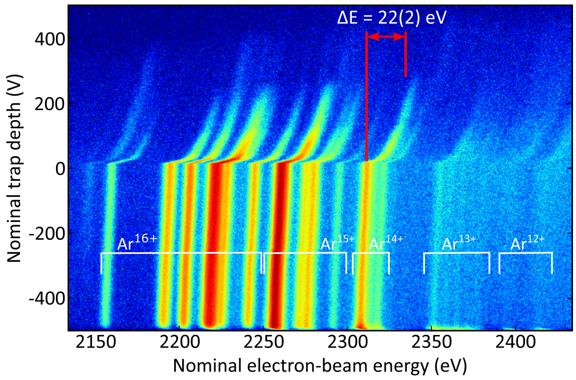

FIG. 17. Dielectronic recombination of argon ions with constant 10 mA electron-beam current as a function of the nominal electron-beam energy, defined by the applied acceleration potentials, and the nominal trap depth for storing the ions, i.e., the difference between the applied voltages of the central trap electrode and adjacent drift tubes. The resonances are assigned to their corresponding charge states. Depending on the trap depth, the number of stored ions and, consequently, their positive space-charge contribution change. Hence, the nominal electron-beam energies at which the resonances appear shift. At +13 V nominal trap depth, the trap starts losing ions, strongly affecting charge-state distribution, resonance intensities, and space-charge compensation. The space-charge contribution of the ions was determined to 22(2) eV. See the text for further details.

resonance condition. At a nominal trap depth of +250 V, only a few ions are still present and the $K\alpha$ fluorescence is very weak. The difference of the required nominal electron-beam energy between the beginning of emptying the trap at the nominal depth of +13 eV and the end of this process is determined to a value of 22(2) eV. This is our estimate for the space-charge contribution Φ_i of the ions at 10 mA electron-beam current. By subtracting this value from $\Phi_{tot} = -4.6$ eV and taking an electrostatic reach-through of 1.2 V into account, we can infer the electronic space-charge potential $\Phi_e \approx -25.4$ eV. However, the total space-charge potential within the electron-beam radius r_e is essentially flat due to the presence of the compensating ions, and therefore −25.4 eV is our assumption for $\Phi_e(r_e)$. Using Eq. (4), we calculate an upper bound for the electron-beam radius of $r_b \leq 74(30)$ μm. Using Eq. (1) from Herrmann's theory, we can confirm operating the cathode in a residual magnetic field on the order of $B_C \approx 1$ mT. This is in good agreement with the simulated and measured magnetic field, considering the off-axis geometry and a possible misalignment. According to Herrmann's theory, the radius of such a compressed electron beam only increases by less than 2 μm when increasing the electron-beam current to 30 mA. Consequently, we expect achievable current densities of more than 170 A/cm^2 with a 30 mA electron beam of the off-axis electron gun.

E. Resonant photoexcitation

Operating the transportable FLASH-EBIT[112] at FELs or synchrotron light sources has demonstrated the feasibility of the resonant photoexcitation of electronic transitions in trapped HCIs by employing the laser spectroscopy technique in the XUV and x-ray regime.[12,107–113] Tunable high-resolution monochromators allow high-precision measurements of transition energies and natural line widths. Moreover, such light sources provide femtosecond pulses. The PolarX-EBIT, with its novel off-axis electron gun, has been designed for the purpose of those experiments. We operated it at the BESSY II synchrotron in Berlin, providing a cloud of highly charged oxygen ions as a target for the monochromatized x-ray beam of beamline U49/2-PGM1. The PolarX-EBIT was set up with the electron beam collinear to the photon beam and was equipped with silicon drift detectors to detect the x-ray fluorescence signal of the HCI cloud. After coarse adjustment of the EBIT position using a YAG crystal and a phosphor screen, the spatial overlap of the ion cloud and photon beam was optimized maximizing the fluorescence yield from the resonantly excited line w (following the nomenclature of Gabriel[156]) of He-like oxygen. A typical diameter of the ion cloud of a few hundred micrometers and an even smaller focus size of the photon beam necessitated a positioning accuracy on the order of 100 micrometers. By resonantly exciting electronic transitions in He-like O^{6+} and Li-like O^{5+}, as shown in Fig. 18, we successfully demonstrated the application of a room-temperature EBIT for high-resolution x-ray laser spectroscopy. Details on the measurement campaign and its results will be published elsewhere.

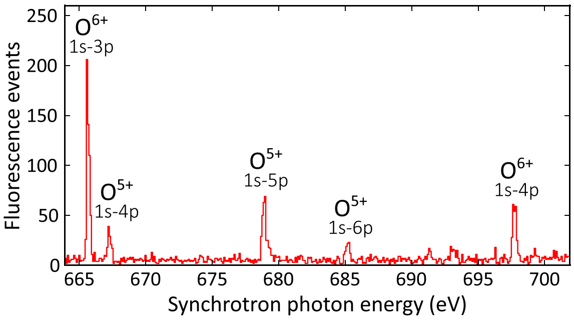

FIG. 18. Resonant photoexcitation of electronic transitions in highly charged oxygen. The number of fluorescence events, recorded with two silicon drift detectors, is shown as a function of the photon beam energy. Five resonances of He- and Li-like oxygen are observed.

IV. APPLICATIONS

Compared to conventional designs based on a superconducting magnet, requiring either a supply of liquid He or the continuous operation of cryocoolers, an HC-EBIT has a much reduced cost of construction and operation. It achieves, in spite of its compact size, the functionality of a traditional superconducting EBIT in many aspects. A large solid angle for detectors compensates for the lower electron currents and shorter trap dimensions to some degree. Mechanical vibrations from cryocoolers are eliminated. For many experiments in which an electron-beam energy below 10 keV and current below 100 mA are sufficient, an HC-EBIT can be employed more conveniently than its larger relatives. With the presently tested parameters, one can expect to produce and study up to H-like iron and He-like or Li-like ions up to Xe.

Once adjusted for an experiment, the HC-EBITs have demonstrated stable operation over months without readjustment. This renders these EBITs particularly attractive for the use as a pulsed or continuous HCI source. For instance, the prototype already successfully delivers HCIs for the Penning-trap experiment ALPHATRAP[121] aiming at the g-factor determination of the bound electron, the PTB-EBIT will provide HCIs for a cryogenic Paul trap to carry out quantum logic spectroscopy testing HCI-based optical atomic clock applications, and the Tip-EBIT is equipped with a wire-probe[76] for rare-isotope injection to supply those HCIs to the Penning trap PENTATRAP[119] where precision mass measurements will be performed.

For spectroscopic applications, the HC-EBITs offer excellent optical access with a large opening angle along the trap axis. Optical, vacuum ultraviolet, and x-ray detectors as well as optics for spectrometers all can be mounted at a close distance of only a few centimeters from the HCI cloud. This proximity and the subsequently possible large solid angles are more troublesome to achieve in superconducting EBITs due to the thermal shielding of the cryogenic parts. Similarly, it seems easier to adopt other EBIT techniques like the wire-probe method[76] for rare-isotope studies. If the desired charge state can be achieved and signal intensity is sufficing, the seemingly disadvantageous low electron-beam current provides a higher resolution since the electron-beam energy spread Φ_0 due to the electronic space charge [see Eq. (5)] is reduced and the HCIs are less heated, resulting in a reduced Doppler broadening.

Moreover, the PolarX-EBIT, now installed at the PETRA III synchrotron, was specifically developed for measurement campaigns at synchrotron or FEL facilities, providing HCIs as the target for x-ray photons. Dedicated to this purpose, we have designed and built a unique off-axis electron gun which allows for clear through access along the axially extended HCI cloud. An external photon beam can pass through the EBIT without being blocked and being available for a downstream experiment, facilitating the operation of the EBIT in a parasitic mode with negligible transmission loss. Photon-energy calibration based on HCIs and photon-polarization diagnostics through the anisotropic angular emission become possible with the potential of providing an atomic absolute wavelength standard in this spectral region. The transport and installation of these compact machines are much more convenient than that of a large superconducting EBIT such as FLASH-EBIT,[112] and space requirements at a photon beamline are significantly relaxed.

V. CONCLUSION

In this paper, we have introduced the Heidelberg Compact EBITs (HC-EBIT) as a novel class of compact room-temperature devices. With possible electron-beam energies of up to 10 keV, more than 80 mA electron-beam current, and radial and axial access to the trapped HCIs, the design has proven its suitability for studies of H-like HCIs up to Fe, He-like and Li-like HCIs up to Xe, as well as all intermediate charge states of heavy elements. Featuring the novel off-axis gun, the operation at synchrotron and FEL light sources allows for innovative experiments with advanced photon-beam diagnostics based on atomic systems.

The HC-EBITs should provide reliable access to HCIs for a wide range of experiments, requiring much less expertise for its use, greatly reducing the investment and cost of operation. Three devices, PTB-EBIT, PolarX-EBIT, and Tip-EBIT, as well as the prototype are in operation. Three more are currently under construction. The HC-EBITs have already shown a performance competitive with fully fledged superconducting EBITs in various applications. We are keen to share our design with other research groups to facilitate new applications of HCIs in, e.g., atomic physics, astrophysics, surface science, and fundamental research.

ACKNOWLEDGMENTS

For their expertise and competent fabrication of numerous parts, we gratefully acknowledge the MPIK engineering design office headed by Frank Müller, the MPIK mechanical workshop led by Thorsten Spranz, the MPIK mechanical apprenticeship workshop led by Stefan Flicker and Florian Säubert, and the MPIK electronics apprenticeship workshop as well as electronics workshop with Jochen Stephan and Thomas Busch. Likewise, we acknowledge the PTB scientific instrumentation department 5.5 headed by Frank Löffler; in particular, we thank Stephan Metschke. We also appreciate expeditious technical help by Christian Kaiser. Financial support was provided by the Max-Planck-Gesellschaft, in particular, through IMPRS-PTFS and IMPRS-QD, the Physikalisch-Technische Bundesanstalt, the Bundesministerium für Bildung und Forschung through Project No. 05K13SJ2, the Deutsche Forschungsgemeinschaft through SFB 1225 ISOQUANT and No. SCHM2678/5-1, and JSPS Grants-in-Aid for Scientific Research through Nos. 24740278 and 15K04707.

[1] A. M. Bykov, F. B. S. Paerels, and V. Petrosian, Space Sci. Rev. **134**, 141 (2008).
[2] C. M. Lisse, D. J. Christian, K. Dennerl, K. J. Meech, R. Petre, H. A. Weaver, and S. J. Wolk, Science **292**, 1343 (2001).
[3] H. Collaboration, Nature **551**, 478–480 (2017).
[4] J. M. Shull, B. D. Smith, and C. W. Danforth, Astrophys. J. **759**, 23 (2012).
[5] C. W. Danforth and J. M. Shull, Astrophys. J. **679**, 194 (2008).
[6] F. Nicastro, S. Mathur, and M. Elvis, Science **319**, 55 (2008).
[7] W. Grotian, Naturwissenschaften **27**, 214 (1939).
[8] B. Edlén, Z. Astrophys. **22**, 30 (1943).
[9] B. Edlén, Physica **13**, 545 (1947).
[10] P. Beiersdorfer, Annu. Rev. Astron. Astrophys. **41**, 343 (2003).
[11] P. Beiersdorfer, K. R. Boyce, G. V. Brown, H. Chen, S. M. Kahn, R. L. Kelley, M. May, R. E. Olson, F. S. Porter, C. K. Stahle, and W. A. Tillotson, Science **300**, 1558 (2003).
[12] S. Bernitt, G. V. Brown, J. K. Rudolph, R. Steinbrügge, A. Graf, M. Leutenegger, S. W. Epp, S. Eberle, K. Kubiček, V. Mäckel, M. C. Simon, E. Träbert, E. W. Magee, C. Beilmann, N. Hell, S. Schippers, A. Müller, S. M. Kahn, A. Surzhykov, Z. Harman, C. H. Keitel, J. Clementson, F. S. Porter, W. Schlotter, J. J. Turner, J. Ullrich, P. Beiersdorfer, and J. R. C. López-Urrutia, Nature **492**, 225 (2012).
[13] C. Shah, S. Dobrodey, S. Bernitt, R. Steinbrügge, J. R. C. López-Urrutia, L. Gu, and J. Kaastra, Astrophys. J. **833**, 52 (2016).
[14] S. Suckewer, E. Hinnov, S. Cohen, M. Finkenthal, and K. Sato, Phys. Rev. A **26**, 1161 (1982).
[15] J. R. Kaufman, V. Kaufman, J. Sugar, T. L. Pittman, and W. L. Rowan, Phys. Rev. A **27**, 1721 (1983).
[16] B. Edlén, Phys. Scr. **T8**, 5 (1984).
[17] M. Finkenthal, R. E. Bell, H. W. Moos, and T. Group, J. Appl. Phys. **56**, 2012 (1984).
[18] P. Beiersdorfer, T. Phillips, V. L. Jacobs, K. W. Hill, M. Bitter, S. von Goeler, and S. M. Kahn, Astrophys. J. **409**, 846 (1993).

[19] A. Iwamae, M. Atake, A. Sakaue, R. Katai, M. Goto, and S. Morita, Phys. Plasmas **14**, 042504 (2007).

[20] P. Beiersdorfer, G. V. Brown, J. Clementson, J. Dunn, K. Morris, E. Wang, R. L. Kelley, C. A. Kilbourne, F. S. Porter, M. Bitter, R. Feder, K. W. Hill, D. Johnson, and R. Barnsley, Rev. Sci. Instrum. **81**, 10E323 (2010).

[21] D. J. Hoarty, P. Allan, S. F. James, C. R. D. Brown, L. M. R. Hobbs, M. P. Hill, J. W. O. Harris, J. Morton, M. G. Brookes, R. Shepherd, J. Dunn, H. Chen, E. Von Marley, P. Beiersdorfer, H. K. Chung, R. W. Lee, G. Brown, and J. Emig, Phys. Rev. Lett. **110**, 265003 (2013).

[22] A. S. Rosen, M. L. Reinke, J. E. Rice, A. E. Hubbard, and J. W. Hughes, J. Phys. B: At., Mol. Opt. Phys. **47**, 105701 (2014).

[23] P. Beiersdorfer, J. Phys. B: At., Mol. Opt. Phys. **48**, 144017 (2015).

[24] P. Beiersdorfer, J. Clementson, K. Widmann, M. Bitter, K. W. Hill, D. Johnson, R. Barnsley, H. K. Chung, and U. I. Safronova, AIP Conf. Proc. **1811**, 190001 (2017).

[25] V. M. Shabaev, J. Phys. B: At., Mol. Opt. Phys. **27**, 5825 (1994).

[26] V. M. Shabaev, M. Tomaselli, T. Kühl, A. N. Artemyev, and V. A. Yerokhin, Phys. Rev. A **56**, 252 (1997).

[27] I. I. Tupitsyn, V. M. Shabaev, J. R. Crespo López-Urrutia, I. Draganić, R. Soria Orts, and J. Ullrich, Phys. Rev. A **68**, 022511 (2003).

[28] M. Vogel and W. Quint, Ann. Phys. **525**, 505 (2013).

[29] S. Sturm, F. Köhler, J. Zatorski, A. Wagner, Z. Harman, G. Werth, W. Quint, C. H. Keitel, and K. Blaum, Nature **506**, 467 (2014).

[30] F. Köhler, S. Sturm, A. Kracke, G. Werth, W. Quint, and K. Blaum, J. Phys. B: At., Mol. Opt. Phys. **48**, 144032 (2015).

[31] F. Köhler, K. Blaum, M. Block, S. Chenmarev, S. Eliseev, D. A. Glazov, M. Goncharov, J. Hou, A. Kracke, D. A. Nesterenko, Y. N. Novikov, W. Quint, E. M. Ramirez, V. M. Shabaev, S. Sturm, A. V. Volotka, and G. Werth, Nat. Commun. **7**, 10246 (2016).

[32] I. Klaft, S. Borneis, T. Engel, B. Fricke, R. Grieser, G. Huber, T. Kühl, D. Marx, R. Neumann, S. Schröder, P. Seelig, and L. Völker, Phys. Rev. Lett. **73**, 2425 (1994).

[33] P. Seelig, S. Borneis, A. Dax, T. Engel, S. Faber, M. Gerlach, C. Holbrow, G. Huber, T. Kühl, D. Marx, K. Meier, P. Merz, W. Quint, F. Schmitt, M. Tomaselli, L. Völker, H. Winter, M. Würtz, K. Beckert, B. Franzke, F. Nolden, H. Reich, M. Steck, and T. Winkler, Phys. Rev. Lett. **81**, 4824 (1998).

[34] A. Gumberidze, T. Stöhlker, D. Banaś, K. Beckert, P. Beller, H. F. Beyer, F. Bosch, S. Hagmann, C. Kozhuharov, D. Liesen, F. Nolden, X. Ma, P. H. Mokler, M. Steck, D. Sierpowski, and S. Tashenov, Phys. Rev. Lett. **94**, 223001 (2005).

[35] S. Sturm, A. Wagner, B. Schabinger, J. Zatorski, Z. Harman, W. Quint, G. Werth, C. H. Keitel, and K. Blaum, Phys. Rev. Lett. **107**, 023002 (2011).

[36] K. Kubiček, P. H. Mokler, V. Mäckel, J. Ullrich, and J. R. C. López-Urrutia, Phys. Rev. A **90**, 032508 (2014).

[37] S. Schiller, Phys. Rev. Lett. **98**, 180801 (2007).

[38] J. C. Berengut, V. A. Dzuba, and V. V. Flambaum, Phys. Rev. Lett. **105**, 120801 (2010).

[39] J. C. Berengut, V. A. Dzuba, V. V. Flambaum, and A. Ong, Phys. Rev. Lett. **106**, 210802 (2011).

[40] J. C. Berengut, V. A. Dzuba, and V. V. Flambaum, Phys. Rev. A **84**, 054501 (2011).

[41] J. C. Berengut, V. A. Dzuba, V. V. Flambaum, and A. Ong, Phys. Rev. Lett. **109**, 070802 (2012).

[42] V. A. Dzuba, A. Derevianko, and V. V. Flambaum, Phys. Rev. A **86**, 054502 (2012).

[43] V. Yudin, A. Taichenachev, and A. Derevianko, Phys. Rev. Lett. **113**, 233003 (2014).

[44] M. Safronova, V. Dzuba, V. Flambaum, U. Safronova, S. Porsev, and M. Kozlov, Phys. Rev. Lett. **113**, 030801 (2014).

[45] M. S. Safronova, V. A. Dzuba, V. V. Flambaum, U. I. Safronova, S. G. Porsev, and M. G. Kozlov, Phys. Rev. A **90**, 042513 (2014).

[46] M. S. Safronova, V. A. Dzuba, V. V. Flambaum, U. I. Safronova, S. G. Porsev, and M. G. Kozlov, Phys. Rev. A **90**, 052509 (2014).

[47] A. Ong, J. C. Berengut, and V. V. Flambaum, *Fundamental Physics in Particle Traps, Springer Tracts in Modern Physics* (Springer, Berlin, Heidelberg, 2014), pp. 293–314.

[48] V. A. Dzuba, V. V. Flambaum, and H. Katori, Phys. Rev. A **91**, 022119 (2015).

[49] V. A. Dzuba, M. S. Safronova, U. I. Safronova, and V. V. Flambaum, Phys. Rev. A **92**, 060502 (2015).

[50] N. S. Oreshkina, S. M. Cavaletto, N. Michel, Z. Harman, and C. H. Keitel, Phys. Rev. A **96**, 030501 (2017).

[51] J. C. Berengut, V. A. Dzuba, V. V. Flambaum, and A. Ong, Phys. Rev. A **86**, 022517 (2012).

[52] V. A. Dzuba, A. Derevianko, and V. V. Flambaum, Phys. Rev. A **86**, 054501 (2012).

[53] V. A. Dzuba, A. Derevianko, and V. V. Flambaum, Phys. Rev. A **87**, 029906 (2013).

[54] A. Derevianko, V. A. Dzuba, and V. V. Flambaum, Phys. Rev. Lett. **109**, 180801 (2012).

[55] A. D. Ludlow, M. M. Boyd, J. Ye, E. Peik, and P. Schmidt, Rev. Mod. Phys. **87**, 637 (2015).

[56] J. R. C. López-Urrutia, J. Phys.: Conf. Ser. **723**, 012052 (2016).

[57] Y.-m. Yu and B. K. Sahoo, Phys. Rev. A **94**, 062502 (2016).

[58] A. Windberger, J. Crespo López-Urrutia, H. Bekker, N. Oreshkina, J. Berengut, V. Bock, A. Borschevsky, V. Dzuba, E. Eliav, Z. Harman, U. Kaldor, S. Kaul, U. Safronova, V. Flambaum, C. Keitel, P. Schmidt, J. Ullrich, and O. Versolato, Phys. Rev. Lett. **114**, 150801 (2015).

[59] G. Kraft, *The Physics of Multiply and Highly Charged Ions* (Springer, Dordrecht, 2003), pp. 149–196.

[60] S. S. Harilal, B. O'Shay, M. S. Tillack, Y. Tao, R. Paguio, A. Nikroo, and C. A. Back, J. Phys. D: Appl. Phys. **39**, 484 (2006).

[61] G. O'Sullivan, B. Li, R. D'Arcy, P. Dunne, P. Hayden, D. Kilbane, T. McCormack, H. Ohashi, F. O'Reilly, P. Sheridan, E. Sokell, C. Suzuki, and T. Higashiguchi, J. Phys. B: At., Mol. Opt. Phys. **48**, 144025 (2015).

[62] A. Windberger, F. Torretti, A. Borschevsky, A. Ryabtsev, S. Dobrodey, H. Bekker, E. Eliav, U. Kaldor, W. Ubachs, R. Hoekstra, J. R. Crespo López-Urrutia, and O. O. Versolato, Phys. Rev. A **94**, 012506 (2016).

[63] F. Torretti, A. Windberger, A. Ryabtsev, S. Dobrodey, H. Bekker, W. Ubachs, R. Hoekstra, E. V. Kahl, J. C. Berengut, J. R. C. López-Urrutia, and O. O. Versolato, Phys. Rev. A **95**, 042503 (2017).

[64] O. Heil, Electron. Ind. **2**, 81 (1946).

[65] L. M. Field, K. Spangenberg, and R. Helm, Electr. Commun. **24**, 108 (1947).

[66] J. R. Pierce, *Theory and Design of Electron Beams*, 2nd ed. (D. Van Nostrand Company, 1954).

[67] E. D. Donets, V. I. Ilyushchenko, and V. A. Alpert, in *Proceedings of the 1st International Conference on Ion Source* (1970), p. 635.

[68] E. D. Donets, Nucl. Instrum. Methods Phys. Res., Sect. B **9**, 522 (1985).

[69] E. D. Donets, Rev. Sci. Instrum. **61**, 225 (1990).

[70] J. Arianer, E. Baron, M. Brient, A. Cabrespine, A. Liebe, A. Sérafini, and T. Ton That, Nucl. Instrum. Methods **124**, 157 (1975).

[71] J. Arianer and C. Goldstein, IEEE Trans. Nucl. Sci. **23**, 979 (1976).

[72] R. E. Marrs, Phys. Rev. Lett. **60**, 1715 (1988).

[73] M. A. Levine, R. E. Marrs, J. R. Henderson, D. A. Knapp, and M. B. Schneider, Phys. Scr. **T22**, 157 (1988).

[74] M. A. Levine, R. E. Marrs, J. N. Bardsley, P. Beiersdorfer, C. L. Bennett, M. H. Chen, T. Cowan, D. Dietrich, J. R. Henderson, D. A. Knapp, A. Osterheld, B. M. Penetrante, M. B. Schneider, and J. H. Scofield, Nucl. Instrum. Methods Phys. Res., Sect. B **43**, 431 (1989).

[75] M. Trinczek, A. Werdich, V. Mironov, P. Guo, A. J. González Martínez, J. Braun, J. R. Crespo López-Urrutia, and J. Ullrich, Nucl. Instrum. Methods Phys. Res., Sect. B **251**, 289 (2006).

[76] S. R. Elliott and R. E. Marrs, Nucl. Instrum. Methods Phys. Res., Sect. B **100**, 529 (1995).

[77] B. M. Penetrante, J. N. Bardsley, D. DeWitt, M. Clark, and D. Schneider, Phys. Rev. A **43**, 4861 (1991).

[78] J. D. Gillaspy, J. Phys. B: At., Mol. Opt. Phys. **34**, R93 (2001).

[79] *The Physics of Multiply and Highly Charged Ions*, edited by F. J. Currell (Springer, The Netherlands, Dordrecht, 2003).

[80] F. Currell and G. Fussmann, IEEE Trans. Plasma Sci. **33**, 1763 (2005).

[81] C. A. Morgan, F. G. Serpa, E. Takács, E. S. Meyer, J. D. Gillaspy, J. Sugar, J. R. Roberts, C. M. Brown, and U. Feldman, Phys. Rev. Lett. **74**, 1716 (1995).

[82] J. R. Crespo López-Urrutia, P. Beiersdorfer, D. W. Savin, and K. Widmann, Phys. Rev. Lett. **77**, 826 (1996).

[83] F. G. Serpa, E. W. Bell, E. S. Meyer, J. D. Gillaspy, and J. R. Roberts, Phys. Rev. A **55**, 1832 (1997).

[84] J. R. Crespo López-Urrutia, P. Beiersdorfer, D. W. Savin, and K. Widmann, Phys. Rev. A **58**, 238 (1998).

[85] J. R. Crespo López-Urrutia, P. Beiersdorfer, K. Widmann, B. B. Birkett, A.-M. Mårtensson-Pendrill, and M. G. H. Gustavsson, Phys. Rev. A **57**, 879 (1998).

[86] S. B. Utter, P. Beiersdorfer, and G. V. Brown, Phys. Rev. A **61**, 030503 (2000).

[87] J. V. Porto, I. Kink, and J. D. Gillaspy, Phys. Rev. A **61**, 054501 (2000).

[88] J. V. Porto, I. Kink, and J. D. Gillaspy, Phys. Rev. A **73**, 039906 (2006).

[89] P. Beiersdorfer, S. B. Utter, K. L. Wong, J. R. Crespo López-Urrutia, J. A. Britten, H. Chen, C. L. Harris, R. S. Thoe, D. B. Thorn, E. Träbert, M. G. H. Gustavsson, C. Forssén, and A.-M. Mårtensson-Pendrill, Phys. Rev. A **64**, 032506 (2001).

[90] H. Watanabe, D. Crosby, F. J. Currell, T. Fukami, D. Kato, S. Ohtani, J. D. Silver, and C. Yamada, Phys. Rev. A **63**, 042513 (2001).

[91] I. Draganić, J. R. Crespo López-Urrutia, R. DuBois, S. Fritzsche, V. M. Shabaev, R. S. Orts, I. I. Tupitsyn, Y. Zou, and J. Ullrich, Phys. Rev. Lett. **91**, 183001 (2003).

[92] K. Hosaka, D. N. Crosby, K. Gaarde-Widdowson, C. J. Smith, J. D. Silver, T. Kinugawa, S. Ohtani, and E. G. Myers, Phys. Rev. A **69**, 011802 (2004).

[93] R. S. Orts, Z. Harman, J. R. C. López-Urrutia, A. N. Artemyev, H. Bruhns, A. J. G. Martínez, U. D. Jentschura, C. H. Keitel, A. Lapierre, V. Mironov, V. M. Shabaev, H. Tawara, I. I. Tupitsyn, J. Ullrich, and A. V. Volotka, Phys. Rev. Lett. **97**, 103002 (2006).

[94] R. Soria Orts, J. R. Crespo López-Urrutia, H. Bruhns, A. J. González Martínez, Z. Harman, U. D. Jentschura, C. H. Keitel, A. Lapierre, H. Tawara, I. I. Tupitsyn, J. Ullrich, and A. V. Volotka, Phys. Rev. A **76**, 052501 (2007).

[95] J. C. López-Urrutia, Can. J. Phys. **86**, 111 (2008).

[96] G. Y. Liang, T. M. Baumann, J. R. C. López-Urrutia, S. W. Epp, H. Tawara, A. Gonchar, P. H. Mokler, G. Zhao, and J. Ullrich, Astrophys. J. **696**, 2275 (2009).

[97] C. Beilmann, P. H. Mokler, S. Bernitt, C. H. Keitel, J. Ullrich, J. R. C. López-Urrutia, and Z. Harman, Phys. Rev. Lett. **107**, 143201 (2011).

[98] C. Beilmann, Z. Harman, P. H. Mokler, S. Bernitt, C. H. Keitel, J. Ullrich, and J. R. C. López-Urrutia, Phys. Rev. A **88**, 062706 (2013).

[99] T. M. Baumann, Z. Harman, J. Stark, C. Beilmann, G. Liang, P. H. Mokler, J. Ullrich, and J. R. Crespo López-Urrutia, Phys. Rev. A **90**, 052704 (2014).

[100] H. Bekker, A. Windberger, O. O. Versolato, M. Binder, R. Klawitter, J. R. C. López-Urrutia, A. Lapierre, S. Schwarz, and T. M. Baumann, AIP Conf. Proc. **1640**, 109 (2015).

[101] H. Bekker, O. O. Versolato, A. Windberger, N. S. Oreshkina, R. Schupp, T. M. Baumann, Z. Harman, C. H. Keitel, P. O. Schmidt, J. Ullrich, and J. R. C. López-Urrutia, J. Phys. B: At., Mol. Opt. Phys. **48**, 144018 (2015).

[102] A. Lapierre, U. D. Jentschura, J. R. Crespo López-Urrutia, J. Braun, G. Brenner, H. Bruhns, D. Fischer, A. J. González Martínez, Z. Harman, W. R. Johnson, C. H. Keitel, V. Mironov, C. J. Osborne, G. Sikler, R. Soria Orts, V. Shabaev, H. Tawara, I. I. Tupitsyn, J. Ullrich, and A. Volotka, Phys. Rev. Lett. **95**, 183001 (2005).

[103] V. Mäckel, R. Klawitter, G. Brenner, J. R. Crespo López-Urrutia, and J. Ullrich, Phys. Rev. Lett. **107**, 143002 (2011).

[104] G. Brenner, J. R. C. López-Urrutia, Z. Harman, P. H. Mokler, and J. Ullrich, Phys. Rev. A **75**, 032504 (2007).

[105] G. Brenner, J. R. C. López-Urrutia, S. Bernitt, D. Fischer, R. Ginzel, K. Kubiček, V. Mäckel, P. H. Mokler, M. C. Simon, and J. Ullrich, Astrophys. J. **703**, 68 (2009).

[106] K. Schnorr, V. Mäckel, N. S. Oreshkina, S. Augustin, F. Brunner, Z. Harman, C. H. Keitel, J. Ullrich, and J. R. C. López-Urrutia, Astrophys. J. **776**, 121 (2013).

[107] M. C. Simon, M. Schwarz, S. W. Epp, C. Beilmann, B. L. Schmitt, Z. Harman, T. M. Baumann, P. H. Mokler, S. Bernitt, R. Ginzel, S. G. Higgins, C. H. Keitel, R. Klawitter, K. Kubiček, V. Mäckel, J. Ullrich, and J. R. C. López-Urrutia, J. Phys. B: At., Mol. Opt. Phys. **43**, 065003 (2010).

[108] M. C. Simon, J. R. Crespo López-Urrutia, C. Beilmann, M. Schwarz, Z. Harman, S. W. Epp, B. L. Schmitt, T. M. Baumann, E. Behar, S. Bernitt, R. Follath, R. Ginzel, C. H. Keitel, R. Klawitter, K. Kubiček, V. Mäckel, P. H. Mokler, G. Reichardt, O. Schwarzkopf, and J. Ullrich, Phys. Rev. Lett. **105**, 183001 (2010).

[109] J. K. Rudolph, S. Bernitt, S. W. Epp, R. Steinbrügge, C. Beilmann, G. V. Brown, S. Eberle, A. Graf, Z. Harman, N. Hell, M. Leutenegger, A. Müller, K. Schlage, H.-C. Wille, H. Yavaş, J. Ullrich, and J. R. Crespo López-Urrutia, Phys. Rev. Lett. **111**, 103002 (2013).

[110] S. W. Epp, R. Steinbrügge, S. Bernitt, J. K. Rudolph, C. Beilmann, H. Bekker, A. Müller, O. O. Versolato, H.-C. Wille, H. Yavaş, J. Ullrich, and J. R. Crespo López-Urrutia, Phys. Rev. A **92**, 020502 (2015).

[111] R. Steinbrügge, S. Bernitt, S. W. Epp, J. K. Rudolph, C. Beilmann, H. Bekker, S. Eberle, A. Müller, O. O. Versolato, H.-C. Wille, H. Yavaş, J. Ullrich, and J. R. Crespo López-Urrutia, Phys. Rev. A **91**, 032502 (2015).

[112] S. W. Epp, J. R. C. López-Urrutia, G. Brenner, V. Mäckel, P. H. Mokler, R. Treusch, M. Kuhlmann, M. V. Yurkov, J. Feldhaus, J. R. Schneider, M. Wellhöfer, M. Martins, W. Wurth, and J. Ullrich, Phys. Rev. Lett. **98**, 183001 (2007).

[113] S. W. Epp, J. R. C. López-Urrutia, M. C. Simon, T. Baumann, G. Brenner, R. Ginzel, N. Guerassimova, V. Mäckel, P. H. Mokler, B. L. Schmitt, H. Tawara, and J. Ullrich, J. Phys. B: At., Mol. Opt. Phys. **43**, 194008 (2010).

[114] P. Beiersdorfer, L. Schweikhard, J. C. López-Urrutia, and K. Widmann, Rev. Sci. Instrum. **67**, 3818 (1996).

[115] M. Schwarz, O. O. Versolato, A. Windberger, F. R. Brunner, T. Ballance, S. N. Eberle, J. Ullrich, P. O. Schmidt, A. K. Hansen, A. D. Gingell, M. Drewsen, and J. R. C. López-Urrutia, Rev. Sci. Instrum. **83**, 083115 (2012).

[116] D. Schneider, D. A. Church, G. Weinberg, J. Steiger, B. Beck, J. McDonald, E. Magee, and D. Knapp, Rev. Sci. Instrum. **65**, 3472 (1994).

[117] L. Gruber, J. P. Holder, J. Steiger, B. R. Beck, H. E. DeWitt, J. Glassman, J. W. McDonald, D. A. Church, and D. Schneider, Phys. Rev. Lett. **86**, 636 (2001).

[118] M. Hobein, A. Solders, M. Suhonen, Y. Liu, and R. Schuch, Phys. Rev. Lett. **106**, 013002 (2011).

[119] J. Repp, C. Böhm, J. R. C. López-Urrutia, A. Dörr, S. Eliseev, S. George, M. Goncharov, Y. N. Novikov, C. Roux, S. Sturm, S. Ulmer, and K. Blaum, Appl. Phys. B **107**, 983 (2012).

[120] S. M. Brewer, N. D. Guise, and J. N. Tan, Phys. Rev. A **88**, 063403 (2013).

[121] S. Sturm, M. Vogel, F. Köhler-Langes, W. Quint, K. Blaum, and G. Werth, Atoms **5**, 4 (2017).

[122] L. Schmöger, M. Schwarz, T. M. Baumann, O. O. Versolato, B. Piest, T. Pfeifer, J. Ullrich, P. O. Schmidt, and J. R. Crespo López-Urrutia, Rev. Sci. Instrum. **86**, 103111 (2015).

[123] L. Schmöger, O. O. Versolato, M. Schwarz, M. Kohnen, A. Windberger, B. Piest, S. Feuchtenbeiner, J. Pedregosa-Gutierrez, T. Leopold, P. Micke, A. K. Hansen, T. M. Baumann, M. Drewsen, J. Ullrich, P. O. Schmidt, and J. R. C. López-Urrutia, Science **347**, 1233 (2015).

[124] L. Schmöger, "Kalte hochgeladene ionen für Frequenzmetrologie," Ph.D. thesis, Heidelberg University, 2017.

[125] P. O. Schmidt, T. Rosenband, C. Langer, W. M. Itano, J. C. Bergquist, and D. J. Wineland, Science **309**, 749 (2005).

[126] J. Nauta, A. Borodin, H. B. Ledwa, J. Stark, M. Schwarz, L. Schmöger, P. Micke, J. R. Crespo López-Urrutia, and T. Pfeifer, in *Proceedings of the 18th International Conference on the Physics of Highly Charged Ions (HCI-2016), Kielce, Poland, 11–16 September 2016* [Nucl. Instrum. Methods Phys. Res., Sect. B **408**, 285 (2017)].

[127] Y. Xue, R. Ginzel, A. Krauß, S. Bernitt, M. Schöffler, K. U. Kühnel, J. R. C. López-Urrutia, R. Moshammer, X. Cai, J. Ullrich, and D. Fischer, Phys. Rev. A **90**, 052720 (2014).

[128] J. W. McDonald, D. Schneider, M. W. Clark, and D. Dewitt, Phys. Rev. Lett. **68**, 2297 (1992).

[129] F. Aumayr, H. Kurz, D. Schneider, M. A. Briere, J. W. McDonald, C. E. Cunningham, and H. Winter, Phys. Rev. Lett. **71**, 1943 (1993).

[130] R. Ritter, R. A. Wilhelm, R. Ginzel, G. Kowarik, R. Heller, A. S. El-Said, R. M. Papaléo, W. Rupp, J. R. C. López-Urrutia, J. Ullrich, S. Facsko, and F. Aumayr, Europhys. Lett. **97**, 13001 (2012).

[131] T. N. Makgato, E. Sideras-Haddad, S. Shrivastava, T. Schenkel, R. Ritter, G. Kowarik, F. Aumayr, J. Crespo López-Urrutia, S. Bernitt, C. Beilmann, and R. Ginzel, in *Eighth International Symposium on Swift Heavy Ions in Matter (SHIM), 2012* [Nucl. Instrum. Methods Phys. Res., Sect. B **314**, 135 (2013)].

[132] R. Ritter, Q. Shen, R. A. Wilhelm, R. Heller, R. Ginzel, J. R. Crespo López-Urrutia, S. Facsko, C. Teichert, and F. Aumayr, in *25th International Conference on Atomic Collisions in Solids (ICACS-25)* [Nucl. Instrum. Methods Phys. Res., Sect. B **315**, 252 (2013)].

[133] R. A. Wilhelm, E. Gruber, J. Schwestka, R. Kozubek, T. I. Madeira, J. P. Marques, J. Kobus, A. V. Krasheninnikov, M. Schleberger, and F. Aumayr, Phys. Rev. Lett. **119**, 103401 (2017).

[134] J. Dilling, R. Baartman, P. Bricault, M. Brodeur, L. Blomeley, F. Buchinger, J. Crawford, J. R. Crespo López-Urrutia, P. Delheij, M. Froese, G. P. Gwinner, Z. Ke, J. K. P. Lee, R. B. Moore, V. Ryjkov, G. Sikler, M. Smith, J. Ullrich, and J. Vaz, "Ultra-accurate mass spectrometry and related topics dedicated to H.-J. Kluge on the occasion of his 65th birthday anniversary," Int. J. Mass Spectrom. **251**, 198 (2006).

[135] S. Ettenauer, M. C. Simon, A. T. Gallant, T. Brunner, U. Chowdhury, V. V. Simon, M. Brodeur, A. Chaudhuri, E. Mané, C. Andreoiu, G. Audi, J. R. C. López-Urrutia, P. Delheij, G. Gwinner, A. Lapierre, D. Lunney, M. R. Pearson, R. Ringle, J. Ullrich, and J. Dilling, Phys. Rev. Lett. **107**, 272501 (2011).

[136] COMSOL Multiphysics Reference Manual 4.3b, COMSOL, Inc., 2013.

[137] H. Khodja and J. P. Briand, Phys. Scr. **T71**, 113 (1997).

[138] V. P. Ovsyannikov and G. Zschornack, Rev. Sci. Instrum. **70**, 2646 (1999).

[139] G. Zschornack, J. König, M. Schmidt, and A. Thorn, Rev. Sci. Instrum. **85**, 02B703 (2013).

[140] K. Motohashi, A. Moriya, H. Yamada, and S. Tsurubuchi, Rev. Sci. Instrum. **71**, 890 (2000).

[141] H. Watanabe and F. Currell, J. Phys.: Conf. Ser. **2**, 182 (2004).

[142] J. Xiao, Z. Fei, Y. Yang, X. Jin, D. Lu, Y. Shen, L. Liljeby, R. Hutton, and Y. Zou, Rev. Sci. Instrum. **83**, 013303 (2012).

[143] E. Takacs, T. D. Kimmel, K. H. Brandenburg, R. K. Wilson, A. C. Gall, J. E. Harriss, and C. E. Sosolik, AIP Conf. Proc. **1640**, 154 (2015).

[144] S. F. Hoogerheide and J. N. Tan, J. Phys.: Conf. Ser. **583**, 012044 (2015).

[145] V. P. Ovsyannikov and A. V. Nefiodov, Nucl. Instrum. Methods Phys. Res., Sect. B **370**, 32 (2016).

[146] G. Herrmann, J. Appl. Phys. **29**, 127 (1958).

[147] J. R. Harries, "A novel permanent-magnet electron-beam ion trap using in-vacuum pole pieces" (unpublished).

[148] J. R. Pierce, J. Appl. Phys. **11**, 548 (1940).

[149] C. D. Child, Phys. Rev. (Ser. I) **32**, 492 (1911).

[150] I. Langmuir, Phys. Rev. **21**, 419 (1923).

[151] M. C. Simon, M. Schwarz, B. L. Schmitt, C. Beilmann, S. W. Epp, T. M. Baumann, K. Kubicek, R. Ginzel, S. G. Higgins, R. Klawitter, V. Mäckel, S. Bernitt, P. H. Mokler, J. Ullrich, and J. R. C. López-Urrutia, J. Phys.: Conf. Ser. **194**, 012009 (2009).

[152] R. Ginzel, S. G. Higgins, P. Mrowcynski, P. Northway, M. C. Simon, H. Tawara, J. R. Crespo López-Urrutia, J. Ullrich, G. Kowarik, R. Ritter, W. Meissl, C. Vasko, C. Gösselsberger, A. S. El-Said, and F. Aumayr, Nucl. Instrum. Methods Phys. Res., Sect. B **268**, 2972 (2010).

[153] H. S. W. Massey and D. R. Bates, Rep. Prog. Phys. **9**, 62 (1942).

[154] S. Kühn, "Inbetriebnahme und Charakterisierung einer Elektronenkanone mit optischem Zugang zur Strahlachse in einer kompakten Elektronenstrahlionenfalle," M.Sc. thesis, Heidelberg University, 2017.

[155] M. F. Gu, Can. J. Phys. **86**, 675 (2008).

[156] A. H. Gabriel, Mon. Not. R. Astron. Soc. **160**, 99 (1972).

P2 Closed-cycle, low-vibration 4 K cryostat for ion traps and other applications

Journal: Review of Scientific Instruments

Copyright and license notice:
©2019 Author(s). All article content, except where otherwise noted, is licensed under a Creative Commons Attribution (CC BY) license. (http://creativecommons.org/licenses/by/4.0/)

Reproduced from

P. Micke, J. Stark, S. A. King, T. Leopold, T. Pfeifer, L. Schmöger, M. Schwarz, L. J. Spieß, P. O. Schmidt, and J. R. Crespo López-Urrutia (2019). "Closed-cycle, low-vibration 4 K cryostat for ion traps and other applications." *Review of Scientific Instruments* 90, 065104.
DOI: 10.1063/1.5088593

with the permission of AIP Publishing.

Review of
Scientific Instruments

ARTICLE

scitation.org/journal/rsi

Closed-cycle, low-vibration 4 K cryostat for ion traps and other applications

Cite as: Rev. Sci. Instrum. 90, 065104 (2019); doi: 10.1063/1.5088593
Submitted: 11 January 2019 • Accepted: 15 May 2019 •
Published Online: 5 June 2019

P. Micke,[1,2,a)] J. Stark,[1,3] S. A. King,[2] T. Leopold,[2] T. Pfeifer,[1] L. Schmöger,[1,2] M. Schwarz,[1,2] L. J. Spieß,[1] P. O. Schmidt,[2,4] and J. R. Crespo López-Urrutia[1]

AFFILIATIONS

[1] Max-Planck-Institut für Kernphysik, Saupfercheckweg 1, 69117 Heidelberg, Germany
[2] Physikalisch-Technische Bundesanstalt, Bundesallee 100, 38116 Braunschweig, Germany
[3] Heidelberg Graduate School of Fundamental Physics, Ruprecht-Karls-Universität Heidelberg, Im Neuenheimer Feld 226, 69120 Heidelberg, Germany
[4] Institut für Quantenoptik, Leibniz Universität Hannover, Welfengarten 1, 30167 Hannover, Germany

[a)] Author to whom correspondence should be addressed: peter.micke@mpi-hd.mpg.de

ABSTRACT

In vacuo cryogenic environments are ideal for applications requiring both low temperatures and extremely low particle densities. This enables reaching long storage and coherence times, for example, in ion traps, essential requirements for experiments with highly charged ions, quantum computation, and optical clocks. We have developed a novel cryostat continuously refrigerated with a pulse-tube cryocooler and providing the lowest vibration level reported for such a closed-cycle system with 1 W cooling power for a <5 K experiment. A decoupling system suppresses vibrations from the cryocooler by three orders of magnitude down to a level of 10 nm peak amplitudes in the horizontal plane. Heat loads of about 40 W (at 45 K) and 1 W (at 4 K) are transferred from an experimental chamber, mounted on an optical table, to the cryocooler through a vacuum-insulated massive 120 kg inertial copper pendulum. The 1.4 m long pendulum allows installation of the cryocooler in a separate, acoustically isolated machine room. At the experimental chamber, we measured the residual vibrations using an interferometric setup. The positioning of the 4 K elements is reproduced to better than a few micrometer after a full thermal cycle to room temperature. Extreme high vacuum on the 10^{-15} mbar level is achieved. In collaboration with the Max-Planck-Institut für Kernphysik, such a setup is now in operation at the Physikalisch-Technische Bundesanstalt for a next-generation optical clock experiment using highly charged ions.

© 2019 Author(s). All article content, except where otherwise noted, is licensed under a Creative Commons Attribution (CC BY) license (http://creativecommons.org/licenses/by/4.0/). https://doi.org/10.1063/1.5088593

I. INTRODUCTION

Cryogenic temperatures are needed in many fields of research, such as in studies of superconductivity and superfluidity, surface studies employing scanning probe techniques, the development of low-noise detectors and electronics, or to generate high magnetic fields. They can also generate extreme high vacuum (XHV) conditions, an advantage exploited in cryogenic Penning traps[1,2] or Paul traps,[3–5] and nearly impurity-free vacua in multipole radio-frequency (rf) traps.[6] Furthermore, superconducting detectors for fluorescence photons integrated into surface Paul traps for scalable quantum information processing require operation at cryogenic temperatures.[7,8] For these reasons, cryogenics is gaining ground in the last years within the communities working in atomic and quantum physics. Moreover, an extremely low residual gas density is crucial for suppressing charge-exchange-induced ion recombination[9] of highly charged ions (HCIs), a key aspect for the current development of optical atomic clocks using HCIs.[10] Recently, retrapping of HCIs in a cryogenic Paul-trap experiment (CryPTEx)[3,11,12] and sympathetic cooling of those HCIs through interactions with a laser-cooled Coulomb crystal were demonstrated at the Max-Planck-Institut für Kernphysik (MPIK). High-resolution spectroscopy of HCIs using advanced spectroscopic methods like quantum logic[13] requires that collisions have to be avoided for many minutes. This is also important for quantum-physics research, e.g., in scalable setups for quantum simulations or quantum

© Author(s) 2019

computing[4,5,14–17] since collisions with background gas molecules or atoms cause decoherence or even unacceptable ion losses, which are suppressed at cryogenic temperatures. In addition, a cryogenic trap suppresses ion heating[18–20] due to reduced electric field noise. Optical atomic clocks aiming at sub-10^{-18} fractional frequency inaccuracy also benefited in recent years from the strong suppression of residual systematics in a cryogenic environment such as the ac Stark shift from black-body radiation and collisional shifts due to background gas.[21–27]

Inside a closed vessel the total vapor pressure given by the sum of partial pressures is tremendously reduced by cooling down the entire vessel or some surfaces therein. At temperatures below the boiling point of nitrogen (77 K at normal pressure) only neon, helium, and hydrogen are still gases. At 4 K, all gases are either condensed, frozen out or cryo-adsorbed. Residual gas particles impinging on cryogenic surfaces lose kinetic energy, stick to the surface (dubbed cryopumping) and do not outgas (desorb). At around 4 K, XHV pressures below 10^{-14} mbar are routinely achieved.[28] Values down to the 10^{-17} mbar level were reported[29,30] for sealed cryogenic traps.

Two methods are chiefly used to reach 4 K temperatures. The first is liquid helium (LHe) refrigeration in continuous-flow or bath cryostats (see, e.g., Ref. 31 and the references therein, and Refs. 17 and 32 as sample applications). For precooling and also for the outer heat shields of such systems, liquid nitrogen (LN_2) is commonly used. The inner stage is then cooled with LHe down to 4 K. There is the option of achieving lower temperatures through the so-called lambda-point refrigeration under pumping (down to approximately 1.8 K[31]), subsequent cooling through adiabatic demagnetization or in ^{3}He-^{4}He mixing cryostats. Inconveniently, since LHe and LN_2 continuously evaporate from these open systems, regular refilling is needed. Evaporation of LHe at the rate of approximately 1 l every hour per watt of cooling power at 4 K causes considerable running costs. The LHe and LN_2 reservoirs, their thermal shields and insulation are bulky and hinder access to the experimental region. In many cases, the cryogenic support of the cold mass and reservoirs is feeble in order to reduce the thermal load from room temperature. This can cause sensitivity to vibrations and mechanical shifts due to thermal expansion and the changing level of the cryogen.

As a second method, continuously operating closed-cycle refrigerators supplied by various vendors can be employed (see, e.g., Refs. 31, 33, and 34 and references therein). They do not need refilling and offer very stable temperatures during operation. Frequently used types are Gifford-McMahon and pulse-tube cryocoolers, both typically as two-stage systems providing cooling powers on the order of 40 W at the first stage (around 40 K) and 1 W at the second stage (around 4 K). A major drawback of such systems is the cycling flow (around 1 s period) of strongly pressurized cooling gas, resulting in mechanical vibrations and noise at the cold head and other parts. Many cryogenic experiments are sensitive to mechanical vibrations on a level of submicrometer: laser spectroscopy of trapped atoms or ions,[5,17,22] silicon cavities for optical oscillators,[35–37] sapphire oscillators,[38,39] frequency references based on spectral hole burning,[40–42] x-ray monochromators,[43,44] bolometers, and detectors searching for, e.g., neutrinoless double-beta decay[45] or dark matter,[46] instruments, and microcalorimeters for infrared, x-ray and gamma astronomy,[34] and gravitational wave detectors.[47] For such applications, pulse-tube cryocoolers[48] offer lesser inherent vibrations than Gifford-McMahon cryocoolers and are more reliable since there are no movable parts at the cold head itself.[31,34] Typical maintenance intervals are on the order of 20 000 h for the cold head and 30 000 h for its compressor. Since a 1 Hz alternating compression and expansion of He gas driven by a rotary valve is needed for the cooling, vibrations at the cold head with amplitudes at the 10 μm level are still induced.

Commercial vibration-insulation systems are available for closed-cycle refrigerators. Some use a He gas heat-exchange unit, i.e. He volume enclosed by edge-welded or rubber bellows, as a thermal link between the cryocooler and the cold stage (see, e.g., Refs. 5, 49, and 50). Except for the flexible bellows, no rigid mechanical contact exists. The He gas needs continuous replenishment to maintain a pressure of typically 30 mbar above atmospheric pressure. It is crucial to operate such a gas-exchange unit above the He boiling point of 4.2 K to prevent mechanical contact through condensed He.[51] Consequently, the experiment has to be operated at a sufficiently high temperature, in cases several kelvins above 4.2 K[5] depending on the thermal coupling of the experiment to the gas-exchange unit. This comes at the price of a reduced cryopumping performance. Some research groups have developed vibration-decoupling systems. Active noise cancellation of pulse-tube cryocooler vibrations was implemented.[52] However, most groups have applied passive decoupling schemes based on flexible metallic links[3,53–55] which must satisfy the conflicting needs of high thermal but low mechanical coupling.

All this considered, we started developing a cryogenic system with vibration decoupling based on our experience from CrypTEx[3] with the goal of improving mechanical stability and lowering the achievable temperatures. A pulse-tube cryocooler ensures reliable, low-maintenance operation over months, low running costs, and stable ion trap temperatures. Our design achieves high reproducibility of the trap position after thermal cycling. By installing the cryocooler and other noisy components in a separate room, the Paul trap mounted onto a pneumatically floating optical table in the adjacent laser laboratory meets the stability demands for optical atomic clocks. It is already in operation for studying forbidden optical transitions of HCIs. These are produced by a Heidelberg Compact Electron Beam Ion Trap (HC-EBIT),[56] transferred through an ion beamline, decelerated, and retrapped in a cryogenic Paul trap.[57]

In this paper, we describe the cryogenic system in detail which we initially designed and assembled at MPIK in Heidelberg, Germany. After completion, we moved it to the Physikalisch-Technische Bundesanstalt (PTB) in Braunschweig, Germany, where various measurements reported here characterized its performance regarding temperatures, vacuum level, and residual vibrations. Currently, the setup is operated there at the QUEST Institute for a cryogenic linear Paul trap, aiming at quantum logic spectroscopy of HCIs. A similar setup was also recently assembled by our collaborators at Aarhus university for the spectroscopy of molecules in a cryogenic Paul trap. Another slightly modified version is currently under construction at MPIK. Its intended application is HCI trapping in a monolithic radio-frequency trap and resonator,[58] aiming at direct frequency-comb spectroscopy in the extreme ultra-violet range using high-harmonic generation in an optical enhancement cavity.[59]

© Author(s) 2019

II. DESIGN

A. Concept

Detrimental vibrations can propagate from the cold head and pumping system through air, the floor, the vacuum chambers, and the thermal transfer elements. We address these paths in our design by (a) acoustically separating the noisy elements from the quiet area, (b) installing the various components on vibration-reducing supports attached to the floor, (c) introducing highly flexible bellows in the vacuum system, and (d) using a low-pass, heavy inertial vibration filter as the thermal transfer unit (TTU). In the following, we will describe these measures.

The cryogenic system (an overview is shown in Fig. 1) extends over two rooms which are separated by an acoustically insulating wall. One of them is the laser laboratory, in which the experimental chamber, containing a linear Paul trap,[57] is rigidly mounted on top of a pneumatically floating optical table to decouple it from the floor. Although this cryogenic system was intended for use with an ion trap, any object of study could be cooled with it. For simplicity, we will refer to this object as just the *ion trap* in this article. In the adjacent room, referred to as the *machine room*, a two-stage closed-cycle pulse-tube cryocooler is installed at a distance of 1.4 m from the ion trap region, which is larger than in most other cryogenic setups. The helium compressor is located at the far end of the machine room for better vibration suppression. A vacuum tube containing the thermal transfer unit (TTU) runs through the wall and connects the two sections of the cryogenic system. Massive high-purity oxygen-free high thermal conductivity (OFHC) copper parts, linked by two flexible vibration-decoupling sections, are used in the TTU between the cryocooler and the ion trap. Together, they constitute an inertial low-pass vibration filter. Moreover, the rigidity of the vacuum chamber surrounding the TTU is also broken at several locations by introducing flexible edge-welded bellows that absorb the noise components above their lowest oscillation frequencies (a few hertz). Hence, several vacuum chambers "float" between bellows, with their mass also acting as low-pass filter for vibrations. Due to our space and technical constraints, such as the required orientation of the pulse tube, the system is divided into three segments: I (vertical) with the cryocooler, II (horizontal) with the inertial pendulum, and III (vertical) with the TTU connecting to the ion trap. The cold masses are divided in two stages: the first one (35–50 K) is the thermal heat shield surrounding the second one (3.5–5.0 K), which cools the ion trap. The thermal insulation vacuum is differentially connected with the vacuum of the ion trap where an XHV level is required once the system is cold. All mechanical pumps for initial pumping and maintaining an ultra-high vacuum (UHV) room-temperature base pressure are located in the machine room. The vacuum chambers enclosing the TTU are vibration-decoupled by six edge-welded bellows in total. Since the diameter of the larger DN160CF bellows is around 170 mm, strong forces arise when the vacuum system is pumped out due to the outer atmospheric pressure. Two outer counteracting DN160CF bellows in extension of the segment II are attached on their outer flanges to rigid pillars anchored to the ground of each room to balance the horizontal pressure forces, leaving zero net forces acting on the vacuum chambers. The chamber of segment I is mounted on an aluminum frame supported by damping rubber feet to the noise-damping screed used in the floor of the machine room. Segment II runs horizontally at 50 cm height through a hole in the noise-insulating wall and is also held by two aluminum frames, one in the machine room and the second in the laser laboratory. Both are again supported by damping rubber feet. The vacuum chamber of segment III runs from below through a hole in the aforementioned floating optical table and is stiffly mounted to its top, the only rigid connection of this chamber. This arrangement provides 360° optical access on the table top in the horizontal plane and leaves also the top lid of the ion-trap chamber free, offering convenient access to the inside.

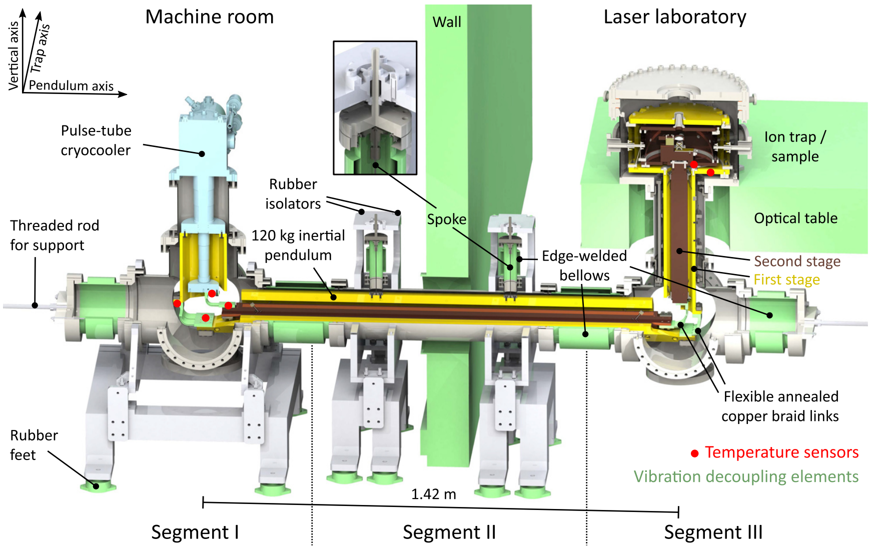

FIG. 1. Cutaway drawing of the cryogenic system. The system extends over two rooms separated by a noise-insulating wall, with the pulse-tube cryocooler located in the machine room on the left and the cooled ion trap/sample on the right on top of a pneumatically floating optical table in the laser laboratory. The cryogenic system is subdivided into three segments. The heat shields which enclose the second stage vibration-decoupling sections with the flexible copper links are not shown for visibility. The inset magnifies the position adjustment of the inertial pendulum. See the text for further details.

© Author(s) 2019

B. Vacuum system

In total, the system comprises three vacuum chambers: two custom-made six-way crosses with DN200CF ports and the DN160CF tube of segment II with two vertical DN40CF flanges. Additionally, two DN160CF tubes are used in segments I and III, respectively (see Fig. 1). All parts are made of low-magnetic stainless steel and are electropolished to reduce outgassing and the radiation-emission coefficient, thus reducing the radiative heat transfer to the cryogenic elements. In segment I, the pulse-tube cryocooler is mounted on a DN160CF vertical tube attached to the top of the first six-way cross, which is connected to segment II by means of an edge-welded DN160CF bellows with 40 diaphragm pairs. On the opposite side of segment II, an identical one connects to the second six-way cross (of segment III). Attached to the top flange of this cross, a second vertical DN160CF tube holds the in-vacuum room-temperature frame of the last segment of the TTU (detailed in Sec. II D 3). This tube passes through the 350-mm diameter hole in the optical table and is connected to the bottom of the ion-trap chamber.[57] For balancing the compressive forces, two edge-welded DN160CF bellows with 20 diaphragm pairs are mounted to the outer flanges of each of the two six-way crosses. These bellows are terminated with blind flanges fixed by means of M12-threaded rods to massive pillars anchored to the floor in each of the two rooms. Two edge-welded DN40CF bellows are installed vertically on the horizontal chamber, with their top flanges closed by modified DN40CF blind flanges. On their vacuum side, each one holds a 150-mm long spoke from which the inertial pendulum of the TTU is suspended (see Sec. II D 2 for further details). On the air side, adjustable threaded rods are welded. They run vertically through oversize holes on aluminum plates, with nuts and larger 25 mm-diameter washers allowing for horizontal position adjustment of the TTU by means of three set screws (see inset of Fig. 1). The height is adjusted by turning the nut on the threaded rod, lifting or lowering the pendulum.

A single 300 l/s turbomolecular pump (TMP) attached to segment I, backed by a smaller 70 l/s TMP and an oil-free scroll pump is used for pumping. This two-stage TMP system increases the H_2 compression ratio by more than three orders of magnitude compared to a single-stage system and provides additional safety during cryogenic operation: If the 300 l/s TMP fails, the smaller TMP can maintain a vacuum level good enough to avoid too much frozen gas on the cryogenic surfaces; a failure of the smaller pump does not cause any immediate problem either. The room-temperature base pressure in the TTU is determined by the limited vacuum conductance across the whole system, where some components cannot be baked due to the use of the cryogenic vacuum grease Apiezon N which starts to flow at 42 °C. Nonetheless, after turning on the cryocooler, the large inner surfaces cryosorb residual gas, quickly reducing the pressure to UHV levels. As for the ion-trap chamber, the first and second stage are differentially separated from the vacuum chamber and the vacuum conductance to the segment III tube is rather small. Therefore, to enhance pumping there, an ion-getter pump is installed. It can be separated from the main vacuum during activation by means of a DN63CF gate valve. The main residual gas in the space between the chamber wall and the first cryogenic stage is H_2, which is removed by the getter pump with a speed of 200 l/s. Cryopumping at the ion trap is further enhanced by gluing approximately 1 g of activated charcoal to a container placed inside the second stage. It acts as a strong getter at cryogenic temperatures due to the surface area of its pores, which can reach thousands of square meters per gram.[60]

It is also possible to close a DN100CF gate valve between the 300 l/s TMP and the cryogenic system, which allows switching off all mechanical pumps during a measurement, eliminating their vibrations. However, measurements have shown that pump vibrations are also well suppressed by our cryogenic system (see Sec. III C).

C. Cryocooler

We use a model RP-082 pulse-tube cryocooler from Sumitomo Heavy Industries,[61] with an F-70H compressor driving it through 20 m long supply and return lines. The manufacturer specifies vibration levels of 7 μm and 9 μm for its first and second stages, respectively. A thermal load of 40 W can be refrigerated by the first stage at 45 K, and 1 W by the second stage at 4.2 K. The rotary valve and drive are directly attached to the cold head without vibration decoupling. It only operates in upright orientation, therefore segment I, where it is mounted, is vertically oriented.

Higher thermal loads raise the achievable temperatures. Our target temperatures were around 45 K and 4.5 K for the first and second stage respectively, to reach long HCI storage times on the order of 1 h. A low temperature of the first stage allows for a lower temperature of the second one. The presented system does not necessarily rely on the employed cryocooler, and small mechanical modifications of segment I would accommodate other models with less vibrations or larger refrigeration powers.

D. Thermal transfer unit

The TTU bridges a horizontal distance of 1.4 m between the cryocooler and the ion trap. It is vacuum-insulated from the room-temperature chamber. Long, heavy and stiff nested sections carry the heat in each segment. Vibration-decoupling soft links suppress transmission of vibrations between them. The first (outer) stage serves as a heat shield for the second one for both radiation and conductive heat loads. Owing to the distance they have to bridge, the cold stages have large surface areas and consequently a high radiation load. To minimize this load, most of the copper parts are plated with a 10 μm silver layer as a diffusion barrier and a 0.5 μm layer of gold, which prevents surface oxidation and provides a low radiation-emission coefficient.

In segments II and III, low thermal conductivity stainless-steel spokes of 2 mm diameter are used to suspend the TTU from the room-temperature vacuum chambers as well as the second stage of the TTU from the first one. The spokes are made as long as possible within the given geometry to reduce thermal conduction. In contrast, thermal conduction along the TTU is enhanced by making it as short (and large in cross section) as possible and by using OFHC copper with purities between 4N and 5N (99.99% and 99.999%, respectively). Furthermore, most of the copper parts were vacuum-annealed to partially recrystallize them, further increasing their residual-resistivity ratio (RRR) and thermal conductivity λ.[62] Thereby, λ values of thousands of W m^{-1} K^{-1} can be achieved,[63] corresponding to RRR values of a few hundreds. For parts that were brazed together, such as the first stage of segment I and III, the annealing procedure was carried out simultaneously with the vacuum brazing at a temperature beyond 850 °C. Annealing was

© Author(s) 2019

performed individually for elements which were bolted together, such as the bars for the pendulum. These were vacuum-annealed at a temperature of only 450 °C over a period of 2–3 h. Annealing under oxygen atmosphere would generally lead to even higher RRR values due to oxidation of magnetic impurities,[63] but safety concerns precluded this. To reduce the thermal boundary resistance between different surfaces which are clamped together, we use thin films of the cryogenic vacuum grease Apiezon N to close microscopic irregularities.[64,65]

1. Segment I

A 220 mm-long first-stage hollow octagon is vacuum brazed from eight prismatic copper bars of 10 mm thickness (see Fig. 2). It is attached to the first stage of the cryocooler and houses the second stage. It ends inside the six-way cross, where flexible copper links connect it to the next segment of the TTU. The second stage of the pulse-tube cryocooler is directly connected by means of flexible copper links to the next segment.

2. Segment II

The first stage of the pendulum (see Figs. 2 and 3) is also a hollow octagon made by bolting together eight ~1.4 m-long and 25 mm-thick copper bars of trapezoidal cross section. On top of it, two stainless-steel inserts hold two vertical 150 mm long stainless-steel spokes that are screwed by their other end to the vacuum side of DN40CF blind flanges. These close the vertical DN40CF bellows connected to the DN40CF ports of the horizontal vacuum chamber and are externally supported by the structure described in Sec. II B. Inside the octagon, the second-stage rod is held by six counteracting spokes of 110 mm length. The rod, made from OFHC 4N5 (99.995%) copper, has a diameter of 50 mm and a length of 1.34 m.

3. Segment III

The two stages of segment III are supported by a room-temperature frame made of stainless steel (see Figs. 2 and 4) resting inside of its DN160CF vacuum tube (see Sec. II B). From the frame, twelve 120 mm-long spokes are arranged in counteracting pairs to hold the hollow 0.45 m-long first-stage dodecagon, vacuum brazed from 12 trapezoidal copper bars. The spokes are vacuum-brazed into fitting bores drilled along the axis of Allen-head screws. A nut on the thread of each screw is used to adjust position and tension (see Fig. 4). The low-temperature ends of the spokes are held by a stainless-steel girdle screwed to the first stage. The warm ends are hooked into the room-temperature frame. From the first stage, a 50 mm-diameter second-stage copper rod with a length of 0.44 m, made from OFHC 4N5 (99.995%) copper, is suspended again by means of 12 spokes with lengths between 80 mm and 90 mm in a similar arrangement.

4. Flexible copper links

Vibration transmission from the pulse tube along the TTU is suppressed by flexible copper links mounted between the three segments. We use customized links from Technology Applications, Inc., based on OFHC copper-wire braids (UltraFlex)[61] with an estimated purity between 4N5 and 4N8. The braids are cold-pressed into copper plates of at least 4N purity. This did not seem to reduce their conductance at operating temperature.[54] The braids have a diameter of 2.54 mm and lengths between 35 mm and 68 mm. The links for the second stages use 32 individual ropes each, whereas for the first stage connections 68 and 64 ropes on the pulse-tube and trap side are used, respectively. We vacuum annealed them at 550 °C for 6 h to increase the RRR value and soften them. Higher annealing temperatures should in principle

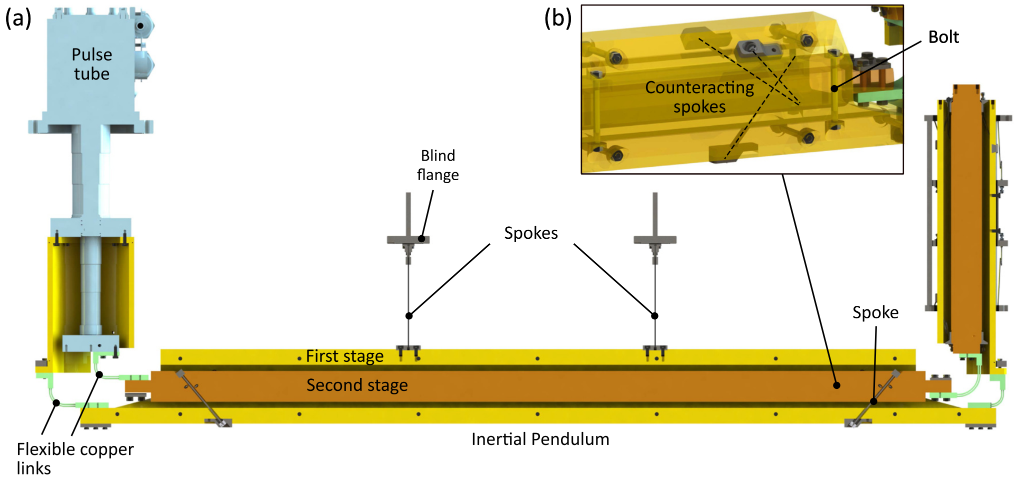

FIG. 2. (a) Cross section of the thermal transfer unit (TTU) with its two temperature stages. The inner parts of the three segments are connected by flexible copper links. Interlaced heat shields enclosing the vibration-decoupling sections are not shown. (b) Mounting structure of the inertial pendulum (both stages are depicted as transparent for visibility). The hollow first stage of the pendulum is assembled from prismatic copper bars bolted together. As second stage, a massive copper rod is held inside the first stage by six counteracting spokes. See the text for further details.

© Author(s) 2019

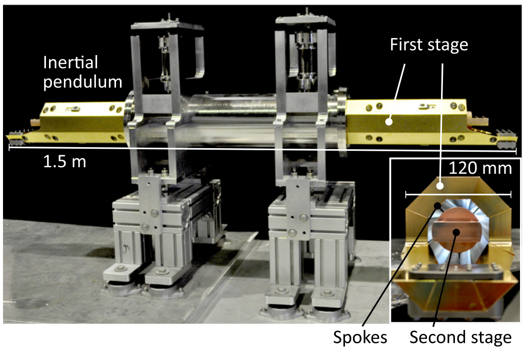

FIG. 3. Photograph of segment II prior to the installation through the noise insulating wall. The pendulum hangs freely inside the vacuum chamber, suspended by two spokes from the top flanges of two vertical DN40CF bellows. The inset shows a view along the pendulum exposing the spokes holding the second stage from the first one.

lead to even better results, but tests on a sample indicated partial fusing of the individual copper strands in the ropes, making them stiffer. Up to 8 bolts per end plate ensured a large number of contact points, used with molybdenum washers for compensation of the differential thermal contraction of copper and stainless-steel parts. As elsewhere, a thin Apiezon N layer was used between contact surfaces. Some of the fittings have holes for mounting temperature sensors. Threaded inserts (Helicoil Nitronic 60) were used in the copper end plates having a high resistance to galling. This permits application of strong force for good thermal contact. The braids are bent by 90°, with several millimeters of excess length and the outer ropes are longer than the inner ones to prevent tension. The links installed beneath segment III are shown in Fig. 5.

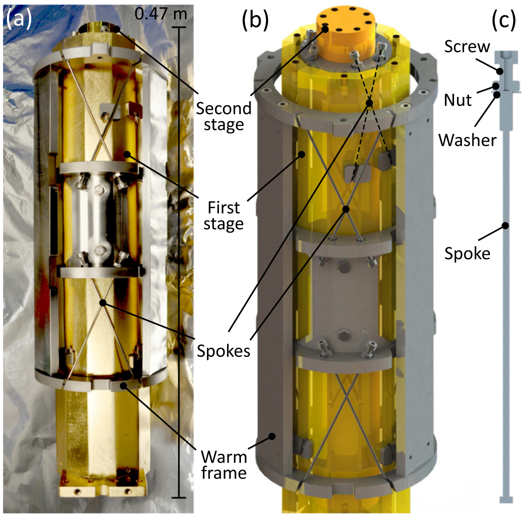

FIG. 4. (a) Photograph of segment III of the TTU. The first stage is suspended by spokes from a room-temperature frame. In the 3D model (b), the first stage is displayed as transparent to show the inside mounting of the second stage, also by means of spokes. (c) shows a cross section of a vacuum-brazed spoke. See the text for further details.

E. Heat shields

In each cross, the flexible links and sensors are enclosed within assemblies of bent 1 mm-thick copper sheets (3N5 99.95%) as shown in Fig. 6. Thermally connected to the first stages of segment I and III, respectively, they shield parts within from room-temperature black-body radiation. Furthermore, the sensors require shielding to exclude perturbations due to radiation directly heating them. To prevent transmission of vibrations through these heat shields, care was taken to avoid contact with the pendulum of segment II.

F. Temperature sensors

Six sensors monitor temperatures at various locations (see Fig. 1). Four of them are permanently installed before and after the first and second stage flexible links in the first cross. Here, we employ calibrated Cernox-type sensors, since these are magnetic-field insensitive and operate in closer proximity to the magnetic field of the EBIT used for HCI production. These sensors measure the temperature gradient across the flexible links. Temporarily, we also installed two silicon-diode temperature sensors at the beginning of the first and second stage of segment III to measure the temperature gradient up to the ion trap where two more silicon sensors are permanently installed on the first and second stage inside the respective temperature stage enclosures. Since these are completely enclosed there, thermal radiation from a warmer stage is blocked. Thin cryogenic 0.127 mm-diameter (Cernox sensors) and 0.202 mm-diameter (silicon diodes) phosphor-bronze wires are used for connecting the sensors to the vacuum-feedthrough flange in a 4-wire arrangement. The wiring was thermally anchored with vacuum-compatible Kapton tape to the temperature stages and had sufficient length in between for heat-load reduction.

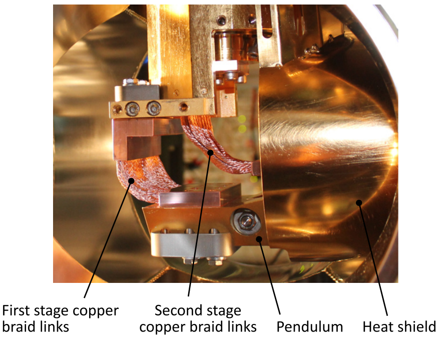
First stage copper braid links
Second stage copper braid links
Pendulum
Heat shield

FIG. 5. Flexible copper braid connections between segments II and III. The gold-plated heat shield (see Fig. 6) that protects the braids from room-temperature radiation is temporarily removed to allow access.

© Author(s) 2019

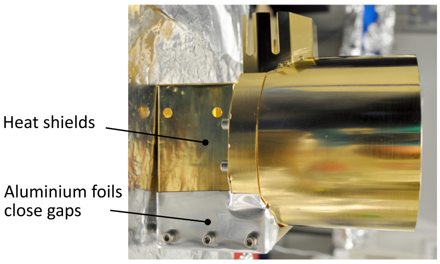

FIG. 6. Photograph of a copper-sheet heat-shield assembly enclosing the flexible copper braids in the second cross. Thick aluminum foil is used to cover gaps in order to reduce thermal radiation from the vacuum chamber reaching the second stage. See the text for further details.

G. Restricting the motion of the optical table

For suppression of vibrations, free relative motion of the different segments, bound together by bellows, is needed. Owing to the small gaps between both, the cryogenic stages themselves in the different segments and the vacuum chamber walls, undesired contact can occur when the floating optical table moves by more than a few millimeters. To avoid thermal shorts, we restrict the motion of the optical table to less than ±1 mm in each direction by means of a strong aluminum frame, shown in Fig. 7. It is rigidly anchored to the concrete floor and has adjustable mechanical stops that can, if needed, withstand the force exerted by the pneumatic legs, which are equipped with position regulators that keep the table within those limits.

H. Installation

The TTU was assembled within a few days after completion of its different components. First, segment II (see Fig. 3) was mounted. Second, the fully assembled segment I and the six-way cross of segment III (second cross) were attached with the inner edge-welded bellows to segment II. Temporarily, we used for the second cross a similar support structure as for the first cross, shown in Fig. 1. Then, the vertical element of Sec. III, (i.e., the DN160CF tube with its inner elements) was passed through the hole in the optical table (see Fig. 7) and connected to the top of the second cross. Following that, the ion trap vacuum chamber was installed on top of it and rigidly attached to the optical table. The outer edge-welded bellows were mounted to the crosses and anchored to the pillars fixed on the floor. The TTU was completed by installing the flexible links inside the crosses through the DN200CF flanges. At the same time, the temperature sensors and the heat shielding enclosures were installed. Finally, the optical table was floated, lifting the second cross from its temporary support structure.

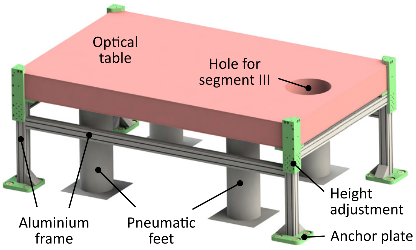

FIG. 7. Optical table and frame restricting its motion range within adjustable mechanical stops. The four corner pillars are firmly anchored to the concrete floor; horizontal bars stiffen the frame.

III. PERFORMANCE CHARACTERIZATION

A. Vacuum

The residual gas pressure between the vacuum chamber and the first stage is measured by a hot-cathode ion gauge installed at the first cross behind a DN40CF elbow to prevent thermal radiation from the gauge reaching the first stage. Without cryopumping, the pressure reaches the 10^{-8} mbar level after a few days of pumping. With the cryocooler switched on, the pressure drops to 3×10^{-10} mbar at the end of the cooldown. Inside the second stage, no pressure gauges are installed, but the vacuum pressure can be estimated by the lifetime of the ions stored in the Paul trap. At temperatures below 5 K molecular hydrogen is the dominant residual gas. As in other experiments, singly charged Be^+ ions under excitation by the 313 nm Doppler-cooling laser can undergo a chemical reaction forming BeH^+.[66,67] With a large cloud of stored Be^+, the residual gas pressure can thus be estimated. At the National Institute of Standards and Technology (NIST), a pressure of 5×10^{-11} mbar was estimated from a Be^+ lifetime of 2.2 h when the ions were continuously excited with a saturation parameter of 0.3.[67] Before installing the activated charcoal getter in our system, we also observed BeH^+ formation on such time scales a few days after a cooldown, indicating a degradation of the initially much better pressure. This is in agreement with our experiences from CryPTEx.[3,11] The increasing amount of adsorbed residual gas on the cryogenic surfaces reduces their pumping speed. Short warm up cycles had to be performed every evening to restore initial vacuum conditions.

For our new system, a short warm up cycle takes approximately one to 3 h, allowing the second stage to typically reach 20–30 K. Shortly after switching off the cryocooler, the pressure measured by the hot-cathode ion gauge typically increases to the 10^{-7} mbar range, then slowly returning to below 10^{-8} mbar over a period of typically 1 h as the TMPs remove the desorbed gas. After passing through a minimum, the pressure would raise again if the warm up were continued. Here, we switch the cryocooler back on.

After installation of the getter, we have never seen BeH^+ formation and trap single Be^+ routinely for a whole week without losing them. This is due to the much greater adsorption capacity of the charcoal compared to the mostly polished metal surfaces. Be^+ ions are only lost if the cooling laser is turned off for many days. Assuming a Be^+ ion exposed to the same 313 nm cooling laser saturation as for the aforementioned NIST experiment, for about 10 h/day and for a conservative estimate of five days storage time without reaction, we can place an upper limit of 2×10^{-12} mbar on our pressure. A more sensitive and efficient vacuum probe is an HCI on which charge exchange (CX) reactions with hydrogen can be observed (see, e.g., Ref. 68 and references therein). Following this approach, we stored a single highly charged Ar^{13+} ion, sympathetically cooled by a

© Author(s) 2019

single laser-cooled Be$^+$ ion, in our Paul trap and measured the lifetime of this two-ion crystal. CX is immediately observable through the temporary decrystallization of the Coulomb crystal or through loss of one or both ions from the trap. Figure 8 shows the recorded lifetimes of a set of 122 two-ion crystals within two weeks after a warm up cycle. By a maximum likelihood estimate, we obtain a mean lifetime of $\tau = 43.1(3.9)$ min. In the classical over-barrier model (see, e.g., Ref. 69), the critical distance for CX between H_2 and the HCI is proportional to $\sqrt{q}$, where q is the HCI charge. According to the Langevin model,[70] the residual-gas particle density is given by

$$n = \frac{1}{\tau \cdot k_L}, \tag{1}$$

where τ is the HCI lifetime and $k_L = q/(2\varepsilon_0)\sqrt{\alpha/\mu}$ is the Langevin rate coefficient, ε_0 the electric constant, $\alpha = 4\pi\varepsilon_0(0.787 \times 10^{-24})\ \mathrm{cm}^3$ the H_2 polarizability, and μ the reduced mass of the HCI-H_2 system. For (Ar^{13+}, H_2) k_L has a value of $1.957 \times 10^{-8}\ \mathrm{cm}^3\ \mathrm{s}^{-1}$ (see Ref. 68). The pressure is then given by

$$p = n \cdot k_B \cdot T \tag{2}$$

with the Boltzmann constant k_B and the residual gas temperature T, which is assumed to be in thermal equilibrium with the second stage. Based on Eqs. (1) and (2), we can give an upper limit for the cryogenic vacuum pressure at the Paul trap inside the second stage since the measured lifetime is only a lower limit for the actual lifetime of the described loss process. Additional non-negligible loss processes, e.g., due to collisions or imperfections of the trap drive electronics, which cause a configuration change of the crystal or a temporary heating, as well as collisions with ballistic room-temperature gas entering the trap region through the open laser access ports,[57] shorten the lifetime to the above measured value. Hence, we derive an upper XHV pressure limit of $p < 1.26\ (-0.11/+0.12) \times 10^{-14}$ mbar at $T = 4.6$ K, strongly indicating operation on the 10^{-15} mbar level as expected for such a cryogenic setup. Arguably, the cryogenic vacuum pressure could be improved and the HCI lifetimes prolonged by closing some of the laser ports in the first stage with windows, though this was not done here due to concerns about birefringence and potentially longer initial pumpdown times due to the decreased pumping conductance. With all laser ports open, 0.01% of the total solid angle exposes the ion to room temperature.[57]

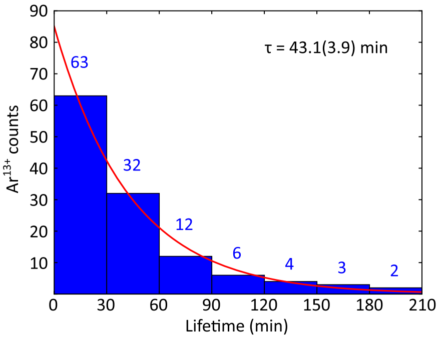

FIG. 8. Lifetime measurement of highly charged Ar^{13+}. The data visualized in the histogram yield a lifetime of 43.1(3.9) min, evaluated by a maximum likelihood estimate. The corresponding exponential decay function is shown in red.

As mentioned above, the HCI lifetime and the vacuum pressure degrade over time. Thus, the measured lifetime is an average over the period of two weeks after a warm up cycle. Significantly longer HCI lifetimes are observed shortly after such a cycle. It is a pragmatic choice when to perform a short warm up with the tradeoff of losing parts of a day due to the cycle time.

B. Temperatures

1. Cooldown

It is important to consider that before a cooldown the pressure inside the cold stages of such a nested design is significantly worse than the pressure measured by an outside gauge which is closer to the pumps. Therefore, a cooldown is usually not started before reaching a vacuum in the 10^{-8} mbar range as measured by the gauge in the first cross. This reduces the amount of freezing residual gas and prolongs the time to the first warm up cycles in order to restore initial vacuum conditions. Furthermore, an increase of the emissivity of the cryogenic surfaces due to adsorbed layers of residual gas is prevented.

We continuously log the temperatures of the different segments of the TTU with sensors mounted at the locations shown in Fig. 1. We reach 49 and 4.6 K with cooldown times of 72 and 36 h for the first and second stage, respectively [see Fig. 9(a)]. After cooling down for about 36 h the second stage temperatures quickly decrease to values near steady-state. This effect is due to the freezing of degrees-of-freedom in the copper, that result in a much-reduced specific heat capacity and an increased thermal conductivity below 40 K, especially for the annealed parts. In many cases experiments can already proceed 36 h after the start of the cooldown. However, thermal contraction could still change the ion trap alignment with the laser. In practice, cooling times of three days over the course of a weekend were a sensible option. We usually maintain cryogenic temperatures over months. In contrast, to restore UHV/XHV conditions after venting in a room-temperature setup requires several weeks of cumbersome high-temperature bake-out procedure to reach pressures in the 10^{-11} mbar range.

2. Warm up

Before venting the system to perform work in the vacuum chamber, it has to warm up above the dew point (around 8 °C at a relative humidity of 40% at 22 °C). Due to the good thermal insulation of the cold stages, the whole system is basically only warmed up through the switched-off pulse tube, and this process takes two weeks [see Fig. 9(b)]. To speed it up, a small amount of helium gas can be leaked into the chambers, increasing the pressure to 10^{-2} mbar or even more, but yet keeping the vacuum chamber temperature around 12 °C—just above the dew point to avoid water condensation on the laser windows. Since He does not freeze out and is a light atom, it ensures a fast heat transfer, causing a cooling of the vacuum chamber wall while the inside temperatures quickly rise. To keep the helium from being pumped away, the gate valve to the TMPs is closed. To exclude a damaging overpressure due to the release of cryosorbed gas, we first warm up the two stages to approximately 100 and 200 K under pumping before closing the gate valve and letting helium into the chamber.

© Author(s) 2019

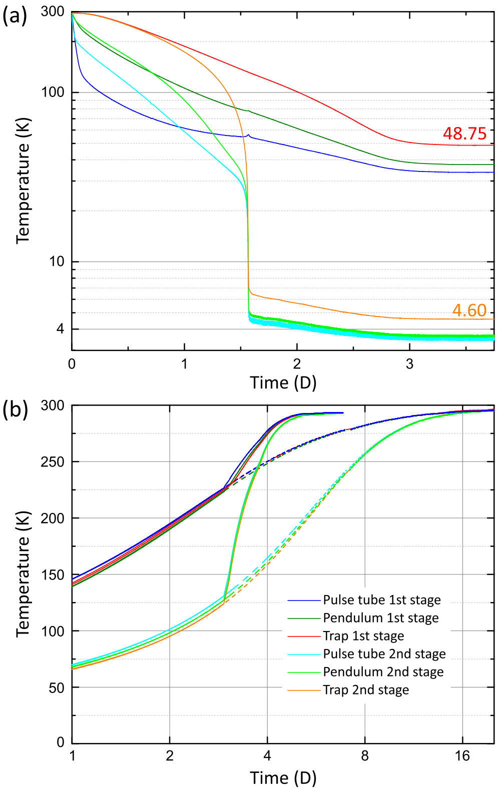

FIG. 9. Cooldown (a) and warm up (b) behavior. (a) Temperature evolution measured by six sensors. At the ion trap, the steady-state temperatures are 48.8 K and 4.6 K on the first and second stage, respectively. The pendulum temperature is measured at the first cross behind the flexible copper links. (b) A warm up of the system after switching off the pulse tube takes more than 14 days (dashed lines). A faster warm up is aided by letting a small amount of helium into the vacuum chamber after about 3 days for increased thermal coupling between the temperature stages (solid lines). Then, the system reaches room temperature in less than two days. Note the different scales in (a) and (b). See the text for further details.

3. Thermal budget

We performed thermal calculations, using established methods as described, e.g., in Ref. 31, taking into account thermal resistances, conductances, and radiation for optimizing the heat load and cryogenic temperatures. These calculations are fairly consistent with the performance of the built systems.

The thermal resistances R_{th} of the various rigid copper elements were minimized along the TTU. They were derived from Fourier's law of heat conduction at a constant nominal temperature (of 4 and 40 K for the second and first stage, respectively), yielding

$$R_{th} = \frac{l}{A \cdot \lambda(T)}, \tag{3}$$

depending on the cross section A, the length l, and the material-specific and temperature-dependent thermal conductivity λ. We maximized the cross sections of the various parts given the geometric constraints of the system; the lengths were determined by the size of the apparatus. Extremely pure copper was used for high λ values with vacuum annealing applied wherever practicable to further increase the conductivity at low temperatures.

The conductances of the flexible copper links can be roughly estimated with the capacity map of the pulse tube[71] yielding the total thermal loads of the two temperature stages as a function of their steady-state temperatures. The temperature gradients across the links are measured in the first cross by temperature sensors on their end plates (see Fig. 1). For the first stage, we observe a thermal load of 22 W (with the ion trap chamber[57] installed) and a temperature gradient of 3.8 K, leading to a conductance of 5.8 W K^{-1}. For the second stage, we obtain a value of 0.8 W/0.15 K = 5.3 W K^{-1}. Since the links attached to the first and second stage have comparable lengths, but differ in the number of copper ropes by a factor of two, these measurements imply that the conductivity of the copper material at 3.5 K is twice as high as its value at 33.8 K. This indicates RRR values between 500 and 1200[72]—a substantial improvement upon a measured value of 77 for an unannealed strap[54] resulting in a five- to tenfold increase of the thermal conductivity at 4 K. The conductances of the flexible links in the second cross can be estimated by scaling the values of the first links regarding the slightly different lengths. The estimated values R_{th} for the different parts of the TTU are listed in Table I.

Estimates of the total heat load onto the two cryocooler stages include heat conduction by the spokes, connecting parts of different temperatures, and thermal radiation from warmer surfaces. The heat flow through a spoke from a thermal reservoir at temperature T_2 to another reservoir at T_1 is given by

$$\dot{Q}_{cond} = \frac{A}{l}\int_{T_1}^{T_2} \lambda(T)\,\mathrm{d}T \tag{4}$$

$$= \frac{A}{l}\left(\int_{4K}^{T_2} \lambda(T)\,\mathrm{d}T - \int_{4K}^{T_1} \lambda(T)\,\mathrm{d}T\right). \tag{5}$$

TABLE I. Estimated thermal resistances R_{th} of the connecting copper elements of the TTU. An RRR of about 1000 is assumed for the annealed copper of the rigid parts with purities between 4N5 and 5N; thermal conductivities $\lambda(T)$ are taken from Refs. 72 and 73. For the flexible links, R_{th} was estimated as described in the text. The nominal temperatures assumed for the two temperature stages are 4 and 40 K, respectively.

Stage	Element	λ (W cm^{-1} K^{-1})	R_{th} (K W^{-1})
2nd	1st flexible link	...	0.19
2nd	Pendulum rod	70	0.10
2nd	2nd flexible link	...	0.25
2nd	Vertical rod	70	0.03
1st	1st vertical shield	20	0.04
1st	1st flexible link	...	0.17
1st	Pendulum shield	20	0.12
1st	2nd flexible link	...	0.11
1st	2nd vertical shield	20	0.09

© Author(s) 2019

The thermal conductivity integral values for stainless steel, 3060 W/m at $T_2 = 300$ K and 82 W/m at $T_1 = 40$ K, were taken from Ref. 31. We minimized the heat flow through the spokes by making them as long as practically possible, using lengths between 79 mm and 150 mm, yielding 1.06 W and 60 mW onto the first and second stage, respectively (see Table II).

The thermal radiation heat loads onto the first and second stages were estimated by approximating the cryogenic system as three long, concentric cylinders. For diffuse reflection, the Stefan-Boltzmann law and the cylindrical geometry yield

$$\dot{Q}_{rad} = \frac{A_1 \sigma \left(T_2^4 - T_1^4\right)}{\frac{1}{\epsilon_1} + \frac{A_1}{A_2}\left(\frac{1}{\epsilon_2} - 1\right)}, \qquad (6)$$

where the power $\dot{Q}_{rad}$ is emitted from the outer surface with area A_2 at temperature T_2 with emissivity ϵ_2, and is received by the inner surface A_1 at temperature T_1 with emissivity ϵ_1. σ is the Stefan-Boltzmann constant. For specular reflection, $A_1 = A_2$ holds in the denominator,[31] resulting in only minor corrections. For the nominal temperatures of 300 K (vacuum chamber), 40 K (first stage), and 4 K (second stage) and estimated emissivities of $\epsilon_1 = \epsilon_2 = 0.05$ for the electropolished stainless-steel vacuum chamber and the mainly gold-plated copper parts, we calculate radiative heat loads of 10.7 W onto the first stage and 1.5 mW onto the second stage.

In Table III, the estimated total heat loads of only the cryostat without the ion trap chamber and ion trap are given. The dominant heat load onto the first stage is the thermal radiation, while for the second stage the thermal conduction is dominant. Additional heat loads onto the first and second stages are introduced by thermal radiation from the ion trap chamber, conduction through further spokes and the rf ion trap wiring, and dissipation of rf power.[57] Thus, we reach final temperatures of 33.8 K at the pulse-tube first stage and of 3.50 K at the second stage, respectively. These values can be compared with the capacity map of the pulse-tube cryocooler,[71] roughly yielding heat loads of about 22 W (first stage) and 0.8 W (second stage).

TABLE II. Heat load by thermal conduction through the spokes. The elements given in the first column, being at the nominal temperature T_1, receive the heat input, given in the last column, by a certain number of spokes of a certain length from the warmer reservoir at T_2. The vertical rod has two different types of spokes, (I) and (II), which differ in their length by about 10 mm.

Element	T_2 (K)	T_1 (K)	Number	Length (mm)	Heat input (W)
Pendulum shield	300	40	2	150	0.12
Vertical shield	300	40	12	120	0.94
Total 1st stage	...	...	14	...	1.06
Pendulum rod	40	4	6	100	0.02
Vertical rod (I)	40	4	6	79	0.02
Vertical rod (II)	40	4	6	89	0.02
Total 2nd stage	...	...	18	...	0.06

TABLE III. Estimated steady-state heat loads of the cryostat without the ion trap.

	1st stage (W)	2nd stage (W)
Black-body radiation	10.7	0.0015
Conduction through spokes	1.06	0.06
Conduction through sensor wiring	0.01	<0.01
Total	11.8	0.07

C. Stability

1. Decoupling from vibration and noise sources

Sources of vibrations are the pulse-tube cryocooler (1.7 Hz) and its compressor, the forevacuum scroll pump (around 25 Hz), the TMPs (1000 Hz and 1500 Hz, respectively), and others that couple through the laboratory floor: building vibrations, air-conditioning, water-cooling systems, and fans. All of these also produce acoustic noise coupling through the air and walls. We installed noisy parts in the machine room, which is acoustically insulated from the laser laboratory, achieving a noise reduction of approximately 20 dB. The machine-room floor has a vibration-damping screed. The compressor is mounted on a vibration-insulation platform on passive pneumatic feet which decouple it from the floor. However, vibrations can still be transmitted along the cryogenic helium lines. To damp such compressor noise, we guide the helium hoses through a heavy metal box filled with 100 kg of fine quartz sand placed right next to the pulse tube (see Fig. 10). Also, the forevacuum scroll pump rests on a pneumatic vibration-insulation platform, and the flexible stainless steel hose connecting it to the segment I TMPs is guided through a second metal box with 25 kg quartz sand. To keep vibrations, arising in segment I by the He gas flow in the pulse tube, from being transmitted towards the ion trap, the three segments are mechanically decoupled. As described in Sec. II, the TTU employs flexible copper links while the vacuum chambers are decoupled by edge-welded bellows with 40 diaphragm pairs each. Segment I rests on

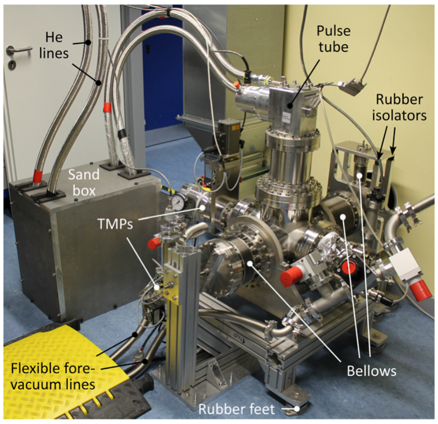

FIG. 10. Photograph of the cryostat in the machine room. Vibration sources and decoupling elements are labeled. TMPs – turbomolecular pumps.

© Author(s) 2019

rubber feet on the machine-room floor. Segment II with the pendulum acting as a low-pass filter also rests on rubber feet on the floors of both rooms. These feet decouple it from vibrations from the pulse tube and vacuum pumps. The two plates from which the pendulum hangs (as described in Sec. II) are supported by four rubber isolators each (as shown in Figs. 1 and 10). Segment III is connected to segment II through the second vibration-decoupling section and attached to the optical table without any rigid connection to the floor. The pneumatically floating optical table with a mass of >600 kg acts as a second inertial filter for vibration damping. In this way, high-frequency vibrations are efficiently suppressed. Beyond 100 Hz, we can rule out vibration peaks above the measurement white noise plateau of $2\,\mathrm{nm}/\sqrt{\mathrm{Hz}}$ root mean square amplitude spectral density. In particular, no vibration peaks were observed at the TMP rotational frequencies of 1000 Hz and 1500 Hz, respectively. Low-frequency vibrations are less strongly damped, as shown by the measured vibration peak amplitude spectra (see Sec. III C 2 for further details).

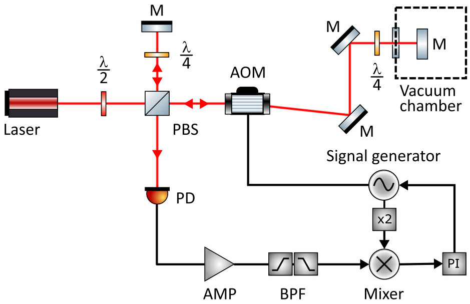

FIG. 11. Interferometric setup to measure the vibrations at the ion trap. Two of the three directions were measured with such a closed-loop setup; the third direction was measured in open-loop. See text for further details. AMP—amplifier, AOM—acousto-optic modulator, BPF—band-pass filter, $\lambda/2$—half-wave plate, $\lambda/4$—quater-wave plate, M—mirror, PBS—polarizing beamsplitter cube, PD—photodiode, PI—proportional-integral controller.

2. Vibration measurement

The inherent vibrations arising in the pulse tube have an amplitude of ~10 μm at the cold stages and appear mostly at its operating frequency (1.7 Hz) plus its harmonics, mostly odd ones (here up to 11th order). The impact on the ion trap of these vibrations, in addition to the other aforementioned noise sources, must be characterized. Vibrations propagating through the TTU and the vacuum chamber walls can cause unacceptable motion of the ion trap. In precision laser spectroscopy for instance, differential vibrations between the optical table and the ion trap lead to Doppler shifts of the interrogating lasers. For coherent operation, the vibration amplitudes should be smaller than the involved wavelengths of the lasers.

To evaluate the mechanical stability of our system, we measured the vibration spectra in three dimensions using self-heterodyne interferometers, with the reference arm located on the optical table and the signal arm connecting to the second stage close by the ion trap using retroreflecting mirrors. The interferometers employ acousto-optic modulators (AOMs) in the signal arms for frequency shifting twice and silver-coated mirrors installed on three laser access ports for retro-reflection of the incident beam (see the scheme in Fig. 11). Due to access constraints, we could not use mutually orthogonal ports. Thus, simultaneous measurements had to be taken to reconstruct the 3D vibrations along the principal axes. For each single direction, the interferometric beat note was detected with a fast photodiode and demodulated with a frequency mixer driven by twice the AOM frequency. These signals passed proportional-integral (PI) loop filters and were fed to the (phase or frequency) modulation input of the signal generators driving the AOMs, thereby stabilizing the laser phases at the mirror positions inside the vacuum chamber. Depending on the type of feedback provided by the signal generators, displacement amplitudes (phase modulation) or velocities (frequency modulation) were measured. Calibration of the modulation inputs of the signal generators returned absolute displacements. The outputs of the loop filter signals were sent to a fast-Fourier transform device, recording the spectrum of the feedback signals necessary to close the loop, or to an oscilloscope. Figure 12 shows such time traces where the signal, recorded as a voltage, was already converted into displacement amplitudes. As there were only two signal generators with modulation inputs available for the measurement, vibrations on the third axis were measured in an open-loop configuration by observing fluctuations in the error signal after demodulation. The phase of the signal generator output for this dimension was tuned to ensure operation in the linear range of the mixer output.

Vibrations along the horizontal pendulum axis could be directly sampled under an angle of 0°. Vibrations along the other two principal axes, namely, the ion trap axis (also horizontal) and the vertical axis, could be estimated by reconstructing the time traces by vector addition. The measurements for these two axes had to be taken at angles of 60° with respect to the trap axis in the horizontal plane and at 75° with respect to the vertical axis in the vertical

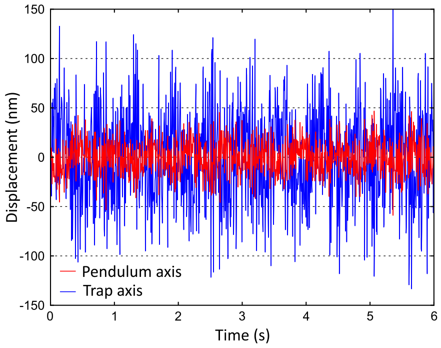

FIG. 12. Vibrations in the horizontal plane along the pendulum axis (red) and the perpendicular trap axis (blue). The time traces were recorded with an oscilloscope at a sampling frequency of 200 Hz. Here, a slow drift was removed by processing the time traces with a cut-off frequency of 1 Hz. The vibrations along the trap axis had to be reconstructed with the pendulum axis measurement and a vibration measurement taken at 60° with respect to the trap axis. A division by cos(60°) results in a deteriorate accuracy. See the text for further details.

plane through the trap axis, respectively. The subsequent reconstructions involve divisions by cos(60°) ≈ 0.5 and cos(75°) ≈ 0.26, also increasing their absolute errors. Consequently, the vertical axis is the least accurate one; however, it is also the least important one since spectroscopy lasers enter the trap in the horizontal plane. In Fig. 13, the vibration amplitude spectra along the three principal axes are displayed, obtained by a discrete Fourier transform of the reconstructed time traces. The left hand column shows the vibrations with the pulse tube switched on and off as well as the measurement noise floor, recorded by blocking the photodiode in Fig. 11. Additionally, the pulse tube-induced vibration spectra are shown in the right hand column, i.e., the difference of the spectra with the pulse tube switched on and off. The individual horizontal vibration amplitudes are well below 20 nm, with the dominating peak at the pulse-tube repetition rate of 1.7 Hz and ~10 nm at the fifth harmonic (8.5 Hz). These oscillations lead to a peak first order Doppler shift on the order of 10^{-16}. Most of the vibrations at 20–60 Hz can be attributed to resonances of the floor or optical table excited by the compressor. In spectroscopic measurements, vibrations lead to line broadening if their period is shorter than the interrogation time, as it is the case for narrow transitions. Second-order Doppler shifts induced by the measured vibration velocities are negligible.

The measured vibration level in the horizontal plane is about one order of magnitude lower than reported for a Gifford-McMahon cryocooler equipped with a helium-gas exchange cell, when operating the system at a similar temperature of about 4.5 K.[5]

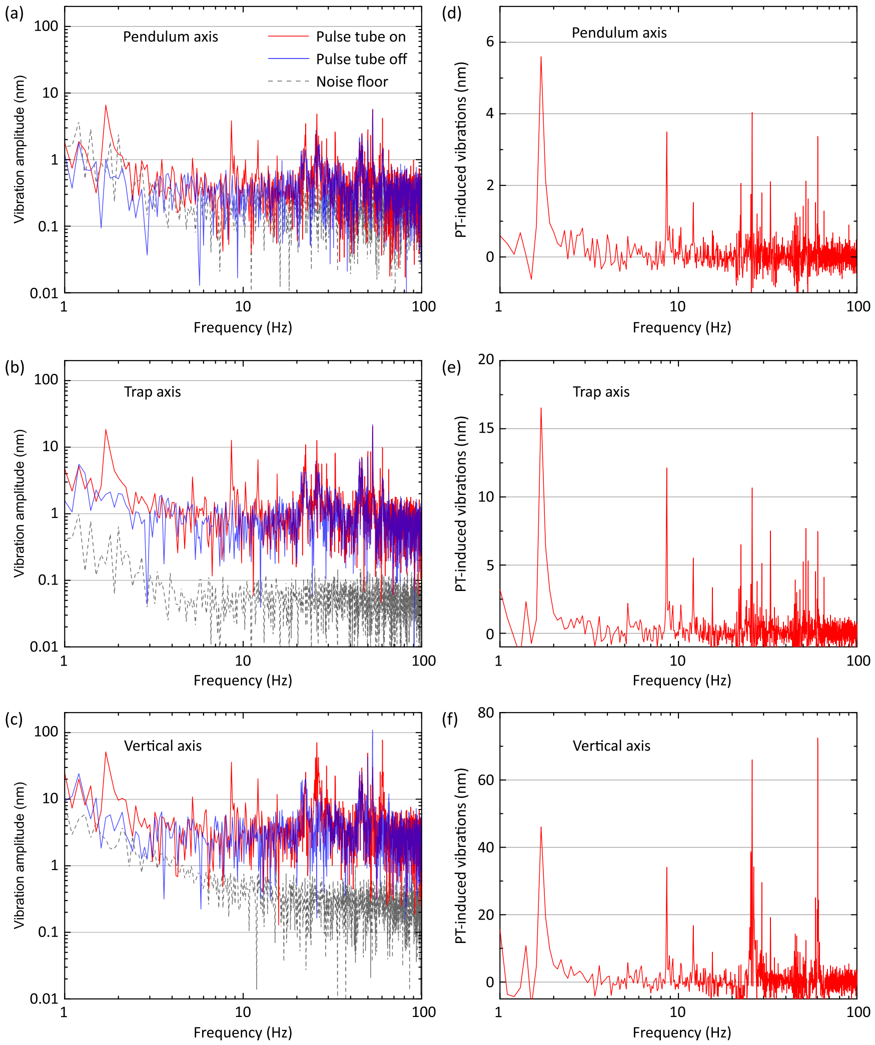

FIG. 13. Left column: Vibration peak amplitude spectra along three orthogonal axes [(a): pendulum axis, (b): trap axis, (c): vertical axis]. The data were taken with the pulse-tube cryocooler on (red) and off (blue) in order to determine its contribution to the vibration levels. Also displayed is the measurement noise floor (dashed), which indicates the sensitivity of the applied method. Right column: Pulse tube-induced vibration amplitudes along the axes to show the effect of the operation of pulse tube and compressor [(d): pendulum axis, (e): trap axis, (f): vertical axis; note the different y-scales]. The spectra were derived from a discrete Fourier transform of 10 s-long measurements of the mirror displacements with a sampling frequency of 200 Hz. This results in a corresponding resolution bandwidth of 0.1 Hz. Measurements taken at higher sampling frequencies did not show vibration peaks beyond 100 Hz. Note that the spectra for the trap and vertical axes had to be reconstructed by measurements taken at 60° and 75°. See the text for further details.

© Author(s) 2019

IV. CONCLUSION

We have introduced a novel closed-cycle cryostat capable of suppressing cryocooler vibrations by about three orders of magnitude to a level of 10 nm. It provides <5 K temperatures, an XHV pressure in the 10^{-15}-mbar range, and 1 W of cooling power. Installation of noisy components in an adjacent room and several stages of vibration suppression are applied. We installed a radio-frequency ion trap on a pneumatically floating optical table, reproducing its position after a full thermal cycle to room temperature and back to below 5 K with respect to several aligned laser beams to better than a few micrometer. These conditions are needed for high precision experiments and optical clock operation with HCIs.[10] Our system has stably operated over months, requires little maintenance, and offers convenient vacuum access from the top. To our knowledge, our vibration suppression surpasses all other reported closed-cycle systems with comparable cooling power. The concept can be adapted to other geometries, for example, with a vertical pendulum. Further vibration suppression could be achieved by separating the rotary valve unit from the pulse-tube cryocooler, decoupling the pulse tube from the first cross with vertical bellows, employing a cryocooler with lower inherent vibrations, and by mounting segment I and II onto air springs. We are keen to share our design with other research groups.

ACKNOWLEDGMENTS

We gratefully acknowledge the MPIK engineering design office headed by Frank Müller, the mechanical workshops of MPIK under the direction of Thorsten Spranz, and of PTB headed by Frank Löffler for their expertise and fabrication of numerous intricate parts. We thank the MPIK mechanical apprenticeship workshop, led by Stefan Flicker, where a major number of parts were made and a significant amount of development work took place. We thank, in particular, Florian Säubert for devising sophisticated procedures for the manufacturing of complex parts. Additionally, we appreciated the help by Stephan Metschke, Christian Kaiser, and Alexander Ruhz. We thank Julian Glässel, Michael Drewsen, Timko Dubielzig, and Matthias Brandl for helpful discussions. Financial support was provided by the Max-Planck-Gesellschaft and the Physikalisch-Technische Bundesanstalt. S.A.K. acknowledges support by the Alexander von Humboldt Foundation. We acknowledge support from the Deutsche Forschungsgemeinschaft through Grant No. SCHM2678/5-1 and the Collaborative Research Centre "SFB 1225 (ISOQUANT)."

REFERENCES

[1] J. Repp, C. Böhm, J. R. C. López-Urrutia, A. Dörr, S. Eliseev, S. George, M. Goncharov, Y. N. Novikov, C. Roux, S. Sturm, S. Ulmer, and K. Blaum, Appl. Phys. B **107**, 983 (2012).

[2] S. Sturm, M. Vogel, F. Köhler-Langes, W. Quint, K. Blaum, and G. Werth, Atoms **5**, 4 (2017).

[3] M. Schwarz, O. O. Versolato, A. Windberger, F. R. Brunner, T. Ballance, S. N. Eberle, J. Ullrich, P. O. Schmidt, A. K. Hansen, A. D. Gingell, M. Drewsen, and J. R. C. López-Urrutia, Rev. Sci. Instrum. **83**, 083115 (2012).

[4] M. Niedermayr, K. Lakhmanskiy, M. Kumph, S. Partel, J. Edlinger, M. Brownnutt, and R. Blatt, New J. Phys. **16**, 113068 (2014).

[5] G. Pagano, P. W. Hess, H. B. Kaplan, W. L. Tan, P. Richerme, P. Becker, A. Kyprianidis, J. Zhang, E. Birckelbaw, M. R. Hernandez, Y. Wu, and C. Monroe, Quantum Sci. Technol. **4**, 014004 (2019).

[6] D. Gerlich, Phys. Scr. **T59**, 256 (1995).

[7] D. H. Slichter, V. B. Verma, D. Leibfried, R. P. Mirin, S. W. Nam, and D. J. Wineland, Opt. Express **25**, 8705 (2017).

[8] E. E. Wollman, V. B. Verma, A. D. Beyer, R. M. Briggs, B. Korzh, J. P. Allmaras, F. Marsili, A. E. Lita, R. P. Mirin, S. W. Nam, and M. D. Shaw, Opt. Express **25**, 26792 (2017).

[9] A. Müller and E. Salzborn, Phys. Lett. A **62**, 391 (1977).

[10] M. G. Kozlov, M. S. Safronova, J. R. Crespo López-Urrutia, and P. O. Schmidt, Rev. Mod. Phys. **90**, 045005 (2018).

[11] L. Schmöger, O. O. Versolato, M. Schwarz, M. Kohnen, A. Windberger, B. Piest, S. Feuchtenbeiner, J. Pedregosa-Gutierrez, T. Leopold, P. Micke, A. K. Hansen, T. M. Baumann, M. Drewsen, J. Ullrich, P. O. Schmidt, and J. R. C. López-Urrutia, Science **347**, 1233 (2015).

[12] L. Schmöger, M. Schwarz, T. M. Baumann, O. O. Versolato, B. Piest, T. Pfeifer, J. Ullrich, P. O. Schmidt, and J. R. Crespo López-Urrutia, Rev. Sci. Instrum. **86**, 103111 (2015).

[13] P. O. Schmidt, T. Rosenband, C. Langer, W. M. Itano, J. C. Bergquist, and D. J. Wineland, Science **309**, 749 (2005).

[14] J. Kim, S. Pau, Z. Ma, H. R. Mclellan, J. V. Gates, A. Kornblit, R. E. Slusher, R. M. Jopson, I. Kang, and M. Dinu, Quantum Inf. Comput. **5**, 515 (2005).

[15] J. Alonso, F. M. Leupold, Z. U. Solèr, M. Fadel, M. Marinelli, B. C. Keitch, V. Negnevitsky, and J. P. Home, Nat. Commun. **7**, 11243 (2016).

[16] K. R. Brown, J. Kim, and C. Monroe, npj Quantum Inf. **2**, 16034 (2016).

[17] M. F. Brandl, M. W. van Mourik, L. Postler, A. Nolf, K. Lakhmanskiy, R. R. Paiva, S. Möller, N. Daniilidis, H. Häffner, V. Kaushal, T. Ruster, C. Warschburger, H. Kaufmann, U. G. Poschinger, F. Schmidt-Kaler, P. Schindler, T. Monz, and R. Blatt, Rev. Sci. Instrum. **87**, 113103 (2016).

[18] L. Deslauriers, S. Olmschenk, D. Stick, W. Hensinger, J. Sterk, and C. Monroe, Phys. Rev. Lett. **97**, 103007 (2006).

[19] J. Labaziewicz, Y. Ge, P. Antohi, D. Leibrandt, K. R. Brown, and I. L. Chuang, Phys. Rev. Lett. **100**, 013001 (2008).

[20] M. Brownnutt, M. Kumph, P. Rabl, and R. Blatt, Rev. Mod. Phys. **87**, 1419 (2015).

[21] T. Rosenband, D. B. Hume, P. O. Schmidt, C. W. Chou, A. Brusch, L. Lorini, W. H. Oskay, R. E. Drullinger, T. M. Fortier, J. E. Stalnaker, S. A. Diddams, W. C. Swann, N. R. Newbury, W. M. Itano, D. J. Wineland, and J. C. Bergquist, Science **319**, 1808 (2008).

[22] T. Middelmann, C. Lisdat, S. Falke, J. Winfred, F. Riehle, and U. Sterr, IEEE Trans. Instrum. Meas. **60**, 2550 (2011).

[23] K. Gibble, Phys. Rev. Lett. **110**, 180802 (2013).

[24] I. Ushijima, M. Takamoto, M. Das, T. Ohkubo, and H. Katori, Nat. Photonics **9**, 185 (2015).

[25] M. Takamoto, I. Ushijima, M. Das, N. Nemitz, T. Ohkubo, K. Yamanaka, N. Ohmae, T. Takano, T. Akatsuka, A. Yamaguchi, and H. Katori, C. R. Phys. **16**, 489 (2015).

[26] A. D. Ludlow, M. M. Boyd, J. Ye, E. Peik, and P. Schmidt, Rev. Mod. Phys. **87**, 637 (2015).

[27] A. C. Vutha, T. Kirchner, and P. Dubé, Phys. Rev. A **96**, 022704 (2017).

[28] C. Benvenuti, J. Vac. Sci. Technol. **11**, 591 (1974).

[29] G. Gabrielse, X. Fei, L. A. Orozco, R. L. Tjoelker, J. Haas, H. Kalinowsky, T. A. Trainor, and W. Kells, Phys. Rev. Lett. **65**, 1317 (1990).

[30] M. Diederich, H. Häffner, N. Hermanspahn, M. Immel, H. Kluge, R. Ley, R. Mann, W. Quint, S. Stahl, and G. Werth, Hyperfine Interact. **115**, 185 (1998).

[31] J. Ekin, *Experimental Techniques for Low-Temperature Measurements: Cryostat Design, Material Properties and Superconductor Critical-Current Testing* (Oxford University Press, Oxford, 2006).

[32] M. E. Poitzsch, J. C. Bergquist, W. M. Itano, and D. J. Wineland, Rev. Sci. Instrum. **67**, 129 (1996).

[33] R. Radenbaugh, Proc. IEEE **92**, 1719 (2004).

© Author(s) 2019

[34] R. Radebaugh, J. Phys.: Condens. Matter **21**, 164219 (2009).

[35] T. Kessler, C. Hagemann, C. Grebing, T. Legero, U. Sterr, F. Riehle, M. J. Martin, L. Chen, and J. Ye, Nat. Photonics **6**, 687 (2012).

[36] D. Matei, T. Legero, S. Häfner, C. Grebing, R. Weyrich, W. Zhang, L. Sonderhouse, J. Robinson, J. Ye, F. Riehle, and U. Sterr, Phys. Rev. Lett. **118**, 263202 (2017).

[37] J. M. Robinson, E. Oelker, W. R. Milner, W. Zhang, T. Legero, D. G. Matei, F. Riehle, U. Sterr, and J. Ye, Optica **6**, 240 (2019).

[38] S. Grop, P. Bourgeois, R. Boudot, Y. Kersale, E. Rubiola, and V. Giordano, Electron. Lett. **46**, 420 (2010).

[39] J. G. Hartnett, N. R. Nand, and C. Lu, Appl. Phys. Lett. **100**, 183501 (2012).

[40] M. J. Thorpe, L. Rippe, T. M. Fortier, M. S. Kirchner, and T. Rosenband, Nat. Photonics **5**, 688 (2011).

[41] Q.-F. Chen, A. Troshyn, I. Ernsting, S. Kayser, S. Vasilyev, A. Nevsky, and S. Schiller, Phys. Rev. Lett. **107**, 223202 (2011).

[42] S. Cook, T. Rosenband, and D. R. Leibrandt, Phys. Rev. Lett. **114**, 253902 (2015).

[43] T. Mochizuki, Y. Kohmura, A. Awaji, Y. Suzuki, A. Baron, K. Tamasaku, M. Yabashi, H. Yamazaki, and T. Ishikawa, in *7th International Conference on Synchrotron Radiation Instrumentation* [Nucl. Instrum. Methods Phys. Res., Sect. A **467-468**, 647 (2001)].

[44] T. S. Toellner, A. Alatas, A. Said, D. Shu, W. Sturhahn, and J. Zhao, J. Synchrotron Radiat. **13**, 211 (2006).

[45] CUORE Collaboration, C. Alduino, F. Alessandria, K. Alfonso, E. Andreotti, C. Arnaboldi, F. Avignone, O. Azzolini, M. Balata, I. Bandac, T. Banks, G. Bari, M. Barucci, J. Beeman, F. Bellini, G. Benato, A. Bersani, D. Biare, M. Biassoni, F. Bragazzi, A. Branca, C. Brofferio, A. Bryant, A. Buccheri, C. Bucci, C. Bulfon, A. Camacho, A. Caminata, L. Canonica, X. Cao, S. Capelli, M. Capodiferro, L. Cappelli, L. Cardani, M. Cariello, P. Carniti, M. Carrettoni, N. Casali, L. Cassina, R. Cereseto, G. Ceruti, A. Chiarini, D. Chiesa, N. Chott, M. Clemenza, D. Conventi, S. Copello, C. Cosmelli, O. Cremonesi, C. Crescentini, R. Creswick, J. Cushman, A. D'Addabbo, D. D'Aguanno, I. Dafinei, V. Datskov, C. Davis, F. Del Corso, S. Dell'Oro, M. Deninno, S. Di Domizio, M. Di Vacri, L. Di Paolo, A. Drobizhev, L. Ejzak, R. Faccini, D. Fang, M. Faverzani, E. Ferri, F. Ferroni, E. Fiorini, M. Franceschi, S. Freedman, B. Fujikawa, R. Gaigher, A. Giachero, L. Gironi, A. Giuliani, L. Gladstone, J. Goett, P. Gorla, C. Gotti, C. Guandalini, M. Guerzoni, T. Gutierrez, E. Haller, K. Han, E. Hansen, K. Heeger, R. Hennings-Yeomans, K. Hickerson, H. Huang, M. Iannone, L. Ioannucci, R. Kadel, G. Keppel, L. Kogler, Y. Kolomensky, A. Leder, C. Ligi, K. Lim, X. Liu, Y. Ma, C. Maiano, M. Maino, L. Marini, M. Martinez, C. Martinez Amaya, R. Maruyama, Y. Mei, N. Moggi, S. Morganti, P. Mosteiro, S. Nagorny, T. Napolitano, M. Nastasi, S. Nisi, C. Nones, E. Norman, V. Novati, A. Nucciotti, I. Nutini, T. O'Donnell, M. Olcese, E. Olivieri, F. Orio, D. Orlandi, J. Ouellet, C. Pagliarone, M. Pallavicini, V. Palmieri, L. Pattavina, M. Pavan, M. Pedretti, R. Pedrotta, A. Pelosi, G. Pessina, V. Pettinacci, G. Piperno, C. Pira, S. Pirro, S. Pozzi, E. Previtali, F. Reindl, F. Rimondi, L. Risegari, C. Rosenfeld, C. Rossi, C. Rusconi, M. Sakai, E. Sala, C. Salvioni, S. Sangiorgio, D. Santone, D. Schaeffer, B. Schmidt, J. Schmidt, N. Scielzo, V. Singh, M. Sisti, A. Smith, F. Stivanello, L. Taffarello, L. Tatananni, M. Tenconi, F. Terranova, M. Tessaro, C. Tomei, G. Ventura, M. Vignati, S. Wagaarachchi, J. Wallig, B. Wang, H. Wang, B. Welliver, J. Wilson, K. Wilson, L. Winslow, T. Wise, L. Zanotti, C. Zarra, G. Zhang, B. Zhu, S. Zimmermann, and S. Zucchelli, Phys. Rev. Lett. **120**, 132501 (2018).

[46] C. P. Aguirre, D. R. Artusa, F. T. Avignone, O. Azzolini, M. Balata, T. I. Banks, G. Bari, J. Beeman, F. Bellini, A. Bersani, M. Biassoni, C. Brofferio, C. Bucci, X. Z. Cai, A. Camacho, L. Canonica, X. Cao, S. Capelli, L. Carbone, L. Cardani, M. Carrettoni, N. Casali, D. Chiesa, N. Chott, M. Clemenza, C. Cosmelli, O. Cremonesi, R. J. Creswick, I. Dafinei, A. Dally, V. Datskov, A. De Biasi, M. M. Deninno, S. Di Domizio, M. L. di Vacri, L. Ejzak, D. Q. Fang, H. A. Farach, M. Faverzani, G. Fernandes, E. Ferri, F. Ferroni, E. Fiorini, M. A. Franceschi, S. J. Freedman, B. K. Fujikawa, A. Giachero, L. Gironi, A. Giuliani, J. Goett, P. Gorla, C. Gotti, T. D. Gutierrez, E. E. Haller, K. Han, K. M. Heeger, R. Hennings-Yeomans, H. Z. Huang, R. Kadel, K. Kazkaz, G. Keppel, Y. G. Kolomensky, Y. L. Li, C. Ligi, X. Liu, Y. G. Ma, C. Maiano, M. Maino, M. Martinez, R. H. Maruyama, Y. Mei, N. Moggi, S. Morganti, T. Napolitano, S. Nisi, C. Nones, E. B. Norman, A. Nucciotti, T. O'Donnell, F. Orio, D. Orlandi, J. L. Ouellet, M. Pallavicini, V. Palmieri, L. Pattavina, M. Pavan, M. Pedretti, G. Pessina, G. Piperno, C. Pira, S. Pirro, E. Previtali, V. Rampazzo, C. Rosenfeld, C. Rusconi, E. Sala, S. Sangiorgio, N. D. Scielzo, M. Sisti, A. R. Smith, L. Taffarello, M. Tenconi, F. Terranova, W. D. Tian, C. Tomei, S. Trentalange, G. Ventura, M. Vignati, B. S. Wang, H. W. Wang, L. Wielgus, J. Wilson, L. A. Winslow, T. Wise, A. Woodcraft, L. Zanotti, C. Zarra, B. X. Zhu, and S. Zucchelli, in *13th International Conference on Topics in Astroparticle and Underground Physics, TAUP 2013* [Phys. Procedia **61**, 13 (2015)].

[47] K. Somiya, Classical Quantum Gravity **29**, 124007 (2012).

[48] R. Radebaugh, *Low Temperature and Cryogenic Refrigeration*, NATO Science Series (Springer, Dordrecht, 2003), pp. 415–434.

[49] J. M. Sage, A. J. Kerman, and J. Chiaverini, Phys. Rev. A **86**, 013417 (2012).

[50] E. Olivieri, J. Billard, M. De Jesus, A. Juillard, and A. Leder, Nucl. Instrum. Methods Phys. Res., Sect. A **858**, 73 (2017).

[51] T. Dubielzig, private communication (2019).

[52] A. D'Addabbo, C. Bucci, L. Canonica, S. Di Domizio, P. Gorla, L. Marini, A. Nucciotti, I. Nutini, C. Rusconi, and B. Welliver, Cryogenics **93**, 56 (2018).

[53] Y. Ikushima, R. Li, T. Tomaru, N. Sato, T. Suzuki, T. Haruyama, T. Shintomi, and A. Yamamoto, Cryogenics **48**, 406 (2008).

[54] R. C. Dhuley, M. Ruschman, J. T. Link, and J. Eyre, Cryogenics **86**, 17 (2017).

[55] M. de Wit, G. Welker, K. Heeck, F. M. Buters, H. J. Eerkens, G. Koning, H. van der Meer, D. Bouwmeester, and T. H. Oosterkamp, Rev. Sci. Instrum. **90**, 015112 (2019).

[56] P. Micke, S. Kühn, L. Buchauer, J. R. Harries, T. M. Bücking, K. Blaum, A. Cieluch, A. Egl, D. Hollain, S. Kraemer, T. Pfeifer, P. O. Schmidt, R. X. Schüssler, C. Schweiger, T. Stöhlker, S. Sturm, R. N. Wolf, S. Bernitt, and J. R. Crespo López-Urrutia, Rev. Sci. Instrum. **89**, 063109 (2018).

[57] T. Leopold, S. A. King, P. Micke, A. Bautista-Salvador, J. C. Heip, C. Ospelkaus, J. R. C. López-Urrutia, and P. O. Schmidt, e-print arXiv:1901.03082 (2019).

[58] J. Stark *et al.*, "Superconducting monolithic 35 MHz radio-frequency quadrupole as ion trap" (unpublished).

[59] J. Nauta, A. Borodin, H. B. Ledwa, J. Stark, M. Schwarz, L. Schmöger, P. Micke, J. R. Crespo López-Urrutia, and T. Pfeifer, in *Proceedings of the 18th International Conference on the Physics of Highly Charged Ions (HCI-2016), Kielce, Poland, 11–16 September 2016* [Nucl. Instrum. Methods Phys. Res., Sect. B **408**, 285 (2017)].

[60] C. Day, in *CAS-CERN Accelerator School and ALBA Synchrotron Light Facility: Course on Vacuum in Accelerators, Platja d'Aro, E., Geneve, May 16–24, 2006*, edited by D. Brandt (CERN Accelerator School, 2007), also published in the web (2007), pp. 241–274.

[61] Model and supplier are just given for reference. This should not be considered as a recommendation.

[62] K. Mimura, Y. Ishikawa, M. Isshiki, and M. Kato, Mater. Trans., JIM **38**, 714 (1997).

[63] A. L. Woodcraft, Cryogenics **45**, 626 (2005).

[64] L. J. Salerno, P. Kittel, and A. L. Spivak, Cryogenics **34**, 649 (1994).

[65] E. Gmelin, M. Asen-Palmer, M. Reuther, and R. Villar, J. Phys. D: Appl. Phys. **32**, R19 (1999).

[66] B. Roth, P. Blythe, H. Wenz, H. Daerr, and S. Schiller, Phys. Rev. A **73**, 042712 (2006).

[67] B. C. Sawyer, J. G. Bohnet, J. W. Britton, and J. J. Bollinger, Phys. Rev. A **91**, 011401 (2015).

[68] L. Schmöger, "Kalte hochgeladene ionen für frequenzmetrologie," Ph.D. dissertation (Heidelberg University, 2017).

[69] A. Niehaus, J. Phys. B: At. Mol. Phys. **19**, 2925 (1986).

[70] M. P. Langevin, Ann. Chim. Phys. **5**, 245 (1905).

[71] "RP-082b2 4k pulse tube cryocooler series," Technical Report (SHI Cryogenics Group, 2018), Available at http://www.shicryogenics.com//wp-content/uploads/2012/11/SRP-082B_Capacity_Map.pdf.

[72] N. J. Simon, E. S. Drexler, and R. P. Reed, *Properties of Copper and Copper Alloys at Cryogenic Temperatures*, NIST Monograph No. 177 (U.S. Government Printing Office, Washington, 1992).

[73] V. J. Johnson, *A Compendium of the Properties of Materials at Low Temperature (Phase I-II)* (Wright Air Development Division, Air Research and Development Command, United States Air Force, Wright-Patterson Air Force Base, Ohio, 1961).

© Author(s) 2019

P3

A cryogenic radio-frequency ion trap for quantum logic spectroscopy of highly charged ions

Journal: Review of Scientific Instruments

Copyright and license notice:
©2019 Author(s). All article content, except where otherwise noted, is licensed under a Creative Commons Attribution (CC BY) license.
(http://creativecommons.org/licenses/by/4.0/)

Reproduced from

T. Leopold, S. A. King, **P. Micke**, A. Bautista-Salvador, J. C. Heip, C. Ospelkaus, J. R. Crespo López-Urrutia, and P. O. Schmidt (2019). “A cryogenic radio-frequency ion trap for quantum logic spectroscopy of highly charged ions.” *Review of Scientific Instruments* 90, 073201.
DOI: 10.1063/1.5100594

with the permission of AIP Publishing.

Review of Scientific Instruments ARTICLE scitation.org/journal/rsi

A cryogenic radio-frequency ion trap for quantum logic spectroscopy of highly charged ions

Cite as: Rev. Sci. Instrum. 90, 073201 (2019); doi: 10.1063/1.5100594
Submitted: 18 April 2019 • Accepted: 7 July 2019 •
Published Online: 29 July 2019

View Online Export Citation CrossMark

T. Leopold,[1] S. A. King,[1] P. Micke,[1,2] A. Bautista-Salvador,[1] J. C. Heip,[1] C. Ospelkaus,[1,3] J. R. Crespo López-Urrutia,[2] and P. O. Schmidt[1,3,a)]

AFFILIATIONS

[1] Physikalisch-Technische Bundesanstalt, Bundesallee 100, 38116 Braunschweig, Germany
[2] Max-Planck-Institut für Kernphysik, Saupfercheckweg 1, 69117 Heidelberg, Germany
[3] Institut für Quantenoptik, Leibniz Universität Hannover, Welfengarten 1, 30167 Hannover, Germany

[a)] Author to whom correspondence should be addressed: piet.schmidt@quantummetrology.de.
URL: http://www.quantummetrology.de.

ABSTRACT

A cryogenic radio-frequency ion trap system designed for quantum logic spectroscopy of highly charged ions (HCI) is presented. It includes a segmented linear Paul trap, an in-vacuum imaging lens, and a helical resonator. We demonstrate ground state cooling of all three modes of motion of a single ^{9}Be$^+$ ion and determine their heating rates as well as excess axial micromotion. The trap shows one of the lowest levels of electric field noise published to date. We investigate the magnetic-field noise suppression in cryogenic shields made from segmented copper, the resulting magnetic field stability at the ion position and the resulting coherence time. Using this trap in conjunction with an electron beam ion trap and a deceleration beamline, we have been able to trap single highly charged Ar^{13+} (Ar XIV) ions concurrently with single Be$^+$ ions, a key prerequisite for the first quantum logic spectroscopy of a HCI. This major stepping stone allows us to push highly-charged-ion spectroscopic precision from the gigahertz to the hertz level and below.

© 2019 Author(s). All article content, except where otherwise noted, is licensed under a Creative Commons Attribution (CC BY) license (http://creativecommons.org/licenses/by/4.0/). https://doi.org/10.1063/1.5100594

I. INTRODUCTION

Over the last decade, there has been growing interest in high precision spectroscopy of highly charged ions (HCI) for applications in frequency metrology and fundamental physics,[1,2] such as the search for a possible variation of fundamental constants,[3–6] violation of local Lorentz invariance,[7] or probing for new long-range interactions.[8] The strong scaling of energy levels with charge state shifts fine and hyperfine transitions into the optical regime,[1,5,9] enabling high-precision laser spectroscopy. The highest sensitivity to many of the tests of fundamental physics can be found in optical transitions between levels of different electronic configuration near energy-level crossings as a function of charge state.[10] The small size of electron orbitals in HCI and correspondingly the reduced atomic polarizability and the electric quadrupole moment suppress field-induced systematic frequency shifts, suggesting HCI as promising optical clock candidates.[3,5,11–15]

Up to now, precision spectroscopy of HCI at rest was mostly performed in electron beam ion traps (EBITs).[16–18] However, high ion temperatures ($T > 10^5$ K) due to the electron impact heating in a deep trapping potential and magnetic field inhomogeneities as well as drifts have limited the achievable spectroscopic resolution and accuracy in most cases to the parts-per-million level. Recently, the transfer of HCI from an EBIT to a Paul trap and sympathetic cooling to millikelvin temperatures using co-trapped laser-cooled Coulomb crystals was demonstrated.[19] Combined with ultrastable local oscillator technology[20,21] and the techniques used in optical frequency standards based on quantum logic,[22,23] this paves the way for a 10^9–10^{13}-fold improvement over the current most accurate spectroscopic measurements for HCI.[24,25]

Currently there are only two approaches for high-precision optical spectroscopy of HCI. One is the use of Penning traps, where a single HCI is trapped and resistively cooled to the temperature of the cryogenic ion trap.[26–28] Successful laser-induced excitation of the

© Author(s) 2019

transition is detected by electronic readout of the ion spin by coupling it to its motion in an inhomogeneous magnetic field.[29] The other approach, followed by this experiment, is based on the detection of Rabi flopping on the spectroscopy HCI using a co-trapped singly charged ion such as $^9Be^+$, which also provides sympathetic cooling. Optical excitation of the HCI is transferred to the Be^+ ion exploiting the coupled motion of the ions using well-established quantum logic protocols.[22] Then, the excitation of the Be^+ ion is read out by fluorescence detection.

The HCI lifetime in a trap is limited by charge-exchange reactions with background gas particles. For frequency metrology, useful lifetimes in the minutes to hours regime can only be achieved in cryogenic environments with pressure levels typically below 10^{-14} mbar.[30–33] Here, a cryogenic ion trap setup including a newly designed segmented blade trap, an in-vacuum helical resonator and a imaging system with high collection efficiency is presented. The segmented blade trap is characterized in terms of ion heating rates and excess axial micromotion. Furthermore, ground state cooling of all three normal modes of motion of a single Be^+ ion confined far outside the Lamb-Dicke regime is demonstrated. The magnetic shielding due to the cryogenic heat shields and the corresponding passive stability of the magnetic field is evaluated. We report on measurements of the coherence time and suppression of low-frequency magnetic field noise. Finally, we demonstrate the successful loading and storage of a single ion of Ar^{13+} (Ar XIV).

The entire system is inspired by the "Cryogenic Paul Trap Experiment"[30] located at the Max-Planck-Institute for Nuclear Physics in Heidelberg and has consequently been named "Cryogenic Paul Trap Experiment PTB" (CryPTEx PTB). Compared to CryPTEx[30] our much smaller trap size yields higher secular frequencies, which are required for high-fidelity quantum logic operations.[34] Furthermore, the trap is connected to a low-vibration cryogenic supply line[35] and a compact EBIT producing the desired HCI.[36]

II. APPARATUS

Cryogenic quadrupole-Paul traps already exist in several laboratories around the world, mainly as surface-electrode ion traps.[37–41] There, a suppression of the anomalous heating rates due to reduced electric field noise is exploited.[37,42] Macroscopic cryogenic Paul traps are in use for reaching extremely low pressures,[30,33] serving as a reservoir for buffer-gas cooling of molecules,[43] or reducing black-body radiation shifts in optical clocks.[44] The setup presented here is the first cryogenic Paul trap designed for sub-Hertz-level spectroscopy of optical transitions in HCI.

The lifetime of trapped HCI depends on the mean free time between collisions with the background gas. Due to the kilo-electron-volt-level ionization potential of HCI, collisions of that type will likely result in charge exchange between the HCI and the neutral partner. This can cause HCI ejection from the trap, which typically has a depth of only a few electron volt/charge in the axial direction. Even if the ion is retained after the charge-exchange event, it does not longer belong to the required spectroscopic species, i.e., the charge state, and must be replaced. With cryopumping, pressures of less than 10^{-16} mbar can be achieved.[32,45] As a comparison, most atomic physics experiments operate at pressures of 10^{-11} mbar or above at room temperature.

A. Cryogenic setup

In addition to the usual requirements, the design of a cryogenic ion trap for frequency metrology calls for the following:

1. Extremely stable cold trap mounting inside the room-temperature vacuum chamber, while thermally insulating the cold stages.
2. Multiple optical ports for lasers, imaging, and external ion delivery while keeping blackbody radiation (BBR) heat load from outside as low as possible.
3. Electrical connections, including the radio-frequency drive, should use long cables with very low thermal conductivity.
4. Repeated thermal cycling needed without trap damage or misalignment relative to the external optical setup.
5. Vibrations generated at the liquid-helium cryostat or the mechanical cryocooler need to be suppressed at the position of the ion trap.

The ion trap setup is attached to a closed-cycle low-vibration cryogenic system, reaching temperatures of <5 K and 50 K on the cold stage and heat shield, respectively, despite the ~1.4 m separation from the cold head.[35] It suppresses the pulse tube vibrations to values below 20 nm in the horizontal plane spanned by the laser beams and below 100 nm in the vertical direction. Figure 1 shows a computer-aided design (CAD) cross-sectional view of the setup. It consists of a nested structure of temperature stages, each mounted symmetrically to the previous one using ~15 cm-long stainless-steel spokes to minimize heat conduction between them despite the rigid mechanical connection. The vacuum chamber is fixed on the optical table, where the laser setup rests. Both the heat shield and the cold stage consist of a base plate, a wide tube and a lid made of high-purity (99.99%), gold-plated oxygen-free high conductivity (OFHC) copper. Gold plating both enhances the thermal conductivity at contact points and prevents tarnishing of the copper during periods when the system is vented, thus maintaining a low emissivity in order to reduce heat transfer via BBR. A wall thickness of 15 mm on the heat shield and 10 mm on the cold stage efficiently shield external AC electromagnetic fields, and particularly well at low temperatures, where the electrical conductivity of the copper is two orders of magnitude higher than at room temperature. Convenient access to the inside of the cold stage is provided by just removing three lids, allowing maintenance work without detaching the cryogenic setup.

Symmetric arrangement of the stainless steel spokes, as in Refs. 30 and 35, minimizes displacements during thermal cycling. After a complete thermal cycle, the trapped ions can be optically addressed without realignment of the lasers or imaging system. Optical access is provided by 16 ports, 12 of which are equally spaced in the horizontal plane. Four additional ports are provided at 15° off the horizontal plane, spanning a vertical plane with the trap axis. The ports restrict the solid angle using two nested concentric, 5 cm-long aluminum tubes on the cold stage and the heat shield with an inner diameter of 5 mm and 11 mm, respectively. This minimizes both the exposure of the cold stage to room-temperature BBR and the flux of residual-gas particles into the cold stage, thereby enhancing differential pumping from the room-temperature sections. The solid angle fraction of room-temperature elements visible to the ion is only 0.1%, which improves upon the ~2% reported previously.[30]

© Author(s) 2019

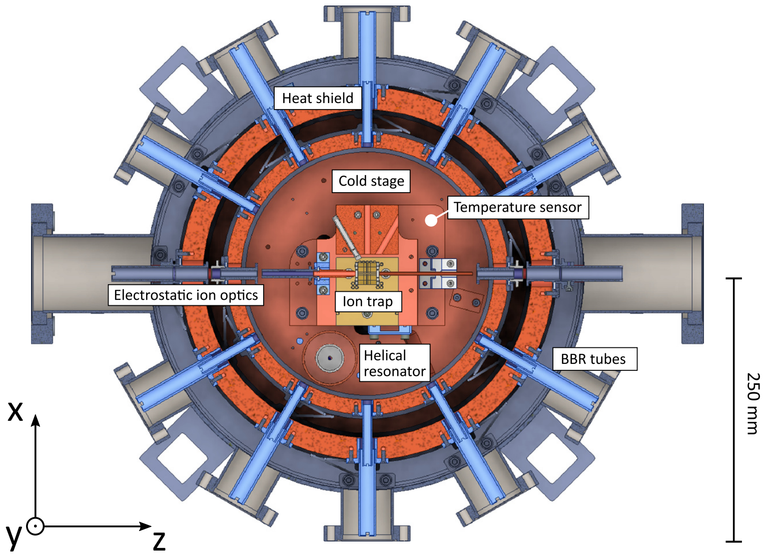

FIG. 1. Top view cross section of the CryPTEx PTB apparatus described in the text. The in-vacuum imaging system is not shown. In addition to the in-plane optical access shown here, there are 4 optical ports with a projection onto the y-axis. These ports are aligned along two axes in the y-z-plane which are tilted by ±15° with respect to the z-axis. Three mutually orthogonal pairs of magnetic field coils span a cuboid around the chamber with outer dimensions of 525× 525 × 245 mm, centered on the position of the ion. Reprinted with permission from T. Leopold, "A cryogenic ion trap system for quantum logic spectroscopy of highly charged ions," Ph.D. dissertation (Leibniz Universität Hannover, 2018).[93]

All necessary DC electrical connections are provided by means of 2 m-long phosphor-bronze wires with a diameter of 200 μm (Lakeshore QT-32), thermally anchored at the heat shield and cold stage with 1 m of wire between the different temperature stages to reduce the thermal flow to the trap electrodes. For the trap drive radio-frequency (RF) signal and a microwave antenna, designed to drive the 1.25 GHz Be^+ ground state hyperfine structure splitting, we use semirigid coaxial beryllium-copper wire (Coax Co., SC-219/50-SB-B).

The estimated heat load of the ion trap setup onto the cryostat is given in Table I. It is apparent, that the heat load on the cold stage is dominated by room-temperature BBR, while the heat load onto the cold stage is dominated by the dissipated RF power of the ion trap and thermal conduction through mechanical and electrical connections.

B. The ion trap

Our present design meets the requirements for quantum logic spectroscopy of HCI. The most important design goals were:

1. low differential contraction between parts when cooling the trap to 4 K,
2. wide axial access and large trap aperture for efficient injection of HCI from the deceleration beamline,
3. a long axial trap for confining Coulomb crystals of several hundred Be^+ ions capable of efficiently stopping the HCI after injection,[46]
4. small RF electrode separations causing high secular frequencies needed for quantum logic spectroscopy.

To meet the first criterion, the trap consists of alumina (sintered Al_2O_3), with adequate thermal conductivity[47] at both room and cryogenic temperatures of 30 and 0.3 W/(m K), respectively, and a low RF loss tangent[48] of 2×10^{-4}. Our geometry is inspired by a segmented blade design;[49] however, the end caps are removed from the axis.[50–52] Instead, the DC blades are segmented into five separate electrodes, whereby radially opposing electrodes can be biased to provide axial confinement. This breaks the cylindrical symmetry of the trap, lifting the degeneracy of the radial secular motional frequencies into a focused and defocused mode and thus strongly defining the principal radial axes of the trap to be along the blade axes. This ensures efficient cooling of all ion motional modes by laser beams at oblique angles in the horizontal plane. A 0.9 mm ion-electrode distance guarantees sufficient axial access for HCI injection while taking advantage of the strong inverse scaling of

TABLE I. Estimated steady-state heat load for temperatures of 50 K and 4.5 K on the heat shield and cold stage, respectively.

Heating mechanism	Heat load on heat shield (mW)	Heat load on cold stage (mW)
Conduction through spokes	780	38
Conduction through wires	65	7
Trap drive RF	...	200
Black-body radiation	4000	19
Total	4845	264

© Author(s) 2019

the anomalous ion-heating rate on the ion-electrode characteristic distance d (between d^{-2} and d^{-4}, depending on the nature of the noise source[53]).

To avoid a direct line-of-sight from the ion to the insulator separating the DC electrodes, small slits with a width and depth of 100 μm are first cut into the blades at the desired electrode boundaries using a dicing saw. The electrode surfaces carry a 20 μm-thick gold layer. At first, a 20 nm-thick titanium seed layer and a 100 nm-thick gold layer were deposited on the alumina substrate using the multidirectional evaporation technique at the PTB surface-technology laboratory. Thereafter, a 20 μm-thick layer of gold was galvanically grown at the PTB clean-room facilities. This thickness was chosen to exceed the skin depth of the RF frequency drive [15 μm at 24 MHz at room temperature, decreasing to 1.5 μm at 4 K for a residual-resistivity ratio (RRR) of 100]. The gold layer thickness was measured before and after the galvanic gold deposition using an optical microscope. After that, gold standing between the individual electrodes on the DC blade was removed by femtosecond-laser cutting at an external company (Micreon GmbH). Slits were also cut into the RF-carrying blades in the same pattern as in the DC blades to minimize axial micromotion,[54] however they were not laser-structured.

The fully assembled trap is mounted on a gold-coated alumina carrier board, which provides the RF and DC electrical ground. The carrier board also features a Rogers 4350B printed-circuit board (PCB) with surface-mounted device (SMD) filter elements and solder patches to connect to the DC blades; see Fig. 2. This provides a short path between filters and electrodes, reducing noise pickup. Additionally, mounting the filter components on the cold stage greatly reduces their Johnson noise. Connections from this filter board to the trap electrodes were made of Kapton-insulated copper wire, soldered at both ends using UHV compatible solder. The dielectric material of the SMD capacitors (Vishay VJ1206A472FF) is class C0G, proven to work at cryogenic temperatures with a subpercent change in capacitance from room temperature.[55] All components were selected to be nonmagnetic, including the Rogers PCB, which uses pure silver layers as conductor instead of the standard copper-nickel-gold combination. On the 6 inner DC blade electrodes and the compensation electrodes, the resistors (1 MΩ, Vishay PNM1206E1004BST) and capacitors (4.7 nF) were selected to build a single-stage low-pass filter with a cutoff frequency of 34 Hz. For the outermost blade electrodes, 1 kΩ resistors of the same series were chosen, increasing the cutoff frequency to 34 kHz to enable faster voltage switching whilst maintaining a low impedance for the RF pickup.

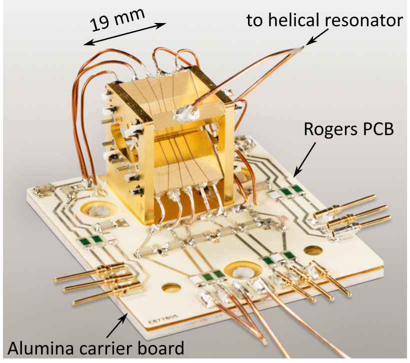

FIG. 2. Fully assembled ion trap with carrier and filter board. The gold-coated top layer of the carrier board (electrical ground of the trap) is electrically isolated from the vacuum chamber and can be biased to several 100 V for HCI deceleration. Reprinted with permission from T. Leopold, "A cryogenic ion trap system for quantum logic spectroscopy of highly charged ions," Ph.D. dissertation (Leibniz Universität Hannover, 2018).

The trap assembly is mounted on an OFHC copper block together with the imaging lens and ion-optic electrodes, see Fig. 3. The ion trap is driven by a miniature OFHC copper helical resonator placed next to the trap on the cold stage. The resonator coil is inductively coupled to a primary coil connected to an amplified low-noise signal generator (Rhode and Schwarz SML01) using a resistive beryllium-copper coaxial cable and an insulated SubMiniature version A (SMA) connector feedthrough. For the resonator design, we follow Ref. 56 for a room-temperature, unloaded quality factor $Q \approx 700$. It provides an unloaded resonance frequency near 50 MHz, and after loading with the trap electrodes 24.1 MHz. We monitor the value of Q as a function of temperature during a thermal cycle using a network analyzer: At room temperature, $Q = 230$ and increases to $Q = 385$ when cooled to 4.5 K as shown in Fig. 4. This increase is much smaller than predicted based on to the RRR values of copper and gold and shows a saturation behavior starting at a temperature of around 50 K. This could be due to losses in the solder joints or the polytetrafluoroethylene (PTFE) former around which the secondary coil is wound.

By purposefully degrading the impedance matching between the primary and secondary coils, the mutual inductance of the resonator coils is reduced,[57] increasing Q. The voltage on the secondary coil scales with $\sqrt{Q \cdot P_{\text{in}}}$, where P_{in} is the coupled power. Figure 4(b) shows Q and the calculated resonator output voltage as a function of P_{in}. We find that the output voltage for a given power dissipated in the resonator exhibits a maximum at slightly below 90% coupling. This is a relevant figure of merit in cryogenic systems only, where the dissipated power in the resonator can be the dominant heat load for the cold stage. Additionally, higher Q leads to more effective filtering of noise on the trap drive signal, reducing ion heating through parametric excitation.[58,59]

For the final deceleration step of the HCI before they are loaded into the trap, we bias the whole trap to +200 V. This potential is added to the signal wire of the beryllium-copper coaxial cable using a bias-tee, keeping the shield of the helical resonator electrically isolated from the cold stage. A capacitor insulates the shield of the coaxial cable from the primary coil of the helical resonator. All other voltages required for ion trapping are referenced to this bias potential, which can be adjusted without affecting the trap operation.

C. Loading and cooling of ^{9}Be$^+$

^{9}Be$^+$ ions are loaded into the trap by pulsed laser ablation and two-step photoionization with a resonant intermediate level.[60] A Q-switched frequency-doubled Nd:YAG laser at 532 nm with a pulse length of 4 ns and energy of up to 10 mJ is focused to a $1/e^2$ waist of 120 μm onto a beryllium wire located 18 mm from the trap center. Ablated beryllium atoms are ionized using a 235 nm laser tuned to the $^1S_0$–$^1P_1$ transition.[61] Typically, two laser pulses separated

© Author(s) 2019

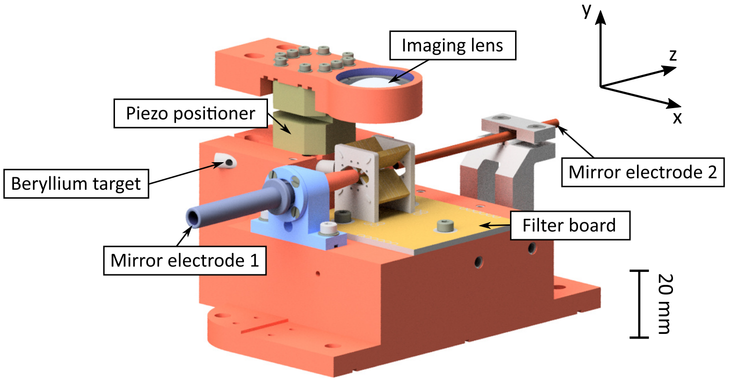

FIG. 3. CAD rendering of the ion trap assembly showing the in-vacuum imaging lens and electrostatic optics around the trap. Reprinted with permission from T. Leopold, "A cryogenic ion trap system for quantum logic spectroscopy of highly charged ions," Ph.D. dissertation (Leibniz Universität Hannover, 2018).

by 0.5 s are used for ablation, with a peak laser energy density of approximately 1.2 J/cm^2 for single ion loading and 4 J/cm^2 for loading of tens of ions, corresponding to peak intensities of around 300 MW/cm^2 and 1000 MW/cm^2, respectively.

For secular motional frequencies of a single ^{9}Be$^+$ ion of 2.5 MHz in the radial direction and 1 MHz in the axial direction, 8 V have to be applied to the trap endcaps at an RF power of 200 mW. The RF-power dissipation raises the temperature of the cold stage by 0.3 K.

The ions are Doppler cooled on the strong, cycling $^2S_{1/2}$ $(F = 2)$ to $^2P_{3/2}$ $(F = 3)$ transition using a laser with a wavelength of 313 nm.[61,62] To lift the degeneracy of the Zeeman sublevels and define the quantization axis, a bias magnetic field of 160 μT is applied at an angle of 30° to the trap axial direction in the horizontal plane using three mutually orthogonal pairs of coils. The cooling laser is delivered along the magnetic bias field axis with circular polarization, as the cooling transition is closed for pure σ-polarized light. Residual polarization impurities optically pump the ion to the $^2S_{1/2}$ $(F = 1)$ state, from which they are repumped with a separate laser tuned to the $^2S_{1/2}$ $(F = 1)$ to $^2P_{1/2}$ $(F = 2)$ transition. This beam is collinear to and has the same polarization as the cooling laser.

A third 313 nm laser with a red detuning of 103 GHz to the cooling laser allows driving stimulated Raman transitions between the ground state hyperfine levels, used for ground-state cooling using resolved sidebands[63,64] and quantum logic operations.[22] A set of three Raman beams enables cooling and logic operations with projection purely onto either the axial or radial direction as necessary. The linear polarization of each of the Raman beams was carefully tuned in order to minimize associated Stark shifts, albeit at the cost of reduced Rabi frequencies.[65] For a single ion cooled to the motional ground state, carrier (first blue sideband) π-times of approximately 13 (15) μs and 5 (23) μs in the axial and radial directions, respectively, are achieved with 1 mW of light per beam focused to a waist of 40 μm. The laser systems were set up following Ref. 62, except the repumper laser which is based on a frequency-doubled distributed Bragg reflector (DBR) diode laser.[66] To ensure long-term alignment of the laser beams onto the ion, all 313 nm beams are delivered to the trap through hydrogen-loaded, large mode area optical fibers which have a typical transmission of 50% for 1.5 m length.[67,68]

The relatively low secular frequencies somewhat complicate ground-state cooling of the ion, in particular, in the axial direction where the Lamb-Dicke parameters for spontaneous emission and stimulated Raman excitation are 0.48 and 0.82, respectively. However, we can exploit this large value for Raman excitation by utilizing the high strength of higher-order red sidebands. Several phonons can be removed at once to counteract the effect of recoil heating.[64,69,70] The cooling process is split into two stages. First, a

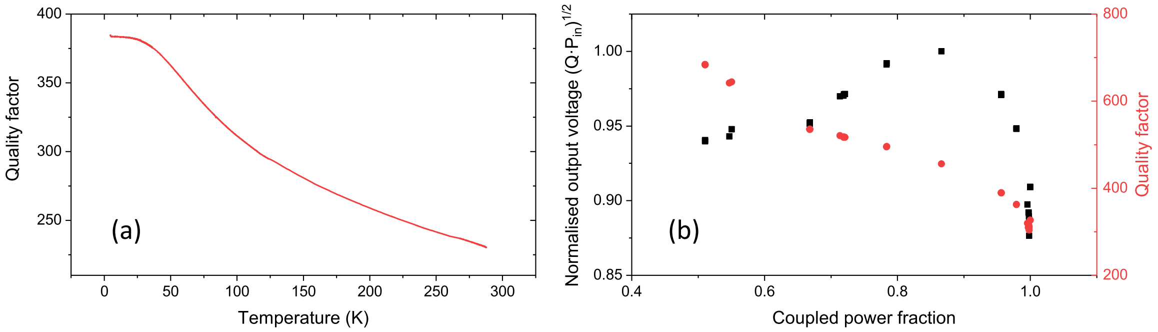

FIG. 4. (a) Helical resonator loaded quality factor Q vs temperature. (b) Output voltage and Q of the unloaded resonator as a function of the coupled power. The output voltage is optimized for a given level of power dissipation when there is a slight impedance mismatch. Reprinted with permission from T. Leopold, "A cryogenic ion trap system for quantum logic spectroscopy of highly charged ions," Ph.D. dissertation (Leibniz Universität Hannover, 2018).

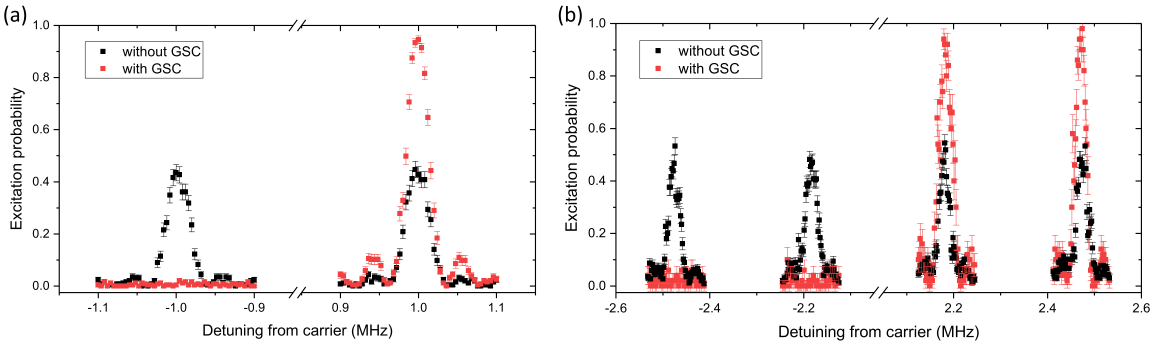

FIG. 5. Scan over the red and blue sidebands of the axial motional mode (a) and the radial modes (b) of a ^{9}Be$^+$ ion. The black data points were taken with a Doppler-cooled ion, the red data points after ground state cooling. Reprinted with permission from T. Leopold, "A cryogenic ion trap system for quantum logic spectroscopy of highly charged ions," Ph.D. dissertation (Leibniz Universität Hannover, 2018).

precooling step consisting of 15 interleaved pulses on each of the fifth, fourth, and third red sidebands is applied. This interleaving prevents optical pumping of the ion into "trap" Fock states that have near-zero excitation probability on a particular red sideband. Simulations indicate that this precooling leaves negligible population in Fock states higher than $n = 3$. Then, the final cooling step comprises 10 interleaved pulses on each of the second and first order red sidebands. For simplicity, all pulses have the same power and duration, judiciously chosen to match a π-pulse on the $n = 1 \rightarrow n' = 0$ transition. A pulse time on the order of 10 μs leads to a Fourier broadening of the resonances to about 100 kHz, reducing the sensitivity of the sideband cooling efficiency to potential drifts of the secular frequencies which is typically on the order of 10^{-4}. In this manner, we are able to reach within 1.8 ms an axial mode ground-state probability of 98% with a total of 65 red sideband pulses. The ground state population is calculated using the sideband asymmetry after sideband cooling; see Fig. 5.

For radial Raman excitation, the Lamb-Dicke parameter is 0.21, and there are no significant Fock states for which the coupling to red sidebands of a certain order is vanishing. Hence, 20 interleaved sideband pulses on each of the second and first order red sidebands are applied.

D. Imaging system

Fluorescence of the Be$^+$ ions on the cooling transition at 313 nm is imaged onto an electron-multiplying CCD camera (Andor iXon3 DU885-KC-VP) and a photomultiplier tube (PMT, Hamamatsu H10682-210). The fluorescence is split 1:99 between camera and PMT for simultaneous observation of the ion position and its electronic state.

The first imaging lens is a custom biaspheric lens (Asphericon) mounted inside the cold stage. It has a free aperture diameter of 22 mm and a working distance of 20 mm. Given its numerical aperture of ~0.5, it covers 6.9% of the total solid angle around the ion. Taking the dipole pattern of circularly polarized spontaneous emission into account reduces the collection efficiency to 5.5%.

At cryogenic temperatures, the imaging lens focus must be corrected for thermal contraction. For this purpose, the lens is installed in a stress-free copper holder which is in turn mounted onto a piezoelectric translation stage (Attocube Anz101) to adjust the focal distance. To minimize the size of the viewing apertures in the cold stages, the lens relays a near-diffraction-limited image with a magnification of ×3 at the exit of a tube analogous to those for the laser beams. This—only slightly magnified—image appears close to a reentrant room-temperature viewport. It is then further magnified by an air-side lens doublet consisting of an off-the-shelf aspheric lens and a standard planoconvex lens, leading to a total magnification of ×22.

With the laser tuned to resonance and a heavily saturated cooling transition, we observe a fluorescence rate of 340 counts/ms from a single ion, a mere 50% of the predicted value including expected losses and the specified PMT quantum efficiency. This could be due to residual misalignment and surface imperfections of the optical elements. For Doppler cooling and state detection, we work with an on-resonance count rate of 60 counts/ms, corresponding to 0.2 times the saturation intensity. In this way, we prevent saturation broadening that would affect the ion temperature after Doppler cooling and reduce state detection errors due to off-resonant depumping of the $F = 1$ state during detection of the ion internal state. At this rate and inserting a pinhole of 1 mm diameter in front of the PMT for blocking stray light, the total background-count rate (including approximately equal contributions from the PMT dark current and laser scatter) is 2.1 counts/s. Therefore, the signal-to-background ratio reaches a value of 28 500. We discriminate between $|\downarrow\rangle$ and $|\uparrow\rangle$ states (see Fig. 8) by counting fluorescence photons during a fixed time (200 μs) induced by a resonant beam connecting the $^2S_{1/2}$ $(F = 2)$ manifold to the $P_{3/2}$ manifold and applying a standard thresholding technique.[71] At the given detection efficiency, the state-discrimination fidelity is limited to 98% by off-resonant depumping of the dark state $|\uparrow\rangle$.[72]

III. TRAP CHARACTERIZATION

A. Heating rates

The low mass of ^{9}Be$^+$ and the high charge state of a HCI make both species highly susceptible to electric field noise on the trap electrodes, which leads to ion heating and thus higher

© Author(s) 2019

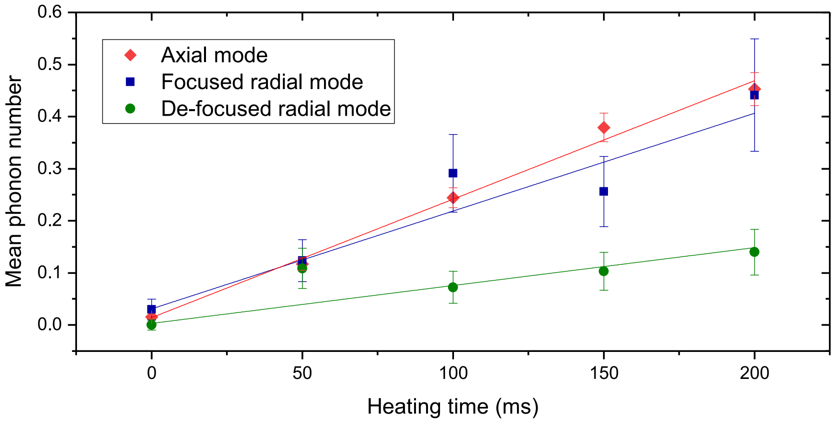

FIG. 6. Ion heating on the defocused (circles) and focused (squares) radial motional mode, as well as the axial mode (diamonds). Adapted with permission from T. Leopold, "A cryogenic ion trap system for quantum logic spectroscopy of highly charged ions," Ph.D. dissertation (Leibniz Universität Hannover, 2018).

temperatures after laser cooling. It will also cause systematic shifts of the clock resonance during interrogation if continuous cooling is not applied.[73] In view of the favorable scaling of the heating rate with the secular frequency,[74] it would be desirable to operate with the tightest possible confinement of the ion. However, to minimize the RF power dissipated in the cold stages and thus achieve the lowest possible temperature of those parts, the opposite becomes true, and we therefore work with the weakest possible ion confinement which still allows motional ground state cooling. Hence, it is important to minimize electric field noise as far as possible.

Measurements of the heating rate were carried out by initializing a single ^{9}Be$^+$ ion in the ground state of one or more of its motional modes, then all lasers are turned off to allow the ion to heat freely during periods of up to 200 ms. The final ground-state population was then determined by evaluating the asymmetry of the first order blue and red sidebands of the mode of interest.[74] From this, the heating rate was determined to be 2.3(1) phonons/s in the axial mode at a frequency near 1.0 MHz, and 0.7(2) and 1.9(3) phonons/s for the two radial modes with frequencies near 2.2 MHz (defocused) and 2.5 MHz (focused) as shown in Fig. 6. This corresponds to an electric field noise spectral density (in units of 10^{-15} V^2 m^{-2} Hz^{-1}) of 3.6(2) for the axial direction and 2.6(7) and 7.1(11) for the radial directions. Such values compare well to other cryogenic traps of this size and are between one and two orders of magnitude lower than in traps of similar designs that are operated at room temperature.[75]

For measuring the frequency dependence of the heating rate in the radial direction, we scan the RF-drive power. The observed heating rate in quanta per second was independent of the secular frequency over the range 1.9–3.2 MHz. Noise with an f^1 spectrum, or residual uncompensated RF electric field at the position of the ion could explain this effect.

Strong filtering of the DC voltages did not affect the anomalous heating rate in the axial direction. Unexpectedly, it was observed that it increased with growing RF drive power, though the radial and axial directions should be mutually independent. In conjunction with the observed independence of the radial heating rate from the RF-trap depth, this indicates that the heating rate in this mode is also limited by RF-drive noise. This couples to the ion through the residual axial RF electric field and causes parametric excitation of the intrinsic micromotion sidebands.[59] A further reduction of the heating rate could therefore be achieved by means of a helical resonator with a higher loaded Q factor thus improving electronic filtering and causing higher trap frequencies for a given level of RF-power dissipation.

B. Micromotion

If the ion is displaced from the RF nodal line of the trap, or if any on-axis RF field component is induced by electrode alignment inaccuracies, ion motion will be driven at the RF frequency, an effect known as excess micromotion. This is expected to dominate the error budget of an optical frequency standard based on HCI.[1]

During curing of the glue holding the various trap parts together, an axial misalignment of approximately 15 μm, determined with an optical microscope, developed between the blade pairs, a value greater than machining tolerances of 5 μm for the individual parts.

We measured the axial micromotion with the resolved sideband method[76,77] for a radial confinement of ν_r = 1.5 MHz for a

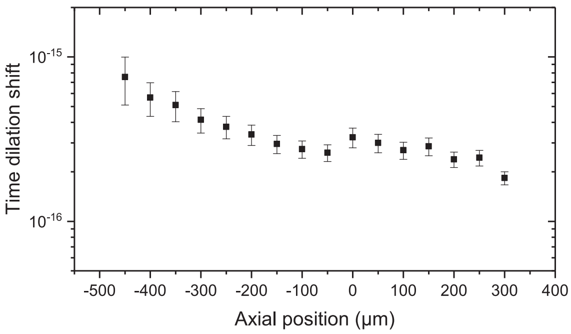

FIG. 7. Micromotion-induced fractional time-dilation shift as a function of the ion position along the trap axis. Data were taken with an RF field amplitude corresponding to a radial confinement of ν_r = 1.5 MHz for a Be$^+$ ion.

© Author(s) 2019

single ^{9}Be$^+$ ion. Figure 7 shows the axial micromotion-induced time-dilation shift as a function of the axial position in the trap given relative to the ion position for symmetric voltages on the DC electrodes. We swept over the entire central segment length under stable trapping conditions, compensating radial micromotion at every point before an axial micromotion measurement. Only a small variation of the micromotion amplitude along the axis was observed, with no zero-crossing of the RF electric field amplitude along the axis. The observed modulation index for the central position was $\beta = 1.5$. The important figure of merit for precision spectroscopy is the experimental error of the determination of the time dilation shift. With standard spectroscopic methods the size of the error can be 1–2 orders of magnitude below the absolute shift,[78] estimating a time-dilation shift error on the order of 10^{-17} for ^{9}Be$^+$. The lack of a zero-crossing within the center segment of the trap is most likely induced by misalignment of the trap electrodes in the axial direction with respect to each other.

C. Magnetic field stability

Figure 8 shows a partial term scheme of the ^{9}Be$^+$ ion, with the hyperfine and Zeeman structure in the $^2S_{1/2}$ ground state. Under an external magnetic bias field of about 160 μT, we measure the magnetic field at the position of the ion by means of microwave spectroscopy on the first order magnetic field-sensitive transition $|\downarrow\rangle = |F = 2, m_F = -2\rangle$ to $|\uparrow\rangle = |F = 1, m_F = -1\rangle$. The linear Zeeman shift of $\Delta\nu/B = (3/2)\mu_B/h \simeq 21$ Hz/nT leads to a transition frequency of 1253.366 MHz. Since the hyperfine constant of Be$^+$ is known[79] to a precision of 10^{-11} with $A = -625\,008\,837.048(10)$ Hz, we can calculate the linear and quadratic Zeeman shift from the observed splitting between $|\downarrow\rangle$ and $|\uparrow\rangle$, which will subsequently be referred to as the qubit transition.

Despite the lack of magnetic shielding around the vacuum chamber, the short-term stability of the magnetic field at the ion position is improved by the two, at 50 K and 4.5 K highly conductive, copper thermal shields. Alternating magnetic fields induce eddy currents, suppressing magnetic field changes inside the shields.[80] Assuming a low-pass filtering effect of first order, the decay time of these currents gives the corner frequency of the filter function. Although one could expect a double-exponential decay due to the two nested shielding layers, our measurements are compatible with a single low-pass behavior.

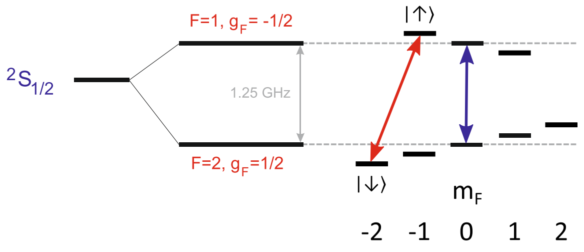

FIG. 8. Partial term scheme of ^{9}Be$^+$ showing the ground state hyperfine and Zeeman structure. Microwave transitions used for setup characterization are indicated. Red arrow: first-order Zeeman sensitive transition used as the hyperfine qubit, with a shift coefficient of $\Delta\nu/B = 21$ Hz/nT. Blue arrow: first-order-insensitive transition.

We measured the ring-down time by observing the step response of the Zeeman splitting for current steps on the magnetic field coils in all three principal axes: x, the horizontal direction perpendicular to the trap axial direction; y, vertical; z, trap axial direction. In order to observe the frequency change of the Zeeman splitting, we produced an error signal applying two-point sampling with a linear range matched to the observed frequency shift. Several up and down steps in current were applied, and the exponential rise times averaged.

Symmetry suggests that the shielding effect in both horizontal directions is identical. In the vertical direction, the shielding should be better as there are solid horizontal OFHC-copper parts close to and aligned concentrically to the ion position. Shielding in both horizontal directions however suffers from the contact resistances between base, wall, and lid elements. Experimental data confirmed these considerations. Table II shows the derived time constants and corresponding corner frequencies for the three different principal axes. Within statistics, the values along x and z are the same and about half the one in the y direction.

Complementary measurements of the shielding factor at higher frequencies were obtained by applying an alternating current to another magnetic coil pair placed outside the main coil set, with the magnitude of the applied field determined using a magnetic flux sensor next to the vacuum chamber. The noise at the ion position was spectroscopically measured using the quantum lock-in amplifier technique,[81] and indicated a shielding factor of 30–40 dB at frequencies between 60 Hz and 1 kHz.

For evaluation of the low-frequency temporal stability of the magnetic bias field, a closed-loop frequency measurement of the qubit transition was carried out. The microwave power and interaction time were matched to produce a linewidth of 100 Hz with 98% contrast using Rabi excitation. With the two-point sampling method, an error signal was created that steered the microwave source.

It was found that, occasionally, changes of up to 50 nT occurred in the field on time scales of several seconds. This was traced down to the motion of an elevator in the building. To compensate for this, two pairs of active magnetic field coils were constructed along the x and z axis, as the quantization axis lies in the corresponding plane. Field variations are detected using a 3-axis magnetic flux sensor located next to the main vacuum chamber, and feedback with a bandwidth of 1 kHz is then applied to the coil currents for compensation. With this active stabilization engaged, the elevator no longer affects the field at the ion position to within our resolution of 0.15 nT.

TABLE II. Experimentally determined time constants and corresponding corner frequencies for magnetic field changes along the different axes. Reprinted with permission from T. Leopold, "A cryogenic ion trap system for quantum logic spectroscopy of highly charged ions," Ph.D. dissertation (Leibniz Universität Hannover, 2018).

Axis	Time constant (s)	Low-pass corner frequency (Hz)
x	0.66(18)	0.24(7)
y	1.11(17)	0.14(2)
z	0.53(10)	0.30(6)

© Author(s) 2019

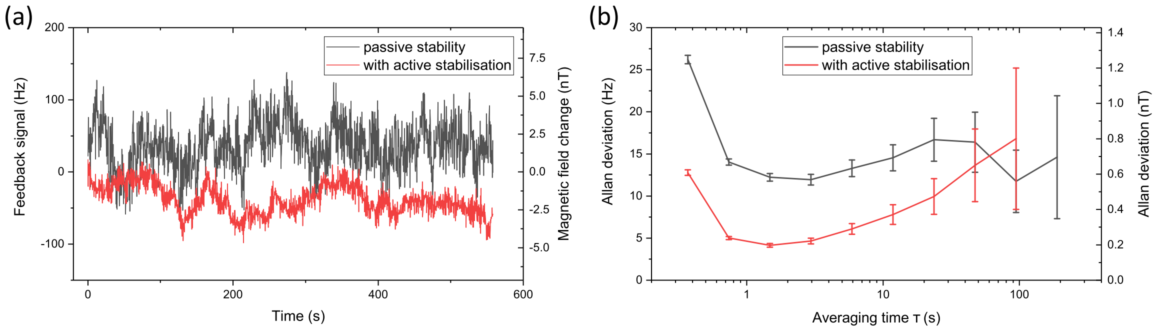

FIG. 9. (a) Time trace of the Zeeman splitting of our qubit states relative to the initial value for passive and active magnetic field stability. (b) Allan deviation corresponding to the data from (a) showing the Zeeman-shift stability and the corresponding magnetic field stability. Reprinted with permission from T. Leopold, "A cryogenic ion trap system for quantum logic spectroscopy of highly charged ions," Ph.D. dissertation (Leibniz Universität Hannover, 2018).

Figure 9 shows a time trace of the frequency feedback necessary to lock to the qubit transition for the cases of active and passive magnetic field stabilization. It is apparent from the reduced rms amplitude of the feedback loop that the active method greatly improves the short-term stability of the field. The Allan deviation shows a passive magnetic field stability of better than 1 nT at time scales from 1 s up to 100 s. A fractional magnetic field stability corresponding to 1 nT is below 6×10^{-6} and thus at the limits of commercially available current supplies. Our active stabilization suppresses fluctuations up to several 10 s with an optimum stability of about 200 pT at 1 s. This is close to the limit given by the resolution of the employed magnetic field sensor. Further improvements could result when shielding the vacuum chamber with high-permeability materials to suppress low frequency drifts.[82]

D. Coherence time

Decoherence on the qubit transition is caused by energy level shifts due to (a) fluctuating magnetic fields, and (b) fluctuations in power and frequency of the source driving the transition. For microwave excitation, frequency fluctuations of the source can be excluded, as all our radio-frequency devices are referenced to a maser with a stability better than $10^{-12}/\sqrt{\tau}$. Frequency excursions will thus be smaller than the Fourier-limited transition linewidth for all reasonable interrogation times.

In most ion trap experiments, coherence times are limited by technical magnetic field noise at 50 Hz and its harmonics, originating from various electronic devices, as well as switch-mode power supplies radiating at tens of kilohertz. Commonly reported coherence times are in the 100 μs range for unshielded room temperature experiments.[52,83]

We measure the coherence time by performing a microwave Ramsey experiment on our qubit transition. With the microwave drive tuned to resonance, the relative phase of the second Ramsey pulse is scanned with respect to the first. The amplitude of the resulting sinusoidal signal indicates the maximum fringe contrast. Measurements for different Ramsey times allow to extract the coherence time, as shown in Fig. 10. It should be noted that we neither use AC-line triggering nor apply spin-echo sequences[81,84,85] to artificially extend the coherence time, as we want to determine the intrinsic decoherence time scale. The coherence decay exhibits a Gaussian shape, scaling with $e^{-(t^2/2\tau^2)}$ if the intrinsic decoherence time is longer than the experimental Ramsey time.[86,87] A fit to the data yields a $1/\sqrt{e}$ coherence time of $\tau = 36(1)$ ms. If the intrinsic decoherence is shorter than a single experimental cycle, the contrast falls off exponentially with $e^{-t/\tau}$. The graph also shows a fit to the data

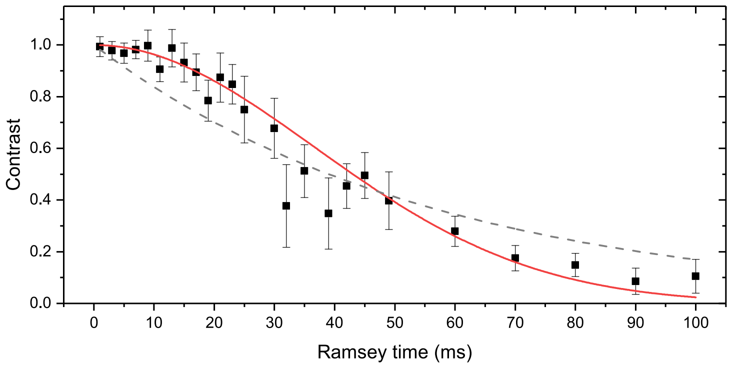

FIG. 10. Measured qubit coherence given by the contrast of Ramsey experiments at varying Ramsey delays. The coherence shows a Gaussian envelope (red line) with a $1/\sqrt{e}$ time constant of $\tau = 36(1)$ ms. The steep loss of contrast for Ramsey times above τ is characteristic of our dominant noise process, slow magnetic field drifts. The gray dashed line is a $e^{-t/\tau}$ fit to the data.

© Author(s) 2019

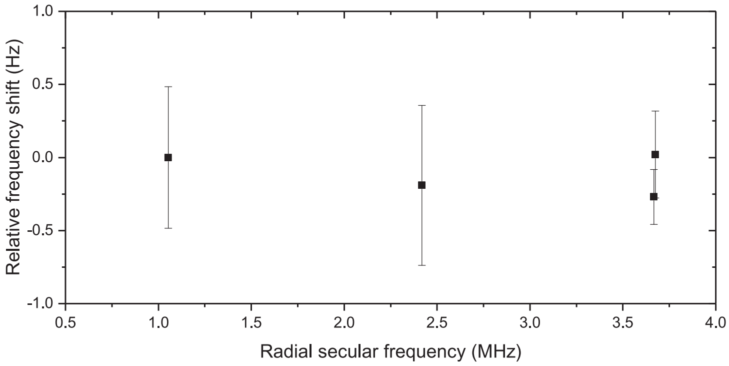

FIG. 11. Relative frequency shift of the $|F = 2, m_F = 0\rangle$ to $|F = 1, m_F = 0\rangle$ transition as a function of one of the radial secular frequencies. Reprinted with permission from T. Leopold, "A cryogenic ion trap system for quantum logic spectroscopy of highly charged ions," Ph.D. dissertation (Leibniz Universität Hannover, 2018).

using the exponential decay, which yields $\tau = 56(5)$ ms. However, especially at Ramsey times below 30 ms it is apparent that the data is reproduced more appropriately by the Gaussian envelope, validating the former fit function (Fig. 10).

The measured coherence time is about a factor of three higher than reported for an optical transition in a similar cryogenic system[80] and comparable to that of a double layer μ-metal shielded room temperature system, when operating with magnetic field coils inside the shield.[87]

With the measured coherence time τ, the rms magnetic field fluctuations can be expressed as[87]

$$\sqrt{\langle \Delta B^2 \rangle} = 2\hbar/(3\mu_B \tau) = 210 \text{ pT}, \qquad (1)$$

taking the magnetic field sensitivity of the transition of $(3/2)\mu_B/h$ into account, where μ_B is Bohr's magneton. This value is consistent with the measured Allan deviation of the qubit transition frequency at averaging times of 0.5–5 s, corresponding to the measurement time of a single phase scan.

E. Trap-induced AC Zeeman shift

The oscillating currents on the RF trap electrodes lead to a time-averaged second-order Zeeman shift induced by the radial trapping potential. Due to imbalanced currents in opposing electrodes, this can even be the case for operation at the AC electric field null of the trap.[73,88] To investigate this effect, we performed Ramsey spectroscopy on the $|F = 2, m_F = 0\rangle$ to $|F = 1, m_F = 0\rangle$ transition; see Fig. 8. This transition is insensitive to first order to magnetic field changes, which enables us to use Ramsey times of 100 ms to resolve the line with a width of 5 Hz. A two-point sampling frequency feedback servo is employed to track the transition frequency. By running interleaved servos on both the magnetic field sensitive transition $|\downarrow\rangle$ to $|\uparrow\rangle$ and the insensitive transition $|F = 2, m_F = 0\rangle$ to $|F = 1, m_F = 0\rangle$, we can correct for the second order frequency shift due to drifts in the DC bias field. The first order-sensitive transition is interrogated with a Ramsey time of 10 ms due to its larger frequency fluctuations.

We measure the bias-field-corrected transition frequency $|F = 2, m_F = 0\rangle$ to $|F = 1, m_F = 0\rangle$ for three different radial trap depths, corresponding to Be$^+$ secular frequencies of 1.05, 2.42, and 3.68 MHz, see Fig. 11. Any AC Zeeman shift increases the transition frequency for higher radial secular frequencies. We see no significant shift at the level of our statistics-limited resolution of ~1 Hz. With an AC Zeeman sensitivity of 314 mHz/μT^2, this provides an upper bound of $\langle B^2 \rangle < 3\ \mu\text{T}^2$ for trap-induced magnetic fields. Owing to the strong scaling of the frequency of magnetic dipole transitions with charge state,[9] the equivalent AC Zeeman sensitivity in HCI is expected to be 3–4 orders of magnitude smaller than in singly charged systems.[10]

IV. TRAPPING OF HCI

Highly charged argon ions with a charge state of $q+$ are extracted in bunches from an EBIT with a mean energy of 700 eV per q and decelerated in a beamline to approximately 150 eV per q using a pair of pulsed drift tubes, similar as described in Ref. 89. Operation of the EBIT is described in detail elsewhere.[36]

A single charge state (Ar^{13+}) is selected by its time of flight for gated injection into the Paul trap. The final deceleration step is performed by raising the trap DC and RF ground to a few volts below the remaining kinetic energy per unit charge. Once the ions have passed the mirror electrode 1 (see Fig. 3), the electrode is switched to a higher potential, confining the HCI axially, together with the second pair of outer endcaps. The inner endcaps provide a weak axial confinement for a Be$^+$ Coulomb crystal with 200 mV of applied voltage. Repeated passes and interactions with the Be$^+$ dissipate the kinetic energy of the HCI[89–92] until a HCI becomes embedded in the Coulomb crystal, leaving as signature a large dark spot in the otherwise fluorescing crystal (Fig. 12). For quantum logic operations, a two-ion crystal of a Be$^+$ ion and the spectroscopy ion is needed.

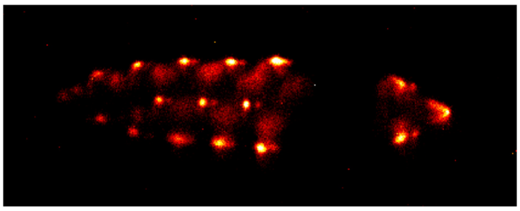

FIG. 12. A single Ar^{13+} ion in a Coulomb crystal of several 10 fluorescing Be$^+$ ions. Due to its high charge, the Ar^{13+} displaces several Be$^+$, appearing as a large dark spot in the crystal.

© Author(s) 2019

Thus, after co-crystallization of the HCI, the excess Be$^+$ ions are ejected from the trap by parametric heating using the RF drive.

The resulting two-ion crystal exhibits a very low configuration hopping rate, as a collision preferably results in charge exchange. Thus, the crystal lifetime is given by the mean time between collisions of about 43 min, consistent with a residual vacuum pressure of about 10^{-14} mbar or below,[35] assuming residual gas in thermal equilibrium with the cold stage. Next steps toward quantum logic spectroscopy of Ar^{13+} include the preparation of a two-ion crystal in the ground state of axial motion, and a search for the transition frequency with a laser which is frequency-stabilized to the Hertz-level.

V. CONCLUSION

We have presented a cryogenic ion trap system specifically designed for spectroscopy of single HCI and characterized the ion trap with respect to heating rates, excess micromotion, and magnetic field stability. Ground state cooling of all the normal modes of a single ^{9}Be$^+$ ion has been demonstrated outside the Lamb-Dicke regime. With the demonstrated specifications matching the design values, the system is well suited for performing quantum logic spectroscopy not only with HCI, as planned, but also in other species such as molecular ions that would undoubtedly benefit from the extremely low level of BBR, the long coherence times resulting from the active cancellation of external magnetic field fluctuations and the double Faraday shielding by the high-conductivity thermal shields, and the very low density of residual gas particles resulting from the operation near 4 K. Further additions such as passive magnetic shielding will help improving its advantages.

The possibility of Doppler-free spectroscopy of HCI in a system such as this one is a key enabler to improve upon state-of-the-art spectroscopic precision in HCI by more than seven orders of magnitude, from the parts per million level to the hertz level and below.

ACKNOWLEDGMENTS

The authors gratefully thank Julia Fenske for the design and manufacturing of the electronics required for operation of the trap. We acknowledge the PTB scientific instrumentation department 5.5 headed by Frank Löffler for their expertise and fabrication of numerous parts, including the cryogenic environment; in particular, we thank Michael Müller and Stephan Metschke. We thank the PTB surface technology laboratory and Manuel Stompe from IMPT Hannover for their technical help with manufacturing of the ion trap. We thank the MPIK mechanical apprentice workshop headed by Stefan Flicker for fabrication of parts. Financial support was provided by Physikalisch-Technische Bundesanstalt, Max-Planck-Gesellschaft zur Förderung der Wissenschaften e. V., and Deutsche Forschungsgemeinschaft through Grant No. SCHM2678/5-1, and Collaborative Research Centers' Grant No. SFB 1227 (DQ-mat), Project Nos. A01 and B05, as well as Grant No. SFB 1225 (ISOQUANT), Project No. B01. S.A.K. acknowledges support by the Alexander von Humboldt Foundation. This project has received funding from the European Metrology Programme for Innovation and Research (EMPIR) co-financed by the participating states and from the European Union's Horizon 2020 research and innovation programme (Project No. 17FUN07 CC4C).

REFERENCES

[1] M. G. Kozlov, M. S. Safronova, J. R. Crespo López-Urrutia, and P. O. Schmidt, Rev. Mod. Phys. **90**, 045005 (2018).

[2] M. S. Safronova, D. Budker, D. DeMille, D. F. J. Kimball, A. Derevianko, and C. W. Clark, Rev. Mod. Phys. **90**, 025008 (2018).

[3] S. Schiller, Phys. Rev. Lett. **98**, 180801 (2007).

[4] J. Berengut, V. Dzuba, and V. Flambaum, Phys. Rev. Lett. **105**, 120801 (2010).

[5] J. C. Berengut, V. A. Dzuba, V. V. Flambaum, and A. Ong, Phys. Rev. Lett. **109**, 070802 (2012).

[6] M. S. Safronova, V. A. Dzuba, V. V. Flambaum, U. I. Safronova, S. G. Porsev, and M. G. Kozlov, Phys. Rev. A **90**, 042513 (2014).

[7] V. A. Dzuba, V. V. Flambaum, M. S. Safronova, S. G. Porsev, T. Pruttivarasin, M. A. Hohensee, and H. Häffner, Nat. Phys. **12**, 465 (2016).

[8] J. C. Berengut, D. Budker, C. Delaunay, V. V. Flambaum, C. Frugiuele, E. Fuchs, C. Grojean, R. Harnik, R. Ozeri, G. Perez, and Y. Soreq, Phys. Rev. Lett. **120**, 091801 (2018).

[9] J. D. Gillaspy, J. Phys. B: At., Mol. Opt. Phys. **34**, R93 (2001).

[10] J. C. Berengut, V. A. Dzuba, V. V. Flambaum, and A. Ong, Phys. Rev. A **86**, 022517 (2012).

[11] A. Derevianko, V. A. Dzuba, and V. V. Flambaum, Phys. Rev. Lett. **109**, 180801 (2012).

[12] J. C. Berengut, V. V. Flambaum, and A. Ong, EPJ Web Conf. **57**, 02001 (2013).

[13] M. S. Safronova, V. A. Dzuba, V. V. Flambaum, U. I. Safronova, S. G. Porsev, and M. G. Kozlov, Phys. Rev. Lett. **113**, 030801 (2014).

[14] V. A. Dzuba, V. V. Flambaum, and H. Katori, Phys. Rev. A **91**, 022119 (2015).

[15] Y.-m. Yu and B. K. Sahoo, Phys. Rev. A **97**, 041403 (2018).

[16] M. A. Levine, R. E. Marrs, J. R. Henderson, D. A. Knapp, and M. B. Schneider, Phys. Scr. **T22**, 157 (1988).

[17] R. E. Marrs, M. A. Levine, D. A. Knapp, and J. R. Henderson, Phys. Rev. Lett. **60**, 1715 (1988).

[18] M. A. Levine, R. E. Marrs, J. N. Bardsley, P. Beiersdorfer, C. L. Bennett, M. H. Chen, T. Cowan, D. Dietrich, J. R. Henderson, D. A. Knapp, A. Osterheld, B. M. Penetrante, M. B. Schneider, and J. H. Scofield, Nucl. Instrum. Methods Phys. Res., Sect. B **43**, 431 (1989).

[19] L. Schmöger, O. O. Versolato, M. Schwarz, M. Kohnen, A. Windberger, B. Piest, S. Feuchtenbeiner, J. Pedregosa-Gutierrez, T. Leopold, P. Micke, A. K. Hansen, T. M. Baumann, M. Drewsen, J. Ullrich, P. O. Schmidt, and J. R. C. López-Urrutia, Science **347**, 1233 (2015).

[20] T. Kessler, C. Hagemann, C. Grebing, T. Legero, U. Sterr, F. Riehle, M. J. Martin, L. Chen, and J. Ye, Nat. Photonics **6**, 687 (2012).

[21] D. G. Matei, T. Legero, S. Häfner, C. Grebing, R. Weyrich, W. Zhang, L. Sonderhouse, J. M. Robinson, J. Ye, F. Riehle, and U. Sterr, Phys. Rev. Lett. **118**, 263202 (2017).

[22] P. O. Schmidt, T. Rosenband, C. Langer, W. M. Itano, J. C. Bergquist, and D. J. Wineland, Science **309**, 749 (2005).

[23] A. D. Ludlow, M. M. Boyd, J. Ye, E. Peik, and P. O. Schmidt, Rev. Mod. Phys. **87**, 637 (2015).

[24] I. Draganić, J. Crespo López-Urrutia, R. DuBois, S. Fritzsche, V. Shabaev, R. Orts, I. Tupitsyn, Y. Zou, and J. Ullrich, Phys. Rev. Lett. **91**, 183001 (2003).

[25] H. Bekker, C. Hensel, A. Daniel, A. Windberger, T. Pfeifer, and J. R. Crespo López-Urrutia, Phys. Rev. A **98**, 062514 (2018).

[26] S. L. Rolston and G. Gabrielse, Hyperfine Interact. **44**, 233 (1989).

[27] N. P. M. Brantjes, D. v. Lindenfels, G. Birkl, W. Quint, and M. Vogel, Hyperfine Interact. **199**, 161 (2011).

[28] M. Vogel, H. Häffner, K. Hermanspahn, S. Stahl, J. Steinmann, and W. Quint, Phys. Rev. A **90**, 043412 (2014).

[29] H. Häffner, T. Beier, S. Djekić, N. Hermanspahn, H.-J. Kluge, W. Quint, S. Stahl, J. Verdú, T. Valenzuela, and G. Werth, Eur. Phys. J. D **22**, 163 (2003).

[30] M. Schwarz, O. O. Versolato, A. Windberger, F. R. Brunner, T. Ballance, S. N. Eberle, J. Ullrich, P. O. Schmidt, A. K. Hansen, A. D. Gingell, M. Drewsen, and J. R. C. López-Urrutia, Rev. Sci. Instrum. **83**, 083115 (2012).

© Author(s) 2019

[31] J. Repp, C. Böhm, J. R. C. López-Urrutia, A. Dörr, S. Eliseev, S. George, M. Goncharov, Y. N. Novikov, C. Roux, S. Sturm, S. Ulmer, and K. Blaum, Appl. Phys. B **107**, 983 (2012).

[32] S. Sellner, M. Besirli, M. Bohman, M. J. Borchert, J. Harrington, T. Higuchi, A. Mooser, H. Nagahama, G. Schneider, C. Smorra, T. Tanaka, K. Blaum, Y. Matsuda, C. Ospelkaus, W. Quint, J. Walz, Y. Yamazaki, and S. Ulmer, New J. Phys. **19**, 083023 (2017).

[33] G. Pagano, P. W. Hess, H. B. Kaplan, W. L. Tan, P. Richerme, P. Becker, A. Kyprianidis, J. Zhang, E. Birckelbaw, M. R. Hernandez, Y. Wu, and C. Monroe, Quantum Sci. Technol. **4**, 014004 (2019).

[34] D. J. Wineland, C. Monroe, W. M. Itano, D. Leibfried, B. E. King, and D. M. Meekhof, J. Res. Natl. Inst. Stand. Technol. **103**, 259 (1998).

[35] P. Micke, J. Stark, S. A. King, T. Leopold, T. Pfeifer, L. Schmöger, M. Schwarz, L. J. Spieß, P. O. Schmidt, and J. R. C. López-Urrutia, Rev. Sci. Instrum. **90**, 065104 (2019).

[36] P. Micke, S. Kühn, L. Buchauer, J. R. Harries, T. M. Bücking, K. Blaum, A. Cieluch, A. Egl, D. Hollain, S. Kraemer, T. Pfeifer, P. O. Schmidt, R. X. Schüssler, C. Schweiger, T. Stöhlker, S. Sturm, R. N. Wolf, S. Bernitt, and J. R. Crespo López-Urrutia, Rev. Sci. Instrum. **89**, 063109 (2018).

[37] J. Labaziewicz, Y. Ge, P. Antohi, D. Leibrandt, K. Brown, and I. Chuang, Phys. Rev. Lett. **100**, 013001 (2008).

[38] P. B. Antohi, D. Schuster, G. M. Akselrod, J. Labaziewicz, Y. Ge, Z. Lin, W. S. Bakr, and I. L. Chuang, Rev. Sci. Instrum. **80**, 013103 (2009).

[39] S. X. Wang, Y. Ge, J. Labaziewicz, E. Dauler, K. Berggren, and I. L. Chuang, Appl. Phys. Lett. **97**, 244102 (2010).

[40] M. Niedermayr, K. Lakhmanskiy, M. Kumph, S. Partel, J. Edlinger, M. Brownnutt, and R. Blatt, New J. Phys. **16**, 113068 (2014).

[41] G. Vittorini, K. Wright, K. R. Brown, A. W. Harter, and S. C. Doret, Rev. Sci. Instrum. **84**, 043112 (2013).

[42] L. Deslauriers, S. Olmschenk, D. Stick, W. Hensinger, J. Sterk, and C. Monroe, Phys. Rev. Lett. **97**, 103007 (2006).

[43] A. K. Hansen, O. O. Versolato, Ł. Kłosowski, S. B. Kristensen, A. Gingell, M. Schwarz, A. Windberger, J. Ullrich, J. R. C. López-Urrutia, and M. Drewsen, Nature **508**, 76 (2014).

[44] R. J. Rafac, B. C. Young, J. A. Beall, W. M. Itano, D. J. Wineland, and J. C. Bergquist, Phys. Rev. Lett. **85**, 2462 (2000).

[45] M. Diederich, H. Häffner, N. Hermanspahn, M. Immel, H. J. Kluge, R. Ley, R. Mann, W. Quint, S. Stahl, and G. Werth, Hyperfine Interact. **115**, 185 (1998).

[46] L. Schmöger, "Kalte hochgeladene ionen für frequenzmetrologie," Ph.D. thesis, University of Heidelberg, 2017.

[47] N. Simon, Technical Report NISTIR 5030, National Institute of Standards and Technology (Materials Reliability Division), 1994.

[48] M. Doležal, P. Balling, P. B. R. Nisbet-Jones, S. A. King, J. M. Jones, H. A. Klein, P. Gill, T. Lindvall, A. E. Wallin, M. Merimaa, C. Tamm, C. Sanner, N. Huntemann, N. Scharnhorst, I. D. Leroux, P. O. Schmidt, T. Burgermeister, T. E. Mehlstäubler, and E. Peik, Metrologia **52**, 842 (2015).

[49] S. Gulde, "Experimental realization of quantum gates and the Deutsch-Josza algorithm with trapped ^{40}Ca^{+}-ions," Ph.D. thesis, University of Innsbruck, 2003.

[50] M. A. Rowe, A. Ben-Kish, B. DeMarco, D. Leibfried, V. Meyer, J. Beall, J. Britton, J. Hughes, W. M. Itano, B. Jelenkovic, C. Langer, T. Rosenband, and D. J. Wineland, Quantum Inf. Comput. **2**, 257 (2002), available at https://www.rintonpress.com/journals/qicabstracts/qicabstracts2-4.html.

[51] T. Schaetz, A. Friedenauer, H. Schmitz, L. Petersen, and S. Kahra, J. Mod. Opt. **54**, 2317 (2007).

[52] B. Hemmerling, F. Gebert, Y. Wan, D. Nigg, I. V. Sherstov, and P. O. Schmidt, Appl. Phys. B **104**, 583 (2011).

[53] J. A. Sedlacek, A. Greene, J. Stuart, R. McConnell, C. D. Bruzewicz, J. M. Sage, and J. Chiaverini, Phys. Rev. A **97**, 020302 (2018).

[54] N. Herschbach, K. Pyka, J. Keller, and T. E. Mehlstäubler, Appl. Phys. B **107**, 891 (2012).

[55] F. Teyssandier and D. Prêle, in Ninth International Workshop on Low Temperature Electronics-WOLTE9, 2010.

[56] J. D. Siverns, L. R. Simkins, S. Weidt, and W. K. Hensinger, Appl. Phys. B **107**, 921 (2012).

[57] S. Panja, S. De, S. Yadav, and A. Sen Gupta, Rev. Sci. Instrum. **86**, 056104 (2015).

[58] D. Wineland, C. Monroe, W. Itano, B. King, D. Leibfried, D. Meekhof, C. Myatt, and C. Wood, Fortschr. Phys. **46**, 363 (1998).

[59] J. A. Sedlacek, J. Stuart, W. Loh, R. McConnell, C. D. Bruzewicz, J. M. Sage, and J. Chiaverini, J. Appl. Phys. **124**, 214904 (2018).

[60] N. Kjærgaard, L. Hornekaer, A. M. Thommesen, Z. Videsen, and M. Drewsen, Appl. Phys. B **71**, 207 (2000).

[61] H.-Y. Lo, J. Alonso, D. Kienzler, B. C. Keitch, L. E. de Clercq, V. Negnevitsky, and J. P. Home, Appl. Phys. B **114**, 17 (2014).

[62] A. C. Wilson, C. Ospelkaus, A. P. VanDevender, J. A. Mlynek, K. R. Brown, D. Leibfried, and D. J. Wineland, Appl. Phys. B **105**, 741 (2011).

[63] C. Monroe, D. M. Meekhof, B. E. King, S. R. Jefferts, W. M. Itano, D. J. Wineland, and P. Gould, Phys. Rev. Lett. **75**, 4011 (1995).

[64] Y. Wan, F. Gebert, F. Wolf, and P. O. Schmidt, Phys. Rev. A **91**, 043425 (2015).

[65] D. J. Wineland, M. Barrett, J. Britton, J. Chiaverini, B. DeMarco, W. M. Itano, B. Jelenković, C. Langer, D. Leibfried, V. Meyer, T. Rosenband, and T. Schätz, Philos. Trans. R. Soc., A **361**, 1349 (2003).

[66] S. A. King, T. Leopold, P. Thekkeppatt, and P. O. Schmidt, Appl. Phys. B **124**, 214 (2018).

[67] Y. Colombe, D. H. Slichter, A. C. Wilson, D. Leibfried, and D. J. Wineland, Opt. Express **22**, 19783 (2014).

[68] C. D. Marciniak, H. B. Ball, A. T.-H. Hung, and M. J. Biercuk, Opt. Express **25**, 15643 (2017).

[69] J.-S. Chen, S. M. Brewer, C. W. Chou, D. J. Wineland, D. R. Leibrandt, and D. B. Hume, Phys. Rev. Lett. **118**, 053002 (2017).

[70] H. Che, K. Deng, Z. T. Xu, W. H. Yuan, J. Zhang, and Z. H. Lu, Phys. Rev. A **96**, 013417 (2017).

[71] A. Myerson, D. Szwer, S. Webster, D. Allcock, M. Curtis, G. Imreh, J. Sherman, D. Stacey, A. Steane, and D. Lucas, Phys. Rev. Lett. **100**, 200502 (2008).

[72] B. Hemmerling, F. Gebert, Y. Wan, and P. O. Schmidt, New J. Phys. **14**, 023043 (2012).

[73] T. Rosenband, D. B. Hume, P. O. Schmidt, C. W. Chou, A. Brusch, L. Lorini, W. H. Oskay, R. E. Drullinger, T. M. Fortier, J. E. Stalnaker, S. A. Diddams, W. C. Swann, N. R. Newbury, W. M. Itano, D. J. Wineland, and J. C. Bergquist, Science **319**, 1808 (2008).

[74] Q. A. Turchette, D. Kielpinski, B. E. King, D. Leibfried, D. M. Meekhof, C. J. Myatt, M. A. Rowe, C. A. Sackett, C. S. Wood, W. M. Itano, C. Monroe, and D. J. Wineland, Phys. Rev. A **61**, 063418 (2000).

[75] M. Brownnutt, M. Kumph, P. Rabl, and R. Blatt, Rev. Mod. Phys. **87**, 1419 (2015).

[76] D. J. Berkeland, J. D. Miller, J. C. Bergquist, W. M. Itano, and D. J. Wineland, J. Appl. Phys. **83**, 5025 (1998).

[77] J. Keller, H. L. Partner, T. Burgermeister, and T. E. Mehlstäubler, J. Appl. Phys. **118**, 104501 (2015).

[78] S. M. Brewer, J.-S. Chen, A. M. Hankin, E. R. Clements, C. W. Chou, D. J. Wineland, D. B. Hume, and D. R. Leibrandt, Phys. Rev. Lett. **123**, 033201 (2019).

[79] D. J. Wineland, J. J. Bollinger, and W. M. Itano, Phys. Rev. Lett. **50**, 628 (1983).

[80] M. F. Brandl, M. W. van Mourik, L. Postler, A. Nolf, K. Lakhmanskiy, R. R. Paiva, S. Möller, N. Daniilidis, H. Häffner, V. Kaushal, T. Ruster, C. Warschburger, H. Kaufmann, U. G. Poschinger, F. Schmidt-Kaler, P. Schindler, T. Monz, and R. Blatt, Rev. Sci. Instrum. **87**, 113103 (2016).

[81] S. Kotler, N. Akerman, Y. Glickman, A. Keselman, and R. Ozeri, Nature **473**, 61 (2011).

[82] I. Altarev, E. Babcock, D. Beck, M. Burghoff, S. Chesnevskaya, T. Chupp, S. Degenkolb, I. Fan, P. Fierlinger, A. Frei, E. Gutsmiedl, S. Knappe-Grüneberg, F. Kuchler, T. Lauer, P. Link, T. Lins, M. Marino, J. McAndrew, B. Niessen, S. Paul, G. Petzoldt, U. Schläpfer, A. Schnabel, S. Sharma, J. Singh, R. Stoepler, S. Stuiber, M. Sturm, B. Taubenheim, L. Trahms, J. Voigt, and T. Zechlau, Rev. Sci. Instrum. **85**, 075106 (2014).

[83] F. Schmidt-Kaler, S. Gulde, M. Riebe, T. Deuschle, A. Kreuter, G. Lancaster, C. Becher, J. Eschner, H. Häffner, and R. Blatt, J. Phys. B: At., Mol. Opt. Phys. **36**, 623 (2003).

© Author(s) 2019

[84] M. J. Biercuk, H. Uys, A. P. VanDevender, N. Shiga, W. M. Itano, and J. J. Bollinger, Nature **458**, 996 (2009).

[85] Y. Wang, M. Um, J. Zhang, S. An, M. Lyu, J.-N. Zhang, L.-M. Duan, D. Yum, and K. Kim, Nat. Photonics **11**, 646 (2017).

[86] T. Monz, "Quantum information processing beyond ten ion-qubits," Ph.D. thesis, University of Innsbruck, 2011.

[87] T. Ruster, C. T. Schmiegelow, H. Kaufmann, C. Warschburger, F. Schmidt-Kaler, and U. G. Poschinger, Appl. Phys. B **122**, 254 (2016).

[88] H. C. J. Gan, G. Maslennikov, K.-W. Tseng, T. R. Tan, R. Kaewuam, K. J. Arnold, D. Matsukevich, and M. D. Barrett, Phys. Rev. A **98**, 032514 (2018).

[89] L. Schmöger, M. Schwarz, T. M. Baumann, O. O. Versolato, B. Piest, T. Pfeifer, J. Ullrich, P. O. Schmidt, and J. R. C. López-Urrutia, Rev. Sci. Instrum. **86**, 103111 (2015).

[90] L. Gruber, J. Holder, J. Steiger, B. Beck, H. DeWitt, J. Glassman, J. McDonald, D. Church, and D. Schneider, Phys. Rev. Lett. **86**, 636 (2001).

[91] M. Bussmann, U. Schramm, D. Habs, V. Kolhinen, and J. Szerypo, Int. J. Mass Spectrom. **251**, 179 (2006).

[92] M. Bussmann, U. Schramm, and D. Habs, Hyperfine Interact. **173**, 27 (2007).

[93] T. Leopold, "A cryogenic ion trap system for quantum logic spectroscopy of highly charged ions," Ph.D. dissertation (Leibniz Universität Hannover, 2018).

© Author(s) 2019

P4

Coherent laser spectroscopy of highly charged ions using quantum logic

Journal: Nature

Copyright and license notice:
© The Author(s), under exclusive licence to Springer Nature Limited 2020.

Reproduced from

P. Micke, T. Leopold, S. A. King, E. Benkler, L. J. Spieß, L. Schmöger, M. Schwarz, J. R. Crespo López-Urrutia, and P. O. Schmidt (2020). “Coherent laser spectroscopy of highly charged ions using quantum logic.” *Nature* 578, 60–65.
DOI: 10.1038/s41586-020-1959-8

with the permission of Springer Nature Limited.

Article

Coherent laser spectroscopy of highly charged ions using quantum logic

https://doi.org/10.1038/s41586-020-1959-8

Received: 16 July 2019

Accepted: 25 October 2019

Published online: 29 January 2020

P. Micke[1,2,4]*, T. Leopold[1,4], S. A. King[1,4], E. Benkler[1], L. J. Spieß[1], L. Schmöger[1,2], M. Schwarz[1,2], J. R. Crespo López-Urrutia[2] & P. O. Schmidt[1,3]*

Precision spectroscopy of atomic systems[1] is an invaluable tool for the study of fundamental interactions and symmetries[2]. Recently, highly charged ions have been proposed to enable sensitive tests of physics beyond the standard model[2–5] and the realization of high-accuracy atomic clocks[3,5], owing to their high sensitivity to fundamental physics and insensitivity to external perturbations, which result from the high binding energies of their outer electrons. However, the implementation of these ideas has been hindered by the low spectroscopic accuracies (of the order of parts per million) achieved so far[6–8]. Here we cool trapped, highly charged argon ions to the lowest temperature reported so far, and study them using coherent laser spectroscopy, achieving an increase in precision of eight orders of magnitude. We use quantum logic spectroscopy[9,10] to probe the forbidden optical transition in $^{40}\mathrm{Ar}^{13+}$ at a wavelength of 441 nanometres and measure its excited-state lifetime and g-factor. Our work unlocks the potential of highly charged ions as ubiquitous atomic systems for use in quantum information processing, as frequency standards and in highly sensitive tests of fundamental physics, such as searches for dark-matter candidates[11] or violations of fundamental symmetries[2].

Like a microscope aimed at the quantum world, laser spectroscopy pursues ever higher resolving power. Every increase in resolution enables deeper insights into the subtle effects that all known fundamental interactions have on the atomic wavefunction. Advances in optical-frequency metrology have improved resolution drastically in the last three decades[1] and have made laser spectroscopy an extremely sensitive tool for studying open physics questions, such as the nature of dark matter, the strength of parity violation and a possible violation of Einstein's theory of relativity[2]. However, only a few atomic and ionic species are currently within the reach of cutting-edge optical-frequency metrology. Expanding this field of exploration to systems with high sensitivity to such effects is therefore crucial. Owing to the very high binding energies of their outer electrons, highly charged ions (HCIs) are promising candidates for such fundamental tests. The fractional contributions to the electronic transition energies from special relativity, quantum electrodynamics (QED) and the nucleus are several orders of magnitude larger than those in neutral atoms. This renders them ideal systems for benchmarking the most advanced theories and calculations, which has been repeatedly demonstrated via optical fluorescence spectroscopy in electron-beam ion traps (EBITs)[6,7], X-ray spectroscopy in storage rings[12] and EBITs[13–15], and ground-state g-factor studies in Penning traps[16,17]. The hyperfine splitting of the 1s state in heavy hydrogen-like ions can even shift into the optical range, providing laser-accessible transitions (see, for example, refs. [18–20]) with nuclear-size contributions of the order of several per cent of the total transition energy.

It was realized recently that non-gravitational coupling of dark matter to ordinary matter would affect atomic energy levels[11] and thus become observable in optical-clock comparisons as an apparent drift or modulation of the fine-structure constant α. HCIs offer narrow-linewidth optical transitions that are among the most sensitive to a possible variation of α (ref. [4]). In addition, their inherent insensitivity to external electric fields[3] leads to considerably smaller systematic perturbations compared to neutral and singly charged atoms. This makes them potentially superior references for high-accuracy optical atomic clocks, with many proposed species reviewed in ref. [5]. However, so far no experiment has performed laser spectroscopy at the required level of precision. The major limitation was set by the high temperature of a few million kelvins at which HCIs are produced and typically stored. This induces Doppler broadenings with full-width-at-half-maximum (FWHM) linewidths of several tens of gigahertz and corresponding line-centre uncertainties of a few hundreds of megahertz in the best cases[6–8]. Because HCIs generally do not offer suitable transitions for direct laser cooling, sympathetic cooling of multiple HCIs by laser-cooled $^{9}\mathrm{Be}^{+}$ ions was implemented in a Penning trap at the Lawrence Livermore National Laboratory[21], reaching an ion temperature of around 4 K. More recently, the Cryogenic Paul Trap Experiment[22] demonstrated reliable Coulomb crystallization of single $^{40}\mathrm{Ar}^{13+}$ ions in a crystal of many $^{9}\mathrm{Be}^{+}$ ions. Sympathetic Doppler cooling down to the 10-mK level and two-ion crystal preparation[23,24] paved the way for high-accuracy spectroscopy. Even so, spectroscopy of narrow transitions in single ions requires efficient state detection on a different, fast-cycling transition[1], which is typically also used for laser cooling. If such a transition is not available, quantum logic spectroscopy (QLS) can be employed[9,10]. In QLS, the 'spectroscopy ion' (in

---

[1]Physikalisch-Technische Bundesanstalt, Braunschweig, Germany. [2]Max-Planck-Institut für Kernphysik, Heidelberg, Germany. [3]Institut für Quantenoptik, Leibniz Universität Hannover, Hannover, Germany. [4]These authors contributed equally: P. Micke, T. Leopold, S. A. King. *e-mail: Peter.Micke@quantummetrology.de; Piet.Schmidt@quantummetrology.de

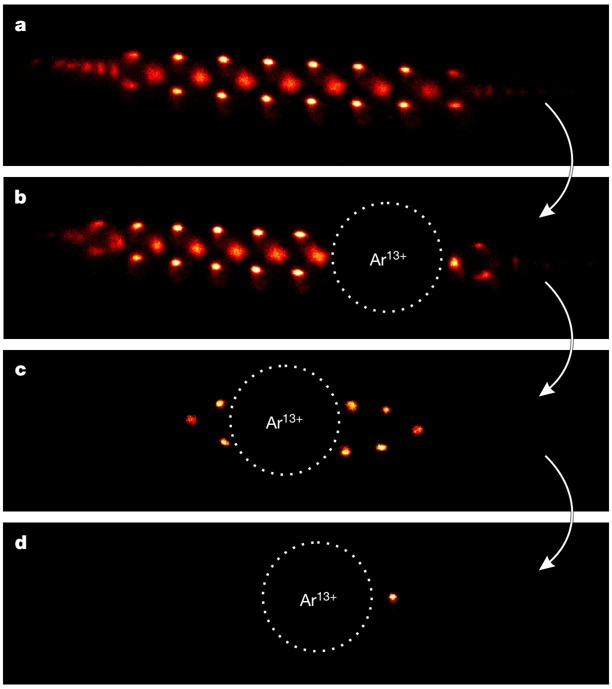

Fig. 1 | Time sequence of HCI recapture and two-ion crystal preparation. a, A laser-cooled Coulomb crystal of 50–100 fluorescing ^{9}Be^{+} ions is confined in the Paul trap. **b**, A single Ar^{13+} ion is injected along the crystal axis, sympathetically cooled and finally co-crystallized with ^{9}Be^{+}. It appears as a large dark void owing to the repulsion of the ^{9}Be^{+} by the high charge state. **c**, Excess ^{9}Be^{+} ions are removed by modulating the Paul trap radio-frequency potential in the absence of laser cooling, resulting in heating and ion losses. **d**, Finally, the Ar^{13+}–^{9}Be^{+} two-ion crystal is prepared.

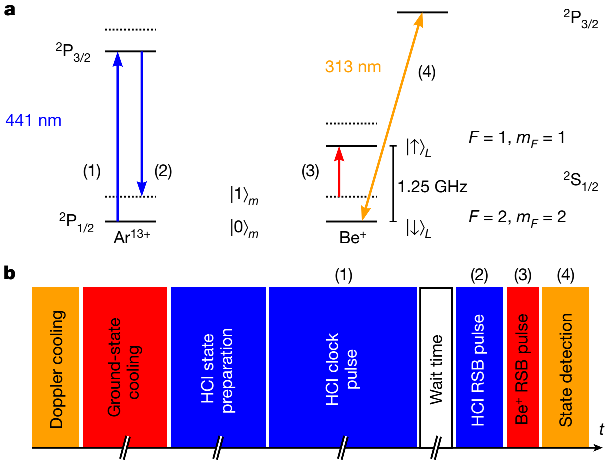

Fig. 2 | Schematic illustration of the experimental cycle. a, Level diagrams (not to scale) of boron-like Ar^{13+} and ^{9}Be^{+}. The motional Fock state of the crystal is denoted as $|n\rangle_m$. Solid and dotted black lines indicate the corresponding ground and first excited motional states, respectively. **b**, Experimental sequence. After Doppler cooling on the ^{9}Be^{+} $|\downarrow\rangle_L$–^{2}P$_{3/2}$ transition followed by ground-state cooling to $|0\rangle_m$ by stimulated Raman transitions, the internal state of Ar^{13+} is prepared (see also Fig. 4c and Extended Data Fig. 3). A clock laser pulse addressing the carrier of the Ar^{13+} transition is then applied (1). After an optional wait time for lifetime measurements, a clock laser π-pulse on the Ar^{13+} red sideband (RSB) maps the Ar^{13+} electronic state onto the common motional state (2). A red-sideband π-pulse on the ^{9}Be^{+} hyperfine transition $|\downarrow\rangle_L$–$|\uparrow\rangle_L$ maps it onto the ^{9}Be^{+} electronic state (3). Finally, this state is detected using the Doppler cooling laser (4).

this case the HCI) is co-trapped with a so-called 'logic ion' (^{9}Be^{+}) that provides sympathetic cooling and state preparation and is used for state detection. These functions are enabled by the Coulomb interaction between the two ions, allowing lasers to couple their internal electronic levels with their quantised joint motion in the trap. This technique and variations thereof have been successfully employed for optical atomic clocks based on Al^{+} ions[25–27], for internal state detection and spectroscopy of molecular ions[28,29] and for spectroscopy of broad transitions in atomic ions[30,31].

Here, we demonstrate QLS of an HCI—specifically, of the electric-dipole-forbidden transition between the ^{2}P$_{1/2}$ and ^{2}P$_{3/2}$ fine-structure levels of ^{40}Ar^{13+} at a wavelength of 441 nm, the most accurately known transition in any HCI[6]. We achieve an FWHM well below 100 Hz, close to the natural linewidth of 17 Hz. Single line scans taken on a timescale of a few minutes determine the line centre with an uncertainty of less than 2 Hz. This corresponds to a fractional statistical uncertainty of 3×10^{-15} for a transition frequency of approximately 680 THz and compares favourably to previous measurements taken over hours or even days, which achieved relative uncertainties[6–8] of 2×10^{-7}. Quantum logic-assisted state preparation of the ^{40}Ar^{13+} ion allows us to measure all six Zeeman components of the transition, which split up on a megahertz scale in a 160-µT magnetic quantization field. This allows us to determine the g-factor of the ^{2}P$_{3/2}$ excited state with unprecedented accuracy. Furthermore, we demonstrate a quantum logic-assisted excited-state lifetime measurement.

Preparation of a single HCI

A detailed description of the experimental setup is given in Methods (see also Extended Data Figs. 1, 2). In brief, argon HCIs are produced by an EBIT, PTB-EBIT[32], and ejected from it in triggered bunches of ~200 ns duration with a mean kinetic energy of approximately 700q V, where q is the ion charge. The HCIs are guided to the spectroscopy trap through an ion optical beamline. Based on their time of flight, we select the ^{40}Ar^{13+} ions by rapidly switching a gate electrode. A pulsed gradient potential decelerates them electrodynamically[33] to about 146q V. Then, a single ^{40}Ar^{13+} ion stochastically enters the cryogenic linear Paul trap[34]. The trap is globally biased to +138 V, thereby slowing the HCI down to 8q V upon entry. After passing through the trapping region, the HCI is reflected back by an electrode at the end of the Paul trap. A mirror electrode in front of the trap is switched up to prevent the ion from escaping again, thereby capturing the HCI in an oscillatory axial motion. The repeated crossing through a pre-prepared laser-cooled ^{9}Be^{+} Coulomb crystal within the trap dissipates the residual kinetic energy of the HCI. After sufficient sympathetic cooling, the ^{40}Ar^{13+} ion joins the Coulomb crystal. Excess ^{9}Be^{+} ions are removed until a two-ion crystal has been prepared (see Fig. 1). The entire preparation procedure of the two-ion crystal takes only a few minutes. The Paul trap is refrigerated to less than 5 K by a mechanically decoupled, closed-cycle cryostat to provide a vacuum below 10^{-12} Pa (corresponding to a particle density of less than 20,000 cm^{-3}), thus suppressing charge-exchange collisions and achieving HCI storage times[35] of the order of 45 min.

Ground-state cooling and quantum logic

The implementation of QLS requires control and preparation of the motional and internal states of both ions using coherent laser pulses on carrier and sideband transitions. After the two-ion crystal preparation, the strong Coulomb coupling between the two ions results in joint motional modes within the trap. Sympathetic cooling, state preparation and QLS are performed by repeating the experimental sequence shown in Fig. 2. First, Doppler cooling and optical pumping on the ^{9}Be^{+} ^{2}S$_{1/2}$–^{2}P$_{3/2}$ cycling transition (see Fig. 2a) are applied. The two axial normal

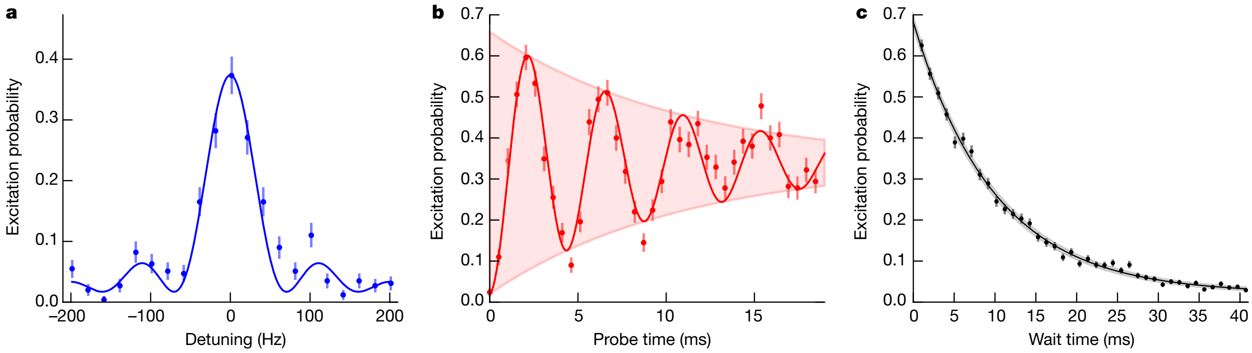

Fig. 3 | Rabi spectroscopy and excited-state lifetime measurement. a, Clock laser frequency scan across Zeeman component 1 (see Fig. 4c) of the ^{40}Ar^{13+} fine-structure transition. The fixed probe time of 12 ms is longer than the excited-state lifetime of 9.6 ms. The line is fitted by a Rabi line shape (blue curve), reaching a Fourier-limited FWHM of about 65 Hz. **b**, On-resonance coherent excitation of this transition. The coherent state Rabi flopping signal (fitted by the red curve, which represents a damped sine with offset) exhibits a 2.2-ms π-time (in which the maximum transferable population is transferred to the excited state) and decays exponentially with the excited-state lifetime (red-shaded envelope). The error bars in **a** and **b** represent the quantum projection noise of 255 measurements per data point. **c**, Excited-state lifetime measurement. Quantum logic sequences (see text) are carried out as a function of the wait time between carrier and red-sideband clock laser pulses. During the wait time, the excited state can decay spontaneously. From a three-parameter maximum-likelihood estimation, we obtain a lifetime of 9.97(27) ms, limited by the quantum projection noise of 1,100 measurements per data point (error bars). The black curve and grey-shaded area show the estimated exponential decay with the corresponding 1σ uncertainty band.

modes of the Coulomb crystal with secular frequencies of about $\nu_{\mathrm{IP}} = 1.37$ MHz (in phase) and $\nu_{\mathrm{OP}} = 1.86$ MHz (out of phase) are then cooled to the quantum mechanical ground state of motion with final average occupation numbers of $\bar{n} = 0.05$ (in phase) and $\bar{n} = 0.02$ (out of phase), corresponding to an effective temperature of less than 50 μK for each mode. For this purpose, we use laser pulses that coherently couple the electronic degrees of freedom to the common motional modes (a technique referred to as resolved sideband cooling). To do this, stimulated Raman transitions are driven between the ^{9}Be$^+$ hyperfine qubit states $|{\downarrow}\rangle_L|n\rangle_m \rightarrow |{\uparrow}\rangle_L|n-1\rangle_m$ (where $|n\rangle_m$ denotes the motional quantum state of the in-phase or out-of-phase modes and $|{\uparrow}\rangle_L$ refers to the upper qubit state of the logic ion ^{9}Be$^+$) using two laser beams with a wavelength of 313 nm. In our low magnetic field, the states are separated by a frequency of approximately 1.25 GHz. A repumping laser couples the ^{9}Be$^+$ ^{2}S$_{1/2}$ and ^{2}P$_{1/2}$ levels (not shown in Fig. 2a) for electronic-state preparation and for depopulation of state $|{\uparrow}\rangle_L$ (ref. [36]). The Ar^{13+} Zeeman ground state is then deterministically prepared with clock laser sideband pulses (see Extended Data Fig. 3). After full state preparation, QLS[9] is performed in four steps (see Fig. 2): (1) a clock laser pulse of tuneable length and power is applied, which couples the ground and excited states in Ar^{13+} coherently. (2) After a variable wait time for excited-state lifetime measurements, a clock laser red-sideband π-pulse maps the excitation from the electronic Ar^{13+} state onto the common axial out-of-phase mode and (3) another red-sideband π-pulse on the ^{9}Be$^+$ hyperfine qubit transition maps it onto the ^{9}Be$^+$ electronic state. (4) Finally, the qubit state of ^{9}Be$^+$ (dark, $|{\uparrow}\rangle_L$, or bright, $|{\downarrow}\rangle_L$) is detected with a fidelity of up to 98% by counting the fluorescence photons that it scatters from the Doppler cooling laser within 200 μs. A threshold value discriminates between the two states. The sequence is carried out multiple times (about 100) within a few seconds with a fixed set of parameters to average the quantum projection noise and evaluate a mean excitation probability. To resolve linewidths approaching the natural linewidth of 17 Hz, a narrow-linewidth clock laser is required. Our home-built laser system is composed of a commercial extended-cavity diode laser (ECDL) at 882 nm, which is prestabilized with a high locking bandwidth of 4 MHz to a passive external reference cavity using the ECDL pump current and grating piezo as actuators for the feedback. Thereby, we suppress laser high-frequency noise and obtain an instantaneous linewidth of about 2 kHz, which is limited by the relatively low cavity finesse (of about 1,000) and lack of vibration-insensitive design. To suppress the residual noise, the laser is then further stabilized by phase-locking it to an ultrastable laser operating at a wavelength of 1.5 μm. The latter is itself stabilized to a cryogenic cavity made from crystalline silicon (referred to as Si2)[37]. This achieves a fractional frequency instability at the thermal noise limit of the cavity of 4×10^{-17} at averaging times of 1–50 s. Using a femtosecond optical frequency comb as a transfer oscillator, we generate a virtual beatnote between the two lasers[38]. By demodulating it, we register their relative frequency and phase fluctuations, which are dominated by the substantially higher noise level of the 882-nm prestabilization cavity. The demodulated beatnote is used to generate a feedback signal for phase-locking the two lasers, which is applied to an acousto-optic modulator between the ECDL and the prestabilization cavity. The considerably lower bandwidth of the second locking stage ensures that the two loops do not compete with one another, but drifts and noise on the prestabilization cavity of up to kilohertz level are suppressed at the ECDL output, from which the spectroscopy light is derived. This suppresses the residual noise of the 882-nm clock laser, narrows its linewidth and reduces the daily drift to a level of about 10 Hz, which is dictated by Si2. The laser is frequency-doubled to 441 nm in an external enhancement cavity containing a periodically poled potassium titanyl phosphate crystal. Active power stabilization on a pulse-by-pulse basis at the ion trap is implemented for the clock, Doppler cooling and Raman lasers to achieve stable system parameters such as Rabi frequencies and a.c. Stark shifts.

Coherent laser spectroscopy of ^{40}Ar^{13+}

By applying this technique, we carried out the first coherent laser spectroscopy of an HCI. Figure 3a shows the excitation profile of the $m_{1/2} = -1/2$ to $m_{3/2} = -3/2$ Zeeman component of the ^{40}Ar^{13+} ^{2}P$_{1/2}$–^{2}P$_{3/2}$ fine-structure transition. The blue curve shows a fit to the line by a Rabi line shape, as expected for the top-hat laser pulse of 12-ms duration. This pulse length results in a Fourier-limited linewidth of 65 Hz FWHM. We do not observe any additional line broadenings on this first-order Zeeman sensitive transition at this level, which confirms our previous measurements[34] of a magnetic-field stability better than 1 nT achieved via active stabilization of the field in the vicinity of the vacuum chamber. Additionally, alternating external magnetic fields are shielded by the highly conductive cryogenic thermal shields made of high-purity copper with a low-pass corner frequency of ≤0.3 Hz and suppression

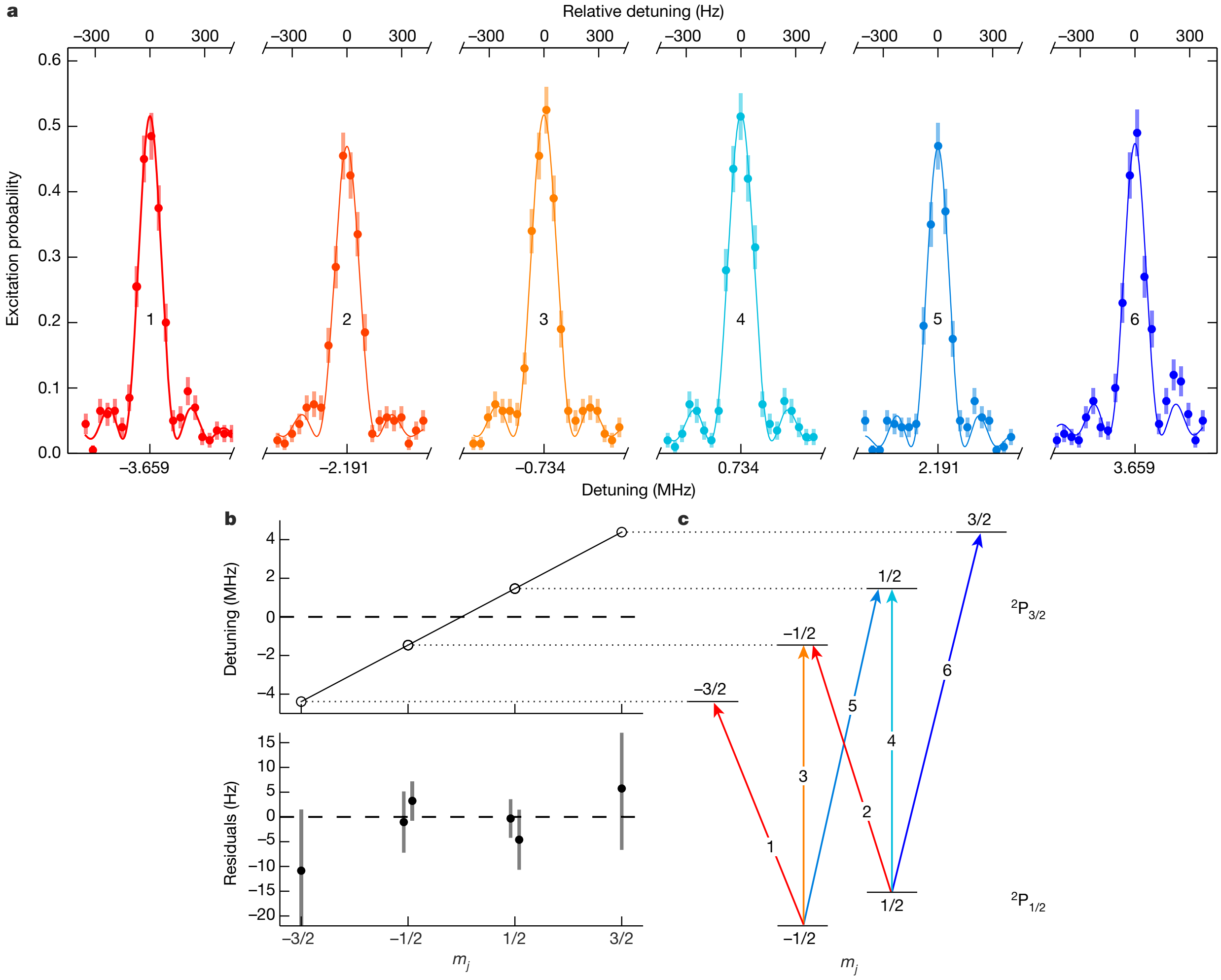

Fig. 4 | Zeeman structure of the $^{40}\mathrm{Ar}^{13+}$ $^{2}P_{1/2}$–$^{2}P_{3/2}$ fine-structure transition. **a**, Excitation probability as a function of the clock laser detuning from the degenerate line centre, showing the six individual Zeeman components. Comparable laser–ion couplings (π-times of 5–6 ms) were chosen for each component, corresponding to Fourier-limited linewidths of around 150 Hz. The solid curves are Rabi line-shape fitting functions used to determine the centre frequencies. Error bars represent the quantum projection noise of 200 repetitions. The varying excitation probabilities of the six components are caused by slightly different state preparation efficiencies. **b**, Reconstructed Zeeman shifts of the $^{2}P_{3/2}$ substates (upper panel) and their residuals (lower panel) with respect to a linear fit (solid black line). Note the different vertical scales. For each of the substates $m_j = \mp 1/2$, two data points are obtained from transitions 2, 3 and 4, 5, respectively. A magnetic-field instability of about 0.5 nT contributes to the standard uncertainties of the line centres, which become larger for the outer components. The slope of the linear fit is proportional to the ratio of the *g*-factors of the excited and ground states. **c**, Level diagram of the $^{2}P_{1/2}$ and $^{2}P_{3/2}$ Zeeman substates and corresponding Zeeman components of the fine-structure transition.

of 30–40 dB in the frequency range 60 Hz–1 kHz (ref. [34]). The maximum fringe contrast of about 0.4 at this probe duration was mostly limited by the excited-state lifetime, with contributions from the ~90% fidelity of the sideband operations on the two ions, as well as from imperfect state preparation and detection. Frequency scans with longer probe times can in principle resolve the natural linewidth, albeit at a reduced excitation probability. Figure 3b shows the on-resonance excitation probability as a function of the probe time for a higher intensity of the clock laser. Under continuous illumination, Rabi flopping between the two electronic states is observed (fitted by the red curve). The coherence decays with the known excited-state lifetime[39] of $9.573(^{+4}_{-4})_{\mathrm{stat}}(^{+12}_{-5})_{\mathrm{syst}}$ ms (where the statistical and systematic standard deviations are given in parentheses), indicated by the red-shaded exponential envelope of the fit. This measurement confirms coherence beyond this timescale for both the clock laser and the magnetic field.

We also performed a direct measurement of the excited-state lifetime. For this, a carrier π-pulse (step (1) in Fig. 2) with maximum laser intensity was applied, which populated the $^{40}\mathrm{Ar}^{13+}$ excited state in about 16 μs. After a variable wait time, the full transfer sequence was performed, and the remaining $^{40}\mathrm{Ar}^{13+}$ excited-state fraction was mapped onto the $^{9}\mathrm{Be}^{+}$ qubit state (see also Methods). During the wait time, a series of ground-state-cooling pulses on both axial motional modes was applied every millisecond to keep the two-ion crystal in the motional ground state in the presence of anomalous heating of 12 and 29 phonons per second for the out-of-phase and in-phase modes, respectively. By incrementing the wait time in 1-ms steps, an axial mode temperature independent of the wait time was ensured. The observed exponential spontaneous decay of the excited state is shown in Fig. 3c and results in a lifetime of 9.97(27) ms. This is about 1.5 standard deviations longer than the more accurate experimental result of

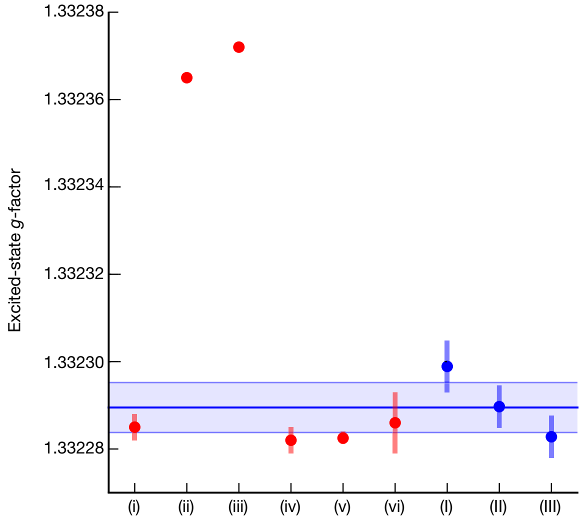

Fig. 5 | Comparison of calculated (red) and measured (blue) excited-state *g*-factors. Shown are results from Glazov et al.[42] (i), Verdebout et al.[43] (ii), Marques et al.[44] (iii), Shchepetnov et al.[46] (iv), Agababaev et al.[45] (v) and Maison et al.[47] (vi). The error bars of (iii) and (v) are smaller than the data points. No uncertainty is provided for data point (ii). (I), (II) and (III) represent *g*-factors evaluated from the three datasets produced in this work with their standard uncertainty. The solid blue line displays the weighted average with the 1σ uncertainty band, with the largest contribution coming from the systematic uncertainty. See Methods for details.

$9.573(^{+4}_{-4})_{\mathrm{stat}}(^{+12}_{-5})_{\mathrm{syst}}$ ms obtained from an in-EBIT measurement[39] and than advanced calculations of 9.538(2) ms (ref. [40]) and 9.5354(20) ms (ref. [41]). Our result is consistent with the previous measurement and calculations within the uncertainty. Further details are provided in Methods.

Measurement of the excited-state *g*-factor

A magnetic field of about 160 μT is applied at the location of the ions to define a quantization axis and to deliberately split the Zeeman substates of ^{9}Be$^+$ and ^{40}Ar^{13+} on the megahertz scale. With quantum logic-assisted HCI state preparation (see Fig. 2b and Extended Data Fig. 3), all six Zeeman components of the ^{40}Ar^{13+} $^2P_{1/2}$–$^2P_{3/2}$ transition can be coherently excited, as shown in Fig. 4a. The bottom horizontal axes represent the clock laser detuning from the degenerate line centre, and the top horizontal axes represent the relative detunings from the centres of the individual Zeeman components. We can reconstruct the Zeeman shifts of the $^2P_{3/2}$ substates from these data (see Fig. 4b, c and Methods) and derive the ratio of the *g*-factors of the excited and ground states from the measured frequencies. Within our current experimental precision of a few hertz over a splitting of several megahertz, we do not observe any quadratic contribution, which for instance could arise from coupling of electric field gradients to the electric quadrupole moment of the $^2P_{3/2}$ state, or from a quadratic Zeeman shift. A quadratic term added to the fitting function of Fig. 4b is consistent with zero. Recently, the ground-state *g*-factor $g_{1/2}$ of ^{40}Ar^{13+} was measured in the Penning trap experiment ALPHATRAP with an accuracy of parts per billion using the continuous Stern–Gerlach method[17]. Using this value, we obtain a weighted average of $g_{3/2} = 1.3322895(13)_{\mathrm{stat}}(56)_{\mathrm{syst}}$ from three individual measurements (see Fig. 5). This is an improvement of more than two orders of magnitude over previous in-EBIT measurements[7], revealing the contributions that arise from special relativity, interelectronic interactions and QED to an HCI excited-state *g*-factor. It also settles a discrepancy between previous theoretical values[42–47], confirming the configuration-interaction calculations of refs. [42,45,46] and very recent coupled-cluster calculations[47].

Conclusions

We have cooled HCIs to the ground state of motion in a linear Paul trap, making them the coldest HCIs prepared in a laboratory so far. This enabled us to perform coherent, optical-clock-like laser spectroscopy of an electric-dipole-forbidden optical transition in an HCI using quantum logic, at a level of precision that is eight orders of magnitude higher than the previous state of the art. This proves the feasibility of hertz-level optical spectroscopy of HCIs and opens up this large class of atomic systems to the tools of cutting-edge frequency metrology and quantum information processing.

The determination of the absolute frequency of the ^{40}Ar^{13+} fine-structure transition with a fractional uncertainty of 3×10^{-15} and even higher levels of precision requires further evaluation of systematic shifts, such as the small time dilation shift from the residual motion of the ion[48] or the electric quadrupole shift[49], which is typically suppressed in HCIs. By restricting measurements to the points of maximum frequency sensitivity of each line, frequency information can be obtained faster than when scanning the full line profiles, as demonstrated here, further reducing the statistical uncertainty at a given averaging time[50]. At the same time, averaging over the Zeeman components on second—rather than minute—timescales will suppress systematic uncertainties arising from drifting magnetic fields[51].

The presented techniques are not limited to our proof-of-principle HCI, ^{40}Ar^{13+}, but can be applied more generally to forbidden transitions in other HCIs. Several of the candidate species have properties that are even better suited for optical-clock experiments, including much longer excited-state lifetimes and suppressed systematic shifts. Certain HCIs are particularly sensitive to physics beyond the standard model, such as possible variations of the fine-structure constant[4], or to effects arising from fundamental interactions. Particularly, HCIs allow the systematic study of relativistic effects in bound electronic systems and of bound-state QED along isoelectronic sequences at ultrahigh precision[5].

Furthermore, the techniques that we have demonstrated here are not limited to the optical domain. Our work also unlocks the new frontiers of the vacuum ultraviolet and X-ray regimes for ultrahigh precision spectroscopy—regions of the electromagnetic spectrum that are incompatible with neutral and singly charged atoms owing to unavoidable photoionization. This will enable novel high-accuracy atomic clocks based on HCIs and unrivalled tests of fundamental physics.

We note that during the revision of the manuscript, a complementary work demonstrating incoherent laser spectroscopy of ^{40}Ar^{13+} in a Penning trap was published[52].

Online content

Any methods, additional references, Nature Research reporting summaries, source data, extended data, supplementary information, acknowledgements, peer review information; details of author contributions and competing interests; and statements of data and code availability are available at https://doi.org/10.1038/s41586-020-1959-8.

1. Ludlow, A. D., Boyd, M. M., Ye, J., Peik, E. & Schmidt, P. O. Optical atomic clocks. *Rev. Mod. Phys*. **87**, 637–701 (2015).
2. Safronova, M. S. et al. Search for new physics with atoms and molecules. *Rev. Mod. Phys*. **90**, 025008 (2018).
3. Schiller, S. Hydrogenlike highly charged ions for tests of the time independence of fundamental constants. *Phys. Rev. Lett*. **98**, 180801 (2007).
4. Berengut, J., Dzuba, V. & Flambaum, V. Enhanced laboratory sensitivity to variation of the fine-structure constant using highly charged ions. *Phys. Rev. Lett*. **105**, 120801 (2010).
5. Kozlov, M. G., Safronova, M. S., Crespo López-Urrutia, J. R. & Schmidt, P. O. Highly charged ions: optical clocks and applications in fundamental physics. *Rev. Mod. Phys*. **90**, 045005 (2018).
6. Draganić, I. et al. High precision wavelength measurements of QED-sensitive forbidden transitions in highly charged argon ions. *Phys. Rev. Lett*. **91**, 183001 (2003).
7. Soria Orts, R. et al. Zeeman splitting and g factor of the $1s^22s^22p$ $^2P_{3/2}$ and $^2P_{1/2}$ levels in Ar^{13+}. *Phys. Rev. A* **76**, 052501 (2007).

8. Mäckel, V., Klawitter, R., Brenner, G., Crespo López-Urrutia, J. R. & Ullrich, J. Laser spectroscopy on forbidden transitions in trapped highly charged Ar^{13+} Ions. *Phys. Rev. Lett*. **107**, 143002 (2011).
9. Schmidt, P. O. et al. Spectroscopy using quantum logic. *Science* **309**, 749–752 (2005).
10. Wineland, D. J., Bergquist, J. C., Bollinger, J. J., Drullinger, R. E. & Itano, W. M. Quantum computers and atomic clocks. In *Proc. 6th Symp. on Frequency Standards and Metrology* (ed. Gill, P.) 361–368 (World Scientific, 2002).
11. Derevianko, A. & Pospelov, M. Hunting for topological dark matter with atomic clocks. *Nat. Phys*. **10**, 933–936 (2014).
12. Gumberidze, A. et al. Quantum electrodynamics in strong electric fields: the ground-state Lamb shift in hydrogenlike uranium. *Phys. Rev. Lett*. **94**, 223001 (2005).
13. Beiersdorfer, P., Osterheld, A. L., Scofield, J. H., Crespo López-Urrutia, J. R. & Widmann, K. Measurement of QED and hyperfine splitting in the $2s_{1/2}$–$2p_{3/2}$ X-ray transition in Li-like $^{209}Bi^{80+}$. *Phys. Rev. Lett*. **80**, 3022–3025 (1998).
14. Beiersdorfer, P., Chen, H., Thorn, D. B. & Träbert, E. Measurement of the two-loop Lamb shift in lithiumlike U^{89+}. *Phys. Rev. Lett*. **95**, 233003 (2005).
15. Beiersdorfer, P. et al. Hyperfine splitting of the $2s_{1/2}$ and $2p_{1/2}$ levels in Li- and Be-like ions of $^{141}_{59}Pr$. *Phys. Rev. Lett*. **112**, 233003 (2014).
16. Sturm, S. et al. *g* factor of hydrogenlike $^{28}Si^{13+}$. *Phys. Rev. Lett*. **107**, 023002 (2011).
17. Arapoglou, I. et al. *g*-factor of boronlike argon $^{40}Ar^{13+}$. *Phys. Rev. Lett*. **122**, 253001 (2019).
18. Crespo López-Urrutia, J. R., Beiersdorfer, P., Savin, D. W. & Widmann, K. Direct observation of the spontaneous emission of the hyperfine transition $F = 4$ to $F = 3$ in ground state hydrogenlike $^{165}Ho^{66+}$ in an electron beam ion trap. *Phys. Rev. Lett*. **77**, 826–829 (1996).
19. Seelig, P. et al. Ground state hyperfine splitting of hydrogenlike $^{207}Pb^{81+}$ by laser excitation of a bunched ion beam in the GSI experimental storage ring. *Phys. Rev. Lett*. **81**, 4824–4827 (1998).
20. Ullmann, J. et al. High precision hyperfine measurements in Bismuth challenge bound-state strong-field QED. *Nat. Commun*. **8**, 15484 (2017).
21. Gruber, L. et al. Evidence for highly charged ion Coulomb crystallization in multicomponent strongly coupled plasmas. *Phys. Rev. Lett*. **86**, 636–639 (2001).
22. Schwarz, M. et al. Cryogenic linear Paul trap for cold highly charged ion experiments. *Rev. Sci. Instrum*. **83**, 083115–083115–10 (2012).
23. Schmöger, L. et al. Coulomb crystallization of highly charged ions. *Science* **347**, 1233–1236 (2015).
24. Schmöger, L. *Kalte hochgeladene Ionen für Frequenzmetrologie*. PhD thesis, Univ. of Heidelberg (2017).
25. Rosenband, T. et al. Frequency ratio of Al^+ and Hg^+ single-ion optical clocks; metrology at the 17th decimal place. *Science* **319**, 1808–1812 (2008).
26. Chou, C. W., Hume, D. B., Koelemeij, J. C. J., Wineland, D. J. & Rosenband, T. Frequency comparison of two high-accuracy Al^+ optical clocks. *Phys. Rev. Lett*. **104**, 070802 (2010).
27. Brewer, S. M. et al. $^{27}Al^+$ quantum-logic clock with a systematic uncertainty below 10^{-18}. *Phys. Rev. Lett*. **123**, 033201 (2019).
28. Wolf, F. et al. Non-destructive state detection for quantum logic spectroscopy of molecular ions. *Nature* **530**, 457–460 (2016).
29. Chou, C. et al. Preparation and coherent manipulation of pure quantum states of a single molecular ion. *Nature* **545**, 203–207 (2017).
30. Hempel, C. et al. Entanglement-enhanced detection of single-photon scattering events. *Nat. Photon*. **7**, 630–633 (2013).
31. Wan, Y. et al. Precision spectroscopy by photon-recoil signal amplification. *Nat. Commun*. **5**, 3096 (2014).
32. Micke, P. et al. The Heidelberg compact electron beam ion traps. *Rev. Sci. Instrum*. **89**, 063109 (2018).
33. Schmöger, L. et al. Deceleration, precooling, and multi-pass stopping of highly charged ions in Be^+ Coulomb crystals. *Rev. Sci. Instrum*. **86**, 103111 (2015).
34. Leopold, T. et al. A cryogenic radio-frequency ion trap for quantum logic spectroscopy of highly charged ions. *Rev. Sci. Instrum*. **90**, 073201 (2019).
35. Micke, P. et al. Closed-cycle, low-vibration 4 K cryostat for ion traps and other applications. *Rev. Sci. Instrum*. **90**, 065104 (2019).
36. King, S. A., Leopold, T., Thekkeppatt, P. & Schmidt, P. O. A self-injection locked DBR laser for laser cooling of beryllium ions. *Appl. Phys. B* **124**, 214 (2018).
37. Matei, D. G. et al. 1.5 μm lasers with sub-10 mHz linewidth. *Phys. Rev. Lett*. **118**, 263202 (2017).
38. Stenger, J., Schnatz, H., Tamm, C. & Telle, H. Ultraprecise measurement of optical frequency ratios. *Phys. Rev. Lett*. **88**, 073601 (2002).
39. Lapierre, A. et al. Lifetime measurement of the Ar XIV $1s^2 2s^2 2p^2 P^{o}_{3/2}$ metastable level at the Heidelberg electron-beam ion trap. *Phys. Rev. A* **73**, 052507 (2006).
40. Tupitsyn, I. I. et al. Magnetic-dipole transition probabilities in B-like and Be-like ions. *Phys. Rev. A* **72**, 062503 (2005).
41. Bilal, M., Volotka, A. V., Beerwerth, R. & Fritzsche, S. Line strengths of QED-sensitive forbidden transitions in B-, Al-, F- and Cl-like ions. *Phys. Rev. A* **97**, 052506 (2018).
42. Glazov, D. A. et al. *g* factor of boron-like ions: ground and excited states. *Phys. Scr*. **T156**, 014014 (2013).
43. Verdebout, S. et al. Hyperfine structures and Landé g_J-factors for $n = 2$ states in beryllium-, boron-, carbon-, and nitrogen-like ions from relativistic configuration interaction calculations. *At. Data Nucl. Data Tables* **100**, 1111–1155 (2014).
44. Marques, J. P., Indelicato, P., Parente, F., Sampaio, J. M. & Santos, J. P. Ground-state Landé *g* factors for selected ions along the boron isoelectronic sequence. *Phys. Rev. A* **94**, 042504 (2016).
45. Agababaev, V. A. et al. *g* factor of the $[(1s)^2(2s)^2 2p]^2P_{3/2}$ state of middle-*Z* boronlike ions. *X-ray Spectrom*. **49**, 143–148 (2019).
46. Shchepetnov, A. A. et al. Nuclear recoil correction to the *g* factor of boron-like argon. *J. Phys. Conf. Ser*. **583**, 012001 (2015).
47. Maison, D. E., Skripnikov, L. V. & Glazov, D. A. Many-body study of the *g* factor in boronlike argon. *Phys. Rev. A* **99**, 042506 (2019).
48. Berkeland, D. J., Miller, J. D., Bergquist, J. C., Itano, W. M. & Wineland, D. J. Minimization of ion micromotion in a Paul trap. *J. Appl. Phys*. **83**, 5025–5033 (1998).
49. Itano, W. M. External-field shifts of the $^{199}Hg^+$ optical frequency standard. *J. Res. Natl Inst. Stand. Technol*. **105**, 829–837 (2000).
50. Madej, A. A., Dubé, P., Zhou, Z., Bernard, J. E. & Gertsvolf, M. $^{88}Sr^+$ 445-THz single-ion reference at the 10^{-17} level via control and cancellation of systematic uncertainties and its measurement against the SI second. *Phys. Rev. Lett*. **109**, 203002 (2012).
51. Barwood, G. P., Huang, G., King, S. A., Klein, H. A. & Gill, P. Frequency noise processes in a strontium ion optical clock. *J. Phys. At. Mol. Opt. Phys*. **48**, 035401 (2015).
52. Egl, A. et al. Application of the continuous Stern–Gerlach effect for laser spectroscopy of the $^{40}Ar^{13+}$ fine structure in a Penning trap. *Phys. Rev. Lett*. **123**, 123001 (2019).

Publisher's note Springer Nature remains neutral with regard to jurisdictional claims in published maps and institutional affiliations.

© The Author(s), under exclusive licence to Springer Nature Limited 2020

Methods

HCI production, transfer and recapture

We show a top view of the laboratory setup in Extended Data Fig. 1 and a simplified schematic of the potential landscape in Extended Data Fig. 2a. HCIs are produced by electron impact ionization and stored by PTB-EBIT, a Heidelberg-type compact EBIT[32]. After extraction of ions in bunches, a beamline with multiple electrostatic elements is used to guide the ions towards the Paul trap and to manipulate their kinetic-energy distribution. Five segmented einzel lenses[53] and an electrostatic double-focusing 90° deflector[54] are employed for focusing and steering. A pair of pulsed drift tubes (following the approach described in ref. [33]) is used for deceleration and pre-cooling, reducing the phase-space volume of the bunches. Downstream, two microchannel plate (MCP) detectors can be moved into the ion beam in front of and behind the Paul trap to optimize ion yield and beam transmission. The first MCP detector also features a retarding field analyser that is used to determine the mean kinetic energy and the energy spread of the ion bunches. Although this method of HCI production, transfer and recapture combining the EBIT, beamline and Paul trap can handle a large variety of elements and charge states, the following section refers specifically to the present case of optimized $^{40}\mathrm{Ar}^{13+}$ recapture.

Highly charged argon ions are produced in a distribution of charge states using a 13-mA, 1-keV electron beam in the approximately 50-V-deep axial trapping potential of the EBIT. In each cycle, the central trap electrode is rapidly switched from about 450 V (for the aforementioned 50-V-deep trap) to a repulsive extraction potential of 700 V (200 V higher than the outer trap electrode potential) for a period of 200 ns at a rate of 4 Hz to eject the ions. The kinetic energy relative to the ground potential of the beamline (0 V), and thus the velocity of the extracted ions, depend on the total extraction potential of 700 V and on the ionic charge q, allowing separation of the different charge states by their different times of flight (Extended Data Fig. 2a, b). $^{40}\mathrm{Ar}^{13+}$ is selected with the help of an electrode of the third segmented einzel lens immediately behind the 90° deflector. This electrode acts as a gate by rapidly switching to a passing voltage at the $^{40}\mathrm{Ar}^{13+}$ arrival time, and back to a deflecting voltage after the ion passage. Thus, the trajectories of all other charge states are deflected away from the Paul trap. We measure a mean kinetic energy of $694q$ V with respect to ground for the fast $^{40}\mathrm{Ar}^{13+}$ bunches using the retarding field analyser (Extended Data Fig. 2e). An associated axial energy spread of $32q$ V was also determined. To decrease the mean kinetic energy and its spread to values more amenable for trapping and efficient cooling in the cryogenic Paul trap, we perform an electrodynamic deceleration step with the pair of pulsed drift tubes. By biasing them to approximately 510 V and 590 V before the extraction, a linear axial potential gradient is generated on the beamline axis between the two electrodes. Thus, when the ion bunch arrives at that position, about 9.7 µs after ion ejection, it is exposed to a mean potential of 550 V. Then, both drift tube potentials are rapidly grounded using a fast high-voltage switch. This slows down the ion bunch to a kinetic energy of $146q$ V and reduces the axial energy spread to $13q$ V (Extended Data Fig. 2f). The deceleration step also shortens the length of the ion bunches considerably, from about 5.2 cm to about 1.7 cm FWHM, while their temporal width is only slightly reduced (Extended Data Fig. 2c, d). After passing through a final einzel lens and an unbiased mirror tube, the $^{40}\mathrm{Ar}^{13+}$ ions enter the Paul trap. The trap voltages are commonly biased to 138 V to accomplish the final electrostatic deceleration step. This brings the ions to a residual kinetic energy of about $5q$ V to $10q$ V.

The Paul trap is formed by a radially confining radio-frequency potential and an axially confining d.c. potential. Once inside the trap, the HCIs repeatedly pass through a cigar-shaped Coulomb crystal composed of about 50 to 100 $^{9}\mathrm{Be}^{+}$ ions that has been previously loaded into the Paul trap using laser ablation combined with photoionization[34] (see also Fig. 1). This proceeds as follows. During injection into the Paul trap, owing to their relatively high kinetic energy, most HCIs can overcome the weak axially confining potential of 300 mV (above the biased ground of 138 V) applied to the electrostatic endcap at the entrance of the trap. After passing through the $^{9}\mathrm{Be}^{+}$ Coulomb crystal for the first time, the $^{40}\mathrm{Ar}^{13+}$ ions are reflected by the opposite electrostatic endcap potential of about 12 V (above the biased ground of 138 V). In the meantime (17.1 µs after initial ion extraction from the EBIT), the mirror tube at the entrance of the Paul trap is rapidly switched up to a confining axial electrostatic potential to complete the capture of $^{40}\mathrm{Ar}^{13+}$. Then the trap remains closed for 1.9 s, during which the HCIs can dissipate their residual kinetic energy by repeated interactions with the laser-cooled $^{9}\mathrm{Be}^{+}$ ions. If these steps are successful for an $^{40}\mathrm{Ar}^{13+}$ ion, it joins the $^{9}\mathrm{Be}^{+}$ Coulomb crystal (Fig. 1). Otherwise, the mirror-tube potential is lowered again to let the next HCI bunch enter the Paul trap. This whole recapture process is rather efficient and succeeds in less than 30 s on average.

Excited-state lifetime measurement

The data for the lifetime measurement were acquired from 440 measurements, each of which includes 100 experimental realizations, adding up to a total measurement time of about two hours. Eleven measurements were averaged for every single wait time, with the error bars in Fig. 3c indicating the quantum projection noise of 1,100 experimental implementations. To cancel the effects of parameter drifts on the observed signal, the wait time was scanned in a pseudo-random sequence.

Drifts of the atomic resonance frequencies could lead to systematic variations in the detected excitation probabilities. The shortest achievable π-times, 16 µs for the initial HCI excitation and 225 µs for the HCI sideband transition, lead to an interaction broadening of the respective lines of 62 kHz and 4.4 kHz, respectively. Our typical short-term magnetic-field fluctuations lead to line shifts of <10 Hz level, and thus affect the measured excited-state population of the order of 10^{-4}. The axial trap frequency has fluctuations below 100 Hz over the course of a day. The distribution of data points for a given wait time is consistent with the expected quantum projection noise, thereby ruling out systematic drifts at the level of the statistical uncertainty.

The clock laser pulses are generated by the first diffraction order of an acousto-optic modulator (AOM). Despite the typical 100-dB level of extinction of the radio-frequency drive power provided by an active radio-frequency switch, the optical extinction ratio does not reach this level owing to scattered light within the AOM crystal. However, this leaked light is unshifted by the AOM and therefore detuned from the ion resonance by the radio-frequency drive frequency of about 200 MHz, or 10^{7} natural linewidths. This alone reduces the de-excitation probability by approximately 14 orders of magnitude.

Spontaneous decay of the HCI on the red sideband is suppressed as the square of the Lamb–Dicke parameter, $\eta^2 \approx 0.01$. However, residual decay on this sideband leads to heating of the motional mode and may thus appear as spurious excitation in the quantum logic detection. A few sideband cooling pulses applied immediately before the quantum logic transfer pulse suppress this effect by returning the crystal to its ground state. Off-resonant depumping of the excited state of $^{40}\mathrm{Ar}^{13+}$ by the $^{9}\mathrm{Be}^{+}$ lasers is negligible because of the narrow natural linewidth and the large detuning. Collisional deshelving, as discussed in refs. [55,56], is absent in this experiment owing to the extremely high vacuum. Furthermore, collisions of an HCI with a neutral particle probably lead to charge exchange and total, but inconsequential, ion loss.

g-factor evaluation

The $^{40}\mathrm{Ar}^{13+}\,{}^{2}P_{3/2}$ excited-state g-factor, denoted as $g_{3/2}$, is determined by a linear fit of the Zeeman substate energy shifts. We use the well known ground-state g-factor of the clock transition from a recent high-accuracy measurement[17] to operate a co-magnetometer and measure the magnetic field by an appropriate combination of the Zeeman components.

The energy shifts $\Delta E_{3/2,\, m_{3/2,i}} = m_{3/2,i}\, g_{3/2} \mu_{\mathrm{B}} B$ of the Zeeman substates of the excited $^2\mathrm{P}_{3/2}$ state that are due to an external magnetic field B are obtained from the measured Zeeman shifts f_i (in units of frequency) of the six Zeeman components (i ranging from 1 to 6, according to Fig. 4c) and analogously the shifts $\Delta E_{1/2,\, m_{1/2,i}}$ of the $^2\mathrm{P}_{1/2}$ Zeeman substates. h and μ_{B} are the Planck constant and the Bohr magneton, respectively. The shifts are referenced with respect to the degenerate line/level centres. One then obtains

$$\frac{\Delta E_{3/2,\, m_{3/2,i}}}{h} = f_i + \frac{\Delta E_{1/2,\, m_{1/2,i}}}{h} \tag{1}$$

$$m_{3/2,i}\, g_{3/2} \frac{\mu_{\mathrm{B}} B}{h} = f_i + m_{1/2,i}\, g_{1/2} \frac{\mu_{\mathrm{B}} B}{h} \tag{2}$$

B is eliminated from the above equation by using the four inner Zeeman components 2–5, which are less sensitive to magnetic-field fluctuations than the two outer ones. Components f_2 and f_3 share the common excited state $m_{3/2} = -1/2$ (see Fig. 4c), and therefore their difference yields the ground-state Zeeman splitting directly, without relying on the excited-state g-factor. Using the known ground-state g-factor $g_{1/2}$ from the work of Arapoglou et al.[17], we obtain the magnetic field

$$B_1 = \frac{h\,(f_3 - f_2)}{g_{1/2}\, \mu_{\mathrm{B}}} \tag{3}$$

Similarly, components f_4 and f_5 share the excited state with $m_{3/2} = +1/2$, and we acquire a second measurement of

$$B_2 = \frac{h\,(f_5 - f_4)}{g_{1/2}\, \mu_{\mathrm{B}}} \tag{4}$$

Introducing $U = f_5 - f_4 + f_3 - f_2$ for simplicity, we average the magnetic field B from these two relations to reduce the uncertainty

$$B = \frac{B_1 + B_2}{2} = \frac{h\, U}{2\, g_{1/2}\, \mu_{\mathrm{B}}} \tag{5}$$

This expression is inserted into equation (2) to obtain

$$y_i(m_{3/2,i}) = \frac{g_{3/2}\, U}{2\, g_{1/2}}\, m_{3/2,i} = f_i + m_{1/2,i}\, \frac{U}{2} \tag{6}$$

On the right-hand side of the equation, the measured shifts of the excited Zeeman substates are given, which fulfil a linear relation in $m_{3/2,i}$ (left-hand side of the equation). A linear fit (see black line in Fig. 4b) of the form

$$y_i(m_{3/2,i}) = a m_{3/2,i} + b \tag{7}$$

with offset b to account for the global frequency offset in the measured f_i, allows us to determine the excited-state g-factor $g_{3/2}$ from the slope a

$$g_{3/2} = \frac{2\, g_{1/2}\, a}{U} \tag{8}$$

The uncertainties σ_{yi} of the excited Zeeman substates are obtained from the right-hand side of equation (6) by expressing U again as $U = f_5 - f_4 + f_3 - f_2$, followed by standard uncertainty propagation with the independently measured f_i

$$\sigma_{y_i} = \sqrt{\sum_j \left(\frac{\partial y_i}{\partial f_j} \sigma_{f_j} \right)^2} \tag{9}$$

The uncertainties σ_{fi} of the Zeeman components depend on the statistical uncertainty of the line centre from the fit, $\sigma_{f_{i,\mathrm{fit}}}$ (fitting the lines by Rabi line shapes) and the relative systematic magnetic-field uncertainty σ_B/B. The latter is time-dependent and is estimated from the observed magnetic-field stability measured previously by using the $^9\mathrm{Be}^+$ qubit transition frequency (see ref. [34] for details) to be 4.1×10^{-6} (measurement 1) and 3.2×10^{-6} (measurements 2 and 3) on relevant timescales. Accordingly, one has

$$\sigma_{f_i} = \sqrt{{\sigma_{f_{i,\mathrm{fit}}}}^2 + \left(\frac{\sigma_B}{B} f_i \right)^2} \tag{10}$$

The linear fit shown in Fig. 4b is weighted with the σ_{yi} uncertainties, which are displayed in the lower panel. For completeness, we state the fit offsets for the three sets of measurements: $b = -17(3)$ Hz, $-45(2)$ Hz and $-30(2)$ Hz. The reduced χ^2 of the linear fits are 1.45, 0.57 and 0.21.

To estimate the uncertainty of $g_{3/2}$, we replace a and U in equation (8) by their analytical expressions. $a = \overline{(m_{3/2,i} y_i)} / \overline{m^2_{3/2,i}}$ is obtained from the closed-form solution of a linear fit. The y_i values are given by the right-hand side of equation (6), and $U = f_5 - f_4 + f_3 - f_2$. We can neglect the parts-per-billion uncertainty of the experimental result $g_{1/2} = 0.66364845532(93)$ from the very recent Penning trap measurement[17] because it is more than three orders of magnitude smaller than our experimental uncertainties in the 25,000-times-weaker magnetic field. Finally, the only uncertainties are introduced by the independently measured f_i. Thus, the uncertainty $\sigma_{g_{3/2}}$ is obtained from the typical formula of uncertainty propagation

$$\sigma_{g_{3/2}} = \sqrt{\sum_i \left(\frac{\partial g_{3/2}}{\partial f_i} \sigma_{f_i} \right)^2} \tag{11}$$

The calculated $g_{3/2}$ values are $1.3322989(19)_{\mathrm{stat}}(56)_{\mathrm{syst}}$, $1.3322897(23)_{\mathrm{stat}}(43)_{\mathrm{syst}}$ and $1.3322828(24)_{\mathrm{stat}}(43)_{\mathrm{syst}}$ for the three measurement sets obtained on two different days, where we have stated the statistical and systematic uncertainties separately. The results are shown in Fig. 5 together with recent calculations. The uncertainties of the individual measurements are the root of the sum of the squared statistical and systematic uncertainties. The measurements agree within their uncertainties, and the largest deviation between measurement 1 and the weighted average is 1.6 standard deviations. We obtain the weighted average $g_{3/2} = 1.3322895(13)_{\mathrm{stat}}(56)_{\mathrm{syst}}$, where we have combined the statistical uncertainties and stated the largest systematic uncertainty of the individual measurements as a conservative estimate for the systematic uncertainty of the average.

Data availability

The datasets generated and analysed during this study are available from the corresponding author upon reasonable request.

53. Mandal, P., Sikler, G. & Mukherjee, M. Simulation study and analysis of a compact einzel lens-deflector for low energy ion beam. *J. Instrum.* **6**, P02004 (2011).
54. Kreckel, H. et al. A simple double-focusing electrostatic ion beam deflector. *Rev. Sci. Instrum.* **81**, 063304 (2010).
55. Barton, P. A. et al. Measurement of the lifetime of the $3d^2D_{5/2}$ state in $^{40}\mathrm{Ca}^+$. *Phys. Rev. A* **62**, 032503 (2000).
56. Letchumanan, V., Wilson, M., Gill, P. & Sinclair, A. Lifetime measurement of the metastable $4d^2D_{5/2}$ state in $^{88}\mathrm{Sr}^+$ using a single trapped ion. *Phys. Rev. A* **72**, 012509 (2005).

Acknowledgements We acknowledge I. Arapoglou, H. Bekker, S. Bernitt, K. Blaum, A. Egl, S. Hannig, S. Kühn, T. Legero, R. Müller, J. Nauta, J. Stark, U. Sterr, S. Sturm and A. Surzhykov for support and discussions. We also thank the MPIK engineering design office, the electronics workshops of QUEST and MPIK, IMPT Hannover, and PTB division 4 for support and technical help. In particular, we thank the mechanical workshop of MPIK and the scientific instrumentation department (5.5) of PTB for their skilful and timely manufacturing of our devices. The project was supported by the Physikalisch-Technische Bundesanstalt, the Max-

Planck Society, the Max-Planck–Riken–PTB–Center for Time, Constants and Fundamental Symmetries, and the Deutsche Forschungsgemeinschaft (DFG, German Research Foundation) through SCHM2678/5-1, the collaborative research centres SFB 1225 ISOQUANT and SFB 1227 DQ-mat, and Germany's Excellence Strategy – EXC-2123/1 QuantumFrontiers. This project also received funding from the European Metrology Programme for Innovation and Research (EMPIR), which is co-financed by the Participating States, and from the European Union's Horizon 2020 research and innovation programme (project number 17FUN07 CC4C). S.A.K. acknowledges financial support from the Alexander von Humboldt Foundation.

Author contributions P.M., T.L., S.A.K., E.B., L.S., M.S., J.R.C.L.-U. and P.O.S. developed the experimental setup. P.M., T.L., S.A.K. and L.J.S. carried out the experiments. P.M. and T.L. analysed the data. J.R.C.L.-U. and P.O.S. conceived and supervised the study. P.M. and P.O.S. wrote the initial manuscript with contributions from T.L., S.A.K. and J.R.C.L.-U. All authors discussed the results and reviewed the manuscript.

Competing interests The authors declare no competing interests.

Additional information
Correspondence and requests for materials should be addressed to P.M. or P.O.S.
Peer review information *Nature* thanks Andrei Derevianko and the other, anonymous, reviewer(s) for their contribution to the peer review of this work.
Reprints and permissions information is available at http://www.nature.com/reprints.

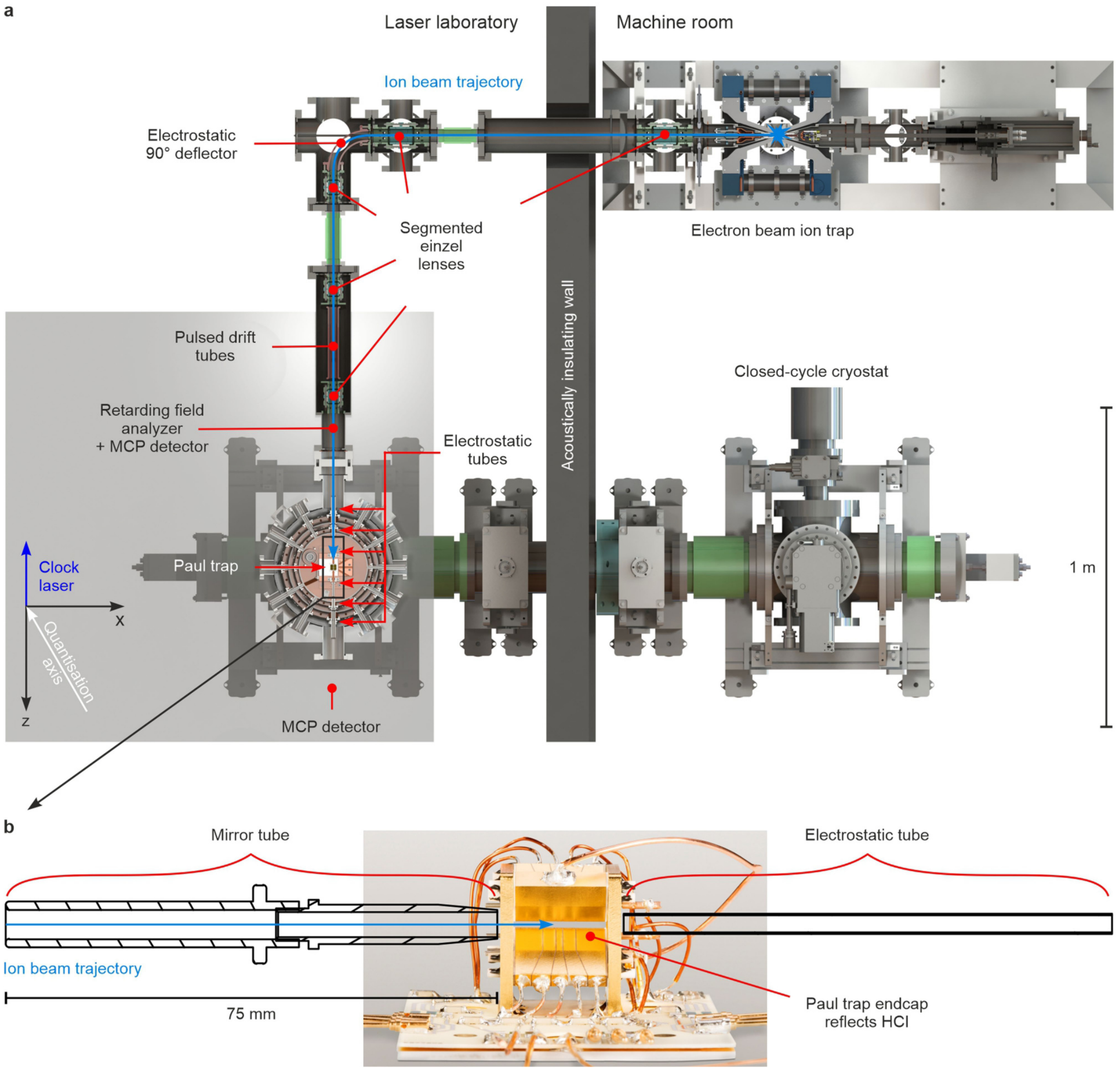
a
Laser laboratory
Machine room
Ion beam trajectory
Electrostatic 90° deflector
Segmented einzel lenses
Electron beam ion trap
Pulsed drift tubes
Retarding field analyzer + MCP detector
Electrostatic tubes
Acoustically insulating wall
Closed-cycle cryostat
1 m
Clock laser
Paul trap
x
Quantisation axis
z
MCP detector
b
Mirror tube
Electrostatic tube
Ion beam trajectory
75 mm
Paul trap endcap reflects HCI

Extended Data Fig. 1 | Experimental setup. a, Top view of the setup. The apparatus extends over two rooms separated by an acoustically insulating wall. Inside the 'machine room' on the right-hand side, HCIs are produced in an EBIT[32] and extracted as ion bunches along the ion beam trajectory (blue line) through a deceleration beamline. At the laser laboratory (left side), they are axially injected into a cryogenic linear Paul trap[34], which is mounted on a pneumatically floating optical table (grey-shaded). The Paul trap is refrigerated by a vibrationally decoupled pulse tube cryocooler[35] located in the machine room. The beamline is composed of several ion optical elements: five segmented einzel lenses and an electrostatic 90° deflector for guiding and focusing the ions, a pair of pulsed drift tubes for deceleration, and six cylindrical electrodes arranged in line in front of and behind the Paul trap. Charge-state separation is accomplished by the different times of flight through the beamline. One electrode of the third segmented einzel lens is used as a gate to select the desired charge state. An MCP detector in front of the Paul trap includes two fine stainless-steel meshes that apply a well defined retarding field, and allows the measurement of the kinetic-energy distribution of the ion bunches (see also Extended Data Fig. 2e, f). A second MCP detector behind the Paul trap is used to optimize the ion beam transmission through the Paul trap. **b**, Magnified side view of the cryogenic Paul trap region. The trap (photograph) is shown with the two adjacent electrostatic tubes. The left one (mirror tube) at the entrance of the Paul trap is used to capture the HCIs by rapidly switching to a confining potential once the HCIs have passed it. Photograph: Physikalisch-Technische Bundesanstalt.

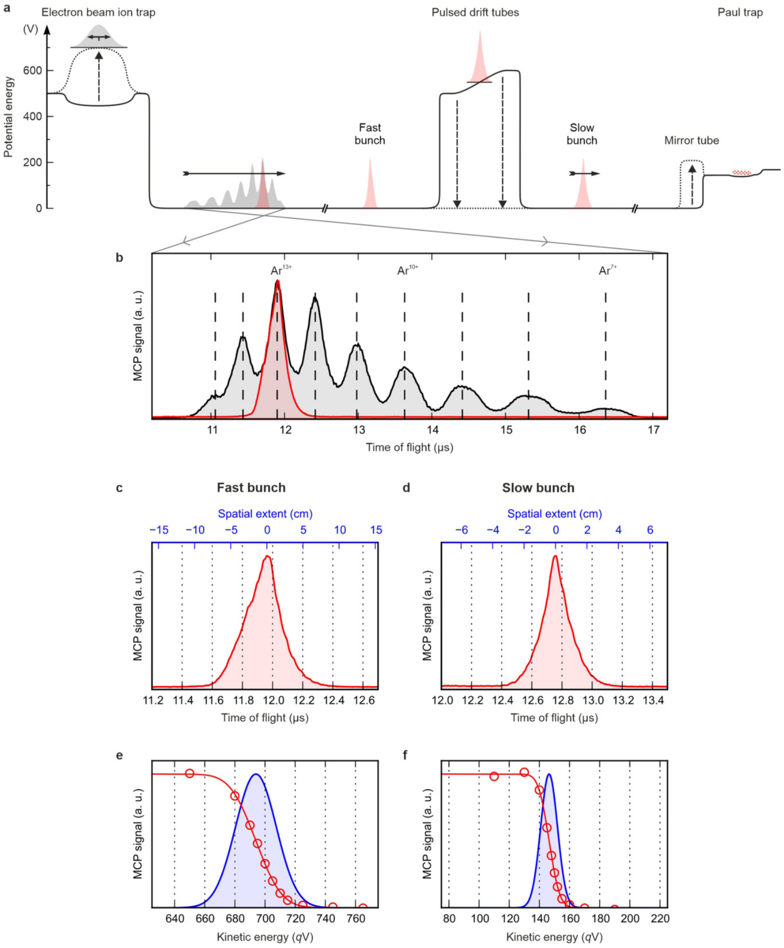

Extended Data Fig. 2 | HCI extraction and transfer. a, Simplified illustration of the electrostatic potential used for the $^{40}\mathrm{Ar}^{13+}$ transfer from the EBIT to the Paul trap. The entire ion inventory stored in the EBIT, with its charge-state distribution displayed as grey-shaded, is ejected by switching the axial trap to a repulsive potential. The charge states separate owing to their distinct initial kinetic energies. $^{40}\mathrm{Ar}^{13+}$ ions (red) are selected by an electrode used as a gate (not shown). The fast $^{40}\mathrm{Ar}^{13+}$ bunch is then slowed down upon entering the pulsed drift tubes. Having arrived there at the centre of a linear potential gradient, the electrode potentials are rapidly switched to ground, and a slower $^{40}\mathrm{Ar}^{13+}$ bunch leaves the pulsed drift tubes. At the Paul trap, the ions are further decelerated by an electrostatic potential and enter the trapping region with a reduced residual kinetic energy of $5q$ V to $10q$ V. They then pass a Coulomb crystal of $^{9}\mathrm{Be}^{+}$ ions and are reflected by an electrostatic endcap electrode biased to a potential of about 12 V above the biased common ground. Meanwhile, an electrostatic mirror tube in front of the Paul trap has been switched up to a confining potential at which $^{40}\mathrm{Ar}^{13+}$ is unable to escape the Paul trap. This causes an oscillatory motion along the trap axis. Through repeated interactions with the laser-cooled $^{9}\mathrm{Be}^{+}$ ions, $^{40}\mathrm{Ar}^{13+}$ dissipates its residual kinetic energy and joins the Coulomb crystal. **b**, Normalized ion yield as a function of the time of flight after ion ejection from the EBIT, measured by the first MCP detector in front of the Paul trap. The black curve shows the entire charge-state distribution, with Ar charge states from +7 through +15. Using the gate electrode, $^{40}\mathrm{Ar}^{13+}$ is chosen for passage, as shown by the red curve. a.u., arbitrary units. **c**, **d**, Normalized $^{40}\mathrm{Ar}^{13+}$ bunches as a function of time and position along the beamline axis (averaged over 16 shots). The FWHM of the fast bunch is about 250 ns (**c**) and that of the slow bunch is about 185 ns (**d**). **e**, **f**, Normalized kinetic-energy distributions of the $^{40}\mathrm{Ar}^{13+}$ bunches along the beamline axis: fast bunch (**e**) and slow bunch after deceleration and phase-space cooling using the pulsed drift tubes (**f**). The red circles show the integrated ion yield of an averaged $^{40}\mathrm{Ar}^{13+}$ bunch (16 shots) for a given retardation potential, measured by the retarding-field analyser. A Gaussian error function (red line) was fitted to the data and differentiated to obtain the Gaussian energy distribution (blue line) to show the mean kinetic energy and longitudinal energy spread.

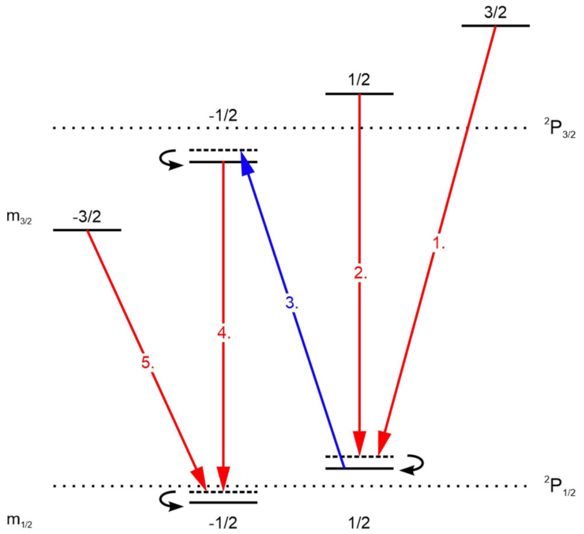

Extended Data Fig. 3 | Quantum logic-assisted internal state preparation of Ar^{13+}. The $m_{1/2} = -1/2$ state of the $^2P_{1/2}$ level is deterministically populated by a series of five clock laser sideband π-pulses (1–5), which excite the two-ion crystal from the motional ground state $|0\rangle_m$ (solid lines) into the excited state $|1\rangle_m$ (dashed lines). By means of Raman sideband cooling pulses acting on the $^9Be^+$ ion, the crystal is returned to the motional ground state after each transfer pulse. This ensures unidirectional optical pumping[9]. To increase the state-preparation efficiency, this sequence is repeated four times. The other Zeeman ground state ($^2P_{1/2}$, $m_{1/2} = +1/2$) is prepared in an analogous manner.

Bibliography

Ade, P. a. R., N. Aghanim, C. Armitage-Caplan, M. Arnaud, M. Ashdown, F. Atrio-Barandela, J. Aumont, C. Baccigalupi, A. J. Banday, R. B. Barreiro, J. G. Bartlett, E. Battaner, K. Benabed, A. Benoît, A. Benoit-Lévy, et al. (2014). "Planck 2013 results. XVI. Cosmological parameters." *Astronomy & Astrophysics* 571, A16. DOI: `10.1051/0004-6361/201321591` (cit. on p. 27).

Agababaev, V. A., D. A. Glazov, A. V. Volotka, D. V. Zinenko, V. M. Shabaev, and G. Plunien (2018). "Ground-state g factor of middle-Z boronlike ions." *Journal of Physics: Conference Series* 1138, 012003. DOI: `10.1088/1742-6596/1138/1/012003` (cit. on pp. 47, 148, 149).

Agababaev, V. A., D. A. Glazov, A. V. Volotka, D. V. Zinenko, V. M. Shabaev, and G. Plunien (2019). "g factor of the $[(1s)^2(2s)^2 2p]^2P_{3/2}$ state of middle-Z boronlike ions." *X-Ray Spectrometry* 49, 143–148. DOI: `10.1002/xrs.3074` (cit. on pp. 47, 147–149).

Agababaev, V. A., A. M. Volchkova, A. S. Varentsova, D. A. Glazov, A. V. Volotka, V. M. Shabaev, and G. Plunien (2017). "Quadratic Zeeman effect in boronlike argon." *Nuclear Instruments and Methods in Physics Research Section B: Beam Interactions with Materials and Atoms* 408, 70–73. DOI: `10.1016/j.nimb.2017.03.130` (cit. on pp. 47, 151).

Alighanbari, S., M. G. Hansen, V. I. Korobov, and S. Schiller (2018). "Rotational spectroscopy of cold and trapped molecular ions in the Lamb–Dicke regime." *Nature Physics* 14, 555–559. DOI: `10.1038/s41567-018-0074-3` (cit. on pp. 30, 35).

Allan, D. W. (1987). "Time and Frequency (Time-Domain) Characterization, Estimation, and Prediction of Precision Clocks and Oscillators." *IEEE Transactions on Ultrasonics, Ferroelectrics, and Frequency Control* 34, 647–654. DOI: `10.1109/T-UFFC.1987.26997` (cit. on p. 13).

ALPHA collaboration (2017). "Observation of the 1S–2S transition in trapped antihydrogen." *Nature* 541, 506–510. DOI: `10.1038/nature21040` (cit. on p. 30).

ALPHA collaboration (2018a). "Characterization of the 1S–2S transition in antihydrogen." *Nature* 557, 71–75. DOI: `10.1038/s41586-018-0017-2` (cit. on p. 30).

ALPHA collaboration (2018b). "Observation of the 1S–2P Lyman-α transition in antihydrogen." *Nature* 561, 211–215. DOI: `10.1038/s41586-018-0435-1` (cit. on p. 30).

Altmann, R. K., L. S. Dreissen, E. J. Salumbides, W. Ubachs, and K. S. E. Eikema (2018). "Deep-Ultraviolet Frequency Metrology of H_2 for Tests of Molecular Quantum Theory." *Physical Review Letters* 120, 043204. DOI: `10.1103/PhysRevLett.120.043204` (cit. on p. 30).

Andersen, T., K. A. Jessen, and G. Sørensen (1969). "Mean-Life Measurements of Excited Electronic States in Neutral and Ionic Species of Beryllium and Boron." *Physical Review* 188, 76–81. DOI: `10.1103/PhysRev.188.76` (cit. on p. 52).

Ann, B.-m., F. Schmid, J. Krause, T. W. Hänsch, T. Udem, and A. Ozawa (2019). "Motional resonances of three-dimensional dual-species Coulomb crystals." *Journal of Physics B: Atomic, Molecular and Optical Physics* 52, 035002. DOI: `10.1088/1361-6455/aaf5ea` (cit. on p. 117).

Antognini, A., F. Nez, K. Schuhmann, F. D. Amaro, F. Biraben, J. M. R. Cardoso, D. S. Covita, A. Dax, S. Dhawan, M. Diepold, L. M. P. Fernandes, A. Giesen, A. L. Gouvea, T. Graf, T. W. Hänsch, et al. (2013). "Proton Structure from the Measurement of 2S–2P Transition Frequencies of Muonic Hydrogen." *Science* 339, 417–420. DOI: `10.1126/science.1230016` (cit. on p. 30).

Aoyama, T., M. Hayakawa, T. Kinoshita, and M. Nio (2015). "Tenth-order electron anomalous magnetic moment: Contribution of diagrams without closed lepton loops." *Physical Review D* 91, 033006. DOI: `10.1103/PhysRevD.91.033006` (cit. on p. 34).

Arapoglou, I., A. Egl, M. Höcker, T. Sailer, B. Tu, A. Weigel, R. Wolf, H. Cakir, V. A. Yerokhin, N. S. Oreshkina, V. A. Agababaev, A. V. Volotka, D. V. Zinenko, D. A. Glazov, Z. Harman, C. H. Keitel, S. Sturm, and K. Blaum (2019). "g Factor of Boronlike Argon $^{40}\mathrm{Ar}^{13+}$." *Physical Review Letters* 122, 253001. DOI: `10.1103/PhysRevLett.122.253001` (cit. on pp. 32, 47, 146, 147, 149, 150).

Artemyev, A. N., V. M. Shabaev, I. I. Tupitsyn, G. Plunien, A. Surzhykov, and S. Fritzsche (2013). "*Ab initio* calculations of the $2p_{3/2}-2p_{1/2}$ fine-structure splitting in boronlike ions." *Physical Review A* 88, 032518. DOI: `10.1103/PhysRevA.88.032518` (cit. on pp. 7, 29, 47).

Artemyev, A. N., V. M. Shabaev, I. I. Tupitsyn, G. Plunien, and V. A. Yerokhin (2007). "QED Calculation of the $2p_{3/2}-2p_{1/2}$ Transition Energy in Boronlike Argon." *Physical Review Letters* 98, 173004. DOI: `10.1103/PhysRevLett.98.173004` (cit. on pp. 7, 29, 47).

Arvanitaki, A., J. Huang, and K. Van Tilburg (2015). "Searching for dilaton dark matter with atomic clocks." *Physical Review D* 91, 015015. DOI: `10.1103/PhysRevD.91.015015` (cit. on p. 39).

ATLAS collaboration (2012). "A Particle Consistent with the Higgs Boson Observed with the ATLAS Detector at the Large Hadron Collider." *Science* 338, 1576–1582. DOI: `10.1126/science.1232005` (cit. on p. 36).

Auzinsh, M., D. Budker, and S. M. Rochester (2010). *Optically Polarized Atoms: Understanding Light-Atom Interactions*. Oxford University Press. URL: `https://cds.cern.ch/record/1297276` (visited on 01/31/2020) (cit. on pp. 65–67, 71).

Bagdonaite, J., P. Jansen, C. Henkel, H. L. Bethlem, K. M. Menten, and W. Ubachs (2013). "A Stringent Limit on a Drifting Proton-to-Electron Mass Ratio from Alcohol in the Early Universe." *Science* 339, 46–48. DOI: `10.1126/science.1224898` (cit. on p. 36).

Barton, P. A., C. J. S. Donald, D. M. Lucas, D. A. Stevens, A. M. Steane, and D. N. Stacey (2000). "Measurement of the lifetime of the $3d^2D_{5/2}$ state in $^{40}\mathrm{Ca}^{+}$."

Physical Review A 62, 032503. DOI: `10.1103/PhysRevA.62.032503` (cit. on p. 158).

Bauch, A., S. Weyers, D. Piester, E. Staliuniene, and W. Yang (2012). "Generation of UTC(PTB) as a fountain-clock based time scale." *Metrologia* 49, 180–188. DOI: `10.1088/0026-1394/49/3/180` (cit. on p. 14).

Beiersdorfer, P., H. Chen, D. B. Thorn, and E. Träbert (2005). "Measurement of the Two-Loop Lamb Shift in Lithiumlike U^{89+}." *Physical Review Letters* 95, 233003. DOI: `10.1103/PhysRevLett.95.233003` (cit. on pp. 7, 31).

Beiersdorfer, P., A. L. Osterheld, J. H. Scofield, J. R. Crespo López-Urrutia, and K. Widmann (1998). "Measurement of QED and Hyperfine Splitting in the $2s_{1/2}$-$2p_{3/2}$ X-Ray Transition in Li-like $^{209}Bi^{80+}$." *Physical Review Letters* 80, 3022–3025. DOI: `10.1103/PhysRevLett.80.3022` (cit. on p. 31).

Beiersdorfer, P., L. Schweikhard, J. R. Crespo López-Urrutia, and K. Widmann (1996). "The magnetic trapping mode of an electron beam ion trap: New opportunities for highly charged ion research." *Review of Scientific Instruments* 67, 3818–3826. DOI: `10.1063/1.1147276` (cit. on pp. 8, 56).

Beiersdorfer, P., E. Träbert, G. V. Brown, J. Clementson, D. B. Thorn, M. H. Chen, K. T. Cheng, and J. Sapirstein (2014). "Hyperfine Splitting of the $2s_{1/2}$ and $2p_{1/2}$ Levels in Li- and Be-like Ions of $^{141}_{59}\mathrm{Pr}$." *Physical Review Letters* 112, 233003. DOI: `10.1103/PhysRevLett.112.233003` (cit. on p. 31).

Beiersdorfer, P., S. B. Utter, K. L. Wong, J. R. Crespo López-Urrutia, J. A. Britten, H. Chen, C. L. Harris, R. S. Thoe, D. B. Thorn, E. Träbert, M. G. H. Gustavsson, C. Forssén, and A.-M. Mårtensson-Pendrill (2001). "Hyperfine structure of hydrogenlike thallium isotopes." *Physical Review A* 64, 032506. DOI: `10.1103/PhysRevA.64.032506` (cit. on p. 32).

Beigang, R., D. Schmidt, and P. J. West (1983). "Laser Spectroscopy of High Rydberg States of Light Alkaline-Earth Elements: Be and Mg." *Le Journal de Physique Colloques* 44, 229–237. DOI: `10.1051/jphyscol:1983719` (cit. on p. 53).

Beilmann, C., P. H. Mokler, S. Bernitt, C. H. Keitel, J. Ullrich, J. R. Crespo López-Urrutia, and Z. Harman (2011). "Prominent Higher-Order Contributions to Electronic Recombination." *Physical Review Letters* 107, 143201. DOI: `10.1103/PhysRevLett.107.143201` (cit. on p. 7).

Bekenstein, J. D. (2004). "Relativistic gravitation theory for the modified Newtonian dynamics paradigm." *Physical Review D* 70, 083509. DOI: `10.1103/PhysRevD.70.083509` (cit. on p. 27).

Bekker, H., A. Borschevsky, Z. Harman, C. H. Keitel, T. Pfeifer, P. O. Schmidt, J. R. Crespo López-Urrutia, and J. C. Berengut (2019). "Detection of the $5p-4f$ orbital crossing and its optical clock transition in Pr^{9+}." *Nature Communications* 10, 1–7. DOI: `10.1038/s41467-019-13406-9` (cit. on pp. 6, 10, 15, 24, 38, 39, 176).

Bekker, H., C. Hensel, A. Daniel, A. Windberger, T. Pfeifer, and J. R. Crespo López-Urrutia (2018). "Laboratory precision measurements of optical emissions from coronal iron." *Physical Review A* 98, 062514. DOI: `10.1103/PhysRevA.98.062514` (cit. on p. 7).

Bekker, H., O. O. Versolato, A. Windberger, N. S. Oreshkina, R. Schupp, T. M. Baumann, Z. Harman, C. H. Keitel, P. O. Schmidt, J. Ullrich, and J. R. Crespo López-Urrutia (2015). "Identifications of $5s_{1/2}$–$5p_{3/2}$ and $5s^2$–5s5p EUV transitions of promethium-like Pt, Ir, Os and Re." *Journal of Physics B: Atomic, Molecular and Optical Physics* 48, 144018. DOI: `10.1088/0953-4075/48/14/144018` (cit. on p. 10).

Benkler, E., C. Lisdat, and U. Sterr (2015). "On the relation between uncertainties of weighted frequency averages and the various types of Allan deviations." *Metrologia* 52, 565–574. DOI: `10.1088/0026-1394/52/4/565` (cit. on p. 13).

Berengut, J. C., V. A. Dzuba, and V. V. Flambaum (2010). "Enhanced Laboratory Sensitivity to Variation of the Fine-Structure Constant using Highly Charged Ions." *Physical Review Letters* 105, 120801. DOI: `10.1103/PhysRevLett.105.120801` (cit. on pp. 6, 38).

Berengut, J. C., V. A. Dzuba, and V. V. Flambaum (2011). "Transitions in Zr, Hf, Ta, W, Re, Hg, Ac, and U ions with high sensitivity to variation of the fine-structure constant." *Physical Review A* 84, 054501. DOI: `10.1103/PhysRevA.84.054501` (cit. on p. 38).

Berengut, J. C., V. A. Dzuba, V. V. Flambaum, and A. Ong (2011). "Electron-Hole Transitions in Multiply Charged Ions for Precision Laser Spectroscopy and Searching for Variations in α." *Physical Review Letters* 106, 210802. DOI: `10.1103/PhysRevLett.106.210802` (cit. on pp. 10, 29, 38).

Berengut, J. C., V. A. Dzuba, V. V. Flambaum, and A. Ong (2012a). "Highly charged ions with $E1$, $M1$, and $E2$ transitions within laser range." *Physical Review A* 86, 022517. DOI: `10.1103/PhysRevA.86.022517` (cit. on pp. 5, 6, 23, 24, 38).

Berengut, J. C., V. A. Dzuba, V. V. Flambaum, and A. Ong (2012b). "Optical Transitions in Highly Charged Californium Ions with High Sensitivity to Variation of the Fine-Structure Constant." *Physical Review Letters* 109, 070802. DOI: `10.1103/PhysRevLett.109.070802` (cit. on p. 38).

Berengut, J. C., D. Budker, C. Delaunay, V. V. Flambaum, C. Frugiuele, E. Fuchs, C. Grojean, R. Harnik, R. Ozeri, G. Perez, and Y. Soreq (2018). "Probing New Long-Range Interactions by Isotope Shift Spectroscopy." *Physical Review Letters* 120, 091801. DOI: `10.1103/PhysRevLett.120.091801` (cit. on pp. 33, 169).

Bergquist, J. C., R. G. Hulet, W. M. Itano, and D. J. Wineland (1986). "Observation of Quantum Jumps in a Single Atom." *Physical Review Letters* 57, 1699–1702. DOI: `10.1103/PhysRevLett.57.1699` (cit. on p. 16).

Berkeland, D. J., J. D. Miller, J. C. Bergquist, W. M. Itano, and D. J. Wineland (1998a). "Laser-Cooled Mercury Ion Frequency Standard." *Physical Review Letters* 80, 2089–2092. DOI: `10.1103/PhysRevLett.80.2089` (cit. on p. 105).

Berkeland, D. J., J. D. Miller, J. C. Bergquist, W. M. Itano, and D. J. Wineland (1998b). "Minimization of ion micromotion in a Paul trap." *Journal of Applied Physics* 83, 5025–5033. DOI: `10.1063/1.367318` (cit. on pp. 22, 58, 59, 117).

Bernard, J. E., A. A. Madej, L. Marmet, B. G. Whitford, K. J. Siemsen, and S. Cundy (1999). "Cs-Based Frequency Measurement of a Single, Trapped Ion Transition in the Visible Region of the Spectrum." *Physical Review Letters* 82, 3228–3231. DOI: `10.1103/PhysRevLett.82.3228` (cit. on p. 167).

Bernard, J. E., L. Marmet, and A. A. Madej (1998). "A laser frequency lock referenced to a single trapped ion." *Optics Communications* 150, 170–174. DOI: `10.1016/S0030-4018(98)00121-7` (cit. on p. 167).

Bernitt, S., G. V. Brown, J. K. Rudolph, R. Steinbrügge, A. Graf, M. Leutenegger, S. W. Epp, S. Eberle, K. Kubiček, V. Mäckel, M. C. Simon, E. Träbert, E. W. Magee, C. Beilmann, N. Hell, et al. (2012). "An unexpectedly low oscillator strength as the origin of the Fe XVII emission problem." *Nature* 492, 225–228. DOI: `10.1038/nature11627` (cit. on p. 7).

Bertone, G. and D. Hooper (2018). "History of dark matter." *Reviews of Modern Physics* 90, 045002. DOI: `10.1103/RevModPhys.90.045002` (cit. on p. 27).

Beyer, A., L. Maisenbacher, A. Matveev, R. Pohl, K. Khabarova, A. Grinin, T. Lamour, D. C. Yost, T. W. Hänsch, N. Kolachevsky, and T. Udem (2017). "The Rydberg constant and proton size from atomic hydrogen." *Science* 358, 79–85. DOI: `10.1126/science.aah6677` (cit. on pp. 29, 30).

Beyer, H. F., V. P. Shevelko, and V. P. Shevelko (2016). *Introduction to the Physics of Highly Charged Ions*. CRC Press. DOI: `10.1201/9781420034097` (cit. on p. 5).

Bezginov, N., T. Valdez, M. Horbatsch, A. Marsman, A. C. Vutha, and E. A. Hessels (2019). "A measurement of the atomic hydrogen Lamb shift and the proton charge radius." *Science* 365, 1007–1012. DOI: `10.1126/science.aau7807` (cit. on pp. 29, 30).

Bieber, D. J., H. S. Margolis, P. K. Oxley, and J. D. Silver (1997). "Studies of magnetic dipole transitions in highly charged argon and barium using an electron beam ion trap." *Physica Scripta* T73, 64–66. DOI: `10.1088/0031-8949/1997/T73/015` (cit. on pp. 7, 47, 164).

Biesheuvel, J., J.-P. Karr, L. Hilico, K. S. E. Eikema, W. Ubachs, and J. C. J. Koelemeij (2016). "Probing QED and fundamental constants through laser spectroscopy of vibrational transitions in HD^+." *Nature Communications* 7, 1–7. DOI: `10.1038/ncomms10385` (cit. on pp. 29, 30, 35).

Bilal, M., A. V. Volotka, R. Beerwerth, and S. Fritzsche (2018). "Line strengths of QED-sensitive forbidden transitions in B-, Al-, F- and Cl-like ions." *Physical Review A* 97, 052506. DOI: `10.1103/PhysRevA.97.052506` (cit. on pp. 29, 47, 48, 70, 156, 159).

Blaum, K. (2006). "High-accuracy mass spectrometry with stored ions." *Physics Reports* 425, 1–78. DOI: `10.1016/j.physrep.2005.10.011` (cit. on pp. 7, 10).

Blaum, K. (2019). *Private communication* (cit. on p. 172).

Bloom, B. J., T. L. Nicholson, J. R. Williams, S. L. Campbell, M. Bishof, X. Zhang, W. Zhang, S. L. Bromley, and J. Ye (2014). "An optical lattice clock with accuracy and stability at the 10^-18 level." *Nature* 506, 71–75. DOI: `10.1038/nature12941` (cit. on p. 18).

Bohr, A. and V. F. Weisskopf (1950). "The Influence of Nuclear Structure on the Hyperfine Structure of Heavy Elements." *Physical Review* 77, 94–98. DOI: `10.1103/PhysRev.77.94` (cit. on p. 32).

Bohr, N. (1913a). "LXXIII. On the constitution of atoms and molecules." *The London, Edinburgh, and Dublin Philosophical Magazine and Journal of Science* 26, 857–875. DOI: `10.1080/14786441308635031` (cit. on p. 28).

Bohr, N. (1913b). "XXXVII. On the constitution of atoms and molecules." *The London, Edinburgh, and Dublin Philosophical Magazine and Journal of Science* 26, 476–502. DOI: `10.1080/14786441308634993` (cit. on p. 28).

Bollinger, J. J., J. S. Wells, D. J. Wineland, and W. M. Itano (1985). “Hyperfine structure of the $2p\,^2P_{1/2}$ state in $^9\mathrm{Be}^+$.” *Physical Review A* 31, 2711–2714. DOI: `10.1103/PhysRevA.31.2711` (cit. on p. 49).

Bothwell, T., D. Kedar, E. Oelker, J. M. Robinson, S. L. Bromley, W. L. Tew, J. Ye, and C. J. Kennedy (2019). “JILA SrI optical lattice clock with uncertainty of 2.0×10^{-18}.” *Metrologia* 56, 065004. DOI: `10.1088/1681-7575/ab4089` (cit. on pp. 17, 18, 105).

Bransden, B. H. and C. J. Joachain (2003). *Physics of atoms and molecules*. Prentice-Hall. URL: `https://cds.cern.ch/record/1095023` (visited on 01/31/2020) (cit. on pp. 65–67).

Breit, G. (1958). “Theory of Isotope Shift.” *Reviews of Modern Physics* 30, 507–516. DOI: `10.1103/RevModPhys.30.507` (cit. on p. 168).

Brenner, G., J. R. Crespo López-Urrutia, S. Bernitt, D. Fischer, R. Ginzel, K. Kubiček, V. Mäckel, P. H. Mokler, M. C. Simon, and J. Ullrich (2009). “On the Transition Rate of the Fe X Red Coronal Line.” *The Astrophysical Journal* 703, 68–73. DOI: `10.1088/0004-637X/703/1/68` (cit. on p. 7).

Brewer, S. M., J.-S. Chen, A. M. Hankin, E. R. Clements, C. W. Chou, D. J. Wineland, D. B. Hume, and D. R. Leibrandt (2019). “$^{27}\mathrm{Al}^+$ Quantum-Logic Clock with a Systematic Uncertainty below 10^{-18}.” *Physical Review Letters* 123, 033201. DOI: `10.1103/PhysRevLett.123.033201` (cit. on pp. 18, 22, 23, 107, 151, 168).

Brewer, S. M. (2012). “Highly-charged ions isolated in unitary Penning traps for precision measurements.” PhD thesis. College Park, Maryland: University of Maryland. URL: `https://hdl.handle.net/1903/13221` (visited on 01/31/2020) (cit. on p. 156).

Brodsky, S. J. and R. F. Lebed (2009). “Production of the Smallest QED Atom: True Muonium $(\mu^+\mu^-)$.” *Physical Review Letters* 102, 213401. DOI: `10.1103/PhysRevLett.102.213401` (cit. on p. 30).

Brossel, J. and F. Bitter (1952). “A New "Double Resonance" Method for Investigating Atomic Energy Levels. Application to Hg $^3P_1$.” *Physical Review* 86, 308–316. DOI: `10.1103/PhysRev.86.308` (cit. on p. 16).

Brownnutt, M., M. Kumph, P. Rabl, and R. Blatt (2015). “Ion-trap measurements of electric-field noise near surfaces.” *Reviews of Modern Physics* 87, 1419–1482. DOI: `10.1103/RevModPhys.87.1419` (cit. on p. 122).

Calmet, X. and M. Keller (2015). “Cosmological evolution of fundamental constants: From theory to experiment.” *Modern Physics Letters A* 30, 1540028. DOI: `10.1142/S0217732315400283` (cit. on p. 36).

Campbell, C. J., A. G. Radnaev, A. Kuzmich, V. A. Dzuba, V. V. Flambaum, and A. Derevianko (2012). “Single-Ion Nuclear Clock for Metrology at the 19th Decimal Place.” *Physical Review Letters* 108, 120802. DOI: `10.1103/PhysRevLett.108.120802` (cit. on p. 25).

Cassidy, D. B. and A. P. Mills (2007). “The production of molecular positronium.” *Nature* 449, 195–197. DOI: `10.1038/nature06094` (cit. on p. 30).

Cassidy, D. B. (2018). “Experimental progress in positronium laser physics.” *The European Physical Journal D* 72, 53. DOI: `10.1140/epjd/e2018-80721-y` (cit. on p. 30).

Chen, J.-S., S. M. Brewer, C. W. Chou, D. J. Wineland, D. R. Leibrandt, and D. B. Hume (2017). “Sympathetic Ground State Cooling and Time-Dilation Shifts in an $^{27}\mathrm{Al}^{+}$ Optical Clock.” *Physical Review Letters* 118, 053002. DOI: `10.1103/PhysRevLett.118.053002` (cit. on pp. 22, 122).

Chou, C. W., D. B. Hume, J. C. J. Koelemeij, D. J. Wineland, and T. Rosenband (2010). “Frequency Comparison of Two High-Accuracy Al^{+} Optical Clocks.” *Physical Review Letters* 104, 070802. DOI: `10.1103/PhysRevLett.104.070802` (cit. on p. 17).

Chou, C.-w., C. Kurz, D. B. Hume, P. N. Plessow, D. R. Leibrandt, and D. Leibfried (2017). “Preparation and coherent manipulation of pure quantum states of a single molecular ion.” *Nature* 545, 203–207. DOI: `10.1038/nature22338` (cit. on p. 17).

Colombe, Y., D. H. Slichter, A. C. Wilson, D. Leibfried, and D. J. Wineland (2014). “Single-mode optical fiber for high-power, low-loss UV transmission.” *Optics Express* 22, 19783–19793. DOI: `10.1364/OE.22.019783` (cit. on p. 114).

Cozijn, F. M. J., P. Dupré, E. J. Salumbides, K. S. E. Eikema, and W. Ubachs (2018). “Sub-Doppler Frequency Metrology in HD for Tests of Fundamental Physics.” *Physical Review Letters* 120, 153002. DOI: `10.1103/PhysRevLett.120.153002` (cit. on p. 30).

Crespo López-Urrutia, J. R. (2008). “The visible spectrum of highly charged ions: A window to fundamental physics.” *Canadian Journal of Physics* 86, 111–123. DOI: `10.1139/p07-115` (cit. on p. 6).

Crespo López-Urrutia, J. R., P. Beiersdorfer, K. Widmann, B. B. Birkett, A.-M. Mårtensson-Pendrill, and M. G. H. Gustavsson (1998). “Nuclear magnetization distribution radii determined by hyperfine transitions in the 1s level of H-like ions $^{185}\mathrm{Re}^{74+}$ and $^{187}\mathrm{Re}^{74+}$.” *Physical Review A* 57, 879–887. DOI: `10.1103/PhysRevA.57.879` (cit. on p. 32).

Crespo López-Urrutia, J. R., P. Beiersdorfer, D. W. Savin, and K. Widmann (1996). “Direct Observation of the Spontaneous Emission of the Hyperfine Transition $F = 4$ to $F = 3$ in Ground State Hydrogenlike $^{165}Ho^{66+}$ in an Electron Beam Ion Trap.” *Physical Review Letters* 77, 826–829. DOI: `10.1103/PhysRevLett.77.826` (cit. on p. 32).

Crespo López-Urrutia, J. R., Z. Harman, W. Quint, and M. Vogel (2014). “Emission and Laser Spectroscopy of Trapped Highly Charged Ions in Electron Beam Ion Traps.” *Fundamental Physics in Particle Traps*. Springer Berlin Heidelberg, pp. 315–373. DOI: `10.1007/978-3-642-45201-7_10` (cit. on p. 6).

Currell, F. J. (2003). *The Physics of Multiply and Highly Charged Ions*. Springer Netherlands. DOI: `10.1007/978-94-017-0542-4` (cit. on pp. 3, 4, 55, 56).

Davis, J., P. Dubé, and A. C. Vutha (2019). “Improved estimate of the collisional frequency shift in Al^{+} optical clocks.” *Physical Review Research* 1, 033137. DOI: `10.1103/PhysRevResearch.1.033137` (cit. on p. 23).

Dehmelt, H. G. (1982). “Monoion oscillator as potential ultimate laser frequency standard.” *IEEE Transactions on Instrumentation and Measurement* IM-31, 83–87. DOI: `10.1109/TIM.1982.6312526` (cit. on p. 17).

Dehmelt, H. G., D. R. Bates, and I. Estermann (1968). “Radiofrequency Spectroscopy of Stored Ions I: Storage.” *Advances in Atomic and Molecular Physics*. Vol. 3.

Academic Press, pp. 53–72. DOI: `10.1016/S0065-2199(08)60170-0` (cit. on p. 60).

Dehmelt, H. G., D. R. Bates, and I. Estermann (1969). “Radiofrequency Spectroscopy of Stored Ions II: Spectroscopy.” *Advances in Atomic and Molecular Physics*. Vol. 5. Academic Press, pp. 109–154. DOI: `10.1016/S0065-2199(08)60156-6` (cit. on p. 60).

Dehmelt, H. G. (1973). “Proposed $10^{14}\,\Delta\nu < \nu$ Laser Fluorescence Spectroscopy on Tl^{+} Mono-Ion Oscillator.” *Bull. Am. Phys. Soc.* 18, 1521 (cit. on p. 16).

Dent, T., S. Stern, and C. Wetterich (2008). “Unifying cosmological and recent time variations of fundamental couplings.” *Physical Review D* 78, 103518. DOI: `10.1103/PhysRevD.78.103518` (cit. on p. 36).

Derevianko, A. and M. Pospelov (2014). “Hunting for topological dark matter with atomic clocks.” *Nature Physics* 10, 933–936. DOI: `10.1038/nphys3137` (cit. on pp. 35, 39).

Derevianko, A. (2018). “Detecting dark-matter waves with a network of precision-measurement tools.” *Physical Review A* 97, 042506. DOI: `10.1103/PhysRevA.97.042506` (cit. on p. 39).

Derevianko, A., V. A. Dzuba, and V. V. Flambaum (2012). “Highly Charged Ions as a Basis of Optical Atomic Clockwork of Exceptional Accuracy.” *Physical Review Letters* 109, 180801. DOI: `10.1103/PhysRevLett.109.180801` (cit. on p. 23).

Deslauriers, L., S. Olmschenk, D. Stick, W. K. Hensinger, J. Sterk, and C. Monroe (2006). “Scaling and Suppression of Anomalous Heating in Ion Traps.” *Physical Review Letters* 97, 103007. DOI: `10.1103/PhysRevLett.97.103007` (cit. on p. 111).

Dickenson, G. D., M. L. Niu, E. J. Salumbides, J. Komasa, K. S. E. Eikema, K. Pachucki, and W. Ubachs (2013). “Fundamental Vibration of Molecular Hydrogen.” *Physical Review Letters* 110, 193601. DOI: `10.1103/PhysRevLett.110.193601` (cit. on p. 30).

Diddams, S. A., T. Udem, J. C. Bergquist, E. A. Curtis, R. E. Drullinger, L. Hollberg, W. M. Itano, W. D. Lee, C. W. Oates, K. R. Vogel, and D. J. Wineland (2001). “An Optical Clock Based on a Single Trapped $^{199}Hg^{+}$ Ion.” *Science* 293, 825–828. DOI: `10.1126/science.1061171` (cit. on p. 18).

Dirac, P. A. M. (1928). “The quantum theory of the electron.” *Proceedings of the Royal Society of London. Series A, Containing Papers of a Mathematical and Physical Character* 117, 610–624. DOI: `10.1098/rspa.1928.0023` (cit. on p. 28).

Dobrin, A. F. (2017). “Particle physics: No sign of asymmetry in the strong force.” *Nature* 546, 477–479. DOI: `10.1038/nature23086` (cit. on p. 34).

Draganić, I., J. R. Crespo López-Urrutia, R. DuBois, S. Fritzsche, V. M. Shabaev, R. S. Orts, I. I. Tupitsyn, Y. Zou, and J. Ullrich (2003). “High Precision Wavelength Measurements of QED-Sensitive Forbidden Transitions in Highly Charged Argon Ions.” *Physical Review Letters* 91, 183001. DOI: `10.1103/PhysRevLett.91.183001` (cit. on pp. 7, 29, 31, 41, 46–48, 138, 164).

Dreiling, J. M., A. S. Naing, J. N. Tan, J. M. Hanson, S. F. Hoogerheide, and S. M. Brewer (2019). “Capture of highly charged ions in a pseudo-hyperbolic Paul trap.”

Journal of Applied Physics 126, 024501. DOI: `10.1063/1.5090338` (cit. on p. 167).

Drewsen, M. (2015). "Ion Coulomb crystals." *Physica B: Condensed Matter* 460, 105–113. DOI: `10.1016/j.physb.2014.11.050` (cit. on p. 57).

Dubé, P., A. A. Madej, J. E. Bernard, L. Marmet, J.-S. Boulanger, and S. Cundy (2005). "Electric Quadrupole Shift Cancellation in Single-Ion Optical Frequency Standards." *Physical Review Letters* 95, 033001. DOI: `10.1103/PhysRevLett.95.033001` (cit. on p. 20).

Dubé, P., A. A. Madej, Z. Zhou, and J. E. Bernard (2013). "Evaluation of systematic shifts of the ^{88}Sr^{+} single-ion optical frequency standard at the 10^{-17} level." *Physical Review A* 87, 023806. DOI: `10.1103/PhysRevA.87.023806` (cit. on p. 18).

Dubin, D. H. E. (1990). "First-order anharmonic correction to the free energy of a Coulomb crystal in periodic boundary conditions." *Physical Review A* 42, 4972–4982. DOI: `10.1103/PhysRevA.42.4972` (cit. on p. 57).

Dumont, V. and J. K. Webb (2017). "Modelling long-range wavelength distortions in quasar absorption echelle spectra." *Monthly Notices of the Royal Astronomical Society* 468, 1568–1574. DOI: `10.1093/mnras/stx381` (cit. on p. 36).

Durante, M., P. Indelicato, B. Jonson, V. Koch, K. Langanke, U.-G. Meißner, E. Nappi, T. Nilsson, T. Stöhlker, E. Widmann, and M. Wiescher (2019). "All the fun of the FAIR: fundamental physics at the facility for antiproton and ion research." *Physica Scripta* 94, 033001. DOI: `10.1088/1402-4896/aaf93f` (cit. on p. 30).

Dzuba, V. A., A. Derevianko, and V. V. Flambaum (2012a). "High-precision atomic clocks with highly charged ions: Nuclear-spin-zero f^{12}-shell ions." *Physical Review A* 86, 054501. DOI: `10.1103/PhysRevA.86.054501` (cit. on pp. 24, 29).

Dzuba, V. A., A. Derevianko, and V. V. Flambaum (2012b). "Ion clock and search for the variation of the fine-structure constant using optical transitions in Nd^{13+} and Sm^{15+}." *Physical Review A* 86, 054502. DOI: `10.1103/PhysRevA.86.054502` (cit. on pp. 24, 38).

Dzuba, V. A., V. V. Flambaum, and H. Katori (2015). "Optical clock sensitive to variations of the fine-structure constant based on the Ho^{14+} ion." *Physical Review A* 91, 022119. DOI: `10.1103/PhysRevA.91.022119` (cit. on pp. 24, 38).

Dzuba, V. A., M. S. Safronova, U. I. Safronova, and V. V. Flambaum (2015). "Actinide ions for testing the spatial α-variation hypothesis." *Physical Review A* 92, 060502. DOI: `10.1103/PhysRevA.92.060502` (cit. on pp. 24, 38).

Edlén, B. (1977). "The ^{2}P interval of 2s^{2}2p^{5} and 2s^{2}2p." *Óptica Pura y Aplicada* 10, 123–129. URL: `http://adsabs.harvard.edu/abs/1977OPurA..10..123E` (visited on 01/31/2020) (cit. on p. 164).

Edlén, B. (1942). "Die Deutung der Emissionslinien im Spektrum der Sonnenkorona. Mit 6 Abbildungen." *Zeitschrift fur Astrophysik* 22, 30. URL: `http://adsabs.harvard.edu/abs/1943ZA.....22...30E` (visited on 01/31/2020) (cit. on p. 7).

Edlén, B. (1982). "Accurate Values of the Energy Intervals in the Configurations 1s^{2}2s^{2}2p^{k} (k = 1–5)." *Physica Scripta* 26, 71–83. DOI: `10.1088/0031-8949/26/2/003` (cit. on pp. 47, 164).

Egl, A., I. Arapoglou, M. Höcker, K. König, T. Ratajczyk, T. Sailer, B. Tu, A. Weigel, K. Blaum, W. Nörtershäuser, and S. Sturm (2019). “Application of the Continuous Stern-Gerlach Effect for Laser Spectroscopy of the $^{40}\mathrm{Ar}^{13+}$ Fine Structure in a Penning Trap.” *Physical Review Letters* 123, 123001. DOI: `10.1103/PhysRevLett.123.123001` (cit. on pp. 7, 9, 10, 29, 41, 47, 138, 147, 150, 164).

Elliott, S. R. and R. E. Marrs (1995). “A wire probe as an ion source for an electron beam ion trap.” *Nuclear Instruments and Methods in Physics Research Section B: Beam Interactions with Materials and Atoms* 100, 529–535. DOI: `10.1016/0168-583X(95)00327-4` (cit. on p. 89).

Epp, S. W., J. R. Crespo López-Urrutia, G. Brenner, V. Mäckel, P. H. Mokler, R. Treusch, M. Kuhlmann, M. V. Yurkov, J. Feldhaus, J. R. Schneider, M. Wellhöfer, M. Martins, W. Wurth, and J. Ullrich (2007). “Soft X-Ray Laser Spectroscopy on Trapped Highly Charged Ions at FLASH.” *Physical Review Letters* 98, 183001. DOI: `10.1103/PhysRevLett.98.183001` (cit. on p. 7).

Essen, L. and J. V. L. Parry (1955). “An Atomic Standard of Frequency and Time Interval: A Cæsium Resonator.” *Nature* 176, 280–282. DOI: `10.1038/176280a0` (cit. on p. 14).

Faber, S. M. and J. S. Gallagher (1979). “Masses and mass-to-light ratios of galaxies.” *Annual Review of Astronomy and Astrophysics* 17, 135. DOI: `10.1146/annurev.aa.17.090179.001031` (cit. on p. 27).

Falke, S., M. Misera, U. Sterr, and C. Lisdat (2012). “Delivering pulsed and phase stable light to atoms of an optical clock.” *Applied Physics B* 107, 301–311. DOI: `10.1007/s00340-012-4952-6` (cit. on p. 125).

Fischer, C. F. (1983). “Multiconfiguration Hartree–Fock Breit–Pauli results for $^2\mathrm{P}_{1/2}$–$^2\mathrm{P}_{3/2}$ transitions in the boron sequence.” *Journal of Physics B: Atomic and Molecular Physics* 16, 157–165. DOI: `10.1088/0022-3700/16/2/005` (cit. on pp. 47, 70).

Fischer, M., N. Kolachevsky, M. Zimmermann, R. Holzwarth, T. Udem, T. W. Hänsch, M. Abgrall, J. Grünert, I. Maksimovic, S. Bize, H. Marion, F. P. D. Santos, P. Lemonde, G. Santarelli, P. Laurent, A. Clairon, C. Salomon, M. Haas, U. D. Jentschura, and C. H. Keitel (2004). “New Limits on the Drift of Fundamental Constants from Laboratory Measurements.” *Physical Review Letters* 92, 230802. DOI: `10.1103/PhysRevLett.92.230802` (cit. on p. 29).

Flambaum, V. V. (2006). “Enhanced Effect of Temporal Variation of the Fine Structure Constant and the Strong Interaction in $^{229}\mathrm{Th}$.” *Physical Review Letters* 97, 092502. DOI: `10.1103/PhysRevLett.97.092502` (cit. on p. 25).

Flambaum, V. V., A. J. Geddes, and A. V. Viatkina (2018). “Isotope shift, nonlinearity of King plots, and the search for new particles.” *Physical Review A* 97, 032510. DOI: `10.1103/PhysRevA.97.032510` (cit. on pp. 33, 169, 171).

Fleurbaey, H., S. Galtier, S. Thomas, M. Bonnaud, L. Julien, F. Biraben, F. Nez, M. Abgrall, and J. Guéna (2018). “New Measurement of the $1S-3S$ Transition Frequency of Hydrogen: Contribution to the Proton Charge Radius Puzzle.” *Physical Review Letters* 120, 183001. DOI: `10.1103/PhysRevLett.120.183001` (cit. on p. 29).

Frugiuele, C., E. Fuchs, G. Perez, and M. Schlaffer (2017). "Constraining new physics models with isotope shift spectroscopy." *Physical Review D* 96, 015011. DOI: `10.1103/PhysRevD.96.015011` (cit. on pp. 33, 169).

Gebert, F. (2015). "Precision measurement of the isotopic shift in calcium ions using photon recoil spectroscopy." PhD thesis. Hannover: Gottfried Wilhelm Leibniz Universität Hannover. DOI: `10.15488/8456` (cit. on p. 170).

Gebert, F., Y. Wan, F. Wolf, C. N. Angstmann, J. C. Berengut, and P. O. Schmidt (2015). "Precision Isotope Shift Measurements in Calcium Ions Using Quantum Logic Detection Schemes." *Physical Review Letters* 115, 053003. DOI: `10.1103/PhysRevLett.115.053003` (cit. on pp. 32, 33, 170).

Ghosh, P. K. (1995). *Ion traps*. Clarendon Press. URL: `https://cds.cern.ch/record/291440` (visited on 01/31/2020) (cit. on pp. 55, 58).

Gillaspy, J. D. (2001). "Highly charged ions." *Journal of Physics B: Atomic, Molecular and Optical Physics* 34, R93–R130. DOI: `10.1088/0953-4075/34/19/201` (cit. on pp. 5, 23, 87).

Gillaspy, J. (1999). *Trapping Highly Charged Ions: Fundamentals and Applications*. Nova Science. URL: `https://cds.cern.ch/record/467865` (visited on 01/31/2020) (cit. on p. 56).

Glazov, D. A., A. V. Malyshev, V. M. Shabaev, and I. I. Tupitsyn (2018). "Nuclear Recoil Effect on the g Factor of Middle-Z Boronlike Ions." *Optics and Spectroscopy* 124, 457–461. DOI: `10.1134/S0030400X18040082` (cit. on p. 149).

Glazov, D. A., A. V. Volotka, A. A. Schepetnov, M. M. Sokolov, V. M. Shabaev, I. I. Tupitsyn, and G. Plunien (2013). "g factor of boron-like ions: ground and excited states." *Physica Scripta* T156, 014014. DOI: `10.1088/0031-8949/2013/T156/014014` (cit. on pp. 21, 47, 147, 151).

Godun, R. M., P. B. R. Nisbet-Jones, J. M. Jones, S. A. King, L. A. M. Johnson, H. S. Margolis, K. Szymaniec, S. N. Lea, K. Bongs, and P. Gill (2014). "Frequency Ratio of Two Optical Clock Transitions in $^{171}\text{Yb}^{+}$ and Constraints on the Time Variation of Fundamental Constants." *Physical Review Letters* 113, 210801. DOI: `10.1103/PhysRevLett.113.210801` (cit. on p. 37).

Gonzalez-Garcia, M. C. and M. Maltoni (2008). "Phenomenology with massive neutrinos." *Physics Reports* 460, 1–129. DOI: `10.1016/j.physrep.2007.12.004` (cit. on p. 34).

Grotti, J., S. Koller, S. Vogt, S. Häfner, U. Sterr, C. Lisdat, H. Denker, C. Voigt, L. Timmen, A. Rolland, F. N. Baynes, H. S. Margolis, M. Zampaolo, P. Thoumany, M. Pizzocaro, et al. (2018). "Geodesy and metrology with a transportable optical clock." *Nature Physics* 14, 437. DOI: `10.1038/s41567-017-0042-3` (cit. on pp. 11, 16).

Gruber, L., J. P. Holder, J. Steiger, B. R. Beck, H. E. DeWitt, J. Glassman, J. W. McDonald, D. A. Church, and D. Schneider (2001). "Evidence for Highly Charged Ion Coulomb Crystallization in Multicomponent Strongly Coupled Plasmas." *Physical Review Letters* 86, 636–639. DOI: `10.1103/PhysRevLett.86.636` (cit. on p. 9).

Guéna, J., M. Abgrall, A. Clairon, and S. Bize (2014). "Contributing to TAI with a secondary representation of the SI second." *Metrologia* 51, 108–120. DOI: `10.1088/0026-1394/51/1/108` (cit. on pp. 14, 37).

Guéna, J., S. Weyers, M. Abgrall, C. Grebing, V. Gerginov, P. Rosenbusch, S. Bize, B. Lipphardt, H. Denker, N. Quintin, S. M. F. Raupach, D. Nicolodi, F. Stefani, N. Chiodo, S. Koke, et al. (2017). “First international comparison of fountain primary frequency standards via a long distance optical fiber link.” *Metrologia* 54, 348–354. DOI: `10.1088/1681-7575/aa65fe` (cit. on p. 14).

Gumberidze, A., T. Stöhlker, D. Banaś, K. Beckert, P. Beller, H. F. Beyer, F. Bosch, S. Hagmann, C. Kozhuharov, D. Liesen, F. Nolden, X. Ma, P. H. Mokler, M. Steck, D. Sierpowski, and S. Tashenov (2005). “Quantum Electrodynamics in Strong Electric Fields: The Ground-State Lamb Shift in Hydrogenlike Uranium.” *Physical Review Letters* 94, 223001. DOI: `10.1103/PhysRevLett.94.223001` (cit. on pp. 7, 31).

Häffner, H., T. Beier, N. Hermanspahn, H.-J. Kluge, W. Quint, S. Stahl, J. Verdú, and G. Werth (2000). “High-Accuracy Measurement of the Magnetic Moment Anomaly of the Electron Bound in Hydrogenlike Carbon.” *Physical Review Letters* 85, 5308–5311. DOI: `10.1103/PhysRevLett.85.5308` (cit. on p. 32).

Hankin, A. M., E. R. Clements, Y. Huang, S. M. Brewer, J.-S. Chen, C. W. Chou, D. B. Hume, and D. R. Leibrandt (2019). “Systematic uncertainty due to background-gas collisions in trapped-ion optical clocks.” *Physical Review A* 100, 033419. DOI: `10.1103/PhysRevA.100.033419` (cit. on p. 23).

Hanneke, D., S. Fogwell, and G. Gabrielse (2008). “New Measurement of the Electron Magnetic Moment and the Fine Structure Constant.” *Physical Review Letters* 100, 120801. DOI: `10.1103/PhysRevLett.100.120801` (cit. on p. 34).

Heisenberg, W. (1925). “Über quantentheoretische Umdeutung kinematischer und mechanischer Beziehungen.” *Zeitschrift für Physik* 33, 879–893. DOI: `10.1007/BF01328377` (cit. on p. 28).

Heiße, F., F. Köhler-Langes, S. Rau, J. Hou, S. Junck, A. Kracke, A. Mooser, W. Quint, S. Ulmer, G. Werth, K. Blaum, and S. Sturm (2017). “High-Precision Measurement of the Proton’s Atomic Mass.” *Physical Review Letters* 119, 033001. DOI: `10.1103/PhysRevLett.119.033001` (cit. on p. 35).

Hempel, C., B. P. Lanyon, P. Jurcevic, R. Gerritsma, R. Blatt, and C. F. Roos (2013). “Entanglement-enhanced detection of single-photon scattering events.” *Nature Photonics* 7, 630–633. DOI: `10.1038/nphoton.2013.172` (cit. on p. 17).

Herrmann, G. (1958). “Optical Theory of Thermal Velocity Effects in Cylindrical Electron Beams.” *Journal of Applied Physics* 29, 127–136. DOI: `10.1063/1.1723053` (cit. on p. 55).

Herrmann, M., M. Haas, U. D. Jentschura, F. Kottmann, D. Leibfried, G. Saathoff, C. Gohle, A. Ozawa, V. Batteiger, S. Knünz, N. Kolachevsky, H. A. Schüssler, T. W. Hänsch, and T. Udem (2009). “Feasibility of coherent xuv spectroscopy on the $1S{-}2S$ transition in singly ionized helium.” *Physical Review A* 79, 052505. DOI: `10.1103/PhysRevA.79.052505` (cit. on p. 29).

Herschbach, N., K. Pyka, J. Keller, and T. E. Mehlstäubler (2012). “Linear Paul trap design for an optical clock with Coulomb crystals.” *Applied Physics B* 107, 891–906. DOI: `10.1007/s00340-011-4790-y` (cit. on p. 17).

Hinshaw, G., D. Larson, E. Komatsu, D. N. Spergel, C. L. Bennett, J. Dunkley, M. R. Nolta, M. Halpern, R. S. Hill, N. Odegard, L. Page, K. M. Smith, J. L. Weiland, B. Gold, N. Jarosik, et al. (2013). “Nine-year Wilkinson Microwave Anisotropy

Probe (WMAP) observations: cosmological parameter results." *The Astrophysical Journal Supplement Series* 208, 19. DOI: `10.1088/0067-0049/208/2/19` (cit. on p. 27).

Holliman, C. A., M. Fan, and A. M. Jayich (2019). "Measurements of electric quadrupole transition frequencies in Ra^+." *Physical Review A* 100, 062512. DOI: `10.1103/PhysRevA.100.062512` (cit. on pp. 33, 170).

Hori, M. and J. Walz (2013). "Physics at CERN's Antiproton Decelerator." *Progress in Particle and Nuclear Physics* 72, 206–253. DOI: `10.1016/j.ppnp.2013.02.004` (cit. on p. 30).

Hori, M. (2018). "Recent progress of laser spectroscopy experiments on antiprotonic helium." *Philosophical Transactions of the Royal Society A: Mathematical, Physical and Engineering Sciences* 376, 20170270. DOI: `10.1098/rsta.2017.0270` (cit. on p. 30).

Hosaka, K., D. N. Crosby, K. Gaarde-Widdowson, C. J. Smith, J. D. Silver, T. Kinugawa, S. Ohtani, and E. G. Myers (2004). "Laser spectroscopy of hydrogen-like nitrogen in an electron beam ion trap." *Physical Review A* 69, 011802. DOI: `10.1103/PhysRevA.69.011802` (cit. on p. 7).

Hume, D. B., C. W. Chou, D. R. Leibrandt, M. J. Thorpe, D. J. Wineland, and T. Rosenband (2011). "Trapped-Ion State Detection through Coherent Motion." *Physical Review Letters* 107, 243902. DOI: `10.1103/PhysRevLett.107.243902` (cit. on p. 10).

Huntemann, N., B. Lipphardt, C. Tamm, V. Gerginov, S. Weyers, and E. Peik (2014). "Improved Limit on a Temporal Variation of m_p/m_e from Comparisons of Yb^+ and Cs Atomic Clocks." *Physical Review Letters* 113, 210802. DOI: `10.1103/PhysRevLett.113.210802` (cit. on p. 37).

Huntemann, N., C. Sanner, B. Lipphardt, C. Tamm, and E. Peik (2016). "Single-Ion Atomic Clock with 3×10^{-18} Systematic Uncertainty." *Physical Review Letters* 116, 063001. DOI: `10.1103/PhysRevLett.116.063001` (cit. on pp. 17, 18, 105, 151).

Imgram, P., K. König, J. Krämer, T. Ratajczyk, R. A. Müller, A. Surzhykov, and W. Nörtershäuser (2019). "Collinear laser spectroscopy at ion-trap accuracy: Transition frequencies and isotope shifts in the $6s\,^2S_{1/2} \to 6p\,^2P_{1/2,3/2}$ transitions in Ba^+." *Physical Review A* 99, 012511. DOI: `10.1103/PhysRevA.99.012511` (cit. on p. 33).

Indelicato, P. (2019). "QED tests with highly charged ions." *Journal of Physics B: Atomic, Molecular and Optical Physics* 52, 232001. DOI: `10.1088/1361-6455/ab42c9` (cit. on p. 31).

International Union of Pure and Applied Chemistry (1997). *Compendium of Chemical Terminology*. Second edition. Blackwell Scientific Publications. DOI: `10.1351/goldbook` (cit. on p. 12).

Itano, W. M., J. C. Bergquist, J. J. Bollinger, J. M. Gilligan, D. J. Heinzen, F. L. Moore, M. G. Raizen, and D. J. Wineland (1993). "Quantum projection noise: Population fluctuations in two-level systems." *Physical Review A* 47, 3554–3570. DOI: `10.1103/PhysRevA.47.3554` (cit. on p. 13).

Itano, W. M. (2000). "External-Field Shifts of the ^{199}Hg^{+} Optical Frequency Standard." *Journal of Research of the National Institute of Standards and Technology* 105, 829–837. DOI: `10.6028/jres.105.065` (cit. on pp. 19, 20, 152).

Itano, W. M., J. C. Bergquist, R. G. Hulet, and D. J. Wineland (1988). "Precise Optical Spectroscopy with Ion Traps." *Physica Scripta* T22, 79. DOI: `10.1088/0031-8949/1988/T22/011` (cit. on p. 16).

Itano, W. M., J. C. Bergquist, and D. J. Wineland (1987). "Laser Spectroscopy of Trapped Atomic Ions." *Science* 237, 612–617. DOI: `10.1126/science.237.4815.612` (cit. on p. 16).

Iwamae, A., M. Atake, A. Sakaue, R. Katai, M. Goto, and S. Morita (2007). "Polarization separated Zeeman spectra from magnetic dipole transitions in highly charged argon in the large helical device." *Physics of Plasmas* 14, 042504. DOI: `10.1063/1.2714506` (cit. on p. 7).

Joint Committee for Guides in Metrology (2008). *Evaluation of measurement data – Guide to the expression of uncertainty in measurement (GUM).* URL: `https://www.bipm.org/en/publications/guides/gum` (visited on 01/31/2020) (cit. on p. 12).

Joint Committee for Guides in Metrology (2012). *International vocabulary of metrology – Basic and general concepts and associated terms (VIM).* URL: `https://www.bipm.org/en/publications/guides/vim` (visited on 01/31/2020) (cit. on p. 12).

Joshi, M. K., P. Hrmo, V. Jarlaud, F. Oehl, and R. C. Thompson (2019). "Population dynamics in sideband cooling of trapped ions outside the Lamb–Dicke regime." *Physical Review A* 99, 013423. DOI: `10.1103/PhysRevA.99.013423` (cit. on pp. 82, 120).

Karshenboim, S. G., A. Ozawa, V. A. Shelyuto, R. Szafron, and V. G. Ivanov (2019). "The Lamb shift of the 1s state in hydrogen: Two-loop and three-loop contributions." *Physics Letters B* 795, 432–437. DOI: `10.1016/j.physletb.2019.06.023` (cit. on p. 29).

Katori, H. (2002). "Spectroscopy of strontium atoms in the Lamb–Dicke confinement." *Proceedings of the 6th Symposium on Frequency Standards and Metrology: University of St. Andrews, Fife, Scotland, 9–14 September 2001.* World Scientific, pp. 323–330. DOI: `10.1142/9789812777713_0036` (cit. on p. 17).

Katori, H., V. D. Ovsiannikov, S. I. Marmo, and V. G. Palchikov (2015). "Strategies for reducing the light shift in atomic clocks." *Physical Review A* 91, 052503. DOI: `10.1103/PhysRevA.91.052503` (cit. on p. 17).

Keller, J., T. Burgermeister, D. Kalincev, A. Didier, A. P. Kulosa, T. Nordmann, J. Kiethe, and T. E. Mehlstäubler (2019). "Controlling systematic frequency uncertainties at the 10^{-19} level in linear Coulomb crystals." *Physical Review A* 99, 013405. DOI: `10.1103/PhysRevA.99.013405` (cit. on p. 17).

Keller, J., T. Burgermeister, D. Kalincev, J. Kiethe, and T. E. Mehlstäubler (2016). "Evaluation of trap-induced systematic frequency shifts for a multi-ion optical clock at the 10^{-19} level." *Journal of Physics: Conference Series* 723, 012027. DOI: `10.1088/1742-6596/723/1/012027` (cit. on pp. 22, 137).

Keller, J., D. Kalincev, T. Burgermeister, A. P. Kulosa, A. Didier, T. Nordmann, J. Kiethe, and T. E. Mehlstäubler (2019). "Probing Time Dilation in Coulomb

Crystals in a High-Precision Ion Trap." *Physical Review Applied* 11, 011002. DOI: `10.1103/PhysRevApplied.11.011002` (cit. on p. 17).

Keller, J., H. L. Partner, T. Burgermeister, and T. E. Mehlstäubler (2015). "Precise determination of micromotion for trapped-ion optical clocks." *Journal of Applied Physics* 118, 104501. DOI: `10.1063/1.4930037` (cit. on pp. 22, 117, 137).

Kessler, T., C. Hagemann, C. Grebing, T. Legero, U. Sterr, F. Riehle, M. J. Martin, L. Chen, and J. Ye (2012). "A sub-40-mHz-linewidth laser based on a silicon single-crystal optical cavity." *Nature Photonics* 6, 687–692. DOI: `10.1038/nphoton.2012.217` (cit. on p. 126).

Kielpinski, D., B. E. King, C. J. Myatt, C. A. Sackett, Q. A. Turchette, W. M. Itano, C. Monroe, D. J. Wineland, and W. H. Zurek (2000). "Sympathetic cooling of trapped ions for quantum logic." *Physical Review A* 61, 032310. DOI: `10.1103/PhysRevA.61.032310` (cit. on p. 122).

Kienzler, D., Y. Wan, S. D. Erickson, J. J. Wu, A. C. Wilson, D. J. Wineland, and D. Leibfried (2020). "Quantum Logic Spectroscopy with Ions in Thermal Motion." *Physical Review X* 10, 021012. DOI: `10.1103/PhysRevX.10.021012` (cit. on p. 17).

Kimura, N., R. Kodama, K. Suzuki, S. Oishi, M. Wada, K. Okada, N. Ohmae, H. Katori, and N. Nakamura (2019a). "Direct determination of the energy of the first excited fine-structure level in Ba^{6+}." *Physical Review A* 100, 052508. DOI: `10.1103/PhysRevA.100.052508` (cit. on p. 167).

Kimura, N., R. Kodama, K. Suzuki, S. Oishi, M. Wada, K. Okada, N. Ohmae, H. Katori, and N. Nakamura (2019b). "Direct Wavelength Measurement of the Visible M1 Transition in Ba^{7+} with a Novel Calibration Method." *Plasma and Fusion Research* 14, 1201021. DOI: `10.1585/pfr.14.1201021` (cit. on p. 167).

King, B. E. (1999). "Quantum State Engineering and Information Processing with Trapped Ions." PhD thesis. Boulder, Colorado: University of Colorado. URL: `https://www.nist.gov/system/files/documents/2017/05/09/bkthesis.pdf` (visited on 01/31/2020) (cit. on p. 52).

King, S. A., T. Leopold, P. Thekkeppatt, and P. O. Schmidt (2018). "A self-injection locked DBR laser for laser cooling of beryllium ions." *Applied Physics B* 124, 214. DOI: `10.1007/s00340-018-7080-0` (cit. on p. 114).

King, W. H. (1963). "Comments on the Article "Peculiarities of the Isotope Shift in the Samarium Spectrum"." *Journal of the Optical Society of America* 53, 638–639. DOI: `10.1364/JOSA.53.000638` (cit. on pp. 33, 169).

King, W. H. (1984). *Isotope Shifts in Atomic Spectra*. Springer. DOI: `10.1007/978-1-4899-1786-7` (cit. on pp. 33, 169).

Klaft, I., S. Borneis, T. Engel, B. Fricke, R. Grieser, G. Huber, T. Kühl, D. Marx, R. Neumann, S. Schröder, P. Seelig, and L. Völker (1994). "Precision Laser Spectroscopy of the Ground State Hyperfine Splitting of Hydrogenlike $^{209}\mathrm{Bi}^{82+}$." *Physical Review Letters* 73, 2425–2427. DOI: `10.1103/PhysRevLett.73.2425` (cit. on pp. 7, 32).

Kluge, H. J., T. Beier, K. Blaum, L. Dahl, S. Eliseev, F. Herfurth, B. Hofmann, O. Kester, S. Koszudowski, C. Kozhuharov, G. Maero, W. Nörtershäuser, J. Pfister, W. Quint, U. Ratzinger, et al. (2008). "Chapter 7 HITRAP: A Facility at GSI for

Highly Charged Ions." *Advances in Quantum Chemistry*. Vol. 53. Academic Press, pp. 83–98. DOI: `10.1016/S0065-3276(07)53007-8` (cit. on p. 9).

Knollmann, F. W., A. N. Patel, and S. C. Doret (2019). "Part-per-billion measurement of the $4\,^2S_{1/2} \rightarrow 3\,^2D_{5/2}$ electric-quadrupole-transition isotope shifts between $^{42,44,48}\mathrm{Ca}^+$ and $^{40}\mathrm{Ca}^+$." *Physical Review A* 100, 022514. DOI: `10.1103/PhysRevA.100.022514` (cit. on pp. 32, 33, 170, 172).

Kobayashi, J., A. Ogino, and S. Inouye (2019). "Measurement of the variation of electron-to-proton mass ratio using ultracold molecules produced from laser-cooled atoms." *Nature Communications* 10, 3771. DOI: `10.1038/s41467-019-11761-1` (cit. on p. 37).

Köhler, F., K. Blaum, M. Block, S. Chenmarev, S. Eliseev, D. A. Glazov, M. Goncharov, J. Hou, A. Kracke, D. A. Nesterenko, Y. N. Novikov, W. Quint, E. M. Ramirez, V. M. Shabaev, S. Sturm, A. V. Volotka, and G. Werth (2016). "Isotope dependence of the Zeeman effect in lithium-like calcium." *Nature Communications* 7, 10246. DOI: `10.1038/ncomms10246` (cit. on p. 32).

Komasa, J., M. Puchalski, P. Czachorowski, G. Łach, and K. Pachucki (2019). "Rovibrational energy levels of the hydrogen molecule through nonadiabatic perturbation theory." *Physical Review A* 100, 032519. DOI: `10.1103/PhysRevA.100.032519` (cit. on p. 29).

Kouvaris, C., E. Papantonopoulos, L. Street, and L. C. R. Wijewardhana (2019). "Probing Bosonic Stars with Atomic Clocks." *arXiv:1910.00567 [hep-ph]*. URL: `https://arxiv.org/abs/1910.00567` (visited on 01/31/2020) (cit. on p. 39).

Kozlov, A., V. A. Dzuba, and V. V. Flambaum (2013). "Transition amplitudes, polarizabilities, and energy levels within optical wavelength of highly charged ions Sm^{14+} and Sm^{13+}." *Physical Review A* 88, 062509. DOI: `10.1103/PhysRevA.88.062509` (cit. on p. 24).

Kozlov, M. G., M. S. Safronova, J. R. Crespo López-Urrutia, and P. O. Schmidt (2018). "Highly charged ions: Optical clocks and applications in fundamental physics." *Reviews of Modern Physics* 90, 045005. DOI: `10.1103/RevModPhys.90.045005` (cit. on pp. 6, 15, 23, 24, 28, 31, 37–39, 62, 63, 169, 173, 176).

Kramida, A. and W. C. Martin (1997). "A Compilation of Energy Levels and Wavelengths for the Spectrum of Neutral Beryllium (Be I)." *Journal of Physical and Chemical Reference Data* 26, 1185–1194. DOI: `10.1063/1.555999` (cit. on p. 53).

Kramida, A., Y. Ralchenko, J. Reader, and NIST ASD Team (2019). *NIST Atomic Spectra Database (version 5.7.1), [Online]*. URL: `https://physics.nist.gov/asd` (visited on 01/31/2020) (cit. on pp. 3, 4, 46, 171, 172, 175).

Krauth, J. J., L. S. Dreissen, C. Roth, E. L. Gründeman, M. Collombon, M. Favier, and K. S. E. Eikema (2019). "Paving the way for fundamental physics tests with singly-ionized helium." *arXiv:1910.13192 [physics.atom-ph]*. URL: `https://arxiv.org/abs/1910.13192` (visited on 01/31/2020) (cit. on p. 29).

Kreckel, H., H. Bruhns, K. A. Miller, E. Wåhlin, A. Davis, S. Höckh, and D. W. Savin (2010). "A simple double-focusing electrostatic ion beam deflector." *Review of Scientific Instruments* 81, 063304. DOI: `10.1063/1.3433485` (cit. on p. 93).

Kühn, S., C. Shah, J. R. Crespo López-Urrutia, K. Fujii, R. Steinbrügge, J. Stierhof, M. Togawa, Z. Harman, N. S. Oreshkina, C. Cheung, M. G. Kozlov, S. G. Porsev, M. S. Safronova, J. C. Berengut, M. Rosner, et al. (2020). "High Resolution Photoexcitation Measurements Exacerbate the Long-Standing Fe XVIII Oscillator Strength Problem." *Physical Review Letters* 124, 225001. DOI: `10.1103/PhysRevLett.124.225001` (cit. on p. 87).

Labaziewicz, J., Y. Ge, P. Antohi, D. Leibrandt, K. R. Brown, and I. L. Chuang (2008). "Suppression of Heating Rates in Cryogenic Surface-Electrode Ion Traps." *Physical Review Letters* 100, 013001. DOI: `10.1103/PhysRevLett.100.013001` (cit. on p. 111).

Lamb, W. E. and R. C. Retherford (1947). "Fine Structure of the Hydrogen Atom by a Microwave Method." *Physical Review* 72, 241–243. DOI: `10.1103/PhysRev.72.241` (cit. on p. 28).

Lapierre, A., J. R. Crespo López-Urrutia, J. Braun, G. Brenner, H. Bruhns, D. Fischer, A. J. González Martínez, V. Mironov, C. Osborne, G. Sikler, R. Soria Orts, H. Tawara, J. Ullrich, V. M. Shabaev, I. I. Tupitsyn, and A. Volotka (2006). "Lifetime measurement of the Ar XIV $1s^2 2s^2 2p\,^2P^o_{3/2}$ metastable level at the Heidelberg electron-beam ion trap." *Physical Review A* 73, 052507. DOI: `10.1103/PhysRevA.73.052507` (cit. on pp. 31, 47, 48, 141, 156, 158, 159).

Lapierre, A., U. D. Jentschura, J. R. Crespo López-Urrutia, J. Braun, G. Brenner, H. Bruhns, D. Fischer, A. J. González Martínez, Z. Harman, W. R. Johnson, C. H. Keitel, V. Mironov, C. J. Osborne, G. Sikler, R. Soria Orts, V. Shabaev, H. Tawara, I. I. Tupitsyn, J. Ullrich, and A. Volotka (2005). "Relativistic Electron Correlation, Quantum Electrodynamics, and the Lifetime of the $1s^2 2s^2 2p\ ^2P^o_{3/2}$ Level in Boronlike Argon." *Physical Review Letters* 95, 183001. DOI: `10.1103/PhysRevLett.95.183001` (cit. on pp. 31, 47).

Leibfried, D., R. Blatt, C. Monroe, and D. Wineland (2003). "Quantum dynamics of single trapped ions." *Reviews of Modern Physics* 75, 281–324. DOI: `10.1103/RevModPhys.75.281` (cit. on pp. 58, 72, 77, 79, 81).

Leopold, T., S. A. King, P. Micke, A. Bautista-Salvador, J. C. Heip, C. Ospelkaus, J. R. Crespo López-Urrutia, and P. O. Schmidt (2019). "A cryogenic radio-frequency ion trap for quantum logic spectroscopy of highly charged ions." *Review of Scientific Instruments* 90, 073201. DOI: `10.1063/1.5100594` (cit. on pp. 57, 82, 83, 105, 106, 110, 111, 120, 123, 137, 163).

Leopold, T. (2018). "A cryogenic ion trap system for quantum logic spectroscopy of highly charged ions." PhD thesis published as PTB-Report Opt-81. Hannover: Gottfried Wilhelm Leibniz Universität Hannover & Physikalisch-Technische Bundesanstalt, Germany. URL: `https://www.schuenemann-verlag.de/fachverlag-nw/ptb/optik/a-cryogenic-ion-trap-system-for-quantum-logic-spectroscopy-of-highly-charged-ions.html` (visited on 01/31/2020) (cit. on pp. 41, 52, 57, 58, 61, 63, 78, 82, 105, 110, 113, 114, 120, 121, 163).

Leroux, I. D., M. H. Schleier-Smith, and V. Vuletić (2010). "Orientation-Dependent Entanglement Lifetime in a Squeezed Atomic Clock." *Physical Review Letters* 104, 250801. DOI: `10.1103/PhysRevLett.104.250801` (cit. on p. 17).

Letchumanan, V., M. A. Wilson, P. Gill, and A. G. Sinclair (2005). "Lifetime measurement of the metastable $4d\,^2D_{5/2}$ state in $^{88}\mathrm{Sr}^+$ using a single trapped ion." *Physical Review A* 72, 012509. DOI: `10.1103/PhysRevA.72.012509` (cit. on p. 158).

Lindenfels, D. von, M. Wiesel, D. A. Glazov, A. V. Volotka, M. M. Sokolov, V. M. Shabaev, G. Plunien, W. Quint, G. Birkl, A. Martin, and M. Vogel (2013). "Experimental access to higher-order Zeeman effects by precision spectroscopy of highly charged ions in a Penning trap." *Physical Review A* 87, 023412. DOI: `10.1103/PhysRevA.87.023412` (cit. on pp. 9, 21, 47, 151).

Lindenfels, D.-F. F. v. (2015). "Experimental Studies of Highly Charged Ions in a Penning Trap for the Measurement of Electron Magnetic Moments by Double-Resonance Spectroscopy." PhD thesis. Heidelberg: Ruprecht-Karls-Universität Heidelberg. DOI: `10.11588/heidok.00019835` (cit. on pp. 71, 151, 152).

Lisdat, C., G. Grosche, N. Quintin, C. Shi, S. M. F. Raupach, C. Grebing, D. Nicolodi, F. Stefani, A. Al-Masoudi, S. Dörscher, S. Häfner, J.-L. Robyr, N. Chiodo, S. Bilicki, E. Bookjans, et al. (2016). "A clock network for geodesy and fundamental science." *Nature Communications* 7, 12443. DOI: `10.1038/ncomms12443` (cit. on p. 16).

Lo, H.-Y., J. Alonso, D. Kienzler, B. C. Keitch, L. E. d. Clercq, V. Negnevitsky, and J. P. Home (2014). "All-solid-state continuous-wave laser systems for ionization, cooling and quantum state manipulation of beryllium ions." *Applied Physics B* 114, 17–25. DOI: `10.1007/s00340-013-5605-0` (cit. on p. 115).

Ludlow, A. D., M. M. Boyd, J. Ye, E. Peik, and P. O. Schmidt (2015). "Optical atomic clocks." *Reviews of Modern Physics* 87, 637–701. DOI: `10.1103/RevModPhys.87.637` (cit. on pp. 12, 13, 15, 17, 18, 39, 117).

Lyons, H. (1949a). "The atomic clock." *Instruments* 22, 133–135 (cit. on p. 13).

Lyons, H. (1949b). "The Atomic Clock: An Atomic Standard of Frequency and Time, Part 1." *Journal of the Horological Institute of America*, 11–20 (cit. on p. 13).

Lyons, H. (1949c). "The Atomic Clock: An Atomic Standard of Frequency and Time, Part 2." *Journal of the Horological Institute of America*, 7–14 (cit. on p. 13).

Lyot, B. and A. Dollfus (1953). "Étude des spectres de la couronne solaire obtenus à Khartoum pendant l'éclipse totale de Soleil du 25 février 1952." *Comptes rendus hebdomadaires des séances de l'Académie des Sciences* 237, 855–859 (cit. on pp. 47, 164).

Ma, L.-S., P. Jungner, J. Ye, and J. L. Hall (1994). "Delivering the same optical frequency at two places: accurate cancellation of phase noise introduced by an optical fiber or other time-varying path." *Optics Letters* 19, 1777–1779. DOI: `10.1364/OL.19.001777` (cit. on p. 125).

Machado, J., C. I. Szabo, J. P. Santos, P. Amaro, M. Guerra, A. Gumberidze, G. Bian, J. M. Isac, and P. Indelicato (2018). "High-precision measurements of $n = 2 \to n = 1$ transition energies and level widths in He- and Be-like argon ions." *Physical Review A* 97, 032517. DOI: `10.1103/PhysRevA.97.032517` (cit. on p. 7).

Mäckel, V., R. Klawitter, G. Brenner, J. R. Crespo López-Urrutia, and J. Ullrich (2011). "Laser Spectroscopy on Forbidden Transitions in Trapped Highly Charged Ar^{13+} Ions." *Physical Review Letters* 107, 143002. DOI: `10.1103/PhysRevLett.107.143002` (cit. on pp. 7, 10, 47, 138, 164).

Mäckel, V., R. Klawitter, G. Brenner, J. R. Crespo López-Urrutia, and J. Ullrich (2013). "Laser spectroscopy of highly charged argon at the Heidelberg electron beam ion trap." *Physica Scripta* T156, 014004. DOI: `10.1088/0031-8949/2013/T156/014004` (cit. on pp. 7, 47, 164).

Madej, A. A., P. Dubé, Z. Zhou, J. E. Bernard, and M. Gertsvolf (2012). "^{88}Sr^{+} 445-THz Single-Ion Reference at the 10^{-17} Level via Control and Cancellation of Systematic Uncertainties and Its Measurement against the SI Second." *Physical Review Letters* 109, 203002. DOI: `10.1103/PhysRevLett.109.203002` (cit. on p. 18).

Maiman, T. H. (1960). "Stimulated Optical Radiation in Ruby." *Nature* 187, 493–494. DOI: `10.1038/187493a0` (cit. on p. 15).

Maison, D. E., L. V. Skripnikov, and D. A. Glazov (2019). "Many-body study of the g factor in boronlike argon." *Physical Review A* 99, 042506. DOI: `10.1103/PhysRevA.99.042506` (cit. on pp. 47, 147, 149).

Malyshev, A. V., D. A. Glazov, I. A. Aleksandrov, I. I. Tupitsyn, and V. M. Shabaev (2020). "Relativistic Calculation of the Nuclear Recoil Effect on the g Factor of the $^2P_{3/2}$ State in Highly Charged B-like Ions." *Optics and Spectroscopy* 128, 297–306. DOI: `10.1134/S0030400X20030145` (cit. on p. 149).

Mandal, P., G. Sikler, and M. Mukherjee (2011). "Simulation study and analysis of a compact einzel lens-deflector for low energy ion beam." *Journal of Instrumentation* 6, P02004. DOI: `10.1088/1748-0221/6/02/P02004` (cit. on p. 91).

Manovitz, T., R. Shaniv, Y. Shapira, R. Ozeri, and N. Akerman (2019). "Precision Measurement of Atomic Isotope Shifts Using a Two-Isotope Entangled State." *Physical Review Letters* 123, 203001. DOI: `10.1103/PhysRevLett.123.203001` (cit. on p. 170).

Marques, J. P., P. Indelicato, F. Parente, J. M. Sampaio, and J. P. Santos (2016). "Ground-state Landé g factors for selected ions along the boron isoelectronic sequence." *Physical Review A* 94, 042504. DOI: `10.1103/PhysRevA.94.042504` (cit. on pp. 47, 147, 148).

Matei, D. G., T. Legero, S. Häfner, C. Grebing, R. Weyrich, W. Zhang, L. Sonderhouse, J. M. Robinson, J. Ye, F. Riehle, and U. Sterr (2017). "1.5 µm Lasers with Sub-10 mHz Linewidth." *Physical Review Letters* 118, 263202. DOI: `10.1103/PhysRevLett.118.263202` (cit. on p. 126).

Matveev, A., C. G. Parthey, K. Predehl, J. Alnis, A. Beyer, R. Holzwarth, T. Udem, T. Wilken, N. Kolachevsky, M. Abgrall, D. Rovera, C. Salomon, P. Laurent, G. Grosche, O. Terra, T. Legero, H. Schnatz, S. Weyers, B. Altschul, and T. W. Hänsch (2013). "Precision Measurement of the Hydrogen $1S{-}2S$ Frequency via a 920-km Fiber Link." *Physical Review Letters* 110, 230801. DOI: `10.1103/PhysRevLett.110.230801` (cit. on p. 29).

McGrew, W. F., X. Zhang, R. J. Fasano, S. A. Schäffer, K. Beloy, D. Nicolodi, R. C. Brown, N. Hinkley, G. Milani, M. Schioppo, T. H. Yoon, and A. D. Ludlow (2018). "Atomic clock performance enabling geodesy below the centimetre level." *Nature* 564, 87–90. DOI: `10.1038/s41586-018-0738-2` (cit. on pp. 11, 18, 105).

Megidish, E., J. Broz, N. Greene, and H. Häffner (2019). "Improved Test of Local Lorentz Invariance from a Deterministic Preparation of Entangled States." *Physical Review Letters* 122, 123605. DOI: `10.1103/PhysRevLett.122.123605` (cit. on p. 39).

Mehlstäubler, T. E., G. Grosche, C. Lisdat, P. O. Schmidt, and H. Denker (2018). "Atomic clocks for geodesy." *Reports on Progress in Physics* 81, 064401. DOI: `10.1088/1361-6633/aab409` (cit. on p. 11).

Micke, P., S. Kühn, L. Buchauer, J. R. Harries, T. M. Bücking, K. Blaum, A. Cieluch, A. Egl, D. Hollain, S. Kraemer, T. Pfeifer, P. O. Schmidt, R. X. Schüssler, C. Schweiger, T. Stöhlker, S. Sturm, R. N. Wolf, S. Bernitt, and J. R. Crespo López-Urrutia (2018). "The Heidelberg compact electron beam ion traps." *Review of Scientific Instruments* 89, 063109. DOI: `10.1063/1.5026961` (cit. on pp. 46, 83, 87, 88, 90, 163).

Micke, P., J. Stark, S. A. King, T. Leopold, T. Pfeifer, L. Schmöger, M. Schwarz, L. J. Spieß, P. O. Schmidt, and J. R. Crespo López-Urrutia (2019). "Closed-cycle, low-vibration 4 K cryostat for ion traps and other applications." *Review of Scientific Instruments* 90, 065104. DOI: `10.1063/1.5088593` (cit. on pp. 25, 83, 105, 106, 108, 109, 163).

Micke, P., T. Leopold, S. A. King, E. Benkler, L. J. Spieß, L. Schmöger, M. Schwarz, J. R. Crespo López-Urrutia, and P. O. Schmidt (2020). "Coherent laser spectroscopy of highly charged ions using quantum logic." *Nature* 578, 60–65. DOI: `10.1038/s41586-020-1959-8` (cit. on pp. 9, 135, 145, 146, 163, 164).

Milgrom, M. (1983). "A modification of the Newtonian dynamics as a possible alternative to the hidden mass hypothesis." *The Astrophysical Journal* 270, 365–370. DOI: `10.1086/161130` (cit. on p. 27).

Miyake, H., N. C. Pisenti, P. K. Elgee, A. Sitaram, and G. K. Campbell (2019). "Isotope-shift spectroscopy of the $^1S_0 \rightarrow ^3P_1$ and $^1S_0 \rightarrow ^3P_0$ transitions in strontium." *Physical Review Research* 1, 033113. DOI: `10.1103/PhysRevResearch.1.033113` (cit. on pp. 32, 33, 170).

Mohr, P. J., D. B. Newell, and B. N. Taylor (2016). "CODATA recommended values of the fundamental physical constants: 2014." *Reviews of Modern Physics* 88, 035009. DOI: `10.1103/RevModPhys.88.035009` (cit. on p. 29).

Monroe, C., D. M. Meekhof, B. E. King, S. R. Jefferts, W. M. Itano, D. J. Wineland, and P. Gould (1995). "Resolved-Sideband Raman Cooling of a Bound Atom to the 3D Zero-Point Energy." *Physical Review Letters* 75, 4011–4014. DOI: `10.1103/PhysRevLett.75.4011` (cit. on p. 81).

Morgan, C. A., F. G. Serpa, E. Takács, E. S. Meyer, J. D. Gillaspy, J. Sugar, J. R. Roberts, C. M. Brown, and U. Feldman (1995). "Observation of Visible and uv Magnetic Dipole Transitions in Highly Charged Xenon and Barium." *Physical Review Letters* 74, 1716–1719. DOI: `10.1103/PhysRevLett.74.1716` (cit. on pp. 7, 47, 164).

Morigi, G. (2003). "Cooling atomic motion with quantum interference." *Physical Review A* 67, 033402. DOI: `10.1103/PhysRevA.67.033402` (cit. on p. 121).

Müller, R. A. (2019). *Private communication* (cit. on pp. 24, 152).

Müller, R. A., A. V. Volotka, and A. Surzhykov (2019). "Excitation of the ^{229}Th nucleus via a two-photon electronic transition." *Physical Review A* 99, 042517. DOI: `10.1103/PhysRevA.99.042517` (cit. on p. 25).

Myerson, A. H., D. J. Szwer, S. C. Webster, D. T. C. Allcock, M. J. Curtis, G. Imreh, J. A. Sherman, D. N. Stacey, A. M. Steane, and D. M. Lucas (2008). "High-Fidelity Readout of Trapped-Ion Qubits." *Physical Review Letters* 100, 200502. DOI: `10.1103/PhysRevLett.100.200502` (cit. on p. 116).

Nagashima, Y. (2014). "Experiments on positronium negative ions." *Physics Reports* 545, 95–123. DOI: `10.1016/j.physrep.2014.07.004` (cit. on p. 30).

Nandy, D. K. and B. K. Sahoo (2016). “Highly charged W^{13+}, Ir^{16+}, and Pt^{17+} ions as promising optical clock candidates for probing variations of the fine-structure constant.” *Physical Review A* 94, 032504. DOI: `10.1103/PhysRevA.94.032504` (cit. on pp. 24, 38).

Nauta, J., A. Borodin, H. B. Ledwa, J. Stark, M. Schwarz, L. Schmöger, P. Micke, J. R. Crespo López-Urrutia, and T. Pfeifer (2017). “Towards precision measurements on highly charged ions using a high harmonic generation frequency comb.” *Nuclear Instruments and Methods in Physics Research Section B: Beam Interactions with Materials and Atoms* 408, 285–288. DOI: `10.1016/j.nimb.2017.04.077` (cit. on pp. 87, 167, 176).

Nazé, C., S. Verdebout, P. Rynkun, G. Gaigalas, M. Godefroid, and P. Jönsson (2014). “Isotope shifts in beryllium-, boron-, carbon-, and nitrogen-like ions from relativistic configuration interaction calculations.” *Atomic Data and Nuclear Data Tables* 100, 1197–1249. DOI: `10.1016/j.adt.2014.02.004` (cit. on p. 47).

Nemitz, N., A. A. Jørgensen, R. Yanagimoto, F. Bregolin, and H. Katori (2019). “Modeling light shifts in optical lattice clocks.” *Physical Review A* 99, 033424. DOI: `10.1103/PhysRevA.99.033424` (cit. on p. 17).

Niering, M., R. Holzwarth, J. Reichert, P. Pokasov, T. Udem, M. Weitz, T. W. Hänsch, P. Lemonde, G. Santarelli, M. Abgrall, P. Laurent, C. Salomon, and A. Clairon (2000). “Measurement of the Hydrogen $1S$–$2S$ Transition Frequency by Phase Coherent Comparison with a Microwave Cesium Fountain Clock.” *Physical Review Letters* 84, 5496–5499. DOI: `10.1103/PhysRevLett.84.5496` (cit. on p. 29).

Norcia, M. A., A. W. Young, W. J. Eckner, E. Oelker, J. Ye, and A. M. Kaufman (2019). “Seconds-scale coherence on an optical clock transition in a tweezer array.” *Science* 366, 93–97. DOI: `10.1126/science.aay0644` (cit. on p. 17).

Nörtershäuser, W., D. Tiedemann, M. Žáková, Z. Andjelkovic, K. Blaum, M. L. Bissell, R. Cazan, G. W. F. Drake, C. Geppert, M. Kowalska, J. Krämer, A. Krieger, R. Neugart, R. Sánchez, F. Schmidt-Kaler, Z.-C. Yan, D. T. Yordanov, and C. Zimmermann (2009). “Nuclear Charge Radii of ^{7,9,10}Be and the One-Neutron Halo Nucleus ^{11}Be.” *Physical Review Letters* 102, 062503. DOI: `10.1103/PhysRevLett.102.062503` (cit. on pp. 49, 51).

Nörtershäuser, W., C. Geppert, A. Krieger, K. Pachucki, M. Puchalski, K. Blaum, M. L. Bissell, N. Frömmgen, M. Hammen, M. Kowalska, J. Krämer, K. Kreim, R. Neugart, G. Neyens, R. Sánchez, and D. T. Yordanov (2015). “Precision Test of Many-Body QED in the Be^+ $2p$ Fine Structure Doublet Using Short-Lived Isotopes.” *Physical Review Letters* 115, 033002. DOI: `10.1103/PhysRevLett.115.033002` (cit. on p. 49).

Oelker, E., R. B. Hutson, C. J. Kennedy, L. Sonderhouse, T. Bothwell, A. Goban, D. Kedar, C. Sanner, J. M. Robinson, G. E. Marti, D. G. Matei, T. Legero, M. Giunta, R. Holzwarth, F. Riehle, U. Sterr, and J. Ye (2019). “Demonstration of 4.8×10^{-17} stability at 1 s for two independent optical clocks.” *Nature Photonics* 13, 714–719. DOI: `10.1038/s41566-019-0493-4` (cit. on p. 17).

Oreshkina, N. S., S. M. Cavaletto, N. Michel, Z. Harman, and C. H. Keitel (2017). “Hyperfine splitting in simple ions for the search of the variation of fundamental constants.” *Physical Review A* 96, 030501. DOI: `10.1103/PhysRevA.96.030501` (cit. on pp. 24, 38).

Pachucki, K. and J. Komasa (2016). “Schrödinger equation solved for the hydrogen molecule with unprecedented accuracy.” *The Journal of Chemical Physics* 144, 164306. DOI: `10.1063/1.4948309` (cit. on p. 29).

Parker, R. H., C. Yu, W. Zhong, B. Estey, and H. Müller (2018). “Measurement of the fine-structure constant as a test of the Standard Model.” *Science* 360, 191–195. DOI: `10.1126/science.aap7706` (cit. on p. 34).

Parthey, C. G., A. Matveev, J. Alnis, B. Bernhardt, A. Beyer, R. Holzwarth, A. Maistrou, R. Pohl, K. Predehl, T. Udem, T. Wilken, N. Kolachevsky, M. Abgrall, D. Rovera, C. Salomon, P. Laurent, and T. W. Hänsch (2011). “Improved Measurement of the Hydrogen $1S$–$2S$ Transition Frequency.” *Physical Review Letters* 107, 203001. DOI: `10.1103/PhysRevLett.107.203001` (cit. on p. 29).

Particle Data Group (2018). “Review of Particle Physics.” *Physical Review D* 98, 030001. DOI: `10.1103/PhysRevD.98.030001` (cit. on p. 27).

Patra, S., J.-P. Karr, L. Hilico, M. Germann, V. I. Korobov, and J. C. J. Koelemeij (2017). “Proton-electron mass ratio from HD^+ revisited.” *Journal of Physics B: Atomic, Molecular and Optical Physics* 51, 024003. DOI: `10.1088/1361-6455/aa9b92` (cit. on pp. 30, 35).

Peebles, P. J. E. and B. Ratra (2003). “The cosmological constant and dark energy.” *Reviews of Modern Physics* 75, 559–606. DOI: `10.1103/RevModPhys.75.559` (cit. on p. 27).

Peik, E. and C. Tamm (2003). “Nuclear laser spectroscopy of the 3.5 eV transition in Th-229.” *Europhysics Letters* 61, 181–186. DOI: `10.1209/epl/i2003-00210-x` (cit. on p. 25).

Penetrante, B. M., J. N. Bardsley, D. DeWitt, M. Clark, and D. Schneider (1991). “Evolution of ion-charge-state distributions in an electron-beam ion trap.” *Physical Review A* 43, 4861–4872. DOI: `10.1103/PhysRevA.43.4861` (cit. on p. 90).

Pohl, R., A. Antognini, F. Nez, F. D. Amaro, F. Biraben, J. M. R. Cardoso, D. S. Covita, A. Dax, S. Dhawan, L. M. P. Fernandes, A. Giesen, T. Graf, T. W. Hänsch, P. Indelicato, L. Julien, et al. (2010). “The size of the proton.” *Nature* 466, 213–216. DOI: `10.1038/nature09250` (cit. on p. 30).

Pohl, R., F. Nez, L. M. P. Fernandes, F. D. Amaro, F. Biraben, J. M. R. Cardoso, D. S. Covita, A. Dax, S. Dhawan, M. Diepold, A. Giesen, A. L. Gouvea, T. Graf, T. W. Hänsch, P. Indelicato, et al. (2016). “Laser spectroscopy of muonic deuterium.” *Science* 353, 669–673. DOI: `10.1126/science.aaf2468` (cit. on p. 30).

Pohl, R., F. Nez, T. Udem, A. Antognini, A. Beyer, H. Fleurbaey, A. Grinin, T. W. Hänsch, L. Julien, F. Kottmann, J. J. Krauth, L. Maisenbacher, A. Matveev, and F. Biraben (2017). “Deuteron charge radius and Rydberg constant from spectroscopy data in atomic deuterium.” *Metrologia* 54, L1–L10. DOI: `10.1088/1681-7575/aa4e59` (cit. on p. 31).

Poli, N., C. W. Oates, P. Gill, and G. M. Tino (2013). “Optical atomic clocks.” *La Rivista del Nuovo Cimento* 36, 555–624. DOI: `10.1393/ncr/i2013-10095-x` (cit. on pp. 12, 16, 17).

Prior, M. H. (1987). “Forbidden lines from highly charged, metastable ion beams.” *Journal of the Optical Society of America B* 4, 144–147. DOI: `10.1364/JOSAB.4.000144` (cit. on p. 164).

Puchalski, M. and K. Pachucki (2009). “Fine and hyperfine splitting of the 2*P* state in Li and Be^+.” *Physical Review A* 79, 032510. DOI: `10.1103/PhysRevA.79.032510` (cit. on pp. 49, 51).

Quint, W., D. L. Moskovkhin, V. M. Shabaev, and M. Vogel (2008). “Laser-microwave double-resonance technique for g-factor measurements in highly charged ions.” *Physical Review A* 78, 032517. DOI: `10.1103/PhysRevA.78.032517` (cit. on p. 9).

Quint, W. and M. Vogel (2014). *Fundamental Physics in Particle Traps*. Springer. DOI: `10.1007/978-3-642-45201-7` (cit. on pp. 5, 6, 23, 28, 31).

Rabi, I. I. (1937). “Space Quantization in a Gyrating Magnetic Field.” *Physical Review* 51, 652–654. DOI: `10.1103/PhysRev.51.652` (cit. on p. 14).

Rabi, I. I., J. R. Zacharias, S. Millman, and P. Kusch (1938). “A New Method of Measuring Nuclear Magnetic Moment.” *Physical Review* 53, 318–318. DOI: `10.1103/PhysRev.53.318` (cit. on p. 14).

Ramsey, N. F. (1983). “History of atomic clocks.” *Journal of Research of the National Bureau of Standards* 88, 301–320. URL: `https://tf.nist.gov/general/pdf/1916.pdf` (visited on 01/31/2020) (cit. on p. 14).

Ramsey, N. F. (1985). *Molecular beams*. Oxford University Press. URL: `https://inis.iaea.org/search/search.aspx?orig_q=RN:18087073` (visited on 01/31/2020) (cit. on p. 14).

Ramsey, N. F. (1949). “A New Molecular Beam Resonance Method.” *Physical Review* 76, 996. DOI: `10.1103/PhysRev.76.996` (cit. on p. 14).

Reichert, J., R. Holzwarth, T. Udem, and T. W. Hänsch (1999). “Measuring the frequency of light with mode-locked lasers.” *Optics Communications* 172, 59–68. DOI: `10.1016/S0030-4018(99)00491-5` (cit. on p. 15).

Reinhold, E., R. Buning, U. Hollenstein, A. Ivanchik, P. Petitjean, and W. Ubachs (2006). “Indication of a Cosmological Variation of the Proton-Electron Mass Ratio Based on Laboratory Measurement and Reanalysis of H_2 Spectra.” *Physical Review Letters* 96, 151101. DOI: `10.1103/PhysRevLett.96.151101` (cit. on p. 36).

Rellergert, W. G., D. DeMille, R. R. Greco, M. P. Hehlen, J. R. Torgerson, and E. R. Hudson (2010). “Constraining the Evolution of the Fundamental Constants with a Solid-State Optical Frequency Reference Based on the ^{229}Th Nucleus.” *Physical Review Letters* 104, 200802. DOI: `10.1103/PhysRevLett.104.200802` (cit. on p. 25).

Rengelink, R. J., Y. v. d. Werf, R. P. M. J. W. Notermans, R. Jannin, K. S. E. Eikema, M. D. Hoogerland, and W. Vassen (2018). “Precision spectroscopy of helium in a magic wavelength optical dipole trap.” *Nature Physics* 14, 1132–1137. DOI: `10.1038/s41567-018-0242-5` (cit. on p. 30).

Repp, J., C. Böhm, J. R. Crespo López-Urrutia, A. Dörr, S. Eliseev, S. George, M. Goncharov, Y. N. Novikov, C. Roux, S. Sturm, S. Ulmer, and K. Blaum (2012). “PENTATRAP: a novel cryogenic multi-Penning-trap experiment for high-precision mass measurements on highly charged ions.” *Applied Physics B* 107, 983–996. DOI: `10.1007/s00340-011-4823-6` (cit. on pp. 7, 10, 87).

Riedel, F., A. Al-Masoudi, E. Benkler, S. Dörscher, V. Gerginov, C. Grebing, S. Häfner, N. Huntemann, B. Lipphardt, C. Lisdat, E. Peik, D. Piester, C. Sanner,

C. Tamm, S. Weyers, et al. (2020). “Direct comparisons of European primary and secondary frequency standards via satellite techniques.” *Metrologia*. Accepted manuscript. DOI: `10.1088/1681-7575/ab6745` (cit. on p. 16).

Riehle, F. (2004). *Frequency Standards: Basics and Applications*. Wiley-VCH. DOI: `10.1002/3527605991` (cit. on pp. 12, 72).

Roberts, B. M., P. Delva, A. Al-Masoudi, A. Amy-Klein, C. Bærentsen, C. F. A. Baynham, E. Benkler, S. Bilicki, S. Bize, W. Bowden, J. Calvert, V. Cambier, E. Cantin, E. A. Curtis, S. Dörscher, et al. (2020). “Search for transient variations of the fine structure constant and dark matter using fiber-linked optical atomic clocks.” *New Journal of Physics*. Accepted manuscript. DOI: `10.1088/1367-2630/abaace` (cit. on p. 39).

Roberts, B. M., G. Blewitt, C. Dailey, M. Murphy, M. Pospelov, A. Rollings, J. Sherman, W. Williams, and A. Derevianko (2017). “Search for domain wall dark matter with atomic clocks on board global positioning system satellites.” *Nature Communications* 8, 1195. DOI: `10.1038/s41467-017-01440-4` (cit. on p. 39).

Rooij, R. v., J. S. Borbely, J. Simonet, M. D. Hoogerland, K. S. E. Eikema, R. A. Rozendaal, and W. Vassen (2011). “Frequency Metrology in Quantum Degenerate Helium: Direct Measurement of the $2^3S_1 \to 2^1S_0$ Transition.” *Science* 333, 196–198. DOI: `10.1126/science.1205163` (cit. on p. 30).

Rosenband, T., D. B. Hume, P. O. Schmidt, C. W. Chou, A. Brusch, L. Lorini, W. H. Oskay, R. E. Drullinger, T. M. Fortier, J. E. Stalnaker, S. A. Diddams, W. C. Swann, N. R. Newbury, W. M. Itano, D. J. Wineland, and J. C. Bergquist (2008). “Frequency Ratio of Al^+ and Hg^+ Single-Ion Optical Clocks; Metrology at the 17th Decimal Place.” *Science* 319, 1808–1812. DOI: `10.1126/science.1154622` (cit. on pp. 17, 18, 37, 63).

Rosenthal, J. E. and G. Breit (1932). “The Isotope Shift in Hyperfine Structure.” *Physical Review* 41, 459–470. DOI: `10.1103/PhysRev.41.459` (cit. on p. 32).

Rubin, V. C. and W. K. Ford (1970). “Rotation of the Andromeda Nebula from a Spectroscopic Survey of Emission Regions.” *The Astrophysical Journal* 159, 379. DOI: `10.1086/150317` (cit. on p. 27).

Rudolph, J. K., S. Bernitt, S. W. Epp, R. Steinbrügge, C. Beilmann, G. V. Brown, S. Eberle, A. Graf, Z. Harman, N. Hell, M. Leutenegger, A. Müller, K. Schlage, H.-C. Wille, H. Yavaş, J. Ullrich, and J. R. Crespo López-Urrutia (2013). “X-Ray Resonant Photoexcitation: Linewidths and Energies of $K\alpha$ Transitions in Highly Charged Fe Ions.” *Physical Review Letters* 111, 103002. DOI: `10.1103/PhysRevLett.111.103002` (cit. on p. 7).

Rynkun, P., P. Jönsson, G. Gaigalas, and C. Froese Fischer (2012). “Energies and E1, M1, E2, M2 transition rates for states of the $2s^22p$, $2s2p^2$, and $2p^3$ configurations in boron-like ions between N III and Zn XXVI.” *Atomic Data and Nuclear Data Tables* 98, 481–556. DOI: `10.1016/j.adt.2011.08.004` (cit. on p. 171).

Safronova, M. S., D. Budker, D. DeMille, D. F. J. Kimball, A. Derevianko, and C. W. Clark (2018). “Search for new physics with atoms and molecules.” *Review of Modern Physics* 90, 025008. DOI: `10.1103/RevModPhys.90.025008` (cit. on pp. 15, 28, 37–39).

Safronova, M. S., V. A. Dzuba, V. V. Flambaum, U. I. Safronova, S. G. Porsev, and M. G. Kozlov (2014a). “Atomic properties of Cd-like and Sn-like ions for the development of frequency standards and search for the variation of the fine-structure constant." *Physical Review A* 90, 052509. DOI: `10.1103/PhysRevA.90.052509` (cit. on pp. 24, 38).

Safronova, M. S., V. A. Dzuba, V. V. Flambaum, U. I. Safronova, S. G. Porsev, and M. G. Kozlov (2014b). "Highly charged Ag-like and In-like ions for the development of atomic clocks and the search for α variation." *Physical Review A* 90, 042513. DOI: `10.1103/PhysRevA.90.042513` (cit. on pp. 24, 38).

Safronova, M. S., V. A. Dzuba, V. V. Flambaum, U. I. Safronova, S. G. Porsev, and M. G. Kozlov (2014c). "Highly Charged Ions for Atomic Clocks, Quantum Information, and Search for α variation." *Physical Review Letters* 113, 030801. DOI: `10.1103/PhysRevLett.113.030801` (cit. on pp. 24, 38).

Safronova, M. S. (2019). "The Search for Variation of Fundamental Constants with Clocks." *Annalen der Physik* 531, 1800364. DOI: `10.1002/andp.201800364` (cit. on pp. 37, 38).

Safronova, U. I., V. V. Flambaum, and M. S. Safronova (2015). "Transitions between the $4f$-core-excited states in Ir^{16+},Ir^{17+}, and Ir^{18+} ions for clock applications." *Physical Review A* 92, 022501. DOI: `10.1103/PhysRevA.92.022501` (cit. on pp. 24, 38).

Safronova, U. I. and M. S. Safronova (2013). "Relativistic many-body calculation of energies, lifetimes, polarizabilities, and hyperpolarizabilities in Li-like Be^{+}." *Physical Review A* 87, 032502. DOI: `10.1103/PhysRevA.87.032502` (cit. on pp. 49, 52).

Salumbides, E. J., J. C. J. Koelemeij, J. Komasa, K. Pachucki, K. S. E. Eikema, and W. Ubachs (2013). "Bounds on fifth forces from precision measurements on molecules." *Physical Review D* 87, 112008. DOI: `10.1103/PhysRevD.87.112008` (cit. on p. 30).

Sanner, C., N. Huntemann, R. Lange, C. Tamm, E. Peik, M. S. Safronova, and S. G. Porsev (2019). "Optical clock comparison for Lorentz symmetry testing." *Nature* 567, 204–208. DOI: `10.1038/s41586-019-0972-2` (cit. on p. 39).

Scharnhorst, N., J. B. Wübbena, S. Hannig, K. Jakobsen, J. Kramer, I. D. Leroux, and P. O. Schmidt (2015). "High-bandwidth transfer of phase stability through a fiber frequency comb." *Optics Express* 23, 19771–19776. DOI: `10.1364/OE.23.019771` (cit. on p. 126).

Schawlow, A. L. and C. H. Townes (1958). "Infrared and Optical Masers." *Physical Review* 112, 1940–1949. DOI: `10.1103/PhysRev.112.1940` (cit. on p. 15).

Schiller, S. (2007). "Hydrogenlike Highly Charged Ions for Tests of the Time Independence of Fundamental Constants." *Physical Review Letters* 98, 180801. DOI: `10.1103/PhysRevLett.98.180801` (cit. on pp. 23, 38).

Schmidt, P. O., T. Rosenband, C. Langer, W. M. Itano, J. C. Bergquist, and D. J. Wineland (2005). "Spectroscopy Using Quantum Logic." *Science* 309, 749–752. DOI: `10.1126/science.1114375` (cit. on pp. 17, 129).

Schmöger, L., M. Schwarz, T. M. Baumann, O. O. Versolato, B. Piest, T. Pfeifer, J. Ullrich, P. O. Schmidt, and J. R. Crespo López-Urrutia (2015). "Deceleration, precooling, and multi-pass stopping of highly charged ions in Be^{+} Coulomb crystals." *Review of Scientific Instruments* 86, 103111. DOI: `10.1063/1.4934245` (cit. on p. 91).

Schmöger, L., O. O. Versolato, M. Schwarz, M. Kohnen, A. Windberger, B. Piest, S. Feuchtenbeiner, J. Pedregosa-Gutierrez, T. Leopold, P. Micke, A. K. Hansen, T. M. Baumann, M. Drewsen, J. Ullrich, P. O. Schmidt, and J. R. Crespo López-Urrutia (2015). "Coulomb crystallization of highly charged ions." *Science* 347, 1233–1236. DOI: `10.1126/science.aaa2960` (cit. on pp. 9, 163).

Schmöger, L. (2013). "Ein elektrodynamisches System für den Transfer hochgeladener Ionen in eine Paulfalle." Diploma thesis. Heidelberg: Ruprecht-Karls-Universität Heidelberg. URL: `http://hdl.handle.net/11858/00-001M-0000-000E-EDFE-0` (visited on 01/31/2020) (cit. on p. 93).

Schmöger, L. (2017). "Kalte hochgeladene Ionen für Frequenzmetrologie." PhD thesis. Heidelberg: Ruprecht-Karls-Universität Heidelberg. DOI: `10.11588/heidok.00023214` (cit. on pp. 9, 25, 41, 102, 109, 163).

Schneider, D. (1996). "EBIT as a versatile experimental facility." *Hyperfine Interactions* 99, 47–69. DOI: `10.1007/BF02274909` (cit. on p. 9).

Schnorr, K., V. Mäckel, N. S. Oreshkina, S. Augustin, F. Brunner, Z. Harman, C. H. Keitel, J. Ullrich, and J. R. Crespo López-Urrutia (2013). "Coronium in the Laboratory: Measuring the Fe XIV Green Coronal Line by Laser Spectroscopy." *The Astrophysical Journal* 776, 121. DOI: `10.1088/0004-637X/776/2/121` (cit. on p. 7).

Schrödinger, E. (1926a). "Quantisierung als Eigenwertproblem - Dritte Mitteilung." *Annalen der Physik* 385, 437–490. DOI: `10.1002/andp.19263851302` (cit. on p. 28).

Schrödinger, E. (1926b). "Quantisierung als Eigenwertproblem - Erste Mitteilung." *Annalen der Physik* 384, 361–376. DOI: `10.1002/andp.19263840404` (cit. on p. 28).

Schrödinger, E. (1926c). "Quantisierung als Eigenwertproblem - Vierte Mitteilung." *Annalen der Physik* 386, 109–139. DOI: `10.1002/andp.19263861802` (cit. on p. 28).

Schrödinger, E. (1926d). "Quantisierung als Eigenwertproblem - Zweite Mitteilung." *Annalen der Physik* 384, 489–527. DOI: `10.1002/andp.19263840602` (cit. on p. 28).

Schulte, M., N. Lörch, I. D. Leroux, P. O. Schmidt, and K. Hammerer (2016). "Quantum Algorithmic Readout in Multi-Ion Clocks." *Physical Review Letters* 116, 013002. DOI: `10.1103/PhysRevLett.116.013002` (cit. on p. 17).

Schüssler, R. X. (2019). "First High-Precision Mass Measurements at PENTATRAP on highly charged Xe and Re ions." PhD thesis. Heidelberg: Ruprecht-Karls-Universität Heidelberg. DOI: `10.11588/heidok.00027646` (cit. on p. 10).

Schwarz, M., O. O. Versolato, A. Windberger, F. R. Brunner, T. Ballance, S. N. Eberle, J. Ullrich, P. O. Schmidt, A. K. Hansen, A. D. Gingell, M. Drewsen, and J. R. Crespo López-Urrutia (2012). "Cryogenic linear Paul trap for cold highly charged ion experiments." *Review of Scientific Instruments* 83, 083115. DOI: `10.1063/1.4742770` (cit. on pp. 9, 163).

Schweiger, C., C. M. König, J. R. Crespo López-Urrutia, M. Door, H. Dorrer, C. E. Düllmann, S. Eliseev, P. Filianin, W. Huang, K. Kromer, P. Micke, M. Müller, D. Renisch, A. Rischka, R. X. Schüssler, and K. Blaum (2019). "Production of highly charged ions of rare species by laser-induced desorption inside an electron beam ion trap." *Review of Scientific Instruments* 90, 123201. DOI: `10.1063/1.5128331` (cit. on pp. 89, 90).

Seelig, P., S. Borneis, A. Dax, T. Engel, S. Faber, M. Gerlach, C. Holbrow, G. Huber, T. Kühl, D. Marx, K. Meier, P. Merz, W. Quint, F. Schmitt, M. Tomaselli, et al. (1998). "Ground State Hyperfine Splitting of Hydrogenlike $^{207}\mathrm{Pb}^{81+}$ by Laser Excitation of a Bunched Ion Beam in the GSI Experimental Storage Ring." *Physical Review Letters* 81, 4824–4827. DOI: `10.1103/PhysRevLett.81.4824` (cit. on pp. 7, 32).

Seiferle, B., L. v. d. Wense, P. V. Bilous, I. Amersdorffer, C. Lemell, F. Libisch, S. Stellmer, T. Schumm, C. E. Düllmann, A. Pálffy, and P. G. Thirolf (2019). "Energy of the $^{229}\mathrm{Th}$ nuclear clock transition." *Nature* 573, 243–246. DOI: `10.1038/s41586-019-1533-4` (cit. on p. 25).

Serpa, F. G., J. D. Gillaspy, and E. Träbert (1998). "Lifetime measurements in the ground configuration of Ar^{13+} and Kr^{22+} using an electron beam ion trap." *Journal of Physics B: Atomic, Molecular and Optical Physics* 31, 3345. DOI: `10.1088/0953-4075/31/15/008` (cit. on p. 47).

Shabaev, V. M., A. I. Bondarev, D. A. Glazov, M. Y. Kaygorodov, Y. S. Kozhedub, I. A. Maltsev, A. V. Malyshev, R. V. Popov, I. I. Tupitsyn, and N. A. Zubova (2018). "Stringent tests of QED using highly charged ions." *Hyperfine Interactions* 239, 60. DOI: `10.1007/s10751-018-1537-8` (cit. on p. 31).

Shah, C., S. Dobrodey, S. Bernitt, R. Steinbrügge, J. R. Crespo López-Urrutia, L. Gu, and J. Kaastra (2016). "Laboratory Measurements Compellingly Support a Charge-Exchange Mechanism for the "Dark Matter" $\sim$ 3.5 keV X-Ray Line." *The Astrophysical Journal* 833, 52. DOI: `10.3847/1538-4357/833/1/52` (cit. on p. 7).

Shaniv, R., R. Ozeri, M. S. Safronova, S. G. Porsev, V. A. Dzuba, V. V. Flambaum, and H. Häffner (2018). "New Methods for Testing Lorentz Invariance with Atomic Systems." *Physical Review Letters* 120, 103202. DOI: `10.1103/PhysRevLett.120.103202` (cit. on p. 39).

Shaniv, R., T. Manovitz, Y. Shapira, N. Akerman, and R. Ozeri (2018). "Toward Heisenberg-Limited Rabi Spectroscopy." *Physical Review Letters* 120, 243603. DOI: `10.1103/PhysRevLett.120.243603` (cit. on p. 17).

Shchepetnov, A. A., D. A. Glazov, A. V. Volotka, V. M. Shabaev, I. I. Tupitsyn, and G. Plunien (2015). "Nuclear recoil correction to the g factor of boron-like argon." *Journal of Physics: Conference Series* 583, 012001. DOI: `10.1088/1742-6596/583/1/012001` (cit. on pp. 47, 147).

Shi, C., F. Gebert, C. Gorges, S. Kaufmann, W. Nörtershäuser, B. K. Sahoo, A. Surzhykov, V. A. Yerokhin, J. C. Berengut, F. Wolf, J. C. Heip, and P. O. Schmidt (2016). "Unexpectedly large difference of the electron density at the nucleus in the $4p\,^2\mathrm{P}_{1/2,3/2}$ fine-structure doublet of Ca^+." *Applied Physics B* 123, 2. DOI: `10.1007/s00340-016-6572-z` (cit. on pp. 32, 33, 170).

Simon, M. C., J. R. Crespo López-Urrutia, C. Beilmann, M. Schwarz, Z. Harman, S. W. Epp, B. L. Schmitt, T. M. Baumann, E. Behar, S. Bernitt, R. Follath, R. Ginzel, C. H. Keitel, R. Klawitter, K. Kubiček, V. Mäckel, P. H. Mokler, G. Reichardt, O. Schwarzkopf, and J. Ullrich (2010). "Resonant and Near-Threshold Photoionization Cross Sections of Fe^{14+}." *Physical Review Letters* 105, 183001. DOI: `10.1103/PhysRevLett.105.183001` (cit. on p. 7).

Skripnikov, L. V., S. Schmidt, J. Ullmann, C. Geppert, F. Kraus, B. Kresse, W. Nörtershäuser, A. F. Privalov, B. Scheibe, V. M. Shabaev, M. Vogel, and A. V. Volotka (2018). "New Nuclear Magnetic Moment of ^{209}Bi: Resolving the Bismuth Hyperfine Puzzle." *Physical Review Letters* 120, 093001. DOI: `10.1103/PhysRevLett.120.093001` (cit. on p. 33).

Smorra, C., S. Sellner, M. J. Borchert, J. A. Harrington, T. Higuchi, H. Nagahama, T. Tanaka, A. Mooser, G. Schneider, M. Bohman, K. Blaum, Y. Matsuda, C. Ospelkaus, W. Quint, J. Walz, Y. Yamazaki, and S. Ulmer (2017). "A parts-per-billion measurement of the antiproton magnetic moment." *Nature* 550, 371–374. DOI: `10.1038/nature24048` (cit. on p. 30).

Smorra, C., Y. V. Stadnik, P. E. Blessing, M. Bohman, M. J. Borchert, J. A. Devlin, S. Erlewein, J. A. Harrington, T. Higuchi, A. Mooser, G. Schneider, M. Wiesinger, E. Wursten, K. Blaum, Y. Matsuda, et al. (2019). "Direct limits on the interaction of antiprotons with axion-like dark matter." *Nature* 575, 310–314. DOI: `10.1038/s41586-019-1727-9` (cit. on p. 30).

Sobelman, I. I. (1992). *Atomic spectra and radiative transitions*. Second edition. Springer. DOI: `10.1007/978-3-642-76907-8` (cit. on pp. 66, 67, 71).

Sonzogni, A. A. (2020). *NuDat 2.8: Chart of Nuclides (online)*. URL: `https://www.nndc.bnl.gov/nudat2` (visited on 02/12/2020) (cit. on pp. 168, 172).

Soria Orts, R., J. R. Crespo López-Urrutia, H. Bruhns, A. J. González Martínez, Z. Harman, U. D. Jentschura, C. H. Keitel, A. Lapierre, H. Tawara, I. I. Tupitsyn, J. Ullrich, and A. V. Volotka (2007). "Zeeman splitting and g factor of the $1s^2 2s^2 2p$ $^2P_{3/2}$ and $^2P_{1/2}$ levels in Ar^{13+}." *Physical Review A* 76, 052501. DOI: `10.1103/PhysRevA.76.052501` (cit. on pp. 8, 10, 31, 47, 138, 147).

Soria Orts, R., Z. Harman, J. R. Crespo López-Urrutia, A. N. Artemyev, H. Bruhns, A. J. González Martínez, U. D. Jentschura, C. H. Keitel, A. Lapierre, V. Mironov, V. M. Shabaev, H. Tawara, I. I. Tupitsyn, J. Ullrich, and A. V. Volotka (2006). "Exploring Relativistic Many-Body Recoil Effects in Highly Charged Ions." *Physical Review Letters* 97, 103002. DOI: `10.1103/PhysRevLett.97.103002` (cit. on pp. 7, 32, 41, 46–48, 164, 168).

Soria Orts, R. (2005). "Isotopic effect in B-like and Be-like argon ions." PhD thesis. Frankfurt am Main: Johann Wolfgang Goethe-Universität. URL: `http://d-nb.info/978709837/34` (visited on 01/31/2020) (cit. on pp. 31, 71).

Stadnik, Y. V. and V. V. Flambaum (2015). "Can Dark Matter Induce Cosmological Evolution of the Fundamental Constants of Nature?" *Physical Review Letters* 115, 201301. DOI: `10.1103/PhysRevLett.115.201301` (cit. on p. 39).

Stadnik, Y. V. and V. V. Flambaum (2016). "Improved limits on interactions of low-mass spin-0 dark matter from atomic clock spectroscopy." *Physical Review A* 94, 022111. DOI: `10.1103/PhysRevA.94.022111` (cit. on p. 39).

Stark, J. (2020). "An Ultralow-Noise Superconducting Radio-Frequency Ion Trap for Frequency Metrology with Highly Charged Ions." PhD thesis. Heidelberg: Ruprecht-Karls-Universität Heidelberg. DOI: `10.11588/heidok.00028742` (cit. on p. 167).

Stenger, J., H. Schnatz, C. Tamm, and H. R. Telle (2002). "Ultraprecise Measurement of Optical Frequency Ratios." *Physical Review Letters* 88, 073601. DOI: `10.1103/PhysRevLett.88.073601` (cit. on p. 126).

Sturm, S., F. Köhler, J. Zatorski, A. Wagner, Z. Harman, G. Werth, W. Quint, C. H. Keitel, and K. Blaum (2014). "High-precision measurement of the atomic mass of the electron." *Nature* 506, 467–470. DOI: `10.1038/nature13026` (cit. on p. 35).

Sturm, S., A. Wagner, B. Schabinger, J. Zatorski, Z. Harman, W. Quint, G. Werth, C. H. Keitel, and K. Blaum (2011). "g Factor of Hydrogenlike $^{28}\mathrm{Si}^{13+}$." *Physical Review Letters* 107, 023002. DOI: `10.1103/PhysRevLett.107.023002` (cit. on pp. 7, 32).

Sturm, S., I. Arapoglou, A. Egl, M. Höcker, S. Kraemer, T. Sailer, B. Tu, A. Weigel, R. Wolf, J. Crespo López-Urrutia, and K. Blaum (2019). "The ALPHATRAP experiment." *The European Physical Journal Special Topics* 227, 1425–1491. DOI: `10.1140/epjst/e2018-800225-2` (cit. on pp. 7, 31, 87, 108).

Sturm, S., M. Vogel, F. Köhler-Langes, W. Quint, K. Blaum, and G. Werth (2017). "High-Precision Measurements of the Bound Electron's Magnetic Moment." *Atoms* 5, 4. DOI: `10.3390/atoms5010004` (cit. on p. 31).

Tachiev, G. and C. F. Fischer (1999). "Breit-Pauli energy levels, lifetimes, and transition data: beryllium-like spectra." *Journal of Physics B: Atomic, Molecular and Optical Physics* 32, 5805–5823. DOI: `10.1088/0953-4075/32/24/315` (cit. on p. 52).

Takamoto, M., F.-L. Hong, R. Higashi, and H. Katori (2005). "An optical lattice clock." *Nature* 435, 321–324. DOI: `10.1038/nature03541` (cit. on p. 17).

Takano, T., M. Takamoto, I. Ushijima, N. Ohmae, T. Akatsuka, A. Yamaguchi, Y. Kuroishi, H. Munekane, B. Miyahara, and H. Katori (2016). "Geopotential measurements with synchronously linked optical lattice clocks." *Nature Photonics* 10, 662–666. DOI: `10.1038/nphoton.2016.159` (cit. on pp. 11, 18).

Tan, T. R., R. Kaewuam, K. J. Arnold, S. R. Chanu, Z. Zhang, M. S. Safronova, and M. D. Barrett (2019). "Suppressing Inhomogeneous Broadening in a Lutetium Multi-ion Optical Clock." *Physical Review Letters* 123, 063201. DOI: `10.1103/PhysRevLett.123.063201` (cit. on p. 17).

Tanaka, M. and Y. Yamamoto (2019). "Relativistic effects in search for new intra-atomic force with isotope shifts." *arXiv:1911.05345 [hep-ph]*. URL: `https://arxiv.org/abs/1911.05345` (visited on 01/31/2020) (cit. on p. 171).

Taylor, B. N. and C. E. Kuyatt (1994). *Guidelines for Evaluating and Expressing the Uncertainty of NIST Measurement Results*. NIST Technical Note 1297. Gaithersburg: National Institute of Standards and Technology. DOI: `10.6028/NIST.tn.1297` (cit. on p. 12).

Telle, H. R., B. Lipphardt, and J. Stenger (2002). "Kerr-lens, mode-locked lasers as transfer oscillators for optical frequency measurements." *Applied Physics B* 74, 1–6. DOI: `10.1007/s003400100735` (cit. on p. 126).

Telle, H. R., G. Steinmeyer, A. E. Dunlop, J. Stenger, D. H. Sutter, and U. Keller (1999). "Carrier-envelope offset phase control: A novel concept for absolute optical frequency measurement and ultrashort pulse generation." *Applied Physics B* 69, 327–332. DOI: `10.1007/s003400050813` (cit. on p. 15).

Thielking, J., M. V. Okhapkin, P. Głowacki, D. M. Meier, L. Wense, B. Seiferle, C. E. Düllmann, P. G. Thirolf, and E. Peik (2018). "Laser spectroscopic characterization of the nuclear-clock isomer $^{229\mathrm{m}}\mathrm{Th}$." *Nature* 556, 321–325. DOI: `10.1038/s41586-018-0011-8` (cit. on p. 25).

Tiesinga, E., P. J. Mohr, D. B. Newell, and B. N. Taylor (2019). *The 2018 CODATA Recommended Values of the Fundamental Physical Constants (Web Version 8.0)*. National Institute of Standards and Technology. URL: `http://physics.nist.gov/constants` (visited on 01/31/2020) (cit. on pp. 29, 34, 35).

Träbert, E., P. Beiersdorfer, S. B. Utter, G. V. Brown, H. Chen, C. L. Harris, P. A. Neill, D. W. Savin, and A. J. Smith (2000). "Experimental M1 Transition Rates of Coronal Lines from Ar X, Ar XIV, and Ar XV." *The Astrophysical Journal* 541, 506–511. DOI: `10.1086%2F309427` (cit. on pp. 47, 156).

Tupitsyn, I. I., A. V. Volotka, D. A. Glazov, V. M. Shabaev, G. Plunien, J. R. Crespo López-Urrutia, A. Lapierre, and J. Ullrich (2005). "Magnetic-dipole transition probabilities in B-like and Be-like ions." *Physical Review A* 72, 062503. DOI: `10.1103/PhysRevA.72.062503` (cit. on pp. 29, 31, 47, 48, 156, 159).

Turchette, Q. A., Kielpinski, B. E. King, D. Leibfried, D. M. Meekhof, C. J. Myatt, M. A. Rowe, C. A. Sackett, C. S. Wood, W. M. Itano, C. Monroe, and D. J. Wineland (2000). "Heating of trapped ions from the quantum ground state." *Physical Review A* 61, 063418. DOI: `10.1103/PhysRevA.61.063418` (cit. on p. 122).

Ubachs, W., J. Bagdonaite, E. J. Salumbides, M. T. Murphy, and L. Kaper (2016). "*Colloquium:* Search for a drifting proton-electron mass ratio from H_2." *Reviews of Modern Physics* 88, 021003. DOI: `10.1103/RevModPhys.88.021003` (cit. on p. 36).

Ubachs, W. (2017). "Search for Varying Constants of Nature from Astronomical Observation of Molecules." *Space Science Reviews* 214, 3. DOI: `10.1007/s11214-017-0432-y` (cit. on p. 36).

Udem, T., R. Holzwarth, and T. W. Hänsch (2002). "Optical frequency metrology." *Nature* 416, 233–237. DOI: `10.1038/416233a` (cit. on pp. 15, 126).

Ullmann, J., Z. Andelkovic, C. Brandau, A. Dax, W. Geithner, C. Geppert, C. Gorges, M. Hammen, V. Hannen, S. Kaufmann, K. König, Y. A. Litvinov, M. Lochmann, B. Maaß, J. Meisner, et al. (2017). "High precision hyperfine measurements in Bismuth challenge bound-state strong-field QED." *Nature Communications* 8, 15484. DOI: `10.1038/ncomms15484` (cit. on pp. 7, 9, 33).

Ulmer, S., C. Smorra, A. Mooser, K. Franke, H. Nagahama, G. Schneider, T. Higuchi, S. Van Gorp, K. Blaum, Y. Matsuda, W. Quint, J. Walz, and Y. Yamazaki (2015). "High-precision comparison of the antiproton-to-proton charge-to-mass ratio." *Nature* 524, 196–199. DOI: `10.1038/nature14861` (cit. on p. 30).

Ushijima, I., M. Takamoto, M. Das, T. Ohkubo, and H. Katori (2015). "Cryogenic optical lattice clocks." *Nature Photonics* 9, 185–189. DOI: `10.1038/nphoton.2015.5` (cit. on p. 105).

Uzan, J.-P. (2003). "The fundamental constants and their variation: observational and theoretical status." *Reviews of Modern Physics* 75, 403–455. DOI: `10.1103/RevModPhys.75.403` (cit. on pp. 28, 36).

Uzan, J.-P. (2011). "Varying Constants, Gravitation and Cosmology." *Living Reviews in Relativity* 14, 2. DOI: `10.12942/lrr-2011-2` (cit. on pp. 15, 33, 36).

Van Tilburg, K., N. Leefer, L. Bougas, and D. Budker (2015). "Search for Ultralight Scalar Dark Matter with Atomic Spectroscopy." *Physical Review Letters* 115, 011802. DOI: `10.1103/PhysRevLett.115.011802` (cit. on p. 39).

Varentsova, A. S., V. A. Agababaev, D. A. Glazov, A. M. Volchkova, A. V. Volotka, V. M. Shabaev, and G. Plunien (2018). “Interelectronic-interaction contribution to the nonlinear Zeeman effect in boronlike ions.” *Physical Review A* 97, 043402. DOI: `10.1103/PhysRevA.97.043402` (cit. on pp. 47, 151).

Verdebout, S., C. Nazé, P. Jönsson, P. Rynkun, M. Godefroid, and G. Gaigalas (2014). “Hyperfine structures and Landé g_J-factors for $n = 2$ states in beryllium-, boron-, carbon-, and nitrogen-like ions from relativistic configuration interaction calculations.” *Atomic Data and Nuclear Data Tables* 100, 1111–1155. DOI: `10.1016/j.adt.2014.05.001` (cit. on pp. 47, 147, 148).

Vetter, J., H. Ackermann, G. z. Putlitz, and E. W. Weber (1976). “Hyperfine Structure Measurement of the $^9\mathrm{Be}^+\ 2\,^2S_{1/2}$ Ground State by Optical Pumping.” *Zeitschrift für Physik A Atoms and Nuclei* 276, 161–165. DOI: `10.1007/BF01412094` (cit. on p. 49).

Vogel, M., M. S. Ebrahimi, Z. Guo, A. Khodaparast, G. Birkl, and W. Quint (2018). “Electron Magnetic Moment in Highly Charged Ions: The ARTEMIS Experiment.” *Annalen der Physik* 531, 1800211. DOI: `10.1002/andp.201800211` (cit. on p. 9).

Vogel, M. and W. Quint (2010). “Trap-assisted precision spectroscopy of forbidden transitions in highly-charged ions.” *Physics Reports* 490, 1–47. DOI: `10.1016/j.physrep.2009.12.007` (cit. on p. 9).

Wagner, A., S. Sturm, F. Köhler, D. A. Glazov, A. V. Volotka, G. Plunien, W. Quint, G. Werth, V. M. Shabaev, and K. Blaum (2013). “g Factor of Lithiumlike Silicon $^{28}\mathrm{Si}^{11+}$.” *Physical Review Letters* 110, 033003. DOI: `10.1103/PhysRevLett.110.033003` (cit. on p. 32).

Walraven, J. T. M. (2018). *Atomic Physics. Lecture notes*. University of Amsterdam. URL: `https://staff.fnwi.uva.nl/j.t.m.walraven/walraven/Publications_files/2019-AtomicPhysics.pdf` (visited on 01/31/2020) (cit. on p. 66).

Wan, Y., F. Gebert, F. Wolf, and P. O. Schmidt (2015). “Efficient sympathetic motional-ground-state cooling of a molecular ion.” *Physical Review A* 91, 043425. DOI: `10.1103/PhysRevA.91.043425` (cit. on pp. 82, 120).

Wan, Y., F. Gebert, J. B. Wübbena, N. Scharnhorst, S. Amairi, I. D. Leroux, B. Hemmerling, N. Lörch, K. Hammerer, and P. O. Schmidt (2014). “Precision spectroscopy by photon-recoil signal amplification.” *Nature Communications* 5, 4096. DOI: `10.1038/ncomms4096` (cit. on p. 17).

Wang, M., G. Audi, F. G. Kondev, W. J. Huang, S. Naimi, and X. Xu (2017). “The AME2016 atomic mass evaluation (II). Tables, graphs and references.” *Chinese Physics C* 41, 030003. DOI: `10.1088/1674-1137/41/3/030003` (cit. on p. 172).

Webb, J. K., J. A. King, M. T. Murphy, V. V. Flambaum, R. F. Carswell, and M. B. Bainbridge (2011). “Indications of a Spatial Variation of the Fine Structure Constant.” *Physical Review Letters* 107, 191101. DOI: `10.1103/PhysRevLett.107.191101` (cit. on p. 36).

Wense, L. v. d., B. Seiferle, M. Laatiaoui, J. B. Neumayr, H.-J. Maier, H.-F. Wirth, C. Mokry, J. Runke, K. Eberhardt, C. E. Düllmann, N. G. Trautmann, and P. G. Thirolf (2016). “Direct detection of the ^{229}Th nuclear clock transition.” *Nature* 533, 47–51. DOI: `10.1038/nature17669` (cit. on p. 25).

Wetterich, C. (2003). “Probing quintessence with time variation of couplings.” *Journal of Cosmology and Astroparticle Physics* 2003, 002. DOI: `10.1088/1475-7516/2003/10/002` (cit. on p. 36).

Weyers, S., V. Gerginov, M. Kazda, J. Rahm, B. Lipphardt, G. Dobrev, and K. Gibble (2018). “Advances in the accuracy, stability, and reliability of the PTB primary fountain clocks.” *Metrologia* 55, 789–805. DOI: `10.1088/1681-7575/aae008` (cit. on pp. 14, 37).

Whitmore, J. B. and M. T. Murphy (2015). “Impact of instrumental systematic errors on fine-structure constant measurements with quasar spectra.” *Monthly Notices of the Royal Astronomical Society* 447, 446–462. DOI: `10.1093/mnras/stu2420` (cit. on p. 36).

Wilson, A. C., C. Ospelkaus, A. P. VanDevender, J. A. Mlynek, K. R. Brown, D. Leibfried, and D. J. Wineland (2011). “A 750-mW, continuous-wave, solid-state laser source at 313 nm for cooling and manipulating trapped ^{9}Be$^+$ ions.” *Applied Physics B* 105, 741–748. DOI: `10.1007/s00340-011-4771-1` (cit. on p. 113).

Windberger, A., J. R. Crespo López-Urrutia, H. Bekker, N. S. Oreshkina, J. C. Berengut, V. Bock, A. Borschevsky, V. A. Dzuba, E. Eliav, Z. Harman, U. Kaldor, S. Kaul, U. I. Safronova, V. V. Flambaum, C. H. Keitel, P. O. Schmidt, J. Ullrich, and O. O. Versolato (2015). “Identification of the Predicted $5s$-$4f$ Level Crossing Optical Lines with Applications to Metrology and Searches for the Variation of Fundamental Constants.” *Physical Review Letters* 114, 150801. DOI: `10.1103/PhysRevLett.114.150801` (cit. on pp. 7, 10, 176).

Wineland, D. J., M. Barrett, J. Britton, J. Chiaverini, B. DeMarco, W. M. Itano, B. Jelenković, C. Langer, D. Leibfried, V. Meyer, T. Rosenband, and T. Schätz (2003). “Quantum information processing with trapped ions.” *Philosophical Transactions of the Royal Society of London. Series A: Mathematical, Physical and Engineering Sciences* 361, 1349–1361. DOI: `10.1098/rsta.2003.1205` (cit. on pp. 77, 78, 113).

Wineland, D. J., J. C. Bergquist, J. J. Bollinger, R. E. Drullinger, and W. M. Itano (2002). “Quantum computers and atomic clocks.” *Proceedings of the 6th Symposium on Frequency Standards and Metrology: University of St. Andrews, Fife, Scotland, 9–14 September 2001.* World Scientific, pp. 361–368. DOI: `10.1142/9789812777713_0040` (cit. on pp. 17, 129).

Wineland, D. J., J. J. Bollinger, and W. M. Itano (1983). “Laser-Fluorescence Mass Spectroscopy.” *Physical Review Letters* 50, 628–631. DOI: `10.1103/PhysRevLett.50.628` (cit. on pp. 49, 51).

Wineland, D. J. and W. M. Itano (1979). “Laser cooling of atoms.” *Physical Review A* 20, 1521–1540. DOI: `10.1103/PhysRevA.20.1521` (cit. on pp. 79, 80).

Wineland, D. J., C. Monroe, W. M. Itano, B. E. King, D. Leibfried, D. M. Meekhof, C. Myatt, and C. Wood (1998). “Experimental Primer on the Trapped Ion Quantum Computer.” *Fortschritte der Physik* 46, 363–390. DOI: `10.1002/(SICI)1521-3978(199806)46:4/5<363::AID-PROP363>3.0.CO;2-4` (cit. on pp. 55, 77).

Wineland, D. J., C. Monroe, W. M. Itano, D. Leibfried, B. E. King, and D. M. Meekhof (1998). “Experimental Issues in Coherent Quantum-State Manipulation of Trapped Atomic Ions.” *Journal of Research of the National Institute of Standards and Technology* 103, 259–328. DOI: `10.6028/jres.103.019` (cit. on pp. 55, 58, 72, 76, 79, 81).

Wolf, F., Y. Wan, J. C. Heip, F. Gebert, C. Shi, and P. O. Schmidt (2016). “Non-destructive state detection for quantum logic spectroscopy of molecular ions.” *Nature* 530, 457–460. DOI: `10.1038/nature16513` (cit. on pp. 10, 17).

Wolfenstein, L. (1999). “Neutrino physics.” *Reviews of Modern Physics* 71, S140–S144. DOI: `10.1103/RevModPhys.71.S140` (cit. on p. 34).

Wübbena, J. B., S. Amairi, O. Mandel, and P. O. Schmidt (2012). “Sympathetic cooling of mixed-species two-ion crystals for precision spectroscopy.” *Physical Review A* 85, 043412. DOI: `10.1103/PhysRevA.85.043412` (cit. on pp. 62, 63, 80).

Xiong, W., A. Gasparian, H. Gao, D. Dutta, M. Khandaker, N. Liyanage, E. Pasyuk, C. Peng, X. Bai, L. Ye, K. Gnanvo, C. Gu, M. Levillain, X. Yan, D. W. Higinbotham, et al. (2019). “A small proton charge radius from an electron-proton scattering experiment.” *Nature* 575, 147–150. DOI: `10.1038/s41586-019-1721-2` (cit. on p. 30).

Xu, D., P. Delva, O. Lopez, A. Amy-Klein, and P.-E. Pottie (2019). “Reciprocity of propagation in optical fiber links demonstrated to 10^{-21}.” *Optics Express* 27, 36965–36975. DOI: `10.1364/OE.27.036965` (cit. on p. 16).

Yerokhin, V. A. (2008). “Hyperfine structure of Li and Be^+.” *Physical Review A* 78, 012513. DOI: `10.1103/PhysRevA.78.012513` (cit. on pp. 49, 51).

Yerokhin, V. A., R. A. Müller, A. Surzhykov, P. Micke, and P. O. Schmidt (2020). “Nonlinear isotope-shift effects in Be-like, B-like, and C-like argon.” *Physical Review A* 101, 012502. DOI: `10.1103/PhysRevA.101.012502` (cit. on pp. 33, 168, 170–172).

Yerokhin, V. A., K. Pachucki, and V. Patkóš (2019). “Theory of the Lamb Shift in Hydrogen and Light Hydrogen-Like Ions.” *Annalen der Physik* 531, 1800324. DOI: `10.1002/andp.201800324` (cit. on p. 29).

Yu, Y., N. R. Hutzler, J. T. Zhang, L. R. Liu, J. D. Hood, T. Rosenband, and K.-K. Ni (2018). “Motional-ground-state cooling outside the Lamb–Dicke regime.” *Physical Review A* 97, 063423. DOI: `10.1103/PhysRevA.97.063423` (cit. on p. 120).

Yu, Y.-m. and B. K. Sahoo (2016). “Scrutinizing Al-like $^{51}\mathrm{V}^{10+}$, $^{53}\mathrm{Cr}^{11+}$, $^{55}\mathrm{Mn}^{12+}$, $^{57}\mathrm{Fe}^{13+}$, $^{59}\mathrm{Co}^{14+}$, $^{61}\mathrm{Ni}^{15+}$, and $^{63}\mathrm{Cu}^{16+}$ ions for atomic clocks with uncertainties below the 10^{-19} level.” *Physical Review A* 94, 062502. DOI: `10.1103/PhysRevA.94.062502` (cit. on p. 24).

Yu, Y.-m. and B. K. Sahoo (2018). “Selected highly charged ions as prospective candidates for optical clocks with quality factors larger than 10^{15}.” *Physical Review A* 97, 041403. DOI: `10.1103/PhysRevA.97.041403` (cit. on pp. 24, 175).

Yu, Y.-m. and B. K. Sahoo (2019). “Investigating ground-state fine-structure properties to explore suitability of boronlike $\mathrm{S}^{11+} - \mathrm{K}^{14+}$ and galliumlike $\mathrm{Nb}^{10+} - \mathrm{Ru}^{13+}$ ions as possible atomic clocks.” *Physical Review A* 99, 022513. DOI: `10.1103/PhysRevA.99.022513` (cit. on pp. 24, 153).

Yudin, V. I., A. V. Taichenachev, and A. Derevianko (2014). “Magnetic-Dipole Transitions in Highly Charged Ions as a Basis of Ultraprecise Optical Clocks.” *Physical Review Letters* 113, 233003. DOI: `10.1103/PhysRevLett.113.233003` (cit. on p. 24).

Zubova, N. A., A. V. Malyshev, I. I. Tupitsyn, V. M. Shabaev, Y. S. Kozhedub, G. Plunien, C. Brandau, and T. Stöhlker (2016). “Isotope shifts of the $2p_{3/2} - 2p_{1/2}$ transition in B-like ions.” *Physical Review A* 93, 052502. DOI: `10.1103/PhysRevA.93.052502` (cit. on pp. 47, 168).

Danksagung

Das Projekt, in dem diese Doktorarbeit entstanden ist, hat die Hingabe und Arbeit vieler Menschen erfordert. Im Rahmen von zwei Seiten Danksagung kann ich wohl nicht einmal den wichtigsten Personen angemessen danken, die zum Gelingen dieser Arbeit beigetragen haben. Viele weitere Menschen, die hier leider keine explizite Erwähnung finden, haben unterstützt und hilfreiche Beiträge geleistet.

Piet und José, zuallererst möchte ich Euch dafür danken, dass ich an dem Projekt wirken und schaffen durfte und schließlich diese Arbeit einreichen konnte. Ich bin 2014 mit hohen Erwartungen in das Projekt gestartet und – ich kann es kaum glauben – sie sind übertroffen worden. Piet, vielen Dank für Dein Vertrauen schon gleich zu Beginn meiner Heidelberger Zeit. Das war alles andere als selbstverständlich. José, vielen Dank dafür, dass Du mich in Heidelberg so toll aufgenommen hattest, wissend, dass ich mit einem aufwendigen Aufbau wieder verschwinden müsse. Ich habe von Euch viel lernen dürfen und am Ende hat sich alles im Experiment wunderbar ergänzt. Danke für diese vielseitige Doktorandenstelle!
Außerdem vielen Dank an Christian Ospelkaus und Klemens Hammerer für Ihre wertvolle Zeit und Arbeit in der Promotionskommission dieser Doktorarbeit und an Birgit Ohlendorf für Ihre äußerst hilfreiche Unterstützung im Promotionsverfahren.

Tobias und Steven, das Gelingen des Experiments wäre ohne Eure Leidenschaft und harte Arbeit nicht möglich gewesen! Lukas, Du hast nach kürzester Zeit das Experiment durchdrungen und bist nun unverzichtbar geworden. Wir haben uns alle toll ergänzt, uns jederzeit geholfen und mit dieser genau richtigen Mentalität schließlich eine Menge (hoch geladener) Ionen gebändigt, wie es bis vor Kurzem noch undenkbar war. Ich hätte mir kein tolleres Team wünschen können! Tobi, wir haben seit Beginn unseres Studiums einen großen Teil des Weges gemeinsam zurück gelegt und Du warst es auch, der mich auf dieses Projekt aufmerksam gemacht hat. Danke dafür und für diese lange und schöne Zeit.
Auch bei Euch, Lisa, Maria und Oscar, möchte ich mich besonders bedanken. Ihr habt entscheidende Beiträge für das Experiment schon im Vorfeld geleistet und damit auch maßgeblich zum Gelingen dieser Arbeit beigetragen. Außerdem habe ich mit Euch gerne über einige Jahre das Büro in Heidelberg geteilt und viele wertvolle Gespräche geführt.

Liebe Heidelberger et al., ich möchte mich bei Euch für inspirierende Gespräche, wertvolle Ratschläge und tatkräftige Hilfen bedanken – insbesondere bei Euch, Alex, Chintan, Christian, Christoph, Daniel, Hendrik, Janko, Julian, Michael, Michael alias Karl, René, Rima, Robert, Sandra, Steffen, Stepan, SungNam, Sven B. und Sven S. Ich habe die Zeiten genossen, in denen ich eng und gut mit Euch zusammenarbeiten durfte, sei es in endlosen Nachtschichten auf Strahlzeiten oder in ‘fremden’ Labors gewesen.

Liebe QUESTler, insbesondere liebes *IQLOC*-Team mit Fabian, Johannes, Kai, Lennart, Ludwig, Nicolas und Stephan sowie liebes *DIFCOS*- alias *MANFRED*-Team mit Fabian, Jan-Christoph und Max, danke für Eure Unterstützung, Tipps und wertvollen Gespräche. Wir haben einen guten Zusammenhalt, der nicht an den Grenzen der einzelnen Experimente endet – so muss es sein und ich schätze es sehr! Sandra und Sina, Ihr löst viele Probleme bevor wir sie erst bemerken und Ihr kennt die Geheimnisse der PTB. Das ist äußerst wertvoll! Auch Ihr, David, Julia und Tjeerd, habt mit Eurem besonderen Engagement einen wertvollen Beitrag für unser Experiment geleistet.

Many thanks to Andrey, Robert, Sabrina, and Vladimir for valuable discussions and the excellent collaboration!

Vielen Dank an Abteilung 4 der PTB und insbesondere an Dich, Erik! Ohne die Nutzung Eurer Infrastruktur, Expertise und tatkräftigen Unterstützung wären unsere Messungen nicht möglich gewesen.

Im Allgemeinen möchte ich mich bei den hervorragende Strukturen von PTB und MPIK bedanken, den mechanischen und elektronischen Werkstätten, Konstruktionsbüros, der Mediengestaltung und für die Unterstützung von Seiten der Presse- und Öffentlichkeitsabteilungen. Außerdem vielen Dank an jeden Steuerzahler für die Finanzierung solcher großartigen und wichtigen Experimente. Ebenso Dankeschön an all jene, die sich für das Gelingen der PTB-MPIK Kollaboration eingesetzt haben, sei es direkt oder indirekt gewesen – denn ohne diese starke Kollaboration wäre die Arbeit nicht möglich gewesen.

Zusätzlichen Dank an Euch, Erik, Johannes, Lukas, Piet, Robert, Steven, Sven und Tobias für das stundenlange Korrekturlesen meiner Arbeit und Eure wertvollen Kommentare und Hinweise. Ich weiß das sehr zu schätzen!

Liebe Eltern, Ihr habt mir diesen Weg ermöglicht, auf dem ich nun bin und ich kann Euch gar nicht dankbar genug sein für Eure bedingungslose Unterstützung. Liebe Michaela, lieber Tobi, liebe Marlene, ich schätze und genieße den Rückhalt durch Euch und Eure Gegenwart sehr. Ich bin dankbar für Euer aller Vertrauen in meine Arbeit.

Liebe Kathi, allergrößten Dank für Deine wichtige Unterstützung in den letzten sechs Jahren. Du hast in besseren und in schlechteren Zeiten immer zu mir gehalten. Du warst und bist die fundamentale Konstante in meinem Leben.

Peter Micke
Braunschweig, Februar 2020

Curriculum Vitæ

Personal data

Name	Peter Micke
Date of birth	June 15th, 1988
Place of birth	Kassel
Nationality	German
ORCID iD	https://orcid.org/0000-0001-7430-8751

Education

2014–2020	PhD student, Physikalisch-Technische Bundesanstalt, Braunschweig QUEST Group of Prof. Dr. Piet O. Schmidt
2014–2017	Guest scientist, Max-Planck-Institut für Kernphysik, Heidelberg Division of Prof. Dr. Thomas Pfeifer Group of PD Dr. José R. Crespo López-Urrutia
2011–2013	Master of Science, Johannes Gutenberg-Universität Mainz Group of Prof. Dr. Jochen Walz
2008–2011	Bachelor of Science, Martin-Luther-Universität Halle-Wittenberg Group of Prof. Dr. Kay Saalwächter
2007	Abitur, Geschwister-Scholl-Schule, Melsungen

Scholarships

2011–2013	Studienstiftung des deutschen Volkes

Invited talks

Mar 2020	DPG Spring Meeting of the Atomic, Molecular, Plasma Physics and Quantum Optics Section (SAMOP), Hannover, Germany (Canceled due to COVID-19 pandemic)
Jul 2019	XXXIst International Conference on Photonic, Electronic, and Atomic Collisions (ICPEAC), Deauville, France
Dec 2018	Atomic Physics Seminar of the GSI Helmholtzzentrum für Schwerionenforschung, Darmstadt, Germany
Okt 2018	International Symposium on Electron Beam Ion Sources and Traps (EBIST), Shanghai, China

Sep 2018	Stored Particles Atomic Physics Research Collaboration (SPARC) topical workshop, Lisbon, Portugal

Selected poster contributions

Jul 2019	XXXIst International Conference on Photonic, Electronic, and Atomic Collisions (ICPEAC), Deauville, France
Jun 2019	Quantum Metrology and Physics beyond the Standard Model, Hannover, Germany
Sep 2018	International Conference on the Physics of Highly Charged Ions (HCI), Lisbon, Portugal
May 2018	670. WE-Heraeus-Seminar on Fundamental Constants: Basic Physics and Units, Bad Honnef, Germany
Jul 2017	Conference of the European Group on Atomic Systems (EGAS), Durham, United Kingdom
Sep 2016	International Conference on the Physics of Highly Charged Ions (HCI), Kielce, Poland
Sep 2016	Conference of the European Group on Atomic Systems (EGAS) and European Conference on Atoms, Molecules, and Photons (ECAMP), Frankfurt am Main, Germany
Jul 2015	Conference of the European Group on Atomic Systems (EGAS), Riga, Latvia
Sep 2014	European Conference on Trapped Ions (ECTI), Mainz, Germany

Publications

P. Micke, T. Leopold, S. A. King, E. Benkler, L. J. Spieß, L. Schmöger, M. Schwarz, J. R. Crespo López-Urrutia, and P. O. Schmidt (2020). “Coherent laser spectroscopy of highly charged ions using quantum logic.” *Nature* 578, 60–65. DOI: 10.1038/s41586-020-1959-8

V. A. Yerokhin, R. A. Müller, A. Surzhykov, **P. Micke**, and P. O. Schmidt (2020). “Nonlinear isotope-shift effects in Be-like, B-like, and C-like argon.” *Physical Review A* 101, 012502. DOI: 10.1103/PhysRevA.101.012502

Ch. Schweiger, C. M. König, J. R. Crespo López-Urrutia, M. Door, H. Dorrer, Ch. E. Düllmann, S. Eliseev, P. Filianin, W. Huang, K. Kromer, **P. Micke**, M. Müller, D. Renisch, A. Rischka, R. X. Schüssler, and K. Blaum (2019). “Production of highly charged ions of rare species by laser-induced desorption inside an electron beam ion trap.” *Review of Scientific Instruments* 90, 123201. DOI: 10.1063/1.5128331

T. Leopold, S. A. King, **P. Micke**, A. Bautista-Salvador, J. C. Heip, C. Ospelkaus, J. R. Crespo López-Urrutia, and P. O. Schmidt (2019). “A cryogenic radio-frequency ion trap for quantum logic spectroscopy of highly charged ions.” *Review of Scientific Instruments* 90, 073201. DOI: 10.1063/1.5100594

P. Micke, J. Stark, S. A. King, T. Leopold, T. Pfeifer, L. Schmöger, M. Schwarz, L. J. Spieß, P. O. Schmidt, and J. R. Crespo López-Urrutia (2019). “Closed-cycle, low-vibration 4 K cryostat for ion traps and other applications.” *Review of Scientific Instruments* 90, 065104. DOI: 10.1063/1.5088593

P. Micke, S. Kühn, L. Buchauer, J. R. Harries, T. M. Bücking, K. Blaum, A. Cieluch, A. Egl, D. Hollain, S. Kraemer, T. Pfeifer, P. O. Schmidt, R. X. Schüssler, Ch. Schweiger, T. Stöhlker, S. Sturm, R. N. Wolf, S. Bernitt, and J. R. Crespo López-Urrutia (2018). “The Heidelberg compact electron beam ion traps.” *Review of Scientific Instruments* 89, 063109. DOI: 10.1063/1.5026961

J. Nauta, A. Borodin, H. B. Ledwa, J. Stark, M. Schwarz, L. Schmöger, **P. Micke**, J. R. Crespo López-Urrutia, and T. Pfeifer (2017). “Towards precision measurements on highly charged ions using a high harmonic generation frequency comb.” *Nuclear Instruments and Methods in Physics Research Section B: Beam Interactions with Materials and Atoms* 408, 285–288. DOI: 10.1016/j.nimb.2017.04.077

T. Leopold, L. Schmöger, S. Feuchtenbeiner, C. Grebing, **P. Micke**, N. Scharnhorst, I. D. Leroux, J. R. Crespo López-Urrutia, and P. O. Schmidt (2016). “A tunable low-drift laser stabilized to an atomic reference.” *Applied Physics B* 122, 236. DOI: 10.1007/s00340-016-6511-z

K. Schäler, M. Roos, **P. Micke**, Y. Golitsyn, A. Seidlitz, T. Thurn-Albrecht, H. Schneider, G. Hempel, and K. Saalwächter (2015). “Basic principles of static proton low-resolution spin diffusion NMR in nanophase-separated materials with mobility contrast.” *Solid State Nuclear Magnetic Resonance* 72, 50–63. DOI: 10.1016/j.ssnmr.2015.09.001

M. Roos, **P. Micke**, K. Saalwächter, and G. Hempel (2015). “Moderate MAS enhances local ^{1}H spin exchange and spin diffusion.” *Journal of Magnetic Resonance* 260, 28–37. DOI: 10.1016/j.jmr.2015.08.016

L. Schmöger, O. O. Versolato, M. Schwarz, M. Kohnen, A. Windberger, B. Piest, S. Feuchtenbeiner, J. Pedregosa-Gutierrez, T. Leopold, **P. Micke**, A. K. Hansen, T. M. Baumann, M. Drewsen, J. Ullrich, P. O. Schmidt, and J. R. Crespo López-Urrutia (2015). “Coulomb crystallization of highly charged ions.” *Science* 347, 1233–1236. DOI: 10.1126/science.aaa2960

M. Roos, **P. Micke**, and G. Hempel (2012). “Monitoring nuclear spin-flip processes and measuring spin-diffusion constants via hole burning into the magnetization.” *Chemical Physics Letters* 536, 147–154. DOI: 10.1016/j.cplett.2012.03.074

Herausgeber:
Physikalisch-Technische Bundesanstalt
ISNI: 0000 0001 2186 1887

Presse und Öffentlichkeitsarbeit

Bundesallee 100
38116 Braunschweig

Telefon: (05 31) 592-93 21
Telefax: (05 31) 592-92 92
www.ptb.de

Vertrieb:
Fachverlag NW in der
Carl Schünemann Verlag GmbH

Zweite Schlachtpforte 7
28195 Bremen

Telefon: (04 21) 369 03-0
Telefax: (04 21) 369 03-63
www.schuenemann-verlag.de